

**THE BEHAVIOUR OF COMPOSITE
CONCRETE ELEMENTS WITH
UNREINFORCED MULTIPLANAR
INTERFACE**

**DOCTORAL DISSERTATION IN THE DISCIPLINE
CIVIL ENGINEERING, GEODESY
AND TRANSPORT**

Jakub ZAJĄC

**PROMOTOR
Professor Phd, CEng Łukasz DROBIEC**

GLIWICE 2024

CONTENTS

1. INTRODUCTION	9
2. MOTIVATION AND ASSUMPTIONS OF THE DISSERTATION.....	12
2.1. Motivation	12
2.2. Research problem and objectives	12
2.3. Scope	13
3. EVALUATION OF THE STATE OF KNOWLEDGE	15
3.1. Principles of interface mechanics	15
3.2. Shear transfer mechanism.....	18
3.2.1. Coulomb-Mohr theory and modification	22
3.2.2. Shear-friction theory development	23
3.3. Characteristic of the interface.....	25
3.3.1. Effect of roughness on interface.....	25
3.3.2. Influence of concrete strength and time of erection.....	30
3.3.3. Effect of shrinkage and stiffness	38
3.4. Standard rules for the calculation of composite elements	41
3.4.1. Polish and European standards - PN-B-03264:2002, PN-EN 1992-1-1, PN-EN 15037-1:2011	41
3.4.2. Model Code 2010	48
3.4.3. USA standards - ACI, ASSHTO LRFD.....	49
3.4.4. Standard comparison	51
3.5. Test specimens for determining interface parameters	53
3.5.1. Test specimens for interfaces in tension.....	54
3.5.2. Test specimens for interfaces in shear.....	55
3.5.3. Test specimens for interfaces in shear and compression or tension.....	56
3.5.4. Alternative methods of determining interface parameters	58
3.6. Studies and examples of composite elements	59
3.6.1. Studies of composite elements with single plain interface.....	60
3.6.2. Studies of elements with multiplanar interface	65
3.6.3. Examples of new and current precast slabs.....	77

3.7. Modelling of composite elements	79
3.7.1. Approaches to modeling composite elements	80
3.7.2. Modelling of composite elements - examples	84
3.8. Conclusions of the literature review	88
4. OBJECTIVES AND STATEMENTS OF THE THESIS	90
4.1. Objectives of the dissertation	90
4.2. Statement of the thesis	91
5. RESEARCH PROGRAM	92
5.1. Research campaign	92
5.1.1. Initial tests.....	93
5.1.2. Direct shear tests.....	96
5.1.3. Three- and four-point bending test	99
5.2. Measuring methods.....	105
5.2.1. LVDT and LDS sensors	105
5.2.2. DIC	106
6. RESULTS OF EXPERIMENTAL STUDIES	112
6.1. Material test	112
6.1.1. Basic material properties	112
6.1.2. Concrete tensile strength	114
6.1.3. Interface roughness.....	117
6.2. Initial tests.....	120
6.3. Direct shear tests.....	127
6.4. Four-point bending tests	140
6.4.1. 4PBT results for group I.....	142
6.4.2. 4PBT results for group II.....	147
6.4.3. 4PBT results for group III	151
6.4.4. Conclusions of 4PBT.....	154
6.5. Three-point bending tests	155
6.5.1. 3PBT results of group I	159
6.5.2. 3PBT results for group II.....	162
6.5.3. 3PBT results for group III	167
6.5.4. Conclusions of 3PBT.....	170
7. NUMERICAL ANALYSIS	172
7.1. Approach	172
7.2. Numerical model materials.....	173
7.2.1. Material models	173

7.2.2. Material parameters assumed from experimental studies	178
7.2.3. Material parameters of numerical models	180
7.3. Direct shear test modelling	181
7.3.1. Correlation of interface parameters	183
7.3.2. Force-slip characteristic.....	188
7.3.3. Stress at the interface.....	193
7.3.4. Failure mechanism.....	197
7.3.5. Influence of force eccentricity.....	199
7.3.6. Conclusions from FEM models of direct shear test	200
7.4. Numerical models of selected 4PBT beams	201
7.5. Results of the 4PBT FEM models	205
7.5.1. Force-displacement characteristics.....	205
7.5.2. Stresses and displacements at the interface	213
7.5.3. Failure mechanism.....	218
7.5.4. Analysis of supplementary models of type Z1_C	222
7.5.5. Partial conclusions from the modelling of elements in the ZX.1 series	225
7.6. Simplified 4PBT beam models.....	226
7.6.1. Results of Group I models	228
7.6.2. Results of Group II models.....	231
7.6.3. Results of Group III models	233
7.6.4. Results of the Group IV models	235
7.7. FEM modelling conclusions.....	237
8. ANALYSIS AND CONCLUSIONS	240
8.1. Analysis of the effectiveness of the interface surfaces.....	240
8.2. Comparative analysis of EN series standards.....	246
8.3. Analysis of interface stiffness	251
8.4. Conclusions and discussion on the research program	255
9. DESIGN RECOMMENDATIONS	260
9.1. Standard modification proposal – PN-EN 1992-1-1:2024	260
9.2. General design recommendations.....	265
10. FINAL CONCLUSION AND FUTHER RESEARCH AREA.....	267
BIBLIOGRAPHY	273

LIST OF BASIC SYMBOLS

Capital Latin letters

A_i	– cross-sectional area
A_{10}	– ductility at failure of rebars,
A_{gt}	– overall ductility of rebars,
A_s	– area of distributed sand,
E	– modulus of elasticity,
F_{cr}	– cracking force,
F_{max}	– maximum force,
F_{res}	– residual force,
G_f	– fracture energy
I	– moment of inertia,
K_{NN}	– normal stiffness of element,
K_{TT}	– tangential stiffness of element,
K_{init}	– initial flexural stiffness,
R_e	– yield strength of rebars,
R_{eH}	– mean upper elastic limit of rebars,
R_m	– tensile strength of rebars,
R_t	– roughness of surface (defined as in Model Code 2010),
S_{max}	– slip value at maximum force,
$V_{R,i,cr}$	– interface shear cracking force,
$V_{R,c}$	– diagonal cracking force,
V_{Rd}	– design shear force,
V_s	– volume of used sand

Small Latin letters

b_i	– width of the interface
c_i	– cohesion surface factor,

f	– deflection of the beam,
f_c	– compressive strength of concrete,
f_{cm}	– mean compressive strength of concrete,
f_{ctm}	– mean tensile strength of concrete,
r_{bsl}	– beam support length reduction factor
s	– displacement of the upper base relative to the lower base (translation),
s_{err}	– slip determination error,
s_{slip}	– slip in the interface (based on DIC measurement),
w	– interface opening (crack width),
w_{err}	– interface opening error,
w_0	– distance between the centres of mass of the layers,
z	– lever arm of composite section

Capital Greek letters

β	– ratio of the longitudinal force in the new concrete area and the total longitudinal force either in the compression or tension zone
β_i	– angle between lower and upper base,
ϕ	– internal friction angle

Small Greek letters

α_i	– angle between base and diagonal,
μ_i	– friction surface factor
ν	– strength reduction factor
σ_n	– normal stresses
$\tau_{R,cr}$	– shear cracking stresses,
τ_{Rd}	– design shear stresses,

1. INTRODUCTION

In the era of increasing ecological awareness and dynamic changes in the global economy, concrete structures face numerous challenges that require thorough re-evaluation and innovation. Concrete, the world's most produced synthetic material, plays a crucial role in modern infrastructure. Its omnipresence in construction, from residential buildings to critical infrastructure, makes it the foundation of contemporary civilisation [144] and the subject of intensive research.

Ambitious legislative solutions are setting directions and leading trends. The European Union's "Fit for 55" legislative package, part of the European Green Deal, was adopted on 14 July 2021. It mandates a reduction in net emissions by at least 55% by 2030 (relative to 1990 levels) and aims for climate neutrality by 2050. Achieving these goals requires a significant reduction in construction emissions. The Commission has proposed a new EU-wide emissions trading system, effective from 2026, will impose charges on emissions from the construction sector, particularly affecting concrete production.

The COVID-19 pandemic has greatly influenced recent developments in society and is a defining factor throughout the writing of this monograph. The aftermath of the pandemic and subsequent economic recovery have further accelerated this shift. The Multiannual Financial Framework, along with the Next Generation EU, leads the recovery package aligned with the objectives of "Fit for 55," addressing the socio-economic impacts of the pandemic. Over the next six years, 30% of the total expenditure from these funds will be dedicated to climate-related projects, totalling an impressive 2018 billion Euros.

The construction market is continuously evolving, but the pace of these changes varies across different segments. Innovative research on new materials and solutions often does not translate into practical applications in the market. In the context of significant environmentally-driven changes, the Polish market for floor systems still primarily focuses on cost, negatively affecting the quality of the products offered [91]. The necessity for change will be driven not so much by customer requirements but by ongoing price competition linked to the impact of CO₂ emissions on the product. Despite the challenges, this market dynamic could potentially lead to a positive shift, encouraging the adoption of more advanced material technologies and driving the optimisation of the design and

geometry of manufactured components [144]. The way of changes could ultimately lead to a more sustainable and innovation-driven industry.

In that context, market research conducted in Poland on the participants in the floor systems market [86,92] offers valuable insights. That research may serve as a guide to understanding the evolving dynamics influenced by legislative changes, market forces and end-users of floor systems. The findings suggest that while cost is an important consideration, it is not the only factor guiding the selection of a floor system. Often, investors prioritise the cost of precast components, overlooking the holistic view that includes labour costs. The study also highlights a lack of emphasis on adopting new technologies in decision-making processes. Additionally, the time taken to erect a floor system is a significant factor but is not thoroughly integrated into the overall cost evaluation. Surprisingly, ecological and health considerations have a minimal role in influencing the choice of floor systems in Poland. This reveals a potential area for future development and the need for market strategies and consumer education.

Studies have shown that the popularity of floor systems in Poland has changed over the past five years due to economic changes and reduced labour availability. Monolithic floors and beam-and-block systems like Teriva are the most commonly used. Other precast systems like hollow core (HC) slabs, prestressed beam-and-block, or panel slabs are less popular. However, there has been significant change. In 2015, prestressed floors (hollow core slabs, prestressed ribbed slabs, and beams) were chosen as the first choice of floor systems by 8% [92]. In 2019-2020, it rose to 22% in the category of 'very often,' with half-precast concrete slab systems accounting for 8% [86]. An analysis of the half-precast concrete slab system (HPCSS) shows a construction productivity rate 1.7 times higher than traditional slab systems. Although, the cost per productivity unit of HPCSS exceeds that of the traditional system [16]. These results align with the global trend of utilising the potential of precast elements [119], which is crucial for speeding up and simplifying the construction process and improving the environmental efficiency of buildings.

Considering the scale of challenges, ongoing research into developing a new slab system plays an essential role. Notably, successfully implementing innovations relies on a comprehensive understanding of structural behaviour. To achieve imposed global trends, studies explore and unlock new potential in known structures, enabling adaptation based on innovative materials, as well as the development of entirely new floor solutions.

The transfer of research findings into standards significantly impacts the floor system market. This can be observed in the manufacturing differences between the United States, Canada and Europe (Fig. 1.1). Notably, there are significant differences in the design of composite structures without reinforcement. Ongoing research must be paired with leading

to precise standards and guidelines. Research into new and current design will enable the potential of composite elements of many possible shapes (Fig. 1.2), which are in many cases limited by the inadequate load-bearing capacity of the interface according to current standards.

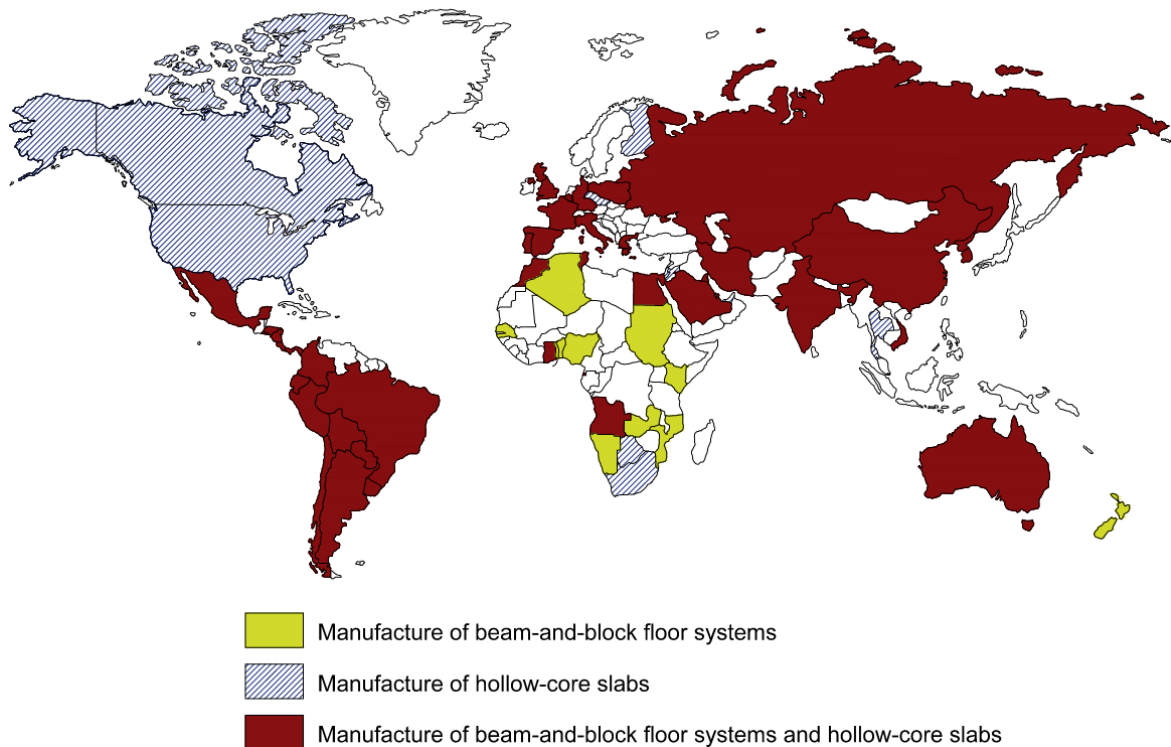


Fig. 1.1. World map with the countries that manufacture precast slabs system [119]

Rys. 1.1. Mapa świata przedstawiająca kraje produkujące prefabrykowane systemy stropowe [119]

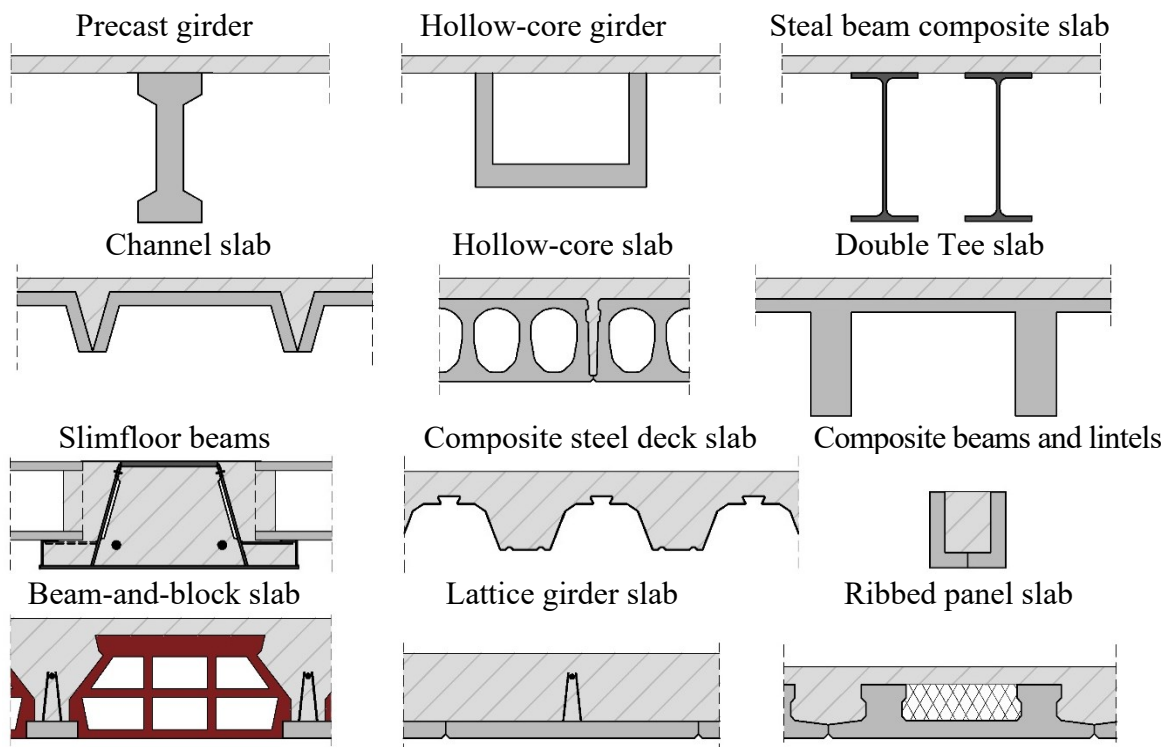


Fig. 1.2. Different types of typical composite concrete beams and slabs

Rys. 1.2. Różne rodzaje przekroji typowych belek i płyt zespolonych

2. MOTIVATION AND ASSUMPTIONS OF THE DISSERTATION

2.1. Motivation

Following the highlighted trends and challenges, the Department of Building Structures of the Silesian University of Technology initiated a research program in collaboration with an industrial partner to evaluate various half-precast concrete slabs [38,40,86,153,157–159]. The tests focused on determining one-way elements' flexural and shear resistance and studying their behaviour under four-edge supported conditions [38,158,159].

Within the scope of the research, the major limitation according to current code requirements, was its design shear interface resistance. While interface shear resistance is usually not the determining factor for the overall resistance of a uniformly loaded slab, it becomes crucial when significant point forces are present. In preliminary studies, none of the test elements failed due to interface delamination [39]. Therefore, that study serves as a starting point towards a more comprehensive analysis of the behaviour of composite elements with unreinforced multiplanar interface presented in this thesis.

2.2. Research problem and objectives

Defining the research problem, it is important to be aware that standards tend to simplify the problem and occasionally distort it as well. Nonetheless, codes also serve as a starting point for analysing the issue. Composite structures are generally designed as quasi-monolithic when the interface resistance conditions are fulfilled. This requirement is one of the ultimate limit states related to shear. Despite the seemingly straightforward procedure for determining the load-bearing capacity of an interface included in PN-EN 1992-1-1:2008 [N15], it provokes a number of questions. These doubts relate to the determination of interface stresses and surface parameters.

Regarding the construction types analysed, i.e. precast slabs, it is also necessary to consider other specific standards such as PN-EN 13747 [N12] and PN-EN 15037-1 [N13]. The second mentioned standard provides various surface parameters based on

the element's production method. These parameters differ significantly from those outlined in PN-EN 1992-1-1:2008, leading to significant discrepancies within a single set of standards. Analysing only the current calculation procedures, several issues and questions can be raised which provide motivation for the research and shape the context and scope of the literature review:

- inconsistent standard recommendations for the parameters of the interface,
- lack of comprehensive consideration of the shear distribution on the interface planes (Eurocode 2),
- impact of interface stiffness and local cracking on the redistribution of internal forces in multiplanar interface,
- effect of different contributions of stresses caused by the external normal forces in dependence on the interface position and plane (vertical or horizontal),
- unclear recommendations for the design of the interface involving long-term effects and shrinkage.

Considering the above aspects, the primary research problem is the behaviour of composite concrete elements with unreinforced multiplanar interface. Following a literature review, sub-objectives and thesis have been determined in the further part of the dissertation (section 4).

2.3. Scope

The scope of the study encloses experimental and analytical research undertaken to verify the scientific problem and goals of the dissertation:

- state of the art review regarding composite elements with concrete-concrete interface,
- own experimental program,
- Finite Element Method analysis,
- proposal for modification and extensions of standards,
- discussion and conclusions.

The dissertation has been divided into chapters focused to particular issues. Chapter 3 provides a comprehensive review of the factors determining interface resistance, standard regulations concerning concrete-concrete interfaces, test procedures, selected tests of composite elements and numerical analysis ending with conclusions. The chapter 4 contains statement of the thesis and outlines the specific intermediate objectives of the dissertation. Chapter 5 establishes the main assumptions of the research campaign. The construction of the test stands, the measurement method, and the design of the test elements are given. Chapter 6 examines the results of three types of tests. Chapter 7 features numerical analyses of composite elements. Chapter 8 analyses the results in the context of the current standards outlined in the literature review and discusses the research program. Chapter 9 proposes modifications and extensions to the existing standards. Chapter 10 provides the final conclusion and determines the potential future scope of work.

Limitations to the scope of work

The scope of analysis excludes slab elements. The study of slab elements would be the next stage of research after establishing the basic dependencies and effects on beam elements. Experimental studies and analyses included a description of the effect of shear, but without an extensive analysis of the maximum shear force of prestressed composite elements with reinforced concrete topping. The coverage was limited to the area relevant to the interface analysis. Addressing the research problems of the dissertation will set the direction for further studies.

3. EVALUATION OF THE STATE OF KNOWLEDGE

3.1. Principles of interface mechanics

The first chapter of the literature review aims to explain the fundamental concepts and phenomena of composite elements. The evaluation of the bond between the elements discussed in this study should be regarded as an assessment of the adhesion phenomenon between two layers of material. Each consists of aggregate and a liquid cement matrix that undergoes hardening over time. At the surface where elements composed of two materials with different parameters meet (even if only due to different hardening times), a thin layer or boundary is formed. This boundary, often referred to as the "interface zone" or "overlay transition zone", is the region where the bond parameters do not align with those of the older or newer material. In this monograph, the boundary between two concrete surfaces, specifically the bonding area, will be referred to as the **"interface"**.

Based on the literature, two different approaches could be described to examine the interphase zone between the overlay and concrete substrate. The first approach, which is more commonly used, involves dividing it into four levels [124,125]. This division has been adopted to describe the phenomena in this monograph (Fig. 3.1). The second approach suggests three levels, one level lower than the division described in [44,78] (the macro level corresponds to the meso level of the first approach, and so on consecutively). The classification into four levels is described below:

- Macro level - the first observation level, the entire element and its interface along its length are evaluated. The interphase zone between layers is primarily assessed based on destructive or nondestructive tests.
- Meso level - the second observation level, the interphase zone, is assessed by examining the surface morphology of the substrate layer.
- Micro level – the assessment level of the density, air pore structure, and hardness of the concrete.
- Nano level - the level of investigating the effects of valence intermolecular forces. The interface is built mainly by prickly calcium silicate hydrates (C–S–H) with ettringite (Aft) and Ca(OH)_2 orientational crystals [78].

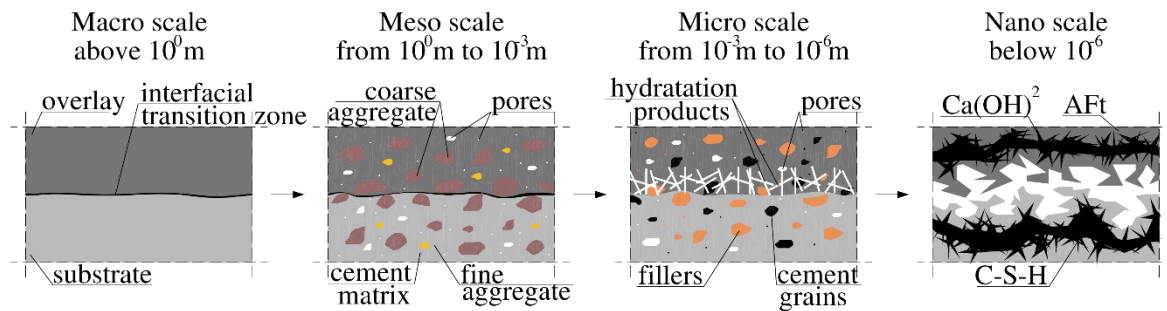


Fig. 3.1. Division of the examination levels of interfaces

Rys. 3.1. Podział na poziomy oceny zespolenia

Adhesion is the term used to describe the physicochemical phenomena that occur at the interface of two materials, resulting in their mutual bonding. Adhesion is formed through three main mechanisms (Fig. 3.3) [125]. The first mechanism is mechanical interlocking, which can be further divided into locking by friction and locking by dovetailing (Fig. 3.2). This concept refers to the micro-level behaviour, where sliding friction at minimal shear slip values and irreversible deformation of the matrix are the essential mechanisms [146].

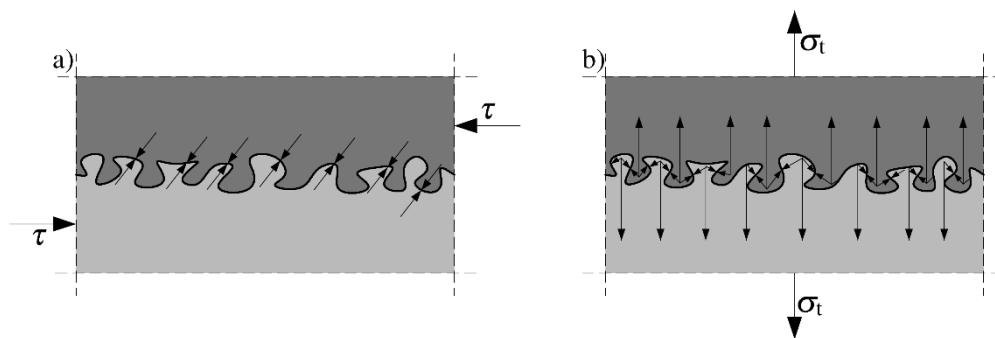


Fig. 3.2. Interlocking mechanism of interface caused by mechanical adhesion: a) shear forces, b) tensile forces

Rys. 3.2. Mechanizm blokowania w styku wynikający z adhezji mechanicznej: a) ścinanie, b) rozciąganie

The second is physical bonding, achieved through Van der Waals and hydrogen bonds. The third mechanism, chemical bonding, is as significant as mechanical interlocking in determining the adhesion force. This mechanism is associated with ionic and atomic bonding. The three categories of mechanisms are commonly referred to as mechanical adhesion (or cohesion between particles as mentioned by some researcher [135]) and specific adhesion, which include both physical and chemical bonding. [43].

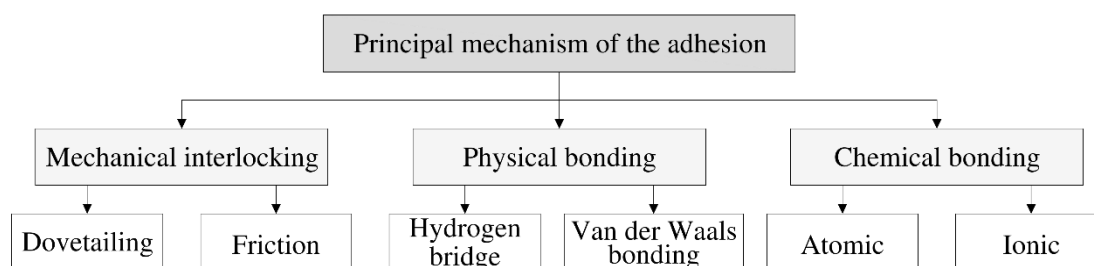


Fig. 3.3. Principal forces constituting adhesion.

Rys. 3.3. Główne oddziaływania składające się na adhezję.

The above description provides a basic overview of the adhesion mechanisms and their division into levels of examination. It allows for the identification of two distinct mechanisms of interface failure (Fig. 3.4) based on the location of the main crack paths [19]. First, the adhesive mechanism is related to the chemical forces that act at the nano-scale and the mechanical interlocking component of adhesion at the micro level. These two factors interact in the range of small displacements (<0.05 mm) [117,134]. Delamination occurs as a result of interface failure, specifically at the contact between layers (adhesion damage). Second, the cohesive mechanism is related to the overlay transition zone (OTZ). At the micro-level, interface failure occurs in a highly porous material zone through the overlay and substrate material [9]. Cohesive failure is commonly regarded as indicative of a “strong bond”, indicating the superior strength of the interface compared to the concrete substrate or overlay. Furthermore, the cohesive mechanism could be a consequence of the adhesion mechanism failure. As a result of debonding, shear stresses are transferred through the interlocking of layers (cohesive mechanism). If the interface is subjected to compression, the development of the cohesive mechanism in transferring the shear stresses is described by the shear-friction mechanism. The following paragraphs will describe shear friction load transfer mechanisms in detail.

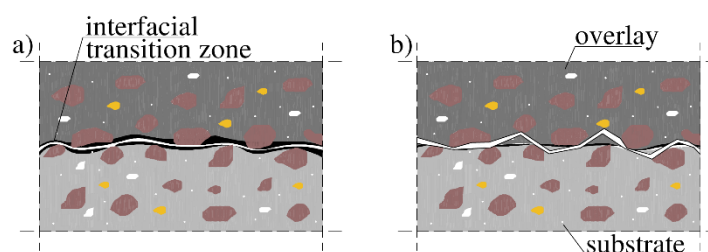


Fig. 3.4. Interface failure mode: a) adhesion mechanism, b) cohesion mechanism

Rys. 3.4. Modele zniszczenia zespolenia: a) mechanizm adhezyjny, b) mechanizm kohezyjny

Based on both the meso and macro structure as well as failure mechanisms, it is possible to identify the factors that affect the condition of the interface. The main factors include the concrete composition and characteristics of the interfacial transition zone (ITZ). The behaviour of concrete-to-concrete interfaces is highly influenced by various parameters, including material strength and stiffness, substrate moisture, the presence of microcracking at the substrate, and the shrinkage of the added concrete. Typically, strengthening the interface involves increasing interfacial roughness, improving the overlay's strength, or using an interfacial bonding agent, particularly for repair purposes. The following sections of the thesis comprehensively analyse specific design parameters and assess their impact on the structural integrity and interface performance of concrete-concrete composites.

3.2. Shear transfer mechanism

In composite structures, three basic factors contribute to the interface strength (Fig. 3.5): the natural adhesion with mechanical interlocking (“interlocking effect” or “aggregate interlocking”), friction between concrete layers and the use of reinforcements [118]. The presence of reinforcement leads to two additional effects. First, friction due to clamping effect and the second the “dowel action” that are a result of resistance to bending of reinforcement.

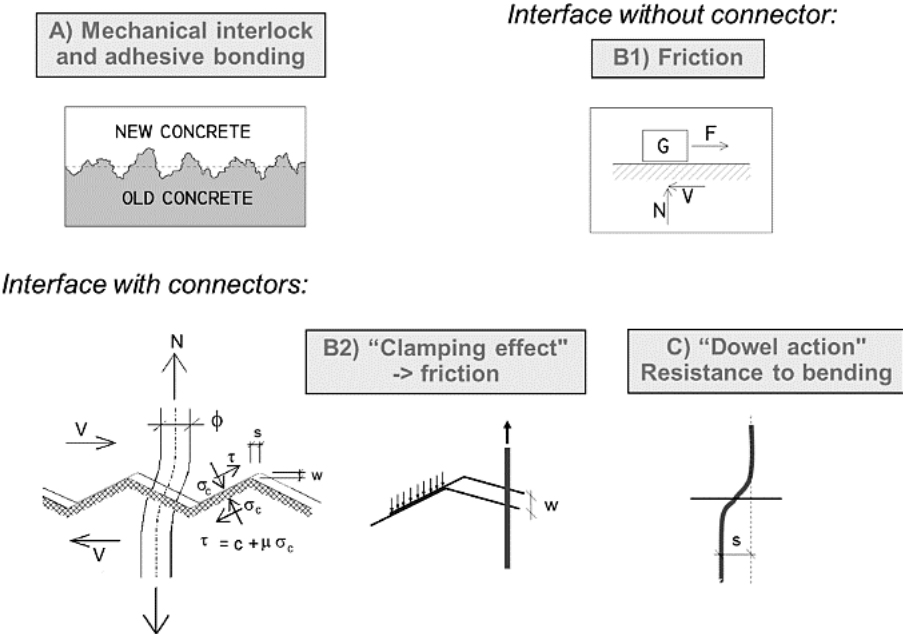


Fig. 3.5. Interface shear resistance mechanism [118]

Rys. 3.5. Mechanizm przenoszenia ścinania w styku [118]

The three principal factors that contribute to the load-bearing capacity of the interface can be attributed to the three-component mechanism [135,166] (Fig. 3.7). The first factor, shear transfer, is associated with adhesive bonding and mechanical interlocking at the micro scale. This mechanism is effective at very small shear slip values, typically below 0.05 mm [19], and is expected to degrade as shear slip increases along the interface. The development of slip, more accurately referred to as crack progression, involves both displacement along the interface and crack opening (Fig. 3.6). The relationships between slip and opening are determined experimentally, and their characteristics depend on the roughness of the interface [12].

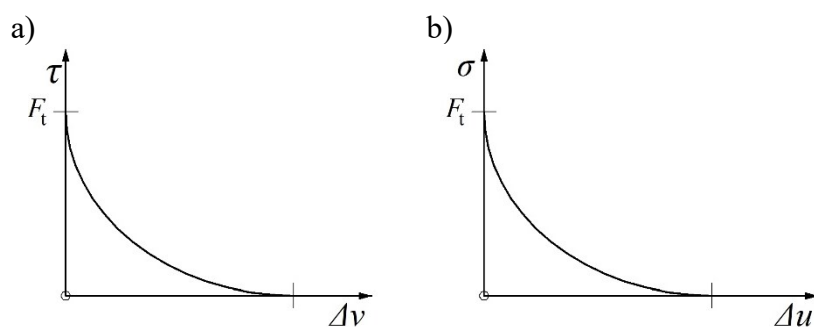


Fig. 3.6. Residual stresses at the interface: a) tangential in relation to the displacement at the interface, b) normal in relation to the opening of the interface [12]

Rys. 3.6. Naprężenia resztkowe w styku: a) styczne w zależności od przemieszczenia w styku, b) normalne w zależności od rozwarcia styku [12]

In second, after degradation of the adhesion, debonding occurs at interface and the shear forces are transferred by friction. If the interface is subjected to compression, the shear transfer are described as shear-friction (friction with normal forces). Shear friction mainly depends upon the interfacial roughness (meso scale), and the magnitude of normal stress at the interface. The first two stages could be described by Coulomb-Mohr theory. In most issues the phenomenon of shear-friction is related to the presence of reinforcement and the pressure force developed from the resistance of the reinforcement to the opening of the interface. Therefore, the development of the shear-friction theory is related to the reinforcement of the interface.

The third occur in interface with additional reinforcement. The steel reinforcement is designed to become the dominant load transfer mechanisms at higher slip value. In this case, the relative shear slip between concrete layers along the interface results in lateral displacement of the upper and lower ends of crossing steel reinforcement bars, inducing bending stresses that are superimposed by the axial tensile forces created in the reinforcement owing to the joint opening. Due to slippage, the shear reinforcement will

be subjected to shear, usually named as dowel action. The magnitude of resisting stresses relies on the type, percentage, flexural resistance of the crossing reinforcement and crushing resistance of the surrounding concrete [45]. The interaction between three components of load transfer mechanism is described by the shear-friction theory.

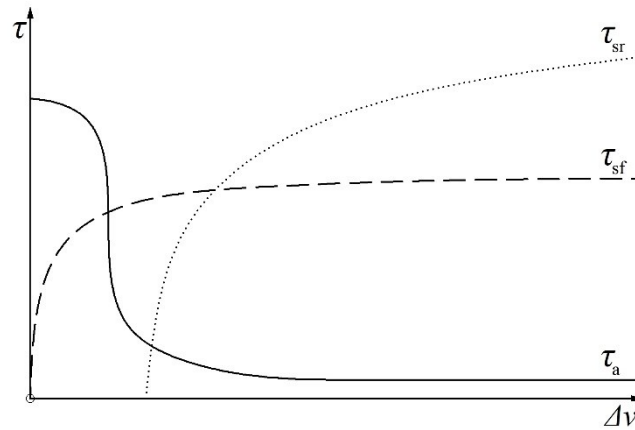


Fig. 3.7. Load transfer mechanisms components [19]: τ_a – adhesion, τ_{sf} – shear-friction, τ_{sr} – reinforcement

Rys. 3.7. Mechanizm przenoszenia ścinania w styku [19]: τ_a – adhezja, τ_{sf} – shear-friction, τ_{sr} – zbrojenie

The contribution of each mechanism to shear resistance at concrete-to-concrete interfaces is significantly affected by the roughness category, the quality of the bond, and the amount of reinforcement (or other steel connectors) crossing the interface (Fig. 3.8). These factors also determine the potential displacements along the interface at the ultimate limit state. In the absence of interface reinforcement, joints typically exhibit relatively brittle behaviour, with failure occurring due to loss of adhesion at slip values of less than 0.05 mm. In contrast, reinforced joints demonstrate more ductile behaviour; depending on the quantity of reinforcement and the roughness of the interface, failure generally occurs at larger slip values ranging from 0.5 mm to approximately 1.5 mm. The roughness of the interface also affects the maximum shear force seen in the load-displacement curve, primarily because of the significant roles of friction and aggregate interlock, which diminish rapidly as displacements increase. A higher amount of reinforcement (at least 0.05%) results in “non-rigid” bond-slip behavior, where friction forces and dowel action become activated due to the increased slip observed at the ultimate load. Conversely, smooth joints with reinforcement and no additional external clamping tend to exhibit dowel action, revealing the kinking effect of the reinforcement at larger displacements.

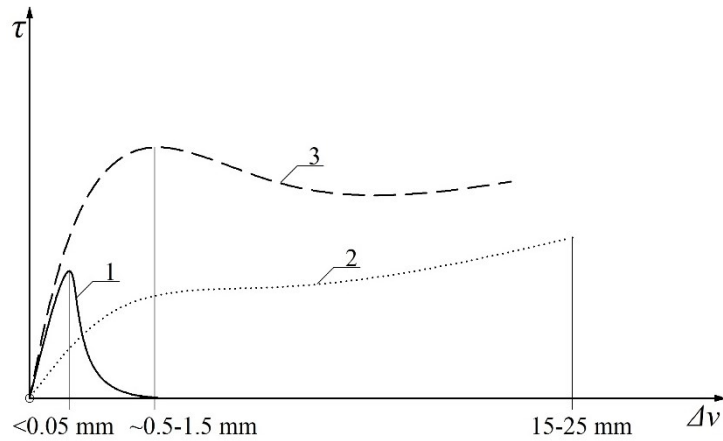


Fig. 3.8. Typical load-displacement characteristic: 1- no reinforcement slightly roughened, 2- reinforced smooth joint, reinforced joint very rough [118]

Rys. 3.8. Typowa charakterystyka siła-przemieszczenie: 1- styk niezbrojony szorstki, 2- styk zbrojony gładki, 3- styk zbrojony szorstki [118]

Ensuring adequate resistance and stiffness at the interface significantly influences the flexural performance of composite elements. When fully composite, the element exhibits behaviour characteristic of a monolithic element. However, as stiffness decrease due to increased slip at the interface, the stress distribution within the individual components undergoes changes. Following the failure of the interface, the components of the composite element function as independent entities, remaining interconnected only through friction (Fig. 3.9).

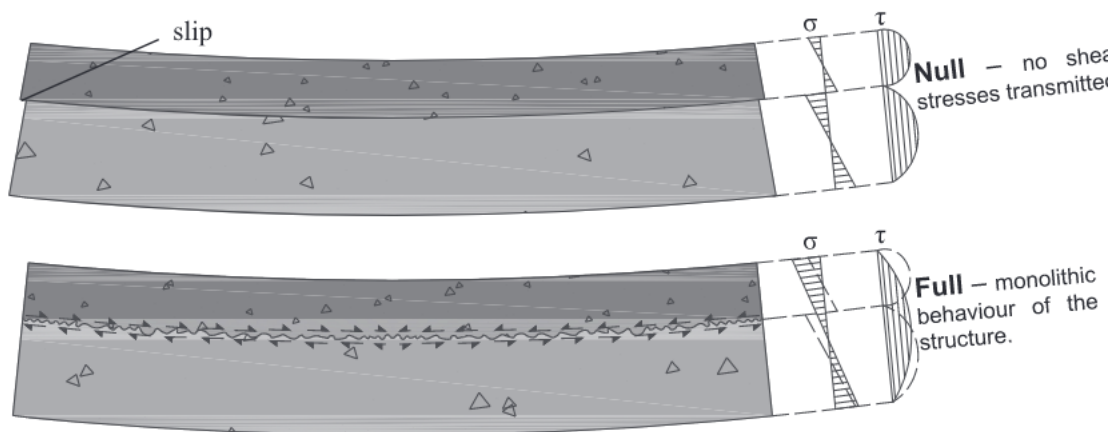


Fig. 3.9. Principles of composite elements performance and stress distribution in the cross-section [45]

Rys. 3.9. Podstawowe zasady zachowania się elementów zespolonych i rozdział naprężeń w przekroju [45]

3.2.1. Coulomb-Mohr theory and modification

The Mohr-Coulomb theory describes the permissible stresses resulting from adhesion and friction. Theoretically, these values have no upper limit. The resulting friction depends on the coefficient of friction related to the internal friction angle.

$$\tau = c + \mu\sigma_n \quad (3.1)$$

in which,

τ – shear stresses

c – adhesion strength

μ – coefficient of friction (related to internal friction angle – ϕ)

σ_n – normal stresses on the interface

The Mohr-Coulomb theory has certain limitations and is therefore subject to modification [44]. In numerical modeling, as detailed in Section 7.2, some overlap occurs. The stresses represented by Equation 3.1 are illustrated by line (A) in Figure 3.10, which delineates the ideal envelope of the interface. The actual tensile strength is consistently lower than the theoretical value, as shown by curve (B), which represents a modified Mohr–Coulomb envelope. Upon reaching the tensile strength of the interface, the primary envelope transitions to an almost "null" tensile strength (C). An additional increase in external forces leads to the degradation of the interface and the cohesion degradation associated with the Coulomb sliding law (D). This stage is characterized by shear cracking, which manifests as an inclined crack path encircling a series of struts transmitting diagonal compression. The final stage of damage (E) occurs when the friction angle of the interface diminishes, causing the interface zone to behave like a frictional soil enclosed by the adjacent unaffected concrete.

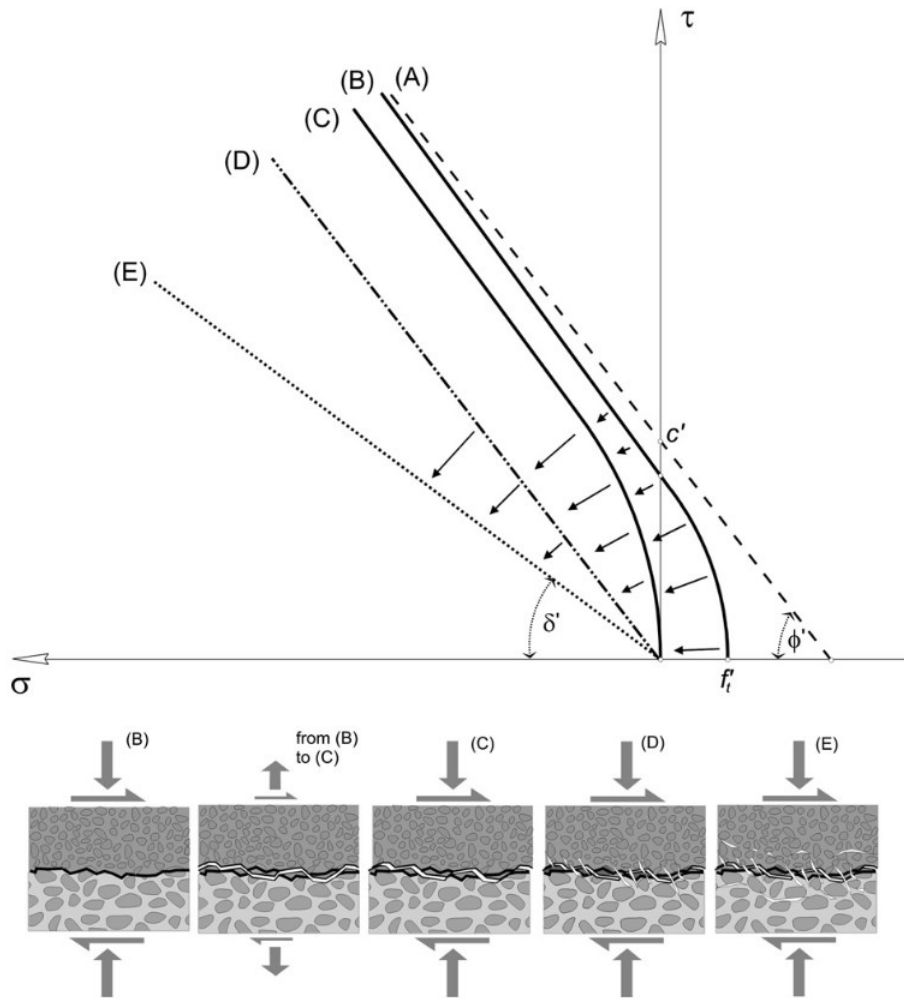


Fig. 3.10. Evolution of interfacial bond-failure based on Carol's concepts [44]

Rys. 3.10. Przebieg zniszczenia styku w oparciu o koncepcje Carolla [44]

3.2.2. Shear-friction theory development

The shear-friction theory is used to evaluate the shear strength between concrete components. The design philosophy originally proposed by Birkeland and Birkeland in 1966 [11] included an integrated reinforcement component, while subsequent revisions (Tab 3.1) also accounted for interface adhesion to varying extents. The most comprehensive design expression was introduced by Randl [116]. Shear-friction theory has been adopted by most major standards, including ACI 318–19 [N2], Eurocode 2, and the fib Model Code 2010 [N9]. The “shear-friction theory” can be used to predict the shear strength of various types of concrete-to-concrete interfaces, such as between a precast element and a cast-in-place component, the interface between two segments of an element cast at different times, the interface between an element and a supporting structure, and the interface between two sections of an element formed by a crack [131].

A simple saw-tooth model is typically employed to illustrate the basic principles of this theory (see Fig. 3.11). This model accounts for the influence of reinforcement positioned across the interface, as well as external forces acting perpendicular to the shear plane. According to this model, shear stress induces not only a parallel displacement but also the opening of the joint, resulting in tensile stresses in any reinforcing bars that intersect the interface. These tensile stresses subsequently generate equalizing compressive stresses in the joint, allowing frictional forces to become established.

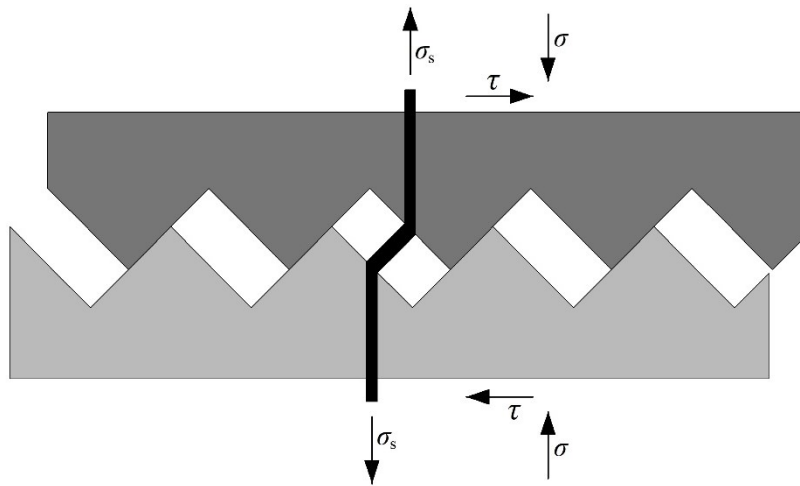


Fig. 3.11. Saw-tooth model [131]

Rys. 3.11. Model „zębów piły” [131]

Table 3.1

Kroki milowe rozwoju teorii shear-friction [131]
 Shear-friction theory development milestones [131]

Researchers	Year	Design expression
Birkeland & Birkeland [11]	1966	$v_u = \mu \rho f_y$
Mattock and Hawkins [104]	1972	$v_u = 1.38 + 0.8(\sigma_n + \rho f_y)$
Loov [98]	1978	$v_u = k \sqrt{f_c(\sigma_n + \rho f_y)}$
Walraven et al. [145]	1987	$v_u = C_1(\rho f_y)^{c_2}$ $C_1 = 0.822 f_c^{0.406}, C_2 = 0.159 f_c^{0.303}$
Randl [116]	1997	$v_u = c f_c^{1/3} + \mu(\sigma_n + \rho k f_y) + \alpha \rho \sqrt{f_y f_c} \leq \beta v f_c$

Dowel action constitutes the third resisting mechanism and is activated when steel reinforcement is placed across the interface and resists bending. The relative slip between concrete layers along the interface induces bending stresses in the rebars, which are superimposed by the axial tensile forces generated in the reinforcement due to joint opening. The magnitude of the resisting stresses relies on the type, percentage, and flexural resistance of the intersecting reinforcement (Fig. 3.12).

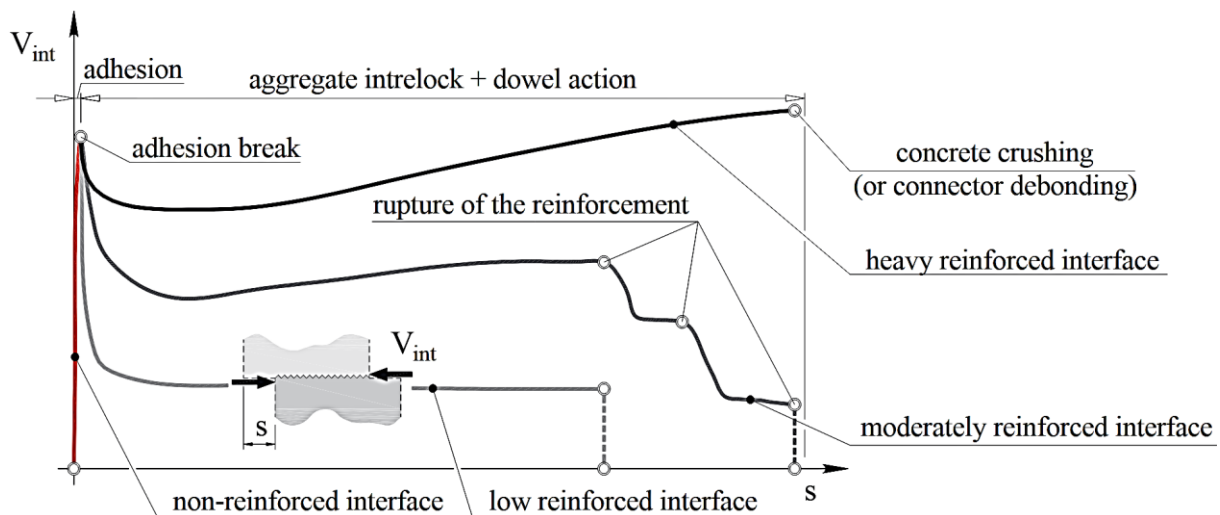


Fig. 3.12. Load-slip characteristic of interfaces with different shear reinforcement [56]

Rys. 3.12. Charakterystyka siła-poślizg styków z różnym zbrojeniem [56]

3.3. Characteristic of the interface

3.3.1. Effect of roughness on interface

Based on empirical observations, the bond quality between layers of concrete cast at different ages is associated with surface roughness [117]. Surface roughness impacts mechanical adhesion by facilitating mechanical interlocking due to irregularities and pores on the surface. Design codes commonly rely on a qualitative assessment of surface roughness through visual inspection [N9]. Surfaces are typically categorised as very smooth, smooth, rough, or very rough [N15] or as intentionally roughened or not intentionally roughened [N16]. These categorisations are often connected to specific finishing treatments of concrete surfaces, with assigned values for friction and cohesion coefficients utilised in design expressions [134]. This approach lacks precision as it is subjective and dependent on the opinions of individual technicians.

To comprehensively characterise surface roughness, a quantitative approach must be adopted, which involves selecting a method for quantifying roughness and defining one or more roughness parameters [134]. These parameters are derived from surface geometrical features, such as the spacing, height, and depth between peaks and valleys. The roughness parameters can be assessed using 2D profiles or 3D surfaces, which can be acquired through roughness quantification techniques. Utilising a quantitative evaluation approach instead of a qualitative approach has the advantage of promoting the standardisation of roughness quantification methods and identifying the most appropriate method for a specific surface. This approach could also explain the difference in concrete-to-concrete interface strength, with the surface prepared using different techniques and occasionally even with the same technique despite similar roughness.

The *fib* Model Code 2010 has already adopted this design philosophy, proposing the correlation between the parameter average roughness (R_a) (Fig. 3.13) and bond strength. This parameter can be obtained from the sand patch test, commonly chosen for its simplicity. It is defined as the average deviation of the profile to its mean line.

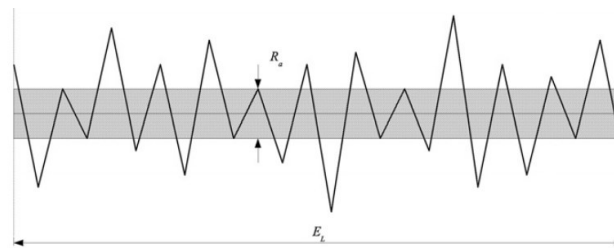


Fig. 3.13. Average roughness interpretation

Rys. 3.13. Interpretacja średniej szorstkości styku

It should be noted that the sand patch test (Fig. 3.14) has some significant drawbacks. This method can only be applied to horizontal surfaces and surfaces with relatively high roughness levels.

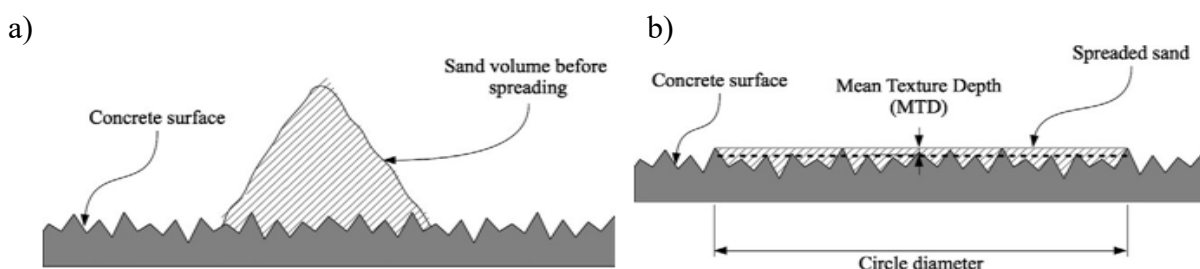


Fig. 3.14. Sand Patch test: a) before spreading, b) after spreading

Rys. 3.14. Pomiar metodą piaskową: a) przed rozproszaniem, b) po rozproszaniu

Nevertheless, the average roughness parameter is not the most suitable option since others demonstrate a stronger correlation coefficient with bond strength. Additionally, this parameter can obtain the same value for concrete surfaces with significantly different textures and, therefore varying bond strengths. More complex assessments have proposed alternative roughness parameters considering the location and spacing between peaks and valleys. Parameters proposed by various authors include Mean Peak Height (R_{pm}), Mean Valley Depth (R_{vm}), Mean Peak-to-Valley Height ($R_z(DIN)$), Ten Points Height ($R_z(ISO)$), Maximum Peak Height (R_p), Maximum Valley Depth (R_v), Maximum Peak-to-Valley Height (R_{max}), and Total Roughness Height (R_y).

In the study of Mohamad et al. [105], an extensive analysis was conducted to investigate the relationship between surface profile parameters (roughness) and shear resistance. Out of the 14 parameters examined, the most accurate were the mean peak height R_{pm} (correlation $R^2 = 0.90-0.92$) and the mean peak-to-valley height R_z (correlation $R^2 = 0.60-0.85$). The correlation for mean roughness (R_a) ranged from $R^2 = 0.15-0.45$. Based on the generally accepted interpretation of correlation coefficients [142], a value of $R^2 < 0.12$ is considered as low or weak correlation. Values between 0.12 and 0.45 are considered moderate correlation, while values between 0.45 and 0.8 are considered strong or high correlation. A correlation coefficient of $R^2 > 0.81$ is considered as very high correlation.

Studies conducted by other researchers suggest alternative roughness measures and their correlation. According to Saldanha et al. [128], the coefficient of correlation (R^2) between the Mean Valley Depth (R_{vm}) and the coefficients of cohesion and friction was 0.92 and 0.94, respectively. It can be concluded that a strong correlation exists between the selected texture parameter, the Mean Valley Depth (R_{vm}), and both coefficients of cohesion and friction. The study by Costa et al. [18] confirmed that increasing roughness of a surface directly impacts shear resistance. The authors proposed equations that describe the adhesion coefficient and friction coefficient in relation to the average profile depth. The cohesion and friction coefficients derived from these equations (3.2) for non-smooth roughness considerably surpass the existing code parameters (Section 3.5).

$$\begin{aligned} c &= 0.86R_{pm}^{0.48} \\ \mu &= 1.16R_{pm}^{0.04} \end{aligned} \tag{3.2}$$

in which,

c – coefficient of cohesion

μ – coefficient of friction

R_{pm} – mean peak depth

The research of Santos [130,133] is an example of using a different parameter (3.3). Based on numerous studies, Santos proposed a function (Fig. 3.15) to determine the parameters, employing the mean valley depth parameter. In line with previous studies by other authors, the obtained adhesion and friction values surpass those specified in the code.

$$c_d = \frac{1.062R_{vm}^{0.145}}{\gamma_{coh}}$$

$$\mu_d = \frac{1.366R_{vm}^{0.041}}{\gamma_{fr}}$$
(3.3)

in which,

c_d – design coefficient of cohesion

μ_d – design coefficient of friction

R_{vm} – mean valley depth

γ_{coh} – partial safety factor for coefficient of cohesion

γ_{fr} – partial safety factor for coefficient of friction

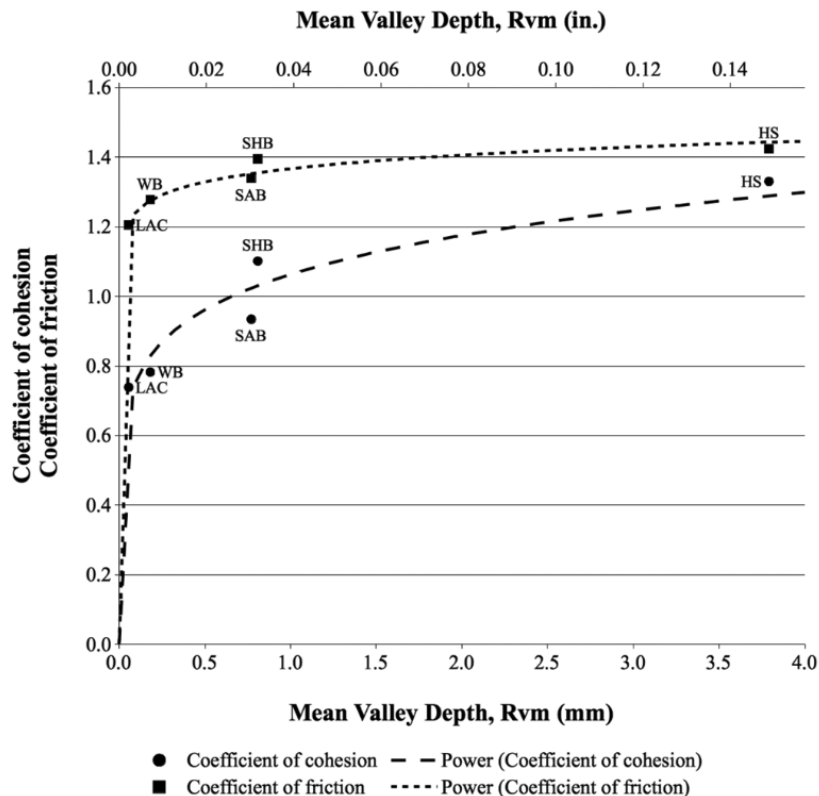


Fig. 3.15. Correlation between mean valley depth R_{vm} and coefficients of cohesion and friction [130,133]

Rys. 3.15. Korelacja między średnią głębokością doliny R_{vm} , a współczynnikami kohezji i tarcia [130,133]

Gohnert [54,55] introduced a unique and simplified approach, highlighting that surface roughness significantly impacts shear capacity and serves as a more reliable indicator of strength compared to the compressive strength of the concrete. Gohnert proposed that shear stress should be considered as a function of the R_z height (3.4), disregarding the influence of concrete strength. Research was conducted on 90 push-off elements related to the geometry of beam and block floors. The design approach employed in this study closely resembles the one outlined in PN-EN 15037-1 [N13], which is applied to the design of beam and block slab systems.

$$\tau_i = 0.2090R_z + 0.7719. \quad (3.4)$$

The quality of surface preparation is no less important than roughness. Impurities such as loose particles or air bubbles and water lenses [66] that remain on the substrate surface after concrete placement and inadequate maintenance lead to reduced adhesion strength (Fig. 3.16). The research conducted by Beushausen et al. [10] demonstrates that pre-wetting the substrate surface prior to the application of the overlay does not confer any additional benefits in terms of enhancing bond strength and may, in certain instances, significantly reduce bond strength. Microstructural investigations revealed that pre-saturated substrates lead to an increase in the water-to-cement (w/c) ratio and porosity within the overlay transition zone (OTZ), which was identified as having a thickness of approximately 100 μm . In contrast, overlays applied to dry substrate surfaces exhibited lower porosity and a higher quantity of anhydrous cement.

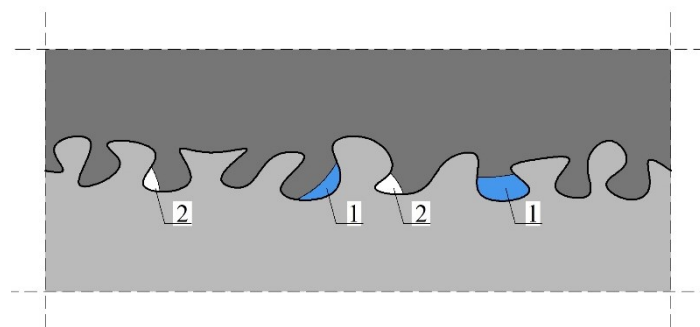


Fig. 3.16. Water lens (1) and air bubble (2) reducing adhesion

Rys. 3.16. Soczewki wody (1) i pęcherzyk powietrza (2) zmniejszające adhezję

Nevertheless, it is crucial to consider the pre-existing substrate and overlay defects, such as micro cracks and specific stress states, which may be introduced during sample preparation. Typically, methods such as chipping, wire-brushing, sand-blasting, shot-blasting, and hydrodemolition are commonly used to prepare the surface of the substrate.

As outlined in a paper from the series "Concrete Surface Engineering" by Garbacz et al. [51,52], an increase in roughness is favourable for high-strength concretes. The opposite tendency has been observed in concretes of lower classes (C20/25), as the treatment causes damage to the near-surface layers of the concrete (microcracks). Similar findings were also presented in the research conducted by Gołdyn and Urban [56,58], which indicated that the ultimate shear stress of interfaces with rough surfaces was 10% or even 43% lower than the shear resistance of interfaces with smooth surfaces. This decrease in shear resistance was found to contribute to local damage in the concrete structure, particularly in relation to the invasive method of surface roughening (milling). These conclusions are consistent with previously described studies conducted by Randl [161], Santos [134] and in the context of repairs by Lourenço [13].

3.3.2. Influence of concrete strength and time of erection

Regarding precast elements, the tensile strength of the weaker concrete (whether it is the precast or overlay concrete) and the roughness are equally important according to code requirements. Additionally, factors such as the execution time of the elements should not be overlooked. For instance, if a prestressed precast element is installed right after it is manufactured, the execution time could be as short as three days. However, in other cases, it may extend for several months. Another factor to consider is the curing process, which affects the concrete's strength development and shrinkage over time.

This chapter provides a detailed description of five studies conducted by various authors that address the factors mentioned above. The research results are often inconclusive and highly dependent on the specific type of interface strength test employed. These studies analyze four key factors to varying degrees: 1) the test scheme, 2) the strength differences between the concretes, 3) the shrinkage differences between the concretes, and 4) the roughness and method of surface preparation. Due to these factors, test results from different authors cannot, in many cases, be directly compared. During the evaluation and description of the studies, particular consideration has been paid to the variation in results obtained by the respective authors. Remarkably, all results are obtained on typical samples in laboratory conditions.

Franczak-Balmas and Halicka

Franczak-Balmas [49] presented the results and analysis of the strength of the interface tested in tension by splitting. The study examined the contribution of both 'old' and 'new' concrete to the adhesion at the unreinforced interface of composite elements.

The specimens were prepared in two stages. First, the "old" concrete was placed in the forms. After curing for 14 days, the "new" concrete was cast. Each series of specimens was labelled with numbers, that the first indicates the class of the 'old' concrete, while the second indicates the 'new' concrete. The test results of the specimens are summarized in Table 3.2. The concrete parameters include the average compressive and tensile strengths and the average tensile contact strength of the composite specimens. Significantly, the coefficient of variation of contact tensile strength ranged from 2.4% to about 9%, and in one series, it reached up to 15%. Excluding only the R20/37 series, the results of the other series fell within the range obtained for each of them.

Table 3.2

Wyniki badań próbek (Franczak-Balmas) [49]
Results of the tests specimen (Franczak-Balmas) [49]

Series	Strength of concrete				Tensile strength of the interface		
	"old" concrete		"new" concrete		$\sigma_{crm,z}$, MPa	$S_{fcrm,z}$, MPa	$\nu_{fcrm,z}$, %
	f_{cm} , MPa	f_{ctm} , MPa	f_{cm} , MPa	f_{ctm} , MPa			
R20/37	25.78	2.14	45.70	2.92	0.74	0.02	2.44%
R37/37	45.26	2.74	45.50	2.75	0.88	0.08	9.21%
R45/15	50.23	3.03	21.56	1.86	0.71	0.06	8.86%
R45/30	50.58	2.79	35.90	2.81	0.82	0.06	7.49%
R45/37	49.70	2.81	46.68	2.90	0.99	0.15	14.64%

The author determined that the bonding efficiency depends on both types of concrete. A coefficient of interface strength, defined as the average of the tensile strengths of the "old" and "new" concrete, was determined:

$$\beta_{cr} = \frac{\sigma_{crm,z}}{\frac{f_{ctm,S} + f_{ctm,N}}{2}} \quad (3.5)$$

in which,

β_{cr} – coefficient of joint effectiveness

$\sigma_{crm,z}$ – average cracking stress of the interface at splitting

$f_{ctm,S}$ – average tensile strength of "old" concrete

$f_{ctm,N}$ – average tensile strength of "new" concrete

The average coefficient of joint effectiveness was found to be approximately 30%, ranging from 29% to 34%. It was observed that when concretes with a slight difference in tensile and compressive strengths were joined, slightly higher values of 32% to 34% were obtained. In the other series of composite specimens, the coefficient was 29%. This indicates that the strength of the interface is not solely dependent on the strength of the weaker concrete.

Prior to the research described above, Franczak-Balmas, co-authoring with Halick, published articles discussing the development of adhesion during concrete hardening [65]. The study focused on testing the tensile contact strength of composite specimens made of concrete of different ages. In the first series, labelled as S28+N3 (or 7, 14, 28), the 'old' concrete, cured for 28 days, was combined with the 'new' concrete, cured for 3, 7, 14, and 28 days. In the second series, labelled as S3 (or 7, 14, 28)+N28, the 'old' concrete, cured for 3, 7, 14, and 28 days, was combined with the 'new' concrete, cured for 28 days. The resistance of the S28+N28 interface increased as the younger of the concretes matured (Fig. 3.17)

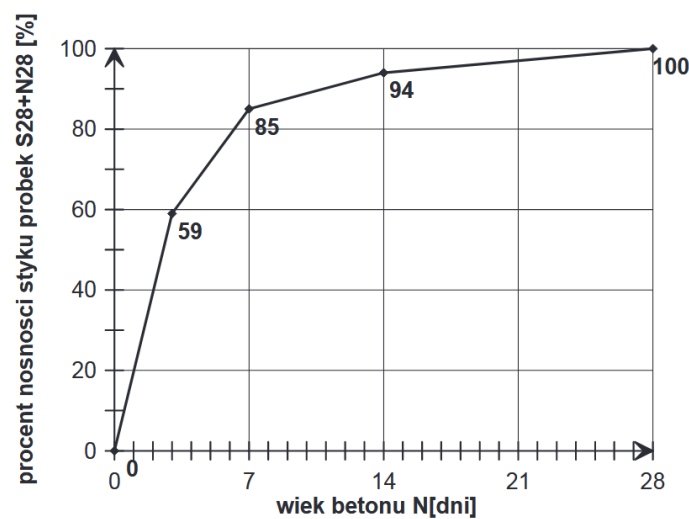


Fig. 3.17. Relative increase of tensile bond strength of specimen S28+N3(or 7, 14) to S28+N28 [65]

Rys. 3.17. Względny przyrost nośności styku na rozciąganie próbek S28+N3(lub 7, 14) do S28+N28 [65]

The results of tests conducted on specimens made of concrete, which were cured for 28 days, along with "new" concrete N, were analyzed on the 3rd, 7th, 14th, and 28th day of concrete curing. These tests reveal that the strength of the interface increases in line with the strength of concrete N. The most rapid increase in interface strength corresponds to the duration of the highest increase in strength of the "new" concrete,

which occurred in the first seven days of its curing. The increase in the coefficient of joint effectiveness also occurs within this phase. The coefficient only exhibits a slight increase during the subsequent curing period of concrete N compared to the initial 7-day increment. The results of the tests on the S3 (or 7, 14)+N28 series of specimens showed that there was no significant increase in the coefficient of joint effectiveness when the S concrete was young at the time of concreting the N concrete (3, 7, or 14 days old). The authors of the research attribute this to a mechanism of specific adhesion. The earlier the "old" concrete, to which "new" concrete is concreted, the more influential this mechanism is. It is particularly important to emphasize and draw attention to the age of the concrete at the time of testing for the first and second series. For the test shown in Table 3.3, the "old" concrete was 31 days old during the test, while the "new" concrete was 3 days old. In contrast, for the second series of tests, the "old" concrete was 31 days old (3 days maturation of concrete one and 28 days of concrete two), and the "new" concrete was 28 days old. Therefore, the first type of test involved concrete that was 3 days old, while the second type of test involved concrete that was 28 days old. It should be noted that the coefficient of variation ranges from 5.12% to 10.08%, representing a smaller variation range compared to the previously described study.

Table 3.3 [65]

Results of the specimen (splitting test)
 Wyniki badan próbek (przez rozłupanie)

Series	Strength of concrete				Tensile strength of the interface		Coefficient of joint effectiveness	Strength gain coefficient
	"old" concrete		"new" concrete		$f_{ctm,z}$ MPa	v_{fc} %		
	f_{cm} MPa	f_{ctm} MPa	f_{cm} MPa	f_{ctm} MPa				
S28+N3	56.00	4.30	34.92	3.17	1.51	6.03	48	59
S28+N7	55.35	4.45	50.06	3.36	2.20	5.12	65	85
S28+N14	51.62	3.65	53.49	3.77	2.42	10.86	66	94
S28+N28	55.35	4.45	46.94	3.84	2.58	6.34	67	100
S14+N28	56.77	3.40	49.69	3.37	2.32	6.08	69	86
S7+N28	54.14	4.39	53.26	4.44	2.57	10.08	59	95
S3+N28	53.03	4.20	48.33	4.22	2.70	8.10	64	100

Based on the research and analysis of the results, the authors conclude that the interface strength and jointing efficiency for the combination of 'old' concrete maturing for 28 days with 'new' concrete increases with the age of the 'new' concrete. The most significant increase in joint efficiency occurs during the greatest strength increase in the "new" concrete. When "young" concrete (curing for 3, 7, 14, or 28 days) is combined with "new" concrete tested after 28 days, no significant differences in interface strength are observed. These findings are particularly relevant in the context of the construction with precast elements, where the joining of precast elements with concrete matured for less than 28 days is common. According to the findings, such a composite provides the necessary interface strength.

The authors conducted additional research on various types of concrete mixtures, which included concretes made from different types of cement [46,47]. These studies validated previous findings. The development of adhesion is influenced by the rate at which the strength of the 'new' concrete increases. It was observed that the interface strength increased more rapidly when the 'new' concrete was made with high early strength cement compared to normal early strength cement.

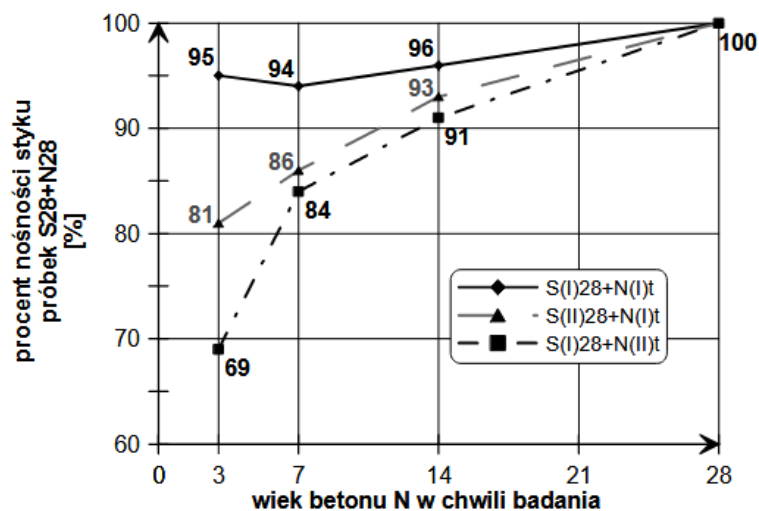


Fig. 3.18. Relative increase in tensile bond strength

Rys. 3.18. Względna wytrzymałość na rozciąganie zespolenia

The ranges of the variation of the tensile strength and the load strengths were similar, with values ranging from 3.5% to 11% (15% in one series) and 2% to 13.5%, respectively. The study's significant contribution is the use of a digital image correlation system to determine the contact cracking force. It was observed that the interface would crack much earlier than the failure of the composite specimens occurred. This indicates that the strength of the specimen tested by splitting is not equivalent to the tensile strength of the interface. The coefficient of composite effectiveness was determined by

calculating the ratio of the average contact cracking stresses to the average tensile strengths of the weaker concrete, resulting in a coefficient value ranging from 0.29 to 0.45. According to the authors, mechanical adhesion is the only bonding mechanism after the joint has been cracked. The contribution of mechanical adhesion to the strength of the interface is significant, as indicated by a cracking force to failure force ratio of no more than 50%.

Concluding the analysis of the authors' study, attention should be focused on the results obtained for the S(I)28+N(I)(t) series [46,47], which consisted of concrete made with C32.5R cement, the same as in the previously described study [65]. The authors themselves note that the S28+N3 series exhibits a surprisingly high initial value for the coefficient of the increment of the interface strength. These results are significantly different from the authors' previous studies on a similar concrete recipe with the same type of cement. In the 2009 study, the S28+N3 samples achieved an interface efficiency of 48% compared to the S28+N28 samples, and in the 2011 study it was as high as 99%. Upon analyzing these results, it is essential to recognize that various factors influence the formation of early interface strength. Therefore, as the authors suggest, further research should be continued and expanded.

Beushausen and Alexander

Beushausen and Alexander [9] also conducted studies on sandblasted specimens in a direct shear test, examining four different concrete strengths. The authors determined that both the concrete's strength and the curing process's duration have a considerable impact on the interface shear strength (Fig. 3.19). The test results represent the mean value of four to six specimens after excluding outliers. It is important to note that the variation coefficient for individual series can reach up to 25%.

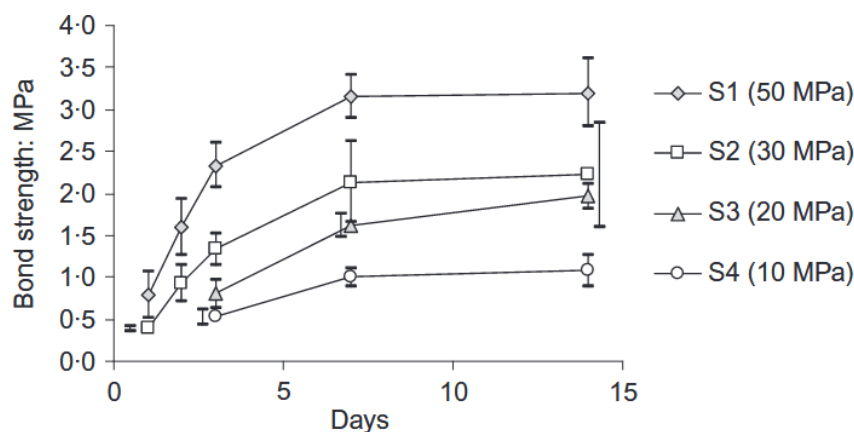


Fig. 3.19. Short-term bond strength development of specimens [9]

Rys. 3.19. Rozwój wytrzymałości styku w krótkim okresie [9]

The research was expanded to investigate the long-term strength of interfaces. The authors prepared three sets of specimens with different surface treatments to achieve this. The specimens were successively sandblasted (S5), smooth (S6) and notched (S7). A guillotine test scheme was used to evaluate the samples. The samples were cured in the laboratory and tested for shear bond strength at 28 days and 26 months. After 26 months, the shear bond strength of the notched interface specimens (S7) was found to be higher compared to the 28-day value. In contrast, the bond strength of the sandblasted (S5) and smooth (S6) interface specimens decreased by approximately 25% after 26 months. The presence of mechanical keys in the notched interface often resulted in the failure of the overlay or substrate material before the interface was affected. Consequently, in the S7 specimens, a significant portion of the shear strength between the substrate and overlay was dependent on the shear strength of the substrate and overlay materials rather than the interface strength. According to the authors, this explains why the bond strength of these specimens was not affected by shrinkage of the overlay.

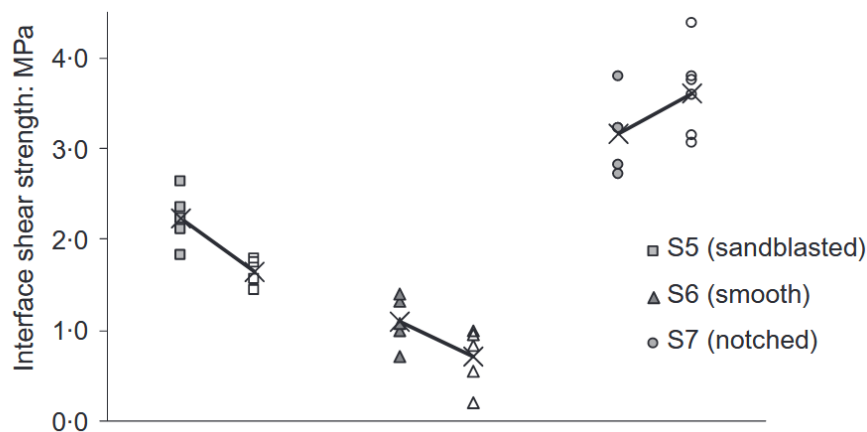


Fig. 3.20. Long-term interface strength development of specimens [9]

Rys. 3.20. Rozwój wytrzymałości styku w długim okresie [9]

The authors conclude that the roughness of the interface significantly impacts the bond's durability. When overlays experience differential shrinkage, interfaces with a relatively low macro-roughness may lead to a loss of strength. The results indicate that overlay shrinkage can cause a significant reduction in interface strength, up to 25%.

Santos et al.

The study conducted by Santos et al. [132] provides a comprehensive analysis of various factors related to surface preparation, interface strength, laying time of 'new' concrete, and the curing conditions of the specimens. The researchers considered two different curing conditions: first set was stored in the laboratory and second set was exposed to environmental conditions (solar radiation, rain, and wind). The time gaps between casting the substrate and adding the concrete layer were set at 28, 56, and 84 days to examine the impact of differential shrinkage between concrete components. The slant shear and splitting tests were employed to evaluate the bond strength of the interface in shear and tension, respectively. The study investigated five surface preparations between the substrate and the added concrete layer. The reference situation, left as-cast (LAC) against steel formwork, was compared to three treatments aimed at increasing the roughness of hardened concrete: wire-brushing (WB), sandblasting (SAB), and shotblasting (SHB). Hand-scrubbing (HS) was adopted to new casted concrete surfaces.

Generally, as expected, the bond strength of the interface increased with higher surface roughness. However, it was observed that the bond strength increased with a greater age difference between the substrate concrete and the added concrete layer. This finding contradicts the assumption that bond strength would decrease with increased differential shrinkage, known to occur with a difference in ages between concrete layers. To investigate this phenomenon, a numerical study, described below, was conducted. As anticipated, curing on the exterior led to lower values of pure shear strength, with an average decrease of 1.12 MPa, equivalent to a 19% decrease.

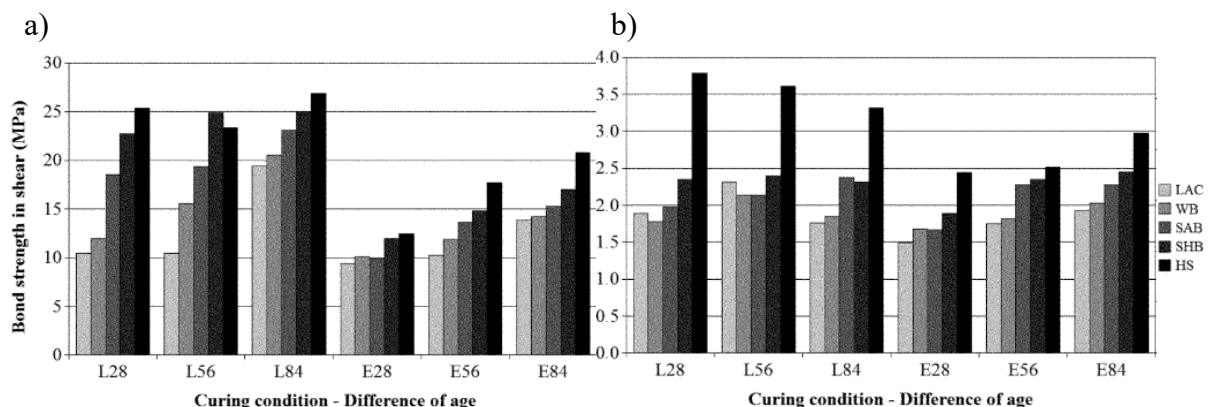


Fig. 3.21. Bond strength: a) in shear, b) in tension

Rys. 3.21. Wytrzymałość styku: a) przy ścinaniu, b) rozciąganiu

The comparative results of the shear and splitting tests are highly valuable. The shear test revealed a more significant impact on surface roughness. This observation can be attributed to the considerable influence of mechanical interlocking on the measured values. Furthermore, the authors have compiled the coefficient of variation results from each test series, yielding an average COV of 15.43% for the slant shear test and 15.7% for the splitting test, respectively. However, the range of COV values for the individual series analysis varied between 2.07% and 38.31%. These findings are consistent with the coefficient of variation results reported in the studies of other authors.

3.3.3. Effect of shrinkage and stiffness

The strength of the interface is influenced by additional factors, such as the shrinkage and stiffness difference between the component concretes. These effects can be attributed to the curing conditions of the substrate and the added concrete. Santos et al. [132] have provided a comprehensive description of the impact of these factors. The described research is a direct continuation of the paper presented at the conclusion of the previous subsection.

Santos and several researchers [7,67,88] have stated that an increase in the difference in stiffness between layers of concrete has an impact on stress distribution at the interface. This leads to stress concentrations at both ends, which has been observed through tests conducted by Santos on slant shear specimens. The stress distribution at the interface provides an explanation for the occurrence of broken corners in these specimens. The authors highlight the significant connection between cohesive failure and differential stiffness, suggesting that modifying the differential stiffness between layers of concrete can alter the failure mode of a composite concrete member. A numerical study was conducted using commercial finite element software to assess the influence of differential shrinkage and differential stiffness on interface bond strength.

Fig. 3.22 presents the stress distributions along the interface for shear and normal stresses. At the edges of the interface, the average increase of the normal stress is 62%. Stresses intensify as the differential shrinkage between concrete layers increases.

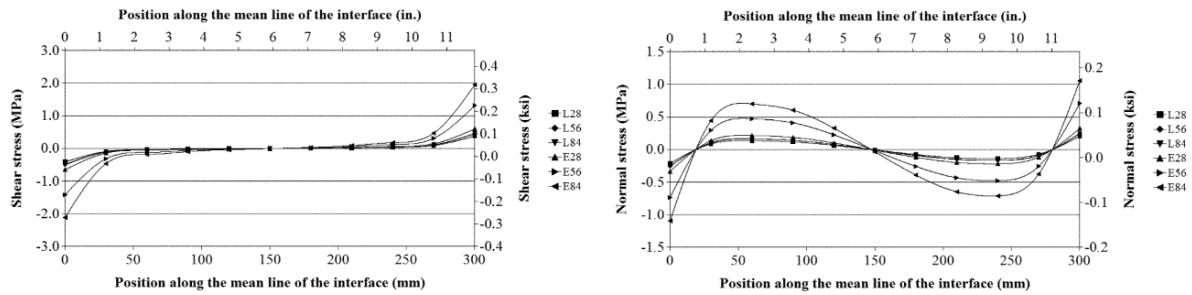


Fig. 3.22. Stress distribution at the interface due to differential shrinkage: a) shear stress, b) normal stress [132]

Rys. 3.22. Rozkład naprężeń w styku na skutek skurczu: a) naprężenie ścinające, b) naprężenie normalne [132]

Authors to investigate the impact of varying stiffness, different concrete classes were chosen between components. The distribution of shear and normal stresses along the mean line of the interface is presented in Fig. 3.23. The differential stiffness directly affects the stress distribution at the interface for both shear and normal stresses. As the differential stiffness increases, stress concentrations appear at both ends, resulting in an S-shaped stress distribution.

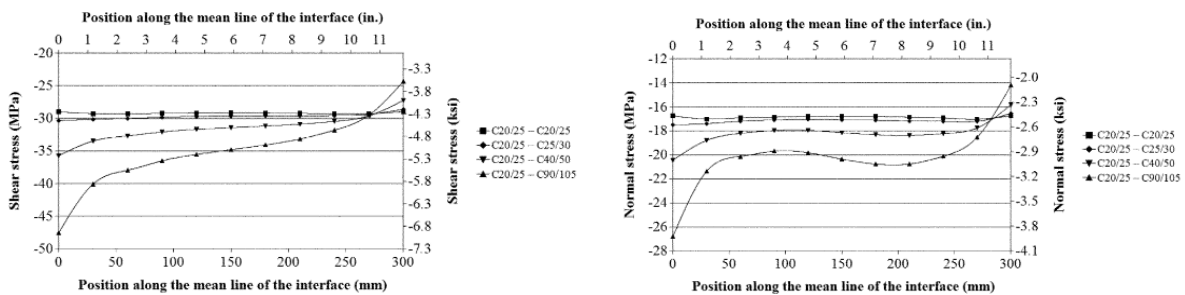


Fig. 3.23. Stress distribution at the interface due to differential stiffness: a) shear stress, b) normal stress [132]

Rys. 3.23. Rozkład naprężeń w styku na skutek różnicy sztywności: a) naprężenie ścinające, b) naprężenie normalne [132]

The combined effect of differential shrinkage, differential stiffness, and compressive loading during testing revealed that the failure load increases as the age difference between concrete layers increases. This is contrary to initial expectations. The numerical model supports these experimental observations by showing that compressive loading eliminates tension stresses caused by differential shrinkage at the interface of slant shear specimens. Therefore, as the age difference between concrete layers increases, leading to greater differential shrinkage, the failure load of the slant shear specimens

correspondingly increases. Santos states that this positive effect should be verified for other structural concrete-concrete interfaces and stress states.

The findings on the modification of the failure model due to shrinkage differences are consistent with Halicka's research [67]. Halicka conducted a comprehensive series of tests on composite elements made of expansive concretes, which presented a situation that contrasted (expansion as opposite to shrinkage) with Santos' study. In Santos' study, the specimens of two shrinkable concrete failed at the interface, while most of the specimens with one half made of expansive concrete failed as monolithic specimens. When 'new' concrete was cast from expansive concrete, the strength of the interface increased by 3-11% (depending on the type of test) for the combined stress-strain state of shear and tension and up to four times in the cylindrical shear test.

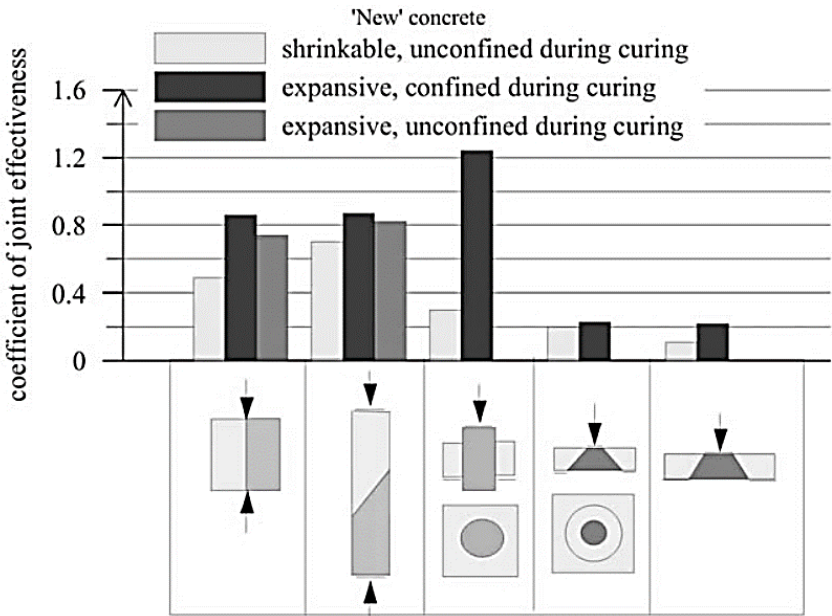


Fig. 3.24. Effectiveness of joint between two concretes in different stress-strain state [67]

Rys. 3.24. Efektywność zespolenia pomiędzy elementami w różnym stanie odkształcenia i naprężenia [67]

The author proposes the following recommendation. The bond strength of an unreinforced joint between expansive and shrinkable concrete can be accurately calculated by multiplying the value specified in PN-EN 1992-1-1:2008 by 1.1 for shrinkage-compensating concrete and 1.5 for expansive concrete.

3.4. Standard rules for the calculation of composite elements

The design of composite elements in design practice is based on standards for the design of reinforced concrete structures. The calculation of the resistance of the interface is intended to verify and check that the condition is fulfilled, i.e. that there is no slip in the interface. Such a condition allows composite structures to be calculated acting as monolithic structures. Current design codes of concrete structures present design expressions for the assessment of the longitudinal shear strength at the interface between concrete layers cast at different ages. These design expressions are most often based on the shear-friction theory. The parameters that are involved in the calculation of the resistance of the interface are usually: compressive strength of the weakest concrete, normal stress at the interface, shear reinforcement crossing the interface, and roughness of the surface. The analysis of the standard provisions was divided into three groups. The first is the PN series of standards, both PN-B and PN-EN. The second group includes the Model Code 2010 [N9] and the third group discusses the American standards ACI [N2] and ASSHTO LRFD [N1]. In the description of the standards, the emphasis has been on the interface basics, while the detailed description of the interface to the reinforcement has been omitted.

3.4.1. Polish and European standards - PN-B-03264:2002, PN-EN 1992-1-1, PN-EN 15037-1:2011

PN-B-03264:2002

The PN-B-03264:2002 [N10] standard was the last edition of the Polish standard before the introduction of the Eurocode series of standards. It was a transitional standard which broadly covered design in accordance with the principles of the Eurocode standards. The formula for calculating the shear resistance in the plane of the interface in the PN-B is similar to the later PN-EN standards. The difference lies in the symbols for the coefficients relating to the surface composite parameter responsible for reducing the tensile strength of the weaker concrete. The surface factors are summarised for the standards in Table 3.4 before which there is a commentary on the values given. The formula, together with an explanation of the symbols, is shown below:

$$\tau_{Rdj} = k_T f_{ctd} + \mu \sigma_N + \rho_j f_{yd} (\mu \sin \alpha + \cos \alpha) \leq 0.5 v f_{cd} \quad (3.6)$$

in which,

τ_{Rdj} – design shear resistance at the interface

f_{cta} – lowest tensile strength of the concrete at the interface

f_{yd} – design steel tensile strength

k_T – the surface factor according to table 3.4, if $\sigma_N < 0$ then it becomes zero.

μ – the friction factor

σ_N – compressive stress over the interface caused by external axial force across the interface, limited to a $\sigma_N \leq f_{cd}$

v – shear strength reduction factor for cracked concrete

$$\begin{aligned}\tau_{sdj} &< \tau_{Rdj} \\ \tau_{sdj} &= \beta \frac{V_{sd}}{zb_j}\end{aligned}\tag{3.7}$$

in which,

τ_{sdj} – design stresses at the interface

V_{sd} – design shear force acting parallel to the interface

β – ratio of the longitudinal force in the new concrete area and the total longitudinal force either in the compression or tension zone

b_j – width of the interface

z – lever arm of composite section, not greater than 0,85d for reinforced concrete structures and 0,80d for prestressed structures

The standard provides information in the notes about the possibility of ignoring shear stresses resulting from differential shrinkage and creep of composite elements. The note is then detailed with reference to the drawings of the composite section. The effects can be neglected when the composite is an infill on the beam between precast slabs, they cannot be neglected when the composite is across the width of the slab.

PN-EN 1992-1-1:2005, PN-EN 1992-1-1:2008

The first Eurocod standard introduced in Poland was PN-EN 1992-1-1:2005 [N14], which is an almost exact implementation of EN 1992-1-1:2004 [N3]. The standard, despite its PN-EN status, was not translated. Compared to the later edition already translated (PN-EN 1992-1-1:2008 [N15]), the calculation of composite structures has not changed. The difference, however, is the value of the surface factors, which have changed radically. This change is described in the following section and summarised in the table. The formula for the calculation of the interface composite resistance according to the 2005 and 2008 standard is presented below:

$$v_{Rdj} = cf_{cta} + \mu\sigma_n + \rho f_{yd}(\mu\sin\alpha + \cos\alpha) \leq 0.5v_{fcd} \quad (3.8)$$

in which,

v_{Rdj} – design shear resistance at the interface, the symbol has changed in relation to the PN-B standard from τ

c – the surface factor according to table 3.4, the symbol has changed in relation to the PN-B standard from k_T

σ_n – compressive stress over the interface caused by external axial force across the interface, the symbol has changed in relation to the PN-B standard from σ_N

$$\begin{aligned} v_{Edi} &< v_{Rdj} \\ v_{Edi} &= \beta \frac{V_{Ed}}{zb_i} \end{aligned} \quad (3.9)$$

in which,

v_{Edi} – design stresses at the interface, the symbol has changed in relation to the PN-B standard

V_{Ed} – design shear force acting parallel to the interface, the symbol has changed in relation to the PN-B standard from V_{Sd}

z – lever arm, without additional limiting conditions as per PN-B

The PN-EN standards do not contain additional notes and explanations as the PN-B standard, no guidelines are given with regard to the consideration of shrinkage and creep.

PN-EN 1992-1-1:2024-05

After 18 years, a new standard, PN-EN 1992-1-1:2024-05 [N16], referred to as the second-generation Eurocode, was introduced in 2024. The formula for calculating stresses at the interface has changed. The main modification is the move away from relying on the tensile strength of concrete to the compressive strength. The symbols as well as the values of the coefficients have also been changed. In the upper limiting condition, the reduction factor for the shear strength of the cracking concrete has been dropped in favour of a reduction of the global factor from 0.5 to 0.3. However, an additional component has been added to increase the maximum stress related to the reinforcement at the interface. The stress symbols have changed and are again in accordance with the latest edition of the PN-B standard. The stresses are again referred to by the symbol tau.

$$\tau_{Rdj} = c_{v1} \frac{\sqrt{f_{ck}}}{\gamma_c} + \mu_v \sigma_n + \rho_i f_{yd} (\mu_v \sin \alpha + \cos \alpha) \leq 0.3 f_{cd} + \rho_i f_{yd} \cos \alpha \quad (3.10)$$

in which,

τ_{Rdj} – design stresses at the interface,

c_{v1} – the surface factor according to table 3.4

σ_n – compressive stress over the interface caused by external axial force across the interface

$$\begin{aligned} \tau_{Edi} &< \tau_{Rdj} \\ \tau_{Edi} &= \frac{\beta_{new} V_{Ed}}{z b_i} \end{aligned} \quad (3.11)$$

in which,

τ_{Edi} – design stresses at the interface

V_{Ed} – design shear force acting parallel to the interface

z – lever arm of composite section

Surface roughness

Over the last more than 20 years, the standards for concrete-concrete interface without reinforcement have been based on the same assumptions derived from the Columbus-Mohr theory. However, the key parameters of the surface have changed several times during this period. The surface description itself remained similar. The interface surfaces were divided into four categories and, with the new edition of the EN standard, into five categories:

- Very smooth: a Surface cast against steel, plastic or specially prepared wooden moulds
- Smooth: a slip formed or extruded surface, or a free surface left without treatment after vibration
- Rough: a surface with at least 3 mm roughness at about 40 mm spacing, achieved by raking, exposing of aggregate or other methods
- Very rough (only PN-EN 1992-1-1:2024): a surface with at least 6 mm roughness at about 40 mm spacing, achieved by raking, exposing of aggregate or other methods.
- Indented/keyed: A surface with indentations complying or shear keys with figure (specified in standard)

Surface parameters are summarised in Table 3.4, surface parameters cannot be fully compared due to the reference of the latest 2024 standard to square root of compression strength of concrete instead of tension strength in previous edition on standard.

Table 3.4
Surface parameters according to PN standards
Parametrów powierzchni według norm PN

Standard Surfaces	PN-B 03264:2002	PN-EN 1992-1-1:2005	PN-EN 1992-1-1:2008	PN-EN 1992-1-1:2024 ¹⁾
Very smooth	0.02	0.25	0.025	0.01
Smooth	0.35	0.35	0.20	0.08
Rough	0.45	0.45	0.40	0.15
Very rough	-	-	-	0.19
Keyed/indented	0.50	0.50	0.50	0.37

1) related to square root of compression strength of concrete

PN-EN 15037-1:2011

In the area of precast concrete, the standard PN-EN 15037-1 [N13] for beam-and-block slab systems gives its own interface parameters for prestressed beams. The standard has its first edition from 2008, and a translated version was published in 2011. The surface types are divided into five types, of which two subtypes are specified for two of them (Tab. 3.5). The surface types depend on the preparation of the top and side surfaces as well as their geometry. The table below summarises the description of the surface type and the interface parameters given for it. The standard specifies the design shear resistances for the three concrete classes, with the proviso that the highest value is also valid for classes above C30/37. The calculated values of the c factor exceed those of the 2005 standard and significantly exceed those of the 2008 standard for smooth surfaces (Tab 3.4). Almost all surface types show a surface roughness factor as rough surfaces (compared to PN-EN 1992), with category c3 to c5 even exceeding keyed/indented surfaces.

Table 3.5

Surface types according to PN-EN 15037-1 standard
 Typy powierzchni według norm PN-EN 15037-1

Type	Beam surface condition	Values for v_{Rdi} , MPa; C25/30 C25/30	Calculation of c surface parameter ¹⁾
c ₁	The top and side surfaces slipformed or extruded (no overhang)	0.48	0.37
c _{2a}	As c ₁ with top of the beam surfaces with at least 3 mm roughness at no more than 20 mm spacing or transversally grooved or corrugated.	0.55	0.43
c _{2b}	The top and sides of the beam are slipformed or extruded and are tapered towards the flange (geometrical parameter according to figure in standard)	0.55	0.43
c _{3a}	The beam is as described in c _{2b} and the top is rough as defined in c _{2a}	0.69	0.54
c _{3b}	The transverse section is similar to the shaped described in c _{2b} . The top and sides of the beam are untreated ale the surfaces of the sides have a floated apperance	0.69	0.54
c ₄	The beam is as described in c _{3b} and the top is rough as defined in c ₂	0.75	0.58
c ₅	The top and sides of the beam are transversally indented as defined in 6.2.5 of EN 1992-1-1:2004	0.75	0.58

1) Recalculated v_{Rdi} to c parameter based on f_{ctd} C25/30 (1.29 MPa)

Note: According to a note in the standard, the v_{Rdi} values can be increased by 25% for verification in accidental situations

Only PN-EN 15037-1 provides guidance on determining the width of the interface for elements with vertical surfaces. The geometrical conditions are given, as shown in fig. 3.25. These conditions define the minimum thickness of concrete topping relative to the rib and adjacent hollow block or other infill element. These conditions are based on a criterion related to the size of the aggregate $1.2d_g$ and the distance - $\min(1.2d_g; 20 \text{ mm})$, in addition the smallest distance between the infill and the corner of the beam must be 35 mm. For the area between adjacent beams, a minimum of 30 mm is required between the edges of the webs. It is relatively unclear to define the depth to which the

height of the interface on the inside of the ribs can be taken. It is not clearly defined whether the height determined by the rules for the surface at the blocks/fills should apply or the total height if the 30 mm requirement is met.

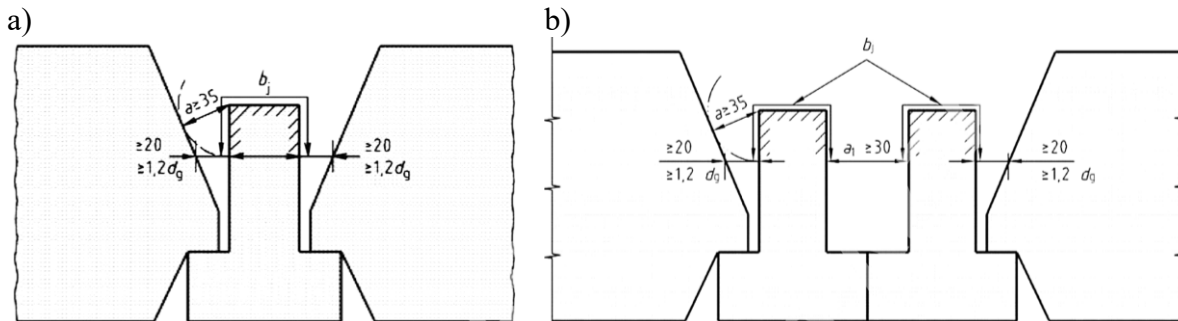


Fig. 3.25. Rules for determining the width of an interface composite according to EN 15037-1
 Rys. 3.25. Zasady określania szerokości zespolenia według PN-EN 15037-1

No similar guidance is given in other precast standards including PN-EN 13747 [N12], in which an example of a precast unit type is shown in the figure (fig. 3.26). The presented example fits into the geometry given in the standard for the beam-and-block slabs, so the provided interface parameters could also apply to some elements of EN 13747. However, no such transfer of provisions was made.

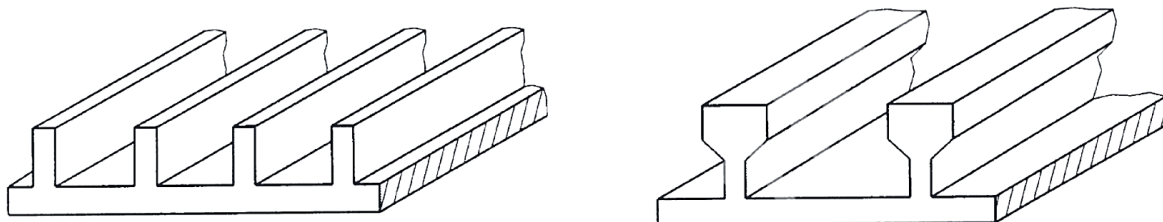


Fig. 3.26. Examples of precast element geometries covered by EN 13747
 Rys. 3.26. Przykładowe geometrie prefabrykatów objęte normą PN-EN 13747

Summary

As part of a summary of the PN series of standards (including PN-B and PN-EN), calculations were made for the example data in order to directly compare the allowable stresses regardless of the formula components. The calculations were carried out for a concrete class C25/30 with a design tensile strength of 1.29 MPa and a characteristic compressive strength of 25 MPa, with a material factor of 1.4 (for comparison to pre-2024 standards). The effect of compression from normal force was neglected and the calculations were performed without reinforcement crossing the interface.

The calculations showed significant differences of up to almost 30% and even 90% between the editions of the PN-EN standards (Tab. 3.6). In one case, the difference is multiple, relating to the 2005 PN-EN standard and very smooth surfaces, which was already revised in 2008. The latest edition from 2024 assigns a lower interface load capacity than in the previous regulations for most surfaces. The difference is between 8 % and 15 % for smooth and rough surfaces. The new edition of the standard adds very rough surfaces that were not present before. An almost doubling of the allowable unreinforced contact stresses occurs for keyed interfaces. At the same time, there is a standard for beam-and-block slab systems, where the allowable stresses differ significantly from the 1992-1-1 standard. Surfaces are assigned according to the manufacturing method, and so for smooth surfaces the difference is more than 90%.

Table 3.6

Stress for concrete C25/30 according to surface types of PN standards
 Naprężenia dla betonu C25/30 według typów powierzchni norm PN

Standard Surface, MPa	PN-B 03264: 2002	PN-EN 1992-1-1: 2005	PN-EN 1992-1-1: 2008	PN-EN 1992-1-1: 2024	PN-EN 15037-1: 2011 ¹⁾
Very smooth	0.03	0.32	0.03	0.03	-
Smooth	0.45	0.45	0.26	0.24	0.48
Rough	0.58	0.58	0.52	0.45	0.55/0.69/0.75
Very rough	-	-	-	0.57	-
Keyed/indented	0.65	0.65	0.65	1.12	0.75
1) PN-EN 15037-1: calculation related to surface type from c ₁ to c ₅					

3.4.2. Model Code 2010

The rules for the calculation of interfaces according to fib Model Code 2010 differ from the Eurocode standard arrangements up to 2023. The new edition of the PN-EN standard is similar to Model Code 2010 in its principles. The similar concerns to the calculation of the reinforcement and the lack of a simple sum of the effects of both adhesion and reinforcement work, which is expressed by separate factors for “rigid” surfaces, where adhesion is the main factor, and ‘non-rigid’ surfaces where reinforcement is responsible for the interface resistance. As for PN-EN 1992-1-1:2024, the analysis of the Model Code 2010 focuses exclusively on the interface without reinforcement.

Regarding the calculation of maximum allowable stresses in an interface without reinforcement, the Model Code does not differ from the PN-EN series of standards. According to Model Code 2010, the determination of the surface roughness and thus the roughness factor should not be based on the manufacturing method of the component, but on the measurement of roughness according to the parameter R_t , calculated from the sand path test [118]. The coefficients take on values similar to those of the PN-EN series for very smooth, smooth and rough surfaces. In addition, the Model Code 2010 includes a category of very rough surfaces that is consistent in value with the notched surfaces of the pre-2024 PN-EN standards.

Table 3.7

Comparison of surface parameters of PN-EN and Model Code
Porównanie parametrów powierzchni norm PN-EN oraz Model Code

Standard Surfaces	Model Code 2010	PN-EN 1992-1-1:2008
Very smooth	0.025	0.025
Smooth	0.20	0.20
Rough	0.40	0.40
Very rough	0.50	-

3.4.3. USA standards - ACI, ASSHTO LRFD

The standards applicable in the USA differ from the Eurocode and Model Code series. The standards ACI 318-19 (ACI - American Concrete Institute) and AASHTO LRFD (AASHTO - American Association of State Highway and Transportation Officials) divide surfaces into intentionally rough surfaces with roughness of approximately 6.4 mm and surfaces without peeling (smooth). Crucially, the ACI standard does not consider adhesion at the interface in the calculations. Therefore, it is not possible to design unreinforced interfaces according to ACI Standard 318-19. The AASHTO LRFD standard, which according to the name of the association is intended for transport-related structures, is used in the design of bridges. This standard allows interface only by adhesion at the joint. Further, however, specifies a requirement for minimum shear reinforcement (5.6.4.5 standard numeration). The formula for allowable stresses at the interface includes the interface area and the part responsible for the reinforcement (3.12):

$$v_u = c + \mu \rho_s f_y \leq \min \left\{ \begin{array}{l} K_1 f_c \\ v_{u,max} \end{array} \right. \quad (3.12)$$

in which,

c – adhesion

μ – coefficient of friction,

K_1 – factor reflecting fraction of concrete strength to resist interface shear

$v_{u,max}$ – limiting interface shear resistance (due to crushing of aggregate)

The interface-dependent coefficients and stress values are given according to the surface type in Table 3.8, as converted to SI units following the publication by Gołdyn [56]. For smooth surfaces, the adhesion value is 0.52 MPa, which is higher than in PN-EN 1992-1-1 for most types of interfaces and very close to the surface parameters of PN-EN 15037-1. Rough surfaces with very high levels of roughness ($R_z > 6.4$ mm) are assigned adhesion stresses of 1.65 and 1.93 MPa, which exceeds the values for notched surfaces according to PN-EN.

Table 3.8
Surface parameters according to ACI 318-19 standards [56]
Parametry powierzchni według normy ACI 318-19 [56]

Type of connection	Concrete placed monolithically	Cast-in-place concrete slab on clean concrete girder surfaces	Concrete placed against surfaces intentionally roughened ($R_z > 6.4$ mm)	Concrete placed against a clean not intentionally roughened surface ($R_z < 6.4$ mm)
c , MPa	2.76	1.93	1.65	0.52
μ	1.40	1.00	1.00	0.60
K_1	0.25	0.30	0.25	0.20
$v_{u,max}$, MPa	10.34	12.4	10.34	5.52

The standard does not provide guidance on the determination of the interface area. The only example is based on a flat area for a typical prestressed concrete girder, where the area is equal to the width of the interface multiplied by the length between the reinforcement of the interface. This area is referred to as the “area of concrete engaged in shear transfer”.

3.4.4. Standard comparison

To compare the standards, calculations were made for the smooth and rough surface and concrete class C25/30 (fig. 3.27). For the smooth surface, almost two times lower stresses were obtained for PN-EN 1992-1-1 in 2008 and 2024, with the highest values allowed by the ASSHTO LRFD. For rough surfaces, the results obtained are more uniform. The lowest stresses were obtained for the latest edition of the Eurocode standard while the highest for PN-EN 15037-1, where the range depending on the type of element can be calculated as 0.55 to 0.75 MPa.

Under the current Eurocode standards, it is possible to obtain allowable stresses that differ by 67% for surfaces of similar roughness and differ only in their execution as precast or on site. The 2024 standard can also be applied to precast elements, due to the more favourable coefficients for notched surfaces.

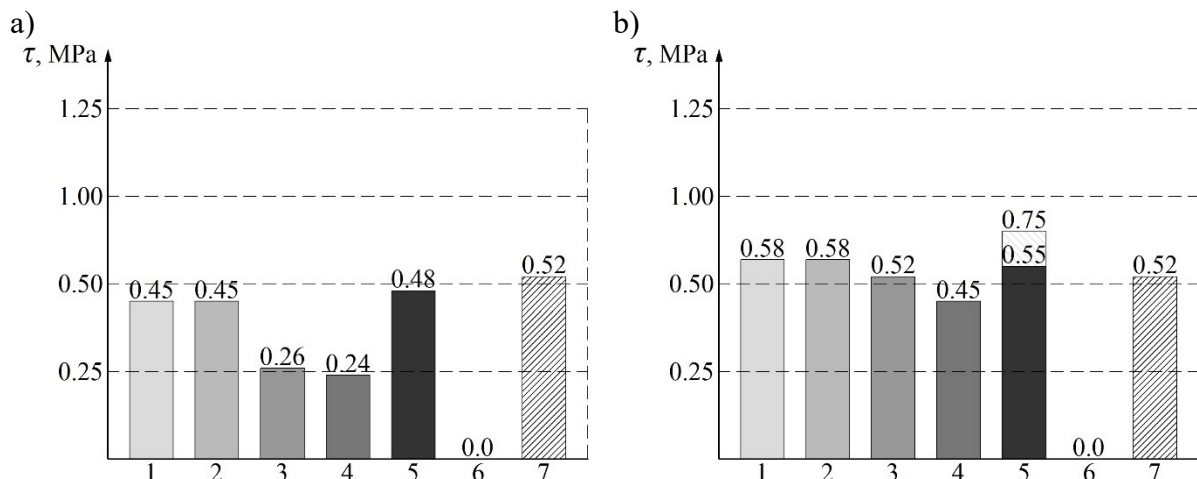


Fig. 3.27. Comparison of stress results for concrete class C25/30 for surfaces: a) smooth, b) rough; 1- PN-B-03264:2002, 2- PN-EN 1992-1-1:2005, 3- PN-EN 1992-1-1:2008, 4- PN-EN 1992-1-1:2024, 5- PN-EN 15037-1:2011, 6- ACI 318-19, 7- ASSHTO LRFD

Rys. 3.27. Porównanie wyników naprężeń dla betonu klasy C25/30 dla powierzchni: a) gładkiej, b) szorstkiej; 1- PN-B-03264:2002, 2- PN-EN 1992-1-1:2005, 3- PN-EN 1992-1-1:2008, 4- PN-EN 1992-1-1:2024, 5- PN-EN 15037-1:2011, 6- ACI 318-19, 7- ASSHTO LRFD

More extensive comparisons can be found in the literature. Goldyn [56,89] compared 184 experimental results on push-off specimens with calculations for PN-EN 1992-1-1:2008, prEN 1992-1-1:2020 [N16], ACI 318-19 and AASHTO-LRFD. The results obtained were mostly on the safe side relative to the standard requirements. The lowest difference between results of the tests and calculations was obtained for the AASHTO-LRFD, at the same time many results were unsafe, with COV = 56%. The ACI standard allows for conservative results. For the ACI standard, there is an apparent difference in

the offset of the results from the expected values due to the lack of consideration of adhesion at the interface. The EN standards allow a higher compliance, but the COV is 37% for prEN. As the degree of reinforcement increases, the standards provide an increasing level of safety, although the range of experimental results is greater.

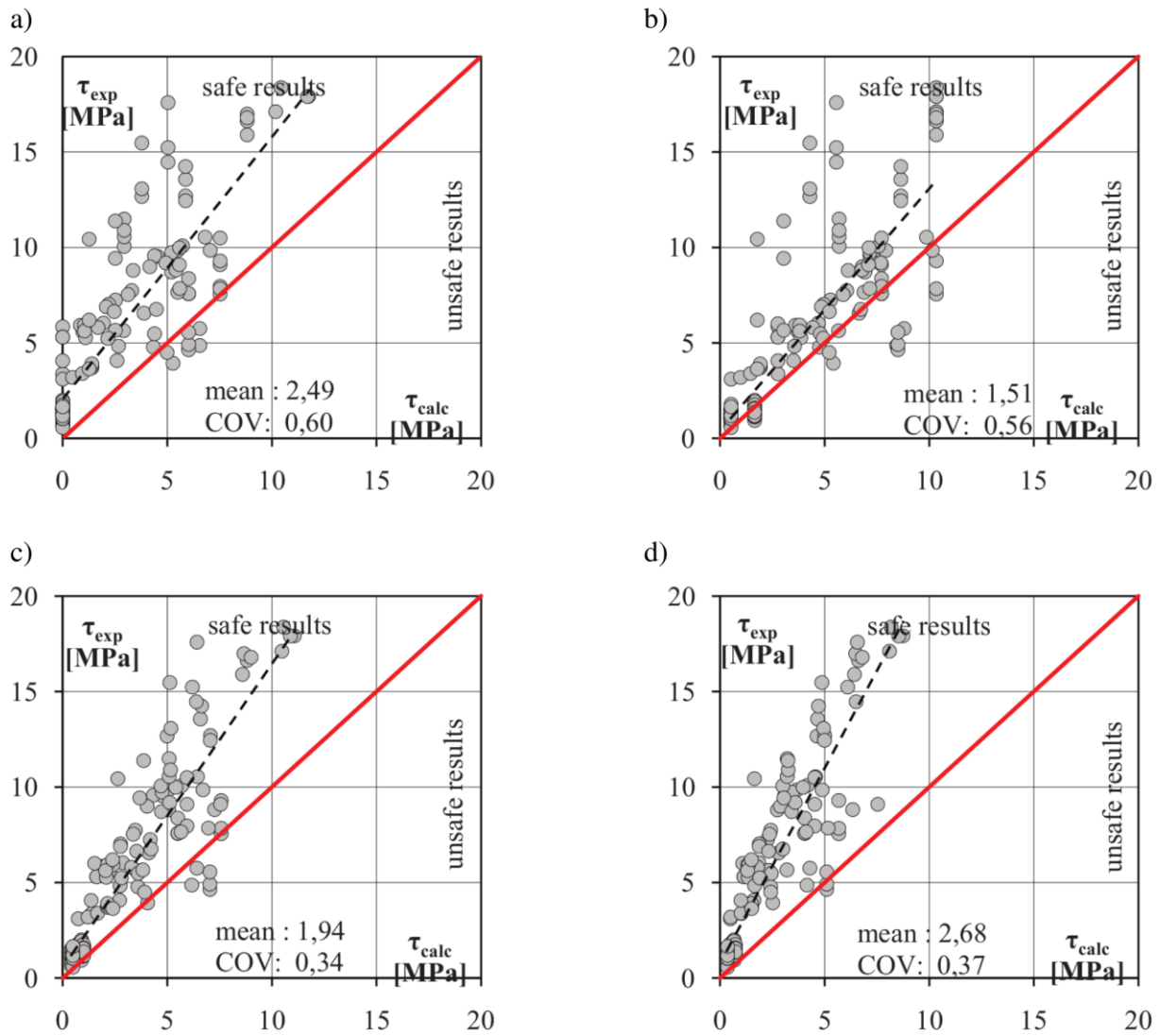


Fig. 3.28. Comparison between results of the test and predictions of the codes: a) ACI 318-19, b) ASSHTO LRFD, c) PN-EN 1992-1-1:2008, d) prEN 1992-1-1:2020 [56]

Rys. 3.28. Porównanie wyników badań doświadczalnych oraz obliczeń normowych: a) ACI 318-19, b) ASSHTO LRFD, c) PN-EN 1992-1-1:2008, d) prEN 1992-1-1:2020 [56]

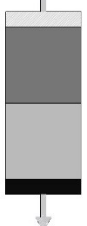
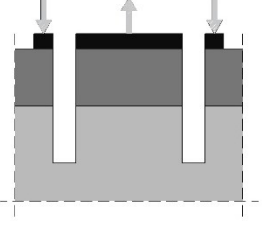
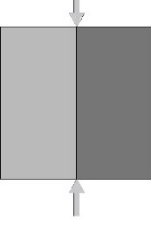
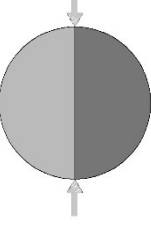
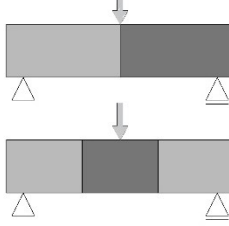


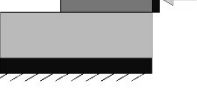
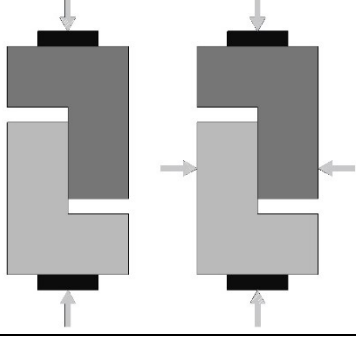
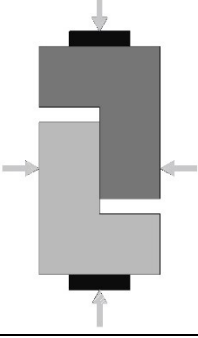



3.5. Test specimens for determining interface parameters

The effectiveness of the interface is often determined on small test specimens. Several types of tests are used, often with different variants. These specimens exhibit differences in the stress state at the interface, resulting from the adopted load arrangement. The variety of bond (interface) tests available in the literature for apparently the same interface strength parameters, whether derived from direct tension, shear or compression shear tests, does not allow a clear comparative assessment. The differing methods also include various methods of preparing the interface, which can lead to microcracking, as well as the use of concrete with distinct shrinkage or curing parameters that are not consistently reported, all of which can significantly influence the results obtained [67].

The strength of the interface is significantly influenced by the test method employed. The coefficients of variation for tests conducted within a single type are often relatively low; however, discrepancies between the same batches of concrete, despite having identical interface parameters, can vary considerably across different test types. A general recommendation is that a test method should be selected that corresponds to the stress state of the designed or tested interface. Based on a comprehensive review of research and analysis, Momayez identified a general relationship among the results from different test types. The strength of the interface decreases in the following order according to test type: slant shear, bi-surface shear, splitting, and pull-off [108]. Given the difficulties associated with routinely performing certain bond tests, particularly for quality control purposes, there is a growing interest in establishing conversion factors between different tests. Specifically, there is interest in using tensile bond test data from simple pull-off or splitting tests to estimate shear bond strength [161]. Currently, there is a lack of international consensus regarding test methods, procedures, and evaluation criteria, leading to significant variability and inconsistencies in the findings reported in the literature [115]. The subsequent section outlines the basic and most common types of tests along with their respective characteristics. The classification into basic test methods, along with the assignment of the stress state at the interface, is presented in Table 3.9.

Table 3.9

Types of interface test specimens (based on [68,108,161,162])
 Rodzaje próbek do badania zespolenia (na podstawie [68,108,161,162])

Tension stresses				
Axial	Pull-off	Splitting	While bending	
				
Shear stresses				
One- and bi-surface shear		Push-off	Direct-shear	
				
Shear and compression stresses				
Slant-shear				
				

3.5.1. Test specimens for interfaces in tension

Interface investigations in tensile tests fall into several quite distinct types. The first is axial tensile, which is relatively difficult to perform due to its sensitivity to small eccentricities and the problem of specimen assembly. The second is the commonly used splitting test, which involves applying a compressive force through a dedicated splitter in the specimen axis. The third is the pull-off test, which involves pulling out a drilled

section of concrete. The fourth type of test is the flexural tensile test. Interface tests are mostly performed on splitting test or pull-off test specimens.

Pull-off tests are subject to numerous issues that can affect the quality of the results [9]. The force must be applied exactly axially to the specimen surface, and the position of this surface may not always be ideally perpendicular to the top surface. Any misalignment of the pull-off force results in non-uniform stress distribution within the member, which can significantly influence the measured strength values. The core drilling process can be a problem, which can damage or weaken the interface, and the core may not be perfectly perpendicular. Bentz points to differences in sample preparation on the results obtained. For the pull-off test, the issue of moisture content of the interface is not clear-cut and, depending on its extent, it may lead to considerable variability in results, potentially impacting the outcomes more than in slant-shear tests [8]. Within the low-wetting range, increased moisture content results in enhanced interface quality due to reduced porosity, which is advantageous in the pull-off test [21], yet may be unfavourable in tests more based on mechanical adhesion, such as slant-shear. Similar alignment issues are also observable in the splitting test. The splitting test is notably more sensitive to the effects of early plastic shrinkage and drying shrinkage, which changes the failure mode from bond-cohesive to bond-adhesive [44]. The splitting test is also sensitive to the effect of scale and its effect decreases with increasing sample size which also allows for more homogeneous results [48,70]. When comparing the results of the splitting test and the pull-off test, relatively higher values for interface strength are to be expected in the splitting test based on the analysis of the test series [19].

3.5.2. Test specimens for interfaces in shear

Tests in shear specimens can be divided into several types with similar characteristics. Bi-surface shear tests are used to test concrete interfaces and, for example, tests on masonry elements [64]. However, each test is subject to eccentricities of load force and bending moments. Bi-surface shear tests especially on elements with a wide base are characterised more by bending and shear failure than pure shear failure. The use of digital image correlation is particularly suitable for analysing tests of this type [96].

Direct-shear tests occur in various configurations of the test component. They are mostly performed on specimens composed of two L-shaped elements. Direct-shear tests are also performed on elements with shapes corresponding to the real interface's shapes, e.g. the gap with the dowel studs [150]. The advantage of direct-shear tests is the possibility of realising an additional compression that reflect normal forces to the

interface [79]. Direct-shear tests are particularly sensitive to the length of the interface section due to disturbances at the edges of the specimen [57]. An attempt to solve this problem was made with some good results by Gremza [59], where the force was applied not as concentrated at the top but uniformly across the lateral edge of the specimen (Fig. 3.29). The modified test configuration resulted in interface stiffnesses that were more than twice as high as those of other researchers, and improved stress distribution by largely eliminating disturbance at the edge of the component and bending effects. Direct-shear tests are most often performed in a single loading cycle which does not necessarily reflect the nature of the interface operation. As Gebreyouhannes points out, direct-shear tests are sensitive to high-repetition cyclic loading that is characterised by gradual increments in shear slip even in the initial range [53]. The greatest effect of deterioration was observed in the initial loading cycles.

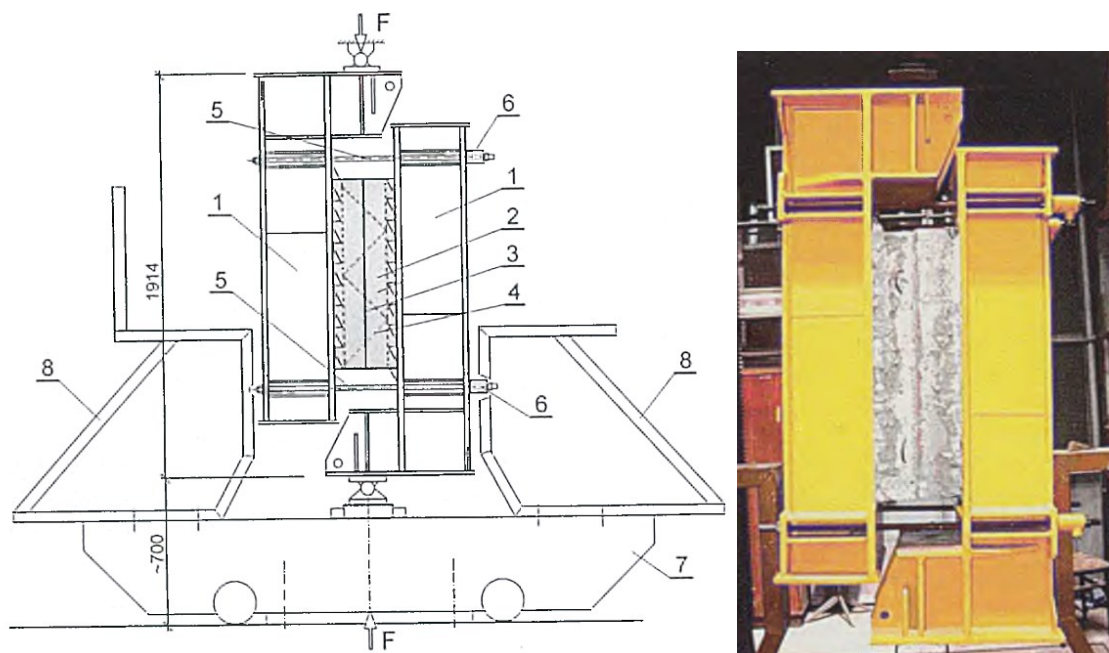


Fig. 3.29. Direct shear test stand as proposed by Gremza [59]

Rys. 3.29. Stanowisko badawcze bezpośredniego ścinania według propozycji Gremzy [59]

3.5.3. Test specimens for interfaces in shear and compression or tension

The third main category of test types refers to tests of interfaces subjected to both shear and tension or compression. The most common test is slant-shear. It involves compressing a concrete cylinder consisting of a diagonal interface. However, this test is sensitive to the effects of shrinkage as described in earlier chapters (sec. 3.3.3). The modification of the angle of inclination additionally has a significant effect on the failure

model. By modifying the angle (Fig. 3.30), it is possible to control the type of failure between bond-adhesive and bond-cohesive (Fig. 3.31) [7,44,129].

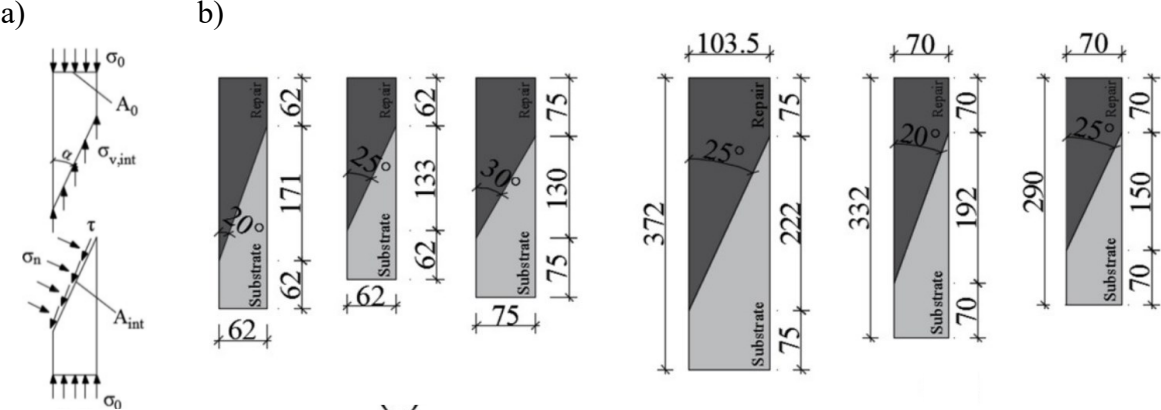


Fig. 3.30 Slant-shear specimens: a) stresses at the interface, b) types of specimens [7,129]
 Rys. 3.30. Próbkki typu slant-shear: a) naprężenia w styku, b) typy próbek [7,129]

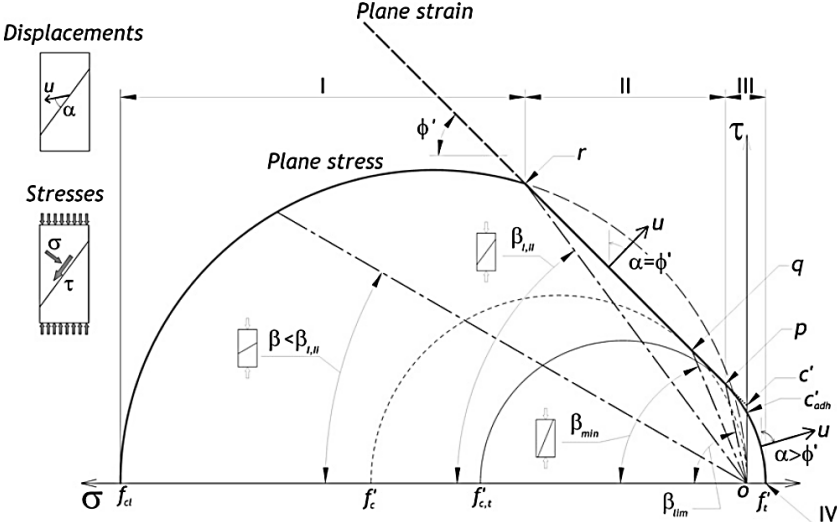


Fig. 3.31 Effect of slant angle in slant-shear specimen on interface stresses [44]
 Rys. 3.31. Wpływ kąta nachylenia w próbce slant-shear na naprężenia w styku [44]

Test configuration combining shear and tension were proposed by Halicka by modifying the bi-surface test with an inclination of the interface so as to achieve tension [68]. A second configuration of the proposed method called the conical shear test is relying on a cone pressed out of a concrete slab supported over the full width of the base.

Some other kinds of tests are based on certain modifications of already known types with the aim of eliminating their drawbacks or extending them with additional aspects. An example of such an approach is the element proposed by Chilwes combining the features of push-off and bi-surface testing [15], which can be extended to include additional forces relative to the interface. The aim of the proposed method was to eliminate the eccentricity problem relative to typical push-off tests and to transmit

a single force axially relative to the specimen (Fig. 3.32), rather than at the edge as is often the case in one- or bi-surface tests.

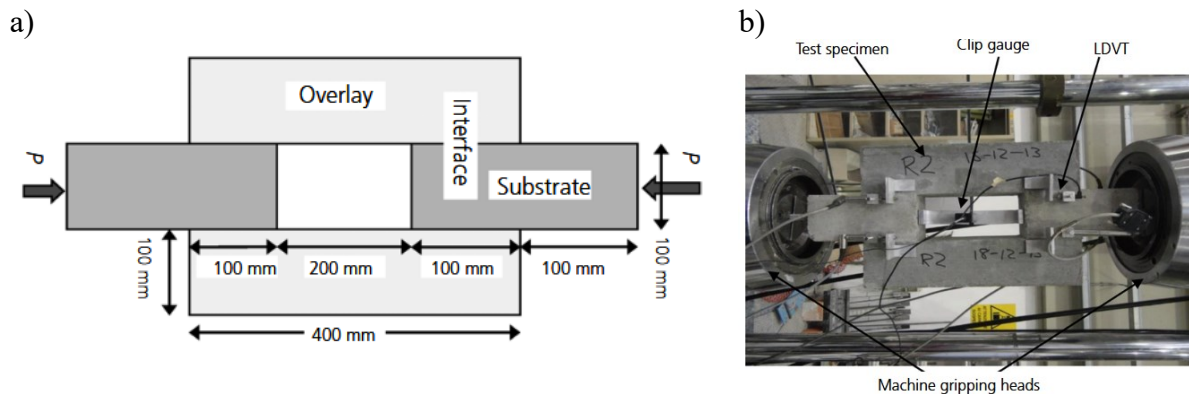


Fig. 3.32. The test configuration proposed by Chilwes: a) dimensions of the specimen, b) view of the test stand [15]

Rys. 3.32. Konfiguracja badania zaproponowana przez Chilwesa: a) wymiary próbki, b) widok stanowiska badawczego [15]

3.5.4. Alternative methods of determining interface parameters

In recent years, a number of new studies are being carried out to determine the state and consequently the strength parameters of an interface by indirect, non-destructive testing (NDT) methods. One group is a combination of destructive testing and non-destructive testing most often based on ultrasonic methods [42,123,151] or surface wave measurement. As indicated by Qian et al. strong correlations demonstrated that the non-destructive ultrasonic pulse test and rapid electrical test could be employed to predict and evaluate the bond strength and permeability of a layered interface [114]. Conclusions from Xu's research show even that delamination lengths can be determined using surface wave measurements [151].

Sadowski proposed a method based on artificial neural networks (ANNs) allowing prediction of the pull-off adhesion of a concrete interface with variable thickness of overlay [126,127]. However, this analysis requires a lot of input data based on three NDT tests: 3D laser scanning method, impact-echo tensile strength prediction and impulse response method to determine the thickness of overlay. Such extensive NDT testing can be difficult to perform in non-laboratory conditions and expensive, but it provides an alternative or additional verification of destructive testing. This method can be useful for analysing very responsible structures, but, due to the need for 3D scanning of the surface, its scope is limited to structures in during assembly rather than subsequent assessment.

3.6. Studies and examples of composite elements

The research review is divided into two sections. The first dealing mainly with the results and experimental aspects of the tests of elements at a scale larger than the samples presented in section 3.5 and the second focusing more on modelling issues. In the numerical modelling section (3.7), the main information related to the experimental investigations, if performed, is also given.

Research on composite elements, apart from laboratory specimen tests, is mainly based on beam elements with single plane interfaces. The research covers a range of issues, focusing on reinforced interfaces due to the relatively well-recognised mechanism of unreinforced flat interfaces. This section presents selected studies of single plane interfaces relevant to the analyses carried out in the thesis, followed by a description of selected studies on interfaces with complex geometries. Lastly, examples of structures employing multiplanar interfaces are given based on research carried out in recent years.

The examination of composite elements covers a wide range of issues, some of which have been partially addressed in Sections 3.3 and 3.5. Several aspects that will not be described in more detail in the study due to being beyond its scope, but are relevant to the overall analysis of composite elements, particularly in relation to their service life, are outlined below:

- Vertical interfaces corresponding to construction joints where shear, tension (longitudinal reinforcement), and compression (within the compression zone) occur, are examined. Research by Cavaco [14] and Park et al. [113] reveal that the vertical interface/construction joint does not significantly impact the element's performance, including its failure mode. However, some influence was observed on the cracking force and the pattern of the diagonal crack near the interface.
- Studies of reinforced interfaces have focused on the stresses within the reinforcement, accompanied by verifications and proposed modifications of calculations based on shear-friction theory. Several studies indicate that the initial contribution of reinforcement to stress transfer is low, but this contribution increases as interface slip arise [71,99,106].
- Strengthening and repairing structures through the application of additional compression or tension layers via concrete is necessary in instances where spatial constraints or inaccessibility to the lower side of the slabs are prevalent, as demonstrated by Fernandes et al. [45]. Research has indicated that the additional

reinforcement at the interface results in ductile behavior, with debonding occurring up to three times more than in slabs without reinforcement.

- A study conducted by Talbot et al. [141] examines the long-term effects of bonding on the durability of plate elements. The authors emphasize the significant impact of surface preparation on both the strength and durability of the bonding, whereas the influence of the concrete mixture on bonding durability is comparatively low.
- Tests conducted under dynamic loading by Supriyadi et al. [139] indicated that the stiffness of the composite slab is slightly lower than that of the monolithic slab. The distribution of shear connectors in an increased quantity within the support zone enhances the stiffness of the slab. Research by Gromysz [61,62] provides a methodology for predicting the failure mode of the slab and assessing the potential for slab delamination at maximum force. As noted by Gromysz, near the peak force (failure), the critical damping fraction begins to decrease, resulting from a transition in the damping characteristics within the joint from viscous damping to damping attributed to the friction of the displacing concrete layers.
- Cyclic tests conducted by Gromysz [60] demonstrated the occurrence of internal friction at the interface within the range of 0.1 mm. This internal friction contributes to the formation of the hysteresis loop observed during the loading and unloading processes. Kinetic friction manifests in scenarios where the relative displacement between the bottom and top layers of concrete exceeds 0.1 mm, indicating the occurrence of delamination. Research involving cyclic loading (fatigue tests) performed by Lemieux indicated that the interface experiences a more pronounced effect in the tensile zones compared to the compressive zones [94]. Additionally, a study by Wienieke and Hegger [148] identified a fatigue effect occurring after more than 1,000,000 cycles, correlated with an increase in stress within the bonding reinforcement. The authors point to a safe verification give against Eurocode 2 and the National Annex of Germany.

3.6.1. Studies of composite elements with single plain interface

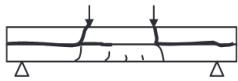


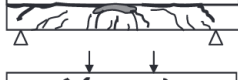



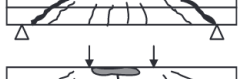
A series of studies by Halicka and her research team determined the behaviour and calculation rules of composite elements with a flat reinforced interface. The crack pattern, and consequently the mode of failure, in a composite concrete unit is influenced

by the shear resistance of the interface between connected concretes resulting from the adhesion and the contribution of transverse reinforcement. Halicka proposed a design criterion based on the analysis of the force that cracks the interface and the forces leading to the formation of diagonal cracks.

Four failure mechanisms (Tab. 3.10) were identified and classified into two groups [69]. Group one are elements with crack propagation at the interface extending to the edge of the element, along with a loss of shear capacity in the separated beam component. Group two includes elements characterized by local cracking at the interface, which is attributed to diagonal cracking (B.1) and like monolithic elements (B.2). The author indicates that only situation B, where cracking of the interface is not allowed before diagonal cracking (situation A), should be considered in the design process. The proposed design criterion incorporates a stress calculation based on the principles of laminar structural mechanics.

Table 3.10

Classification of failure mechanisms of composite concrete beams [69]
Klasyfikacja mechanizmów zniszczenia betonowych belek zespolonych [69]

Description of the situation		Causes of the failure	Crack pattern
'A' Crack propagation in the interface $V_{Rd,i(cr)} < V_{Rd,w(cr)}$	'A.1' $E_{cm,u} I_u E_{cm,l} I_l$	'A.1.1' Delamination	Displacement connected parts in relation to each other in the interface 
		'A.1.2' Excluding of down layer	Exceeding the shear resistance of upper layer 
	'A.2' $E_{cm,u} I_u E_{cm,l} I_l$	'A.2' - Delamination - Exceeding the shear or flexure resistance of the lower layer	
			
'B' Propagation of diagonal crack $V_{Rd,i(cr)} < V_{Rd,w(cr)}$	'B.1' Interface cracking $V_{Ed} \geq V_{Rd,i(cr)}$	'B.1.1' Local cracking of the interface	Exceeding the shear or flexure resistance of the beam 
		'B.1.2' Partial delamination of the interface	- Partial delamination - Exceeding the shear or flexure resistance of the down layer 
	'B.2' Beam behaves like monolithic one $V_{Ed} < V_{Rd,i(cr)}$	'B.2' Exceeding the shear or flexure resistance of the beam	
			

The research was extended in a team with Jabłoński [71,81,82,84] to include elements with T-sections and with Sadowski to notches interface (which will be described in section 3.7) . Tests on T-section elements included the difference in

stiffness at element height and the position of the interface at element height. The tests showed the influence of the interface position on the cracking pattern of the beam. Cracking of the interface positioned in upper part of the beam occurred first with diagonal cracks, and the cracking at the interface was its continuation (Fig. 3.33a). For interfaces at the middle of the beam (Fig. 3.33b, c), a local contact slip connected the two diagonal cracks. The contact cracking force values for the web-height interface of Fig. 3.33b, c was 50% higher than for interface of Fig. 3.33a.

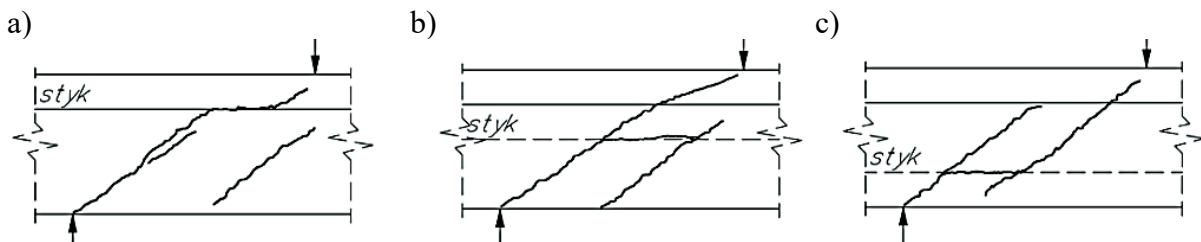


Fig. 3.33. Crack pattern of T-shaped beam depending on the position of the interface [82]

Rys. 3.33. Obraz zarysowania belki teowej w zależności od położenia styku [82]

The phenomenon of cracking at the interface, as well as the associated cracking force, can be attributed to the shear stresses that arise from the geometry of the section, with the maximum stresses occurring at the T flange/web interface (Fig. 3.34a). The study also confirms the observations of other authors (including recent research by Oh and Moon [110]) related to the minimal shear forces (effectiveness) of the shear reinforcement prior to the cracking at the interface (Fig. 3.34b).

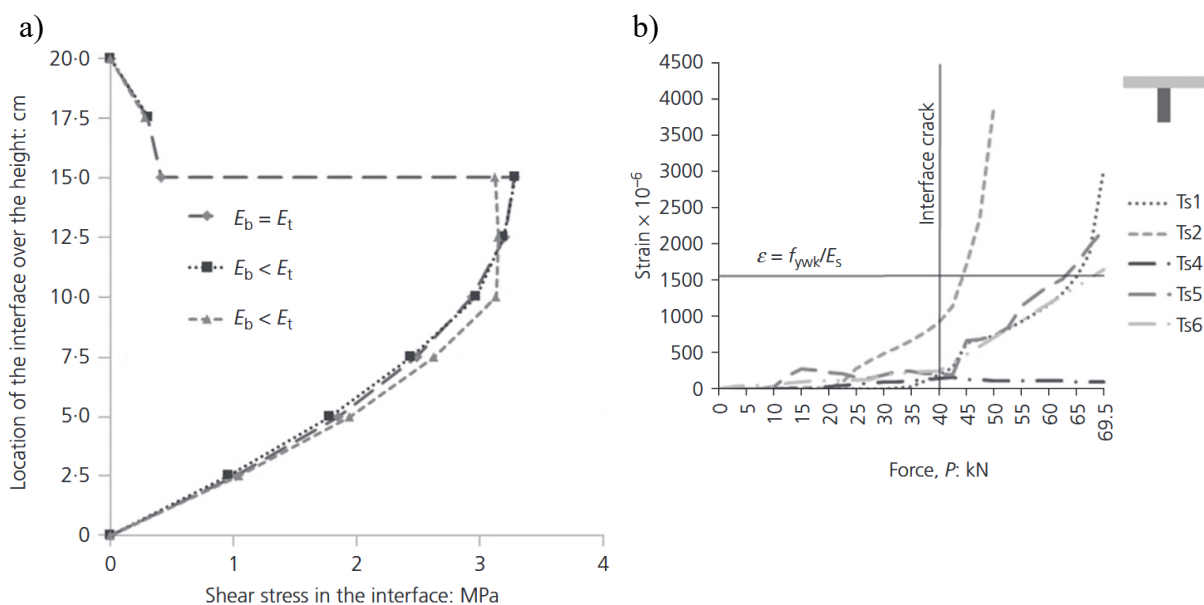


Fig. 3.34. Research on T-shaped beam: a) shear stress in the interface in relation to the element part stiffness of the concrete, b) strain on the stirrups [71,82]

Rys. 3.34. Badania belek teowych: a) wartość naprężeń stycznych w styku belki teowej w zależności od sztywności składowych betonów, b) odkształcenia strzemion [71,82]

Research on elements similar to the presented study by Halicka and Jabłoński was undertaken by Rueda-Garcia et al. [120]. The investigation involved 21 T-shaped composite beams. The authors performed an analysis of the failure mechanism based on the cracking pattern, utilising a strut-and-tie model (Fig. 3.35). The model was divided into three distinct phases: 1) prior to slippage at the interface (Fig. 3.35a), 2) at maximum force (Fig. 3.35b), and 3) post-peak (Fig. 3.35c). Arching action was identified as the principal mechanism of shear transfer following the formation of critical shear cracks. The diagonal cracks that developed limit the effective height of the element, resulting in an ineffective area. The crucial zone in the final phase extends beyond the support axis, with its cracking determining the failure of the element. The authors concluded from their analyses that the codes underestimated the horizontal shear capacity at the interface of composite beams without reinforcement crossing the interface. Notably, the experimental results for vertical shear strength were found to align well with the predictions made by the codes (Eurocode 2, Model Code 2010, and ACI 318-19) when the depth of the composite beam was utilised in the calculations instead of beam depth. In addition, they assessed the impact of shrinkage and found no reduction in shear strength attributable to differential shrinkage. However, these conclusions are limited to the specific geometry that was tested.

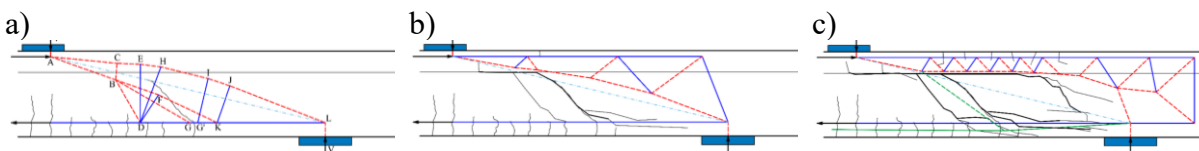


Fig. 3.35. Strut-and tie models of the shear transfer mechanisms: a) development of diagonal cracks, b) after critical shear crack formation, c) failure [120]

Rys. 3.35. Model strut-and tie opisujący mechanizm pracy z uwagi na ścinanie: a) powstanie rysy ukośnej, b) poślizg w styku i powstanie rysy dominującej, c) zniszczenie [120]

Further development of the issue of "anchoring" the interface within the support zone is presented in Gromysz's research on slab elements [63]. The author emphasises that a significant finding from this extensive series of studies is the observation that the bearing capacity of a composite slab can be achieved by anchoring the main bending reinforcement, which is situated in the precast section, outside the support zone within the concrete topping (Fig. 3.36). Ensuring that the strains in the end zones of the element to ensure the effective performance of a composite structure. As indicated by the author, composite behaviour can still be realised even when the entire interface is covered by a membrane that does not facilitate the transfer of tangential stresses. Proper anchorage of the reinforcement, such as within the ring beam, can be a critical factor in ensuring

the composite performance of an element, particularly when it experiences degradation due to cracking. These observations constitute a significant contribution to understanding the behaviour of composite elements and the safety of their application. Gromysz notes that ensuring the adequate anchorage of reinforcement at the support within the concrete topping may provide an alternative method for achieving monolithic behaviour in elements.

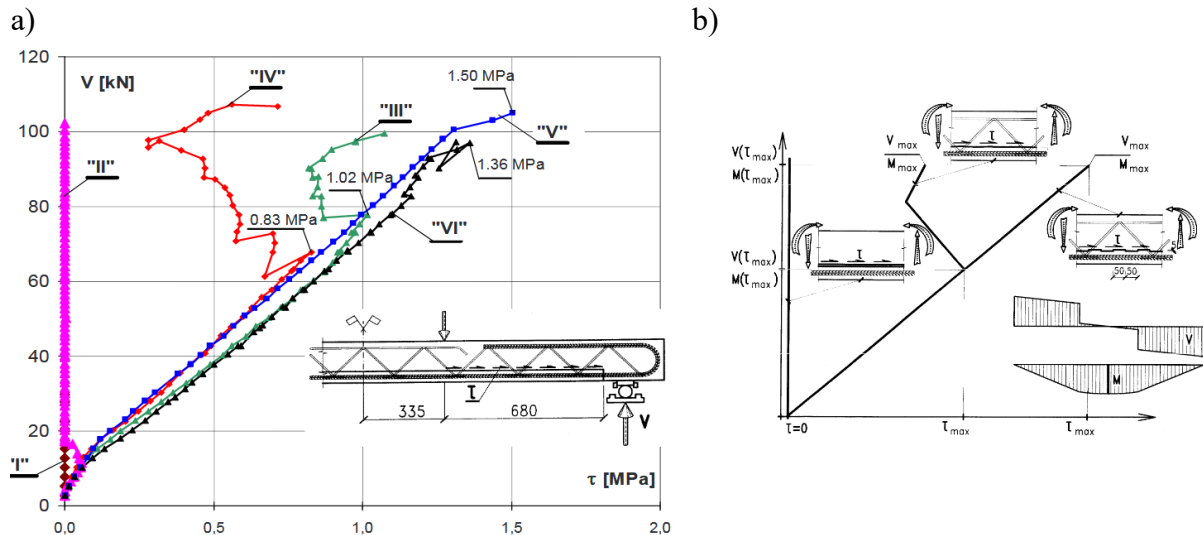


Fig. 3.36. Shear stress in the interface: a) value of shear stresses (V – model with rebars anchorage in topping), b) characteristic of shear stresses in the interface according to the interface type [63]

Rys. 3.36. Naprężenia styczne w styku: a) wartość naprężeń w styku (V – model z zbrojeniem zakotwionym w nadbetonie), b) charakterystyka naprężeń stycznych w zależności od typu powierzchni zespolenia [63]

The study of slab elements with flat interfaces mainly focuses on elements featuring spatial trusses that are designed similarly to beam-and-block slabs [77], where the reinforcement is responsible for ensuring the interface resistance. The second category of slab elements investigated consists of prestressed hollow core slabs, which are mostly executed with unreinforced interfaces. An interesting characteristic from an analytical perspective is their impact on the delayed formation of diagonal cracking due to the prestressing of the precast element. As indicated by previously presented studies, this phenomenon can significantly affect interface behaviour. Furthermore, concrete topping is applied to unsupported slabs, resulting in varying compression stresses on both the precast component and the concrete topping.

Numerous studies have established the beneficial impact of concrete topping on the performance of hollowcore slabs, with full-scale tests on flexural elements demonstrating the absence of delamination. According to Mones [109], horizontal shear strength only governs in short-span slabs with thick webs. A study conducted by Ajdukiewicz [4],

which assesses the PN-EN 1992-1-1:2004 standard with increased adhesion coefficients compared to the current ones, indicates that the standard calculations still lead to conservative results. Additionally, he recommends the implementation of vertical reinforcement at the interface, applicable only in situation where the quality of the interface may be questionable. This reinforcement is supposed to prevent the negative effect of shrinkage. Similar findings are reported by Adawi et al. [1] concerning the ACI standard and the requirement for reinforcement at the interface, which the authors argue should not be mandated for slab elements such as hollowcore slab

An analysis of the experimental tests conducted by various researchers, alongside their own computational analysis, was performed by Derkowski and Surma [28]. The analysis demonstrated that the current European codes provided the lowest possible values of joint bearing capacity, which were significantly lower than the values obtained in the experiments. The authors also conducted their own experimental studies in this area, wherein full-scale research indicated that all tested topped elements exhibited full composite action up to the point of failure [29]. Some inconsistencies can be inferred from other studies by the same authors regarding push-off tests [23]. These tests revealed an adhesion coefficient of 0.21 for the grooved surface, which aligns with the PN-EN 1992-1-1:2008 standard. This finding represents a certain discrepancy when compared to analyses based on tests conducted by other authors presented in the paper [28]. Derkowski and Surma, based on analyses performed by the authors, conclude that in the case of ceiling or roof slabs, the contribution of the friction effect to joint longitudinal shear capacity is negligible and may be omitted in calculations.

3.6.2. Studies of elements with multiplanar interface

Research on elements with multiplanar interfaces is carried out on both separated beams and slabs. A number of studies concern the analysis of beam-and-block slabs. The investigations are often carried out only considering the interface at the top surface and the connection to the slab, which allows a rectangular [54,55] or T-shaped model to be obtained. Similar models are obtained for the analysis of slabs with lightweight infill which leads to the same conclusions as on T-models due to the non-reliance on the lateral surfaces of the ribs [77].

Extensive research involving various tests was conducted by Derkowski and Surma on prestressed beam-and-block slabs [25,26,30,31]. The elements examined were characterized by the wavy geometry of their top surface. Tests were performed on elements with an interface on the side surface as well as those without it in push-off tests

(Fig. 3.37). This approach limits a comprehensive evaluation of the cohesive adhesion and friction characteristics due to the absence of an interface on the side surface. In the push-off test, failure occurred as a result of shear along the axis of the strands. Subsequently, tests were carried out for the delaminated element to determine the coefficient of friction. The cohesion results obtained are an average of 0.56, with a minimum value of 0.48, while friction exceeded 1.0, attributed to the wave locking effect. These values surpass those specified in PN-EN 1992-1-1:2008 but are consistent with PN-EN 15037-1.



Fig. 3.37. View of the tests stands for cohesion and friction test [31]

Rys. 3.37. Widok stanowiska do badań przyczepności kohezyjnej i sił tarcia [31]

Regardless of the test configuration, no delamination was obtained at the interface of the test elements (Fig. 3.38). The failure of the slabs was attributed to the shearing of the ribs at the strand line, as occurred in the push-off tests. The only delamination was obtained, as indicated by the authors, as a result of a secondary mechanism, after the transverse shear resistance had been reached. As a result of secondary delamination failure, the authors observed fall-off of the bottom flanges (cover) of the strands in the support zones, as well as fragments of the infill blocks. Furthermore, there was a loss of anchorage of the prestressing strands over an extensive length.



Fig. 3.38. View of shear failure of the PC girder in slab element [30]

Rys. 3.38. Widok ściętego żebra w elemencie płytowym [30]

Extensive research on 24 prestressed rib elements, specifically within a beam-and-block slab system, was conducted by Ribas and Cladera [119], taking into account the influence of the interface on the side surfaces (see Fig. 3.39a). To incorporate the effects of prestressing and facilitate anchorage, the authors assumed a 500 mm length of beams beyond the support axis. The authors presented several conclusions that align with findings from other studies. Firstly, they noted an increase in shear resistance with T-shaped elements, corroborating the model proposed by Zararis and the ST model by Rueda [120]. The three shear standard formulations evaluated in the paper were found to be overly conservative regarding predictions of beam-and-block shear strength. Notably, the authors indicated that, in the three-point bending tests, the three of the beam specimens failed in the longer shear span rather than the shorter span as anticipated. According to the authors' analysis, this can be attributed to the consideration of three phenomena: the arch effect, the type of prestressing, and the moment-shear interaction. Importantly, no local slip at the interface (see Fig. 3.39b) or any other effects indicative of delamination were observed in any of the element.

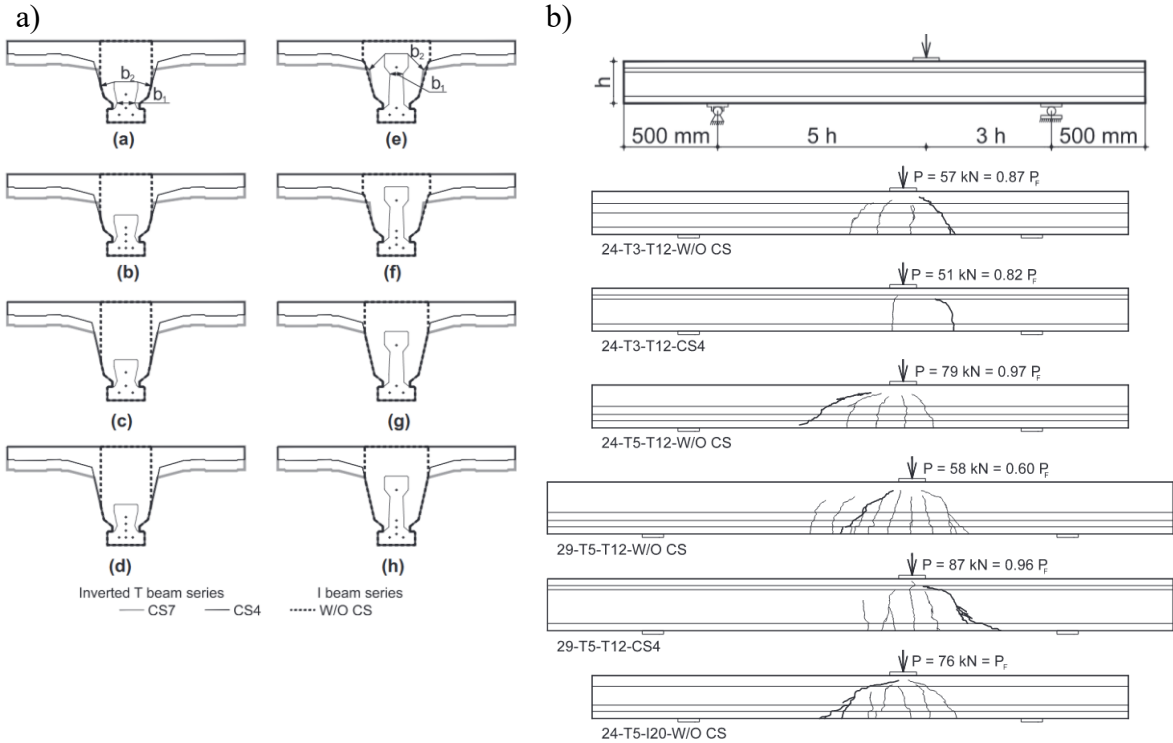


Fig. 3.39. Research of Ribas and Cladera on prestressed slab ribs: a) tested cross-sections, b) crack pattern of shear failure beam [63]

Rys. 3.39. Badania Ribasa i Cladera sprężonych żeber stropowych [63]: a) testowane przekroje, b) obraz zarysowań belek zniszczonych z uwagi na ścinanie.

An experimental research programme on concrete composite slabs featuring precast prestressed rectangular rib panels (see Fig. 3.40) was conducted by various institutions in China, initiated by Wu et al. in 2011 [149], followed by subsequent investigations by Zhang et al. in 2013 and 2019 [164,165], Wenzhond et al. in 2015 [147], Huang et al. in 2018[76], and summarising by Liu et al. in 2020 [97]. The research focused on floor panels designed with a rectangular opening, which permitted reinforcement placement in the opposite direction within the precast unit. The panels were produced in two variants: one variant included a single rib for the arrangement of effective two-way reinforcement, while the other featured two ribs solely for the distribution of reinforcement. The slabs equipped with two ribs were filled with lightweight XPS polystyrene inserts. The primary emphasis of the research was on the flexural and shear behaviour of the slabs. Notably, none of the tests resulted in delamination at the interface. However, it is important to note that the studies predominantly employed flexural schemes rather than applying forces closer to the support to maximise shear forces. Similar conclusions were also reported by Zhang et al. [164] based on long-term studies.

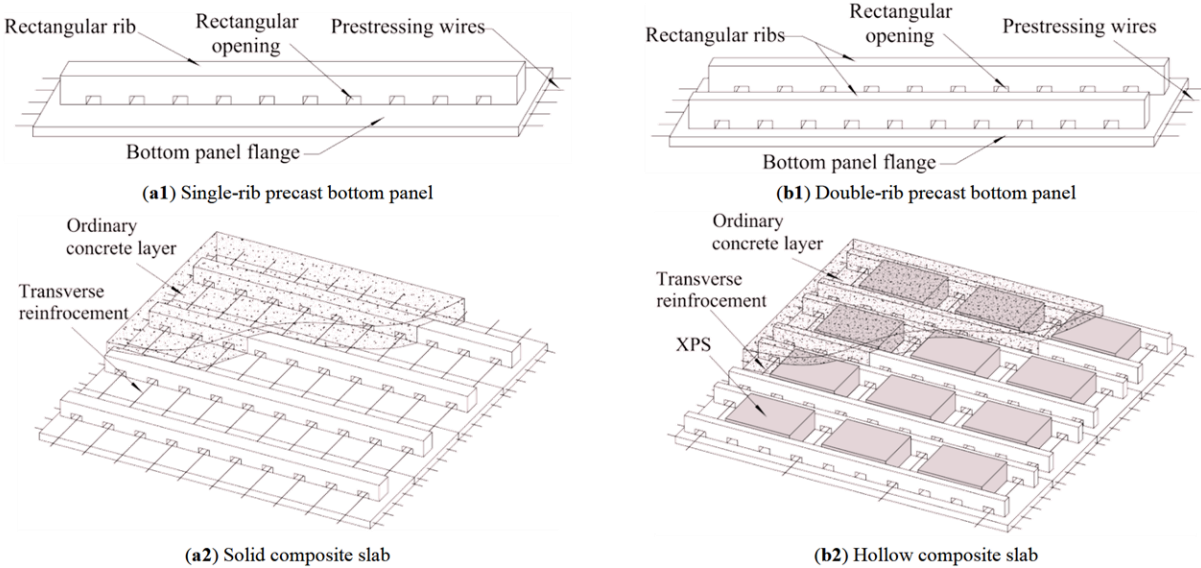


Fig. 3.40. Precast ribbed bottom panels and composite slabs [147]

Rys. 3.40. Prefabrykowany panel żebrowy oraz płyta zespolona [147]

Liu and Zhang conducted experiments on modified panels lacking second direction bottom reinforcement, while incorporating a complete top grid and a modified rib shape (Fig. 3.41). Based on their experimental tests and analyses, they concluded that the precast panel concrete slab can behave compositely. Furthermore, they found that the assumption of a plan-remain-plane condition is valid during the elastic stage. This study was supplemented by an acoustic emission test [137], which confirmed the above conclusions. Additionally, the authors determined the required % of the precast surface

that must remain composite in order not to affect the flexural behaviour. The minimum value to achieve full load-bearing capacity with minimal impact on the cracking force, while at 70%, the element behaves as a fully monolithic structure. The authors observed no differences in the behavior of the slabs based on rib shape, a finding that is further supported by additional research conducted by Huang [75].

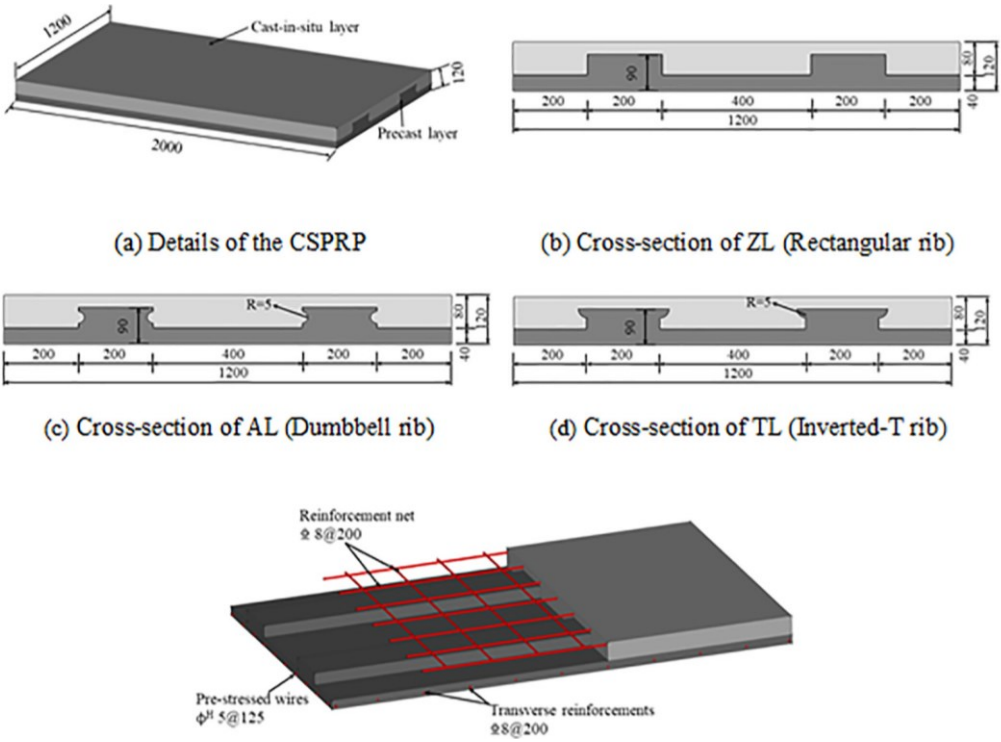


Fig. 3.41. Shaped of tested rib cross-sections of Liu research [97]

Rys. 3.41. Kształt testowanych przekroji poprzecznych żeber w badaniach Liu [97]

Han et al. conducted experiments on prestressed composite slabs featuring inverted multi-ribs, commercially known as the Joint Advanced Slab System (JAS) [72]. The research utilized a 230 mm thick precast slab, which included a 100 mm concrete topping (Fig. 3.42). N-type truss reinforcement was integrated into the ribs to facilitate joint with the concrete topping.

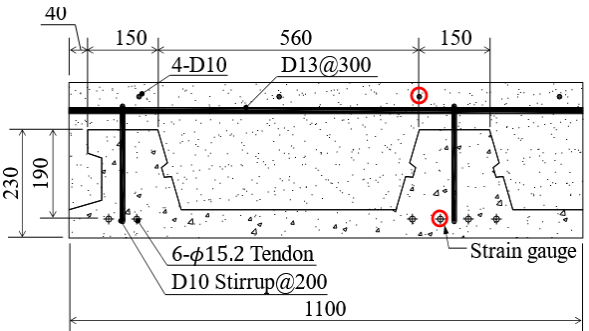


Fig. 3.42. Details of test specimens (CSt and CSf) [72]

Rys. 3.42. Detale badanych elementów (CSt oraz CSf) [72]

Tests were carried out in four configurations, two for the precast alone and two for the composite slab: USt (without topping, force in transfer zone), USf (without topping, force in strain plateau zone), CSt (with topping above ribs, force in transfer zone), CSf (with topping above ribs, force in strain plateau zone). Precast without concrete topping failed due to web-shear crack propagation in the ribs. The angle of the crack was greater for the element where the full prestressing force was present in the test section. The reverse situation occurred in the composite elements, where the crack had the smallest angle in the element with the full prestressing transmission zone. The inclined cracks occurred directly under load point, horizontal interface crack between in the PC unit slab and the cast-in-place concrete were observed. The angle of the shear crack was steeper than the shear crack than supposed. Authors state that was effect of larger cross-section of cast-in-place concrete than that of the PC unit. Also, prestressing is introduced only ic PC unit. The failure for the composite member without an off-support zone occurred for a shear force of 420.1 kN, and for the member with full prestressing in the load zone, 50% more, or 650.7 kN. In the study, the authors did not achieve full delamination of the section, and they identified a dominant diagonal crack as the failure. However, as shown in Fig. 3.43, there was visible slippage up to the support axis at the lower edge of the interface with the precast unit. As the authors indicate, the interface was still ensured by the truss connecting the rib to the concrete topping.

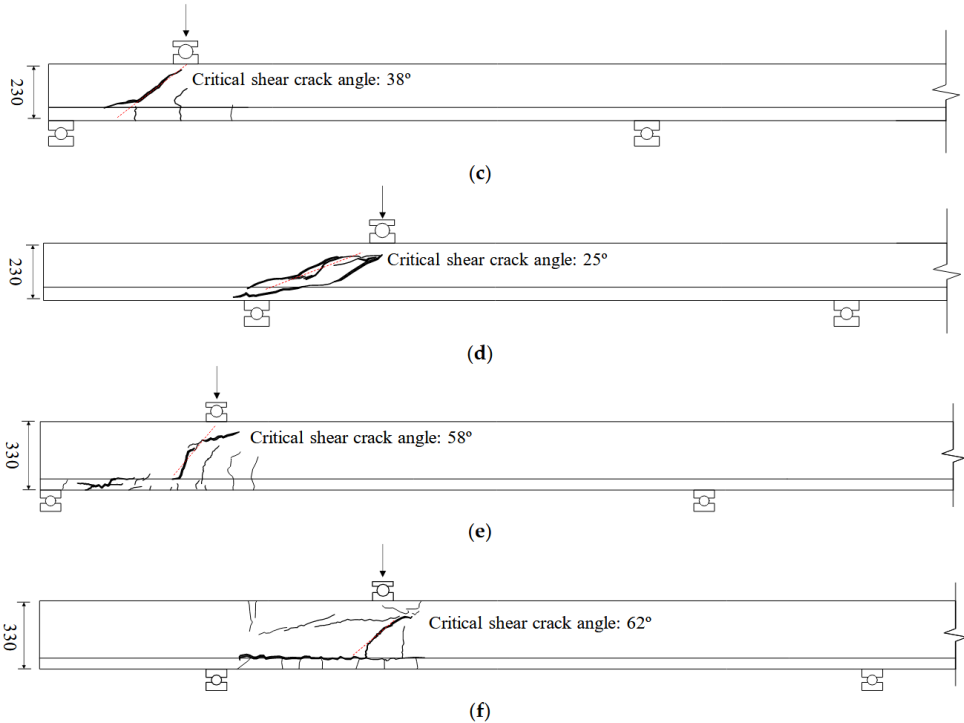


Fig. 3.43. Crack patterns at failure: c-d) precast test, e-f) composite slab [72]

Rys. 3.43. Przebieg zarysowań przy zniszczeniu: c-d) test prefabrykatu, e-f) płyta zespolona [72]

As presented by the authors, the estimation of shear strength for slabs constructed with cast-in-place concrete exhibited significant variability based on the methodology employed to calculate the shear contributions of both the precast concrete unit and the cast-in-place concrete. The authors proposed three computational models for assessing shear resistance (Fig. 3.44). They obtained relatively the best convergence for the second model considering the prestressed section and the plain concrete section. However, for the situation without adequate prestressing transmission, the calculations were on the unsafe side. As indicated by the authors the shear test results indicated that the lattice reinforcement used with concrete topping exhibited effective shear resistance performance, whereas in precast concrete without topping not contribute significantly to the shear resistance.

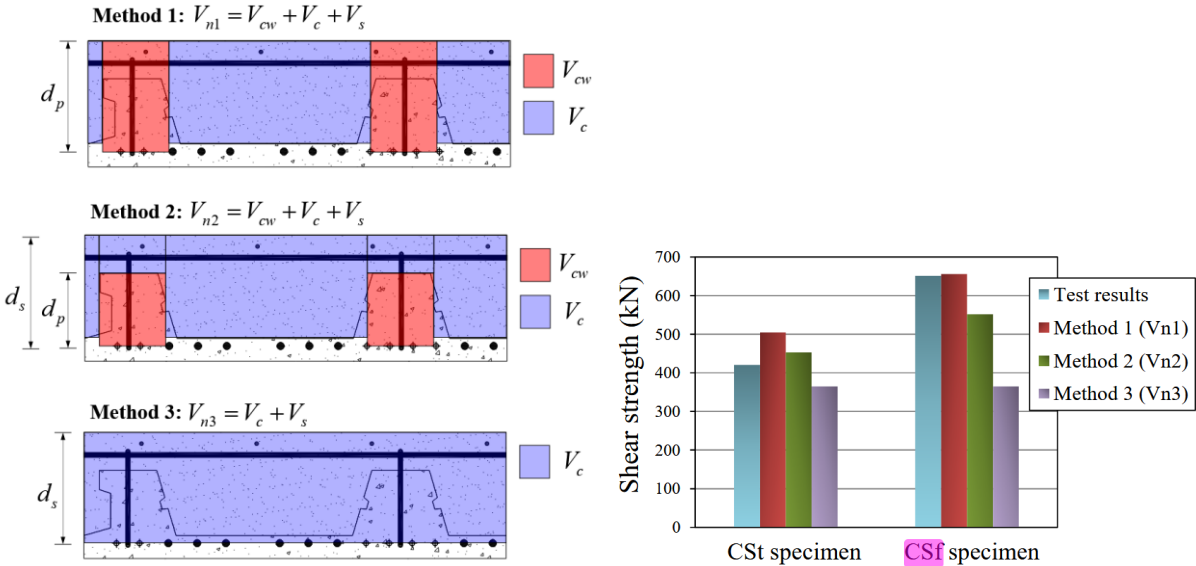


Fig. 3.44. Considered shear strength calculation methods [72]

Rys. 3.44. Rozważane metody obliczeń wytrzymałości na ścinanie [72]

A new type of precast concrete was investigated by Ju et al. [87], focusing on an optimised-section precast slab with a tapered cross-section. The cross-section of the precast element in the end section was modified to enhance interface shear resistance (Fig. 3.45). In the authors' study, no delamination was observed at the interface between the precast slab and the concrete topping. Furthermore, only a short local slip occurred at the interface, which did not extend to the edge of the support. This local slip was associated with a diagonal crack. The results obtained were compared with ACI 318-14, which overestimated the expected results. As indicated by the authors, the shear reinforcement placed in the PC slab unit specimens did not yield even at the ultimate strength. This estimation method not only revealed that the shear strengths of the

specimens (based only on concrete section) are on the safe side but also provided a highly convergence based on experimental test. Additionally, the shear crack angles observed in the composite slab specimens with the topping concrete were significantly steeper than those typically seen in reinforced concrete and prestressed concrete members.

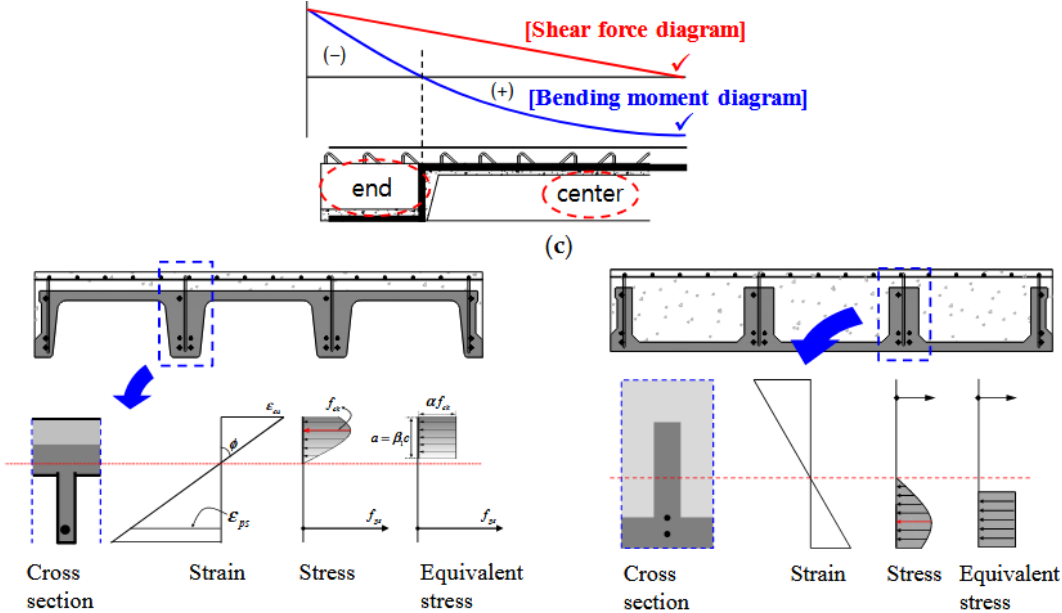


Fig. 3.45. Optimised-section precast slab (OPS) - stress distribution in the centre and end section [72]

Rys. 3.45. Zoptymalizowana płyta zespolona typu OPS – rozkład naprężeń w strefie środkowej oraz podporowej [72]

One group of solutions that are hardly classifiable are elements composite by vertical extrusions/blocks referred to as shear keys. These elements integrate the characteristics of a composite through connectors that create a concrete-to-concrete interface, thereby achieving a high stiffness within the composite system. Shear keys serve as point-to-point joints like reinforcements for girders, or as a form of 'notch' for slabs. An example of such connections in slab elements is presented in the study by Li et al. [95], where shear keys (Fig. 3.46a) are intended to replace steel trusses and fulfil their function under seismic conditions. As noted by the author, the locks at the edges of the plate in the support zones play a crucial role, engaging sequentially as the load increases.

A related concept involves the connections of girders to slabs via shear keys, as discussed by Araujo [6,36] and Afefy [2]. The connections examined incorporated bar reinforcement, with the pockets filled with concrete (Fig. 3.46 a, b). The conclusions drawn by the authors are consistent, highlighting that the most significant factor

influencing the load-bearing capacity of the connection is the strength of the concrete. The connections employed allow the elements to work like monolithic elements, however, with reduced ductility. The proposed methods provide some solutions for girders requiring composite strengthening through the implementation of point shear keys.

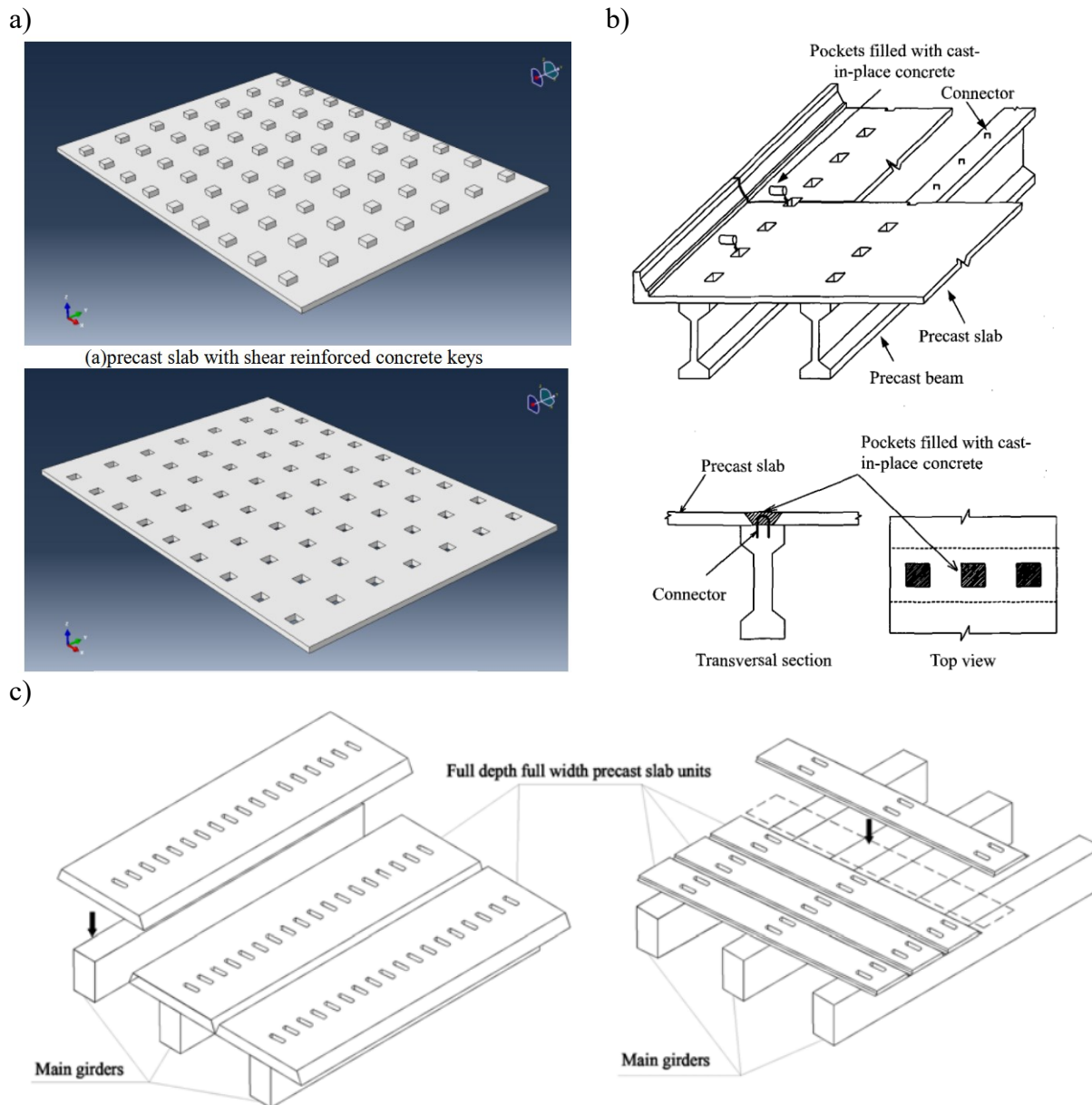


Fig. 3.46. Composite concrete elements with shear-keys: a) slab of Li et al. research [95], b) girder concept of Araujo [36], c) concept of precast system by Afefy et al. [2]
 Rys. 3.46. Elementy zespolone poprzez zamek ścinany: a) płyta z badań Li i in. [95], b) dźwigar według koncepcji Araujo [36], c) koncepcja prefabrykowanego systemu stropowego Afefy i in. [2]

Lastly, a series of tests on composite elements composed partially of concrete are discussed. Although these studies may initially appear unrelated to the primary focus of

the thesis, their implications regarding friction are relevant for further analysis. The principal load-bearing component is either a steel beam or a composite slab. This research is described in greater detail due to the intriguing conclusions drawn about vertical interfaces, which may also be applicable to concrete-concrete interfaces. The interfaces presented below go beyond the current standard framework and do not have established calculation models. The concept of vertical (sheet steel) interfaces functioning through friction and creped surfaces was introduced in studies by Dauner in 2002 [20] and by Thomann and Lebet in 2007 [143], and was designated as “connection by adherence”. This type of interface demonstrated multiple times the stiffness and load-bearing capacity compared to alternative interfaces utilising headed studs or perfobond (Fig. 3.47).

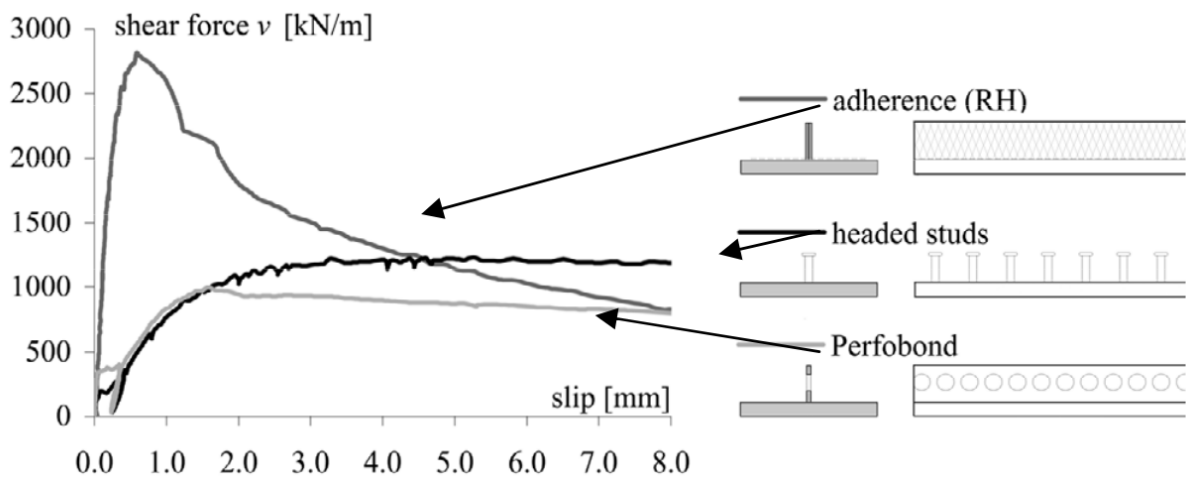


Fig. 3.47. Comparison between different vertical connection types [93]

Rys. 3.47. Porównanie różnych rodzajów łączników pionowych [93]

The concept was further developed by Lebet to cover the steel plate that is bonded with a layer of cement paste. The study described a mechanism for establishing an interface between the concrete topping layer and a vertical steel plate, which serves as an extension of the steel beam web. This plate features diagonal notches to increase friction, leading, after initial slip, to the pushing out of the concrete topping fragments (Fig. 3.48, Fig. 3.49). Consequently, significant normal forces are generated at the interface, leading to increased frictional resistance. These forces must be adequately absorbed by the rigid slab. The author concludes by recommending that reinforcement be applied as close to the abutment as possible, as this approach positively influences both the cracking behavior and stiffness of the element.

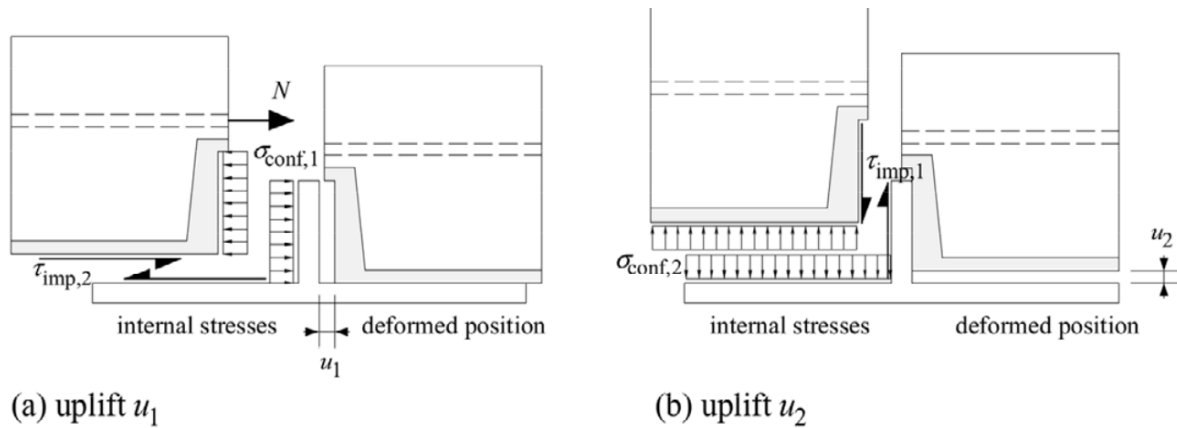


Fig. 3.48. Deformation and internal stresses forces in “connection by adherence” [93]
 Rys. 3.48. Deformacje oraz naprężenia w styku dla „połączeń przez przyleganie” [93]

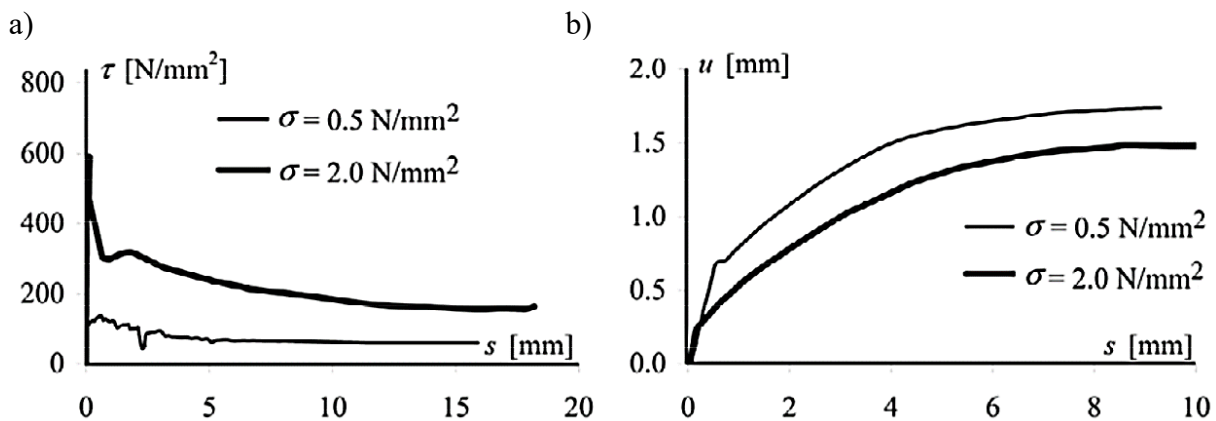


Fig. 3.49. Behaviour in direct shear test: a) slip-shear stress relationship, b) slip-uplift relationship [93]

Rys. 3.49. Zachowanie się w teście bezpośredniego ścinania: a) zależność poślizg-naprężenie styczne, b) zależność poślizg-uniesienie [93]

Research on the interface with a vertical sheet featuring a rough surface was conducted by Diogenes et al. [35], who assessed the resistance of the interface using a Perfobond sheet with an appropriate notch. According to the authors, the presence of a hole in the connector did not lead to a significant increase in resistance. The observed cracking pattern aligned with the model proposed by Thonmann (Fig. 3.48a). The cracks propagated diagonally from the edge of the plate, cutting through the concrete topping along the entire length of the element (Fig. 3.50b). In a similar study of the connectors, Hu et al. demonstrated that employing Ultra-High Performance Concrete for the bond layer resulted in shear connections as high as 15 MPa [73]. Full composite action was developed, and the integrity of the composite action was maintained after testing for two million load cycles.

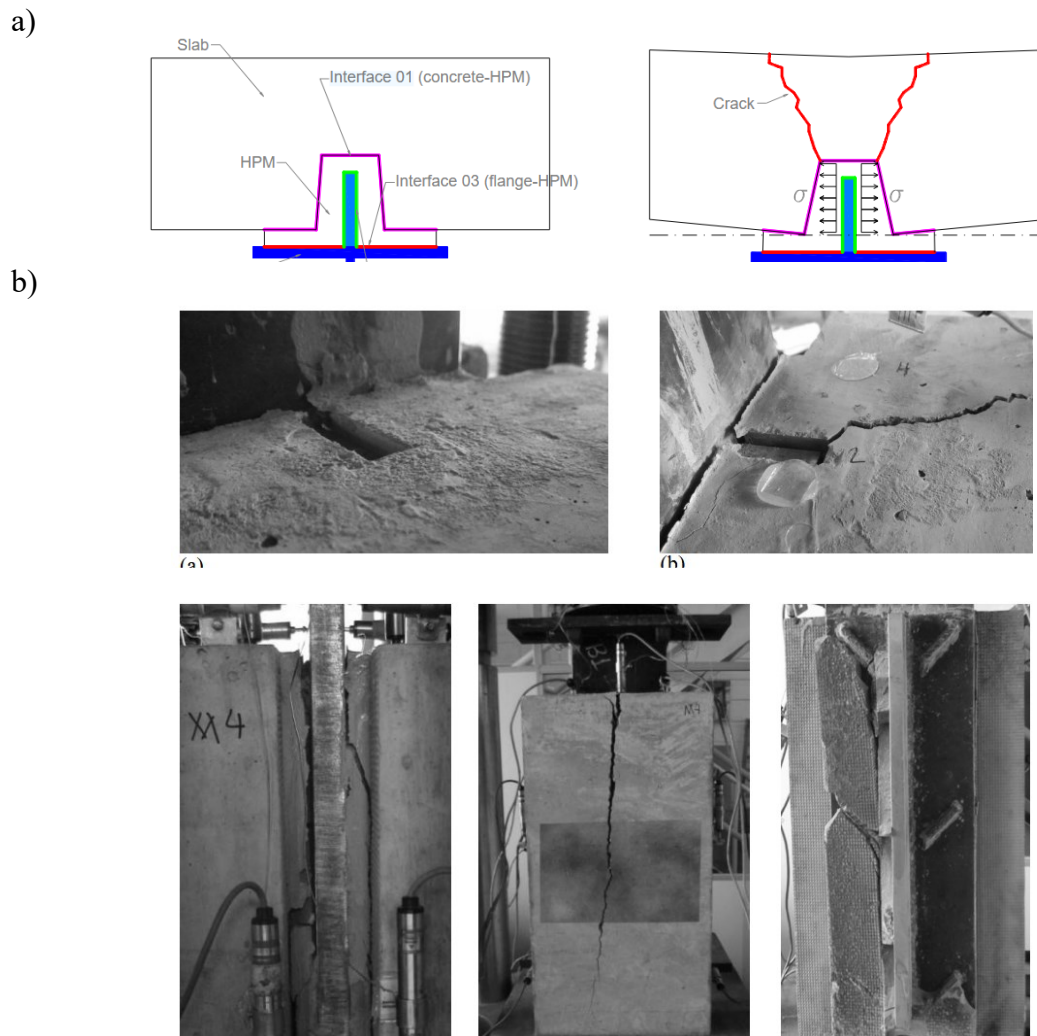


Fig. 3.50. Characteristic of connector: a) initial configuration of connection and post-peak cracking, b) view of element after the test [35]

Rys. 3.50. Charakterystyka pracy styku: a) budowa styku oraz zarysowania po zniszczeniu, b) widok po badaniach elementu [35]

An adherence-type connection was employed in a novel precast floor element characterised by a hybrid slab that integrates a Glass Fibre Reinforced Polymer (GFRP) rib with a concrete upper slab. This research was conducted by the team of Mastali et al. [102,103]. The experimental investigation utilised a 1:2 scale model with a span of 1800 mm (Fig. 3.51). A detailed description of the interface behaviour is provided in section 3.7, which discusses the modelling of the connector interface. The experimental tests revealed both uplift and vertical crack splitting effects in the concrete topping (Fig. 3.52), similar to the observations made with the steel connector. The tested slabs exhibited an almost linear response of force versus mid-span displacement up to the peak load, subsequently transitioning to a gradual softening structural behaviour. The authors conclude that the proposed hybrid slab system demonstrates a lightweight structural configuration with significant load-carrying capacity and considerable stiffness.

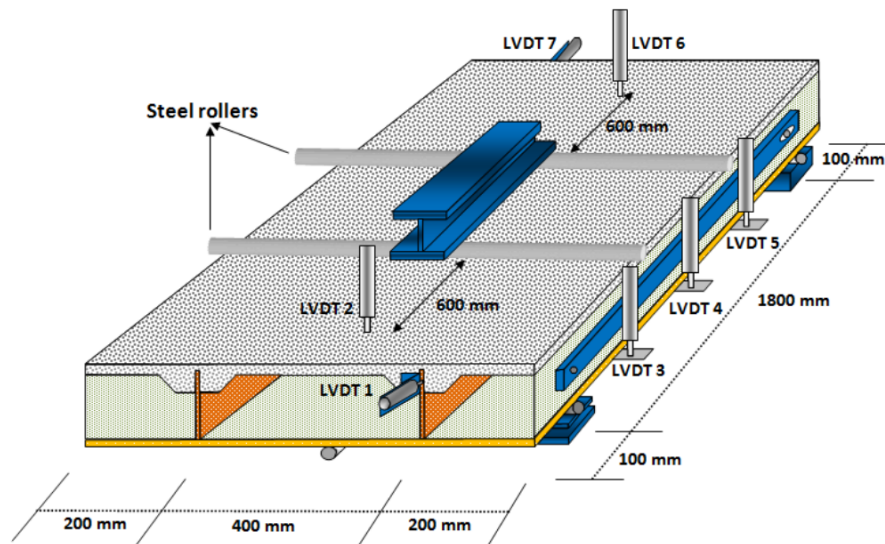


Fig. 3.51. Geometria badanego stropu i stanowiska badawczego [103]

Rys. 3.51. Geometry of the tested slab and the test stand [103]

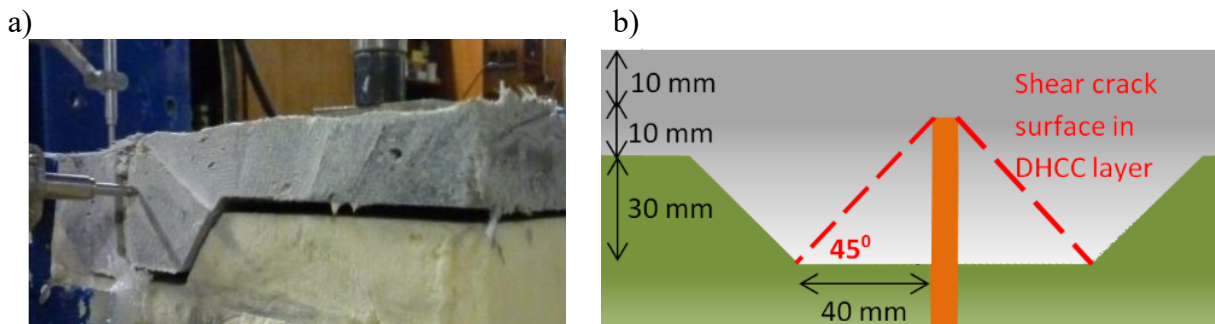


Fig. 3.52. Damages after the hybrid slab test: a) slip and uplift, b) shear crack in concrete layer [102]

Rys. 3.52. Uszkodzenia po badaniu stropu hybrydowego: a) poślizg oraz uniesienie, b) zarysowanie nadbetonu [102]

3.6.3. Examples of new and current precast slabs

The prefabrication of slabs has a history spanning over 100 years, and many of the slabs produced today do not differ significantly from those from the early days of reinforced concrete precasting. Ongoing research is directed towards both existing slabs and innovative constructions, serving as a crucial component in the evolution of slab system markets. The successful implementation of innovations relies on a comprehensive understanding of structural behaviour. Current studies explore new potentials within established structures [3,5,17,27,76,80,90,95,163], facilitating adaptation through the use of innovative materials [6,24,74,102] and the development of entirely new slab solutions [22,36,87,102,138,140]. Figure 3.53 provides a summary of both established and emerging types of slab systems, the majority of which have been examined in preceding subsections.

One- and two-way prestressed concrete planks

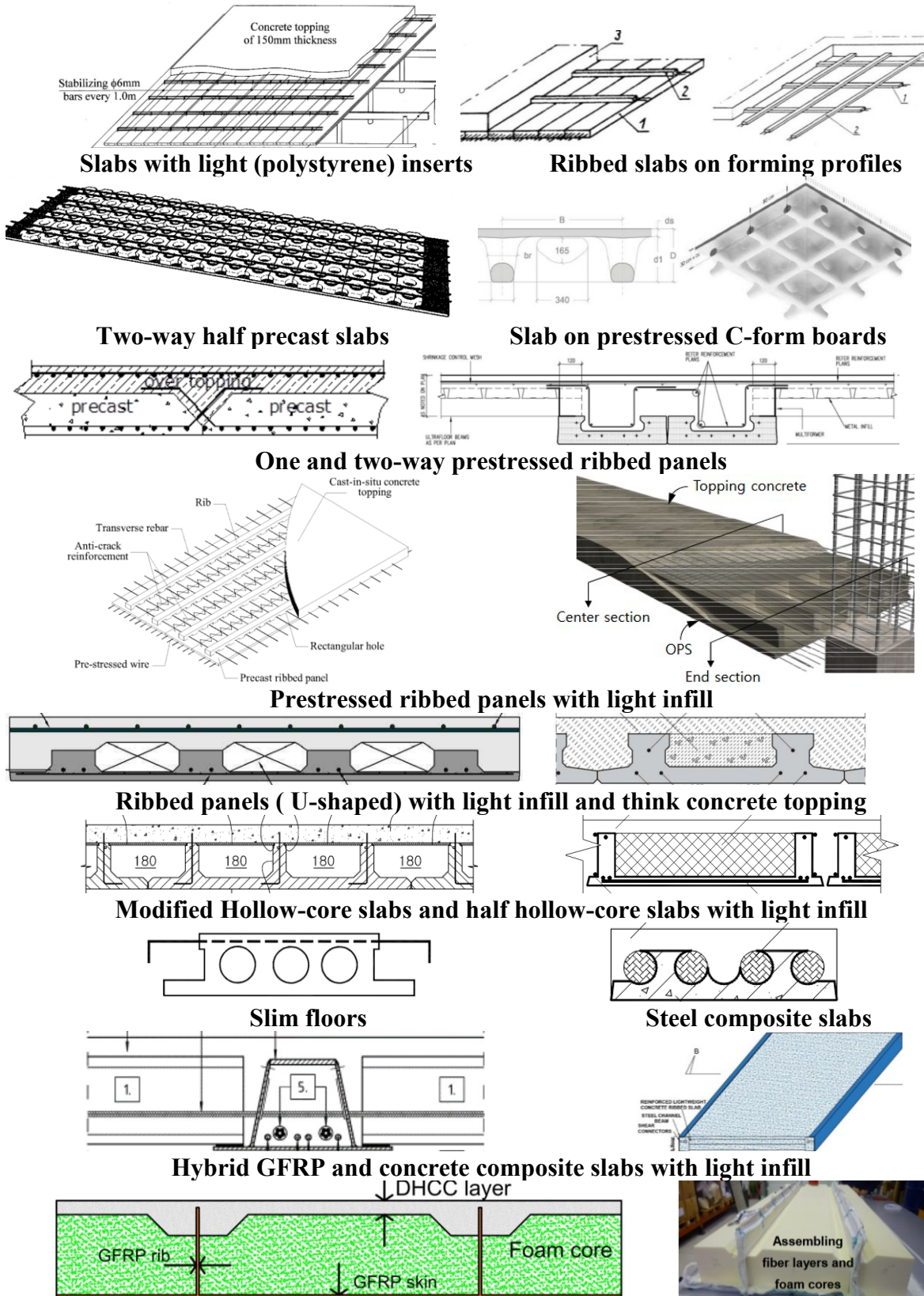


Fig. 3.53. Examples of current and new precast slabs

[3,5,22,27,36,40,76,80,87,90,95,102,138,140,163]

Rys. 3.53. Przykłady obecnych i nowych typów stropów prefabrykowanych

[3,5,22,27,36,40,76,80,87,90,95,102,138,140,163]

3.7. Modelling of composite elements

The modeling of composite structures, including concrete-concrete is based upon three distinct approaches. The first approach is macro modeling, which considers the interface as a surface (or "flat" volume) that serves as the layer connecting the two bonded modeled elements [41,83,84,132,136]. The second, more complex approach permits the incorporation of interfaces without explicit modeling, instead utilizing strong embedded discontinuity approaches (DSDA) within numerical models [34]. The third approach is meso-scale modelling, which represents the entire structural of the element at the level prior to the homogenization of concrete. The meso model considers the features of concrete as three-phase heterogeneous composite material composed of aggregate, cement mortar, and the associated bonding interface. The complex meso-structure of concrete has a direct influence on its macroscopic mechanical properties. These models take roughness into account by accurately representing it [100,111]. Due to the time-consuming calculations and often the lack of required parameters, they are not used in modelling experimental tests. Instead, trials are conducted on smaller models to validate the modeling approach, which will not be elaborated upon further. An example of such a model is illustrated in Fig. 3.54.

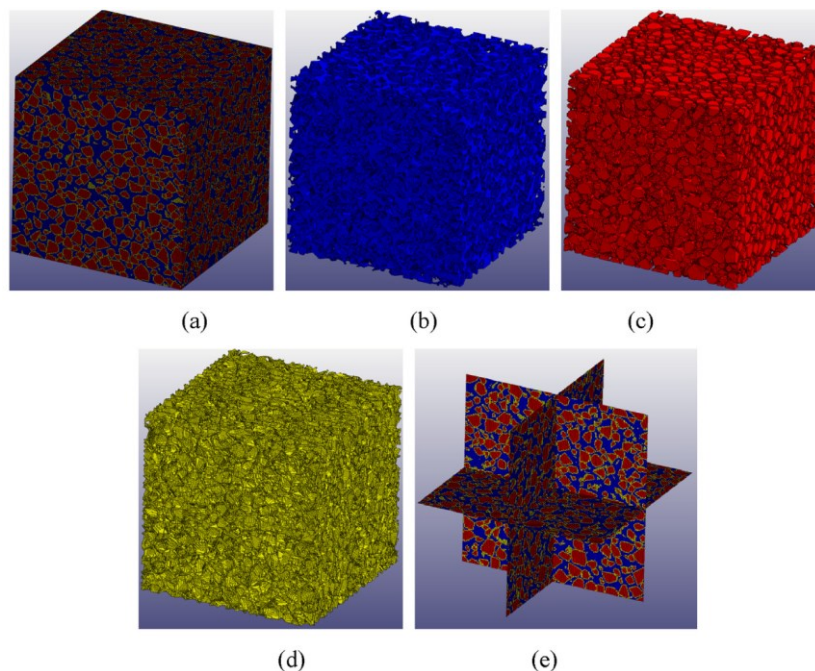


Fig. 3.54. The concrete meso-model: a) meso-finite model, b) mortar, c) aggregate, d) ITZ, e) three-dimensional symmetrical slices [111]

Rys. 3.54. Meso-model betonu: a) meso-finite model, b) zaprawa, c) kruszywo, d) ITZ, e) trójwymiarowe płaszczyzny struktury [111]

The modeling of composite structures using the macro-modeling approach primarily relies on interface models based on Mohr-Coulomb theory up to the limit force. These interfaces are characterized by parameters such as tensile strength, cohesion, tangential stiffness, and normal stiffness. When these limits are exceeded, the interfaces fail. Most models allow for interface separation and incorporate overlays to define weakening after failure [41].

3.7.1. Approaches to modeling composite elements

Modelling of composite elements is typically conducted using a macro approach, where the interface is represented as a flat surface characterised by specific material parameters. For preliminary models, interface parameters may be estimated based on established relationships and existing literature, although this method does not ensure an accurate depiction of interface performance. To accurately model the component, it is crucial to adopt a suitable modelling strategy that considers the correlation of material parameters, including tangential stiffness, tensile strength, shear strength, and failure separation. A comprehensive correlation path for a numerical model is provided in the publication by Dudziak et al. [41]. This article details a complete strategy for the calibration of the concrete-to-concrete interface model within the Abaqus software. A significant conclusion drawn from this work regards the interface model based on Mohr-Coulomb theory, wherein the authors assert that the default traction-separation model implemented in this system does not account for the strength envelope of such interfaces. Additionally, a crucial finding relates to interface failure. The limitations of the proposed approach include the model's inability to address the residual strength envelope induced by the shear-friction phenomenon and irreversible (plastic) slip. The used by authors Abaqus available traction-separation material model was developed within the framework of damage-elasticity without considering plastic behaviour.

Calibration and verification of the model were conducted using slant-shear interface test specimens. The calibrated model enabled the reproduction of test results with a discrepancy of no more than 1% in the maximum force. This calibrated FEM facilitates the extraction of supplementary information regarding the test, including the stress distribution at the interface and the progression of damage (Fig. 3.55). The numerical model was able to cover the chipping of sharp edges in slant-shear specimens. Furthermore, it was observed that the traction stress distribution is not uniform along the interface throughout the entire loading history for slant-shear specimens.

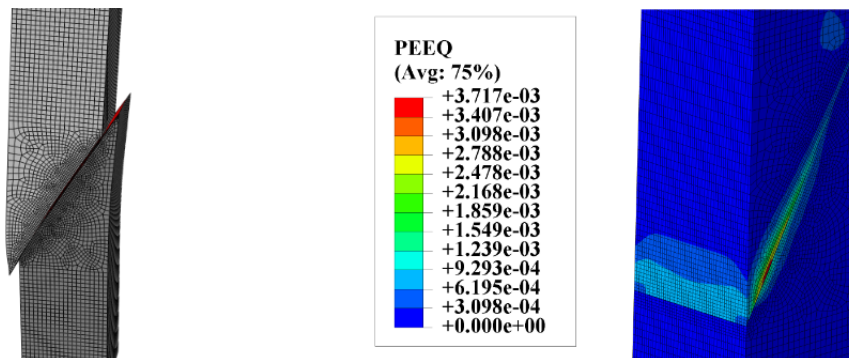


Fig. 3.55. The slant-shear model deformation after failure and map of the plastic strain in compression [41]

Rys. 3.55. Deformacje modelu slant-shear po zniszczeniu oraz mapa odkształceń plastycznych przy ściskaniu [41]

A similar approach was presented in the article by Luu et al. [101], in which direct-shear tests were employed for correlation purposes. The maximum difference at such a correlated interface, when compared to the beam models, was 6.8% for maximum force and 15.9% for displacement. The authors note the problem of accurately determining the initial stiffness in the tests, which contributes to the observed discrepancy in stiffness between the model and the test results (Fig. 3.56a). The difference in initial stiffness of a reinforced concrete beam between experimental and simulated outcomes can be attributed, according to the authors' analysis, to several factors. The first factor to consider is the presence of voids and defects, which can lead to a reduction in stiffness. The second factor pertains to the modeling assumptions, such as the incorporation of embedded reinforcement, which may not accurately depict the actual interaction between the reinforcement and concrete. This discrepancy has the potential to result in an overestimation of the beam's stiffness in the simulated model.

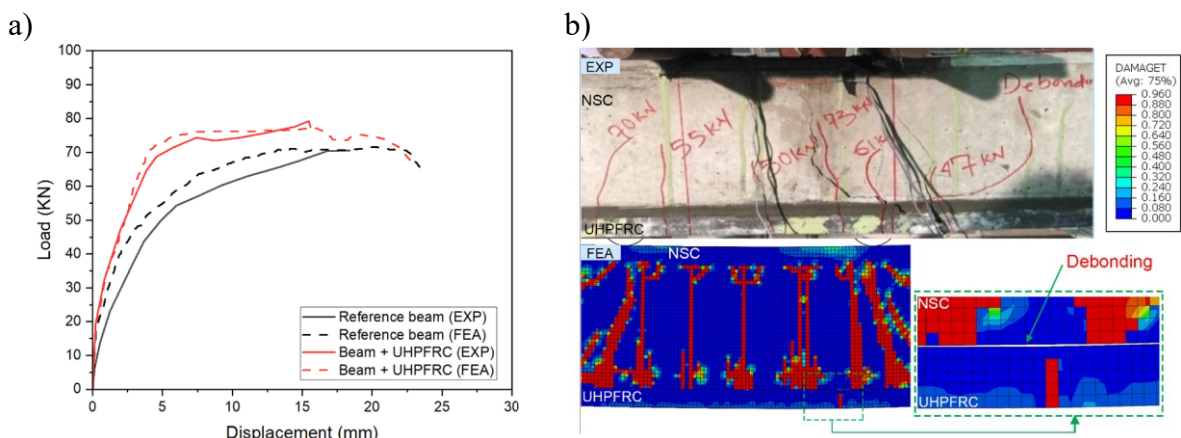


Fig. 3.56. The beam experimental test and FEM simulation: a) load-displacement characteristics, b) comparison of failure between EXP and FEM [101]

Rys. 3.56. Porównanie wyników badań doświadczalnych oraz modelowania MES: a) charakterystyka siła-przemieszczenie, b) porównanie obrazu zarysowań [101]

Calibrated models also make it possible to explain the behaviour of examinee behaviors that may initially appear contrary to established expectations. An example is the comprehensive analysis conducted by Santos and Julio [132] regarding the factors influencing the outcomes of a slant-shear test. Their modeling efforts to the reasons for the positive impact of the age differential of the constituent concretes on the results obtained in the slant-shear test. Based on a thorough stress analysis, the authors concluded that compressive loading negates the tensile stresses at the interface of slant-shear specimens, a phenomenon attributable to differential shrinkage. This analysis led to the conclusion that as the age difference between concrete layers increases, corresponding to greater differential shrinkage, the failure load of the slant-shear specimens also rises. Building upon the work of Julio's team, additional analyses concerning the influence of interface factors were undertaken [36]. Notably, these numerical models had to be calibrated with the tests. Without proper calibration, numerical models alone do not provide a reliable basis for analysis. In the paper, the authors highlighted the problem of modelling interfaces that incorporate reinforcement, particularly due to the utilization of truss elements to represent the reinforcement. They pointed out that truss elements are incapable of simulating bending, which constitutes a significant limitation of the numerical model. Consequently, the precise force of failure in the steel connectors remains indeterminate. Although this aspect lies beyond the scope of the dissertation, it underscores additional complexities in replicating the interface, particularly regarding the later stages of failure of reinforced joints.

Examples of the use of similar interface models for the representation of tests including the determination of weaknesses in the test stands carried out can be found in the literature [50,101]. An example is the analysis of an element where the intermediate layer is bonded to the main layers through two interfaces [50]. Again, the model allowed the representation of local interactions at the interface and cracking (Fig. 3.57). The authors emphasise that even numerical models that reproduce tests accurately must be subjected to additional verification on analytical models. Such analysis aims to verify if the identified failure modes and determined material and interface values can be transferred to practice-oriented applications. If an appropriate calculation model is found, layered concrete elements may be designed, so that interface failure is reliably prevented, thereby avoiding a brittle fracture.

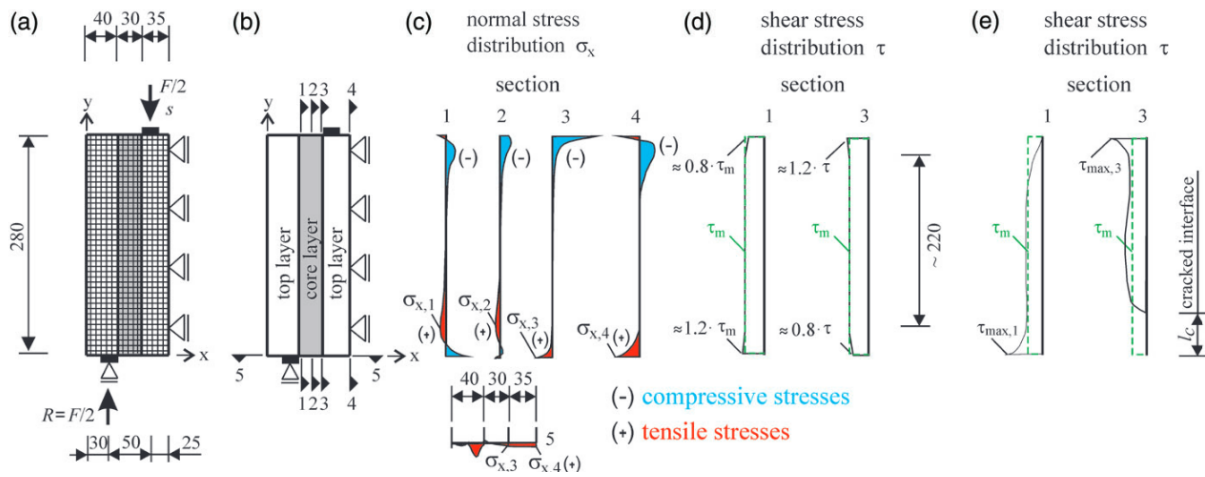


Fig. 3.57. FEM model [50]: a) model boundary condition, b) sections, c/d) normal and shear stresses in uncracked state, e) shear stresses distribution in cracked state
 Rys. 3.57. Model MES [50]: a) warunki brzegowe modelu, b) warstwy, c/d) naprężenia normalne i styczne przed zarysowaniem, e) rozkład naprężeń stycznych po zarysowaniu

More complex approaches to modelling composite structures have been presented based on the discrete strong embedded discontinuity approach (DSDA) and the generalized finite element method (GFEM) with discrete interface elements [34]. The DSDA and the GFEM allow to overcome difficulties in non-prescribed crack problems, namely remeshing. The discontinuity in DSDA (Fig. 3.58a) and GFEM (Fig. 3.58b) is located in the parent finite element, independently of mesh orientation. The use of the DSDA model allows the discrete interface element modelling step to be omitted.

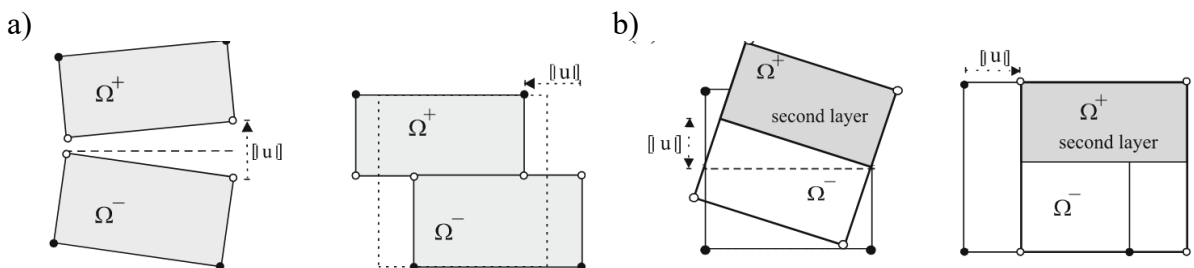


Fig. 3.58. Cracking and slipping in the mesh element [34]: a) DSDA, b) GFEM
 Rys. 3.58. Zarysowanie i poślizg w ramach elementu skończonego [34]: a) DSDA, b) GFEM

Based on numerical analyses, the authors identified two general conclusions defining the scope of applicability of the modeling methods. The discrete-interface approach is favored for modeling fixed geometric discontinuities, such as bond-slip interfaces between concrete and internal or external reinforcement, interfaces between old and new concrete, mixed structures, and masonry joints. In the context (DSDA), the discontinuity is explicitly represented as an interface element (Fig. 3.59), employing identical one-

dimensional shape functions. Consequently, integration along the discontinuity does not present any numerical difficulties; therefore, these formulations are recommended for use with stiff discontinuities, specifically penalty formulations or cracks that have been repaired using epoxy resin injection.

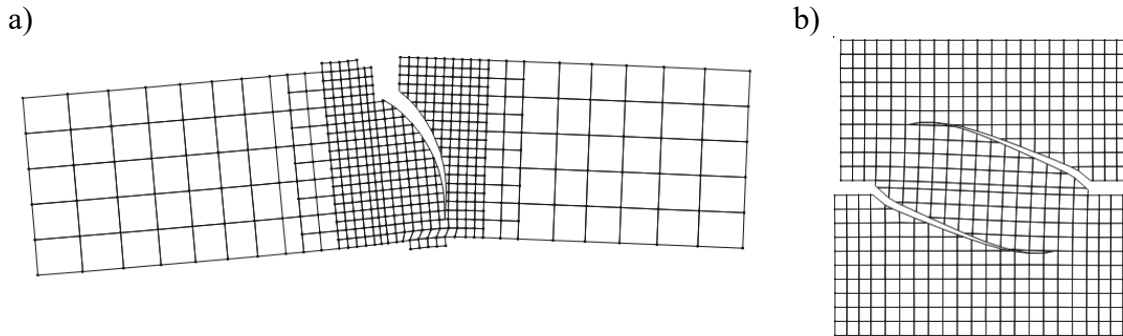


Fig. 3.59. Deformed mesh (magnified 100 times) [34]: a) single edge notched beam, b) shear with tensile force test

Rys. 3.59. Deformacje siatki (powiększenie 100-krotne) [34]: a) belka nacięciem, b) test ścinania z rozciąganiem

3.7.2. Modelling of composite elements - examples

The modelling of near-real-scale tests primarily relies on cohesive interface models in accordance with the fundamental Mohr-Coulomb assumption. When properly calibrated, these tests, particularly those involving push-off or slant-shear models, facilitate a high degree of convergence between experimental results and finite element modelling. The subsequent section presents several modelling examples of tests conducted on composite elements with interfaces of varying geometrical configurations.

Numerical analyses conducted by Jabłoński and Halicka on T-beam elements [83,84], i.e. elements with a significant difference in stiffness between the components, demonstrated a high level of compliance with the results obtained (Fig. 3.60), even in the absence of prior correlation of the interface parameters on laboratory specimens. The authors examined the influence of several factors on the response of the beam. Two parameters had the greatest influence on the behaviour of the beam. The first was the friction coefficient, whose effect became pronounced as the beam experienced cracking and the reinforcement was engaged. The second parameter was the separation displacement (slip) following failure. Based on the analyses, the authors recommend that the values should be established within the range of 0.05 to 0.1 mm. Other parameters had less influence on the behaviour of the beam with a reinforced interface. Variations in the stiffness parameters had an insubstantial effect, leading to the recommendation of a value no less than 10^5 N/mm^3 .

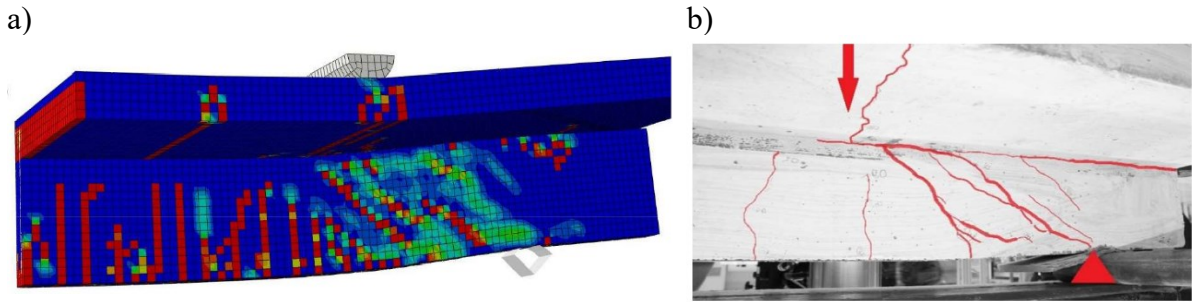


Fig. 3.60. Comparison of T-beam modelling results (a) with experimental studies (b) [83,84]

Rys. 3.60. Porównanie wyników MES belki teowej (a) z badaniami doświadczalnymi (b) [83,84]

Further research by Sadowski was conducted on elements with a notched interface [121,122]. This interface, due to its horizontal and inclined surfaces, is a kind of example of more complex geometries. This interface can operate in different slip states with the same load in different sections of the interface (Fig. 3.61). The delaminated area were the points of increased normal stresses from the reinforcement crossing the interface. The failure of the interface with the notches was also progressive. As the load increases, the cracks interface lengthened, and new ones are formed in the subsequent notches towards the support. The model showed formation of cracks in indented interface related to the appearance and propagation of shear cracks. However, the analyses did not achieve full agreement between the model and the experimental test. The difference in deflection results from the fact that in a MES model, the interface cracks occur at each notch, while in laboratory tests only in notches without crossing stirrups. In the study, the author did not provide values for the vertical opening of the interface, which would have been possible to determine from the DIC and FEM analysis. This parameter would have been interesting from the point of view of the influence of the geometry of the notches and their inclination on the behaviour of the concrete topping including the development of additional axial forces due to the geometry.

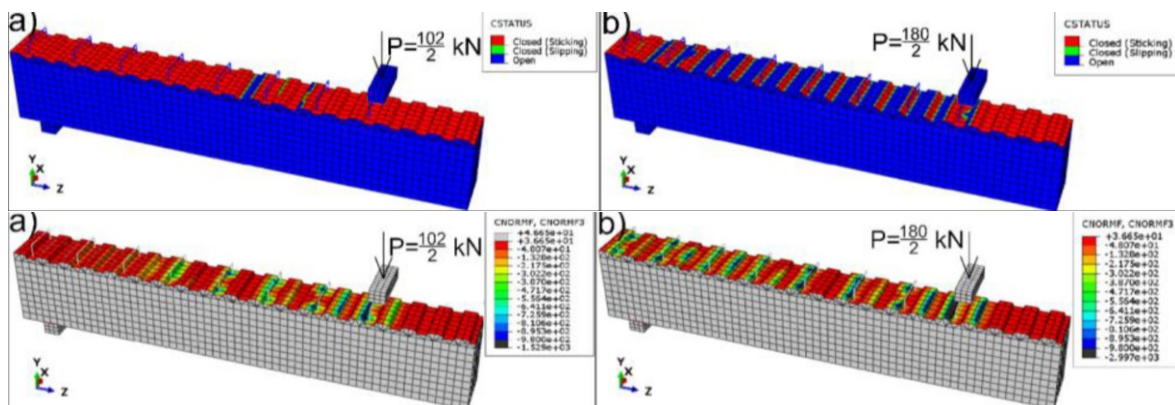


Fig. 3.61. Results of FEM analysis: a-b) slip propagation, c-d) distribution of normal stresses in the interface [121]

Rys. 3.61. Wyniki analiz MES: a-b) postępujący poślizg w styku, c-d) rozkład naprężeń normalnych w styku [121]

An example of analyses of interfaces with differing geometries is the paper by the Minho research group, which investigates a novel hybrid slab integrating glass fibre reinforced polymer (GFRP) ribs with a concrete upper slab [103]. The interface is characterised solely by a vertical configuration. A material model based on cohesion was employed for this analysis. The authors reported a high degree of concordance between the numerical modelling results and the experimental tests. The model effectively simulated the uplift of the interface and the slip between layers (Fig. 3.62). A similar failure pattern was observed for GFRP ribs in hole sections, as well as for splitting cracks in the dense high-performance concrete (DHCC) layer. The crack traversing the concrete layer was correlated with interface failure and the constraint effect exerted by the rib. Substantial shear stresses were recorded in the rib area on the vertical surface, measuring 7.67 MPa. The concrete filling the rib holes, composed of phenolic-core material, experienced shear, and the primary interface mechanism was attributed to the restraint imposed on the vertical surfaces of the rib by the concrete layer. Notably, the authors did not elaborate on their methodology for modelling the roughness (notching) of the vertical rib and, consequently, the effect of its restraint by the concrete topping.

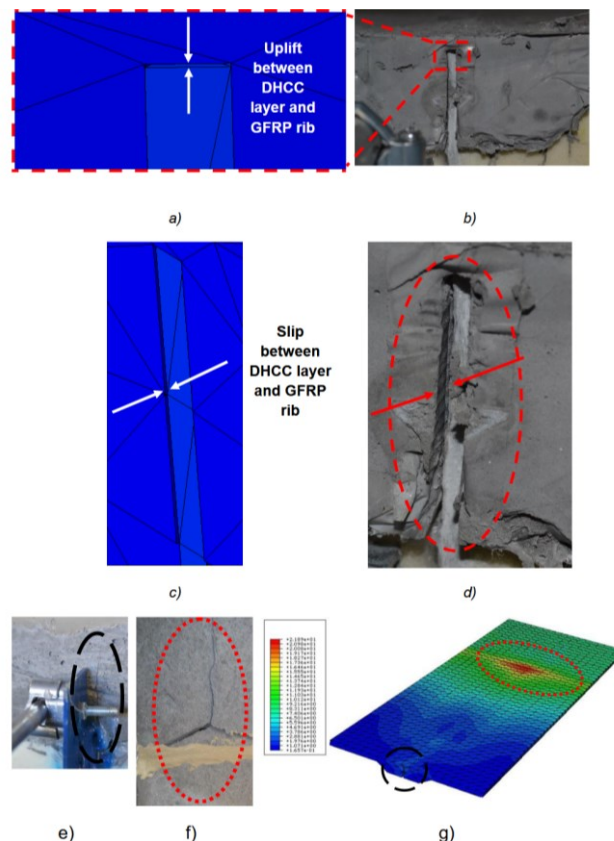


Fig. 3.62. Results of FEM analysis of hybrid slab [121]: a-b) uplift od concrete layer, c-d) slip in the interface, e-f) crack splitting concrete layer, g) stresses in the DHCC layer
Rys. 3.62. Wyniki modelowania MES płyty hybrydowej [121]: a-b) uniesienie nadbetonu, c-d) poślizg styku, e-f) rysa przecinająca nadbetonu, g) naprężenia w warstwie DHCC

The modeling approach presented in Gremza's PhD thesis [59] was discussed last. The author tried to address the phenomenon of uplift, caused by the roughness of flat interfaces, which has been described through his own research as well as other studies. This effect is counteracted by reinforcement, adjacent elements such as concrete toppings or, as explored in Gremza's investigation, by the incorporation of tie rods on which force increments were measured. Gremza proposed an alternative modeling strategy for the interface by implementing single cross-bracing elements (Fig. 3.63) that connect the two layers. These cross-braces are designed to function solely under compression. Depending on the specific model, Gremza constructed cross-braces dedicated to the test direction, as well as opposing ones, to facilitate universal applicability of the method. Furthermore, the author compared this modeling technique involving flat interfaces while also modifying parameters to account for concrete swelling.



Fig. 3.63. Modelling the interface through diagonal cross-bracing: a) idea, b) finite element system [59]

Rys. 3.63. Zamodelowanie styku poprzez ukośne krzyżulce: a) idea, b) układ elementów skończonych [59]

For FEM flat interfaces, there was no observed increase in force within the tie rods. Allowing the concrete to undergo swelling due to plasticization did not lead to convergence with the experimental tests. Only the approach incorporating cross-bracing that permitted the rods to engage effectively. Gremza's numerical analysis highlighted the limitations of modeling interfaces as a single plane (surface), as it failed to account for the inherent natural roughness prior to failure during the linear-elastic phase. The model featuring cross-bracing was the only one that accurately represented the failure of the element with rods and an unreinforced interface.

3.8. Conclusions of the literature review

Based on the literature review presented, it can be concluded that the characteristics of the concrete-concrete interface, particularly regarding the parameters that influence the strength of the interface, have been recognised to a considerable extent. However, the differences identified among various studies are frequently not significantly greater than the range of variation observed in results, which typically falls between 10% and 25% for tensile strength tests of the interface. Frequently, the discrepancies between studies conducted by different authors can be attributed to the use of diverse test specimens. Therefore, it is essential that comparisons are made solely between similar test types, even though different testing methodologies may theoretically lead to equivalent strength parameters. Many of the available methods do not permit the separation of the tested influences and, as seen in push-off or direct-shear tests, are subject to local edge effects or bending influences. The aspects shaping the interface can be summarised in the following points, which relate to the subsequent interface parameters:

- Surface roughness positively influences the strength of the interface, including its ductility.
- An extended interval between the cast of successive layers has a negative effect on the strength of the interface.
- Differences in shrinkage between concretes cast at different times result in additional forces at the interface, the effect of which depends on the loading pattern considered. In the flexural elements, shrinkage should be considered as a negative phenomenon.
- The strength of the interface is not solely determined by the properties of the weaker concrete but is a more complex sum of the factors associated with the constituent concretes.

The current standard provisions do not fully recognise the complexity of interface characteristics, and calculations based on standard procedures result in significant discrepancies with experimental results. Within a single set of PN-EN standards, it is possible to specify interface parameters that differ substantially for similar surface characteristics. The current standards do not provide additional guidance for the multiplanar interface and are limited to general rules for determining joint width, without considering the varying shear stress distributions across the height of the cross-

section. Additionally, the standards do not account for the complex mechanics of interfaces, including phenomena such as local cracking and stress redistribution.

With reference to the experimental results on test specimens and flexural elements, it can be concluded that flat interfaces are relatively well recognised. There are far fewer studies on interfaces with complex geometries. The limited research on multiplanar interface elements, which frequently occur as unreinforced elements, tends to emphasise flexural behaviour rather than the specific complexities of the interface itself. Based on the experimental studies presented, it can be concluded that:

- The interfaces are subject to local cracking, which does not indicate a failure of the composite element.
- The anchoring of the reinforcement within the concrete topping, or a sufficiently extended interface of the support axis, can facilitate a fully composite element, despite the occurrence of cracking at the interface with the support axis.
- In the research on multiplanar interfaces, the majority of the tests did not achieve delamination, with some tests reports local slip.
- The vertical interfaces, despite their small width, have a significant load-bearing capacity due to the frictional restraint provided by the concrete topping, which prevents delamination at the interface.

Experimental studies are often combined with modelling approaches that utilise the finite element method. The models applied to both flat and reinforced interfaces demonstrate a significant correlation with empirical findings. FEM models serve as a reliable tool for analysing stress distribution and the behaviour of interfaces, including local slip phenomena. However, models based on Mohr-Coulomb theory do not comprehensively capture all characteristics of the interface. Notably, accurately accounting for the effects of roughness in unreinforced interfaces poses a particular challenge, as these interfaces are characterised by opening before and after cracking. This limitation inhibits the consideration of additional effects arising from the partial restraint of interfaces by concrete toppings on vertical surfaces, as well as those interfaces subjected to pre-stressing by external elements.

4. OBJECTIVES AND STATEMENTS OF THE THESIS

4.1. Objectives of the dissertation

The literature review identified gaps in the recognition of the behaviour of multiplanar interface elements. Inconsistencies between the standard provisions were highlighted, revealing that current calculation methods insufficiently reflect the complexity of composite element behaviour. To address the identified research gap, this study adopts both theoretical and experimental approaches, with the following primary issues under which specific objectives have been established:

1. Behaviour of an element with multiplanar unreinforced interface subjected to direct shear.
 - 1.1. Analysis of the cooperation between interface planes.
 - 1.2. Influence of element geometry on internal force distribution.
 - 1.3. Force-displacement characteristics of interfaces, including the possibility of a non-linear extent before cracking.
2. Flexural behaviour of elements with multiplanar unreinforced interface.
 - 2.1. Analysis of the cooperation of the interface planes within a beam under bending.
 - 2.2. Analysis of the influence of local cracking on the flexural stiffness of beams.
 - 2.3. Impact of interface stiffness and local slip on the redistribution of internal forces in the multiplanar interface.
 - 2.4. Influence of anchorage length of the element outside the support on the interface resistance and flexural stiffness.
 - 2.5. Analysis of the effect of diagonal cracking on the development of slip at the interface.
 - 2.6. Effect of different contributions of stresses caused by the external normal forces in dependence on the interface position and plane (vertical or horizontal).

- 2.7. Possibility of the beam behaviour as partially composite only due to local compression from a point load.
3. Development of numerical models to represent the test conditions.
 - 3.1. Reflecting interface performance before and after cracking in direct shear and flexural beam elements.
 - 3.2. Analysis of stress distribution and interface planes efficiency.
 - 3.3. Separation of the phenomena impacting the behaviour of composite elements.
 - 3.4. Establishing interface parameters based on a correlation procedure allowing further analysis of elements with a different geometry or under a different set of boundary conditions.
4. Recommendations for the design and calculation of the multiplanar interface.
5. Providing a framework for further analysis of full-scale elements, including composite slabs consisting of multiple elements with a multiplanar unreinforced interface.

4.2. Statement of the thesis

Based on the literature review and the issues outlined in the introduction, the following thesis were assumed:

1. The cooperation between the interface planes in the composite element dependent on the position at the height of the cross-section.
2. Multiplanar unreinforced interfaces responded non-linearly before slip failure.
3. The increased shear resistance of the vertical interface planes results from the restraint effect.
4. The lengthening of the composite beam beyond the support axis allows the quasi-monolithic behaviour despite slip in the interface up to support axis.

5. RESEARCH PROGRAM

5.1. Research campaign

As summarised in the literature review, the majority of systematic research on the composite of beam elements focuses on flat interfaces. Studies on elements with more complex composite geometries are rare and focus on single elements, often not posing the interface issue as the main research subject. To realise the stated objectives and to verify the theses posed, a research programme of experimental studies was designed to determine the behaviour of composite concrete elements with unreinforced multiplanar interface. The research was preceded by preliminary tests on elements with a flat interface. The main study was divided into three stages. Stage one consisted of direct shear tests. Tests were carried out in the second and third stages on beam elements in three-point and four-point bending. The tests were conducted on the ribs of a precast prestressed slab manufactured in Poland. The test elements represent a section of this floor. The tests were divided into three main stages with the following assumptions and objectives:

1. Initial tests:

- 1.1. The elements were prepared using precast pre-stressed beams with 120 x 120 mm sections and a flat interface (trade symbol SBN 120/120). The concrete topping was 40 mm thick.
- 1.2. Four variants of the flat interface surface were made to select materials and methods for preparing the main test elements.
- 1.3. The behaviour of the elements before and after adhesion breakage at the interface and the failure type were verified.
- 1.4. The research aimed to determine the materials for the main elements and verify the suitability of the planned measurement methods, i.e., the Aramis digital image correlation (DIC) system and linear variable differential transformer (LVDT) sensors to measure slip at the interface.

2. Direct shear test:
 - 2.1. The test was carried out on elements with the same geometry and properties prepared for the main research.
 - 2.2. The tests were used to determine the interface's characteristics and the slip's value corresponding to the interface's failure.
 - 2.3. The test results correlated with the FEM modelling will be used to determine the interface parameters.
3. Three- and four-point bending tests:
 - 3.1. Tests were carried out on precast pre-stressed beam elements (with the trademark S-Panel 120) with a concrete overlay. The tested element represents the actual precast slab element (add-on beam).
 - 3.2. The support and anchorage lengths of the element were chosen to ensure the transmission of the prestressing force to the load application point. The design aimed to verify and minimise the influence of the development of cracking on the local slip at the interface.
 - 3.3. To determine the performance characteristics of composite elements with multiplanar unreinforced interface subjected to bending and shear.
 - 3.4. Determination of the influence of the position of the interface.
 - 3.5. Verification of the influence of local compression from a point load.

5.1.1. Initial tests

Initial tests were carried out on prestressed beams of width and height equal to 120 mm, with a 40 mm thick layer of concrete topping. The beams were made of C40/50 design-grade concrete, and the prestressing consisted of three Ø6.85 mm 7-wire strands (1 x Ø2.24 mm + 6 x Ø2.40 mm) of Y2060S7 steel. The results of the concrete and steel tests are presented in section 6.1. The top surface of the precast beam was untreated smooth according to the criteria of Model Code 2010 and EN 1992-1-1. Four different types of top surfaces were prepared (Fig. 5.1), according to which the following symbols were assigned to the test elements:

- B1.X-C - beam with the untreated top surface,
- B2.X_F - beam with top surface half-covered with PE foil,
- B3.X_P - beam with top surface half-covered with PVC mat,
- B4.X_O - beam with the top surface covered with the anti-adhesion agent,

where X indicates the number of the next element of the same type.

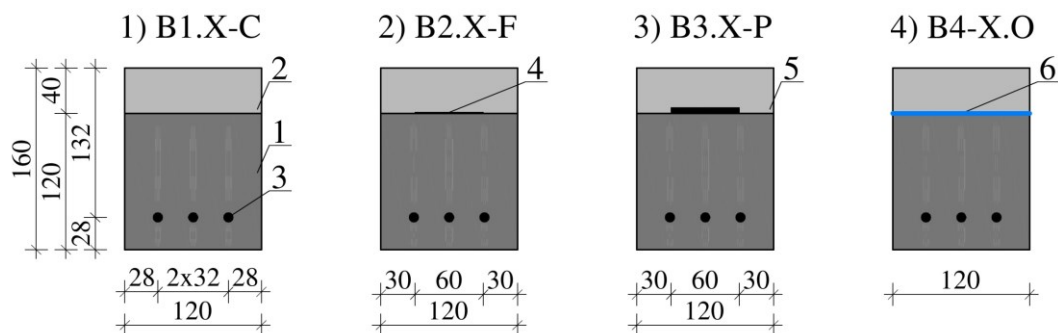


Fig. 5.1. Initial test beam cross-section: 1- precast, 2- overlay, 3- strands, 4- PE foil, 5- PVC mat, 6- antiadhesion agent

Rys. 5.1. Przekrój poprzeczny belek do badań wstępnych: 1- prefabrykat, 2- nadbeton, 3- sploty, 4- folia PE, 5- mata PCW, 6- środek antyadhezyjny

Covering half of the interface with PVC or PE foil was intended to limit adhesion due to chemical adhesion and friction. The PVC or PE was only point-glued to the precast for assembly purposes. In addition, B4.X-AB elements with broken chemical adhesion were tested, but the intention was to maintain the friction of the precast unit surface. In the beam, the composite surface was coated with an antiadhesion agent. The tests were carried out in a four-point bending test, using a steel crosshead to transmit loads at a distance of 400 mm to the support axis ($a/d = 3.0$). The elements were supported, leaving a 250 mm length beyond the support axis (Fig. 5.2).

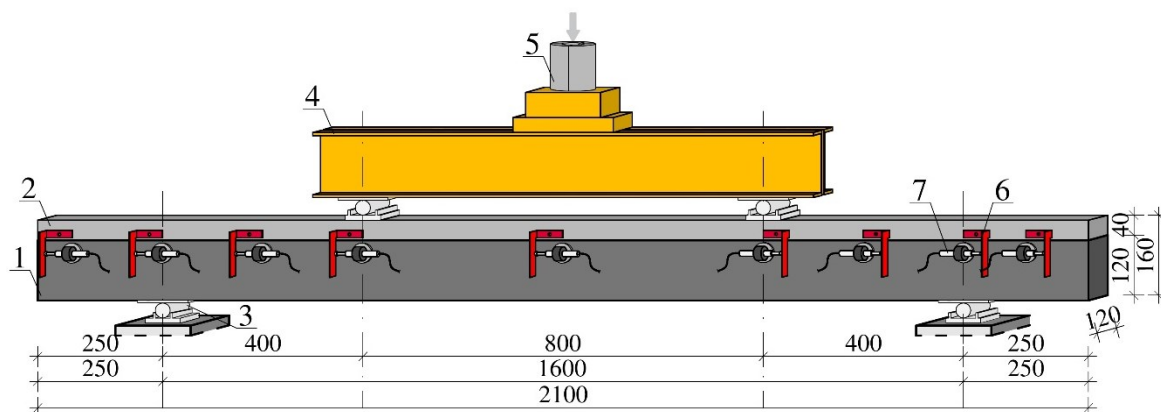


Fig. 5.2. Test stand of initial test beam: 1- precast, 2- overlay, 3- support, 4- steel traverse, 5- force gauge, 6- slip measuring base, 7- LVDT sensor

Rys. 5.2. Stanowisko badawcze belek wstępnych: 1- prefabrykat, 2- nadbeton, 3- podpora, 4- trawers stalowy, 5- siłomierz, 6- baza pomiarowa poślizgu, 7- czujnik LVDT

The load was applied using a hydraulic actuator with an electric pump through a steel crosshead on which an actuator was placed. During the elastic phase, the load was applied uniformly at a speed of approximately 0.5 kN/s, and then the pressure in the

system was adjusted until the beam failure. The measurement results were recorded continuously at a frequency of 0.5 seconds.

Two measurement methods were used. Nine LVDT sensors were attached to one surface of the beam for reference measurement of slip at the interface. The sensors were attached to the precast element, and the measuring base plates were fixed to the concrete topping. The positions of the sensors are shown in Fig. 5.2 and Fig. 5.3. On the second surface, a measurement pattern was prepared to measure with the Aramis digital image correlation (DIC) system. The system was used to measure the displacement of the element, allowing the test bench to be separated from the deformation.

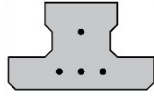




Fig. 5.3. View of the beams: a-b) during and after execution, c-d) on the test stand
Rys. 5.3. Widok belek: a-b) w trakcie i po wykonaniu, c-d) na stanowisku badawczym

5.1.2. Direct shear tests

Direct shear tests were aimed at determining interface parameters such as initial stiffness, coefficient of friction and cohesion. The tests were carried out on elements cut from beams made for the main tests. The elements tested were T-shaped beams with a width of 200 mm and a height of 120 mm, with a concrete topping of 45 mm. The precast beams were made of concrete designed as C40/50, and the concrete topping was designed as class C25/30 (test results in Section 6.1). A detailed description of the reinforcement is given in the next section. Three element types (Table 5.1) from ten elements (described in subsection 5.1.3) were designated for testing. The first was a precast element with a natural untreated surface, the second (AB type) was an element with an interface coated with an anti-adhesion agent, and the third (CB type) was entirely covered with a 0.3 mm thick mat. The anti-adhesion agent reduced chemical adhesion while leaving mechanical adhesion and surface roughness. The matting was used to break chemical and mechanical adhesion and reduce friction between the components. GAMBIT AF-300 mats based on aramid fibres (KEVLAR®), mineral fibres and fillers bound with a binder based on a rubber mixture were used. The mats were coated with a release agent before concreting.

Table 5.1
Designation of elements based on the interface type
Podział elementów ze względu na rodzaj zespolenia

Element designation	Cross-section	Concrete interface width, mm	Effective width ratio	Top surface	Side surface	Bottom surface
Z1.2-C		367	1.0	x	x	x
Z2.2-AB		367* Anti adhesion agent	1.0*	*	*	*
Z3.2-CB		-	-	-	-	-

The composite element has the same thickness as the precast's bottom flange and the concrete topping's top flange. Figure 5.4 shows the centre of mass of the precast and the concrete topping to the centre of mass of the composite element. The load was applied through steel plates at the centre of mass of the composite element.

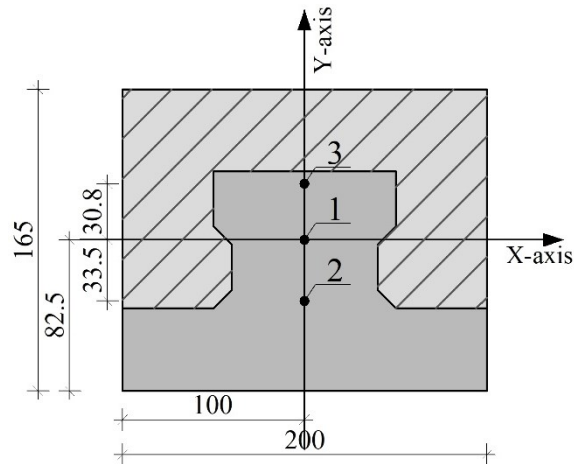


Fig. 5.4. Centres of gravity: 1- composite section, 2- precast, 3- concrete topping

Rys. 5.4. Środek ciężkości: 1- przekroju zespolonego, 2- prefabrykatu, 3- nadbetonu

The load was applied using a hydraulic actuator with an electric pump. To transmit the force to the cross-section of the element, steel plates were designed with a dimension reduced by 5 mm to the concrete topping and precast cross-section (Fig. 5.5). To reduce friction and compensate for surface irregularities, Teflon (PTFE) spacers were placed between the plates and the specimen. The elements were integrated into a dedicated test stand, where the force gauge was mounted to a steel crosshead, a part of the frame (Fig. 5.6) made of two columns and two beams. The load was applied to the test element steadily at a rate of 0.5 kN/s in the elastic phase, and the pressure in the system was then adjusted according to the element's behaviour until failure. Measurement results were recorded continuously at a frequency of 0.2 seconds.

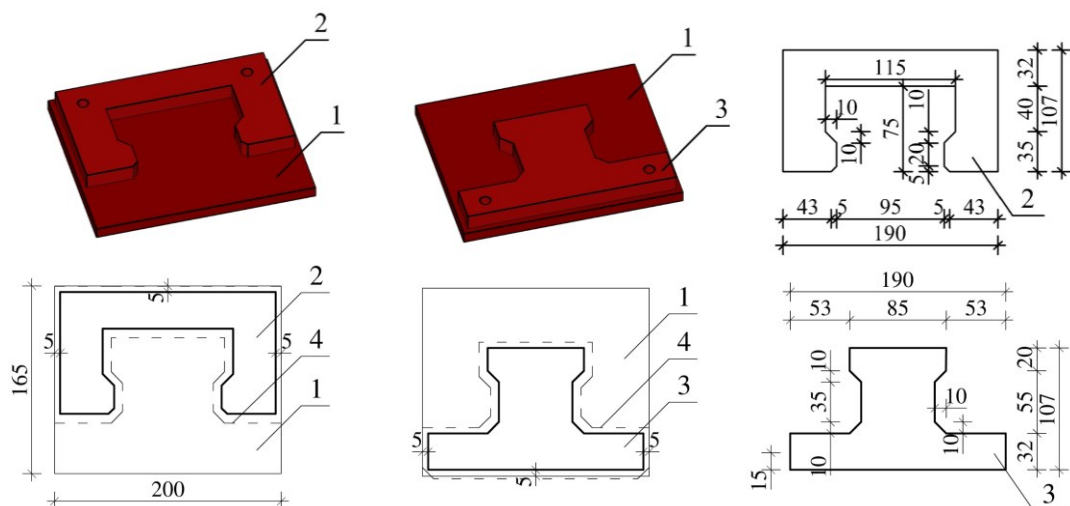


Fig. 5.5. Force transfer steel plate: 1- main steel plate, 2- overlay steel plate, 3- precast steel plate, 4- precast and overlay cross-section outline

Rys. 5.5. Stalowe blachy do przekazania siły: 1- blacha stalowa, 2- blacha o kształcie nadbetonu, 3- blacha o kształcie prefabrykatu, 4- kontur przekroju prefabrykatu i nadbetonu

Two measurement methods were used. A single laser sensor (LDS) was set up on the two side surfaces to measure displacements along the interface. On the bottom surface of the precast element, two opposing LDS sensors were set up to measure displacements of the concrete topping in the plane perpendicular to the rib head. A pattern was made on one of the surfaces for measurements with the Aramis digital image correlation (DIC) system (Fig. 5.7). Using the measurement capabilities in three dimensions, the slip of the interface, the rotation of the element and the outward displacement of the concrete topping (perpendicular to the rib) were verified.

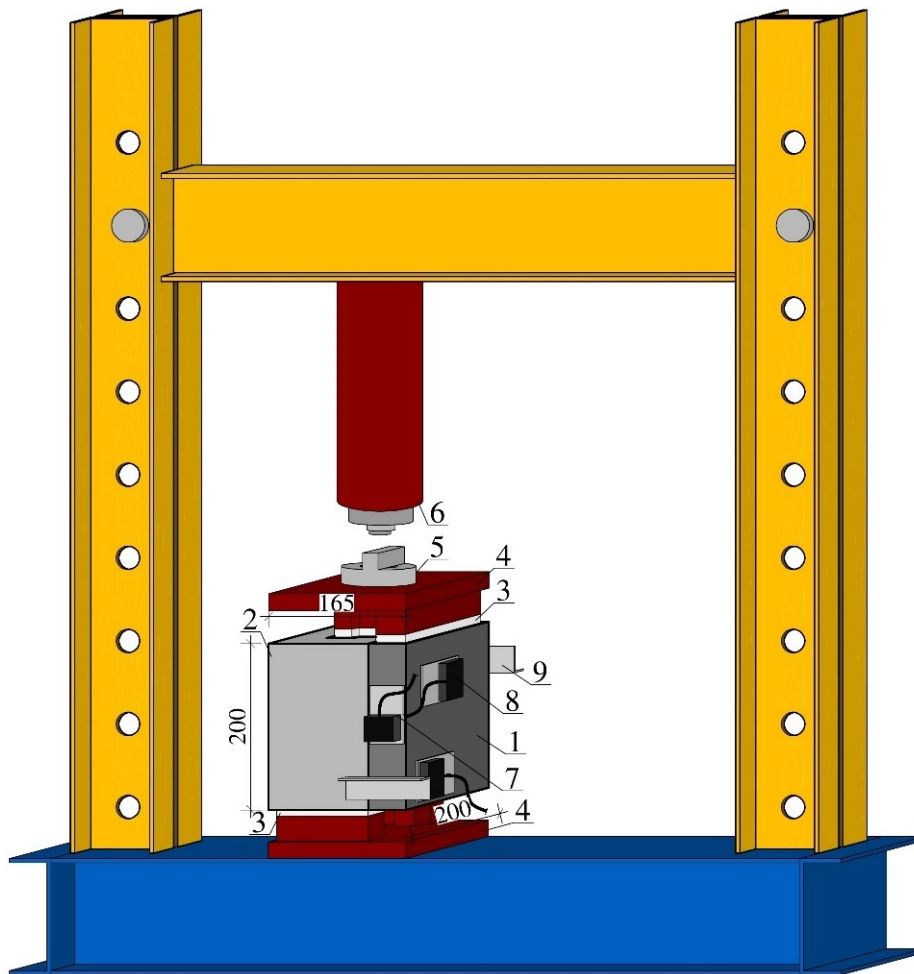


Fig. 5.6. Direct-shear test stand: 1- precast, 2- overlay, 3- PTFE, 4- steel plate, 5- force gauge, 6- hydraulic cylinder, 7- vertical LDS, 8- horizontal LDS, 9- measuring base

Rys. 5.6. Stanowisko badawcze bezpośredniego ścinania: 1- prefabrykat, 2- nadbeton, 3- podpora, 4- trawers stalowy, 5- siłomierz, 6- siłownik hydrauliczny, 7- pionowy czujnik laserowy, 8- poziomy czujnik laserowy, 9- baza pomiarowa



Fig. 5.7. Widok elementu na stanowisku badawczym

Rys. 5.7. View of the element on the test stand

5.1.3. Three- and four-point bending test

The main research was carried out on prestressed ribbed beams as described in Section 5.1.2. The prestressing consisted of four 7-wire strands ϕ 6.85 mm (1 x ϕ 2.24 mm + 6 x ϕ 2.40 mm) of Y2060S7 steel. The lower three were placed at an axial distance of 25 mm from the bottom surface and the upper strand at 80 mm. According to the manufacturer's technical documentation, the theoretical prestressing of the strands after losses was 1340 MPa. The reverse deflection of the element before laying the concrete topping was $\sim L/1000$ (~ 2.0 mm). The over-concrete was reinforced to resist shrinkage and cracking from local pressure under the applied load from the crosshead. Longitudinal reinforcement consisted of 10 mm diameter bars placed in the corner sections of the concrete topping at an axial distance of 25 mm from the edge of the element. Transverse reinforcement was also provided in the form of stirrups with a diameter of 6 mm at a spacing of 60 mm in the zones of increased shear forces and pressure, with a spacing of 120 mm over the remaining length of the element (Fig. 5.8). The entire reinforcement was made of B500B grade ribbed bars.

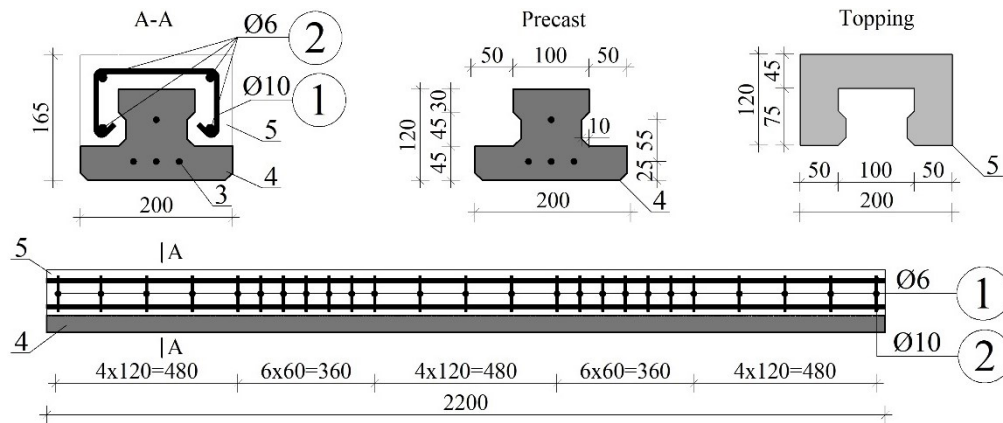


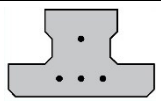
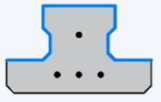
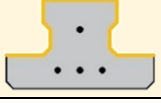
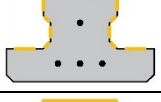
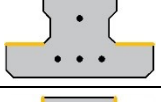
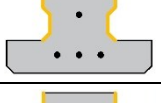
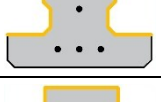
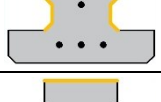
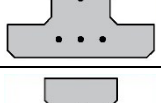
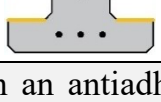
Fig. 5.8. Geometric dimensions of the element and reinforcement of the concrete topping:
 1- topping longitudinal reinforcement, 2- stirrups, 3- strands, 4- precast, 5- topping
 Rys. 5.8. Wymiary geometryczne elementu oraz zbrojenie nadbetonu: 1- zbrojenie podłużne nadbetonu, 2- strzemiona, 3- sploty, 4- prefabrykat, 5- nadbeton

The interface was prepared in ten variations (Table 5.2). The basic type is an element with an untreated surface, the second type is an interface covered with an antiadhesion agent, and the third type is an interface wholly covered with a 0.3 mm thick Kevlar-rubber mat. The other elements were made with a partial covering of the composite surface with the mat. The purpose was to verify the effectiveness of the position of the interface surface in the flexural elements. The table defines the type of covered surface by dividing it into top, bottom, and side surfaces. The variants were given the following designations.

Table 5.2

Division of elements based on the interface surface

Podział elementów ze względu na rodzaj powierzchni zespolenia

Element designation	Cross-section*	Concrete interface width, mm	Effective width ratio	Top surface	Side surface	Bottom surface
Z1.X-C		367	1.0	x	x	x
Z2.X-AB		367**	1.0**	*	*	*
Z3.X-CB		_*	_*	-	-	-
Z4.X-P		200	0.55	x/2	X_{3/5}	x/2
Z5.X-S		167	0.46	x	-	x
Z6.X-TB		200	0.55	-	x	-
Z7.X-T		100	0.27	x	-	-
Z8.X-B		100	0.27	-	-	x
Z9.X-SB		267	0.73	-	x	x
Z10.X-TS		267	0.73	x	x	-

*Surfaces with an antiadhesion agent applied are shown in blue, and mat-covered surfaces are in yellow.

**The entire interface width is stated for surfaces with an antiadhesion agent. Mat-covered surfaces were deducted from the interface width.

Tests were carried out in three- and four-point bending. Four-point bending tests were carried out using a load transfer crosshead at 350 mm from the edge of the support ($a/d = 2.5$). The value of $a/d = 2.5$ was chosen to obtain a bending-shear type rather than a shear-compression type [32] [112]. The beams were set with a 500 mm section (Fig. 5.9), along the length of which the slip of the concrete topping was also verified.

This section was the anchorage length of the prestressing strands while ensuring that the prestressing forces (dispersion) were transmitted to the section.

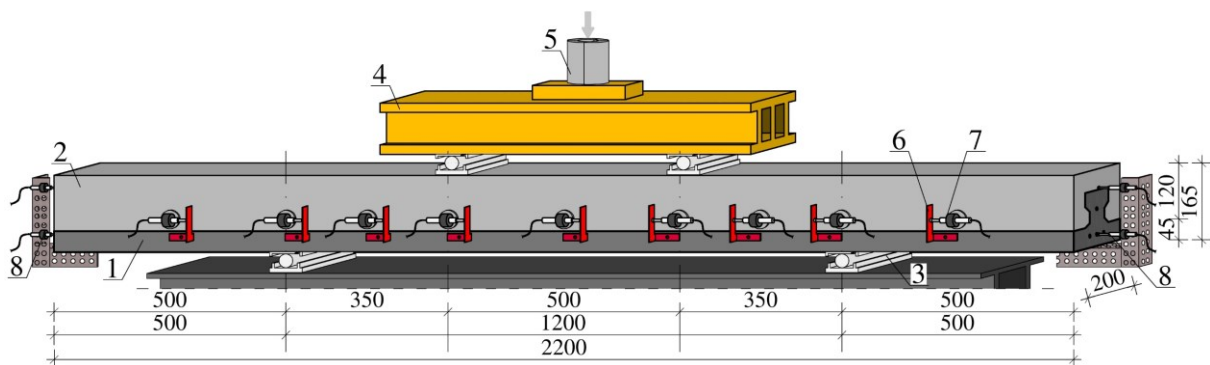


Fig. 5.9. Test stand of four-point bending test (4PBT): 1- precast, 2- overlay, 3- support, 4- steel traverse, 5- force gauge, 6- slip measuring base, 7- LVDT sensor, 8- strand slip sensor (LVDT)

Rys. 5.9. Stanowisko badawcze czteropunktowego zginania: 1- prefabrykat, 2- nadbeton, 3- podpora, 4- trawers stalowy, 5- siłomierz, 6- baza pomiarowa poślizgu, 7- czujnik LVDT, 8- czujnik poślizgu splotu (LVDT)

Three-point bending tests were performed on a DRBM 300 machine, applying the load at a distance of 350 mm from the axis of the right support ($a/d = 2.5$), and the distance to the left support was 750 mm ($a/d \approx 5.4$), as shown in Figure 5.10.

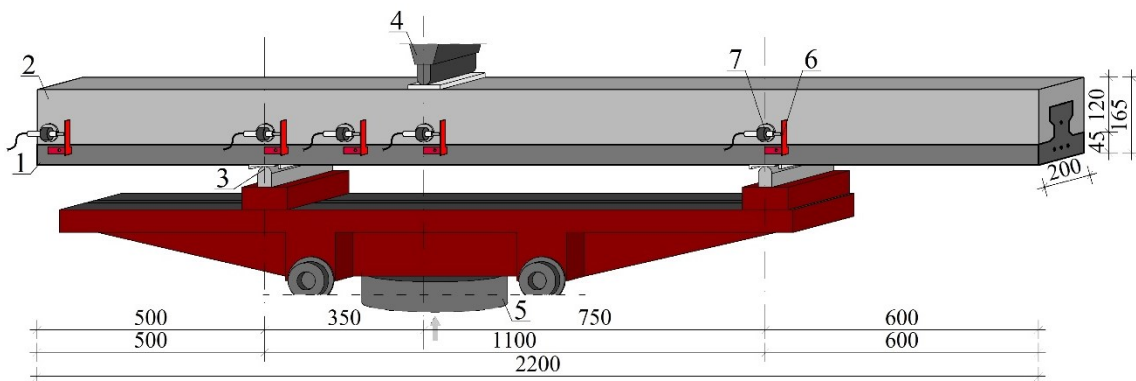


Fig. 5.10. Test stand of three-point bending test (3PBT): 1- precast, 2- overlay, 3- support, 4- steel traverse, 5- hydraulic actuator and force gauge, 6- slip measuring base, 7- LVDT sensor

Rys. 5.10. Stanowisko trójpunktowego zginania (3PBT): 1- prefabrykat, 2- nadbeton, 3- podpora, 4- trawers stalowy, 5- siłownik i siłomierz, 6- baza pomiarowa poślizgu, 7- czujnik LVDT

Two measurement methods were used in the 3PBT and 4PBT study. LVDT sensors were placed on one of the element's side surfaces. As a benchmark, LVDT sensors were applied to measure the slip at the interface. The sensors were attached to the concrete topping, and the measuring base plates were fixed to the precast. A single sensor measuring the displacement of the concrete topping was placed on the face of the element. Also, one sensor was mounted on the centre strand axis to verify the slip during the test. The positions of the sensors are shown in Figures 5.9, 5.10 and 5.12. The front surface was patterned for measurements with an Aramis digital image correlation (DIC) system. The system measured vertical displacements, horizontal displacements near the interface, and perpendicular displacements of the concrete topping relative to the rib. The recorded image of the cracks was used to determine the phases of behaviour and the influence of flexural and diagonal crack lengths on interface slip.

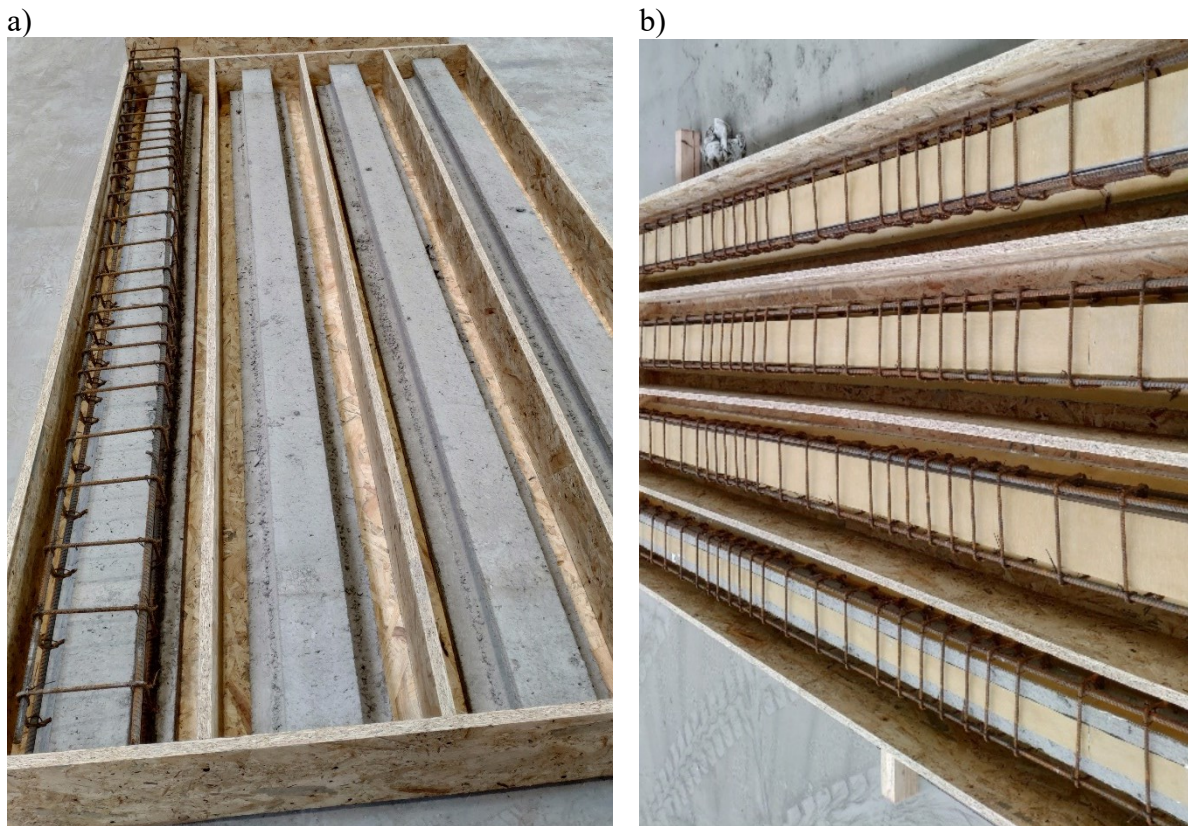


Fig. 5.11. View of the main beams during execution

Rys. 5.11. Widok belek głównych w trakcie wykonywania

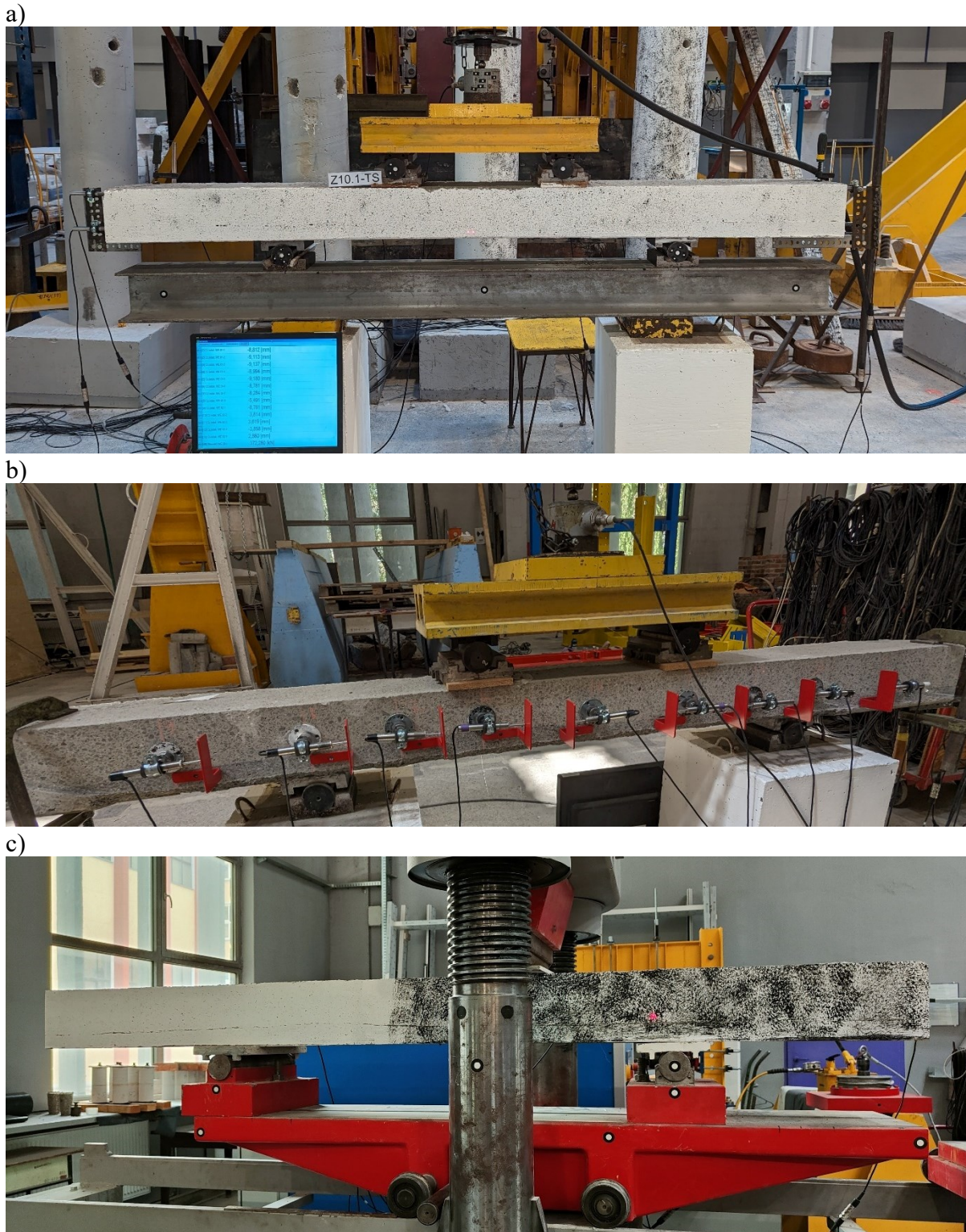


Fig. 5.12. View of the beams on the test stands: a) face with pattern on the 4PBT, b) location of the measuring sensors, c) element on the 3PBT

Rys. 5.12. Widok belek na stanowiskach badawczych: a) powierzchnia czołowa z deseniem na stanowisku do badania czteropunktowego zginania, b) rozmieszczenie czujników pomiarowych, c) element na stanowisku do badania trójpunktowego zginania

5.2. Measuring methods

5.2.1. LVDT and LDS sensors

Linear variable differential transformer (LVDT) sensors were used to measure interface displacements directly in beam element tests. The sensors measured the horizontal displacement between the concrete topping location and the LVDT attachment point on the precast element. The sensors and measuring plates were glued to the elements before testing. The measurement base was the length between the centre of the LVDT sensor head mounting and the measuring plate (Fig 5.13a). Due to the length of the sensor and the design of the measuring points, the LVDT measured not a single point but the displacement changes at the length of the measuring base. The length of the measuring base for the beam elements was 50 mm. LVDT sensors with a measuring range of 20 mm (PJX-20) were mounted. The repeatability of the indications is 0.002 mm. The linearity of the indications is 0.5%, which, for the measuring base used, translates into 0.1 mm.

For direct shear tests, it was decided to use two sets of laser distance sensors (LDS) type optoNCDR Micro-epsilon ILD1420-50 with a measurement range of 50 mm. The LDSs, due to their smaller size, allowed improved localisation of the measurement points. In addition, the LDSs provide improved linearity parameters. The first set was used to perform displacement measurements of the interface slip. The sensors were placed on opposite surfaces in the middle of the specimen side length. Measuring bases made of aluminium angle were placed on the surfaces. The angle brackets were placed diagonally on the opposite surfaces. The first was located in the lower zone (Fig. 5.13b), and the second was in the upper zone. The described positioning allowed the laser sensors to measure two slip zones, the upper zone at the load application point and the lower zone at the support of the specimen. This arrangement was also intended to leave enough space for the installation of laser sensors to measure the horizontal displacement of the concrete topping. The sensors on the precast element's bottom surface were directed horizontally towards the measuring bases. The length of the LDS measuring base was 60 mm, representing the sensor's mid-measuring range. The repeatability of the indications is 0.002 mm. The linearity of the indications is 0.08%, which, for the measuring base used, translates into 0.04 mm.

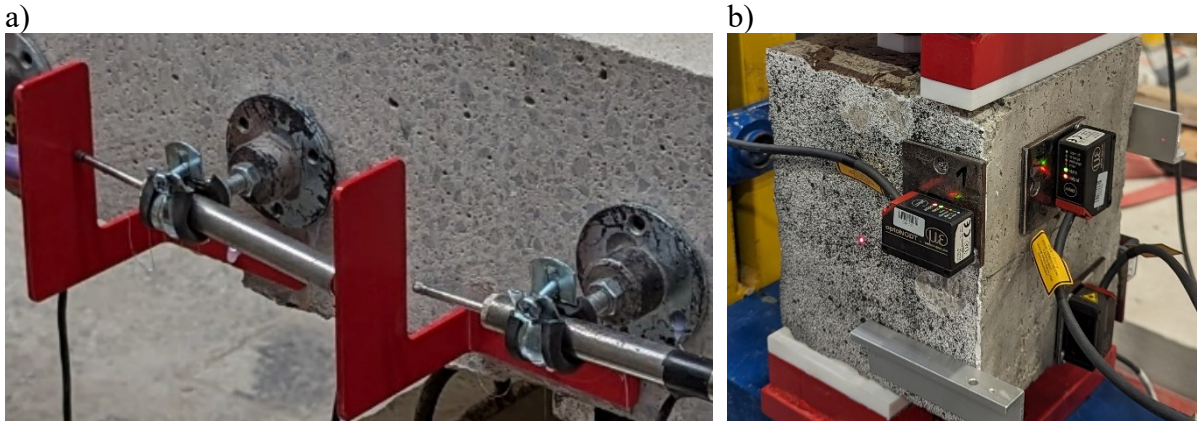


Fig. 5.13. View of the sensor arrangement: a) LVDT at Z-series beams, b) LDS at direct-shear test element

Rys. 5.13. Widok położenia czujników pomiarowych: a) LVDT na belce z serii Z, b) LDS na elemencie w badaniu bezpośredniego ścinania

5.2.2. DIC

Digital image correlation (DIC) measurement technique was used to examine the component's surface. Based on solid mechanics, the technique involves evaluating changes in geometry and the localisation of points before and after material deformation. The measurement relies on small rectangular areas called facets, which are relatively small, such as 15 x 15 pixels (Fig. 5.14). Each facet has a unique pattern and overlaps with neighbouring facets within a range determined by the user (typically, 20-50% overlap is recommended). In this study, an overlap of 40% was chosen to capture local effects. Common areas were used to minimise errors in strain measurement, as each facet included elements from adjacent areas with the same boundary conditions. The size of the facets affects the accuracy and speed of calculations, with larger facets resulting in decreased measurement accuracy.

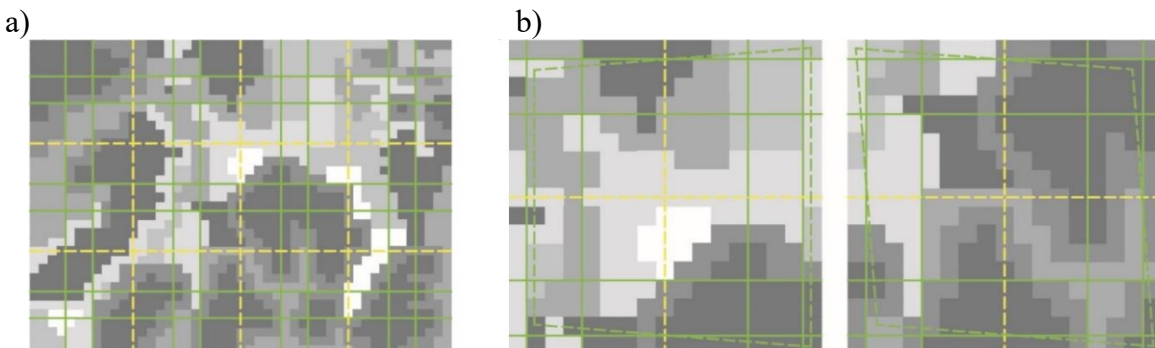


Fig. 5.14. Principle of image correlation [85]: a) area with arranged facets marked with green lines, b) enlarged segment of an analysed area with facet contour

Rys. 5.14. Zasady korelacji obrazu [85]: a) obszar pomiarowy z rozmieszczonymi fasetkami zaznaczonymi zielonymi liniami, b) powiększony segment obszaru z konturem fasetki

The Aramis 6M system, consisting of two digital cameras, each with a resolution of 6 MPx, recording images in grey tones, was used in the tests. The measurements and processing of the results were carried out using GOM Correlate software, which was certified and calibrated for the camera configuration used. The measurement area of the Aramis 6M system ranges from 150x170 mm to 2150x2485 mm. An area with the following dimensions was used in the study:

- Initial test – area of 2150x2485 mm – 112 Px/cm²
- 3PBT and 4PBT – area of 1150x1340 mm – 390 Px/cm²
- Direct shear test – area of 150x170 mm – 23530 Px/cm²

The side surfaces of the elements for the largest of the areas were covered with irregular contrasting patterns obtained by applying black paint with a brush with stiff hair - Fig. 5.15a. For the smallest area, a pattern was made using graphite spray (Fig. 5.15b), allowing a finer pattern for testing the smaller areas. In the intermediate area, both methods were tried, allowing similar surface quality results (verified by the software pattern quality assessment module). In the ZX.3 series and for two items in the ZX.2 series (Z1.2_C and Z2.2_AB), the first method was used to achieve a surface finish, while in the following items from the ZX.2 series, the surface was made entirely with spray.

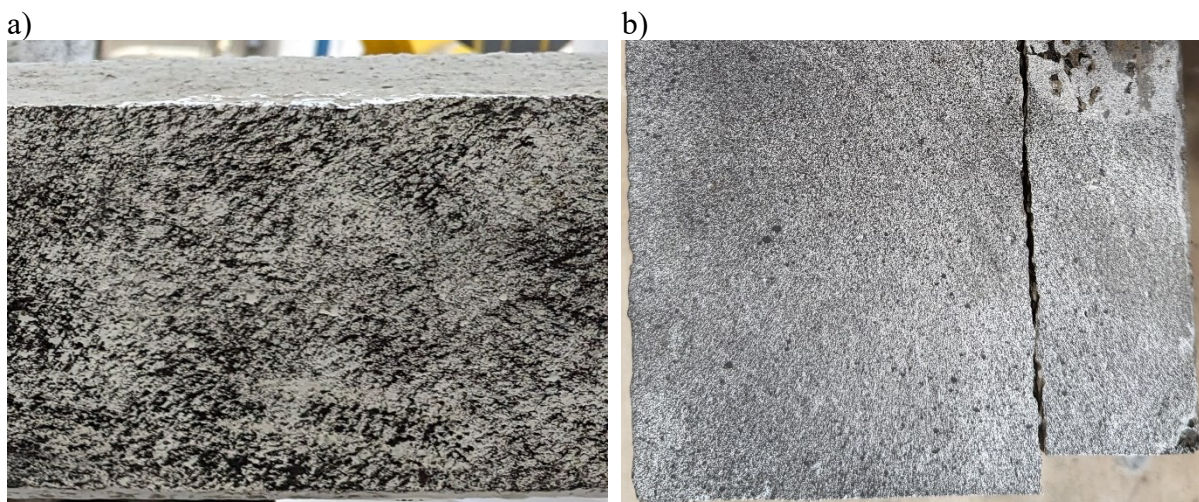


Fig. 5.15. View of the applied pattern on the surface of the elements: a) type I pattern (brush with stiff hair), b) type II pattern (graphite spray)

Rys. 5.15. Widok naniesionego wzoru na powierzchnię elementów: a) wzór typu I (szczotka ze sztywnym włosiem), b) wzór typu II – (grafit w sprayu)

Based on DIC measurements, a calculation method for determining displacements at the interface was developed, which allows the effects of slip at the interface, opening of the interface and flexural cracking crossing the interface to be distinguished. The method

is based on geometric transformations of a closed set of four points connected by perpendicular lines with diagonals. In each measurement step, the values of the lengths of the straights and diagonals and the angles between the diagonals and the straights parallel to the longitudinal edges of the element were measured. Figure 5.16 shows the geometric interpretation of the developed image analysis method.

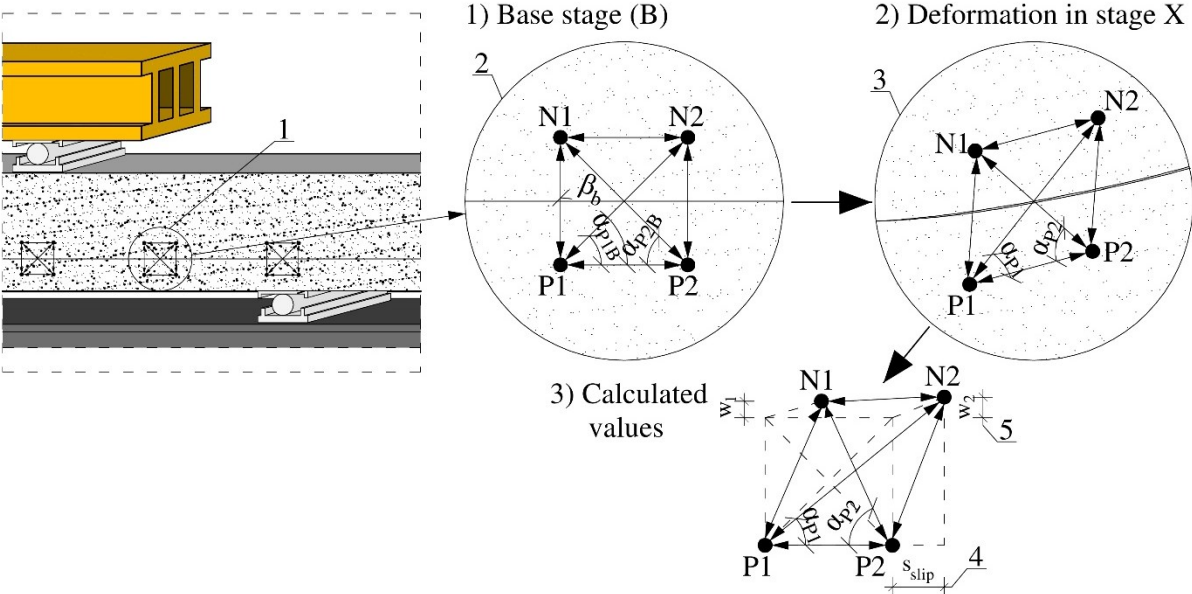


Fig. 5.16. The geometry of the measurement base: 1- position of measuring base on the element, 2- base stage, 3- any subsequent stage, 4- interface slip value, 5- interface opening value
 Rys. 5.16. Geometria bazy pomiarowej: 1- położenie bazy pomiarowej na elemencie, 2- etap bazowy, 3- dowolny następny etap, 4- obliczana wartość poślizgu styku, 5- obliczana wartość rozwarcia styku

Based on the deformation of the measuring points in the subsequent loading steps, it is possible to determine the slip at the interface and the crack width to compensate for its contribution to the slip. In the first step, it is necessary to take into account the lack of perpendicularity of the created points and the straight lines connecting them. Due to the characteristics of the DIC measurement, it is impossible to create a perfectly perpendicular measuring area in the initial step. Thus, the base error understood as deviations from a straight angle, generates an error in the slip and interface opening values. The subsequent calculation steps are shown below:

- Determination of the error in the formation of the measurement area (lack of perpendicularity) in relation to the length of the bottom surface:

$$s_{err} = L_{P1N2B} \times \cos(\alpha_{P1B}) - L_{P1P2B} \tag{5.1}$$

- Displacement of the upper base relative to the lower base (translation):

$$s = L_{P1N2} \times \cos(\alpha_{P1}) - (L_{P1P2} + s_{err}) \quad (5.2)$$

- Crack width in the base area (separately for precast and concrete topping):

$$w_{P1P2} = L_{P1P2} - L_{P1P2B} \quad (5.3)$$

$$w_{N1N2} = L_{N1N2} - L_{N1N2B} \quad (5.4)$$

- Interface slip with crack compensation:

$$s_{slip} = s + (w_{P1P2} - w_{N1N2}) \quad (5.5)$$

It is possible to determine further the value of the interface opening, which is understood as the distance between the surface of the precast element and the concrete topping. Again, starting by calculating the base formation error affecting the interface opening is necessary. The error is because a perfect right angle has not been defined based on the measuring points set in the base step. The error value is calculated as the difference between the right angle and the angle defined by points N1-P1-P2. With the known value of the interface slip and the value of the formation angle error, it is possible to calculate the error when determining the contact opening.

- Error in determining interface opening for N1P1 and N2P2 straight:

$$w_{err1} = s_{slip} \times \sin(\beta_B - 90^\circ) \quad (5.6)$$

$$w_{err2} = (s_{slip} + w_{L1}) \times \sin(\beta_B - 90^\circ) \quad (5.7)$$

- Interface opening for straights between points N1P1 and N2P2:

$$w_{N1P1} = (L_{N1P2} \times \sin(\alpha_{P2})) - (L_{N1P2B} \times \sin(\alpha_{P2B})) - w_{err1} \quad (5.8)$$

$$w_{N2P2} = (L_{N2P1} \times \sin(\alpha_{P1})) - (L_{N2P1B} \times \sin(\alpha_{P1B})) - w_{err2} \quad (5.9)$$

- The average value of the interface opening over the length of the measuring base:

$$w = \frac{w_{N1P1} + w_{N2P2}}{2} \quad (5.10)$$

The size of the measurement bases was chosen according to the size of the selected measurement area. The measurements aimed to verify local effects, so the measuring bases were selected as small as possible. A 40 x 40 mm base was used for the beam elements, while a 10 x 10 mm base was used for the direct shear test. The photos below

show a view of the adopted measurement based on a beam element (Fig. 5.17a) and in the direct shear test (Fig. 5.17b).

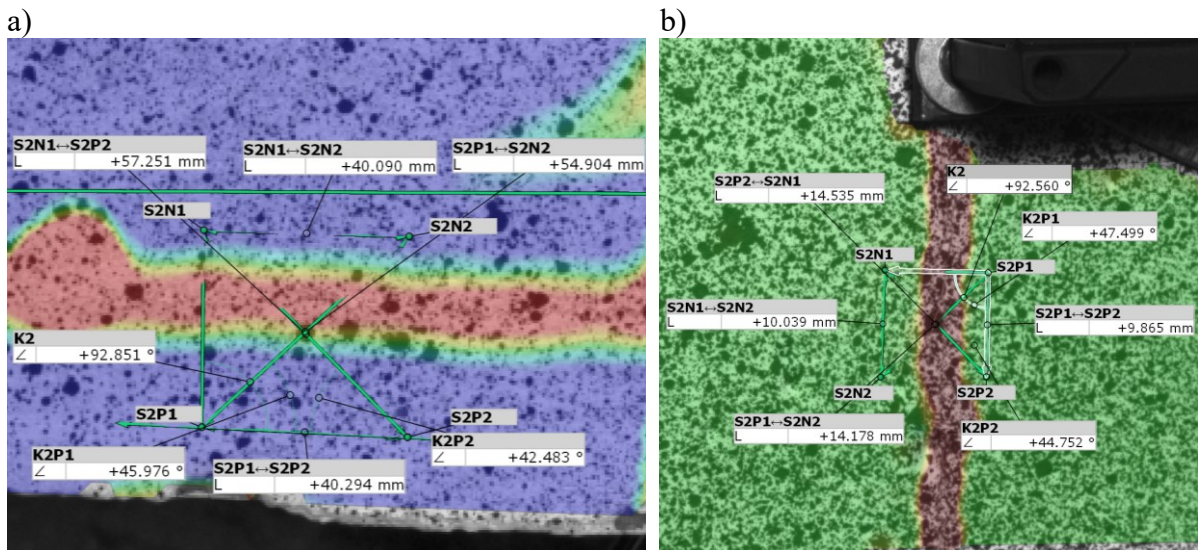


Fig. 5.17. View of the base definitions at the measurement surfaces: a) 3PBT - Z5.1_S, b) direct-shear test - Z1.2_C

Rys. 5.17. Widok definicji baz na tle powierzchni pomiarowych: a) 3PBT – Z5.1_S, b) test bezpośredniego ścinania – Z1.2_C

Element deflections were also recorded using DIC measurements. This measurement makes it possible to isolate possible movements of the test bed from the displacement of the element when covering the entire element in the area of the support locations. Based on the deflection measurements, the flexural stiffness of the beam elements was determined. The basic formulae for calculating the deflections for the 3PBT (Fig. 5.18a) and 4PBT (Fig. 5.18b) schemes were transformed. The flexural stiffness calculated in this manner was used to determine the value of the cracking force, and the stiffness decreased, resulting from the debonding of the elements.

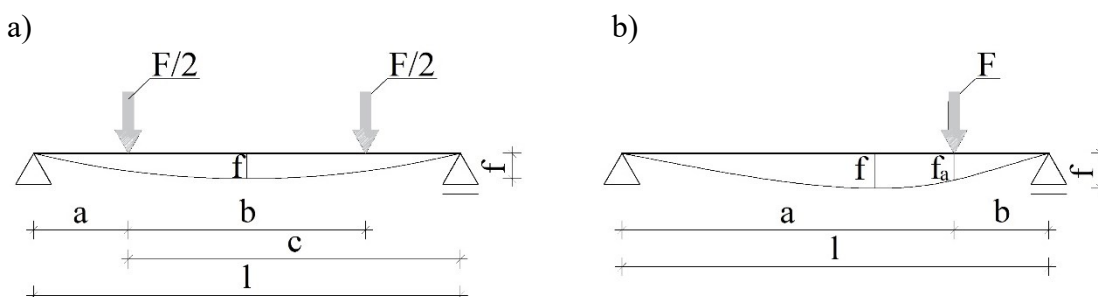


Fig. 5.18. Static scheme with deflection determination points for a) 4PBT, b) 3PBT

Rys. 5.18. Schemat statyczny wraz z punktami określenia ugięcia dla: a) 4PBT, b) 3PBT

The stiffness was calculated by transforming the deflection formulae of the beam elements. For the case of three-point bending, the value of the maximum deflection was converted to the value of the deflection occurring under the force. The conversion is necessary because the deflection is measured under the force instead of at its maximum location.

- Deflection of a beam element in four-point bending:

$$f = \frac{F \times c^2 \times (a^2 + b^2)}{3 \times EI \times l} \quad (5.11)$$

in which,

a , b , and c are the dimensions of the test stand according to Fig. 5.8 and Fig. 5.16a

- Flexural stiffness after transformation of the formula calculated from measured deflection in four-point bending:

$$EI = \frac{F \times c^2 \times (a^2 + b^2)}{3 \times f \times l} \quad (5.12)$$

- Deflection of a beam element in three-point bending:

$$f = \frac{F \times a^2 \times b^2}{3 \times EI \times l} \quad (5.13)$$

in which,

a and b are the dimensions of the test stand according to Fig. 5.9 and Fig. 5.16b

- Flexural stiffness after formula transformation calculated from measured deflection in three-point bending. The ratio of maximum deflection to deflection under force is ~ 1.10 (f/f_a) per dimension, as in Figure 5.9. This factor is included in the formula:

$$EI = \frac{F \times a^2 \times b^2}{3 \times 1.1f_a \times l} \quad (5.14)$$

6. RESULTS OF EXPERIMENTAL STUDIES

6.1. Material test

6.1.1. Basic material properties

The test elements were partly precast and made in the prefabrication facility. The initial tests were based on a typical prestressed lintel with the commercial designation SBN 120/120, and the elements from the main study were made on an S-Panel 120 slab beam. The precast was made of concrete of the design class C40/50. The concrete was made with CEM I (Portland cement) of class 42.5R using basalt aggregate of 2-8 mm fraction, and Sika 3020X plasticiser was added to the mix. The w/c ratio of the mix is 0.23, and the amount of water dosed is adjusted according to the moisture content of the aggregate. The concrete topping of the beams for the initial tests was made under laboratory conditions with CEM I 42.5R cement with a w/c ratio of 0.5 after 28 days of precast production. The topping of the beams for the main tests was made in the prefabrication facility using concrete of the design class C25/30. The concrete was made 28 days after concreting the precast using CEM I 42.5R cement with a w/c ratio of 0.5 on gravel aggregate fraction 2-8 mm. The complete composition of the concrete mixes is given in Table 6.1.

Table 6.1
Quantity of ingredients as kg/m³
Skład mieszanek betonowych kg/m³

Element	Water	Cement	Sand	Coarse aggregate	Super-plasticiser
B and Z – precast concrete	80	342	734	1223	1.83
B – topping concrete	200	400	673	1052	1.43
Z – topping concrete	191	383	1105	810	-

Six samples were taken for each concreting for compressive strength testing. The tests were carried out on cubic elements measuring 150 x 150 x 150 mm. For the elements in the main series, an additional three cylinders, each with a diameter of 150 mm and 300 mm high, were taken to determine the stiffness modulus. The results are summarised in Table 6.2.

Table 6.2
Concrete strength parameters [N5-N7]
Parametry wytrzymałościowe betonu [N5-N7]

Element	Part	Compression strength		Modulus of elasticity	
		Mean value $f_{c,cube}$, N/mm ²	Standard deviation	Mean value E_c , GPa	Standard deviation
B series	Topping	57.02	1.19	-	-
	Precast	62.81	1.39	-	-
Z series	Topping	35.94	1.59	31.75	1.20
	Precast	65.34	1.08	39.08	0.87

The concrete topping reinforcement in the beams was made of ribbed reinforcing steel class B500B with a diameter of 6 mm for the stirrups and 10 mm for the longitudinal bars. The precast elements were made as prestressed without bar reinforcement. Prestressed steel grade Y2060S7 was used. The precast elements were made on 130 m long tracks. The tension was released from the retaining blocks after 24 h, and the elements were then cut to the target length. The parameters of the reinforcing steel tested and the prestressing steel parameters given following the manufacturer's tests (own prestressing strand tests were not performed) are given in Table 6.3.

Table 6.3
Properties of reinforcement steel and prestressing steel [N4, N8]
Parametry stali zbrojeniowej oraz sprężającej [N4, N8]

Element	Steel Grade	Mean upper elastic limit R_{eH} , N/mm ²	Tensile strength to nominal yield stress R_m/R_e	Overall ductility A_{gt} , %	Ductility at failure A_{10} , %
Z series	B500B	554	1.08	6.1	10.3
B and Z series	Y2060S7	1927	1.12	5.4	-

6.1.2. Concrete tensile strength

The concrete tests were extended to include tensile splitting tests and tests of adhesion of concrete in the pull-off test. Splitting tests were carried out on six 150 x 150 x 150 mm cubes of each concrete type for the Z-series beams. In addition, tests were performed on three composite cubes, half of which were made of precast concrete and half of which were made of concrete corresponding to the topping of the beams. The testing of the half elements was treated as an additional test. The surface of the composite, with its roughness and method of preparation, did not correspond to the surface of the manufactured precast elements. Due to the smooth surface (without rubbing), these results are considered to be minimum values for the tensile strength of the interface.

Pull-off tests were carried out on additional beam elements to determine the adhesion of the concrete topping to the precast element with the actual surface roughness. Five of the eight tests carried out were qualified as correct, with the remaining tests resulting in rupture on the bond (glue). The average tensile strength of the pull-off interface of 3.56 MPa is higher than that of the concrete topping in the splitting test, which was 3.34 MPa. This result is inconsistent with the literature data, which indicates that the bond strength measured with the pull-off test was the lowest and can be treated as a conservative estimation [19]. The interface strength should not be greater than the tensile strength of the constituent concrete. This discrepancy will be discussed later when taking parameters for modelling. Pull-off tests were also performed for covered surfaces and surfaces with an antiadhesion agent. For beams with surface types Z2_AB and Z3_CB, it was impossible to carry out the test due to the cylinders breaking during the cutting process.

Based on the view of the interface of the composite after testing the Z1_C series elements, it can be concluded that the adhesion rupture occurred not at the interface with the precast but close to the bond in the topping concretes. The failure image is similar to a cohesion mechanism failure indicative of a “strong bond” [9], pointing to the superior strength of the interface compared to the concrete substrate or overlay. For the Z3_CB series, rupture occurred at the cover material under the overlay concrete. The surface view of the specimens from the Z2_AB series demonstrates the failure of the adhesion mechanism between the precast and the concrete topping, thus indicating the effectiveness of the antiadhesion agent used. Pull-off tests confirmed the effectiveness of the methods to limit and break the bond in the test elements.

Table 6.4 shows the results of the tensile splitting and pull-off tests. Figure 6.1 shows a view of the sample cubes after the tensile splitting test, and Figure 6.2 shows the components after the Pull-off test.

Table 6.4
Concrete strength parameters
Parametry wytrzymałościowe betonu

Element	Tensile splitting test			Pull-off test		
	Mean value $f_{ctm,ts}$, N/mm ²	Standard deviation	COV, %	Mean value $f_{ctm,pot}$, N/mm ²	Standard deviation	COV, %
Z series Topping	3.34	0.83	24.9%	-	-	
Z series Precast	4.37	0.59	13.5%	-	-	
Z series T/P	1.86*	0.25	13.4%	3.56	0.85	23.9%

*smooth surface, not reflecting the surface characteristics of the precast

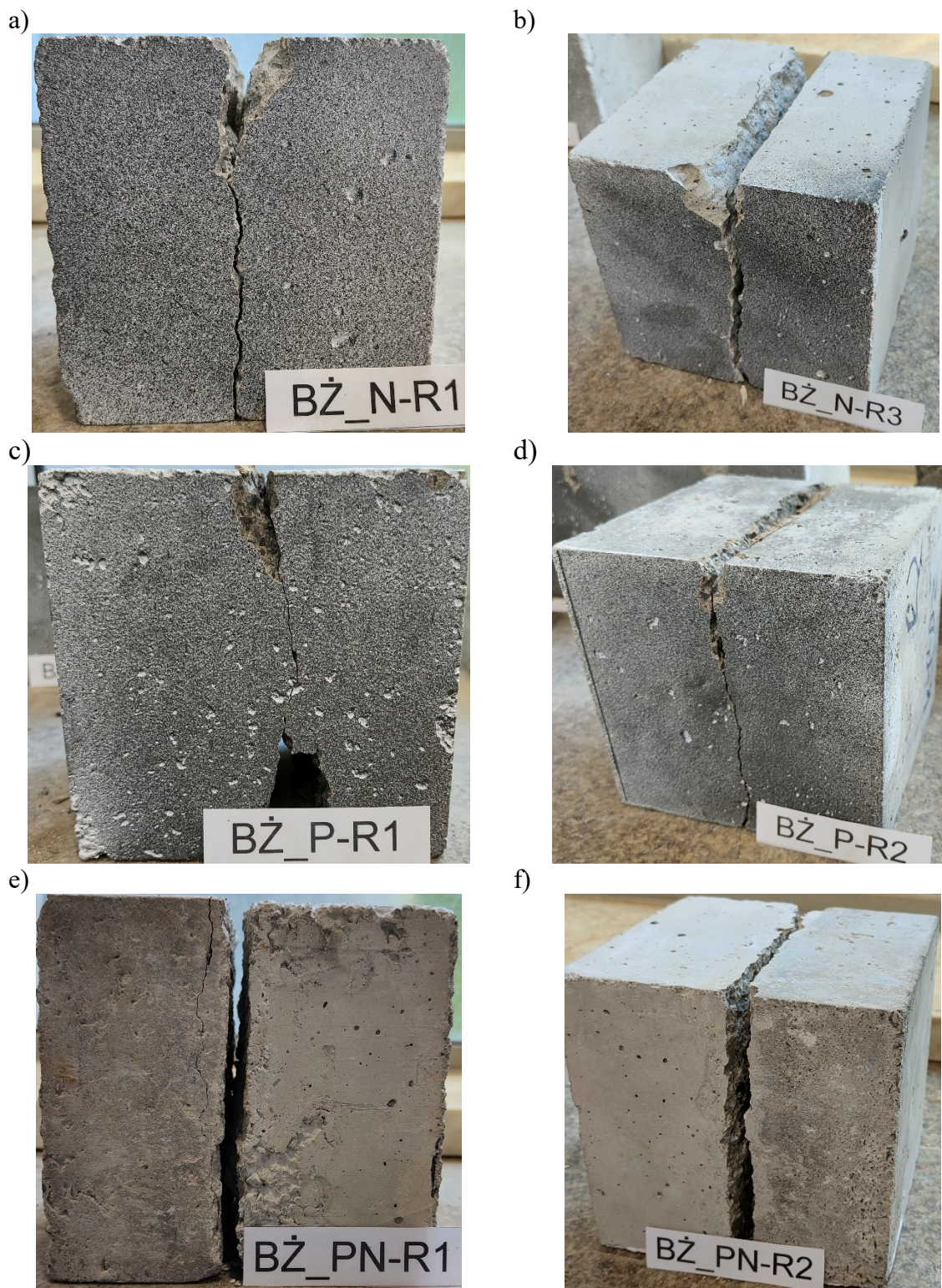


Fig. 6.1. View of the specimen after the splitting test: a-b) Z-series topping concrete elements, c-d) Z-series precast concrete elements, e-f) Z-series composite of topping concrete and precast concrete as for the Z-series precast element

Rys. 6.1. Widok próbek po badaniu na rozłupywanie: a-b) elementy z nadbetonu serii Z, c-d) elementy z betonu jak dla prefabrykatu serii Z, e-f) elementy zespolone z nadbetonu serii Z oraz betonu jak dla prefabrykatu serii Z

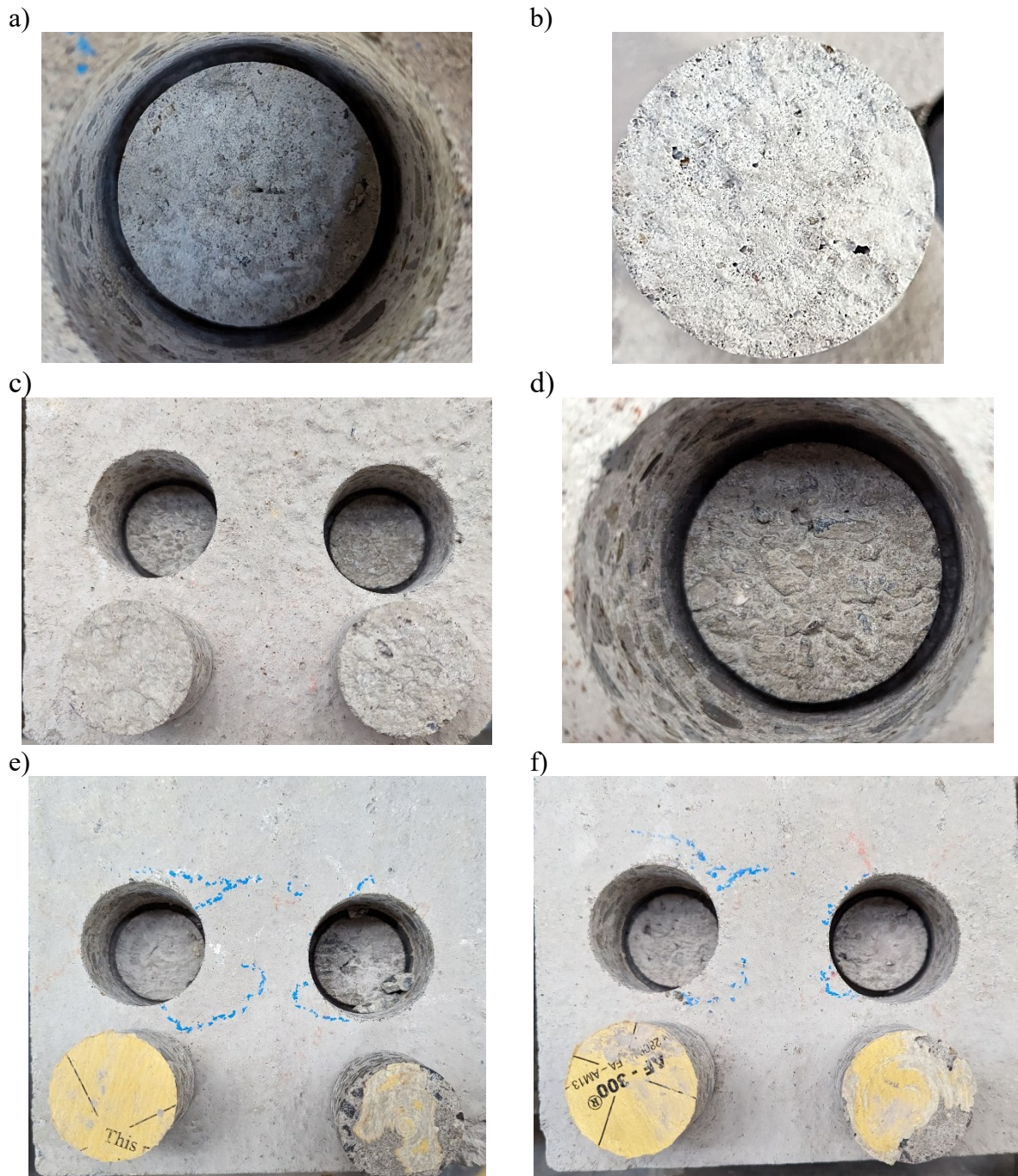


Fig. 6.2. View of samples after pull-off test: a-b) type Z1_C, c-d) type Z2_AB, e-f) type Z3_CB
 Rys. 6.2. Widok próbek po badaniu pull-off: a-b) typ Z1_C, c-d) typ Z2_AB, e-f) typ Z3_CB

6.1.3. Interface roughness

Before preparing the precast elements from the main series (Z-series) for laying concrete topping, surface roughness tests were carried out using the Sand Patch Test, with sand of 0.1-0.3 mm fraction. Due to the small width of the precast surface, it was decided to carry out the test only on the top surface of the rib. Tests were carried out for three different beams, each at four points. A total of 12 measurements converted to

average roughness were carried out. Due to the small width of the head of the beams (100 mm), the method was modified for the test pieces. Six tests were carried out with a small volume of sand ($V = 5.0 \text{ cm}^3$), allowing a circle to be made within the width of the beam head. The diameter of the resulting circle was measured for these tests. The test was performed for the following six points with an increased volume to 10 cm^3 , spreading the sand evenly over the head's surface without maintaining the circle's shape. The irregular surface thus made was measured from the photographs taken with the scale applied to the specimens. The surface of the precast elements can be characterised by dividing into two types of surfaces with similar roughness. The first type is a surface with a visible small local valley (Fig. 6.3. a, c), resulting from the manufacturing method using a concrete mixture with a consistency that can be described as on the level between moist and loose. The second type (Fig. 6.3. b, d) is characterised by less “visible roughness” (meso roughness) but has areas of depressions of about 20 mm in width, leading consequently to roughness similar to the first type.

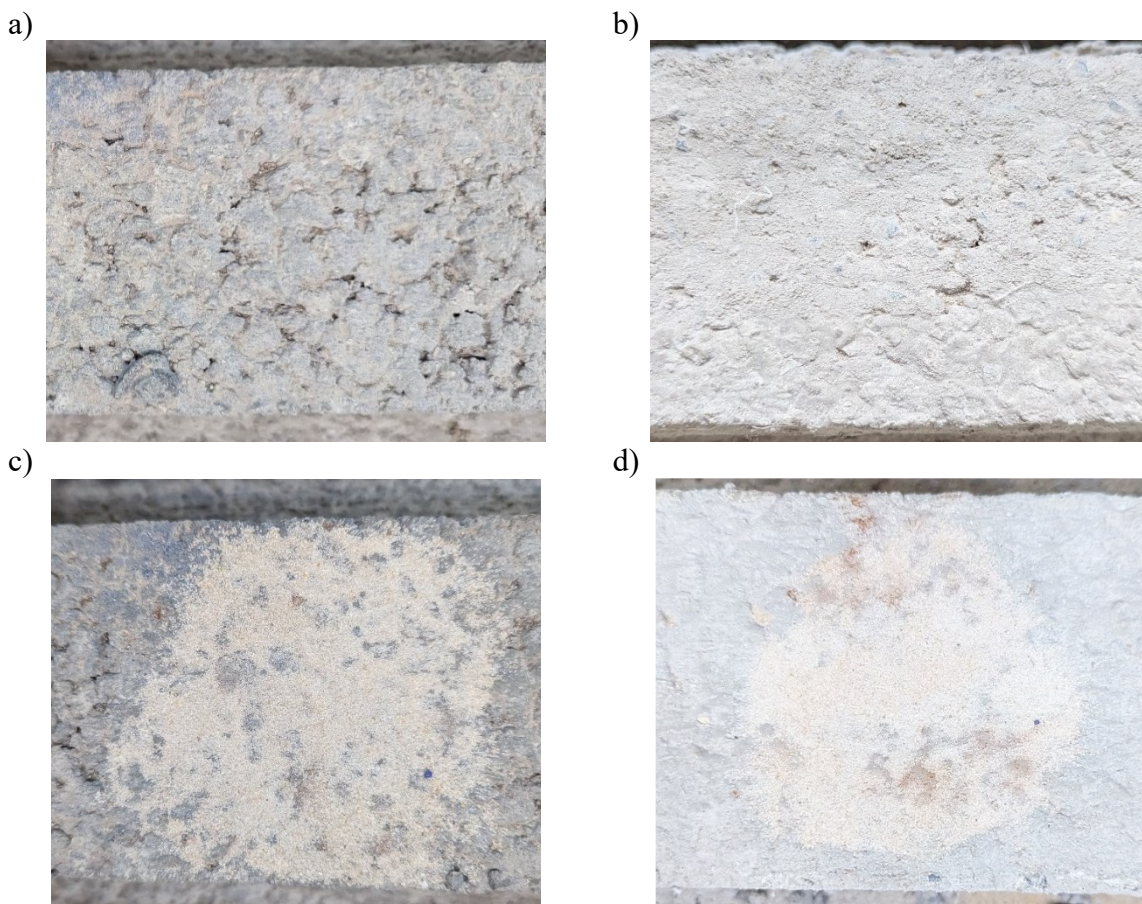


Fig. 6.3. View of the precast element surface: a) top of the beam with type I surface, b) top of the beam with type II surface, c-d) view of the surface after the test

Rys. 6.3. Widok powierzchni prefabrykatu: a) półka górna z powierzchnią typu I, b) półka górna z powierzchnią typu II, c-d) widok powierzchni po badaniu

Calculations were carried out for the parameter defined according to the *fib* Model Code 2010 as roughness R_t based on a simple relation, allowing the roughness to be calculated as a ratio of volume to surface area of the smoothed sand (Eq. 6.1).

$$R_t = \frac{V_s}{A_s} \tag{6.1}$$

in which,

R_t – roughness (defined as in Model Code 2010)

V_s – volume of used sand

A_s – area of distributed sand

The measurements are summarised in Table 6.5. The highest measured surface roughness was 1.96 mm, and the lowest was 1.01 mm. An average roughness value of 1.33 mm was obtained, with a standard deviation of 0.33 and a COV of 25.1%. According to the *fib* Model Code 2010, the interface should be considered as a smooth surface due to the condition $R_t > 1.5$ mm not being exceeded. Due to the single measurements, it would be possible to classify the surface as rough.

Table 6.5
Mean roughness of the interface surface
Średnia szorstkość powierzchni zespolenia

Element	Mean roughness R_t , mm	Standard deviation	Coefficient of variation COV, %
Z series	1.33	0.33	25.1%

According to the latest edition of EN 1992-1-1:2023, the element's surface should also be assigned to smooth surfaces. For a surface like the type I described, it would be possible to locally assign a rough category by looking only at a peak-to-valley parameter greater than 3 mm at a maximum spacing of 40 mm. However, the element does not meet the surface treatment requirements for the rough category described in Figure 8.15a of the standard. Due to the shape and manufacturing method's compatibility with the beams of beam-and-block slabs, the surface type was also analysed according to EN 15037-1:2008. Again, analysing the surface as for the described type I, it would be possible to classify the surface of the beam according to the logic of the standard into category c_{3a} due to the top surface as in category c_{2a} (unevenness of not less than 3 mm at intervals of not more than 20 mm), the sides being slipformed. In addition, the

requirement is to fulfil the shape as for category c_{2b} , i.e. slip-forming extended towards the top flange, with the flange having a local roughness of more than 4 mm. If the requirement for roughness of the head is not met, it would be necessary to assign the element to the lowest category c_1 , described as beams with lateral and horizontal surfaces (without top flange) moulded using the sliding method.

The differences resulting from other definitions of roughness between the standards and the occurrence of element surfaces on the borderline of the standard definitions are analysed in Chapter 8.

6.2. Initial tests

This section presents the results of preliminary tests on beam elements with a flat interface. Due to the supportive nature of the tests, this section presents the results and conclusions without further analysis. Figure 6.4 describes the symbols assigned to the LVDT sensors used. Initial element tests were carried out up to failure, defined as either no increase in the element loading force with a significant increase in displacement or violent element failure due to crushing of the compression zone. Depending on the element under consideration, it was possible to distinguish two primary forms of failure: crushing of the compression zone under concentrated force combined with the development of a diagonal crack and slippage of the strand anchorage (fully composite beams - B1 series) or delamination of the interface for beams of the B2, B3 series. The B4 series beams were delaminated from the beginning of the test. Concrete topping is split into several parts along with the slipping of the interface. After breaking the adhesion at the interface, the precast beam further deflected up to the loss of anchorage of the strands combined with the crushing of the compression zone. Figure 6.5 collects the force-displacement characteristics for each of the tested elements, and Table 6.6 summarises the values of the maximum force, the cracking force at the interface locally and entirely (to the face edge of the beam), as well as the diagonal cracking force and the flexural cracking force.

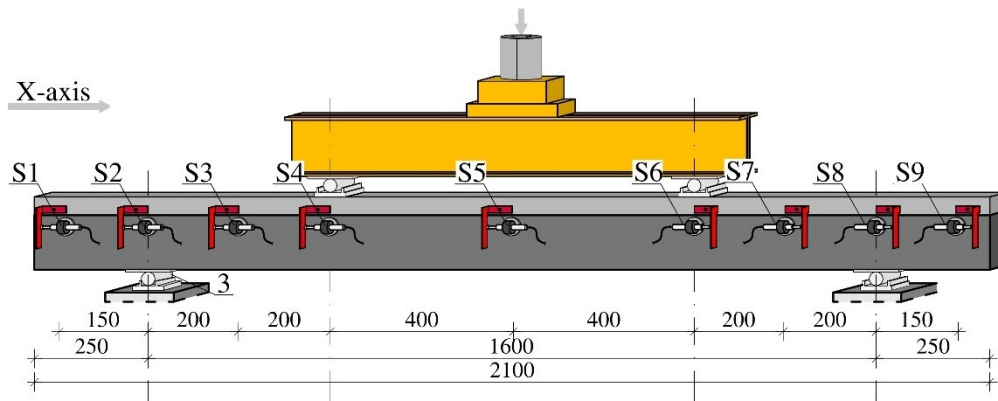


Fig. 6.4. Label of the measurement points and the X axis as seen from the front (DIC), mirror view from the sensor side is shown

Rys. 6.4. Oznaczenie punktów pomiarowych oraz osi X patrząc od frontu (powierzchni DIC), przedstawiono lustrzany widok od strony czujników

Table 6.6
Summary of failure and cracking forces of B-series beams
Zestawienie sił niszczących i rysujących belek serii B

Element	Flexural crack F_{cr} , kN	Local interface slip $V_{R,1,cr}$, kN	Interface slip at face $V_{R,2,cr}$, kN	Diagonal crack $V_{R,c}$, kN	Peak load F_{max} , kN
B1.1-C	39,8	-	-	-	76,7
B1.2-C	44,9	-	-	70,6	77,2
B2.1-F	45,1	49,5	53,3	-	59,8
B.2.2-F	42,3	-	65,2	-	65,2
B3.1-P	40,9	-	64,8	-	64,8
B3.2-P	45,7	-	59,5	-	59,5
B4.1-O	36,7	-	0,0	-	45,2
B4.2-O	36,7	-	0,0	-	56,7

For beams in the B1, B2 and B3 series, a high consistency of flexural cracking force was obtained (Fig. 6.5), with a coefficient of variation for the force of 5.1%. The cracking force was determined from the stiffness analysis of the beams (Fig. 6.6). For the beams of the B2-F and B3-P series, despite the application of similar bond limitation methods, a full cracking of the interface between 53.3 kN and 65.2 kN was recorded, which translates into a COV of 23.3%. The coefficient of variation obtained is within the assumed range based on the literature review. Only for one beam B2.1-F a local cracking at the interface between the point of force application and the support was

obtained (Fig. 6.9a). Local cracking at the interface has a negligible effect on the flexural stiffness of the beam (Fig. 6.7b). The occurrence of slip at the interface can be determined from the crack pattern and the stiffness curve. When the interface was fully cracked, the stiffness of the beams decreased to a value consistent with the stiffness of the beam with the adhesion and friction lowered (beam B4.X) (Fig. 6.6).

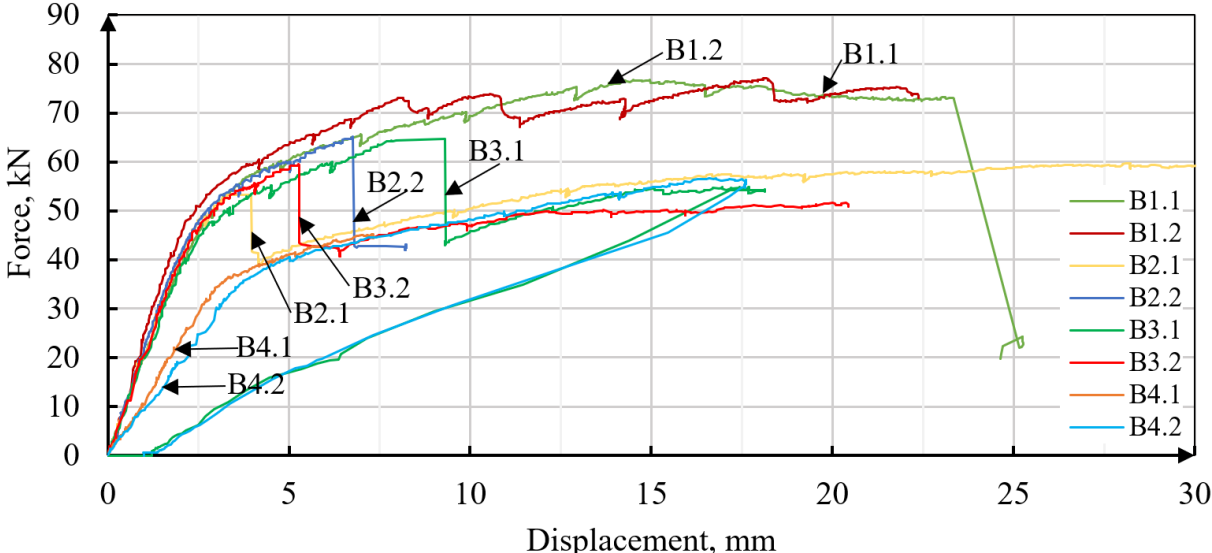


Fig. 6.5. Force-displacement diagram for B-series beams
 Rys. 6.5. Wykres zależności siła-przemieszczenie belek z serii B

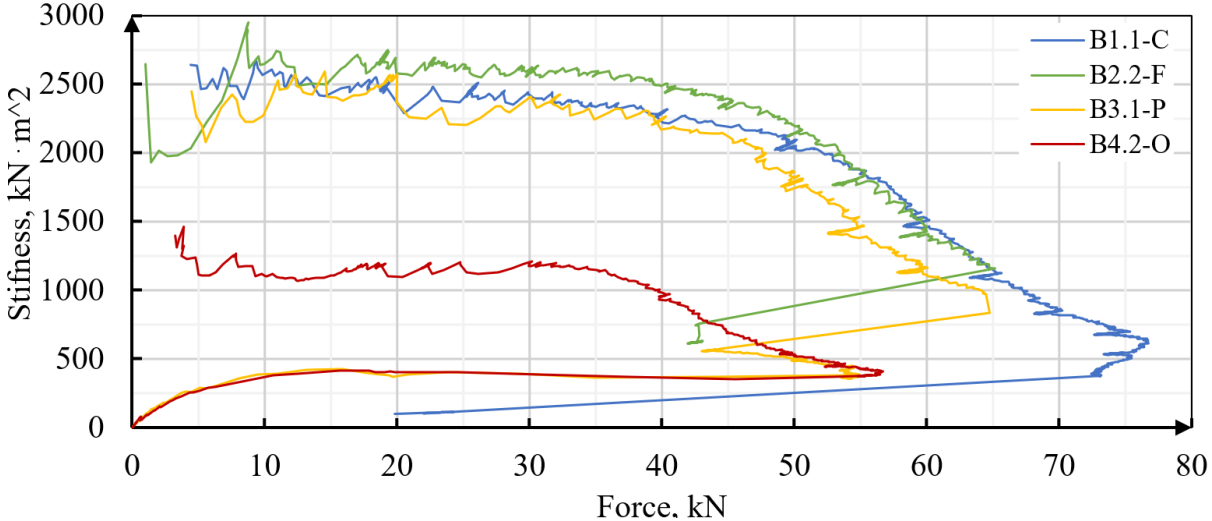


Fig. 6.6. Beam stiffness diagram for selected B-series beams
 Rys. 6.6. Wykres sztywności giętej dla wybranych belek z serii B

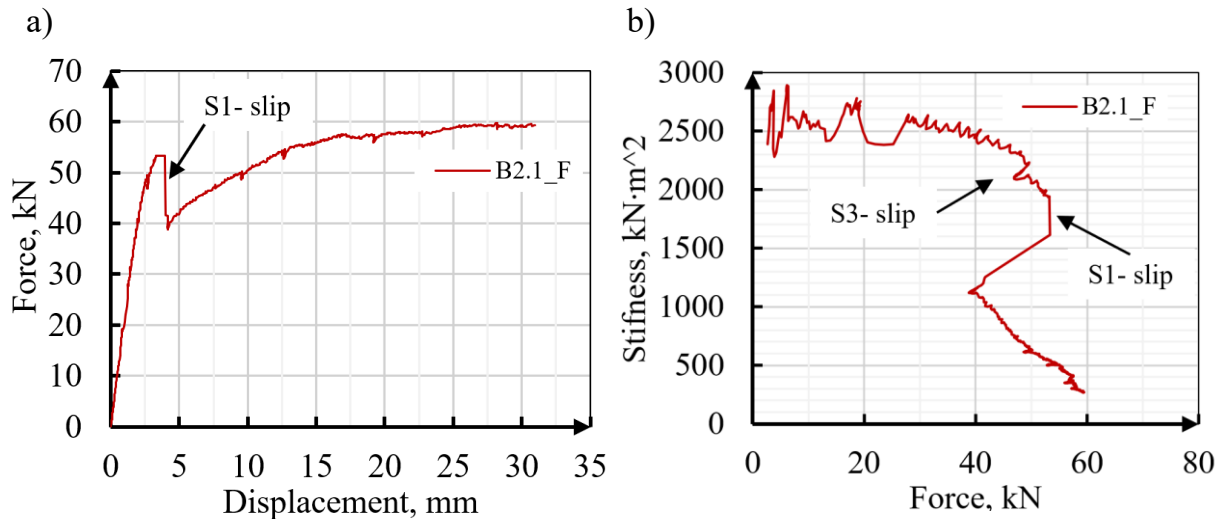


Fig. 6.7. Comparison of force-displacement characteristics with flexural stiffness for beam B2.1-F
 Rys. 6.7. Porównanie charakterystyki siła/przemieszczenie ze sztywnością giętną dla belki B2.1-F

The deformation results obtained in the form of maps from the DIC measurements allow the identification of flexural cracking and interface slip. Due to the insufficient resolution of the measurement, it was not possible to identify the first cracking accurately, close to that of the cracking identification from the beam stiffness analysis. The edge areas of the beams are the areas of greater disturbance in the DIC measurement. These areas are identifiable between successive measurement steps as local 'noise' - significant differences in the strain readings without a change in the force value.

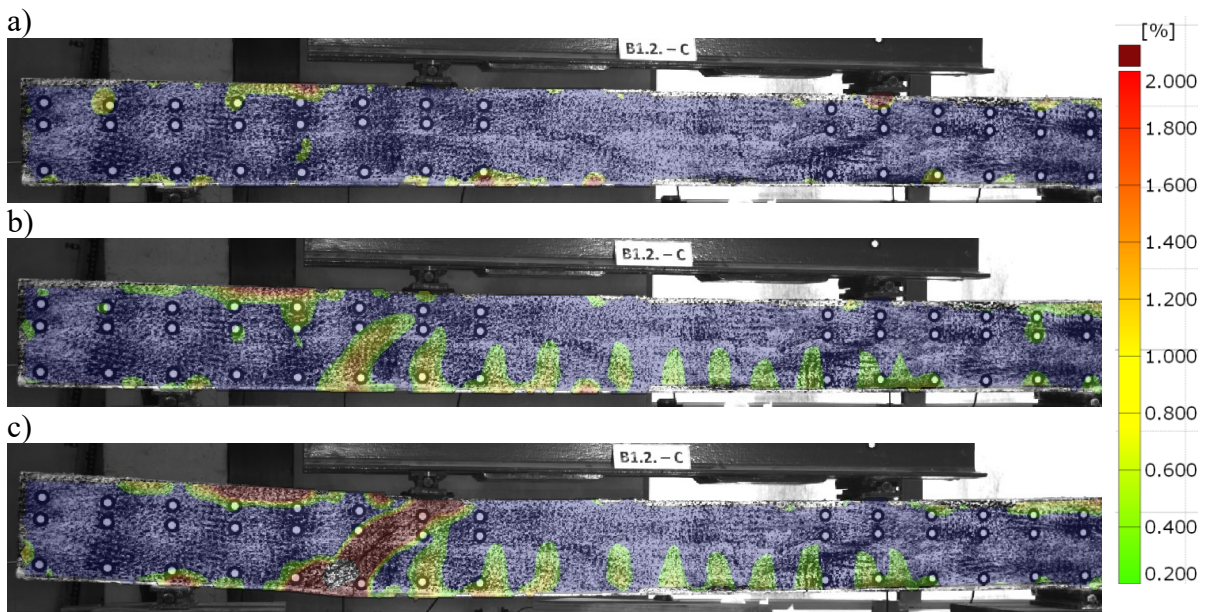


Fig. 6.8. View of principal strain for B2.1-F beam: a) 50.9 kN, b) 70.6 kN, c) 77.2 kN
 Rys. 6.8. Widok odkształceń głównych dla belki B1.2-C: a) 50.9 kN, b) 70.6 kN, c) 77.2 kN

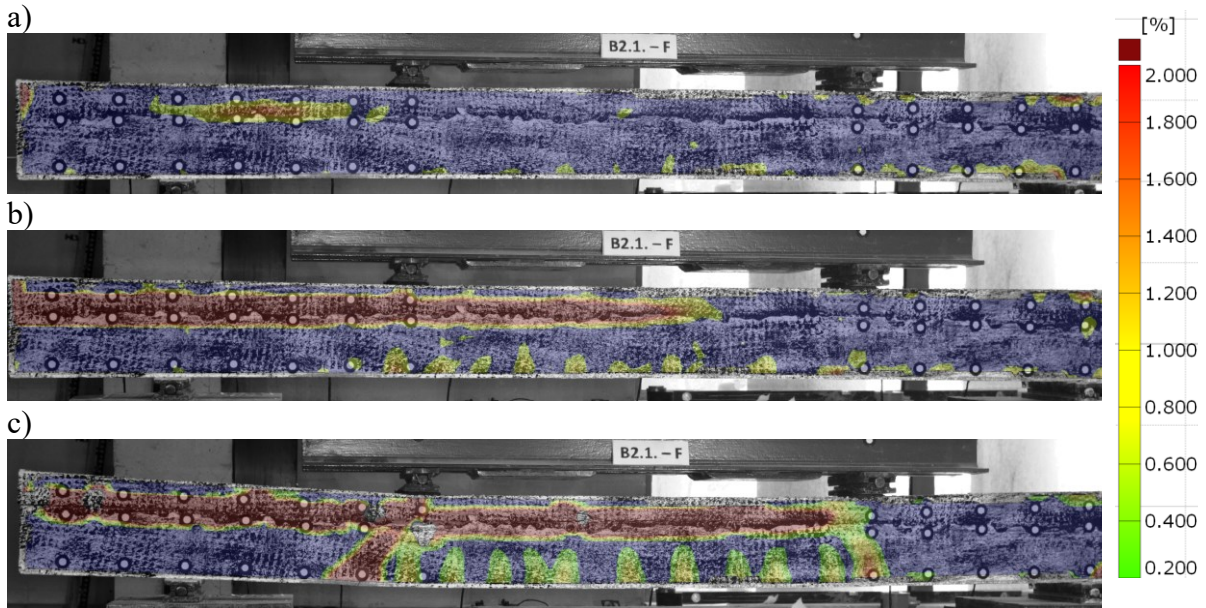


Fig. 6.9. View of principal strain for B2.1-F beam: a) 49.5 kN, b) 53.3 kN, c) 59.8 kN

Rys. 6.9. Widok odkształceń głównych dla belki B2.1-F: a) 49.5 kN, b) 53.3 kN, c) 59.8 kN

The primary objective of the preliminary study was to calibrate the measurement methods used and the relationships developed for the analysis of the interface displacement. Beam B2.1-F was selected for detailed analysis, particularly in the area of local interface cracking. Measurement with LVDT sensors and DIC analysis allowed the identification of the same load value of the interface cracking. The differences in the area marked in the diagram in the red box (Fig. 6.10) are due to slight differences in the synchronisation of the measurements of the test apparatus and the cameras. The same measurement frequency of 2 Hz was used for both methods, but there may be some shift in the measurements due to the lack of direct transmission of the load value to the camera recording module.

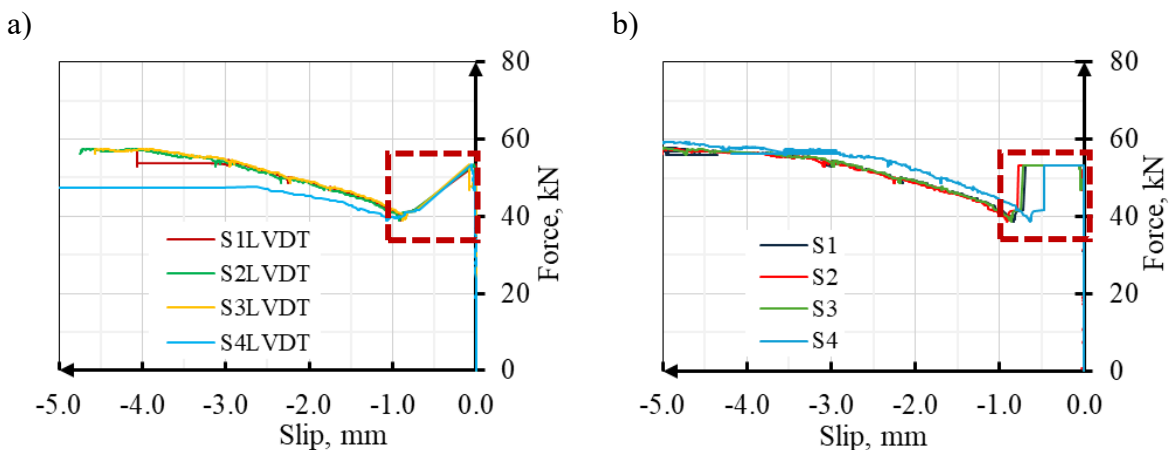


Fig. 6.10. Slip of the interface of B2.1-F beam: a) LVDT measurement, b) DIC measurement

Rys. 6.10. Poślizg w styku belki B2.1-F: a) pomiary LVDT, b) pomiary DIC

Detailed analysis in the small displacement range (Fig. 6.11a) showed a convergence of LVDT and DIC measurements. DIC measurements have a lower precision in the slip

range up to 0.05 mm. An important advantage of DIC measurements is the ability to identify the vertical opening of the interface, as shown in Fig. 6.11b.

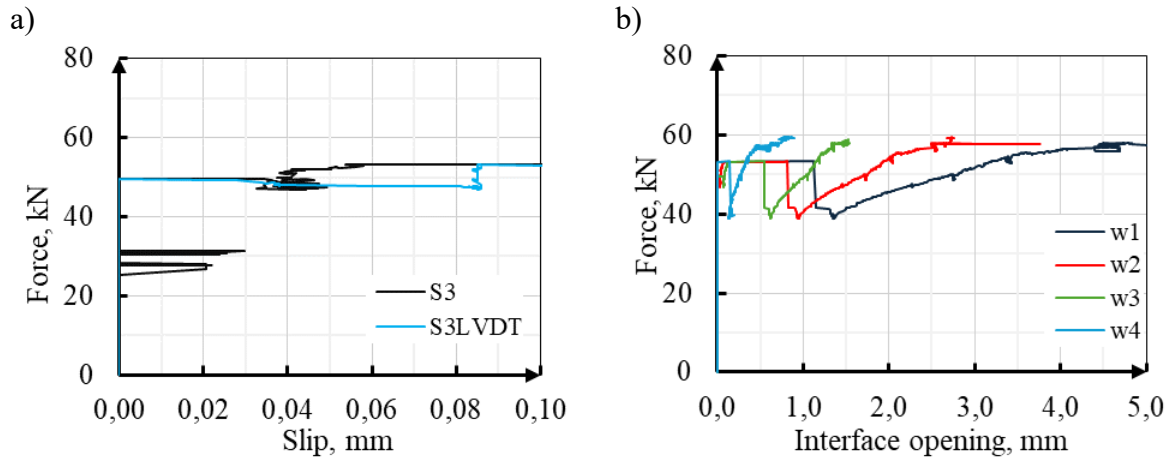


Fig. 6.11. Displacement at the interface of B2.1-F beam: a) slip measurement by LVDT and DIC comparison, b) interface opening (DIC measurement)

Rys. 6.11. Przesunięcia w styku belki B2.1-F: a) porównanie poślizgu zmierzonego czujnikami LVDT i metodą DIC, b) rozwarcie pionowe styku (pomiar DIC)

Measurements of deformation on virtual strain gauges (Fig. 6.12) with a base length of 80 mm allowed identification of the position of the compression zone in beam B1.1-C located in the upper 40 mm of the section height (interface location between precast and concrete topping). The readings for beam B2.1-F allow the approximate identification of the position of the compression zone before delamination and the tension zone in the precast and concrete topping after cracking. Deformation measurements based on virtual strain gauges are characterised by unsatisfactory precision and measurement accuracy in the range of force values lower than close to the maximum.

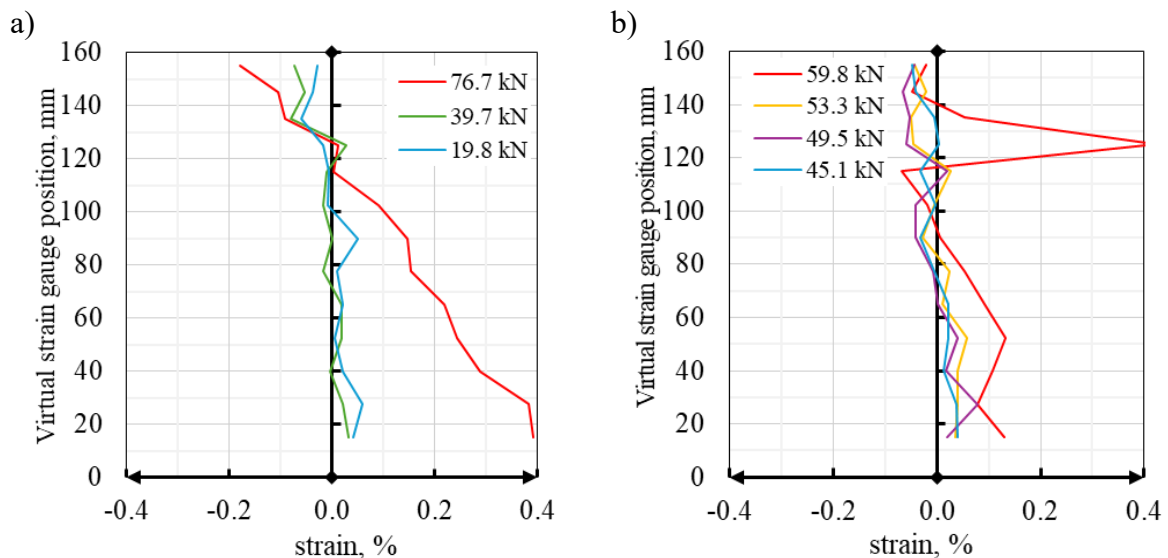


Fig. 6.12. Virtual strain gauge readings: a) B1.1-C, b) B2.1-F

Rys. 6.12. Odczyty wirtualnych tensometrów: a) B1.1-C, b) B2.1-F

For all the beams tested, vertical cracking of the unreinforced concrete layer was observed due to the local pressure (Fig. 6.13a). In beams with delamination of the interface, the concrete topping was divided into sections between the force application points (Fig. 6.13b). For beam B4.1-O, due to the rapid failure, there was a dynamic drop-off of the concrete topping sections, as shown in the stop-frame in Fig. 6.14.

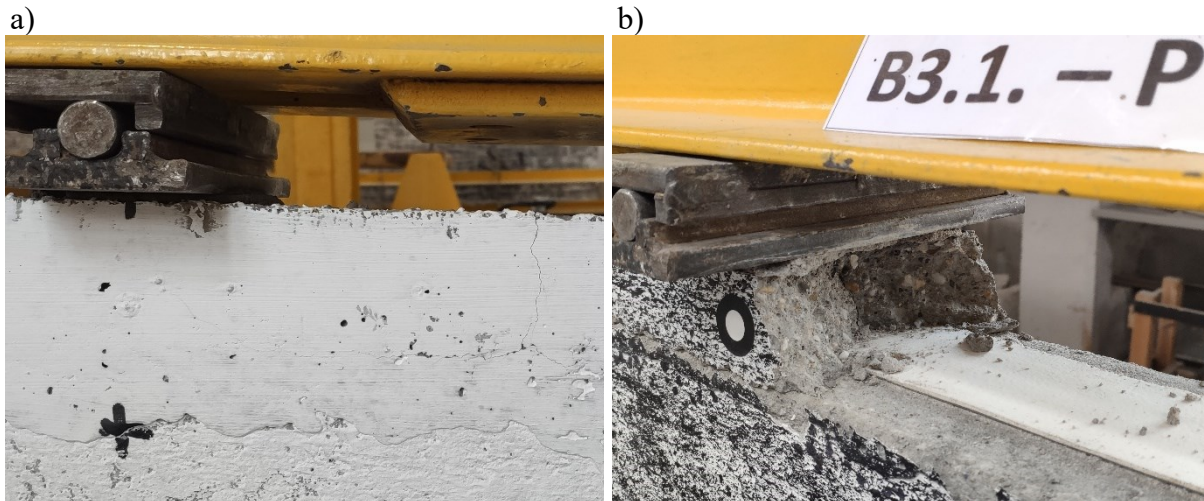


Fig. 6.13. View of topping concrete cracking: a) B1.2-C, b) B3.1-P

Rys. 6.13. Widok zarysowań nadbetonu: a) B1.2-C, b) B3.1-P



Fig. 6.14. View of beam B4.1-O at the failure point

Rys. 6.14. Widok belki B4.1-O w chwili zniszczenia

Based on the preliminary studies carried out, it is possible to present conclusions relevant to further main studies:

- The use of mats reduced the interface strength for the B2-F and B3-P series beams. Used an antiadhesion agent allowed the adhesion to break at the interface of the B4-O series beams.
- Local cracking of the interface did not significantly affect the flexural stiffness of the beam. The loss of element stiffness resulting from the bond to the concrete topping occurred when the interface was cracked to the face of the element.

- The lack of concrete topping reinforcement resulted in cracking due to the pressure. A concrete topping reinforcement was designed for the main series beams.
- The applied displacement measurement of the interface with LVDT sensors and by image analysis of the DIC enables the identification of cracking at the interface with sufficient accuracy.
- The analysis of the flexural stiffness of the beam, based on the DIC displacement data and the load values, makes it possible to determine the value of the flexural cracks.
- Displacement values of the interface based on measurements with LVDT sensors, as well as image analysis (e.g. of beams B2.1-F), make it possible to precisely determine the slip value of the interface (in the range of >0.05 mm).
- The precision of slip measurement in the range up to 0.05 mm is sufficient for analysing beam components. For the analysis of direct shear test elements, a reduced measurement area was used to allow higher accuracy indications, including analysis in the displacement range of less than 0.05 mm.
- Analysis of the DIC image using the geometric transformations of the measurement base described in Section 5.2.2 allows the value of the interface opening to be determined.
- The precision and accuracy of the readings for the virtual strain gauge allow the element to be analysed in the range of strains corresponding to the maximum force. By measuring the strain values at the height of the component, it is possible to determine the height of the compression zone.

6.3. Direct shear tests

The measurements taken by the LDS sensors were mainly used to analyse the results of the direct shear tests (Fig. 6.15a). The DIC measurements taken on one of the surfaces were used as a subsidiary to analyse in detail the behaviour of the interface along the length of the element (Fig. 6.15b). Tests were carried out through reaching the maximum force until the residual force was obtained from the mutual displacement of the elements after the interface was cracked.

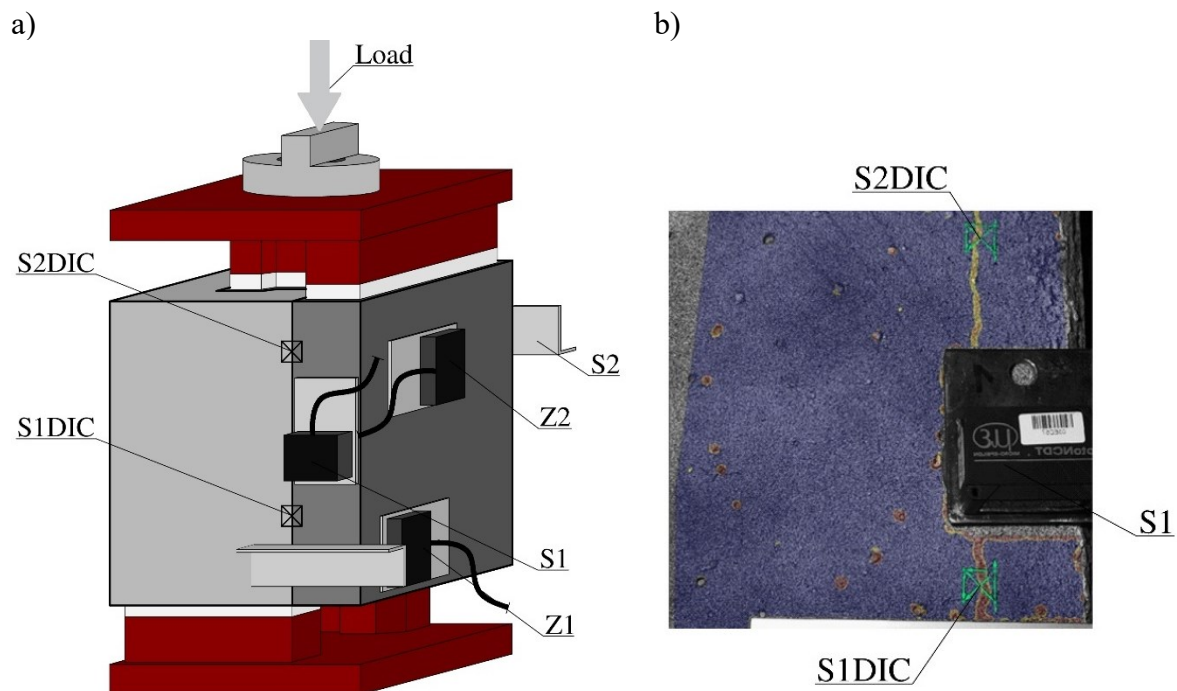


Fig. 6.15. Labels of measuring points: a) placement, b) DIC view

Rys. 6.15. Odczyty wirtualnych tensometrów: a) umiejscowienie, b) widok dla pomiaru DIC

The force/slip characteristics obtained in this study can be discussed in three groups according to the assignment of the elements to the surface preparation type. Only one element (Z2.1_AB1) had a significantly higher maximum force than the other two elements in group AB. The behaviour of all elements can be divided into three phases:

- Phase I - until maximum force is reached with a measured slip value of 0.05 to 0.10 mm for type C elements and 0.05 to 0.30 mm for type AB and CB elements. The slight non-linearity obtained for type C elements is sometimes referred to as phase II in the literature, so the entire interface description is divided into four phases. In this study, however, the description of the interface performance in terms of division into three phases is retained.
- Phase II - an increasing slip of the concrete topping relative to the precast element with decreasing force value. A stable residual force can be determined with slip values in the range of ~5.0 to ~10.0 mm for AB and CB elements. For group C elements, the residual force does not reach a stable value, except for element C1.
- Phase III - failure of elements due to increasing mutual displacement in the interface for AB and CB elements. C-type elements, except for C3, have failed due to diagonal cracking of the precast and concrete topping associated with increasing displacement, mainly on one side of the element. Elements C1 and C2 shifted rapidly from phase I to times III.

After the interface was cracked for element C3, a residual force of similar value (15.65 kN) to elements with intentionally broken adhesion (AB-type) was obtained, averaging 14.52 kN. However, the residual value occurred at three times the slip for element C3. The C1 element slipped unevenly (significantly different slip values for sensors S1 and S2). They, therefore, did not experience a separable phase II as in AB and CB elements with a slip range of several mm. A short residual load phase in the force range of 33.43 kN was recorded. Also, for element C2, a residual force of 22.53 kN (initial value of quasi-phase II) was measured. For elements C1 and C2, phase II only occurred for a displacement increment of ~ 0.7 mm.

By comparing C- and AB-elements, it is possible to define the residual value as the value of the load carried by the interface resulting from the shape and roughness of the element. The effect of shape should be understood as the confinement of the concrete topping relative to the rib. This effect can be intensified due to the bending resulting from the eccentricity of the centre of mass of the concrete topping relative to the precast element after cracking. The CB-type elements were characterised by lower values of residual force, which is attributed to adhesion breaking and roughness compensation. Isolating the effect of adhesion, roughness, and shape will be analysed in the following sections. The split into phases is indicated in Figure 6.16, which shows the results for each element, taking the slip value as the average value obtained from the LDS sensors located on opposite sides of the elements.

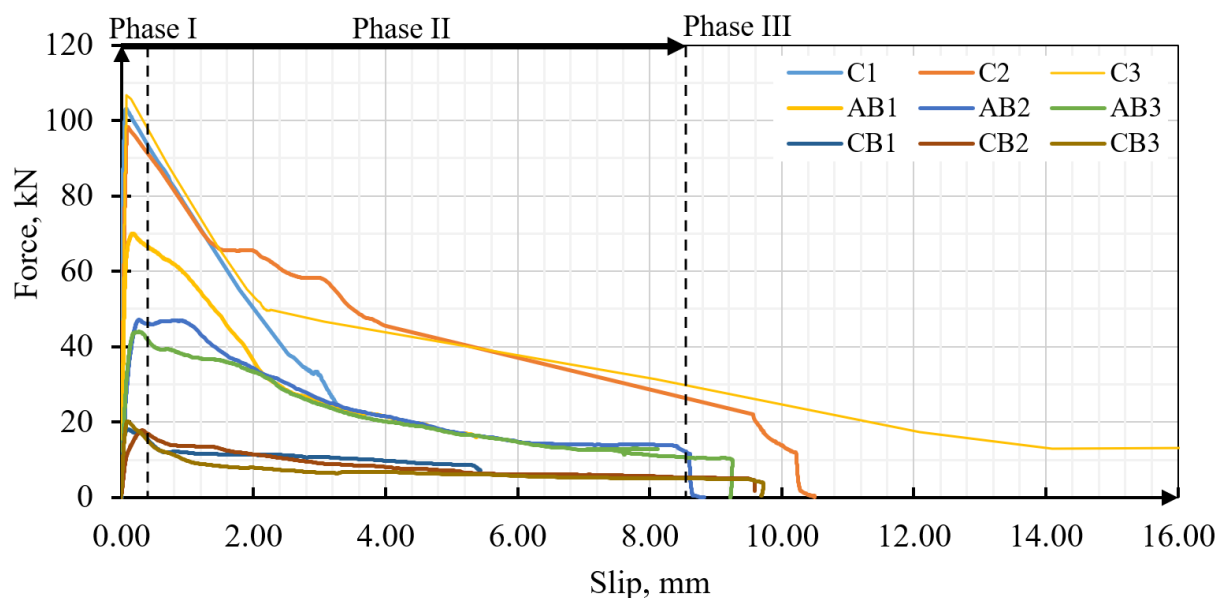


Fig. 6.16. Force/slip characteristics of ZX.2 series elements

Rys. 6.16. Charakterystyka siła/poślizg badanych elementów serii ZX.2

For each test element, displacements at the interface were measured on opposite surfaces. For one surface, the measurement was carried out for the upper part of the interface (closer to the applied load) and the other for the lower part. Figure 6.17a-i summarises the results of the resulting displacements at the interface for each element in the phase I range. The elements with a fully bonded interface (type C) showed a significant difference in the measured displacements at the interface depending on the measurement point. The measurement in the lower part of the element showed significantly higher displacement values in the initial phase than in the upper part. Only for element Z1.2_C2 was the difference compensated for when the maximum force was reached. For elements Z1.2_C1 and Z1.2_C3, the difference between the upper and lower measuring points was twice as at an equal force maximum value. However, significant differences were also noted here. For element Z1.2_C1, the largest displacement at the force cracking the interface was recorded at point S2; for element Z1.2_C3, it was recorded at point S1. Elements C1 and C3 were cracked at the interface with a displacement of less than 0.05 mm at one of the measuring points, while the contact cracking of element C2 occurred with a displacement of 0.10 mm. Despite the differences indicated, the failure force for the elements in group C was 98.26 - 106.79 kN.

Significantly smaller relative differences between opposite measuring points were recorded for AB and CB elements. The element Z2.2_AB1 with the highest maximum force among its group and the difference in slip between sensors S1 and S2 in the initial phase will be analysed further using the DIC measurement. The components with the applied antiadhesion agent were characterised by a loss of adhesion in the range of ~0.20 mm. For the components with the spacer applied, it is possible to distinguish a slightly expanded phase I, which transitions smoothly into phase II without the characteristic rapid decrease in force and increase in displacement as in C-type components. The transition from phase I to phase II is the point where the cross-section of the element at the corners of the concrete topping to the edge of the precast element is cracked.

Based on the analysis of the force-displacement characteristics, it is possible to determine the effectiveness of the adhesion-breaking agents used at the interface (AB elements) and the adhesion-breaking and roughness limitation of the interface (CB elements). Intending further analysis, it is important not only to reduce the value of the maximum force but also to increase the slip value at maximum force, thus lowering the interface's stiffness.

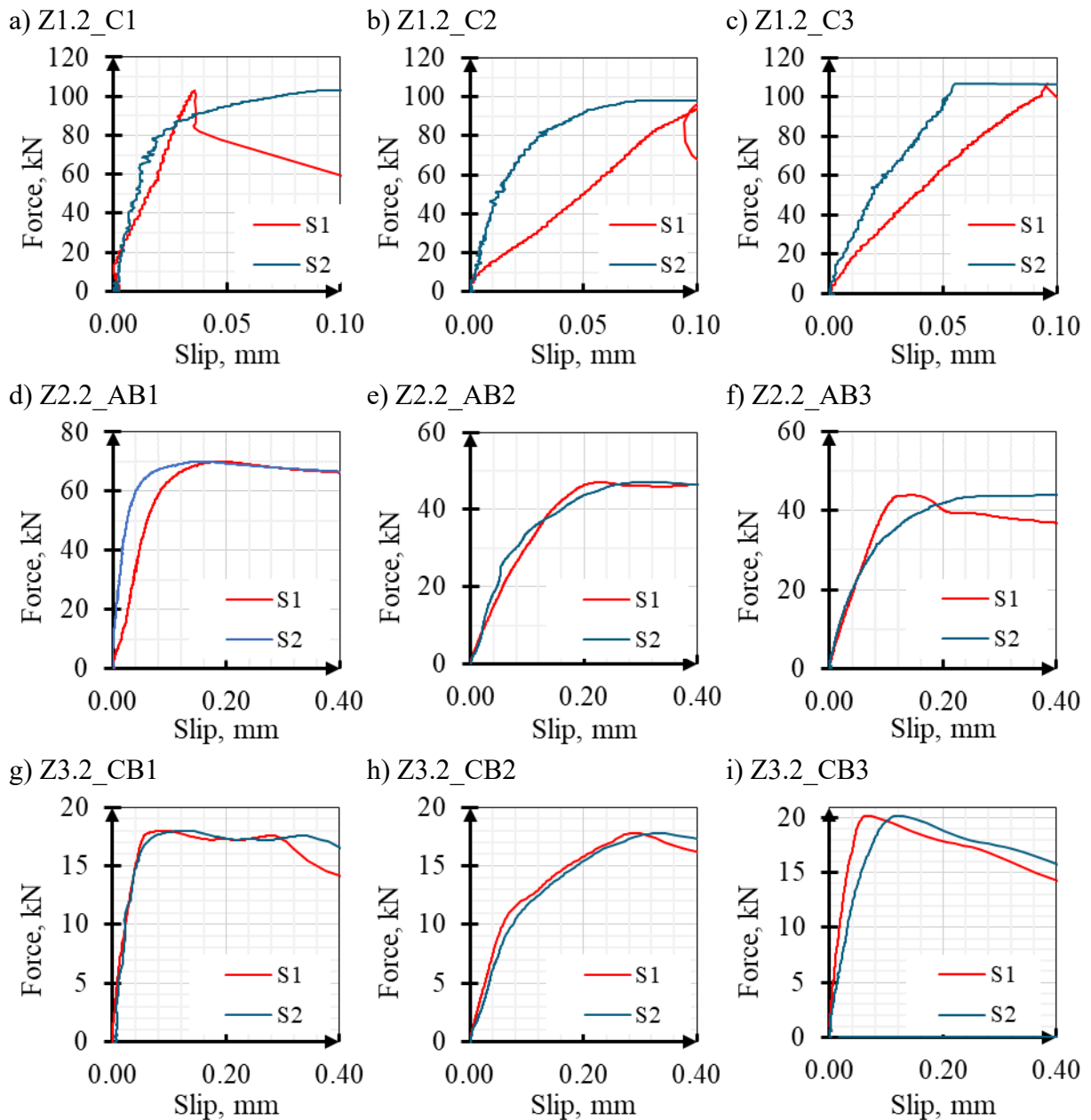


Fig. 6.17. Measured contact slip values: a-c) Type C series, d-f) Type AB series, g-i) Type CB series
 Rys. 6.17. Zmierzone wartości poślizgu w styku: a-c) seria typu C, d-f) seria typu AB, g-i) seria typu CB

For selected elements from each of the three groups, the readings of the interface slip sensors were compared with the outward displacement of the concrete topping (Fig. 6.18). Following the increasing displacement at the interface, concrete topping outwards was noted. The smallest values of horizontal displacement of the concrete topping were recorded for the CB element. This is the group of elements with the slightest roughness, with no direct bond between the concrete topping and the precast. Elements in phase II were characterised by a further increase in horizontal displacements of the concrete topping, reaching values that temporarily exceeded the value of the interface slip.

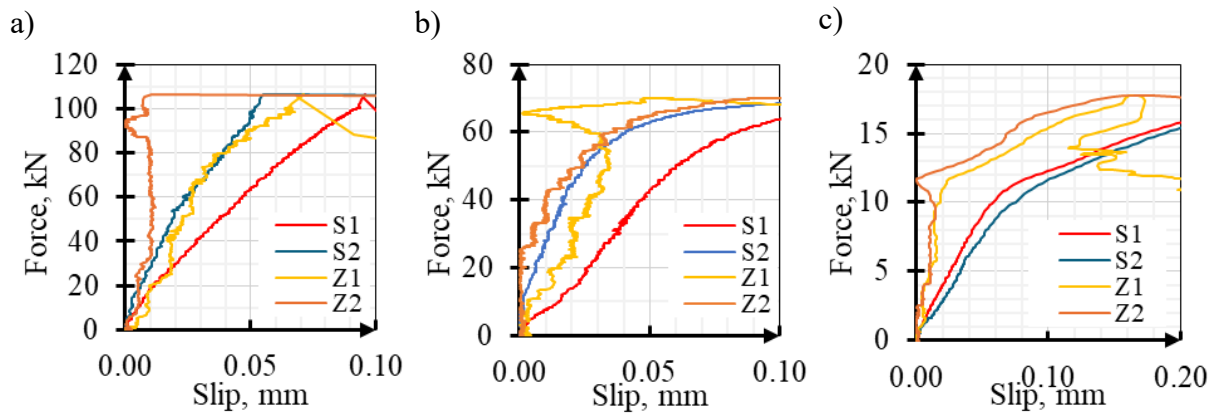


Fig. 6.18. Summary of readings for sensors in the arrangement of type S (slip) and Z (topping deflection): a) Z1.2_C3, b) Z2.2_AB1, c) Z3.2_CB2

Rys. 6.18. Zestawienie odczytów dla czujników w rozmieszczeniu typu S (poślizg) oraz Z (odchylenie nadbetonu): a) Z1.2_C3, b) Z2.2_AB1, c) Z3.2_CB2

Additional DIC measurements were carried out for all components on one of the side surfaces. The image analysis allowed additional data to be acquired, such as the value of the interface opening and the analysis of the slip value in the interface along the length of the element. Figure 6.19 shows the results for elements Z1.2_C3 and Z2.2_AB1 in phase I before reaching the maximum force and after cracking the interface (phase II). The view of the strains (scale 0.1 - 0.3%) confirmed the readings of the opposing LDS sensors, indicating the occurrence of larger interface displacements (slip) at the lower edge of the component than in its upper part closer to the load application surface (Fig. 6.19a, b). Due to the differences in the size of the measurement bases, their location, and the limited area of the DIC measurements (smaller than the surface of the element), it is not possible to compare the readings of the DIC directly with the LDS. For the element Z1.2_C3, the virtual measuring point S1DIC, located in the middle of the length of the sensor base S1LSD, showed smaller displacements for the same force than the LSD measurement (Fig. 6.20a). The measurement at S2DIC showed smaller displacements of the interface than the S2LSD measurement located at the opposite edge. The measurements for element Z1.2_C3 did not show the alignment of interface displacements when reaching a load value close to the maximum force. Measurements taken on element Z2.2_AB1 also identified a difference in interface displacements along the length of the element but with values significantly lower than the difference between the LSD sensors on the opposite faces. This indicates different values for the displacements of the entire surfaces of the element, possibly due to the eccentricity of the load application or the different interface stiffness.

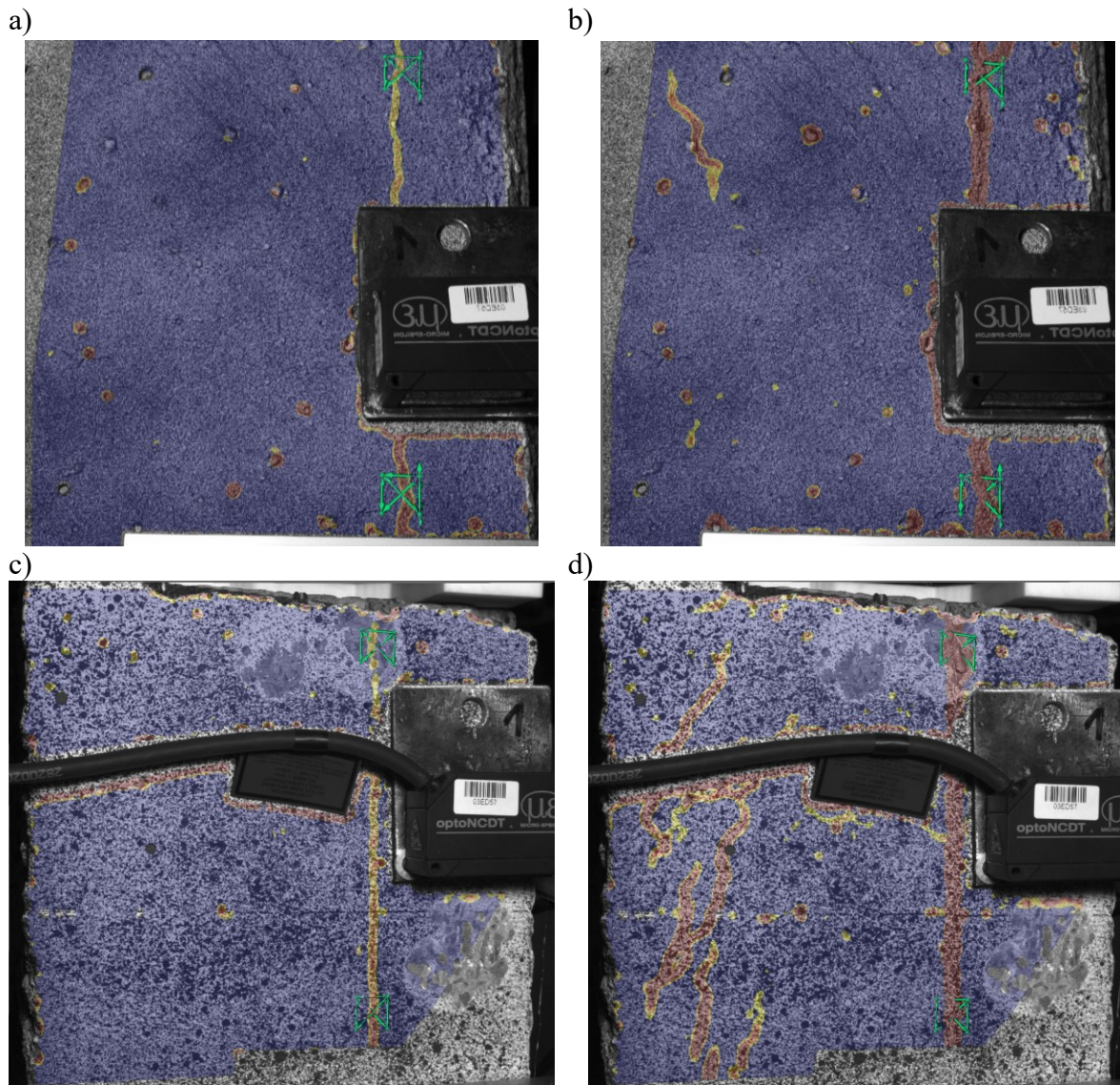


Fig. 6.19. View of principal strain for DIC measurement: a-b) Z1.2_C3, c-d) Z2.2_AB1
 Rys. 6.19. Widok odkształceń głównych dla pomiaru DIC: a-b) Z1.2_C3, c-d) Z2.2_AB1

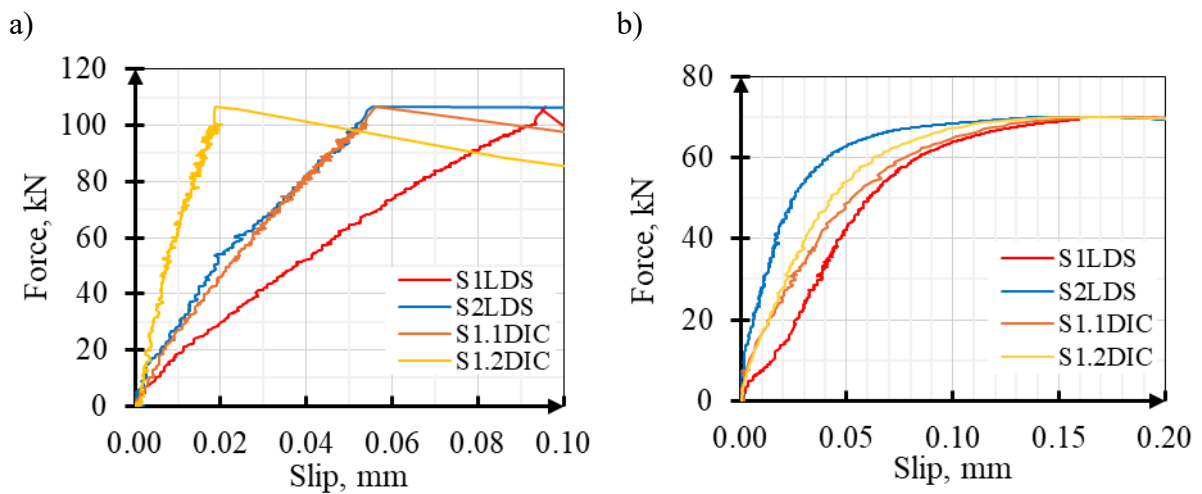


Fig. 6.20. Comparison of LDS and DIC measurements.: a) Z1.2_C3, b) Z2.2_AB1
 Rys. 6.20. Porównanie pomiarów LDS z DIC: a) Z1.2_C3, b) Z2.2_AB1

An increase in the interface opening values with increasing slip was noted. The measured values are in the range of very small displacements (<0.02 mm). Significantly, the values of interface opening in the Z1.2_C3 element are not directly correlated with the slip value (Fig. 6.21a). Identical values of interface opening (~ 0.01 mm) were recorded at both measurement points (W1 and W2) despite a twofold difference in slip value between points S1 and S2. The lack of difference in contact opening along the length of the element indicates that the eccentricity value between the centre of gravity of the precast and the concrete topping has little influence on the behaviour of the interfaces. This feature will be the subject of further analyses, including FEM analyses. The opposite situation occurred for element Z2.2_AB1, where, despite the significant convergence of the measured slip values, the measurements of the interface opening differed significantly (Fig. 6.21b). In contrast to the C-type element, the measurement for the AB-type element indicates the formation of an interface opening due to the interacting force eccentricity. As a result of this eccentric force, an increased opening of the interface was expected at its upper part (measuring point W1.2DIC) relative to the lower part (W1.1DIC). However, it is not possible, based on the DIC measurements alone, to separate the effect of the load eccentricity from the value of the interface opening due to component slip and roughness.

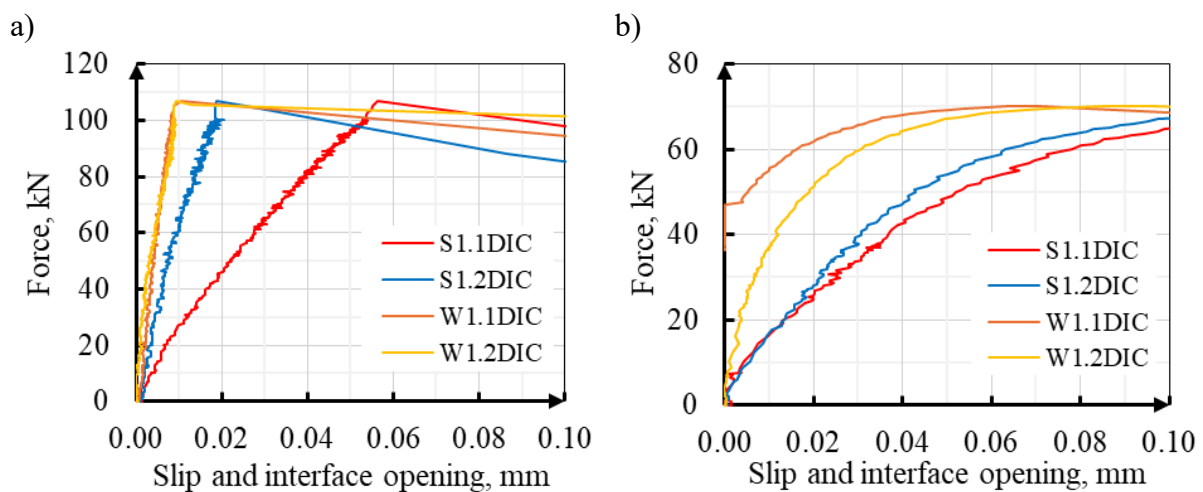


Fig. 6.21. Slip and interface opening - DIC measurements: a) Z1.2_C3, b) Z2.2_AB1

Rys. 6.21. Poślizg oraz rozwarcie styku – pomiary DIC: a) Z1.2_C3, b) Z2.2_AB1

To compare the characteristics of the interfaces and to subsequently correlate the experimental results with the FEM analysis, force-displacement characteristics were converted to interface stiffness. The stiffness was defined as the force required for the slip (displacement) measured at the interface (average value from S1LSD and S2LSD measurements). The stiffness is not calculated with the interface's surface area (width) due to the unknown effective contribution of the surface area to the stress transfer. The distribution will be verified at a later stage by FEM analysis, which will be used in the

subsequent analysis (Section 7). The results are presented for values greater than 20 % of the maximum force (Fig. 6.22) to limit the noise due to the limited precision of the measurement for displacements smaller than <0.02 mm. Such converted values made it possible to define the characteristics of the interface as behaving non-linearly even in phase I before it is fully cracked. One element differed significantly from the other two measurements for both Group C and AB elements. Despite the different characteristics of the stiffness curve (element C1), the final value was significantly consistent with the values for elements C2 and C3 (Fig. 6.22a). Elements from all groups were characterised by decreased stiffness values (non-linear characteristics), particularly at 80% of the maximum force value. The calculated stiffness values for elements in group AB are four times lower than for group C (Fig. 6.22b). Interestingly, despite the significant difference in maximum force achieved, the stiffness of elements CB1 and CB3 converged with that of elements AB2 and AB3 in the initial range. However, this stiffness was degrading (Fig. 6.22c). As for group C, the other element types also recorded an alignment of the interface stiffness values at near maximum force, identical to the transition from Phase I to Phase II. The interface stiffnesses in Phase II for C- and AB-type elements were 200 times lower than in Phase I, and stiffnesses 50 times lower were obtained for C-type elements.

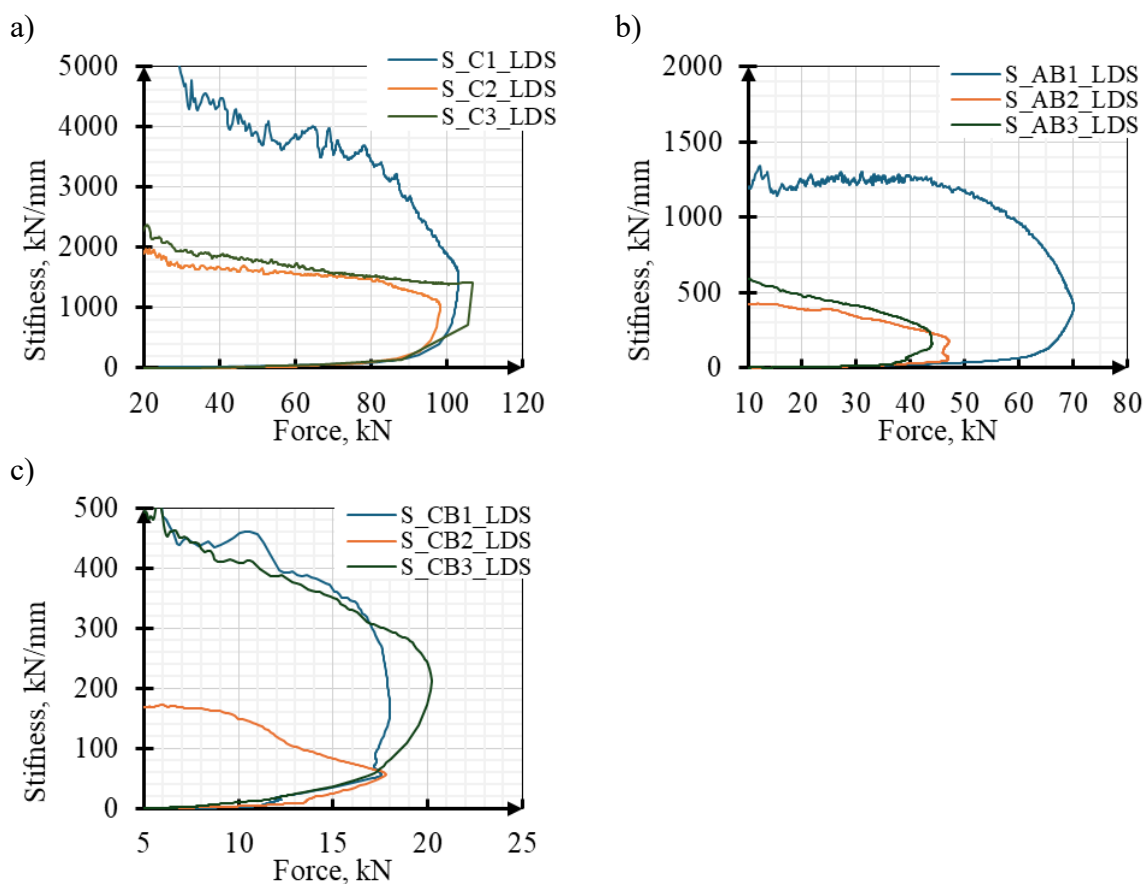


Fig. 6.22. Interface stiffness for average slip values: a) Z1_C, b) Z2_AB, c) Z3_CB

Rys. 6.22. Sztywność styku dla średniej wartości poślizgu: a) Z1_C, b) Z2_AB, c) Z3_CB

Following the test, a crack survey of the elements was carried out. Characteristic cracks extending from the precast head's edge to the concrete topping's outer edge were noted on all elements. These cracking marks out the side sections of the concrete topping relative to the head. These observations are consistent with the concrete topping deflection measurements relative to the precast. Based on the view of the damage, two types of failure were separated:

- Type I - slippage and cracking of the interface over the whole element's width, three-phase element behaviour possible.
- Type II - slippage of the interface with a significantly higher value on only one side of the element, associated with the formation of cracking crossing the concrete topping and the precast element.

Type I failure can be assigned to elements in groups AB and CB. Only one element from group C (Z1.2_C3) was characterised by pure type I destruction. Type II damage was attributed to elements Z1.2_C1 and Z1.2_C2. These elements were cracked across the entire width but with many times larger slip values for one of the sides. These elements were split by cracks with a large opening (>1.0 mm). For Z1.2_C3, this was a crack pulling the rib head from its base (Fig. 6.23f), and in Z1.2_C2, a crack at the extension of the rib lateral surface, cutting through the concrete topping (Fig. 6.23e). The possibility of Type II failure due to a possible eccentricity of the load application to the vertical axis of the elements will be one of the points of the FEM analysis.

Tables 6.7-6.9 summarise the most relevant measured parameters such as maximum force, residual force, displacement value for maximum force, interface stiffness values for the three force levels and type of failure. The calculated COV values are additionally given for the values of maximum force, residual force, and slip. A low COV of 3.4 % was obtained for group C elements and 5.9 % for group CB. A significantly higher COV was recorded for the elements of group AB due to one element achieving a maximum force 56% higher than the other two. COV values greater than 25% were recorded for the residual force, for which it is impossible to clearly determine residual force for the individual element groups, as described in the previous paragraphs.

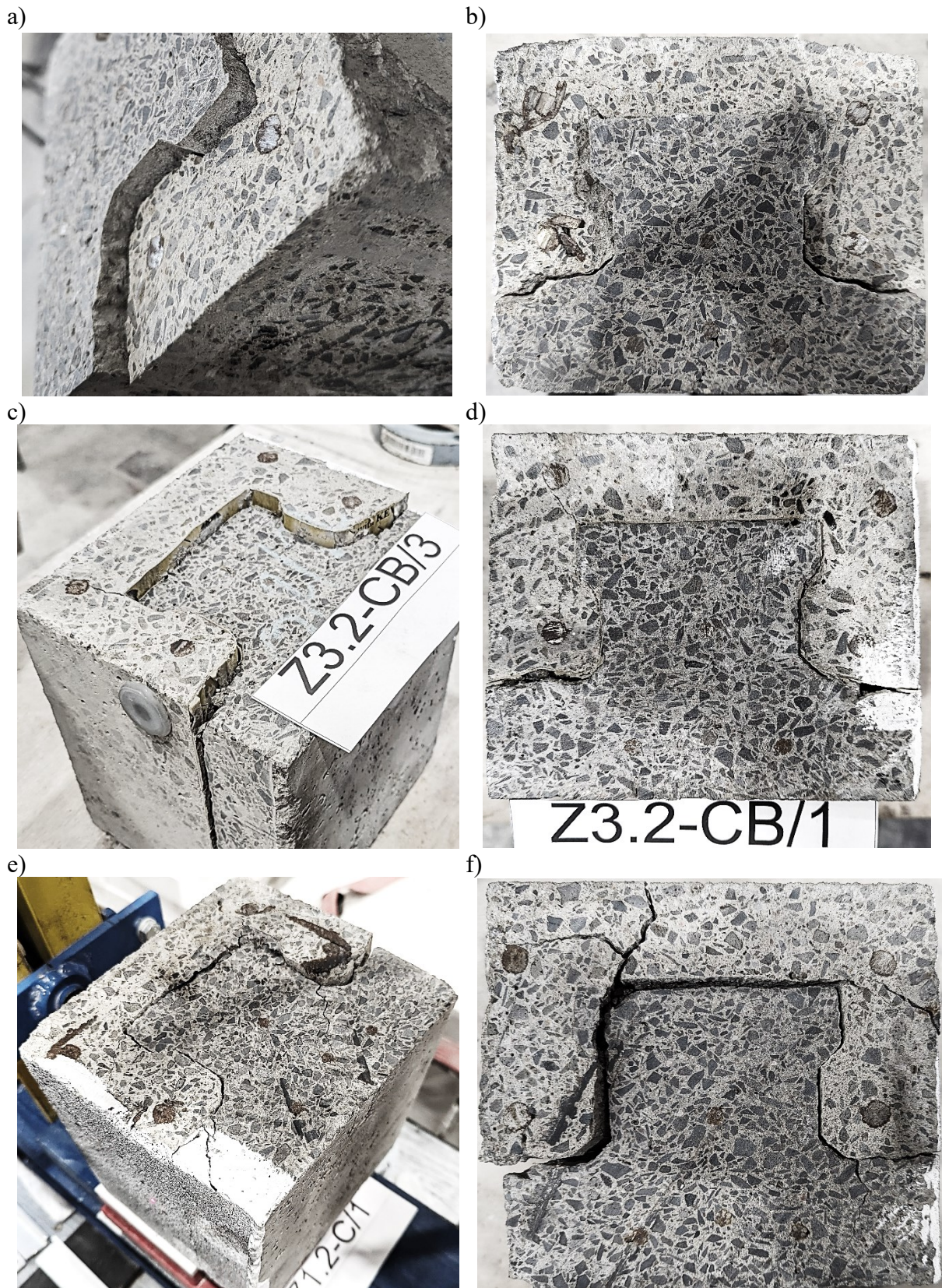


Fig. 6.23. View of elements after test: a-d) failure type I, e-f) failure type II

Rys. 6.23. Widok elementów po badaniu: a-d) zniszczenie typu I, e-f) zniszczenie typu II

Table 6.7

Summary of failure type and cracking forces of C type elements

Zestawienie sił niszczących i rysujących elementów typu C

Element	Peak load F_{max} , kN	Residual load F_{res} , kN	Slip at F_{max} S_{max} , mm	Stiffness 20% F_{max} $K_{20\%}$, kN/mm	Stiffness 50% F_{max} $K_{50\%}$, kN/mm	Stiffness F_{max} $K_{100\%}$, kN/mm	Failure type
Z1.2_C1	103.11	33.43	0.068	5930.8	3780.2	1516.3	II
Z1.2_C2	98.26	22.53	0.097	1989.8	1614.7	1013.0	II
Z1.2_C3	106.79	15.65	0.076	2232.5	1756.7	1405.1	I
Mean	102.72	23.87	0.080	3384.3	2383.9	1311.5	
SD	3.49	7.32	0.012				
COV, %	3.4%	31%	15.2%				

Table 6.8

Summary of failure type and cracking forces of AB type elements

Zestawienie sił niszczących i rysujących elementów typu AB

Element	Peak load F_{max} , kN	Residual load F_{res} , kN	Slip at F_{max} S_{max} , mm	Stiffness 20% F_{max} $K_{20\%}$, kN/mm	Stiffness 50% F_{max} $K_{50\%}$, kN/mm	Stiffness F_{max} $K_{100\%}$, kN/mm	Failure type
Z2.2_AB1	70.07	16.24	0.179	1222.5	1262.9	391.5	I
Z2.2_AB2	47.10	14.15	0.275	420.7	386.7	171.3	I
Z2.2_AB3	43.94	13.17	0.267	591.8	464.1	164.6	I
Mean	53.70	14.52	0.240	745.0	704.6	242.4	
SD	11.64	1.28	0.043				
COV, %	21.7%	9.0%	18.1%				

Table 6.9

Summary of failure type and cracking forces of CB type elements

Zestawienie sił niszczących i rysujących elementów typu CB

Element	Peak load F_{max} , kN	Residual load F_{res} , kN	Slip at F_{max} S_{max} , mm	Stiffness 20% F_{max} $K_{20\%}$, kN/mm	Stiffness 50% F_{max} $K_{50\%}$, kN/mm	Stiffness F_{max} $K_{100\%}$, kN/mm	Failure type
Z3.2_CB1	18.00	11.50	0.110	374.0	448.4	163.6	I
Z3.2_CB2	17.78	7.55	0.311	174.6	155.5	57.2	I
Z3.2_CB3	20.21	6.45	0.095	545.5	407.1	212.7	I
Mean	18.66	8.50	0.172	364.7	337.0	144.5	
SD	1.10	2.17	0.098				
COV, %	5.9%	25.5%	57.2%				

Based on the results of the direct shear tests presented, it is possible to provide some conclusions and points for further analysis:

- The force-displacement characteristics of the interface allowed three phases to be distinguished. Despite the lack of reinforcement at the interface, the elements were characterised by a separable phase II, for which it is possible to determine the residual force with increasing slip value.
- The residual stiffness of the interface was 50 to 200 times lower than in phase I.
- Elements with the interface left rough (type AB and C) were characterised by a higher residual strength than elements with a mat to reduce roughness (type CB).
- Elements of all types were characterised by some non-linearity of interface stiffness in Phase I before slip failure.
- LDS measurements and DIC analysis indicate different interface displacement values along its length within Phase I. This suggests a different degree of stress on the composite plane along its length.
- Cracking (slip) of the interface occurred when a displacement value of >0.05 mm was reached, consistent with the conclusions presented in the literature review.
- Based on the above conclusion, a criterion for filtering slip results with a lower tolerance of 0.05 mm was adopted in the analyses of the beams.
- Based on the failure image of the elements, two types of failure were distinguished. The first is related to the full slip of the concrete topping, and the second one combines slip with cracking, cutting through the topping and the precast element.
- The individual surfaces of an AB element may differ in stiffness due to the different effectiveness of the antiadhesion agent used. This is indicated by the different stiffness and maximum force for element Z2.2_AB1 compared to the others in the AB group.
- The analysis of the values of the interface opening (axial tensile forces), the deflection of the concrete topping, and the interface's slippage will be the subject of further analyses. The FEM analyses will be extended to include the effect of load application eccentricity on the failure model of the element. The distribution of interface displacements in phase I along the length of the element will be verified.

6.4. Four-point bending tests

The measuring points were assigned symbols according to the caption of the sensors in Figure 6.24. The sensors located at the front face of the element were abbreviated as FF (front face) and BF (back face), and measurements of strand slip were also given, referred to as strand front (SF) and strand back (SB). The front and back faces were referenced in the direction of the X-axis.

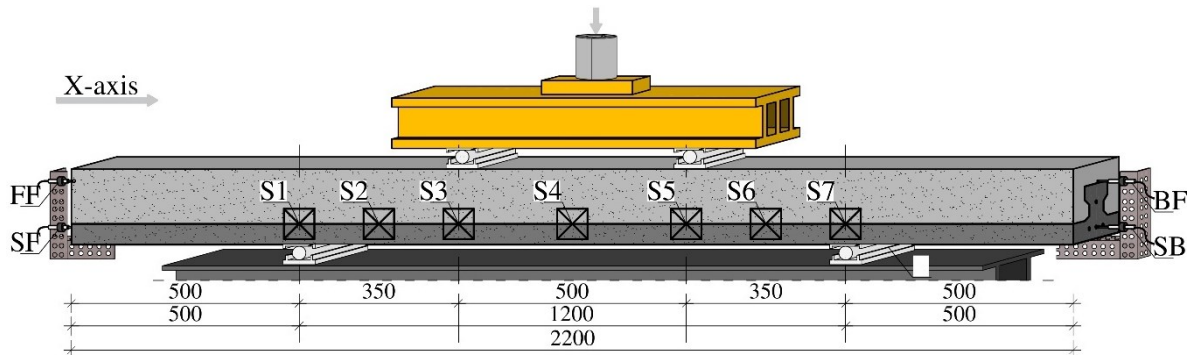


Fig. 6.24. Label of the measurement points and the X axis as seen from the front (DIC surface)
Rys. 6.24. Oznaczenie punktów pomiarowych oraz osi X patrząc od frontu (powierzchni DIC)

Figures 6.25 and 6.26 summarise the test results in force-displacement diagrams for the entire test range (Fig. 6.25) and a close-up of the range covering the drawing force values (Fig. 6.26). These are shown for reference to provide an overview of the results obtained for all elements. Table 6.10 summarises the most relevant parameters obtained from the tests for each element.

To discuss the four-point bending results in detail, the elements are divided into subsections corresponding to dividing the elements into groups. Group one are the basic beams, i.e. a composite beam over the entire interface bond (Z1.1_C), with an antiadhesion agent (Z2.1_AB) and a fully covered mat interface (Z3.1_CB). The second group is represented by elements for which there is an interface over the entire height of the cross-section and, therefore strain compliance. Beams with an interface on the top and bottom surfaces with a covered side surface are also included in this group. The third group includes elements where the requirements of the second group cannot be met. In the elements Z7.1_T and ZZ8.1_B, only one effective interface plane was made, which provides an effective connection until cracking. The results in each group were compared to the basic element Z1.1_C in each case.

The highest failure force value was obtained for element Z1.1_C and the lowest for Z6.1_TB. A visual inspection of each beam was carried out before the test, and for element Z6.1_TB, no slip of strands was observed, which could indicate a loss of

anchorage. The tests showed that the element's stiffness was twice as low in the initial phase. The flexural crack develops at a force of 20 kN, indicating a lack of effective prestressing and anchorage of the strands. The results for this beam were not described due to the defective execution. The analysis of the type Z6_TB element in the following section was based on three-point bending tests.

By analysing the value of the flexural cracking force, slippage-generating force at the interface, the peak force, and the failure mechanism, four phases of beam behaviour were detailed:

- Phase I - reaching the flexural cracking force indicated by the stiffness analysis.
- Phase II - development of interface cracking (slip) up to the edge of one of the supports (if slip is present).
- Phase III - from Phase I or II until reaching the peak force.
- Phase IV - decrease in force up to 50% of the maximum value. In rapid element failure, Phase IV is assigned to the force value immediately after reaching the maximum force. Phase IV is used to describe the failure of the beams at the largest crack width.

Following the completion of the tests, an inspection of the cracking and failure surfaces of the elements was carried out. The outward deflection of concrete topping fragments at the interface slip length was observed for each beam. This effect was observed regardless of the presence of only local cracking at the interface and complete slip-up to the face of the precast element.

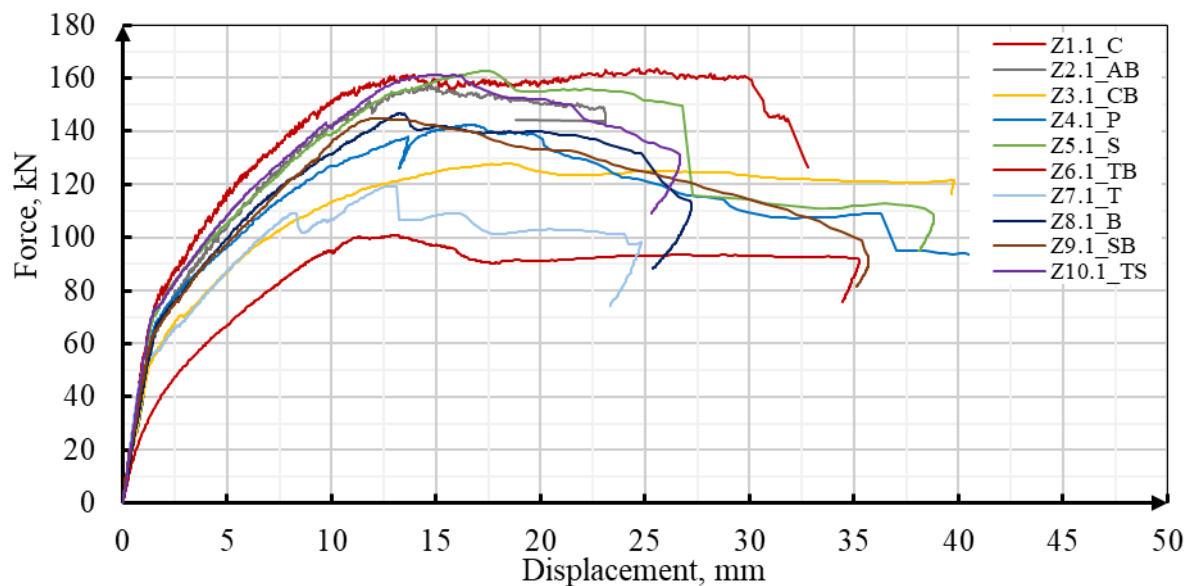


Fig. 6.25. Force-displacement characteristics of ZX.1 series beam

Rys. 6.25. Charakterystyka siła/przemieszczenie dla belek z serii ZX.1

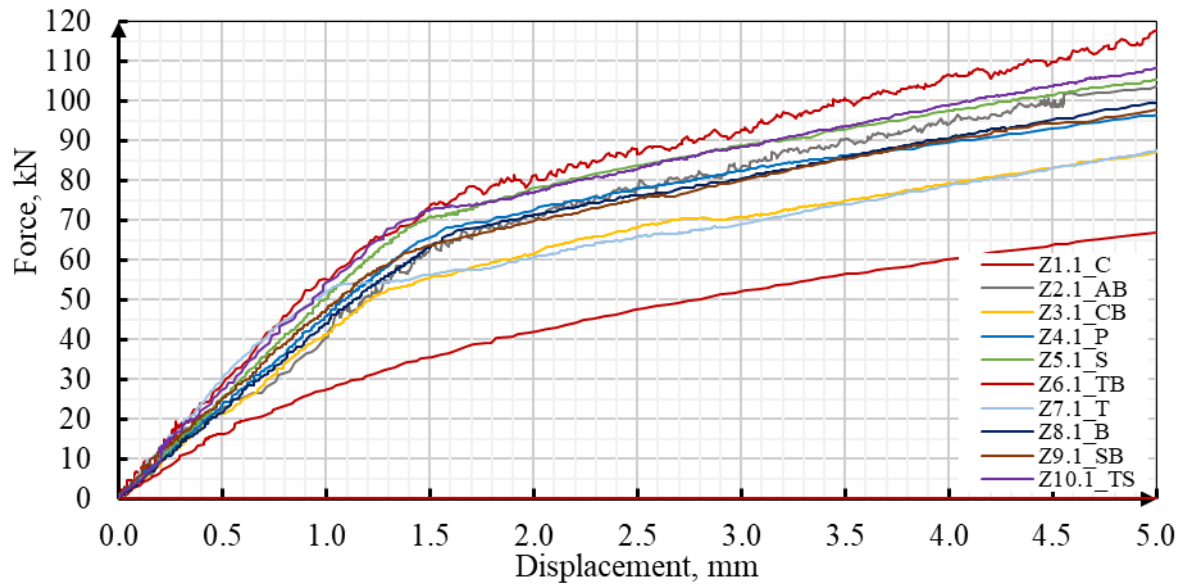


Fig. 6.26. Force-displacement characteristics in flexural crack force range of ZX.1 series beam
 Rys. 6.26. Charakterystyka siła/przemieszczenie w zakresie siły rysującej dla belek z serii ZX.1

Table 6.10

Summary of failure type and characteristic forces of ZX.1 type beams

Zestawienie sił oraz typów zniszczenia belek z serii ZX.1

Element	Initial stiffness K_{init} , kNm ²	Flexural crack F_{cr} , kN	Interface slip at support $V_{R,1,cr}$, kN	Interface slip at face $V_{R,2,cr}$, kN	Diagonal crack $V_{R,c}$, kN	Peak load F_{max} , kN	Failure type
Z1.1_C	2130	65.6	-	-	130.2	163.6	I
Z2.1_AB	1590	63.5	144.3	-	131.2	157.3	I
Z3.1_CB	1560	51.1	57.9	67.1	97.8	127.7	I
Z4.1_P	1730	67.6	126.8	108.8*	126.8	142.5	II
Z5.1_S	1910	70.7	88.7	149.6*	131.0	162.7	III
Z6.1_TB	1270	19.3	100.1	-	88.7	100.9	III
Z7.1_T	2260	52.0	119.1	119.1	103.3	119.1	II
Z8.1_B	1640	67.8	111.1	-	84.1	146.8	III
Z9.1_SB	1840	63.8	-	-	134.6*	144.8	I
Z10.1_TS	2010	68.3	-	-	134.0	161.4	I

*Interface slip or diagonal crack after peak load

6.4.1. 4PBT results for group I

The flexural stiffness of beam Z1.1_C was, as expected, the highest of all the components tested, reaching an initial value of ~ 2100 kNm². Beams Z2.1_AB and Z3.1_CB had a similar initial stiffness with a value of ~ 1560 - 1590 kNm² (Fig. 6.27).

Initial stiffness is defined as a constant value until the first flexural cracks occur, decreasing stiffness. The first flexural cracking occurred earliest for beam Z3.1_CB at a force of 51.1 kN. Despite a 35% difference in initial stiffness, flexural cracking occurred for the other two beams at almost the same value. The decrease in stiffness caused by cracking for beam Z1.1_C occurred at a force of 65.6 kN, followed by beam Z2.1_AB at a force of 63.5 kN. The determination of the flexural force is subject to some error due to the lack of a single measurement directly indicating a decrease in stiffness. The readings representing the transition of an element from phase I (uncracked) to phase II (cracked) represent an interval within approximately 5% of the force reached at a given point. The failure force achieved was successively for the elements: Z1.1_C - 163.6 kN, Z2.1_AB - 157.3 kN, Z3.1_CB - 127.7 kN. The difference between a fully composite element and one with an antiadhesion agent-coated interface was only 4%. The initial stiffness difference between elements Z1.1_C and Z2.1_AB gradually decreased as the applied load increased.

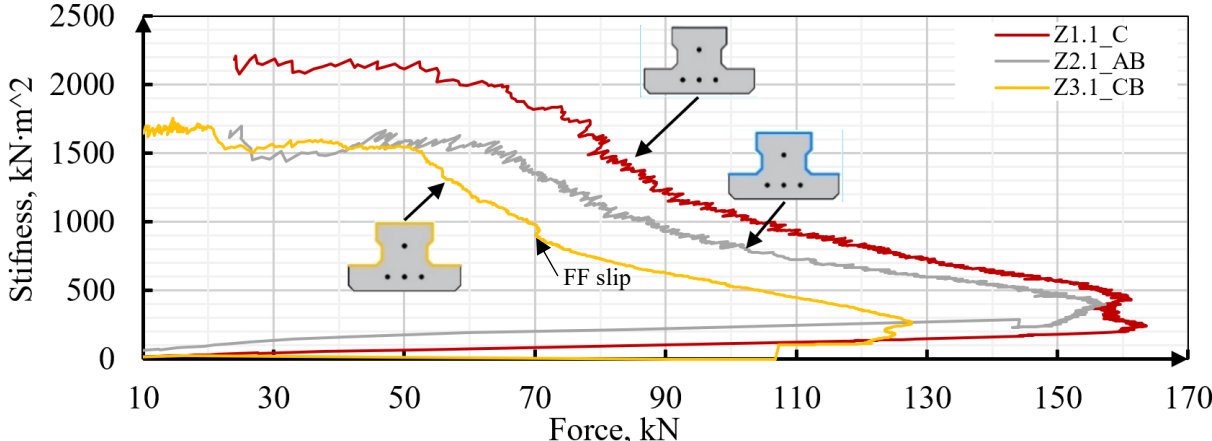


Fig. 6.27. Beam stiffness diagram for selected Z-series beams

Rys. 6.27. Wykres sztywności giętej dla wybranych belek z serii Z

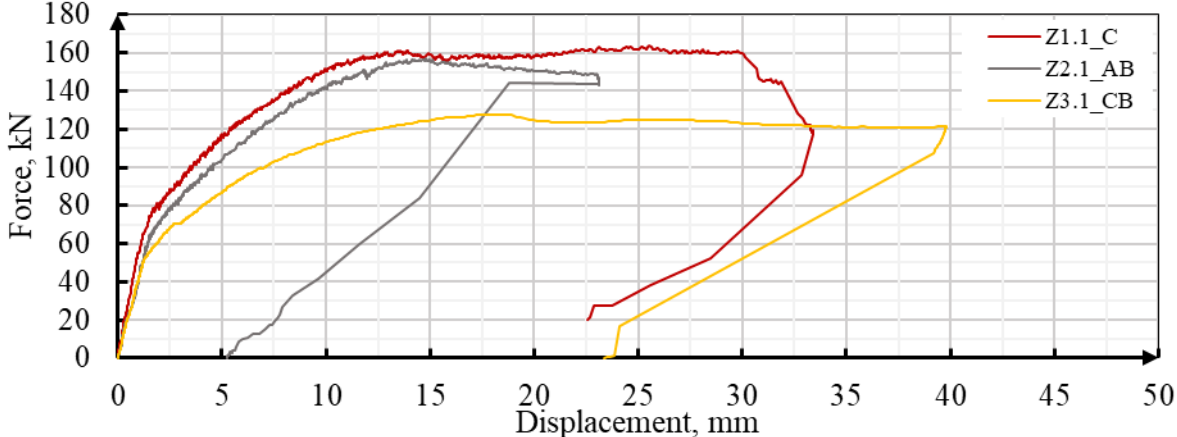


Fig. 6.28. Force-displacement characteristics for selected Z-series beams

Rys. 6.28. Charakterystyka siła/przemieszczenie dla wybranych belek z serii Z

The development of the cracks was not related to strand slip, which occurred in the elements at a force of ~ 100 kN on one side (Fig. 6.29b, h). After a force of 146.9 kN, increasing strand slippage was also noted for the other side in beam Z1.1_C. Due to the faulty assembly of the sensor ('jamming' against the edge of the strand/concrete), no strand slip values were measured in beam Z2.1_AB. For the elements for which the interface slip occurred, the displacement value at the interface is given for the measurement points in the axis of the support and from the face of the element (Fig. 6.29d, g). Due to the lack of interface slip at the support in beam Z1.1_C, measurement results are given for the two measurement points for which the slip was recorded (Fig. 6.29d, a). This was only a local slip due to flexural cracking between the precast element and the concrete topping. Only in beam, Z1.1_C was a compliance between the cracking of the precast and the concrete topping, except for two small areas where the flexural cracks were connected by a section where local slippage occurred at the interface (Fig. 6.30a).

For beam Z3.1_CB, several flexural cracks were noted in the concrete topping and the precast element without a shared path (Fig. 6.30c). There was also slippage of the interface in the axis of the support at a force of 57.9 kN and then to the face edges at a load of 67.1 kN (Fig. 6.29g). Slip at the interface at the edge of support S1 with no slip from the element face was recorded for beam Z2.1_AB at a force of 144.3 kN. For elements Z1.1_C and Z2.1_AB, a diagonal crack was recorded only crossing the concrete topping at similar force values of 130.2 kN and 131.2 kN, respectively. A diagonal crack indicates either shear cracking penetrating both the concrete topping and the precast or local slip of the interface near the cracking. The lack of continuity of the crack into the bottom flange of the precast evidences the lack of a diagonal crack cutting through the precast.

Due to the distortion of the results obtained from the virtual strain gauges by flexural cracks passing through the measurement area, it is only possible to use the measurements taken to determine the height of the compression zone. In beams Z1.1_C and Z2.1_AB, the zone of compression in phase III starts at a height of 45 mm from the top of the cross-section, and in beam Z3.1_AB at 35 mm.

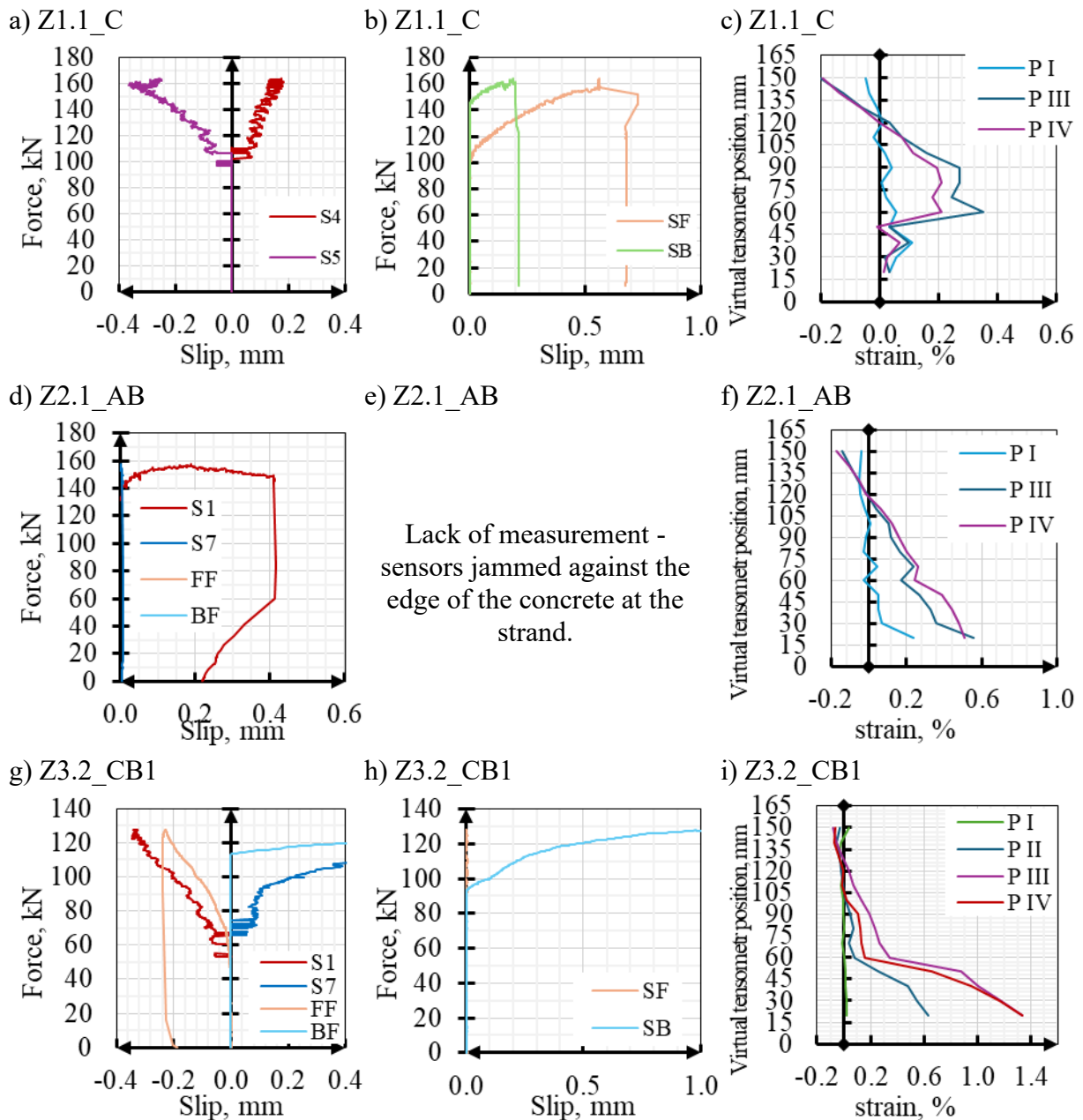


Fig. 6.29. Selected results: a, d, g) slip in the interface, b, e, h) slip of strands, c, f, i) virtual strain gauges
 Rys. 6.29. Wyniki pomiarów: a, d, g) poślizg w styku, b, e, h) poślizg splotów c, f, i) wirtualne tensometry

The failure of all three beams resulted in a very similar appearance (Fig. 6.30 and Fig. 6.31). It is possible to identify a decisive flexural crack directly under one of the force points. The crack crosses the precast element, connecting to the crack in the concrete topping with a short slip section at the interface. The crack ends its path in the compression zone, where concrete crushing occurs when the maximum force is reached. As described above, the element's failure type was defined as **Type I (crushing of the compressed zone and eventual slip)**. For beam Z2.1_AB, the interface slip was measured up to the edge of the left support, and for beam Z3.1_CB, the interface slip was measured along the entire length of the element.

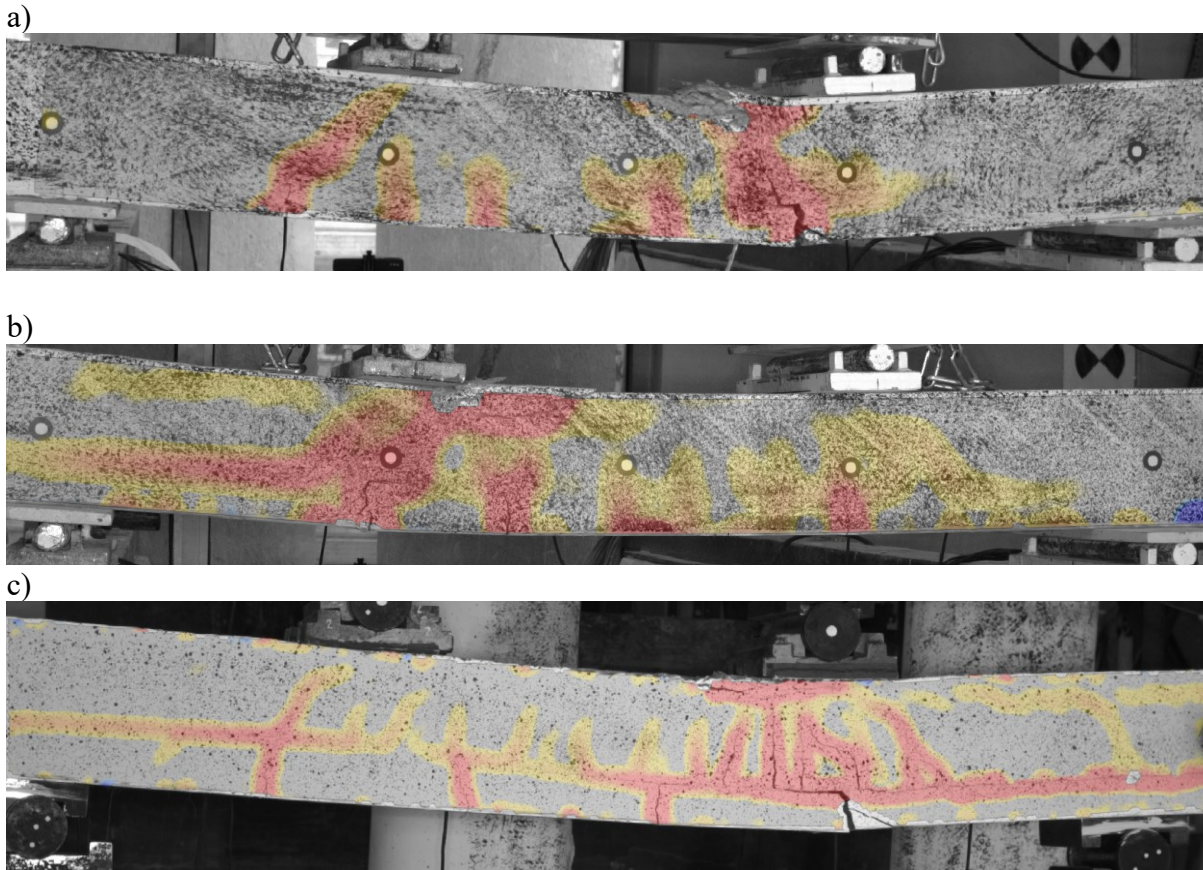


Fig. 6.30. View of principal strain (tensile) after failure: a) Z1.1_C, b) Z2.1_AB, c) Z3.1_CB
 Rys. 6.30. Widok odkształceń głównych (rozciągających) po zniszczeniu: a) Z1.1_C, b) Z2.1_AB, c) Z3.1_CB

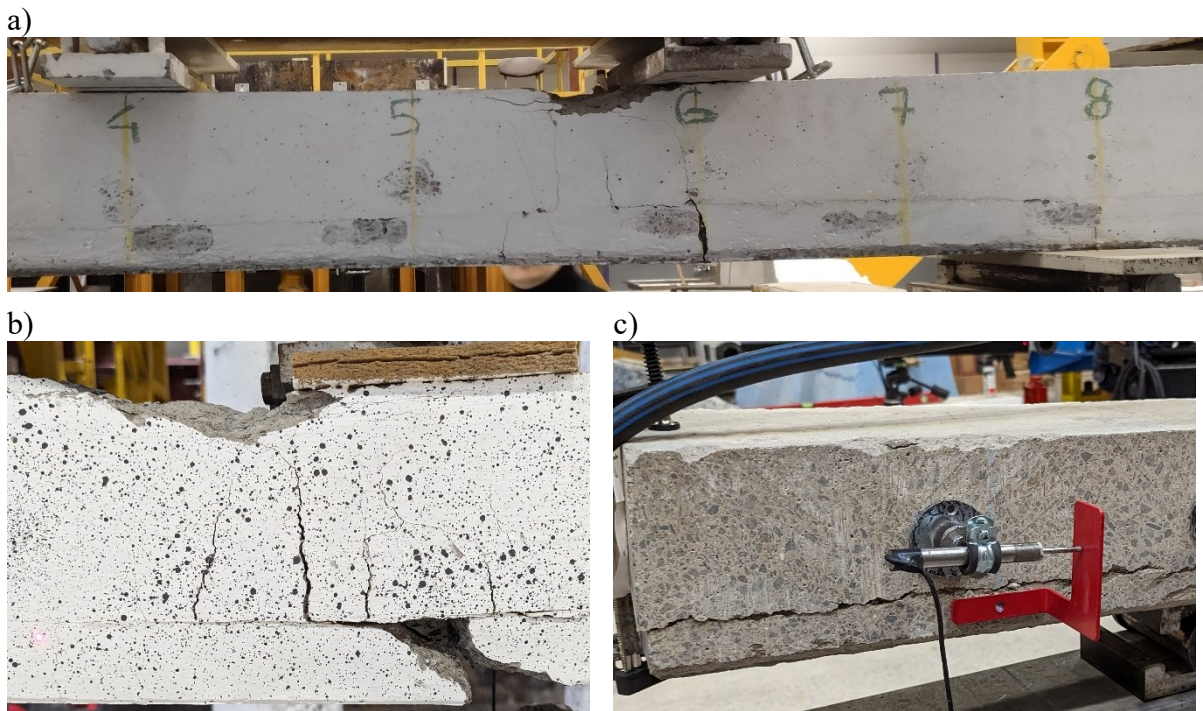


Fig. 6.31. View beams after failure: a) Z2.1_AB, b-c) Z3.1_CB
 Rys. 6.31. Widok belek po zniszczeniu: a) Z2.1_AB, b-c) Z3.1_CB

6.4.2. 4PBT results for group II

Group II elements were characterised by varying initial stiffnesses of the elements in the range ~1730-2010 kNm² (Fig. 6.32), which means that the stiffness of beam Z4.1_P was 23% lower than that of reference beam Z1.1_C. At the same time, the stiffness range is above the values for beam Z2.1_AB or Z3.1_CB. Except for beam Z9.1_SB, the decrease in stiffness due to the development of cracking occurred at similar load values in the range of 67.6-70.7 kN. For beams Z5.1_S and Z10.1_TS, the value of the peak force reached values close to the reference beam, while for elements Z4.1_P and Z9.1_SB, it was ~13% lower.

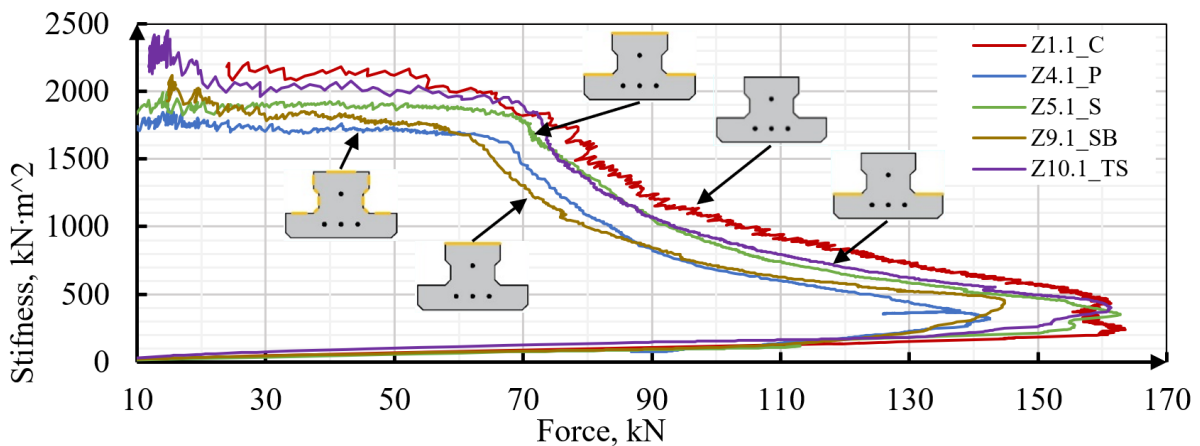


Fig. 6.32. Beam stiffness diagram for selected Z-series beams

Rys. 6.32. Wykres sztywności giętej dla wybranych belek z serii Z

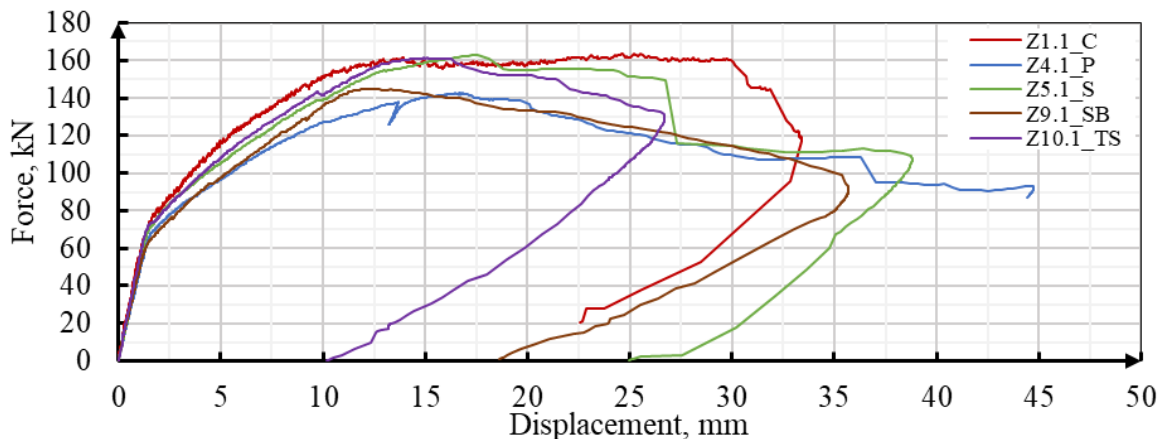


Fig. 6.33. Force-displacement characteristics for selected Z-series beams

Rys. 6.33. Charakterystyka siła/przemieszczenie dla wybranych belek z serii Z

The strand slip measurements showed a partial anchorage loss for each element on one side at a force of 100 kN, or 140 kN if slip also occurred for the other side of the beam (Fig. 6.34b, e, h, k). Slip measurements of the interface on elements Z9.1_SB and Z10.1_TS did not show any slip in the support axes and from the face of the element. For beams Z4.1_P and Z5.1_S, no interface slip was measured from the element face before the maximum force was reached, but only immediately after failure. Before the failure, slippage at the support axis was measured for both elements without this being a point of

brittle decrease in stiffness. On element Z4.1_P, interface slip was associated with the occurrence of a diagonal crack in the concrete topping at a force of 126.8 kN (Fig. 6.34a).

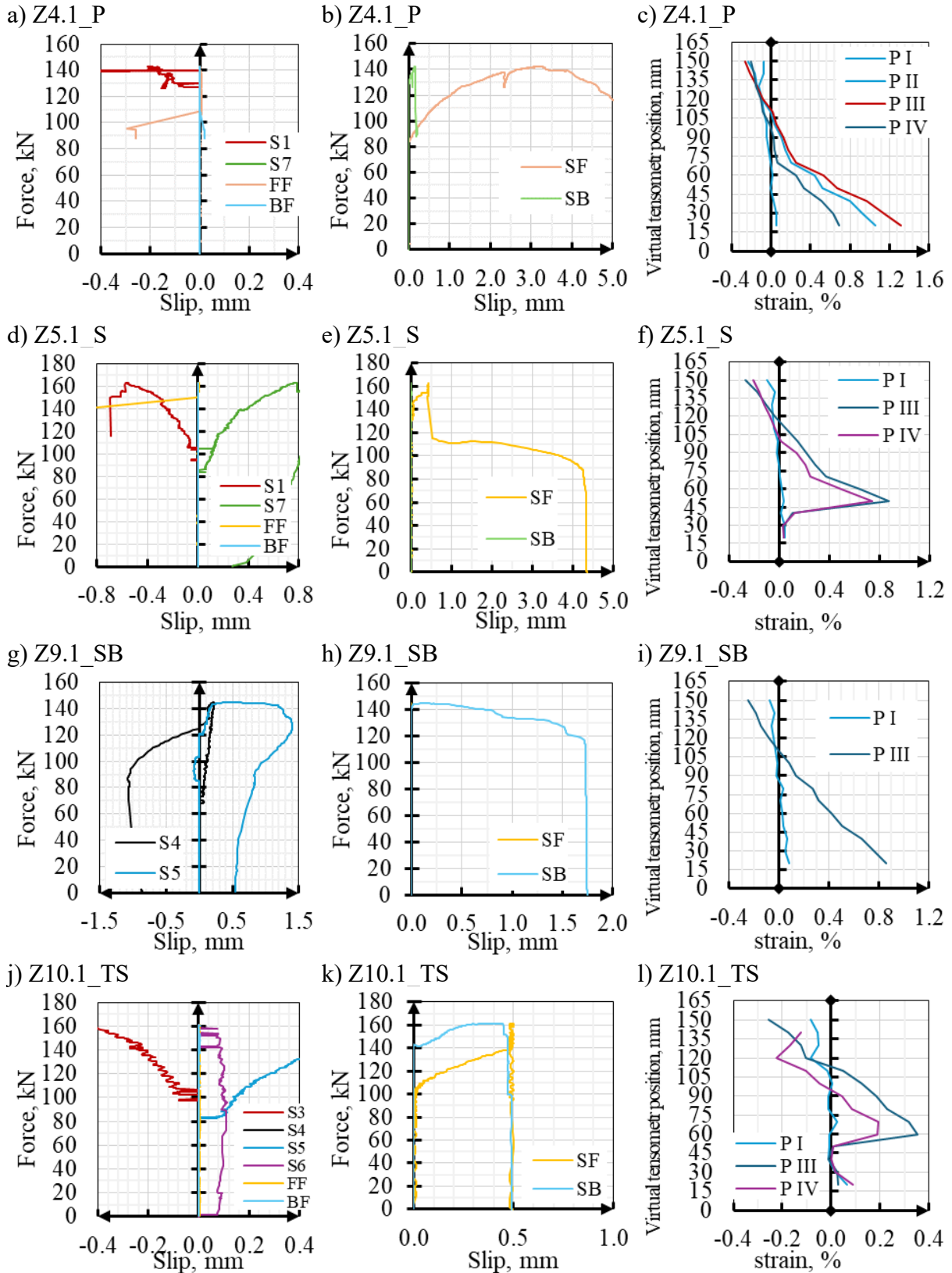


Fig. 6.34. Selected results: a, d, g) slip in the interface, b, e, h) slip of strands, c, f, i) virtual strain gauges
Rys. 6.34. Wyniki pomiarów: a, d, g) poślizg w styku, b, e, h) poślizg splotów c, f, i) wirtualne tensometry

On element Z4.1_P, interface slip was associated with the occurrence of a diagonal crack in the concrete topping at a force of 126.8 kN (Fig. 6.34a). Beams Z9.1_SB and Z10.1_TS are the closest elements to the reference beam due to the lack of cracking in the support axis (Fig. 6.34g, j) and the very similar values of the diagonal forces in the concrete topping. The height of the compressed zone at the maximum force was between 50 and 55 mm from the top edge of the concrete topping in all beams.

Based on the failure image, the same failure type cannot be assigned to all elements in Group II. As described earlier, beams with symbols Z9.1_SB and Z10.1_TS were the closest to the reference beam. This is also true for the failure model. For these elements, a Type I failure is assigned (Fig. 6.35c, d), where the compression zone was crushed, resulting in the buckling the reinforcement bars in the upper concrete topping. Beam Z4.1_P failed due to the **development of diagonal cracks in the concrete topping and propagating through the interface** (Fig. 6.35). **Immediately after failure, the slip of the concrete topping up to the leading edge was measured.** This failure pattern was classified as **Type II. Type III failure was also specified, combining the characteristics of Type I and Type II failure.** Type III failure was characterised by crushing the compression zone with slippage at the interface up to the edge of the support but without a diagonal crack of increasing width. Failure of this type was assigned to beam Z5.1_S (Fig. 6.35c). Based on the strain image, one major difference between the described beams and beam Z1.1_C can be distinguished. For neither of the beams was there a path compliance of cracking in the precast and concrete topping. Despite beams Z9.1_SB and Z10.1_TS reaching a maximum force close to the reference beam, the interface of the beams was locally cracked over a significant length but without reaching the slip up to the edge of the support.

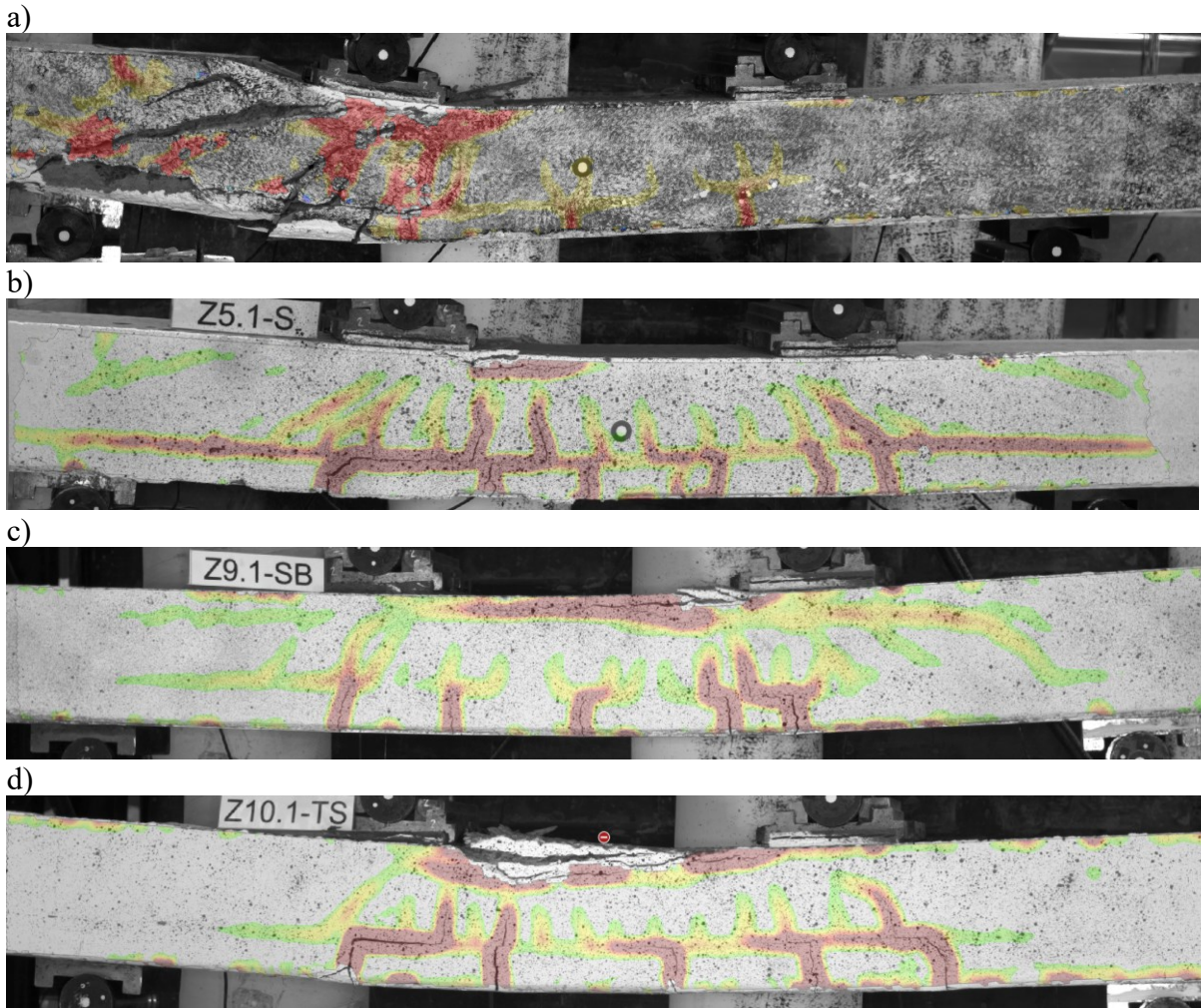


Fig. 6.35. View of tensile strain after failure: a) Z4.1_P, b) Z5.1_S, c) Z9.1_SB, d) Z10.1_TS

Rys. 6.35. Widok odkształceń rozciągających po zniszczeniu: a) Z4.1_P, b) Z5.1_S, c) Z9.1_SB, d) Z10.1_TS

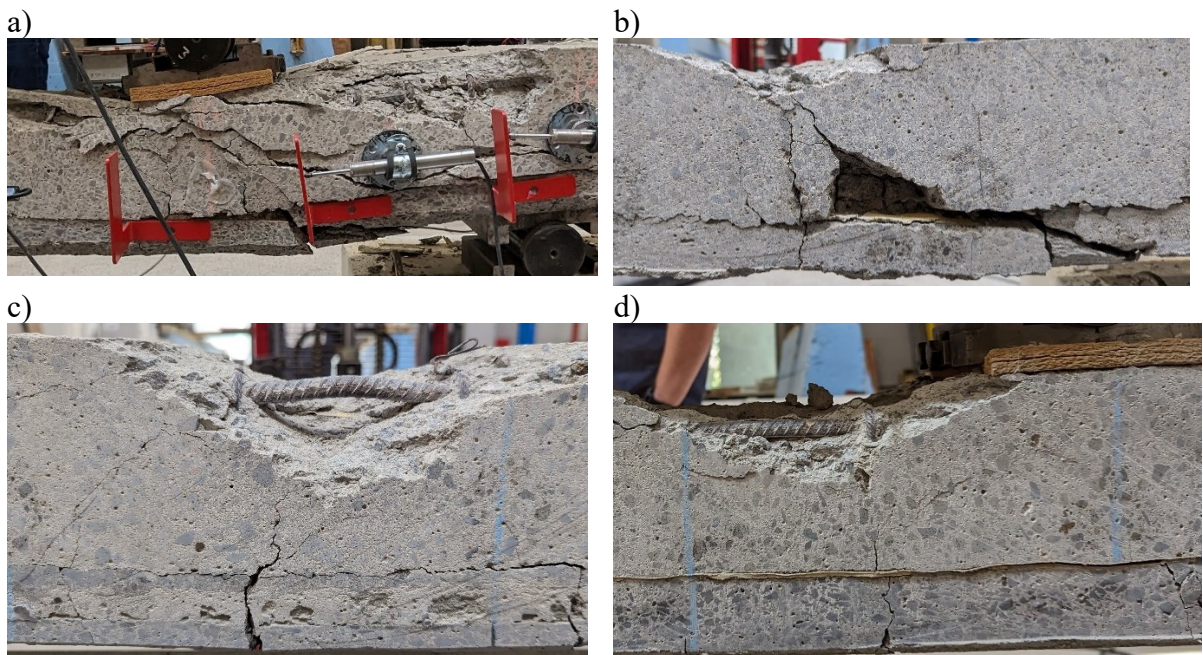


Fig. 6.36. View beams after failure: a) Z4.1_P, b) Z5.1_S, c) Z9.1_SB, d) Z10.1_TS

Rys. 6.36. Widok belek po zniszczeniu: a) Z4.1_P, b) Z5.1_S, c) Z9.1_SB, d) Z10.1_TS

6.4.3. 4PBT results for group III

The beams classified in Group III were characterised by the narrowest interface area, present only in one horizontal plane. Element Z7.1_T can be considered a beam connected to the top flange with an extended width. The bonding only through the top surface can be similar to certain rib-and-block slab beams.

The beams differed significantly in their initial stiffness, 2260 kNm² for beam Z7.1_T, a value 5% higher than for the reference beam. The stiffness of beam Z8.1_B was only 1640 kNm², which corresponds to the stiffness of a beam with the adhesion and roughness of the interface wholly removed (Fig. 6.37). Despite such significant differences in the initial stiffness, a higher maximum force was achieved for beam Z8.1_B, significantly exceeding the values obtained for element Z3.1_CB. At a force of 52.0 kN, flexural cracking was recorded in the precast element propagating into the concrete topping for beam Z7.1_T. After the cracking, the stiffness of the beam dropped to a level consistent with beam Z3.1_CB, which is the reverse of the situation for beam Z8.1_B. For the second element analysed, the value of the cracking force was equal to 67.8 kN, which aligns with the fully composite element.

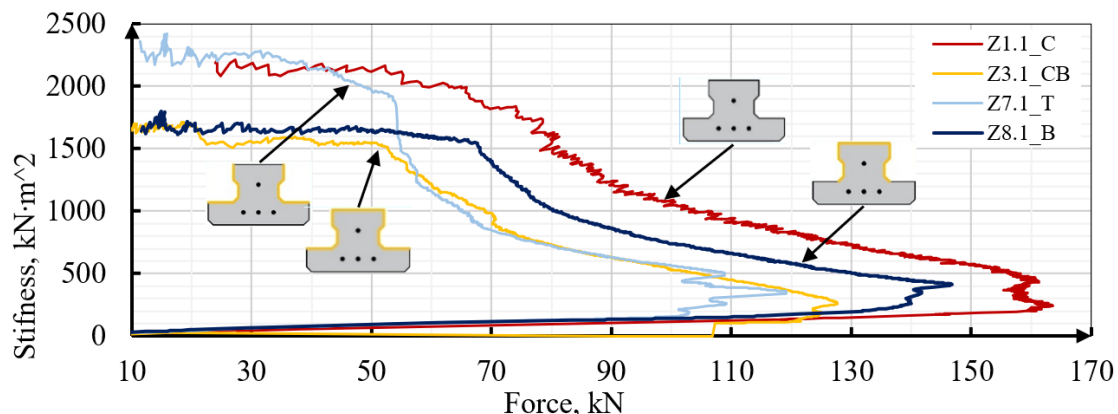


Fig. 6.37. Beam stiffness diagram for selected Z-series beams

Rys. 6.37. Wykres sztywności giętej dla wybranych belek z serii Z

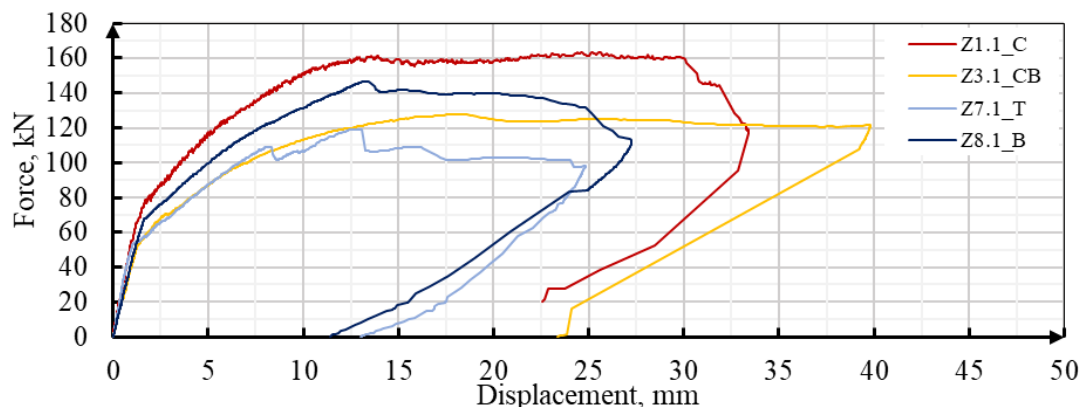


Fig. 6.38. Force-displacement characteristics for selected Z-series beams

Rys. 6.38. Charakterystyka siła/przemieszczenie dla wybranych belek z serii Z

For beam Z7.1_T, the slippage of strands was recorded at a force of 103.3 kN (Fig. 6.39b), which also matches the value of the diagonal crack force. The significantly lower value of the force at which flexural cracking was developed and the subsequent slippage of the strands on both sides of the element indicates a problem with the anchorage of the beam. The failure of beam Z7.1_T occurred due to the failure of the interface. The value of the force cracking the interface to the edge of the support and the face of the element is also the maximum obtained value, which was 119.1 kN. For beam Z8.1_B, the cracking of the interface up to the edge of the support developed at a force of 111.1 kN (Fig. 6.39d), after which there was no sharp decrease in the stiffness of the element. After the diagonal cracking and the interface slip at the support, the maximum force reached 146.8 kN. From a value of 100 kN, the strand's slippage on one side increased with the applied load. The slippage occurred on the same side of the element where the failure occurred.

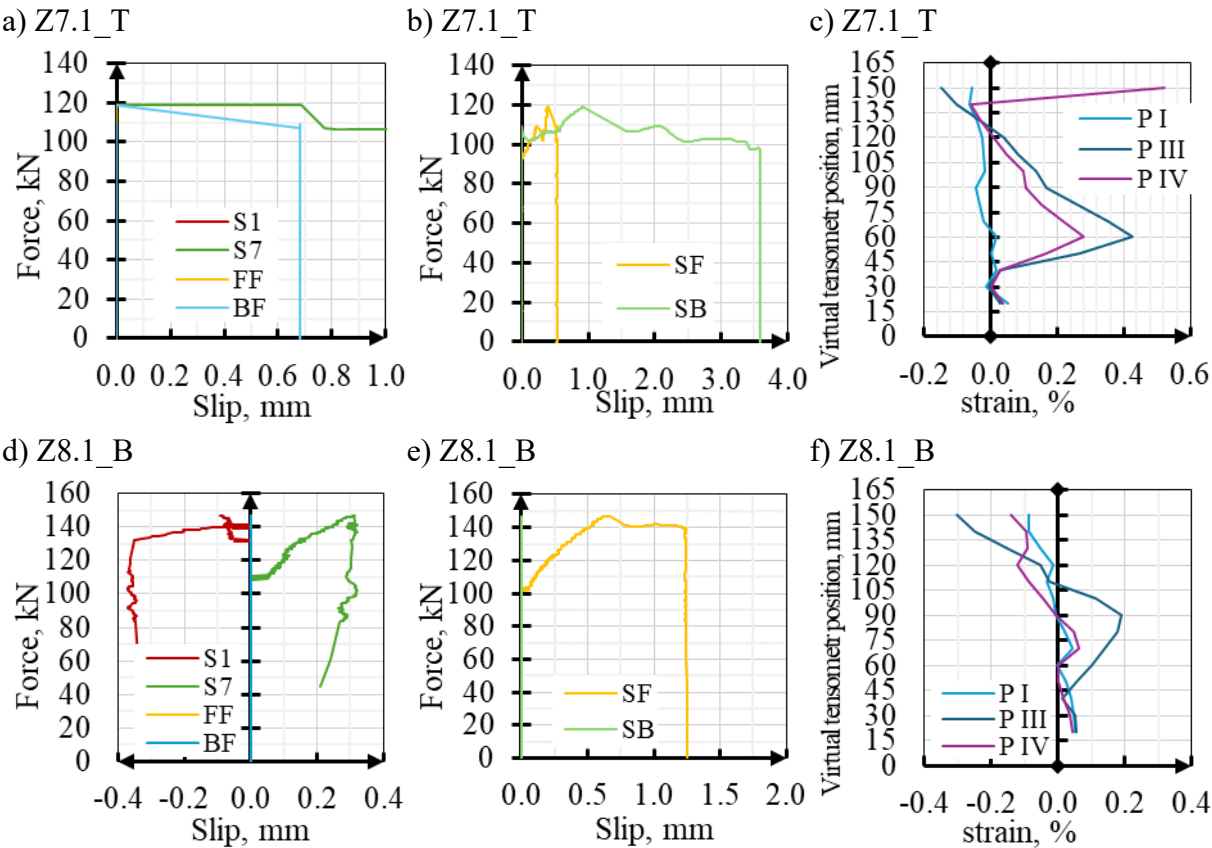


Fig. 6.39. Selected results: a, d,) slip in the interface, b, e,) slip of strands, c, f,) virtual strain gauges
 Rys. 6.39. Wyniki pomiarów: a, d) poślizg w styku, b, e) poślizg splotów c, f) wirtualne tensometry

For the beam Z7.1_T, a type II failure has been assigned, resulting from developing a diagonal crack (Fig. 5.40a, Fig. 5.41a, b). Also, for beam Z8.1_B, a type II failure was attributed, i.e. combining the development of a diagonal crack with slippage of the interface up to the support (Fig. 5.40b, Fig. 5.41c, d).

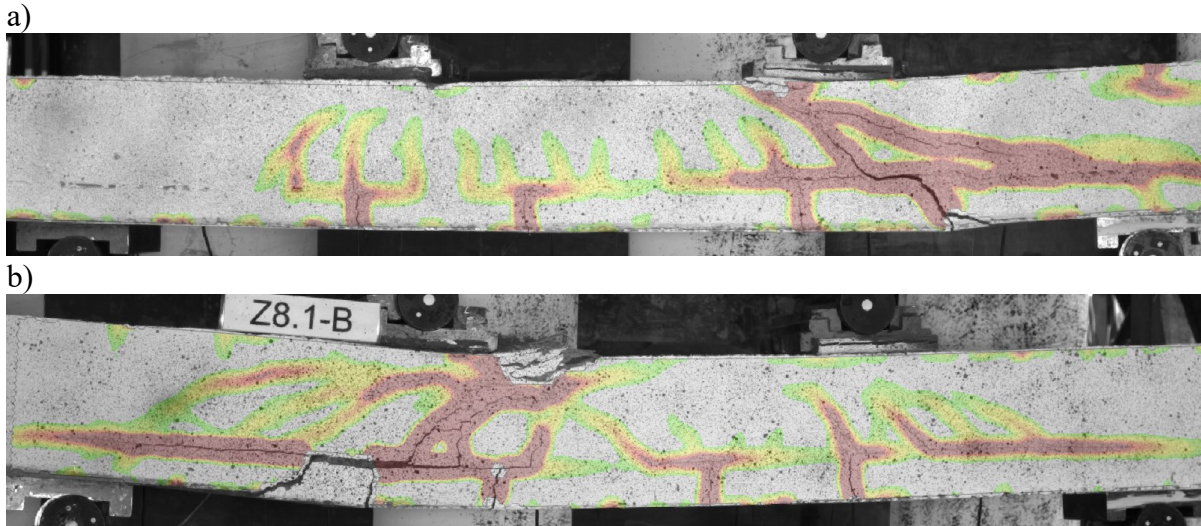


Fig. 6.40. View of tensile strain after failure: a) Z7.1_T, b) Z8.1_B

Rys. 6.40. Widok odkształceń rozciągających po zniszczeniu: a) Z7.1_T, b) Z8.1_B

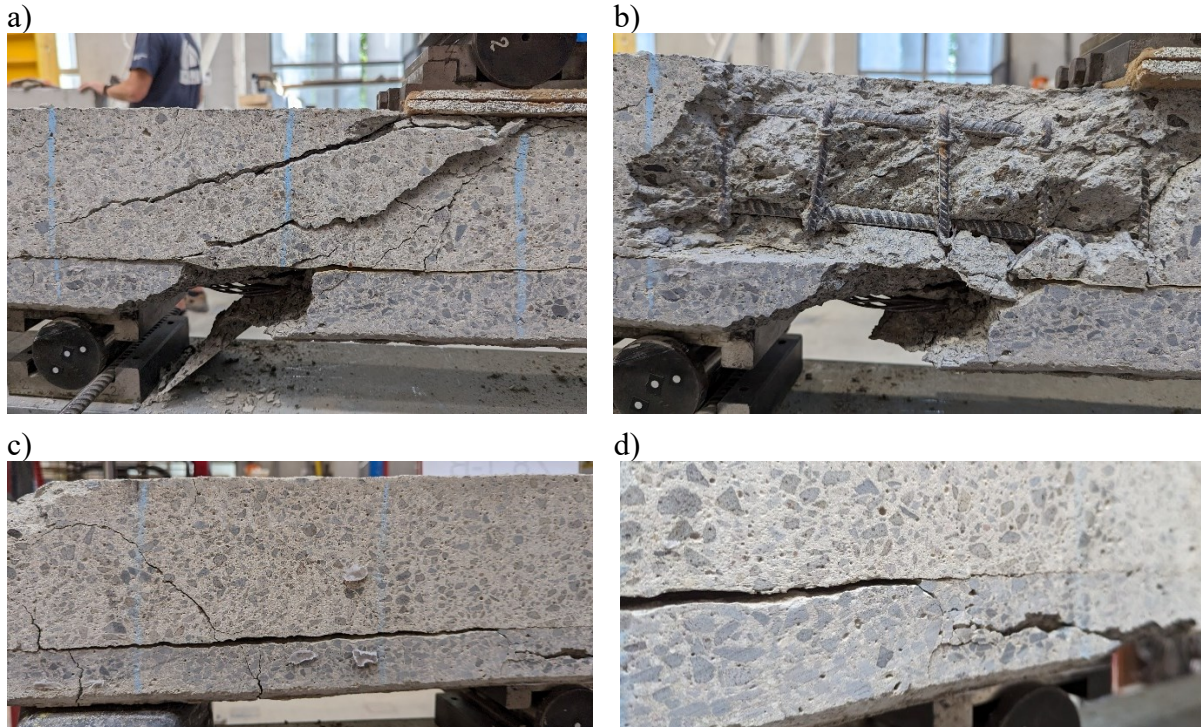


Fig. 6.41. View of beams after failure: a-b) Z7.1_T, c-d) Z8.1_B

Rys. 6.41. Widok belek po zniszczeniu: a-b) Z7.1_T, c-d) Z8.1_B

6.4.4. Conclusions of 4PBT

Based on the presented results of the 4PBT, it is possible to present some conclusions and points for further analysis:

- The beams for which no slip was observed at the interface to the element face and beam Z1.3_CB failed type I due to the crushing of the compression zone and the occurrence of a dominant flexural crack.
- The beams for which slippage occurred at the interface, including slippage to the element face, failed due to a diagonal crack cutting through the precast and concrete topping.
- Beam Z6.1_TB had lower stiffness, which was related to weakened anchorage of the prestressing and loss of prestressing force, so analysis of the beam will only be possible based on 3PBT.
- Beams with limited composite parameters (Z2.1_AB and Z3.1_CB) were characterised by lower flexural stiffness in phase I (before flexural cracking and interface slippage).
- The cracking force due to **flexural cracking** for most of the model was between **63.5 kN and 68.3 kN**. As expected, lower values were obtained for beam Z3.1_CB and beam Z6.1_TB, which is related to the weaker anchorage of the strands.
- Only for the beam, Z1.1_C was high compliance with the crack pattern in the concrete topping and the precast element obtained.
- The occurrence of diagonal cracking was associated with the measured slip of the strands. **Diagonal cracking** was developed for most of the elements for forces between **126.8 kN and 134.6 kN**.
- Failure of Group II beams occurred for a force in the range 142.5 kN to 162.7 kN, and beam Z1.3_C for a force of 163.6 kN.
- Local slip of interface was observed between successive diagonal cracks.
- **Local slip, even up to the support axis, did not result in a sudden drop in the beam's flexural stiffness.**
- **Slip development to the beam face should be taken as failure due to delamination.**
- **At the point of local slip of the interface, lateral outward pushing of the topping was measured and observed for each beam.**
- An analysis of the effect of local interface slip and the effect of the interface length off the support axis will be one element of the FE analysis.

6.5. Three-point bending tests

Three-point bending tests were described based mainly on measurements taken with LVDTs, using DIC for failure image analysis. During the test, no measurements were taken from the face of the elements, being limited to the side surfaces only (Fig. 6.42). Measuring was carried out for the further support only at its axis (LVDT - S1), with no intermediate measurement between the support and the point of load. The 3PBT tests complement the 4PBT tests in assessing the behaviour of the composite. The range of slip propagation at the interface will be verified, and cracking towards the support will be done with a lower shear force.

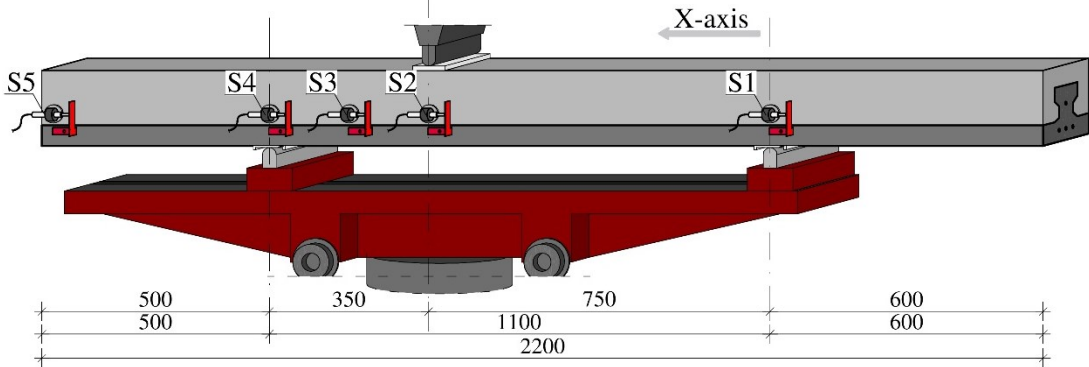


Fig. 6.42. Label of the measurement points and the X-axis as seen from the back side (side LVDT)
 Rys. 6.42. Oznaczenie punktów pomiarowych oraz osi X, widok od tyłu (strona LVDT)

Figure 6.43 shows the results of the force-displacement characteristics for each beam, and Fig. 6.44 the calculated flexural stiffness values. Analysis of the charts does not indicate an early loss of strand anchorage for any of the beams, resulting in reduced initial stiffness. As in the 4PBT study, the highest force value was obtained for the fully composite element Z1.3_C. As expected, the lowest force and stiffness values were obtained for beam Z3.3_CB, and beam Z2.3_AB had the second lowest stiffness for most of the test range. Most of the elements had a significant extent of displacement under near-maximum load. The displacement of half of the elements exceeded the 40 mm value. Further analysis of the test results was again divided into three groups, as was done when describing the 4PBT tests. Table 6.11 summarises the most relevant test results collectively.

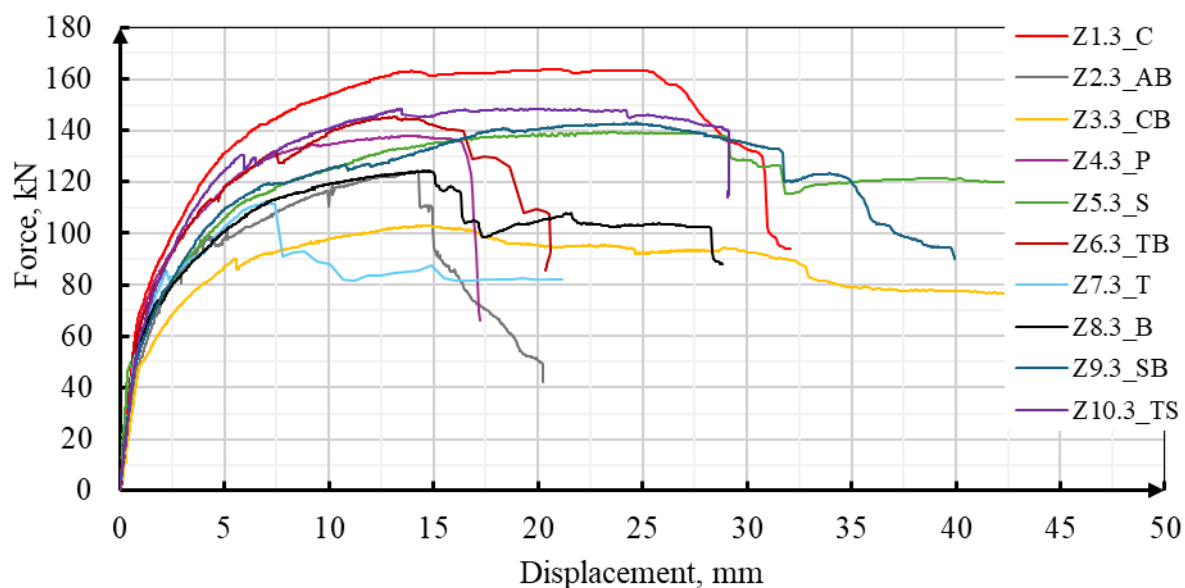


Fig. 6.43. Force-displacement characteristics for selected ZX.3 series beams

Rys. 6.43. Charakterystyka siła/przemieszczenie dla wybranych belek z serii ZX.3

The flexural stiffness diagram of the tested beam elements requires additional discussion. The values obtained differ significantly from the stiffnesses obtained in the 4PBT test. The difference is that for the basic element Z1.3_C, in terms of initial stiffness, it is almost 30%. Only for one beam (Z5.3_S), the measurements did not indicate a reduction in stiffness, but its initial stiffness variation was significantly higher than for the other elements.

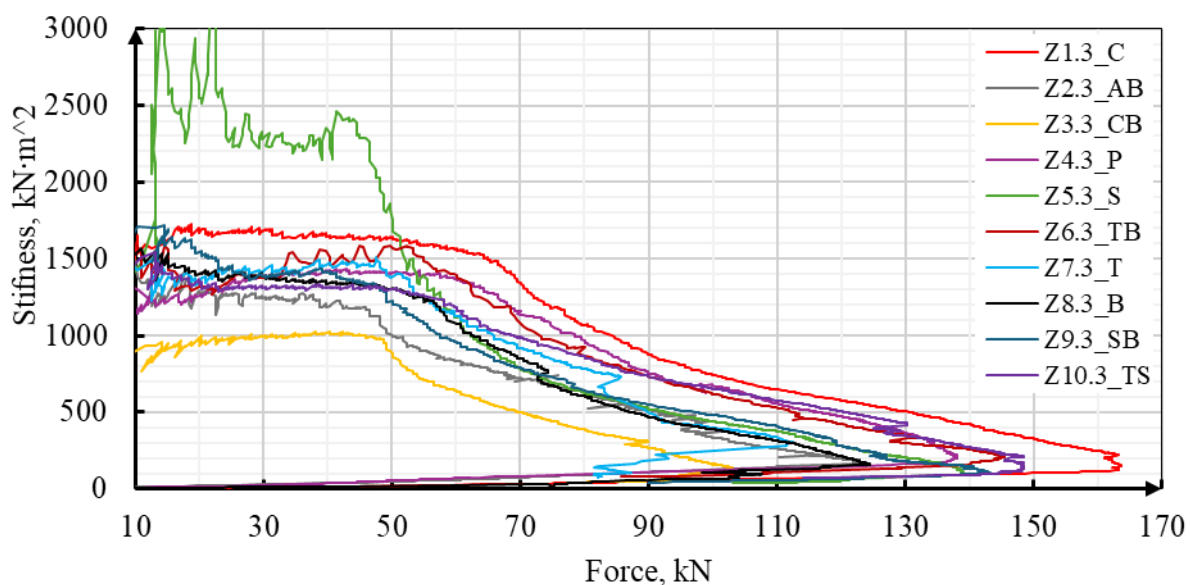


Fig. 6.44. Beam stiffness diagram for selected ZX.3 series beams

Rys. 6.44. Wykres sztywności giętej dla wybranych belek z serii ZX.3

After close analysis of the DIC image, such different stiffness values can be attributed to looseness and the adaptation of the machine hinges to the beam under force. These movements cannot be compensated by a deflection measurement using the DIC method due to the impossibility of covering the second support with cameras due to the test machine setup. Measurements of the displacement of the beam relative to the support elements, including the support roller and the lower base of the testing machine, showed slight movements of the support elements in the range of ~ 0.2 mm (Fig. 6.45b) at load values up to ~ 45 kN. The smallest differences were measured for the element with the highest calculated stiffness, beam Z5.3_S, where support movements were less than 0.02 mm. Even 0.1 mm of possible displacement of the second support, with a deflection of 0.4 mm (at ~ 45 kN), can affect the calculated stiffness difference by up to 33%. Once a sufficiently large load value was obtained, the displacement difference did not increase. To illustrate the problem, images and measurements were collated for element Z5.3_S, for which the measured difference between beam and support was minimal (< 0.02 mm), and beam Z1.3_C.

The zero line of vertical displacement, which should be near the axis of support, for the Z10.3_TS beam (Fig. 6.45b) is located behind the support plate at the end section (anchorage length). This shows the beam displacement and supports occurring relative to the machine base. For beam Z5.3_S, the zero displacement axis passed through the support axis (Fig. 6.45a). Due to the inability to measure the deformation of the support at the sensor S1 axis, it is not possible to determine the correct deflection of the element at the initial stage. The error in determining the stiffness resulting from the phenomenon described above decreases as the element deflection increases. Due to the above, a direct comparison of stiffness values between the 3PBT and 4PBT tests is not possible. The stiffness analysis also cannot be used as the basis for an undoubted determination of the flexural cracking force. The calculated stiffness values were only used in a subsidiary manner, each time using an analysis of the cracking pattern of the beams and a measurement of the displacement of the supports relative to the base of the testing machine. However, the stiffness diagrams obtained can still be used to analyse the range of stiffnesses higher than the cracking force.

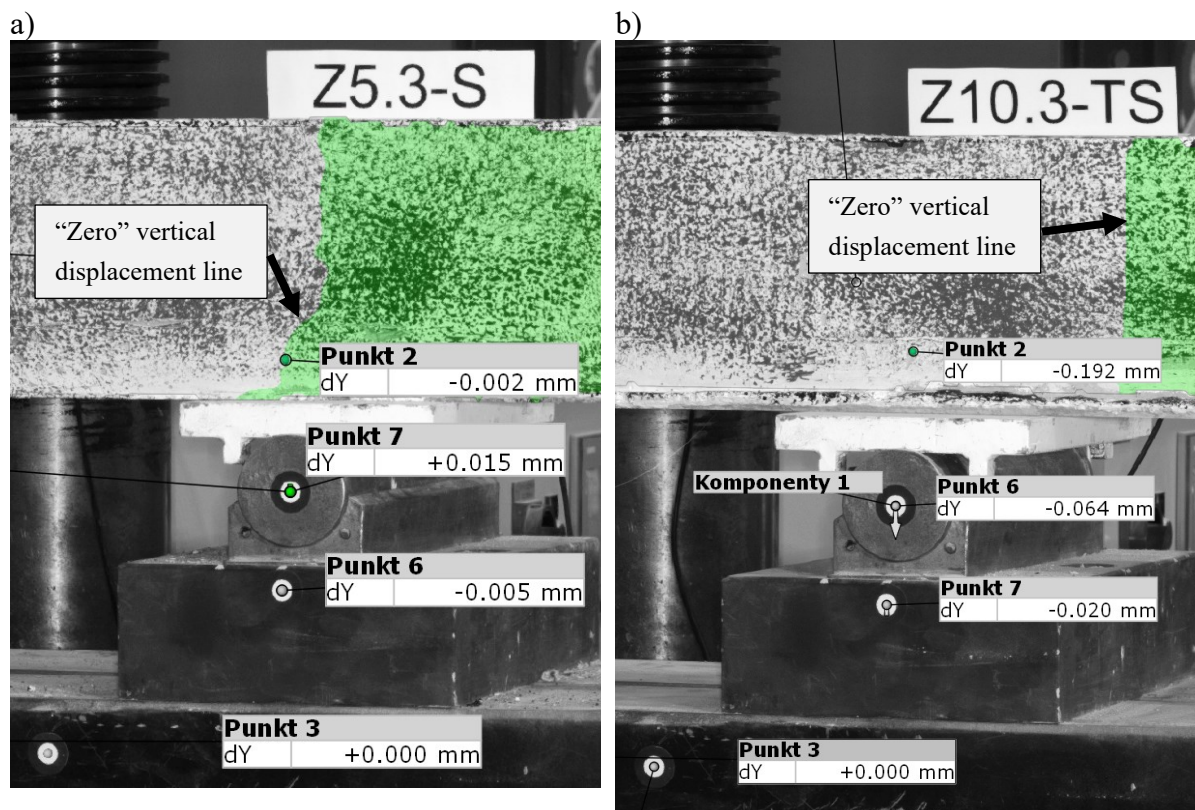


Fig. 6.45. View of beam and test stand (supports) displacement for a force ~ 45 kN.

Rys. 6.45. Widok przemieszczeń belki oraz stanowiska badawczego (podpór) dla siły ~ 45 kN.

Table 6.11

Summary of failure type and characteristic forces of Z type beams

Zestawienie sił oraz typów zniszczenia belek z serii Z

Element	Flexural crack F_{cr} , kN	Interface slip at support $V_{R,1,cr}$, kN	Interface slip at face $V_{R,2,cr}$, kN	Diagonal crack $V_{R,c}$, kN	Peak load F_{max} , kN	Failure type
Z1.3_C	59.6	147.0	-	112.3	163.7	I
Z2.3_AB	46.5	94.7	-	94.7	124.0	II
Z3.3_CB	47.1	66.4	74.8(BF)	66.4	103.0	III
Z4.3_P	54.4	112.5	-	100.0	138.1	II
Z5.3_S	47.6	80.1	-	75.8	139.1	II
Z6.3_TB	53.3	113.0	-	113.0	145.4	II
Z7.3_T	48.1	80.4	88.9(BF)*	80.4	112.5	II
Z8.3_B	53.3	116.1	124.5(FF)	75.3	124.5	II
Z9.3_SB	48.6	110.9	-	85.3	143.3	II
Z10.3_TS	54.9	99.9	-	76.8	148.5	II

*Interface slip or diagonal crack after peak force

6.5.1. 3PBT results of group I

Similar to the 4PBT bending test, the highest failure force was obtained for beam Z1.3_C, with a value of 163.7 kN, compared to 124 kN for beam Z2.3_AB and 103 kN for beam Z3.3_CB (Fig. 6.46). The flexural cracking force was also highest for the fully composite beam, reaching 59.6 kN, against 46.5 kN and 47.1 kN for the other two beams.

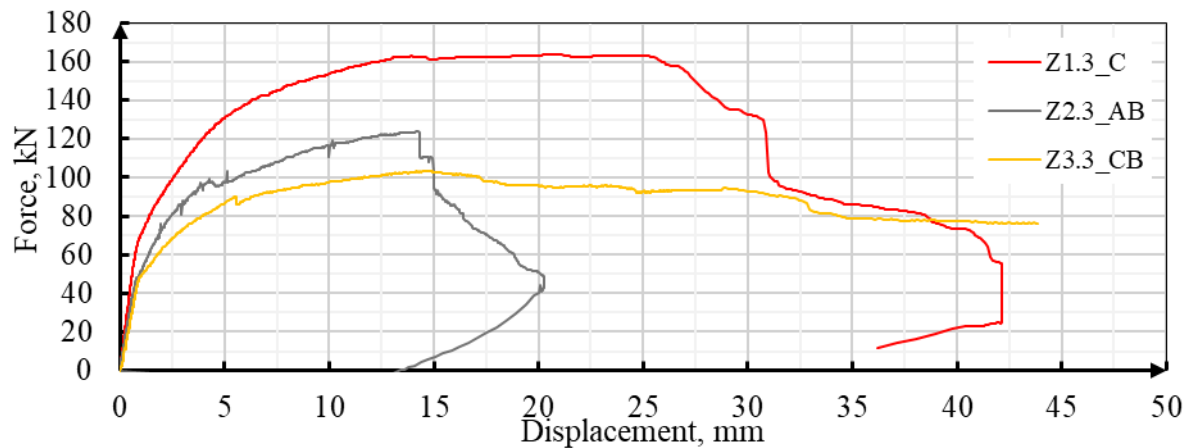


Fig. 6.46. Force-displacement characteristics for selected Z-series beams

Rys. 6.46. Charakterystyka siła/przemieszczenie dla wybranych belek z serii Z

Cracking of the interface, including in the axis of the support, occurred in element Z1.3_C at a force of 147.0 kN. A slip was developed to closer supports relative to the point of load application. The crack did not propagate along the anchorage section towards the end of the element face. Also, for beams Z2.3_AB and Z3.3_CB, slippage was measured in the axis of the support, which did not decrease stiffness. The development of slip in the support axis resulted from forming a diagonal crack. When the cracking load of the interface was reached up to the support axis, a further increase in the value of the applied force was possible. After a load of 74.8 kN was exceeded, the increasing slip was measured at the front edge (beam Z3.3_CB). This slip resulted in a slight decrease in flexural stiffness (Fig. 6.47a).

The development of a diagonal crack in beam Z1.3_C was not related to measurable slip at the interface. Based on the image analysis, it is possible to recognise the occurrence of a diagonal crack connection through the local slip of the interface (Fig. 6.48a). The measured slip of the interface developed at a load of 147 kN but did not result in a decrease in flexural stiffness.

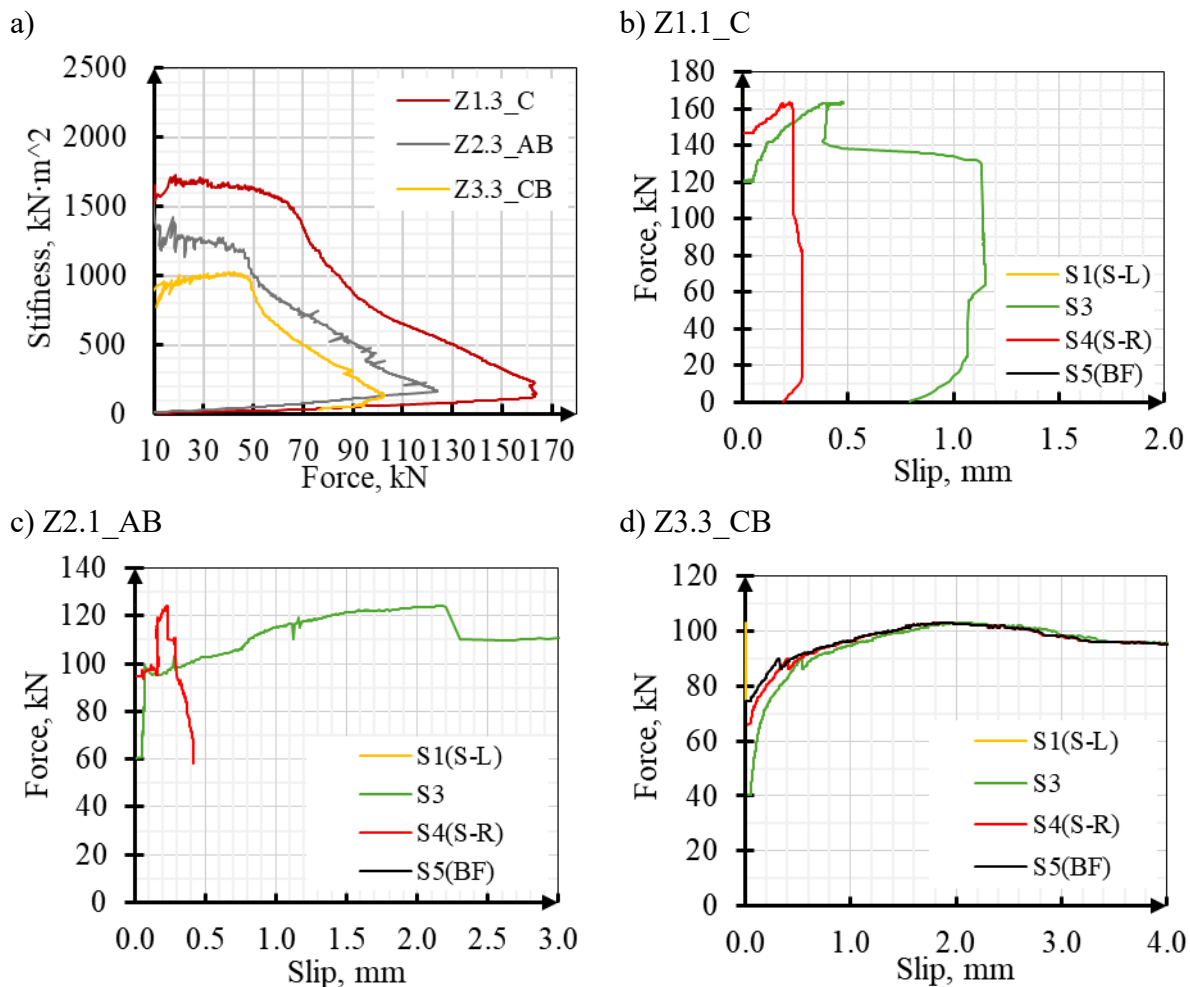


Fig. 6.47. Selected results: a) beam stiffness, b-d) slip in the interface

Rys. 6.47. Wybrane pomiary: a) sztywność giętna belek, b-d) poślizg w styku

The failure of the beams has been identified in three different types, as defined in sec. 5.5. Beam Z1.3_C failed type I due to crushing the compression zone and buckling of the upper reinforcement in the concrete topping (Fig. 6.49a). Two main diagonal cracks can be distinguished (Fig. 6.48a), which, although not significantly widened at failure. Type II failure can be attributed to element Z2.3_AB. One dominant diagonal crack at failure developed, crossing the concrete topping and the precast element (Fig. 6.49b). The third type of failure occurred for beam Z3.3_CB, where the concrete topping slipped up to the front face. The parts of the beam, i.e. the precast and the concrete topping, failed due to bending (Fig. 6.49c).

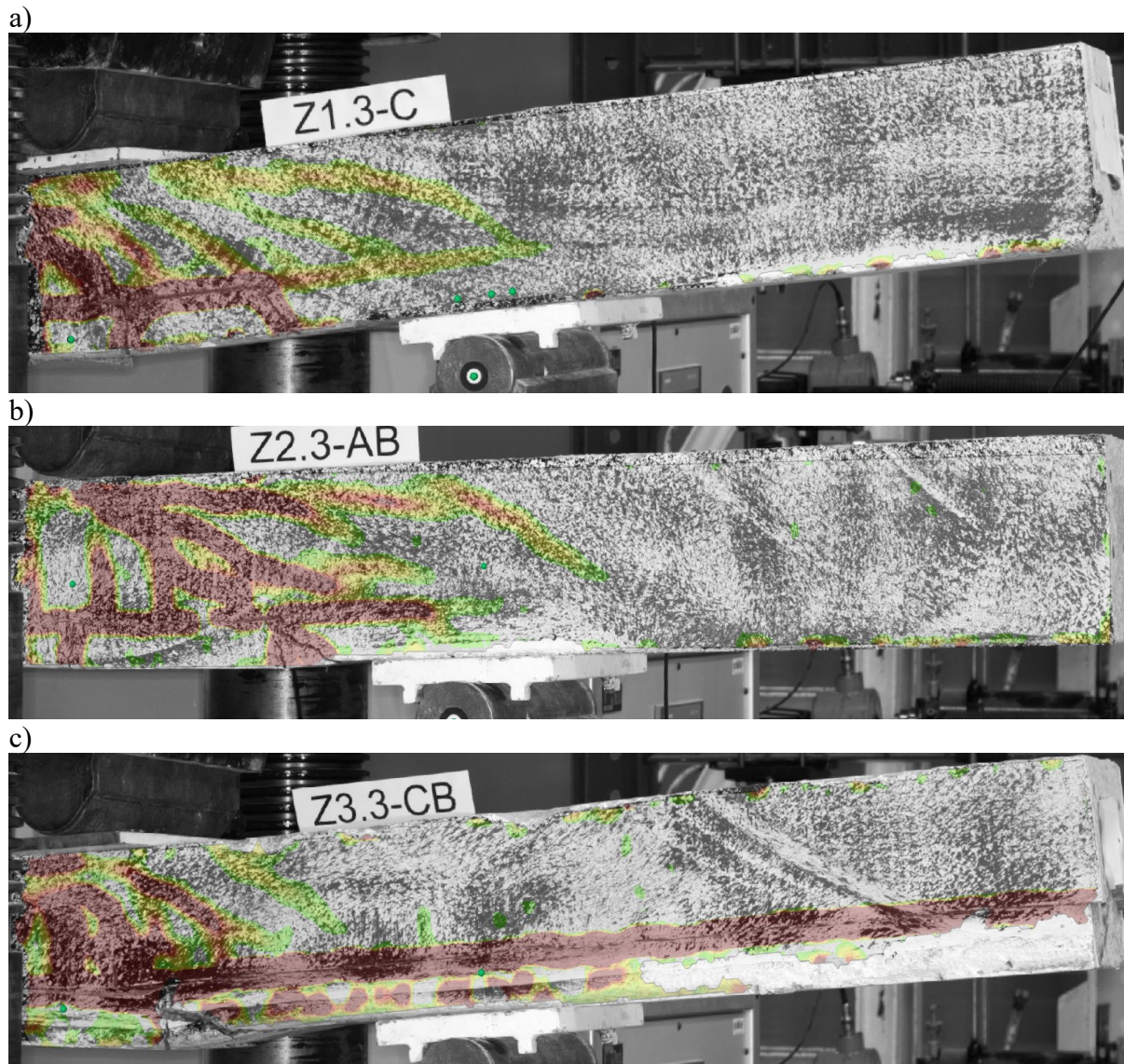


Fig. 6.48. View of principal strain (tensile) after failure: a) Z1.3_C, b) Z2.3_AB, c) Z3.3_CB

Rys. 6.48. Widok odkształceń głównych (rozciągających) po zniszczeniu: a) Z1.3_C, b) Z2.3_AB, c) Z3.3_CB



Fig. 6.49. View beams after failure: a) Z2.3_AB, b-c) Z2.3_AB, d-e) Z3.3_CB
 Rys. 6.49. Widok belek po zniszczeniu: a) Z2.3_AB, b-c) Z2.3_AB, d-e) Z3.3_CB

6.5.2. 3PBT results for group II

The elements in group two had lower stiffness (after cracking) and failure force than the reference beam Z1.3_C. The maximum force (Fig. 6.50) was in the range from 138.1 kN (Z5.3_P) to 148.5 kN (Z10.3_TS), which is ~9-15% lower than the force for beam Z1.3_C. These values were obtained with a beam displacement under a force close to 15 mm. At the relatively high variation between beams (difference of ~15%), cracking force values in the range of 47.6 kN to 54.9 kN were determined. These values are within the range of forces obtained for elements Z1.3_C and Z3.3_CB. For the two beams (Z5.3_S, Z9.3_SB), the obtained cracking force is similar to that for elements with limited interface adhesion.

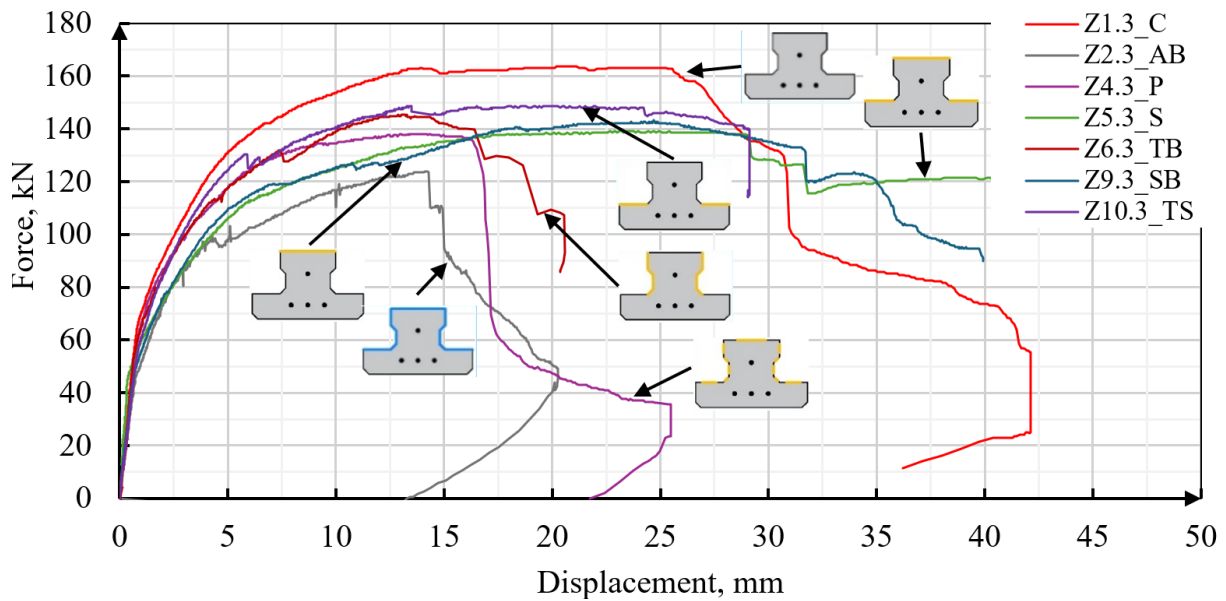


Fig. 6.50. Force-displacement characteristics for selected Z-series beams

Rys. 6.50. Charakterystyka siła/przemieszczenie dla wybranych belek z serii Z

In each beam, interface slippage in the support axis was measured (Fig. 6.51b-f), but was not accompanied by the reaching of the peak load. As in the Group I elements, after local interface slip or slippage in the axis of the support, a further increase in the applied load value was recorded, with no sudden decrease in stiffness (Fig. 6.51a). The occurrence of slip at the interface for half of the elements was linked to the developing of a diagonal crack (Table 6.11). However, interface slip at the support axis always occurs at a force equal to or greater than the diagonal crack initiation force. Despite the local slip of the interface, the selected beams carried a load more than 50 kN higher than the force at which the slip over the support occurred. After the beam's failure and the test's termination, no slip was observed in any of the beams from the face of the element.

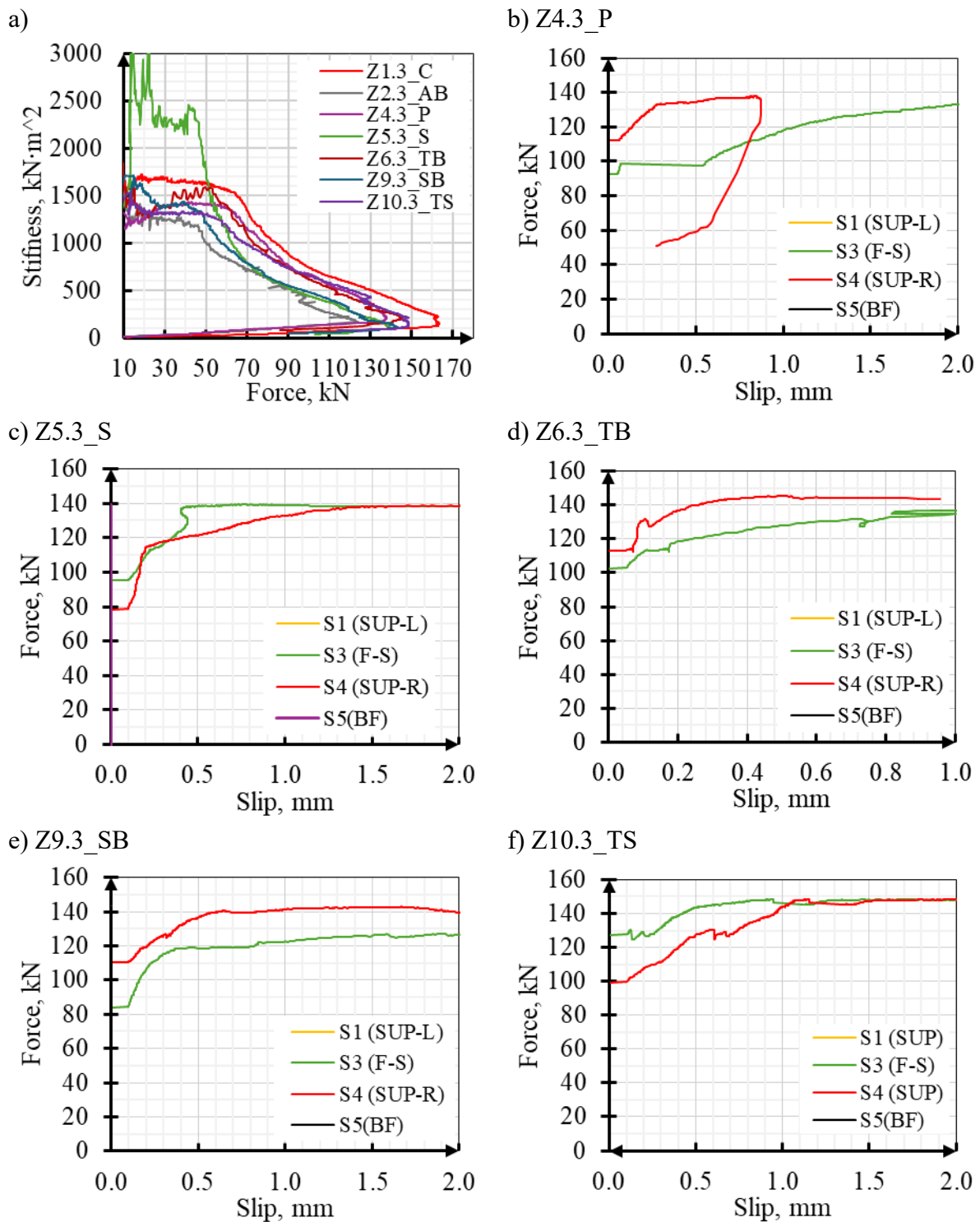


Fig. 6.51. Selected results: a) beam stiffness, b-f) slip in the interface

Rys. 6.51. Wybrane pomiary: a) sztywność giętna belek, b-f) poślizg w styku

The beams in group II were all assigned a type II failure. The failure image of the elements was similar (Fig. 6.52). For each beam, it is possible to identify a dominant diagonal crack reaching the edge of the support. The crack course was not always straight through the concrete topping and the precast element (Fig. 6.52b, c and Fig. 6.53b, c).

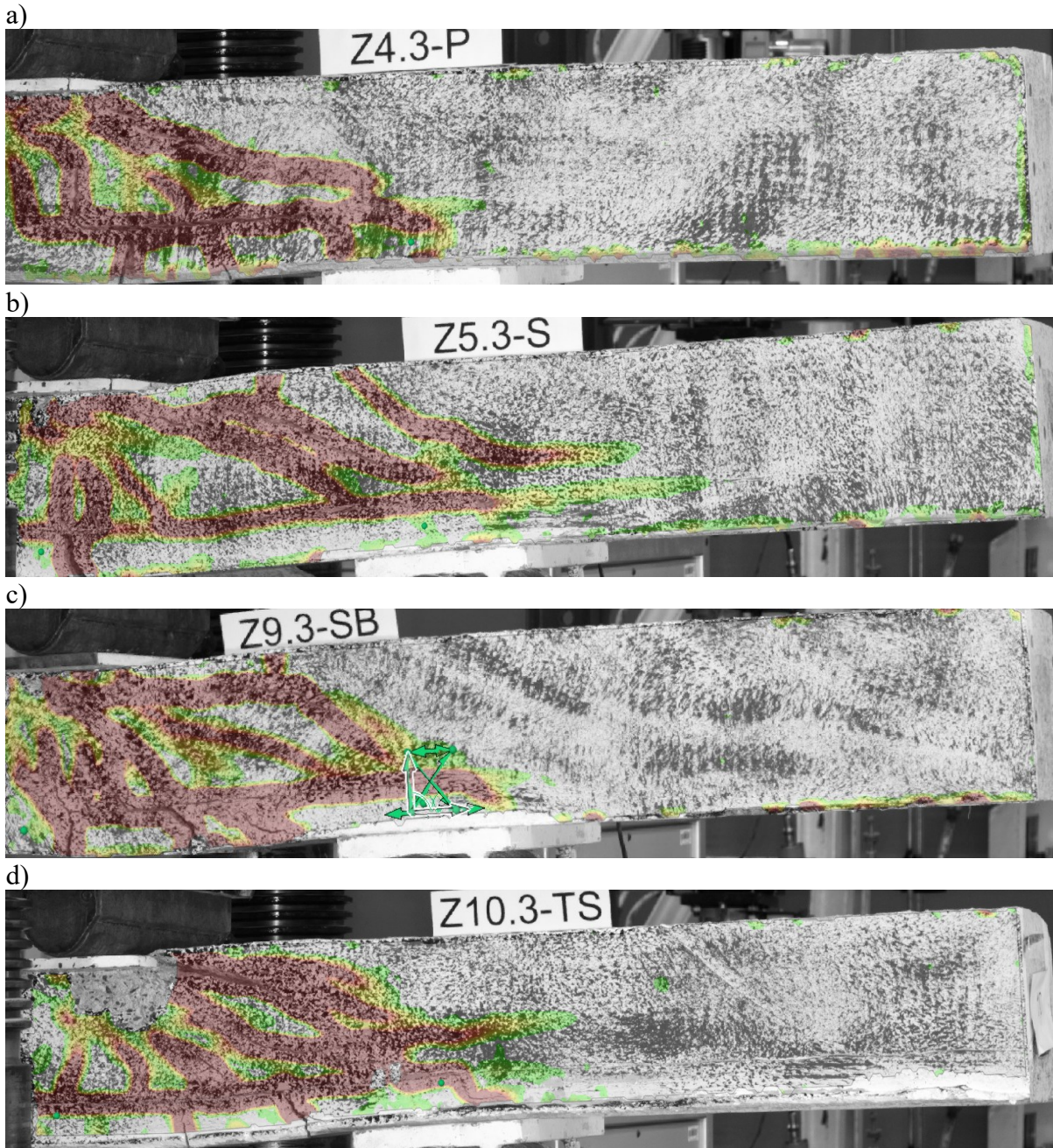


Fig. 6.52. View of tensile strain after failure: a) Z4.3_P, b) Z5.1_S, c) Z9.3_SB, d) Z10.3_TS
 Rys. 6.52. Widok odkształceń rozciągających po zniszczeniu: a) Z4.3_P, b) Z5.3_S, c) Z9.3_SB, d) Z10.3_TS

Diagonal cracks crossing the concrete topping at the lower interface surface with the precast concrete continue horizontally through the precast concrete, cutting off the rib from its bottom flange (Fig. 6.53 c, e). There was always an outward deflection of the concrete topping at the point of the cracks. Around the zone of the applied load, sections of the concrete topping separated from the reinforcement, separating the part inside and outside from the stirrups and longitudinal bars. **In beams Z5.1_S and Z9.1_SB, the diagonal crack and slip of the interface also propagated towards the second,**

further support. Because the tests were carried out up to a significant drop in the applied load and the large displacements of the beams, a considerable part of the concrete topping in the cracked area became detached and locally crushed (Fig. 6.53a)



Fig. 6.53. View beams after failure: a) Z4.3_P, b) Z5.3_S, c) Z9.3_SB, d) Z10.3_TS

Rys. 6.53. Widok belek po zniszczeniu: a) Z4.3_P, b) Z5.3_S, c) Z9.3_SB, d) Z10.3_TS

6.5.3. 3PBT results for group III

Group III elements had a lower stiffness throughout the test than the reference element Z1.3_C (Fig. 6.55a). After cracking at the interface (slip), the stiffness of the beams decreased to the level of the element without adhesion at the interface (Z2.3_AB). Diagonal cracks were formed in both elements at similar load values (80.4 kN - Z7.3_T and 75.3 kN - Z8.3_B). The values of the maximum forces obtained were also similar, 112.5 kN and 124.5 kN, respectively (Fig. 6.54), where the higher value applies to the element with the interface on the bottom surface of the precast unit. These values are consistent with the maximum forces as in element Z2.3_AB.

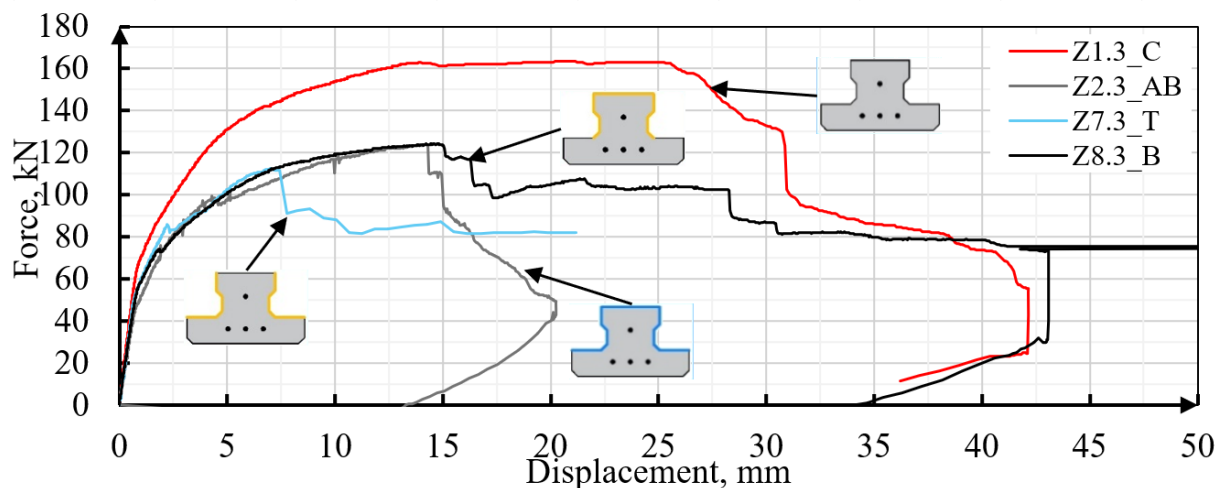


Fig. 6.54. Force-displacement characteristics for selected ZX.3 series beams

Rys. 6.54. Charakterystyka siła/przemieszczenie dla wybranych belek z serii ZX.3

Beams in group three, for which the interface existed only on one of the horizontal surfaces, showed a noticeable decrease in stiffness related to slippage at the interface. In the case of beam Z7.3_T, slippage occurred on the side of the support closer to the point of load application. Measured slippage over the support of more than 0.1 mm (Fig. 6.55b) led to a decrease in stiffness at a load of 80.4 kN. For beam Z7.3_T, the value of the maximum load (112.5 kN) is related to the occurrence of slippage at the interface up to the face of the element. Similarly, the failure of beam Z8.3_B is associated with slippage at the interface up to the leading edge (Fig. 6.55c), but for this element, slippage occurred towards the further support. The measurable local slip between the force (S3 F-S) and the support in both beams did not lead to an identifiable decrease in the stiffness of the elements.

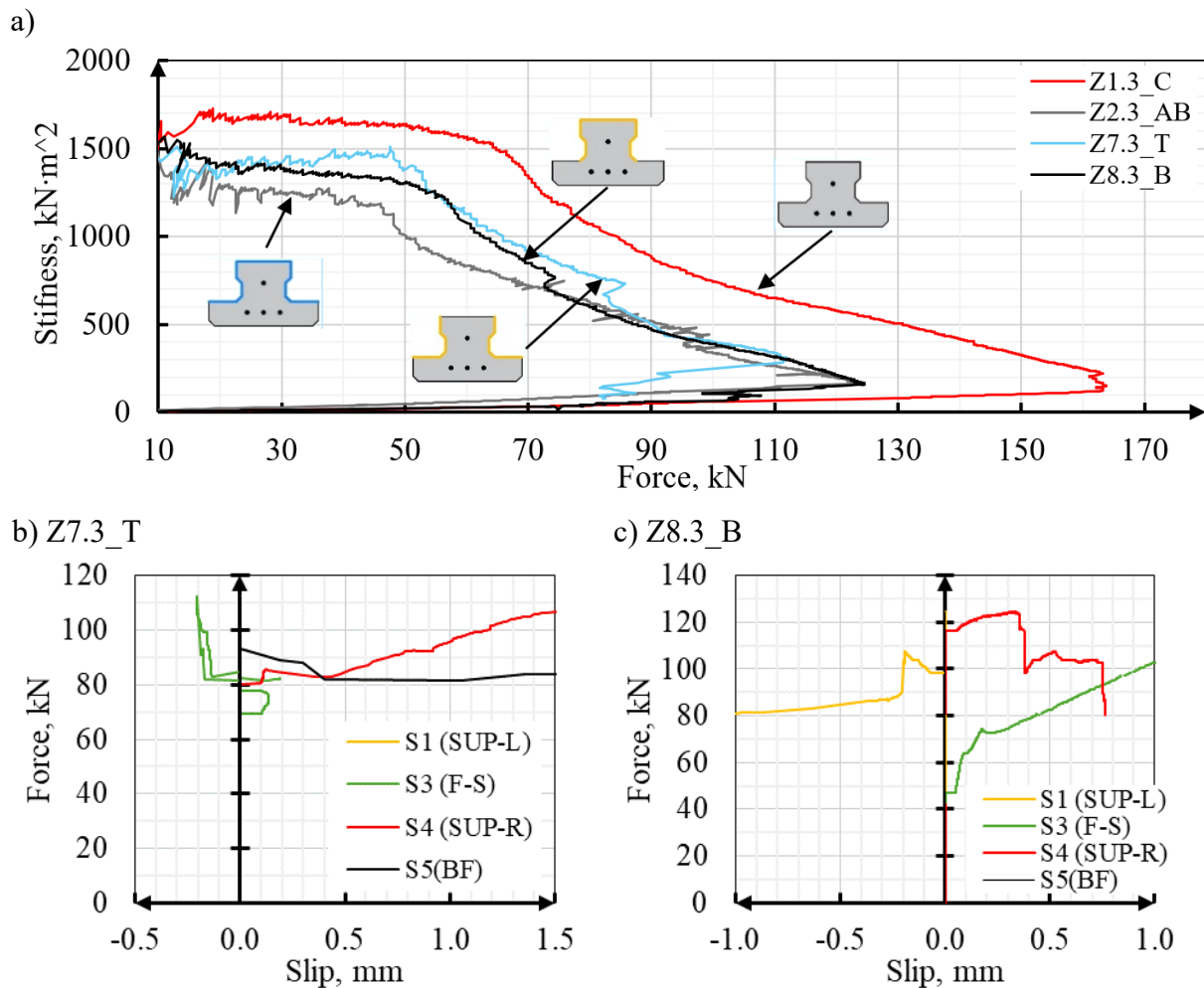


Fig. 6.55. Selected results: a) beam stiffness diagram for selected Z-series beams, b-c) slip in the interface

Rys. 6.55. Wybrane pomiary: a) wykres sztywności giętej dla wybranych belek z serii Z, b-c) poślizg w styku

Both beams were assigned a Type II failure, with the propagation of a diagonal crack through the concrete topping and precast after a short slip section at the interface (Fig. 6.56a, b). Beam Z8.1_B is distinguished from the others by the failure in the direction of further support (Fig. 6.56c-d), where the theoretically lower value of the shear force occurs. Also, the anchorage section of the precast member behind the support is 100 mm longer. As in the other failed beams, an outward deflection of the concrete topping is visible in the section where the slip was noted. An increased vertical interface opening can be seen between the diagonal cracks (Fig. 6.57).

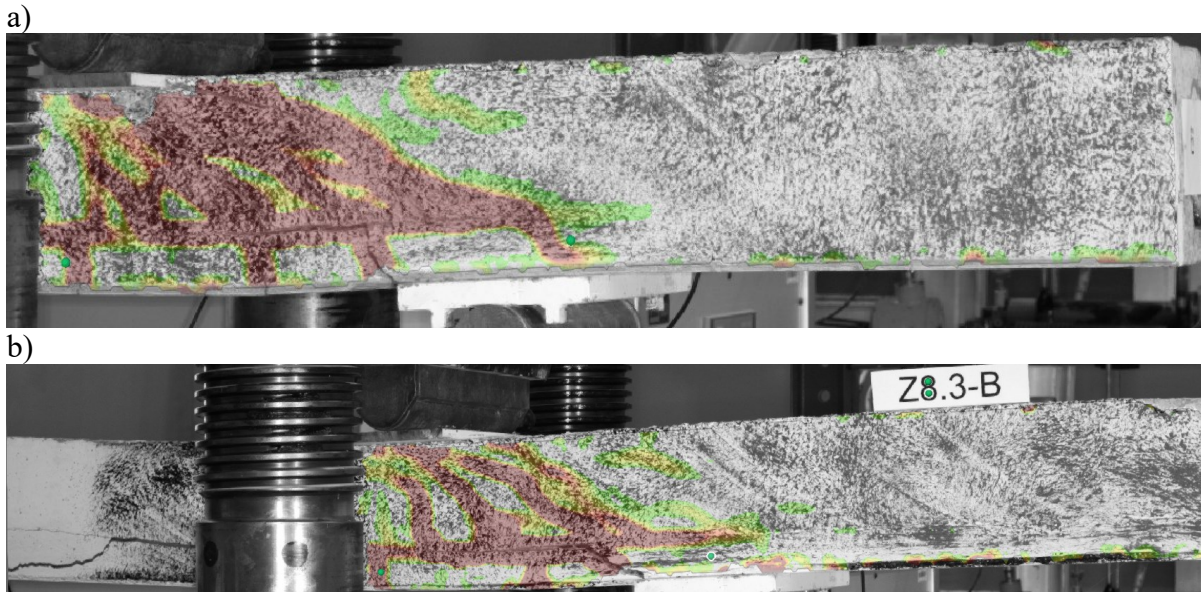


Fig. 6.56. View of tensile strain after failure: a) Z7.3_T, b) Z8.3_B

Rys. 6.56. Widok odkształceń rozciągających po zniszczeniu: a) Z7.3_T, b) Z8.3_B

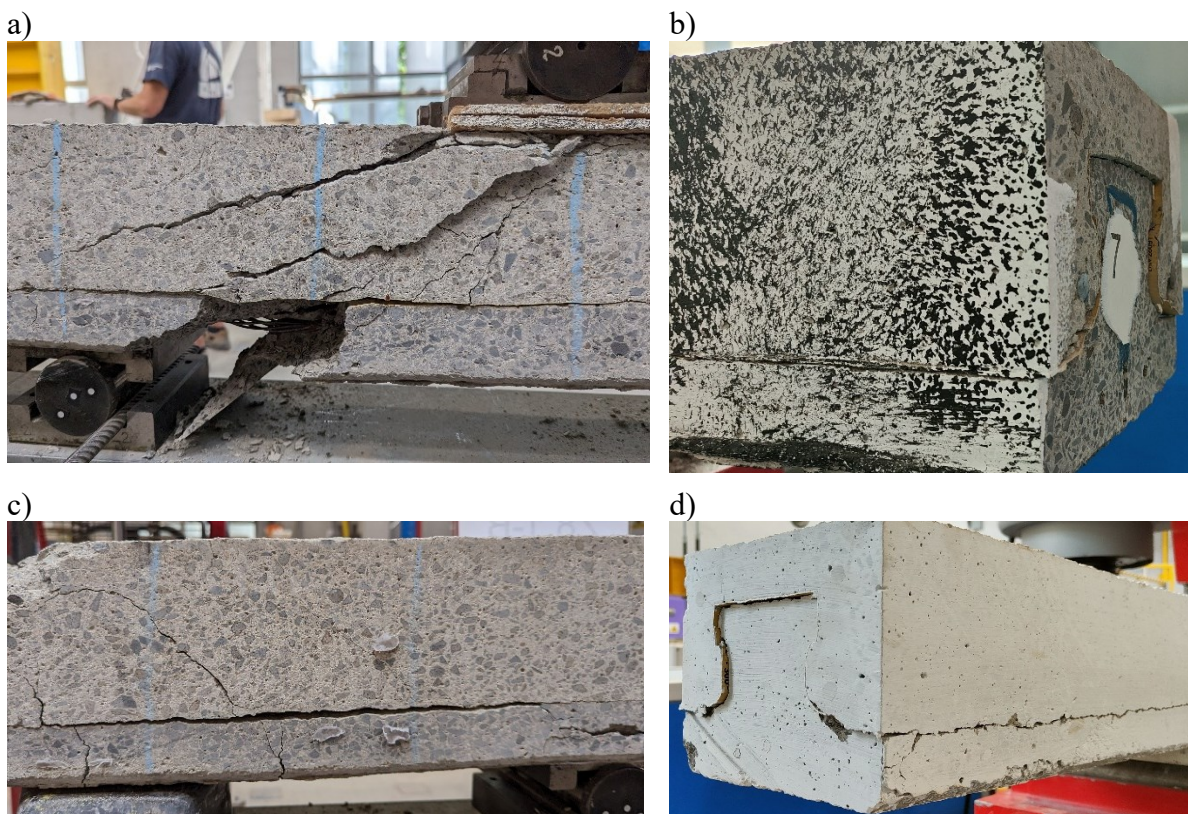


Fig. 6.57. View beams after failure: a-b) Z7.3_T, c-d) Z8.3_B

Rys. 6.57. Widok belek po zniszczeniu: a-b) Z7.3_T, c-d) Z8.3_B

The characteristic concrete topping cracks are evident in all beams on which the slip to the face was measured (Z3.3_CB, Z7.3_T and Z8.3_B). The cracks run from the inner corner at the interface towards the outer edges of the topping (Fig. 6.58). Two of the

cracks cross with the longitudinal reinforcement of the concrete topping, and two pass vertically through the concrete. The crack is associated with an outward deflection of the concrete topping.

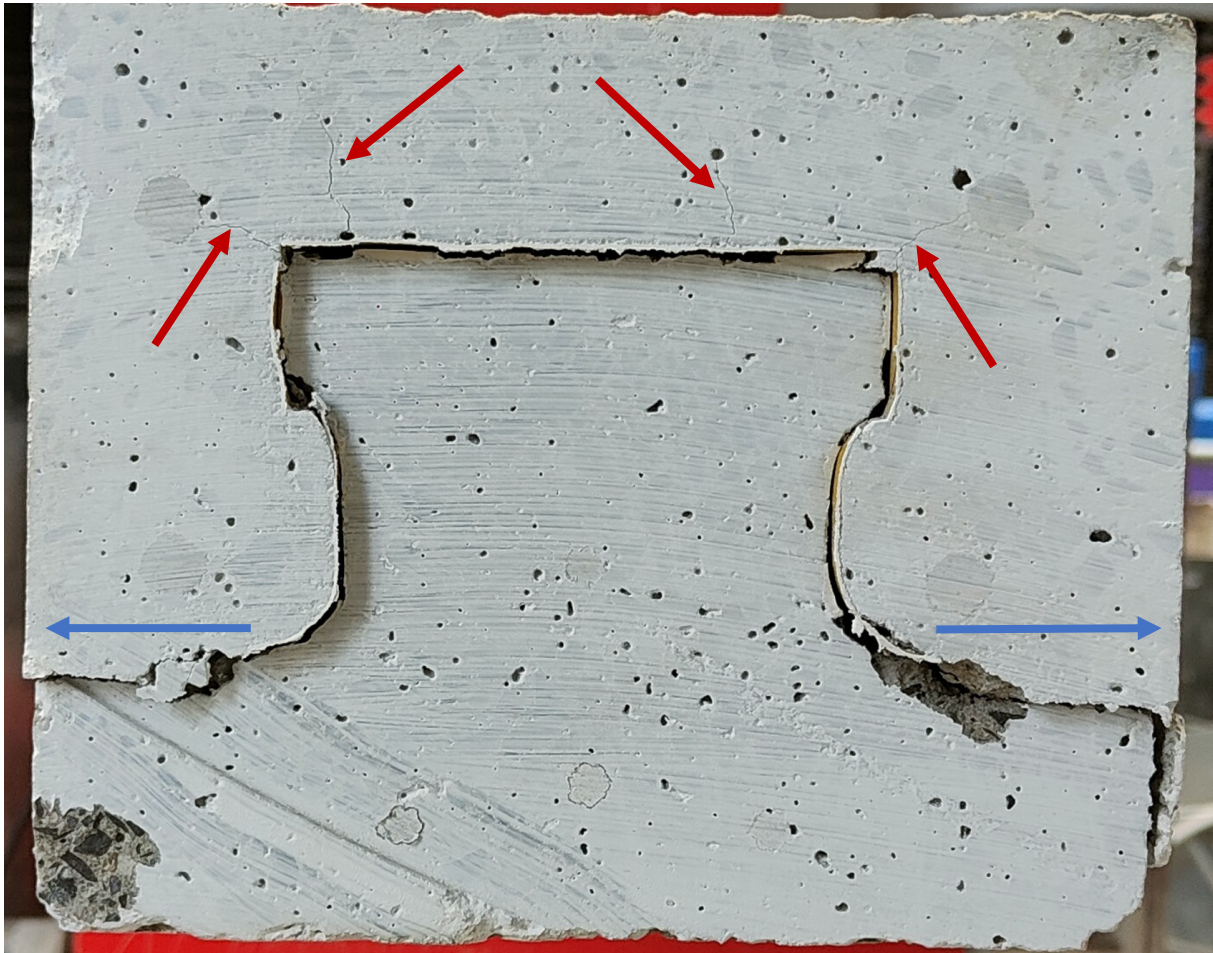


Fig. 6.58. View of the face of beam Z8.3_B after failure – cracks in the corners of the topping
Rys. 6.58. Widok powierzchni czołowej belki Z8.3_B po zniszczeniu - rysy w narożach nadbetonu

6.5.4. Conclusions of 3PBT

Based on the presented results of the 3PBT, it is possible to present several conclusions and points for further analysis, most of which are in line with those presented for the 4PBT:

- Only beam Z1.3_C can be attributed to type I failure - crushing of the compression zone and occurrence of a dominant flexural crack. Despite the slippage towards the support axis and the diagonal crack, there was no slippage to the element face and no increase in the width of the diagonal crack.

- The remaining beams (except for Z3.3_CB) were subjected to Type II failure related to the increased diagonal crack width.
- **For all beams, slip was measured at the interface up to a support axis** closer to the point of load application.
- The cracking force due to **flexural cracking** ranged from **46.5 kN to 59.6 kN**. The highest value was obtained for beam Z1.1_C, 4.7 kN higher than for the second beam Z10.3_TS (54.9 kN).
- The failure of beams in group II occurred for a similar force value in the range 138.1 kN to 148.5 kN, and beam Z1.3_C for a force of 163.7 kN.
- As in the 4PBT study, high compliance of the crack pattern in concrete topping and precast concrete was obtained in the 3PBT study for beam Z1.1_C only.
- The development of a diagonal crack was related to or preceded the slip in the support axis.
- The development of local interface slips between successive diagonal cracks was observed.
- Beams Z5.1_S and Z9.1_SB, in which the vertical surfaces are the main composite surfaces, failed due to slippage in the direction of further support. This may indicate the influence of force application on the slipping value at the interface.
- **Local slippage, even to the support axis, did not result in a sudden drop in the flexural stiffness of the beam.** Visible cracking of the lower interface surface (visible from the side) is not conclusive of delamination over the entire section height. This may justify the lack of stiffness drop with visible delamination up to the support axis. This issue will be part of the FEM analysis.
- **Slipping up to the beam face should be considered as interface failure.**
- **At the point of local slip of the concrete** topping relative to the precast element for each beam, the **outward pushing of the side surfaces** was measured and observed.
- Each beam for which slip was measured to the face of the element was characterised by **diagonal cracks** cutting through the concrete topping **visible from the face of the element**.
- The FEM analysis will be extended to include the effect of local pressure from the concentrated force on the cracking force at the interface and an analysis of the delamination of the interface at the section height.

7. NUMERICAL ANALYSIS

Experimental studies of beams do not allow an unambiguous assessment of the phenomena affecting the behaviour of the elements due to the simultaneous occurrence of several effects. In order to assess the influence of individual effects such as the interface's stiffness, the beam's length after the support edge, the position of interface planes, and the influence of flexural and diagonal cracks, numerical models were made. Numerical modelling is not only a verification of the experimental studies. Therefore, the results of all the experimental tests were not modelled and compared with the numerical models; such an approach would not have been useful from an analytical point of view. The modelling will serve as another separate element to analyse issues that cannot be extracted from the experimental research programme due to limitations in measurements or the size of the research programme. Numerical analyses were carried out only for Z-series beams; preliminary tests on precast rectangular beams were omitted. The calculations were performed using ATENA Studio V5.9.1.21 (Cervenka Consulting).

7.1. Approach

The numerical analyses were divided into several steps, taking a specific correlation path. The approach is based on correlating interface parameters from direct shear tests. This is followed by modelling the tests on beam elements, for which the prestress-related parameters are correlated. For the elements correlated in this way, the results of the experimental tests will be compared in terms of the values of the cracking forces and the failure models. The numerical analyses are divided in detail into three main stages, for which the objectives to be achieved are separated:

1. Stage I – direct shear tests

- 1.1. Objective I - correlation of the interface characteristics in terms of the interface stiffness and the cohesion parameter by varying the K_{TT} stiffness based on the direct shear test of element Z1.2_C3 with the type I failure model and the obtained values of slip and maximum force for elements Z2_AB and Z3_CB.

- 1.2. Objective II - to determine the size of the mesh of the model.
 - 1.3. Objective III - to verify the test configuration's sensitivity to the force application's eccentricity.
 - 1.4. Objective IV - verification of deformation and failure types, including crack pattern.
2. Stage II – modelling of the 4PBT study
- 1.1 Objective I - verification of the failure type with the same interface parameters as in Stage I for beams Z1_C, Z2_AB, Z3_CB and beams Z5_S and Z6_TB.
 - 1.2 Objective II - determination of shear stress distribution at the interface.
3. Stage III – second approach to modelling the 4PBT test. An attempt to isolate the effects affecting cracking force and interface behaviour based on a modified and simplified concrete topping and precast material model.
- 1.1 Objective I - to determine the force cracking the interface locally, to the axis of the support and the edge of the element, and their effect on the flexural stiffness of the element.
 - 1.2 Objective II - to determine the effect of the length of the beam beyond the edge of the support on the flexural stiffness of the element under bending.
 - 1.3 Objective III - to determine the effect of diagonal cracking on the slippage of the interface.
 - 1.4 Objective IV - to determine the distribution of tangential stresses at the interface compared to the models in Stage II.

7.2. Numerical model materials

7.2.1. Material models

Concrete material model

The Athena software implements the Fracture-Plastic Constitutive Model, specifically designed for concrete structures. This model incorporates constitutive models for both tensile (fracturing) and compressive (plastic) behaviour. The fracture model relies on the orthotropic smeared crack formulation and crack band model. It applies the Rankine failure criterion and exponential softening. The hardening/softening plasticity model is based on the Menétrey-Willam failure surface. The model integrates the constitutive equations using a return mapping algorithm.

The combined algorithm, based on a recursive substitution, allows for the independent development and formulation of the two models. It can address situations where both models' failure surfaces are active and physical changes such as crack closure. This model can effectively simulate concrete cracking, crushing under high confinement, and crack closure resulting from crushing in different material directions. The combined algorithm determines the division of strains into plastic and fracturing components while ensuring stress equivalence in both models.

The Rankine criterion is employed in the analysis of concrete cracking, whereby it postulates the transformation of strains and stresses along the material's specific orientations. These orientations correspond to the principal directions in scenarios involving a rotated crack model. In instances of a fixed crack model, the orientations are determined by the principal directions before cracking begins. Solving this equation requires iterative processes since the prevailing tensile strength depends on the extent of crack opening for materials exhibiting softening behaviour, denoted as w . The domain of principal stresses is defined by σ_1 , σ_2 , and σ_3 principal stress. The free parameters define the octahedral domain, which is delineated by Haigh-Westergaard coordinates (Fig. 7.1).

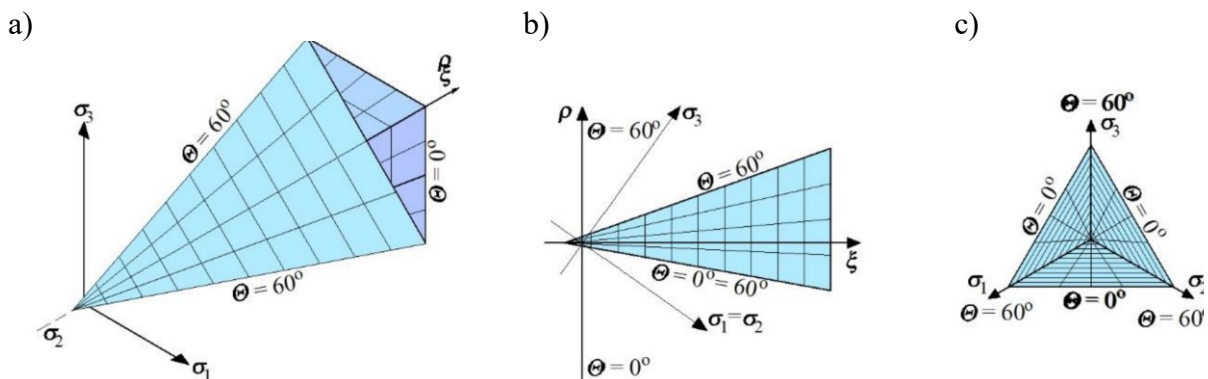


Fig. 7.1. The Rankine criterion in the Haigh-Westergaard space: a) view of principle stress space, b) view of axiatoric section, c) view of deviatoric section [64]

Rys. 7.1. Kryterium Rankina w przestrzeni Haigha-Westergaarda: a) przestrzeń naprężeń głównych, b) przekrój aksjatorowy, c) przekrój dewiacyjny [64]

The Rankine criterion was utilized to determine tension-induced failure. The crack width was calculated by considering known strains and the specified length L_t , which reflects the dimensions of smeared cracks. It is important to note that the position of Menetrey-Willam failure surfaces is not fixed; it can shift depending on the value of the strain hardening/softening parameter. The equivalent plastic strain determines the strain hardening. In the case of the Menetrey-Willam surface, the parameter c governs the hardening/softening (Fig. 7.2), which changes the process of yielding/crushing.

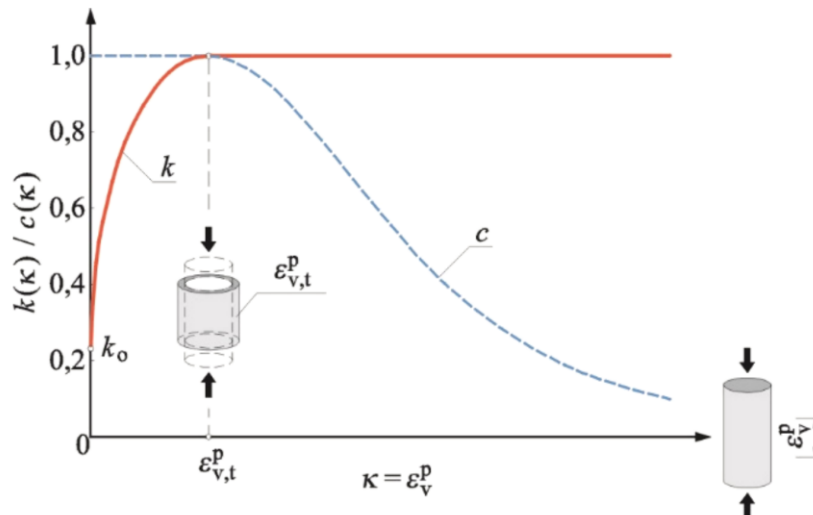


Fig. 7.2. Shape of hardening/softening function with c parameter
 Rys. 7.2. Funkcja wzmocnienia/osłabienia z parametrem c

The Fracture-Plastic Constitutive Model integrates various models into a unified framework, incorporating the Menetrey-Willam model for concrete crushing and the Rankine fracture model for cracking. Each model functions as an operator, mapping strain increments as input to either fracture or plastic strain increments as output. The relative positions of the M-W and Rankine surfaces are determined by the surface matching parameter λt , which is illustrated in Figure 7.3. When λt is equal to 1, the yield surface is contained within the Rankine pyramid. At λt equals 2, the surfaces intersect from the side of hydrostatic tension and minor compression, with the Rankine boundary surface defining the stress states. For higher values of hydrostatic compression, failure is determined by the M-W surface. Movements of the M-W surface along the axis were achieved by simulating the material's hardening or softening stages.

The ATENA material model named *CC3DNonLinCementitious2* based on the above assumptions. The model offers the capability to include effects such as: tensile strength degradation due to lateral compressive stress, tension stiffening, aggregate interlock, and shear factor (cracking shear stiffness).

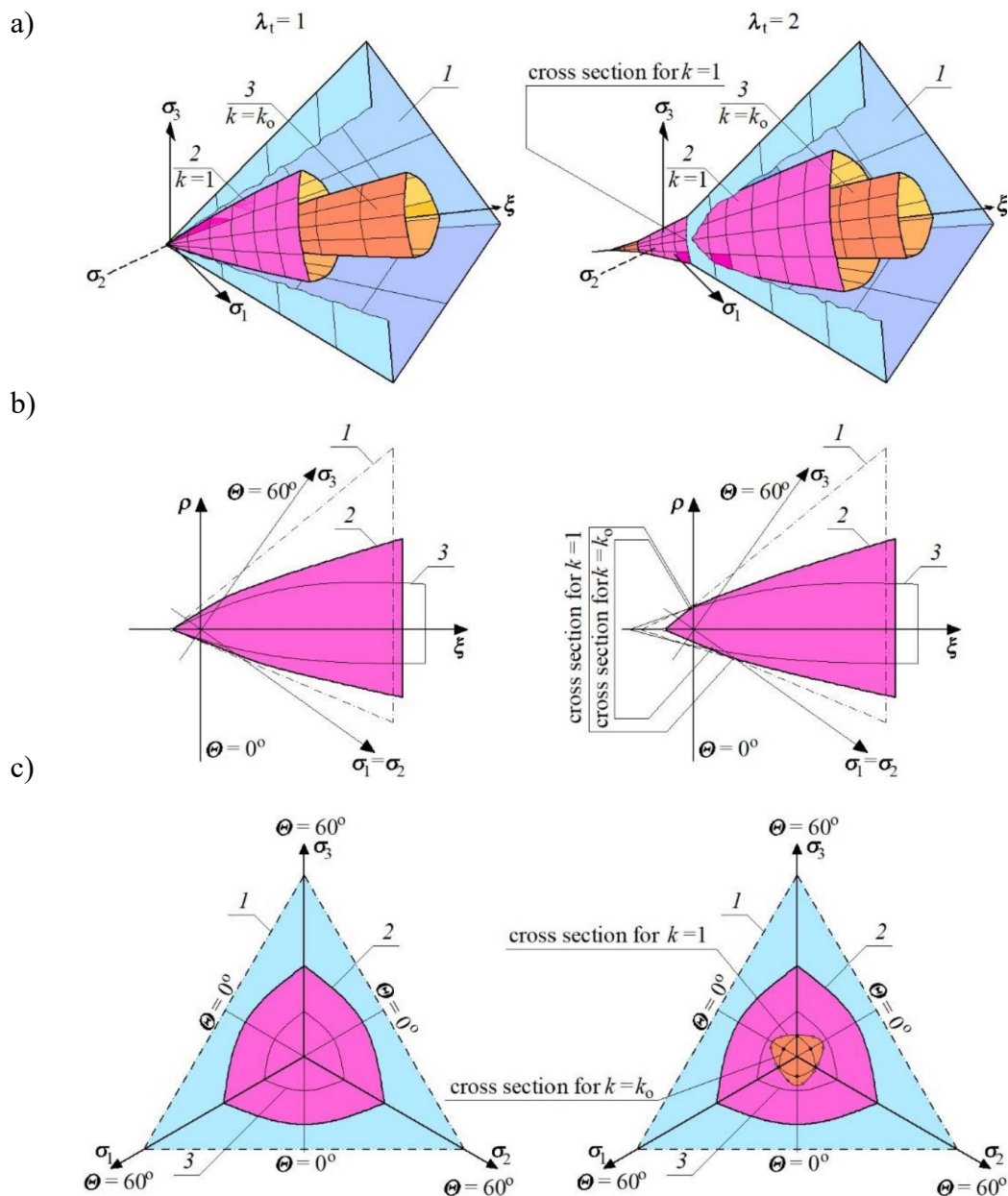


Fig. 7.3. Relative position of Rankine and M-W surfaces: a) view of surfaces, b) axiatic sections, c) deviatoric sections: 1 – Rankine Surface, 2 – M-W surface, the surface at $k = 1$ (yield strength), 3 – M-W surface at k_0 (end of the elastic stage) [64]

Rys. 7.3. Względne położenie powierzchni Rankine'a i M-W: a) widok powierzchni w przestrzeni naprężeń głównych, b) przekroje aksjatorowe, c) przekroje dewiacyjne: 1 - powierzchnia Rankine'a, 2 - M-W, powierzchnia przy $k = 1$ (granica plastyczności), 3 - powierzchnia M-W przy k_0 (koniec fazy sprężystej) [64]

Interface material model

Based on the Mohr-Coulomb criterion, the interface material model simulates contact between two concrete segments. The Mohr-Coulomb criterion is modified by tension cut-off (represented by an ellipse in tension). This ellipse defines the interface criterion in tension, connecting the point of pure cohesion and the point of pure tension. The constitutive relation for a general three-dimensional case is described in terms of tractions acting on interface planes and relative sliding and opening displacements (Eg. 7.1).

$$\begin{Bmatrix} \tau_1 \\ \tau_2 \\ \sigma \end{Bmatrix} = \begin{bmatrix} K_{TT} & 0 & 0 \\ 0 & K_{TT} & 0 \\ 0 & 0 & K_{NN} \end{bmatrix} \begin{Bmatrix} \Delta v_1 \\ \Delta v_2 \\ \Delta u \end{Bmatrix} \quad (7.1)$$

The initial failure surface follows the Mohr-Coulomb condition with an ellipsoid in the tension regime. When stresses exceed this condition, the surface collapses into a residual surface representing dry friction (Fig. 7.4a). The definition of interface parameters should follow the rules:

$$f_t < \frac{c}{\phi} \quad (7.2)$$

$$f_t < c \quad (7.3)$$

$$c > 0 \quad (7.4)$$

$$f_t > 0 \quad (7.5)$$

$$\phi > 0 \quad (7.6)$$

In cases of interface with no cohesion or tensile strength, it is required to assign very small values (due to computational purposes).

The variables K_{NN} and K_{TT} represent the initial elastic normal and shear stiffness, respectively (Fig. 7.4a, b). Additionally, two other stiffness values, referred to as min K_{nn} and min K_{tt} , need to be specified in the input for ATENA. These values are utilised solely for numerical purposes after the element fails to ensure the positive definiteness of the global system of equations. Ideally, the interface stiffness should be zero after the interface fails, leading to an indefinite global stiffness. To resolve this problem, the minimal stiffness values should be approximately 0.001 times the initial values.

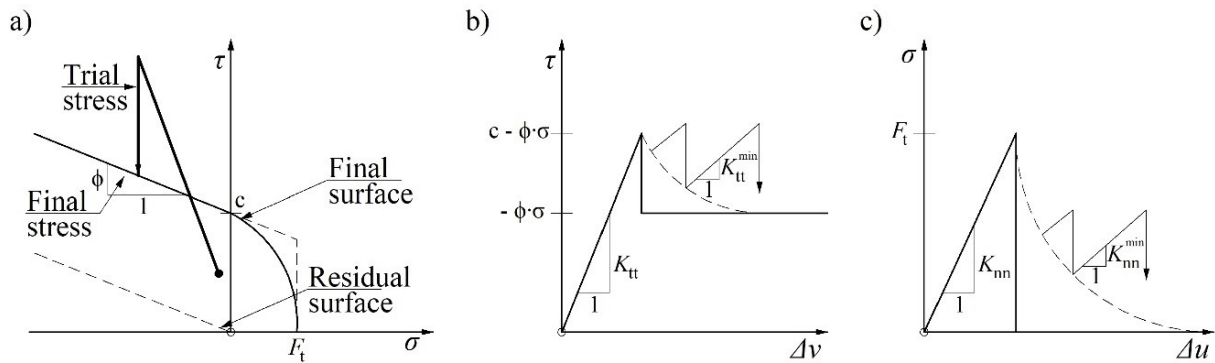


Fig. 7.4. Interface material model: a) failure surface, b) shear behaviour, c) tension behaviour
 Rys. 7.4. Modelu materiałowy styku: a) powierzchnia zniszczenia, b) zależności przy ścinaniu, c) zależności przy rozciąganiu

It is possible to extend the material model of the interface to individually define evolution laws for tensile and shear softening using arbitrary multilinear laws. This approach ensures that shear degradation also affects the tensile strength. In this study, the interface degradation was not correlated with softening law modifications.

Steel

Reinforcement can be introduced through the implementation of discrete reinforcement models. In the case of discrete reinforcement, reinforcing bars and strands are modelled using truss elements. Steel bars and strand material model consistent multi-linear strand law, which represents all four stages of steel behaviour: elastic state, yield plateau, hardening, and fracture. The multi-linear law is defined by four points that can be specified as input. The parameter models employed in this study are based on the two-line models based on the *fib* Model Code 2010 parameter relations. Bond behaviour was included in the reinforcement modelling. The fundamental property of the reinforcement bond model is the bond-slip relationship. This relationship defines the bond strength (cohesion) in relation to the current slip between the reinforcement and the surrounding concrete. ATENA contains the *fib* Model Code 2010 bond-slip model generator. The model is based on concrete compressive strength, reinforcement diameter, reinforcement type, confinement conditions, and the quality of the concrete casting.

7.2.2. Material parameters assumed from experimental studies

The material parameters of the concrete, such as compressive strength and modulus of elasticity, were taken as in Table 7.2, and the tensile strength was taken as in Table 7.1. The reinforcing and prestressing steel parameters were taken as in Table 7.3.

The value of the prestressing force was determined using a FEM model, where the value of the flexural cracking force was correlated with the tension of the strands (initial strain option). The assumption of parameters for the interface requires more extensive discussion. Due to the precast elements' manufacturing process, it was impossible to carry out comparative tensile splitting tests. The concrete topping tensile strengths for the tensile splitting test were lower than for the interface in the pull-off test. If the interface tensile strength is higher or equal to the tensile strength of the weaker materials being connected, it does not make mechanical sense to model the interface. A perfect connection can be used instead because the concrete next to the interface cracks under the same or lower load as the interface (Atena Manual). However, based on experimental investigations, it is possible to determine the occurrence of slippage at the interface on both direct shear and beam elements.

For this reason, a possible range of tensile strength parameters within one standard deviation was defined. For the parameters determined in this way, average values were taken as initial values due to the tensile strength of the concretes. For the interface, the tensile strength minus one standard deviation was taken. The strength thus determined corresponds to a c factor of 0.81 with respect to topping concrete, which finds its justification in the literature (Section X.X). The values selected for modelling are highlighted in Table 7.1.

Table 7.1

Concrete tensile strength parameters

Parametry wytrzymałościowe betonu na rozciąganie

Element	Tensile splitting test			Pull-off test		
	Mean value $f_{ctm,ts}$, N/mm ²	Standard deviation	Mean value +/- SD $f_{ctm,ts}$, N/mm ²	Mean value $f_{ctm,pot}$, N/mm ²	Standard deviation	Mean value +/- SD $f_{ctm,pot}$, N/mm ²
Z series Topping	<u>3.34</u>	0.83	2.51 / 4.17	-	-	
Z series Precast	<u>4.37</u>	0.59	3.78 / 4.96	-	-	
Z series T/P	1.86*	0.25	1.61 / 2.11	3.56	0.85	<u>2.71</u> / 4.41

7.2.3. Material parameters of numerical models

The material parameters of the concrete (Table 7.2) were determined employing an in-built generator based on the relationships given in Model Code 2010, acting on the given average compressive strength of the concrete. The generated parameters were corrected for the tested tensile strength of the concretes in terms of tensile strength and onset of crushing.

The reinforcing steel parameters (Table 7.3) were generated based on the test results based on the Eurocode 2 relationship. The anchorage bond parameters were determined based on the Model Code 2010 relationship, perimeter was defined based on [107] recommendation.

Table 7.2
Material strength parameters in FEM model
Parametry wytrzymałościowe materiałów w modelu MES

Element Parameter	Z series Precast	Z series Topping	Steel plates	PTFE
Mean value $f_{c,cube}$, N/mm ²	65.34	35.94	-	-
Compressive strength, N/mm ²	56.7	31.7	-	-
Young modulus E_c , GPa	39.08	31.75	200	0.7
Poisson ratio	0.2	0.2	0.3	0.46
Tension strenght $f_{cm,ts}$, N/mm ²	4.37	3.34	-	-
Fracture energy, G_f , N/mm	0.151	0.136	-	-
Plastic strains EPS _{CP}	-0.0011	-0.00117	-	-
Onset of crushing N/mm ²	-9.18	-7.02	-	-
Critical compressive displacement, mm	-0.5	-0.5	-	-

Table 7.3

Properties of reinforcement steel and prestressing steel in FEM model
Parametry stali zbrojeniowej oraz sprężającej w modelu MES

Element Parameter	Ribbed reinforcement	PS strands
Yield strength, N/mm ²	554	1927
Tensile strength, N/mm ²	594	2177
Breaking strains	0.05	0.05
Young modulus E_c , GPa	200	195
Bond strength, N/mm ²	7.66	0.81

The interface parameters were determined by correlating the direct shear FEM model. A description of the principles and dependencies adopted to calculate cohesion and stiffness for the models in the Z1_C, Z2_AB and Z3_CB series has been described in the following section.

7.3. Direct shear test modelling

The numerical model was made by modelling all the relevant elements of the test stand. Due to the shape of the force gauge used, a simplified model was also made, consisting of an upper beam supported on a lower ring distributing the applied force (Fig. 7.5a). The force gauge was supported on a steel plate by using the master/slave fixed contact option. A surface support was set on the lower steel plate. The plates were connected to the model with a flexible PTFE material plate (Fig. 7.5b). The interface between the PTFE and the steel plate was set to act in compression only, with a friction coefficient limited to 0.1. The PTFE plate was connected to the model with the master/slave fixed contact option, which allowed the finite element mesh of the plate and the PTFE to be decoupled from the mesh of the test piece. This avoids local disturbance points and complies with the Atena Manual recommendation. An interface was modelled between the concrete topping and the precast element with a material model, as described in Section 7.2.1, with correlated parameters.

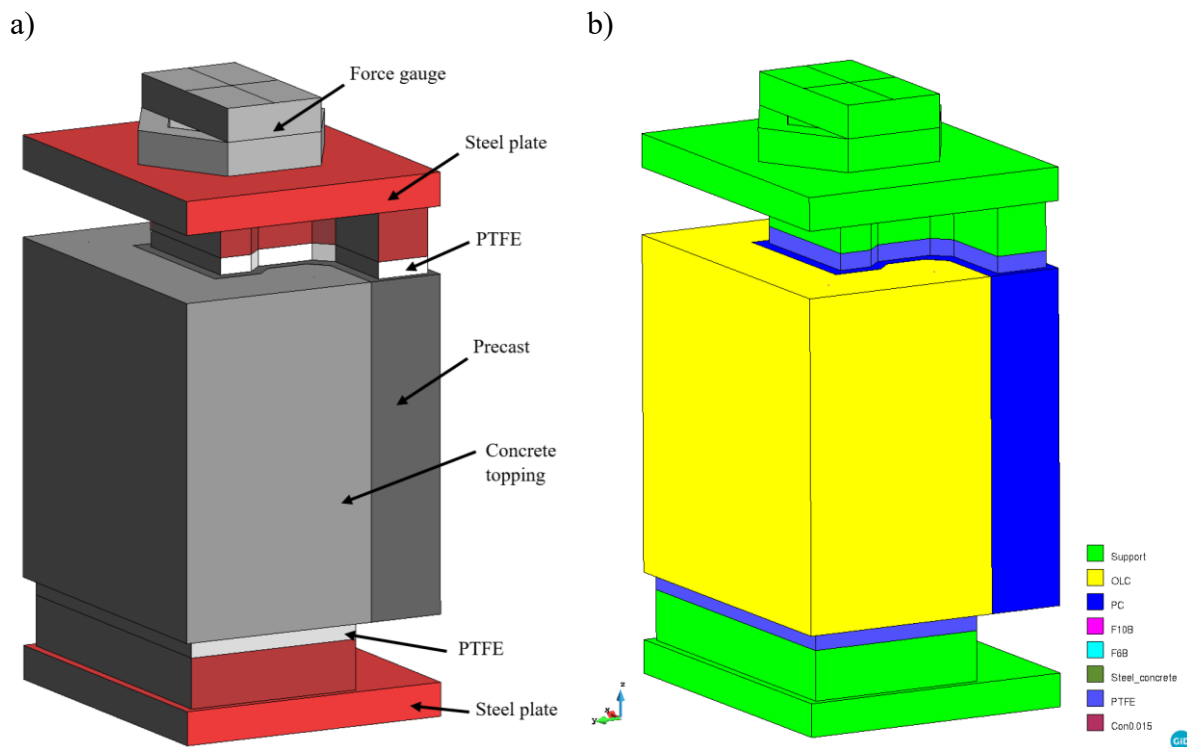


Fig. 7.5. Construction of the numerical model: a) overall view with breakdown by elements, b) view with breakdown by materials

Rys. 7.5. Budowa modelu numerycznego: a) widok ogólny z podziałem na elementy, b) widok z podziałem na materiały

To control the solving of the task due to the relatively small number of elements, the Newton-Rapson method was used with a tangential predictor matrix to predict displacement increments from structural unbalanced forces. In the tangent predictor, the stiffness matrix is assembled in each iteration. The iteration limit is set to 200 with the line-search iteration method. If no match is obtained for a given step, the solver repeats the calculation of the step, reducing the displacement increment by 50%, up to a value of 12.5% of the original increment. The latest available solver, PARDISO (developed by Intel in 2011), was used, enabling the efficient use of multi-core processors with additional logic processes per core. Due to the increased vulnerability of the solved model to step error values, a reduced permissible error of 0.1% was adjusted on a trial basis, compared to the recommended 1% for most tasks. All solver setup parameters are shown in Table 7.4.

Table 7.4
Properties of solver
Parametry solvera

Parameter	Method/Value
Method	Full Newton-Raphson
Displacement, Residual and Absolute Residual error	0.001
Energy error	0.0001
Negligible size relative	0.00001
Iteration limit	200
Iteration process	Line-search with iterations
Optimize bandwidth	Sloan
Stiffness type	Tangent Predictor (each iteration)
Solver	PARDISO
Step size	0.01mm* *(applied to the force gauge, partially compensated by PTFE and model geometry)
Number of load steps	100
Step load reduction allowance	3
Reduce step load coefficient	0.5

7.3.1. Correlation of interface parameters

Preliminary correlation of interface parameters

This study does not describe in detail the entire iterative step-by-step procedure for establishing the model solution parameters, which are presented in Table 7.4. These parameters were established during the iterative work on the numerical models. Some parameters, including those responsible for optimising hardware utilisation, were modified during successive versions of the performed numerical models, agreed upon before all models' final calculations were performed. The following section presents the results of the models for the solution parameters as above. Correlation of the interface parameters was performed for the solution, which was thus defined. The first numerical model was performed on a 10 mm finite element mesh adopted from the literature, consisting of quadrilateral elements for the surface and hexahedra for the volume (Fig. 7.6a). The mesh was defined so that the finite element dimensions were always 10 mm for each surface (edge). Limited variables in the size of the finite elements within the volume were allowed. Displacement measurements were set as monitors at points to

determine slip as in the test, as shown in Fig. 7.6b. The displacement value at the point of load application and the value of the reaction (force) generated by the applied displacement were also set to be tracked.

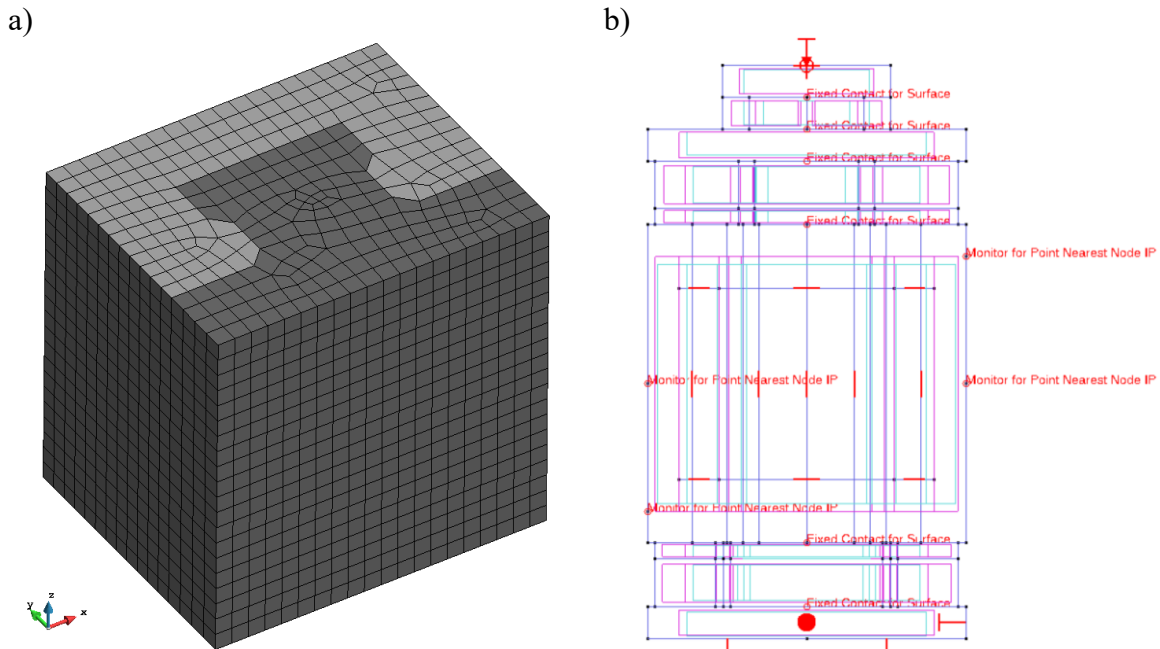


Fig. 7.6. View of the numerical model: a) 10 mm FEM mesh, b) definition of boundary conditions and monitors

Rys. 7.6. Widok modelu numerycznego: a) siatka FEM o wymiarze 10 mm, b) definicja warunków brzegowych oraz monitorów

In order to determine the cohesion parameters initially, a basic relationship under Mohr-Coulomb theory [33] was used, the basic relationship of which is shown as equation 7.7.

$$c = \frac{1}{2} \sqrt{f_c \times f_{ct}} \quad (7.7)$$

The f_{ct} value was assumed in the range between the tensile strength of the concrete topping from the tensile splitting test and the tensile strength of the bond from the pull-off test. For elements without a measurable adhesion value tested, parameters were initially assumed for numerical purposes in the 0.1 to 1.0 MPa range. For model Z2_AB, higher cohesion values are expected to be obtained relative to model Z3_CB due to the presence of a mechanical adhesion component and the removal of only chemical adhesion. The preliminary expected cohesion range was determined in this manner and is summarised in Table 7.5 for the given element and surface types. These values are also within the range definable by the Carol/Espeche-Leon [161] approach.

Table 7.5

Initial extent of cohesion parameter correlation
Wstępny zakres korelacji parametru kohezji

Element	Parameter	Cohesion range
Z1_C	$f_{c,cube} = 35.94$ MPa	4.93 – 5.48 MPa
	$f_{ctm,ts} = 3.34$ MPa	
	$f_{ctm,pot} - SD = 2.71$ MPa	
Z2_AB	$f_{c,cube} = 35.94$ MPa	0.95 – 3.0 MPa
Z3_CB	$f_{ctm,ts} = 0.1 - 1.0$ MPa	

In the case of a concrete-concrete interface as in the Z1_C model, two parameters were correlated: the described cohesion c and the tangential stiffness of the K_{TT} . The tensile strength was also correlated for interfaces coated with antiadhesion agent and the interface with a mat. As shown in the experimental test, the AB and CB interfaces were characterised by initial adhesion, indicating the presence of tensile strength in the range below, which could be tested by the pull-off method. This strength is due to mechanical adhesion for the Z2_AB element in particular. A friction coefficient as for rough surfaces (according to EN 15037-1) of 0.7 was assumed for the elements with concrete-concrete interface and a value of 0.2 for the covered surfaces.

Correlation of the interface on model Z1_C with a 10 mm mesh based on tests on element Z1.2_C3, for which a Type I failure was obtained, i.e. slip over the entire interface width. The interface parameters were obtained after an iterative correlation approach, as shown in Table 7.7, compared to the test result in Table 7.6. The convergence of the maximum force values was 99.8%, with a convergence of slip and stiffness of 97.4%. Convergence was not obtained for the residual force after interface failure.

Table 7.6

Summary of failure type and cracking forces of C type elements
Zestawienie typów zniszczenia i sił rysujących elementów typu C

Element	Peak load F_{max} , kN	Residual load F_{Res} , kN	Slip at F_{max} S_{max} , mm	Stiffness F_{max} $K_{100\%}$, kN/mm	Failure type
Z1.2_C3_0.01	106.79	15.65	0.076	1405.1	I
Z1_C - FEM	106.83	1.90	0.072	1479.6	I
COV, %	0.02%	78.4%	2.56%	2.58%	

The remaining interfaces were correlated analogously to the procedure for the fully composite model. To represent the element's behaviour with an antiadhesion agent, it was necessary to increase the tensile strength of the concrete and, thus the cohesion beyond the initially expected range.

The normal stiffness of the interface each time was determined according to the Athena Manual as ten times the stiffness of the adjacent finite element (concrete stiffness divided by the mesh element size). An interface test with a stiffness of $2 \cdot 10^5$ (10x the stiffness) was also carried out, and a maximum force difference of 1% (1.1 kN) was obtained, so the normal stiffness calculated according to the recommendations of the Athena Manual was retained. No correlation of normal interface stiffness was made for the surface with the mat, leaving the value for the interfaces without the interlayer. The residual value of normal stiffness for numerical purposes was determined according to the recommendation as 1/200 of the basic value. The stiffnesses were specified to the optimised mesh size of 15 mm, as shown later in the description of this subsection. Table 7.7 gives the results from the correlations of the interface, which were adopted in the direct shear and beam models.

Table 7.7
Properties of interface in FEM model
Parametry styków w modelu MES

Element Parameter	Concrete – concrete surface	Adhesion brake surface (AB)	Surface with mat (CB)	Steel – concrete surface (support)
Cohesion, N/mm ²	5.30	3.3	2.0	0.1
Tensile strength, N/mm ²	2.71	1.2	0.45	0.001
Friction coefficient	0.7	0.7	0.2	0.1
Normal stiffness K_{NN} , N/mm ³	21170.0	21170.0	21170.0	21170.0
Tangential stiffness K_{TT} , N/mm ³	45.0	5.0	3.0	2.0
Minimal normal stiffness K_{NN} , N/mm ³	271.0	217.0	217.0	217.0
Minimal tangential stiffness K_{TT} , N/mm ³	0.45	0.05	0.03	0.02

Verification of the sensitivity of the FEM mesh

The model's sensitivity to finite element mesh size was then verified. The analysis was carried out for three mesh sizes

ranging from 22.5 mm to 10 mm (Fig. 7.7), using four-node (normal) and eight-node (quadratic) elements. Due to the solution time (more than 12h) and obtaining high convergence with the other results for the 10 mm grid size, only the four-node elements were verified.

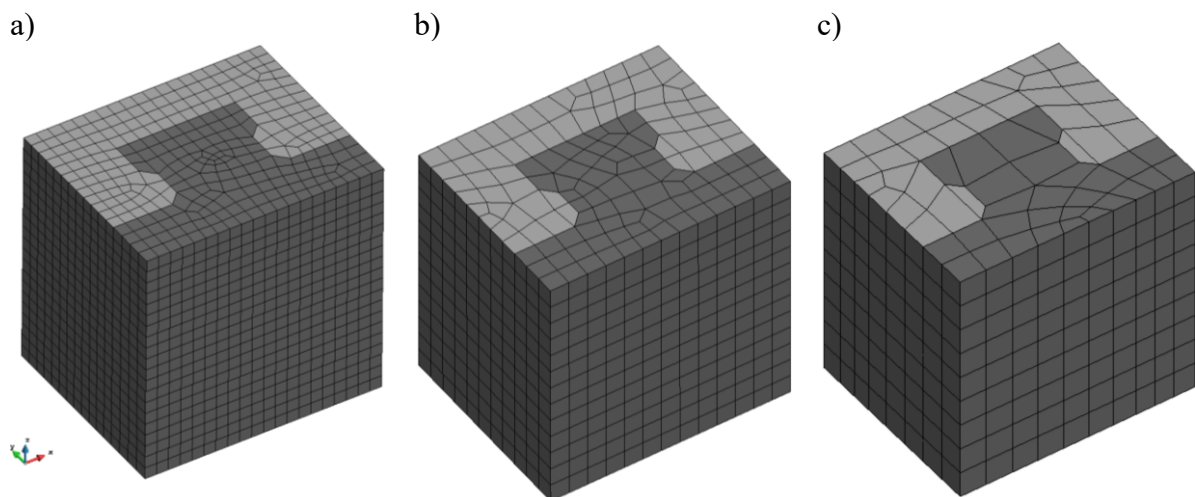


Fig. 7.7. View of the model with mesh size: a) 10 mm, b) 15 mm, c) 22.5 mm

Rys. 7.7. Widok modelu z siatką o rozmiarze: a) 10 mm, b) 15 mm, c) 22.5 mm

The results were sorted according to the number of nodes in the tested element (precast, concrete topping and interface). The values of maximum force and average slip at maximum force were given. A 95% agreement was obtained for both force and slip values for four of the five meshes tested against the model with the highest number of nodes. Only the model with a mesh size of 22.5 mm deviated from the others, its correlation being 78% for force and 85% for slip. The calculation of models with a quadratic mesh takes disproportionately longer than models with a similar number of nodes but with a four-node mesh (normal). This is due to the increased computation time of the stage triangulation, which determines the stiffness matrix performed on only one processor thread. The triangulation process is the most time-consuming phase of single-stage calculation. Based on the verification, it was decided to select a 15 mm grid of the four-node type for further analysis. Due to the dimensions of the element (bottom flange and concrete topping over the head with a dimension of 45 mm), this mesh fits well into the modelled elements. The convergence of the results for force is 97%, and for slip 99%, relative to the model with the highest number of nodes. Further results are presented for models on a 15 mm grid for both direct shear and beam models.

Table 7.8

Summary of calculated values for verified mesh sizes

Zestawienie obliczonych wartości dla weryfikowanych rozmiarów siatki

Number of nodes	Mesh size mm	Mesh type	Computation time, s	Peak load F_{max} , kN	Slip at F_{max} S_{max} , mm
9691	15.0	Quadratic	11646	107.92	0.074
7921	10.0	Normal	4382	106.83	0.072
3509	22.5	Quadratic	3961	104.86	0.075
2566	15.0	Normal	865	107.11	0.077
954	22.5	Normal	563	84.03	0.063

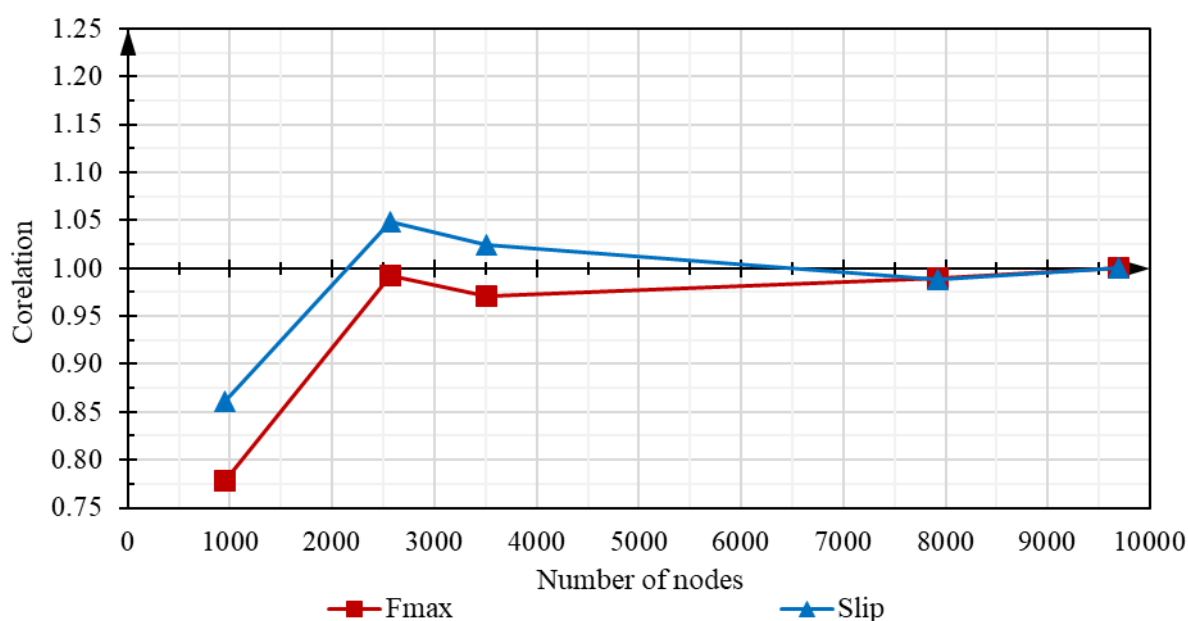


Fig. 7.8. Correlation of verified parameters to the model with the highest number of nodes

Rys. 7.8. Korelacja weryfikowanych parametrów względem modelu o największej liczbie węzłów

7.3.2. Force-slip characteristic

Two types of failure characterised the elements with full adhesion in the tests. Only type I was present in the numerical models; therefore, the model results were compared only to element Z1.2_C3 (table 7.9). Very high conformity was obtained for all verified parameters, such as maximum force, slip value and stiffness, except the residual force. The numerical model obtained almost ten times lower residual force than in the study. Regardless of the initial or minimum stiffness values and the friction coefficient, obtaining a residual force as in the tests was impossible.

Table 7.9

Summary of failure type and cracking forces of C type elements
Zestawienie typów zniszczenia i sił rysujących elementów typu C

Element	Peak load F_{max} , kN	Residual load F_{Res} , kN	Slip at F_{max} S_{max} , mm	Stiffness F_{max} $K_{100\%}$, kN/mm	Failure type
Z1.2_C3	106.79	15.65	0.076	1405.1	I
Z1_C - FEM	107.11	1.90	0.077	1437.6	I
COV, %	0.15%	78.35%	0.65%	1.14%	

In Fig. 7.9, the numerical model results are collected and compared with each test element. As described earlier, no convergence in terms of the failure model was obtained for elements Z1_C1 and Z1_C2. Significant differences are also found in the slip curve at the interface concerning model Z1_C1 in particular (Fig. 7.9a). Relatively good convergence was obtained by comparing the slip behaviour against the Z1_C2 element. The numerical model is characterised by constant stiffness over almost the entire range before maximum force. This represents the main difference to models C2 and C3 (Fig. 7.9b, c). A slight non-linearity resulting from using ellipse in tension described in the material model and the distribution of tangential forces as described further, at values close to the maximum force (Fig. 7.9d). The numerical model confirmed a significant difference in interface slip along the length. The slip value is not constant along the length of the element at the tested and modelled stiffnesses of the composite. The results obtained for the concrete topping deflection outside the precast section are not shown in the diagrams. **The maximum measurement showed a deflection of 0.0064mm, ten times smaller than in the study.** Similar results for horizontal deformation of the concrete topping were obtained on all models.

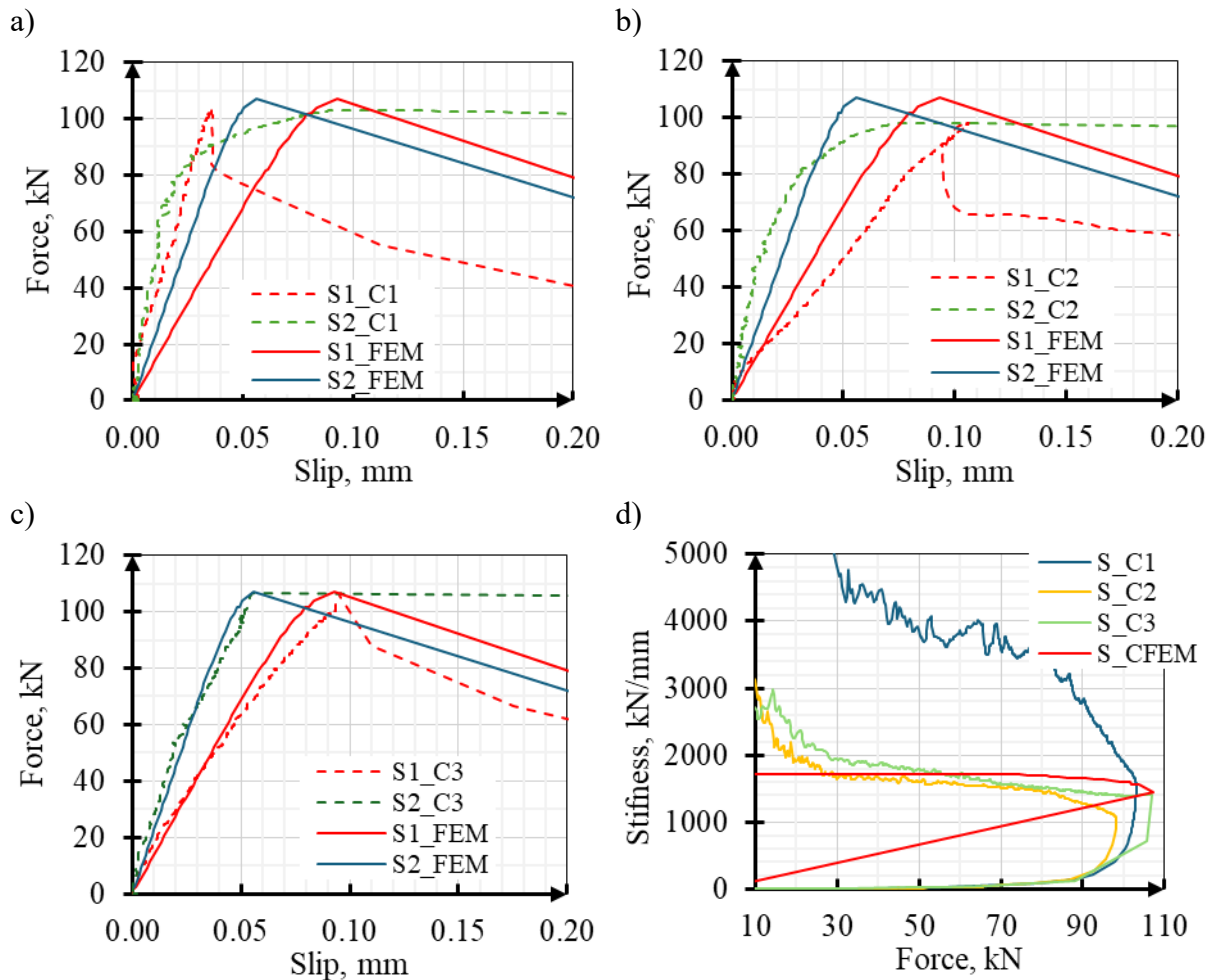


Fig. 7.9. Comparison of test and FEM results for Z1_C elements: a) Z1.2_C1, b) Z1.2_C2, c) Z1.2_C3, d) Z1.2_C interface stiffness

Rys. 7.9. Porównanie wyników analiz MES z wynikami badań dla elementu Z1_C: a) Z1.2_C1, b) Z1.2_C2, c) Z1.2_C3, d) Z1.2_C sztywność zespolenia

To correlate with the test results, the Z2_AB model required the interface to be modelled with a tensile strength of 1.2 MPa despite not obtaining meaningful results in the Pull-off test. The numerical model is highly correlated with the test results of elements Z2.2_AB2 and Z2.2_AB3 regarding maximum force (Table 7.10). For the numerical model, as in the test elements, slip values for the measuring points at different interface lengths showed similar values (Fig. 7.11a-c). Similar to Z1_C, the numerical model showed a more linear interface stiffness than the test models (Fig. 7.11d). Residual values of 5.48 kN were obtained, several times higher than for model Z1_C. The Z2_AB models had a smoother post-failure slip growth and residual force drop path.

Table 7.10

Summary of failure type and cracking forces of AB type elements
Zestawienie typów zniszczenia i sił rysujących elementów typu AB

Element	Peak load F_{max} , kN	Residual load F_{Res} , kN	Slip at F_{max} S_{max} , mm	Stiffness F_{max} $K_{100\%}$, kN/mm	Failure type
Z2.2_AB1	70.07	16.24	0.179	391.5	I
Z2.2_AB2	47.10	14.15	0.275	171.3	I
Z2.2_AB3	43.94	13.17	0.267	164.6	I
Z2_AB - FEM	47.66	5.48	0.205	244.9	I

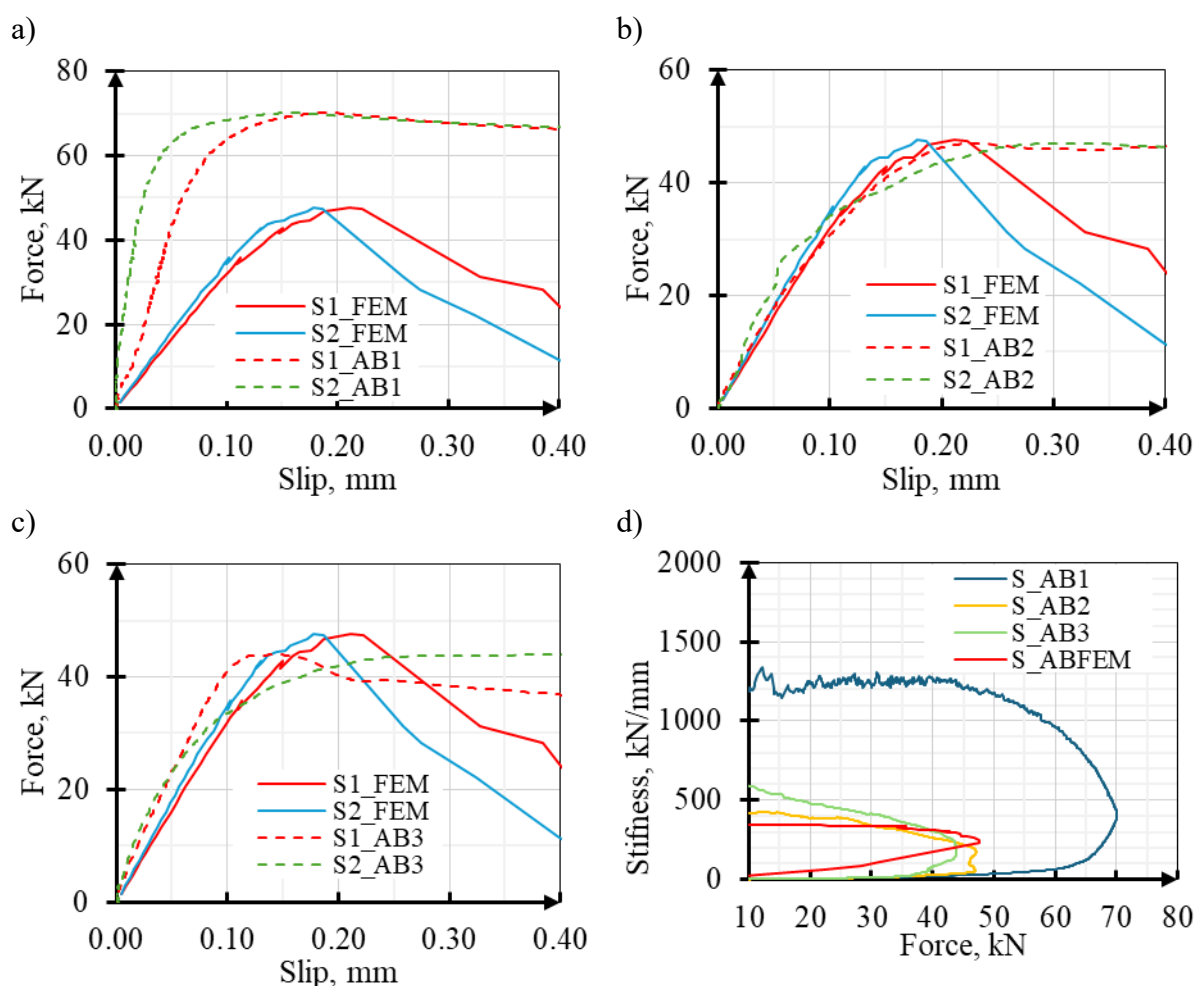


Fig. 7.10. Comparison of test and FEM results for Z2_AB elements: a) Z2.2_AB1, b) Z2.2_AB2, c) Z2.2_AB3, d) Z2.2_AB interface stiffness

Rys. 7.10. Porównanie wyników analiz MES z wynikami badań dla elementu Z2_AB: a) Z2.2_AB1, b) Z2.2_AB2, c) Z2.2_AB3, d) Z2.2_AB sztywność zespolenia

The FEM model Z3_CB represents the performance of the CB-series elements well in terms of maximum force and average slip value (Table 7.11). The measured slip at the interface was similar regardless of the location of the measuring point (Fig. 7.11a-

c). The test elements were characterised by the non-linearity of the slip at the interface over the entire range, which could not be reproduced in the numerical model.

Table 7.11

Summary of failure type and cracking forces of CB type elements
Zestawienie typów zniszczenia i sił rysujących elementów typu CB

Element	Peak load F_{max} , kN	Residual load F_{Res} , kN	Slip at F_{max} S_{max} , mm	Stiffness F_{max} $K_{100\%}$, kN/mm	Failure type
Z3.2_CB1	18.00	11.50	0.110	163.6	I
Z3.2_CB2	17.78	7.55	0.311	57.2	I
Z3.2_CB3	20.21	6.45	0.095	212.7	I
Z3_CB - FEM	19.12	4.40	0.110	174.6	I

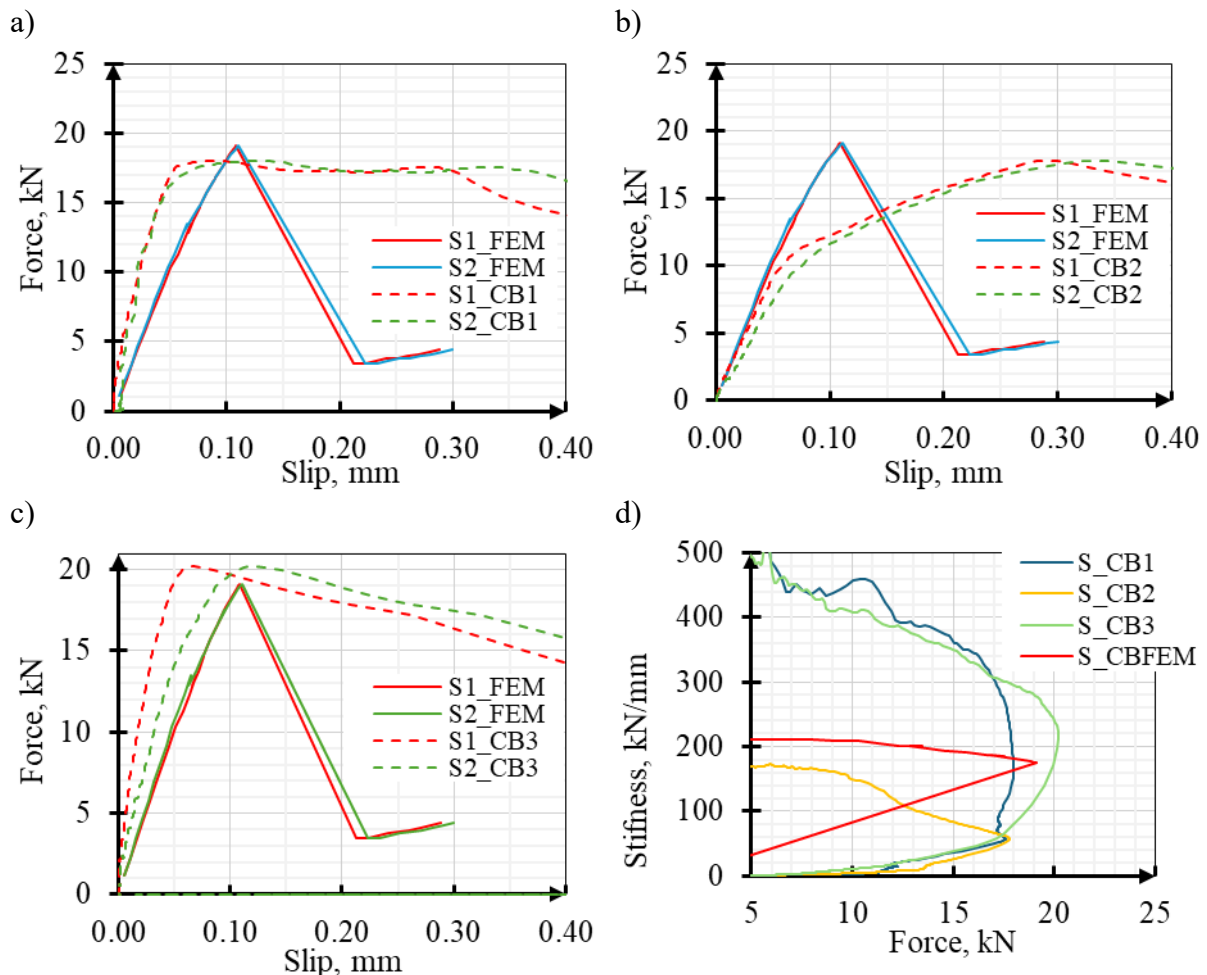


Fig. 7.11. Comparison of test and FEM results for Z3_CB elements: a) Z3.2_CB1, b) Z3.2_CB2, c) Z3.2_CB3, d) Z3.2_CB interface stiffness

Rys. 7.11. Porównanie wyników analiz MES z wynikami badań dla elementu Z1_C: a) Z3.2_CB1, b) Z3.2_CB2, c) Z3.2_CB3, d) Z3.2_CB sztywność zespolenia

7.3.3. Stress at the interface

The slip value at the interface of the numerical model correlated with the test element represents the shear stress interface value. Fig. 7.12 shows the shear stress and displacement readings for a force of 79.2 kN. The figure shows the last computational step for which no local slip was recorded at the interface on the rib side surfaces. The location of maximum displacement (Fig. 7.12a) also has the highest stresses at the interface (Fig. 7.12b). The slip and stress values are not constant along the length of the interface. Similar values are found for the interface between the head and the concrete topping on the face (loaded) and on the bottom surfaces of the rib flange where the model is supported. This load distribution based on the FEM analyses can be attributed to the geometry of the element and the test stand resulting in a slight eccentricity of the force application point to the precast and the concrete topping (as described in Section 5.1). Due to the eccentric rotation of the element, it is possible to analyse the Y-axis's compressive and tensile stress readings (Fig. 7.12c). The compressive stresses occur in the lower part of the cross-section at the side edges of the model. In the same areas, the only significant interface displacements in the lateral direction were read for (Fig. 7.12d). These displacements were consistent in direction (concrete topping outwards) relative to the experimental tests. The difference is the only local presence of horizontal slip of the interface in FEM relative to the measurable slip at different heights during the test. Minor tensile stress values (<0.2 MPa) on the model faces are present at the interface with the PTFE plate. The compressive stress map in Fig. 7.11c shows that the applied load is transmitted only by the pressure of the PTFE spacer against the rib head area. Despite using a force-measuring device with a design that distributes the applied load over the surface of the steel plate, the force was transferred mainly in the axis of the element rather than uniformly over the surface of the precast and concrete topping.

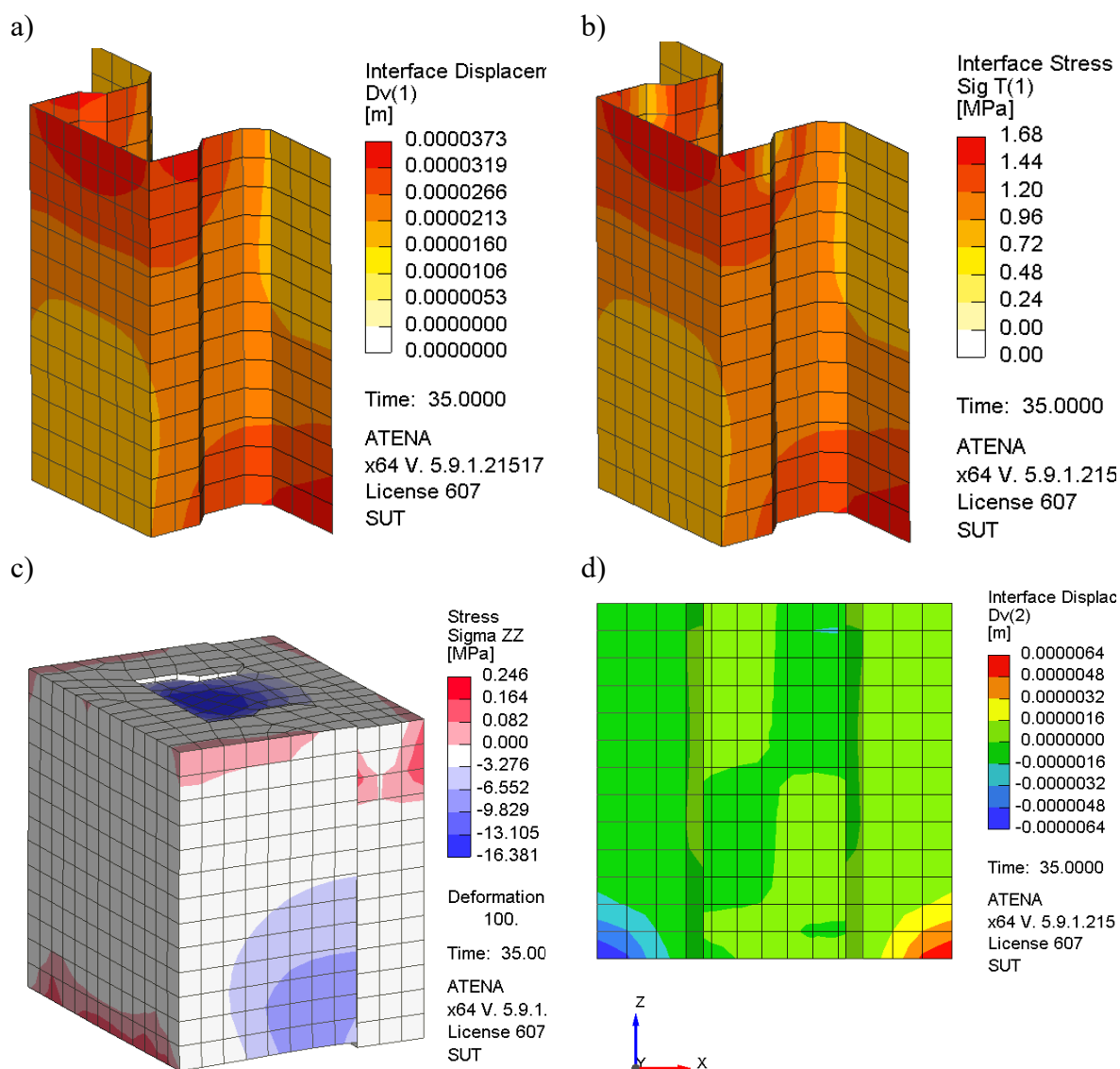


Fig. 7.12. FEM results of model Z1_C: a) z-axis (vertical) deformation of the interface, b) shear stresses at the interface, c) normal stresses of the model, d) z-axis (horizontal) deformation of the interface

Rys. 7.12. Wyniki obliczeń MES modelu Z1_C: a) deformacja na osi z (pionowej) styku, b) naprężenia styczne w styku, c) naprężenia normalne modelu, d) deformacja na osi z (poziomej) styku

The stresses in the interface for the step where the maximum force was obtained (107.1 kN) indicate a lack of effective tangential force transmission across the interface. From the stress map in Fig. 7.13, it can be stated that the side surface of the interface was “plasticised”, understood as exceeding the Mohr-Coulomb material model limit condition. The side surface connected the points of maximum displacement and stress in the interface. At the same time, it was not an area of compressive stresses that raised the maximum allowable tangential stresses. A concentration of compressive stresses

(with values up to 7.6 MPa) occurs at the face's edge. A significantly larger area is subjected to tensile stresses, reaching a maximum value of 1.63 MPa, representing 60% of the tensile strength of the modelled interface. The stress value at the interface of 3.21 MPa (peak force step) was lower than the cohesion of the material model and accounted for 60% of the maximum value. Within the transition step between peak force and full cracking, successive computational iterations indicated increasing sizes of plasticised zones. This was related to increased shear stresses in the edge zones with the highest compression.

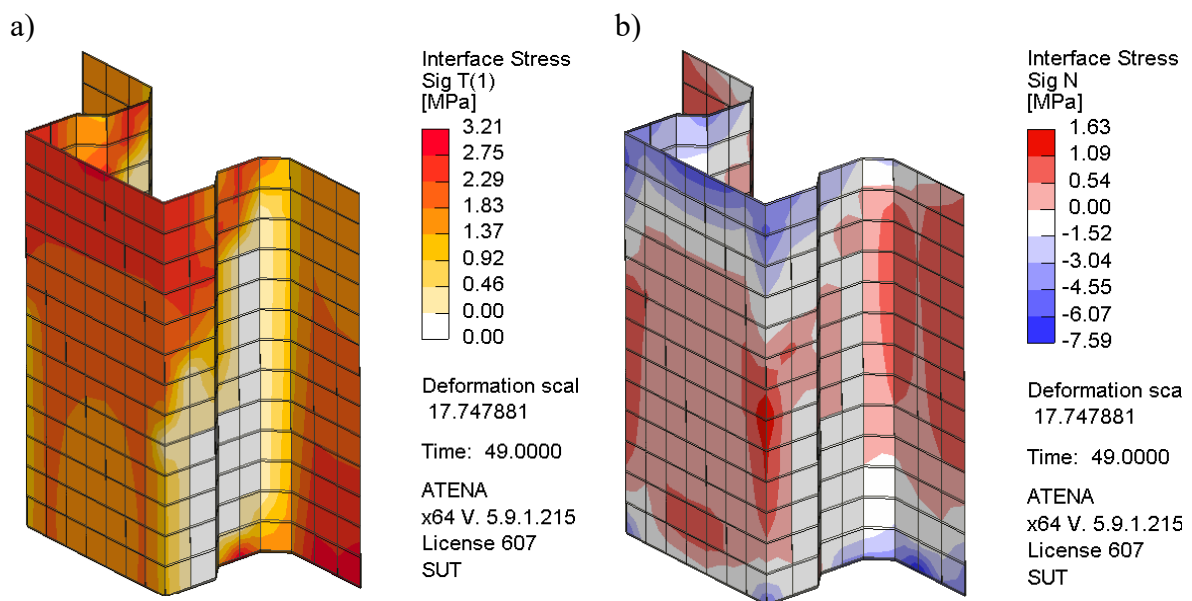


Fig. 7.13. Results of FEM analyses for model Z1_C: a) shear stresses at the interface, b) normal stresses at the interface

Rys. 7.13. Wyniki analiz MES dla modelu Z1_C: a) naprężenia styczne w styku, b) naprężenia normalne w styku

Similar stress distributions to model Z1_C occurred for models Z2_AB and Z3_CB. The differences were the failure progression of the interface, divided into several calculation steps (from 2 to 4 steps with full convergence), in which degradation of the effective (non-plasticised) interface surfaces occurred. The side surfaces were weakened first, followed by the top surfaces of the rib (Fig. 7.11 a, c) at the location of the highest tensile stresses. After plasticisation (local cracking) of the interface, the tensile stresses reach a value close to zero (Fig. 7.11b, d). Despite achieving full convergence of the calculation steps and determining an error value of 0.001, no symmetry was obtained in the subsequent stages of interface cracking at values close to the maximum force. This represents the main difference in the behaviour of FEM models Z2_AB and Z3_CB relative to model Z1_C. As indicated in para. 7.3.2, the element with the lower stiffness

of the interface was characterised by a uniform distribution of deformations along the length of the interface. The above is confirmed by the distribution of shear stresses along the length of the composite.

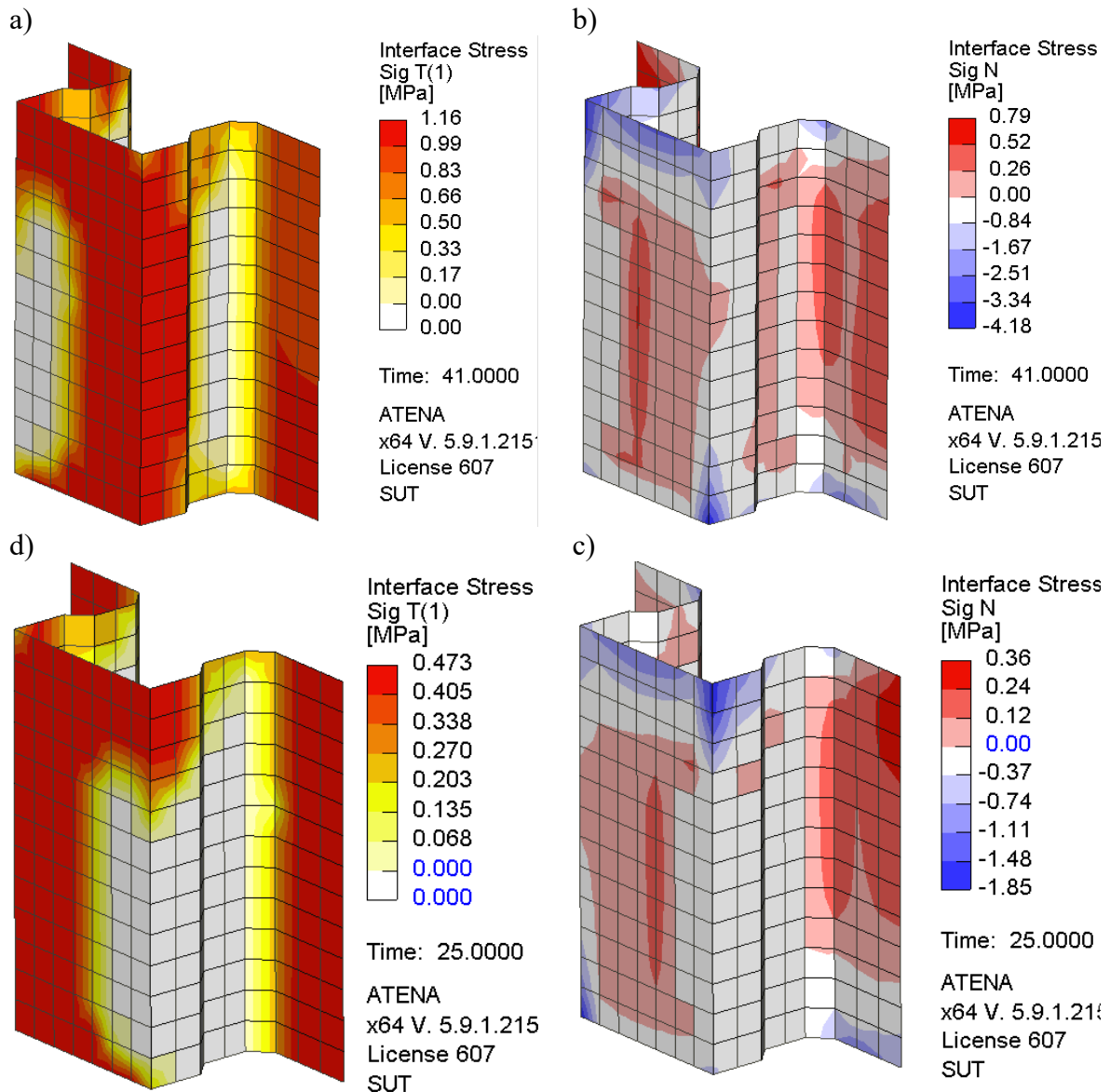


Fig. 7.14. Comparison of the results of FEM analyses for models Z2_AB and Z3_CB: a) shear stresses at the interface of model Z2_AB, b) normal stresses at the interface of model Z2_AB, c) shear stresses at the interface of model Z3_CB, d) normal stresses at the interface of model Z3_CB

Rys. 7.14. Porównanie wyników analiz MES dla modeli Z2_AB oraz Z3_CB: a) naprężenia styczne w styku modelu Z2_AB, b) naprężenia normalne w styku modelu Z2_AB, c) naprężenia styczne w styku modelu Z3_CB, d) naprężenia normalne w styku modelu Z3_CB

7.3.4. Failure mechanism

A global view of the vertical displacements of the numerical models for the steps corresponding to the maximum force is shown in Figure 7.15. The models are shown at 50 times the visual relative magnification of the deformation. In each case, it is possible to observe the effect of the flexibility of the PTFE plate aligning the pressure area with the steel plate and the composite element model. As a result of the eccentricity described earlier, a deflection of the element from the vertical axis is visible. The deflection is, however, less than 0.07 mm (Z1_C) for either model. At the same time, it is 100 times smaller than the vertical deformation of the interface before the complete slippage. The deformation image also shows the effect of interface displacement (elastic slip) relative to the concrete topping and precast (Fig. 7.15a, c, e).

For models Z1_C and Z2_AB, cracks were observed on the support face (bottom), with the largest opening at maximum force. These cracks reached a small width, 0.0013 mm for model Z1_C and 0.0019 mm for Z2_AB. These values are many times smaller than could be observed during the test and smaller than those found in the experimental models. The cracking pattern, with the greatest concentration at the corner of the rib head with concrete topping, is in line with the test image. In model Z3_CB, no cracking was observed, and the tensile stresses of the concrete topping reached a value of 1.76 MPa, which does not exceed the maximum tensile stress for the given material model parameters. In each model, one of the points of cracking concentration was the concrete topping reinforcement occurring on two sides of the rib, slightly above its bottom flange.

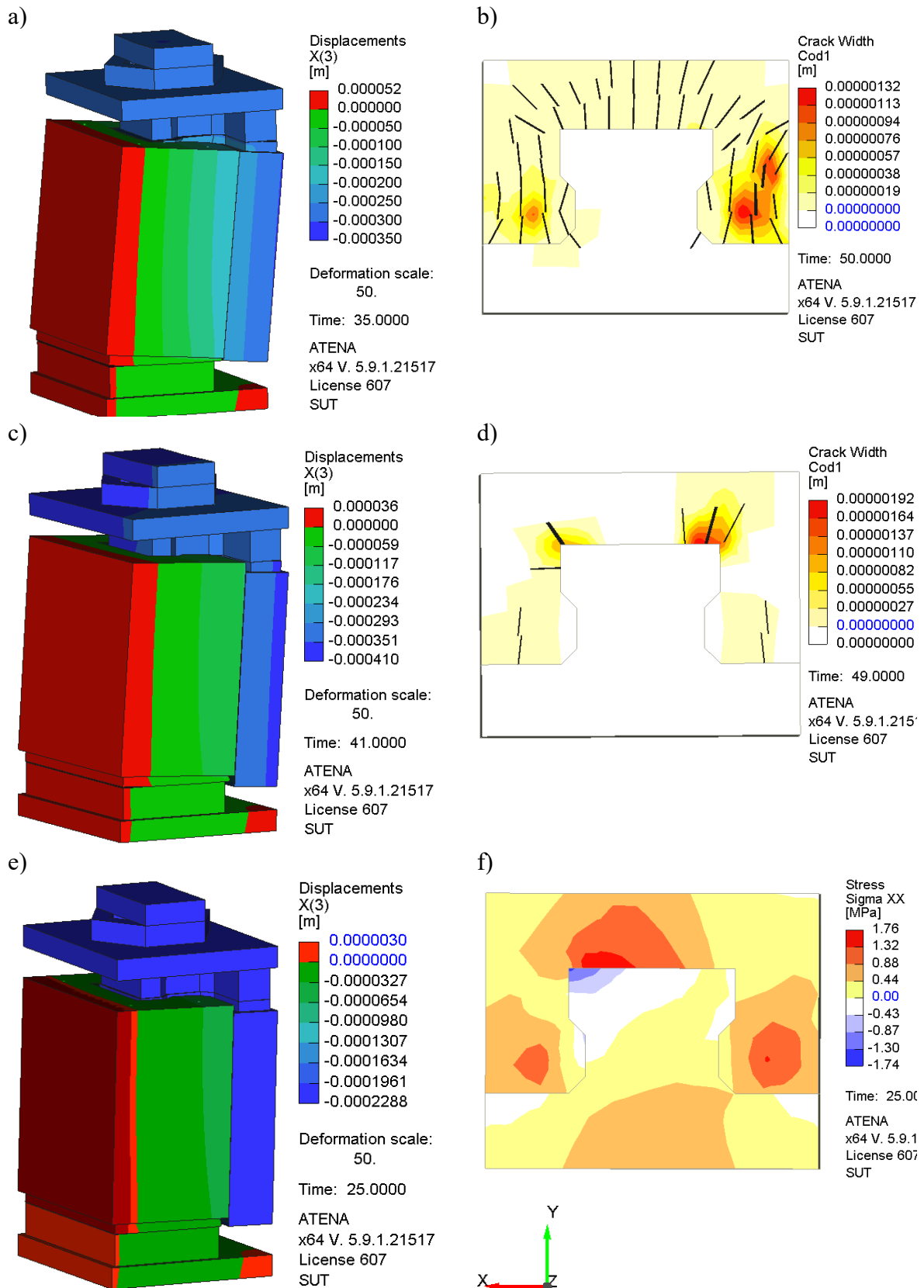


Fig. 7.15. Comparison of global deformation view (a, c, e) and scratch image (b, d) or tensile stress (f) for models: a-b) Z1_C, c-d) Z2_AB, e-f) Z3_CB

Rys. 7.15. Porównanie globalnego widoku deformacji (a, c, e) i obrazu zarysowań (b, d) lub naprężeń rozciągających (f) dla modeli: a-b) Z1_C, c-d) Z2_AB, e-f) Z3_CB

7.3.5. Influence of force eccentricity

The effect of the force eccentricity on the results of the FEM models was verified. The eccentric was modelled as a shift of the force application point to the centre of gravity axis of the composite section. The eccentric was considered on the X and Y axes as described in Fig. 7.16. The considered were an eccentricity of 5 mm, 10 mm and two configurations combining an eccentricity on the X and Y axes of 10 mm.

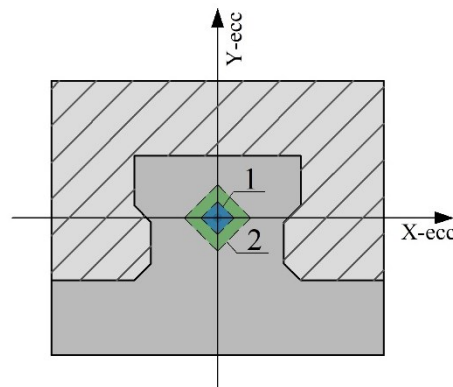


Fig. 7.16. Assignment of the axis and eccentricity of force relative to the model cross-section:
1- 5 mm eccentricity, 2- 10 mm eccentricity

Rys. 7.16. Opis osi oraz mimośrodów przyłożenia siły względem przekroju modelu: 1- mimośród 5 mm, 2- mimośród 10 mm

The results of the simulations are summarised in Table 7.12, where the maximum force, residual force, slip, and stiffness are compared, and the failure model is assigned. All model variants suffered Type I failure due to slippage at the interface. Eccentricity to the Y-axis of the model increased the maximum force value (Fig. 7.17) and decreased residual force. As the eccentricity on the Y-axis increased, the stiffness of the composite decreased. The complete opposite occurred for models with an eccentricity on the X-axis, where an increase in the eccentricity results in a decrease in the maximum force relative to the reference model. However, this decrease was associated with an increase in the stiffness of the composite.

For none of the modelled eccentric variants could type II damage be obtained, as in the two tested elements from the Z1_C series. In addition, two models, including an eccentricity of 10 mm in both the X and Y axes, were verified. For the models, twice the difference in the stiffness of the composite as measured for the selected points was obtained, with a 4% difference in the maximum force. As the eccentricity increased, an increase in crack opening was observed, with the same pattern as in the reference model. Again, there was no outward pushing of the concrete topping relative to the precast unit of the magnitude recorded in the experimental studies.

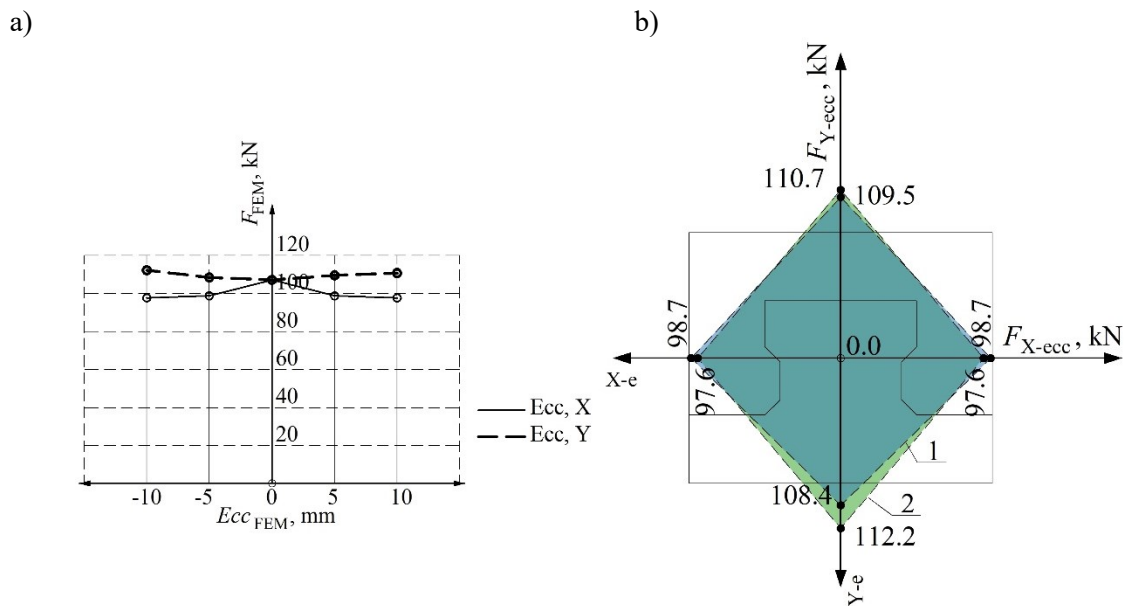


Fig. 7.17. Summary of model results with load eccentricity: a) force-eccentricity diagram, b) value of forces with relation to the eccentricity and model cross-section
 Rys. 7.17. Zestawienie wyników modeli z mimośrodem przyłożenia obciążenia: a) wykres siła-mimośród, b) rozkład sił względem przekroju modelu i mimośrodu

Table 7.12

Summary of failure type and cracking forces of eccentricity models

Zestawienie typów zniszczenia i sił rysujących modeli z mimośrodem obciążenia

Element (eccentricity in mm)	Peak load F_{max} , kN	Residual load F_{Res} , kN	Slip at F_{max} S_{max} , mm	Stiffness F_{max} $K_{100\%}$, kN/mm	Failure type
Z1_X0Y5	109.5	1.3	0.065	1694	I
Z1_X0Y-5	108.4	1.1	0.086	1256	I
Z1_X0Y10	110.7	0.5	0.108	1023	I
Z1_X0Y-10	112.2	0.7	0.105	1074	I
Z1_X+/-5Y0	98.7	1.5	0.064	1547	I
Z1_X+/-10Y0	97.6	1.8	0.057	1706	I
Z1_X10Y10	97.1	1.6	0.046	2118	I
Z1_X-10Y-10	93.2	1.4	0.085	1093	I

7.3.6. Conclusions from FEM models of direct shear test

Based on the presented results of the FEM model of the direct shear test, it is possible to present some conclusions and points for further analysis:

- In the FEM models of the Z1_C series, it is possible to distinguish only two behave phases (phase I and phase III - from the experimental study), rather than

three phases as in the tests. The models were subjected to brittle interface failure without a significant weakening phase (phase II - residual).

- Models with lower interface stiffness are characterised by a uniform distribution of shear stresses and displacements along the length of the interface.
- Models of all types were characterised by some non-linearity of the interface stiffness in the Phase I slippage failure range but to a lesser extent than in the tests.
- FEM analyses confirmed the LDS and DIC measurements indicating the occurrence of different values of interface displacement along its length within Phase I for the Z1_C series. This is related to the difference in stress distribution along the length of the interface.
- A very high convergence of the interface parameters in terms of stiffness and maximum force within the expected range determined by the Mohr-Coulomb theory could be correlated.
- The FEM models were characterised by only one type of failure, corresponding to slippage along the entire length of the interface.
- For none of the FEM models analysed, including those with an eccentric load application, there was no concrete topping outward displacement relative to the precast element of a value close to the tests.
- The numerical models fulfilled the objectives set in correlating the interface parameters, determining the dimension of the finite element mesh, the test's sensitivity to the load application's eccentricity, the deformation and cracking pattern, and the types of failure (for most elements).

7.4. Numerical models of selected 4PBT beams

Five elements from the four-point bending test were selected for FEM models, and these are beam types: Z1_C, Z2_AB, Z3_CB, Z5_S, and Z6_TB. The first three are the basic beam to verify the maximum force, the element with friction left and the element with reduced friction. The Z5_S model was chosen because the interface was only on the side surfaces, and the Z6_TB model had an interface only on the horizontal surfaces.

The supports and force application points were modelled as steel plates (Fig. 7.18a) connected by an interface with parameters as in Table 7.7. In Fig. 7.18b, the concrete topping is described as 'ZERO' due to the need to include the staged construction of the elements in the model. Due to the logic of the software, it is not possible to add more elements at a later stage of the calculation, therefore the concrete topping was modelled

as 'ZERO' material. The 'ZERO' material is only used to properly prestress the precast element without affecting the topping. That material has almost zero stiffness (0.01 kPa due to numerical purpose).

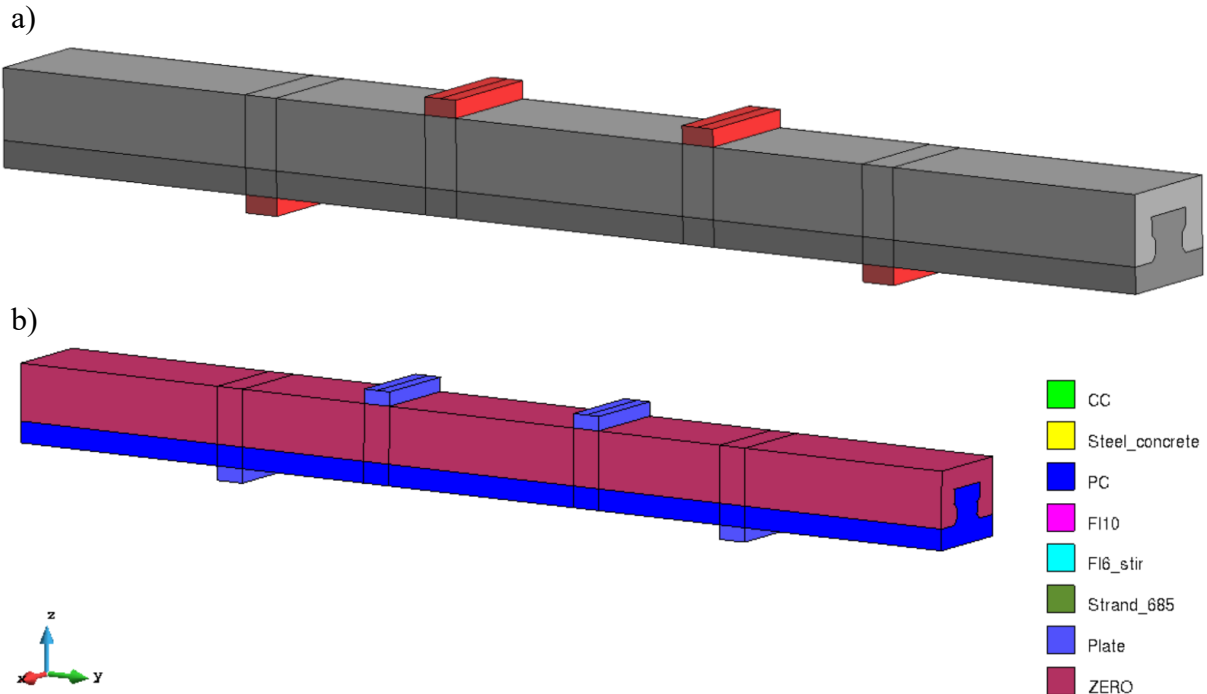


Fig. 7.18. Construction of the 4PBT numerical model: a) overall view with breakdown by elements, b) view with breakdown by materials

Rys. 7.18. Budowa modelu numerycznego 4PBT: a) widok ogólny z podziałem na elementy, b) widok z podziałem na materiały

Staging of FEM model calculations:

1. Compression of the precast element due to imposed initial strains to the strands.
2. Replacement of the concrete topping material from 'ZERO' to the correct parameters according to Table 7.2. Resetting of the strain state in the topping. Activation of reinforcement in the concrete topping.
3. Control of the applied force by displacement set linearly on the upper plates. A displacement of 1 mm divided into 50 calculation steps was set during the entire step. The purpose of dividing it into 50 steps is to determine the flexural cracking force precisely. That allows the convergence of the solution in the steps associated with the appearance of the first cracks and the decrease in stiffness of the model.
4. Further, a displacement of 30 mm was divided into 200 calculation steps.

The Modified Newton-Rapson method with a elastic predictor matrix to predict displacement increments from structural unbalanced forces was used to control the solution. MNRM was chosen because the number of finite elements was higher than in direct shear models. In elastic predictor stiffness matrix is assembled only once at the beginning of the step. The iteration limit was set to 300 with the line-search without iteration method. The solver parameters set in this manner allowed the solution time to be optimised due to the reduced number of stiffness matrix recalculations. If no match is obtained for a given step, the solver repeats the solution of the step, reducing the displacement increment by 50%. The PARDISO solver was used with a maximum permissible error rate set at 1%, which aligns with the ATENA software's general recommendations. All solver setup parameters are shown in Table 7.13.

Table 7.13
Properties of solver
Parametry solvera

Parameter	Method/Value
Method	Modified Newton-Raphson
Displacement, Residual and Absolute Residual	0.01
Energy error	0.0001
Negligible size relative	0.00001
Iteration limit	300
Iteration process	Line-search without iterations
Optimize bandwidth	Sloan
Stiffness type	Elastic Predictor (each step)
Solver	PARDISO
Step size	0.02 mm (phase 3) 0.15 mm (phase 4)
Step load reduction allowance	1
Reduce step load coefficient	0.5

The finite element mesh was made as shown in the direct shear models four-node elements with a size of 15 mm. In the zones beyond the support edges (anchorage zones), a mesh with a side ratio of 2:1 (30 mm by 15 mm) was modelled to optimise the number of finite elements (Fig. 7.19). As illustrated further in (7.5), increasing the size of the finite element mesh in the anchorage direction does not affect the resolution value of the task.

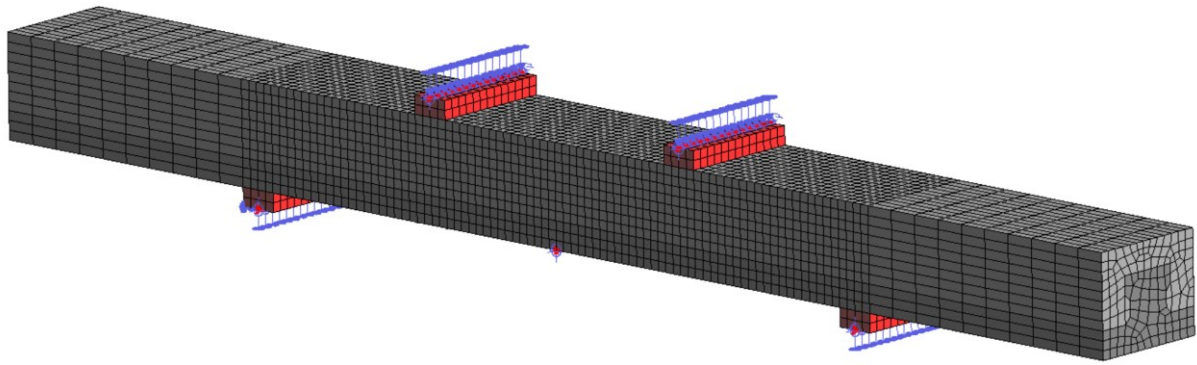


Fig. 7.19. View of the finite element mesh and boundary conditions of the model
 Rys. 7.19. Widok siatki elementów skończonych oraz warunków brzegowych modelu

Based on the provisional Z1_C model, the compression force values were correlated. Compression was set as the initial strain of the strands, and it was applied in stage I. The calibrated strain value was -0.0042 for each of the four prestressing strands. The prestressing force determined in this manner allows the flexural cracking force to be correlated at 98% convergence with the Z1.1_C beam test. The specified prestressing results in a maximum compressive stress of 6.47 MPa at the centre of the beam span, and the dispersion length is slightly greater than the distance of the support from the edge of the beam (Fig. 7.20a). As a result of compression, the FEM model flexes upwards by 0.55 mm (Fig. 7.20b). This is a smaller value than that measured after laying concrete topping (Section 5.1.3). The FEM model does not include the stiffness of the concrete when the tension is released and the effects of creep, increasing upward displacement.

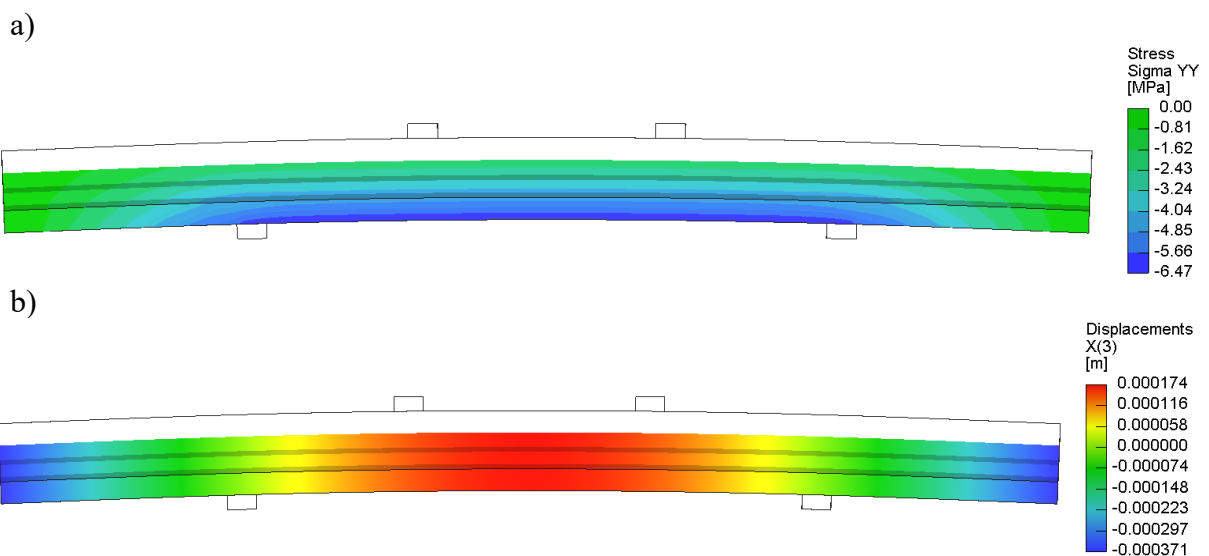


Fig. 7.20. Precast model precast after stage I (prestressing): a) stress, b) deformation
 Rys. 7.20. Model prefabrykatu po etapie I (sprężenie): a) naprężenia, b) deformacje

The analysis of the models in the following subsections is presented for a selection of the five main computational steps defined as:

1. Before flexural cracking development
2. In the flexural cracking development stage
3. At peak load
4. Before failure or slippage of the interface from force point to model face
5. After failure or slippage of the interface from force point to model face

Detailed results of all main parameters are presented for model Z1_C. The results of other models were limited to the issues relevant to the analysis and the objectives of the FEM calculations. An image of cracks with a width greater than or equal to 0.005 mm was drawn for the individual stress maps.

7.5. Results of the 4PBT FEM models

The description of the modelling results as in the previous sections is divided into two groups, the first group consisting of the basic models Z1_C, Z2_AB and Z3_CB and the second group of models Z5_S, Z6_TB.

7.5.1. Force-displacement characteristics

Results for group I

The numerical model of beam Z1_C shows a very good correlation between the experimental tests (Fig. 7.21). The values obtained for the flexural cracks force, diagonal cracks force, and the peak load value differ by no more than 5% from the tests. A significant difference of almost 60% was obtained for the initial stiffness (Fig. 7.21b). This difference decreases with increasing displacement and the development of flexural cracking. This is because of the difference between the actual (variable) and assumed axis of rotation of the beam on the support. This phenomenon is explained in Section 6.5. The numerical model Z1_C was cracked with a small width (<0.005 mm) at a force of 67.1 kN, and a decrease in stiffness occurred at a load of 71.7 kN.

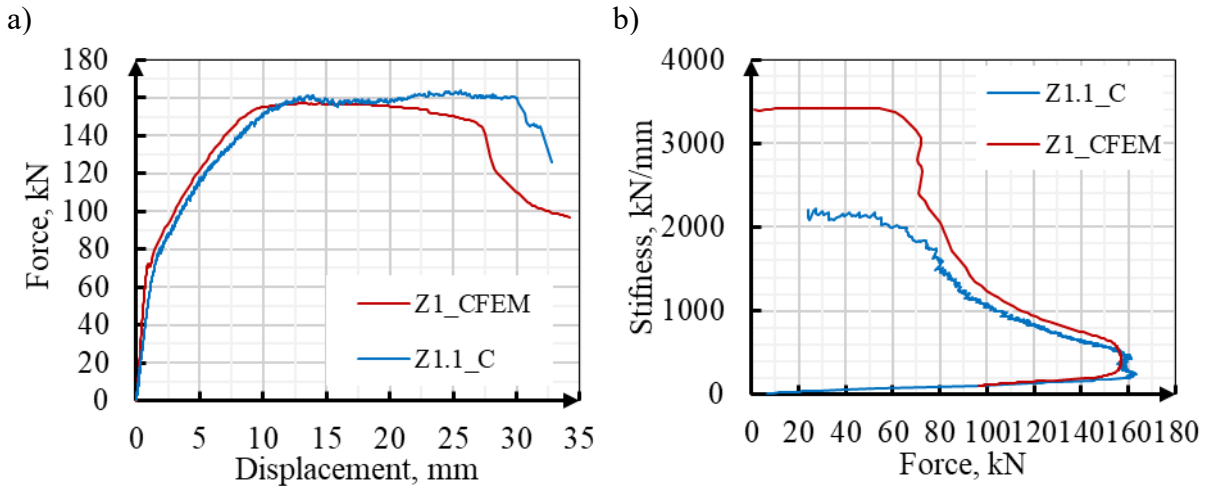


Fig. 7.21. Comparison of test and FEM results for Z1_C type elements: a) force-displacement characteristics, b) flexural stiffness

Rys. 7.21. Porównanie wyników analiz MES z badaniami dla elementów typu Z1_C: a) charakterystyka siła-przemieszczenie, b) sztywność giętna

The calculated force-displacement characteristics for the three models differ in both the initial stiffness and the value of the flexural cracking force (Fig. 7.22a), which is in line with the experimental tests. The numerical models Z2_AB (Fig. 7.22b) and Z3_CB (Fig. 7.22c) were stiffer than the tested beams. For the numerical models, only from the displacement diagram is it possible to determine the forces that crack the interface (slip). Such points represent the locations of the sudden force drop and the displacement increment. Models Z2_AB and Z3_CB significantly differed in stiffness (force versus displacement) for the range after the interface was cracked. This indicates the significance of the increased coefficient of friction for model Z2_AB.

For model Z2_AB, slippage was obtained in the interface up to the face of the element, which determines the value of the maximum force. This slip did not develop during the experimental tests. The value of the force that cracks the interface up to the axis of the support edge is very close at 142.0 kN compared to 144.3 kN for the tests. The development of a crack in the edge of the support resulted in a noticeable decrease in force and an increase in displacement. Cracking on the supports edge occurred for one of the supports at a force of 144.3 kN and a displacement of ~13 mm and for the other at a force of 131.2 kN and a displacement of ~22 mm. In both cases, there was a brittle decrease in force and an increase in displacement. The development for the first diagonal cracking in the concrete topping occurred at a force of 108.0 kN, which is 23.2 kN less than in beam Z2.1_AB.

The Z3_CB model was the only one characterised by the development of the first flexural cracks in the concrete topping (52.9 kN) before the precast cracking (58.7 kN).

The difference between the tests for flexural cracking was only 3.5%. Also, very good compliance was obtained for the cracking force at the interface in the support axis, where the difference was only 2.7%. The occurrence of a crack in the support axis did not result in a significant decrease in stiffness. It is not possible to separate the influence of local interface cracking from that of flexural cracking due to the occurrence of similar force values (Table 7.14). Slippage at the element face (121.1 kN) developed almost twice the test force (67.1 kN). Along with full-length slippage, there was a decrease in force and an increase in displacement.

Overall, all models achieved 95% convergence with the experimental tests in peak load. Models Z1_C and Z2_AB achieved a maximum force value lower than the tested beams, and model Z3_CB slightly higher than the tests. Type I failure was obtained for each element, which was consistent with the image obtained from the DIC analysis. A summary of the most important values for the characteristic points of the FE models is collected and compared with the experimental tests in Table 7.14.

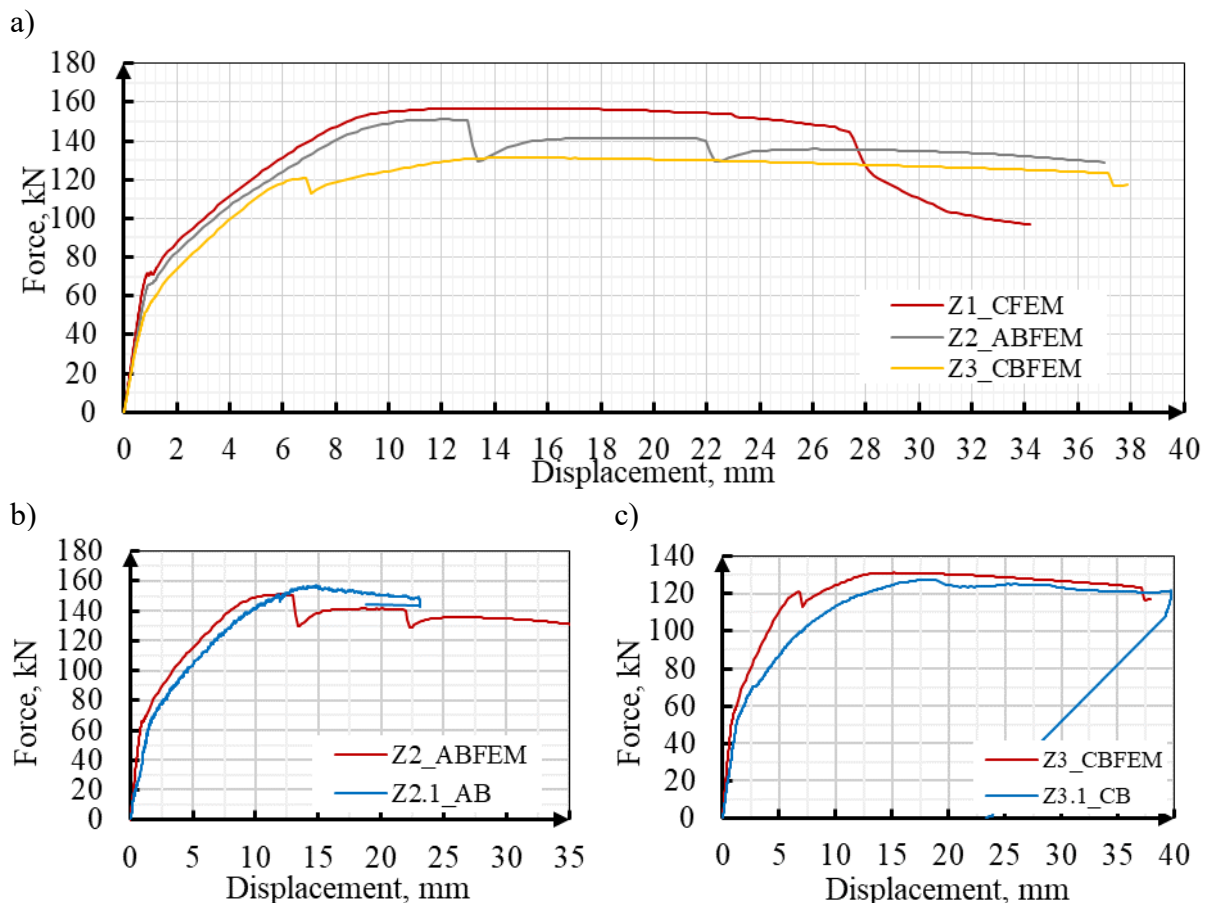


Fig. 7.22. Comparison of test and FEM results for Z1_C, Z2_AB, Z3_CB elements: a) force-displacement characteristic, b) Z2_AB model, c) Z3_CB model,

Rys. 7.22. Porównanie wyników badań z obliczeniami MES dla elementów Z1_C, Z2_AB oraz Z3_CB: a) charakterystyka siła-przemieszczenie, b) model Z2_AB, c) model Z3_CB

Table 7.14

Summary of failure type and cracking forces of models and test elements
Zestawienie typów zniszczenia i sił rysujących dla modeli i elementów badawczych

Element	Flexural crack F_{cr} , kN	Interface slip at support $V_{R,1,cr}$, kN	Interface slip at face $V_{R,2,cr}$, kN	Diagonal crack $V_{R,c}$, kN	Peak load F_{max} , kN	Failure type
Z1.1_C	67.1	-	-	130.2	163.6	I
Z1_CFEM	71.7	-	-	122.7	156.9	I
Z2.1_AB	63.5	144.3	-	131.2	157.3	I
Z2_ABFEM	65.1	142.0	151.1	108.0	151.1	I
Z3.1_CB	51.1	57.9	67.1	97.8	127.7	I
Z3_CBFEM	52.9 (Topping) 58.7 (PC)	56.4	121.1	100.9	131.2	I

Based on the Z1_C beam, a detailed description of the element's behaviour with increasing applied force was carried out. For this purpose, stress maps in the longitudinal direction of the beam were used, together with a visual display of the cracking. The beams are shown in axonometry at twice the deformation scale.

In Figure 7.23a, the beam is shown before cracking. The concrete topping had a compressive stress of 12.6 MPa and a tensile stress of 3.30 MPa, while the precast concrete had a tensile stress of 4.34 MPa. Above the support axis, there are negligible (<0.2 MPa) tensile stresses in the concrete topping. Once the flexural cracking force is exceeded (Fig. 7.23b), a local increase in compressive stresses can be observed directly above the cracks. After diagonal cracking (Fig. 7.23c - image at peak load), the extent of the concrete topping tensile zone was reduced to the area defined by the two diagonal cracks. Despite the lack of slippage of the interface in the topping section between the support and the diagonal cracks, there are no tensile stresses. Between the load application points, the compressive stresses on the concrete topping reach 42.1 MPa, with stress increasing directly under the plates. The flexural cracks intersecting the precast and the concrete topping coincide in position in the range of cracks with the largest width. Between these cracks, there are smaller cracks only in the concrete topping at half the distance between the cracks of the precast unit. After failure, horizontal cracks above the flexural cracks with the largest width indicate crushing of the concrete topping (Fig. 7.23d). There were no diagonal cracks in the precast unit crossing its bottom flange at any stage.

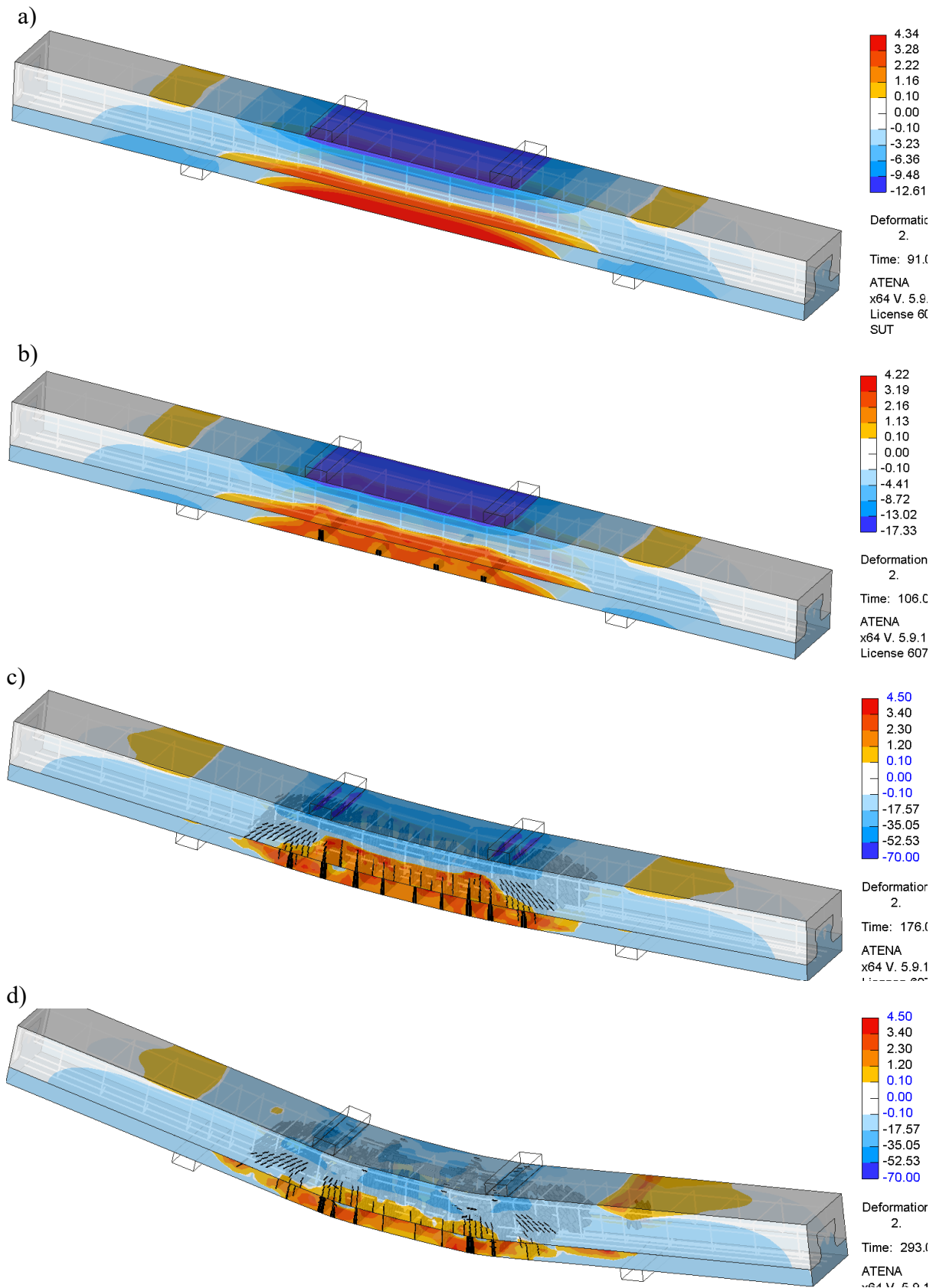


Fig. 7.23. Stress maps in the longitudinal direction of the model Z1_C with the image of cracks for a force: a) 65.1 kN, b) 71.7 kN, c) 156.9 kN, d) 96.3 kN (post-peak)

Rys. 7.23. Mapy naprężeń na kierunku podłużnym modelu Z1_C z obrazem zarysowań dla siły: a) 65.1 kN, b) 71.7 kN, c) 156.9 kN, d) 96.3 kN (po osiągnięciu siły maksymalnej)

The stress distributions of models Z2_AB and Z3_CB differed in particular with regard to the concrete topping relative to model Z1_C. Figures 7.24a, b shows the stress maps after peak load and cracking of the interface along the length from the point of load application to the axis of support. In both cases, there is no convergence of the flexural crack path between the precast and the concrete topping. Tensile stresses occur along the entire length of the concrete topping, and their extent at the height of the concrete topping is greater than that of model Z1_C (Fig. 7.23c). There are also more diagonal cracks in the concrete topping. However, the diagonal cracks remain without cutting through the bottom flange of the precast element.

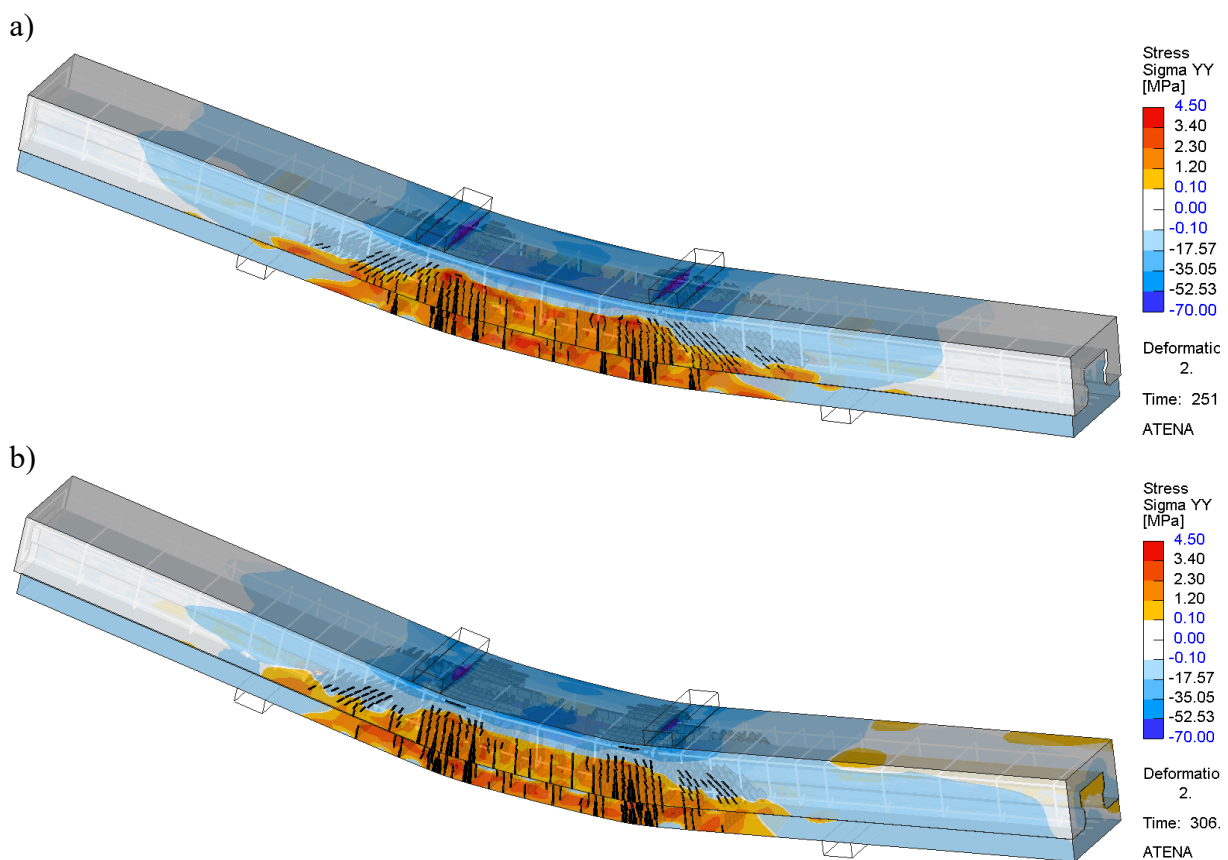


Fig. 7.24. Stress maps in the longitudinal direction of the beam with the image of cracks for a force: a) Z2_AB – 135.7 kN, b) Z3_CB – 123.3 kN

Rys. 7.24. Mapy naprężeń na kierunku podłużnym belki z obrazem zarysowań dla siły: a) Z2_AB – 135.7 kN, b) Z3_CB – 123.3 kN

The tangential stresses occurring in the precast unit prior to cracking (Fig. 7.25a) had a higher value than in the concrete topping (Fig. 7.25b). This is attributed to the higher stiffness of the precast. With the development of flexural cracking, the height of the shear stress zone decreased (Fig. 7.25c). This increases the stress values, resulting in diagonal cracking in the concrete topping (Fig. 7.24b). The highest concentration of shear stresses (Fig.

7.25d) occurred directly above the diagonal cracks (the border of the compression zone). After crushing the concrete topping, the shear stresses in the topping decreased. The highest concentration of shear stresses occurred in the precast at the section between the concrete topping diagonal cracks and the support edge (Fig. 7.25e). The calculations did not show the formation of a diagonal crack in the precast cutting up to the edge of the support. A similar behaviour of shear stress redistribution occurred in models Z2_AB and Z3_CB, for which no stress maps were presented.

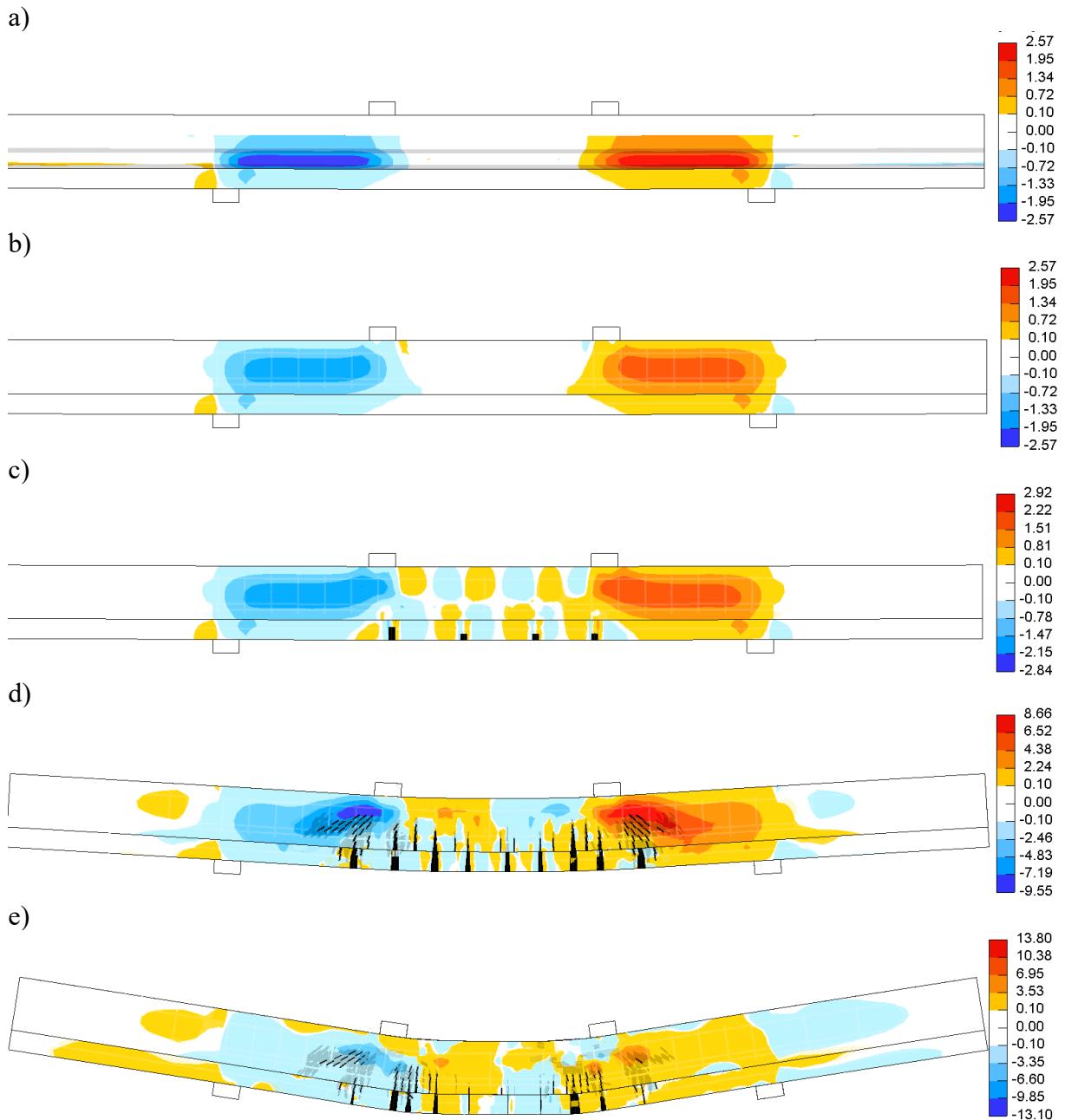


Fig. 7.25. Shear stress maps of the model Z1_C with the image of cracks for a load: a) 65.1 kN = precast, b) 65.1 kN - topping, c) 71.7 kN, d) 156.9 kN, e) 96.3 kN (post-peak)

Rys. 7.25. Mapy naprężeń stycznych modelu Z1_C z obrazem zarysowań dla siły: a) 65.1 kN - prefabrykat b) 65.1 kN - nadbeton, c) 71.7 kN, d) 156.9 kN, e) 96.3 kN (po osiągnięciu siły maksymalnej)

Results for group II

In the description of the results of Group II, only the most important aspects were included, without a detailed description as in the elements of Group I. The values obtained on the Z5_S model for the flexural cracking force and slip in the support axis have been close to the values from the test. However, the difference is in the maximum force values (Fig. 7.26a) and the interface cracking. The first value was as much as 23% lower and the second 27% lower. Along with the slippage in the support axis, a diagonal crack also occurred on the FEM model.

The results for the Z6_TB model differ significantly from the experimental tests due to the described anchorage problems in the Z6.1_TB beam. The values of the interface cracking force, the diagonal crack, and the maximum force converge with the results for model Z1_C. The difference is the occurrence of slippage at the interface, which already took place after the peak load was reached, with a displacement of 28 mm (Fig. 7.26b).

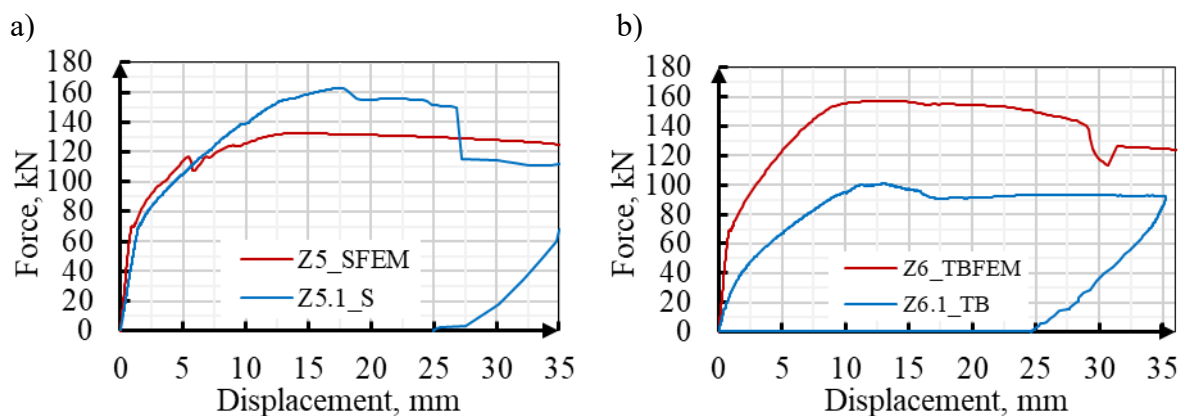


Fig. 7.26. Comparison of test and FEM results at force-displacement characteristics for models: a) type Z5_S, b) type Z6_TB

Rys. 7.26. Porównanie wyników analiz MES z badaniami dla charakterystyki siła-przemieszczenie dla modeli: a) typ Z5_S, b) typ Z6_TB

Analysing the curve in Fig. 7.27, the force-displacement characteristics after the cracking of model Z5_S were the same as those of model Z3_CB. The resulting stiffness was lower than that of model Z2_AB with friction on the horizontal surfaces. This clearly defines the effect of pressure from the applied point force on the performance of the interface resulting from the friction coefficient. As described in an earlier paragraph, the behaviour of model Z6_TB was consistent with model Z1_C. The difference occurs after the peak load is reached, and it is associated with a different failure model related to the slip to the support axis at the interface of model Z6_TB. All relevant load values

are included in Table 7.15, and the assigned failure models are described in subsection 7.5.3.

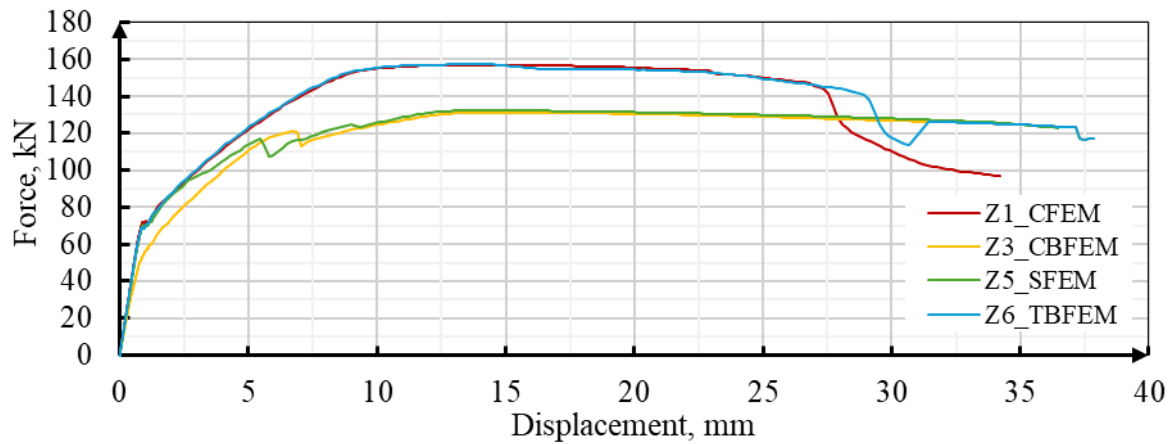


Fig. 7.27. Comparison of force-displacement characteristics for models Z1_CFEM, Z3_CBFEM, Z5_SFEM, Z6_TBFEM

Rys. 7.27. Porównanie charakterystyk siła-przemieszczenia dla modeli Z1_CFEM, Z3_CBFEM, Z5_SFEM, Z6_TBFEM

Table 7.15

Summary of failure type and cracking forces of models and test elements
Zestawienie typów zniszczenia i sił rysujących dla modeli i elementów badawczych

Element	Flexural crack F_{cr} , kN	Interface slip at support $V_{R,1,cr}$, kN	Interface slip at face $V_{R,2,cr}$, kN	Diagonal crack $V_{R,c}$, kN	Peak load F_{max} , kN	Failure type
Z5.1_S	70.7	88.7	149.6*	131.0	162.7	III
Z5_SFEM	70.2	98.4	117.0	98.4	132.3	III
Z6.1_TB	19.3	100.1	-	88.7	100.9	III
Z6_TBFEM	69.2	156.4*	-	130.4	157.1	III

*after peak load

7.5.2. Stresses and displacements at the interface

The development of local slip at the interface is related to the development and spread of flexural cracks in the Z1_C model. As the flexural cracking force is exceeded for model Z1_C, the first slip in the interface was recorded directly above the crack (Fig. 7.28a). As the number of cracks increases, flexural cracks are bridged by slippage (crack) at the interface (Fig. 7.28b) and slip also develops at the section height. The limit for the presence of slip at the interface of model Z1_C was determined by diagonal

cracks crossing the precast web and the concrete topping. These cracks, as described earlier, did not intersect the bottom flange, or reach the edge of the support. The maximum value of the local slip at the interface was 1.63 mm between two adjacent flexural cracks. Slip in the remaining areas ranged from 0.05 mm to 0.44 mm (Fig. 7.28c).

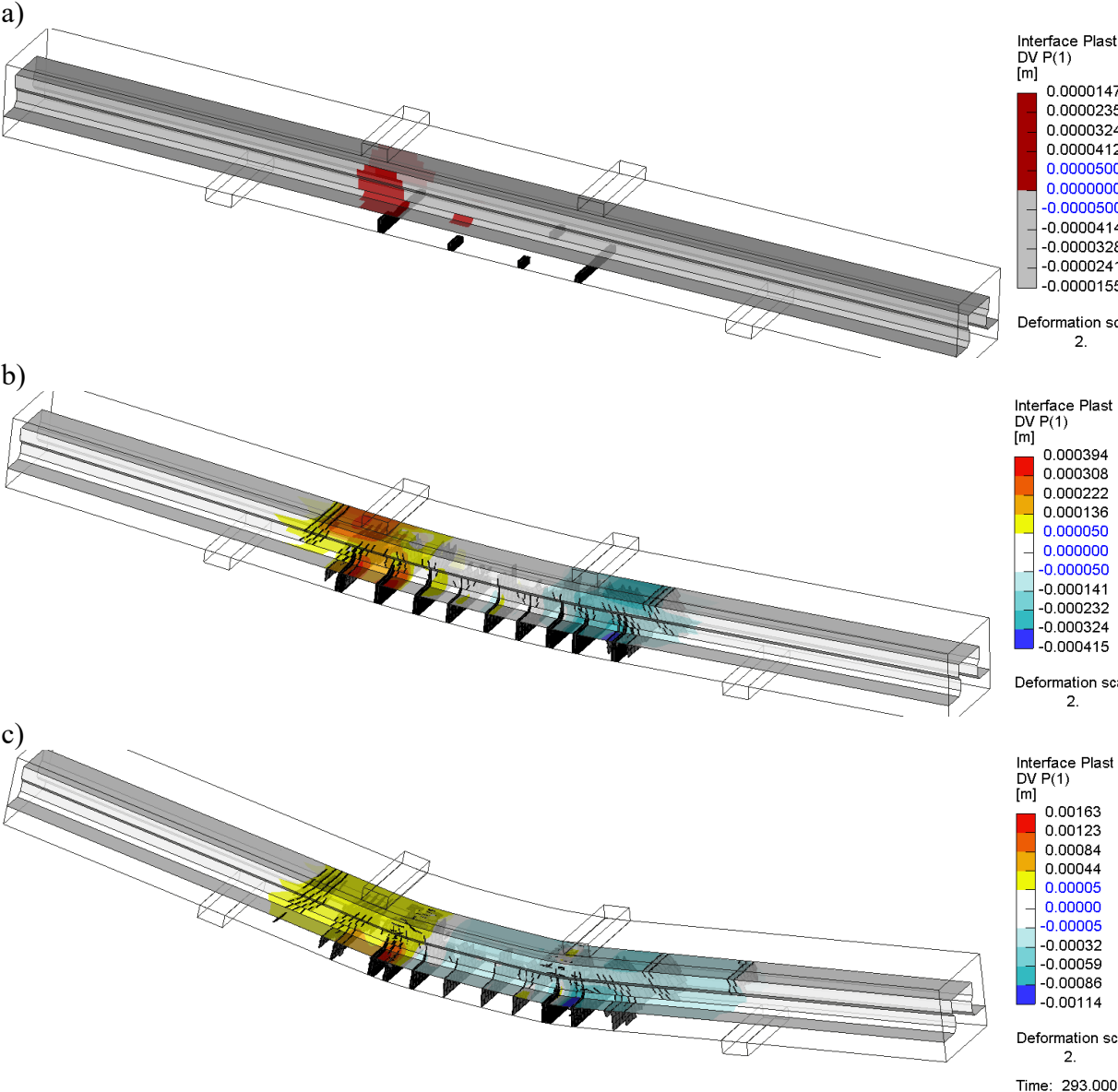


Fig. 7.28. Slip in the interface of the model Z1_C with the image of cracks for a load: a) 71.7 kN, b) 156.9 kN, c) 96.3 kN (post-peak)

Rys. 7.28. Mapy poślizgu w styku modelu Z1_C z obrazem zarysowań dla siły: a) 71.7 kN, b) 156.9 kN, c) 96.3 kN (po osiągnięciu siły maksymalnej)

The stress distribution at the interface was not uniform over the height of the section at any of the loading stages. There are higher stresses for the horizontal surfaces than vertical ones (Fig. 7.30a). This distribution is not consistent with the distribution of shear

stresses in the concrete topping and precast shown in Fig. 7.25a, b even before flexural cracking and local interface cracking just on the vertical surfaces. Before the flexural cracks developed, the stress distribution along the length between the point of force application and the support edge was uniform. This behaviour changed with the development of flexural cracks (local slip), which reduced the effective area of the bottom flange. At the maximum load, the effectiveness of the side surfaces was low. The maximum stresses at the rib side interface were less than 0.1 MPa (Fig. 7.30c). The effective area of the interface was limited by the presence of diagonal cracks (Fig. 7.30d). The highest stress concentration occurred on the horizontal surfaces near the edge of the support, which is related to the increased pressure due to the support reaction (Fig. 7.29).

For the given interface stiffness parameters, it is possible to determine the effective length of the interface cooperation, understood as the area effectively transmitting stresses. The length of this area and its displacement towards the beam end zone can be seen in Figure 7.30b-d. The effect of the beam length beyond the support axis on the interface of the precast unit was analysed using the simplified models and model Z1_C, with the concrete topping beyond the outer edge of the support plate deleted. The results for the additional model Z1_C are presented in Section 7.5.4.

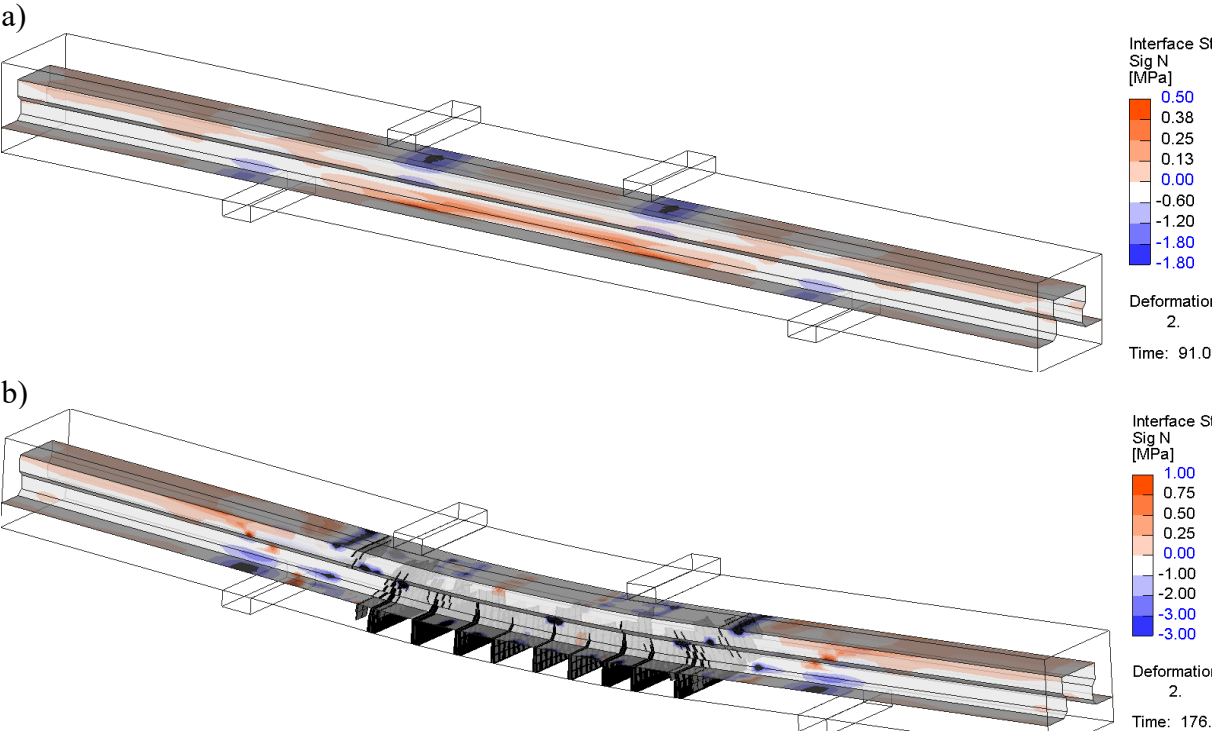


Fig. 7.29. Normal stress in the interface of model Z1_C for a force: a) 65.1 kN, b) 156.9 kN
 Rys. 7.29. Naprężenia normalne w styku modelu Z1_C dla siły: a) 65.1 kN, b) 156.9 kN

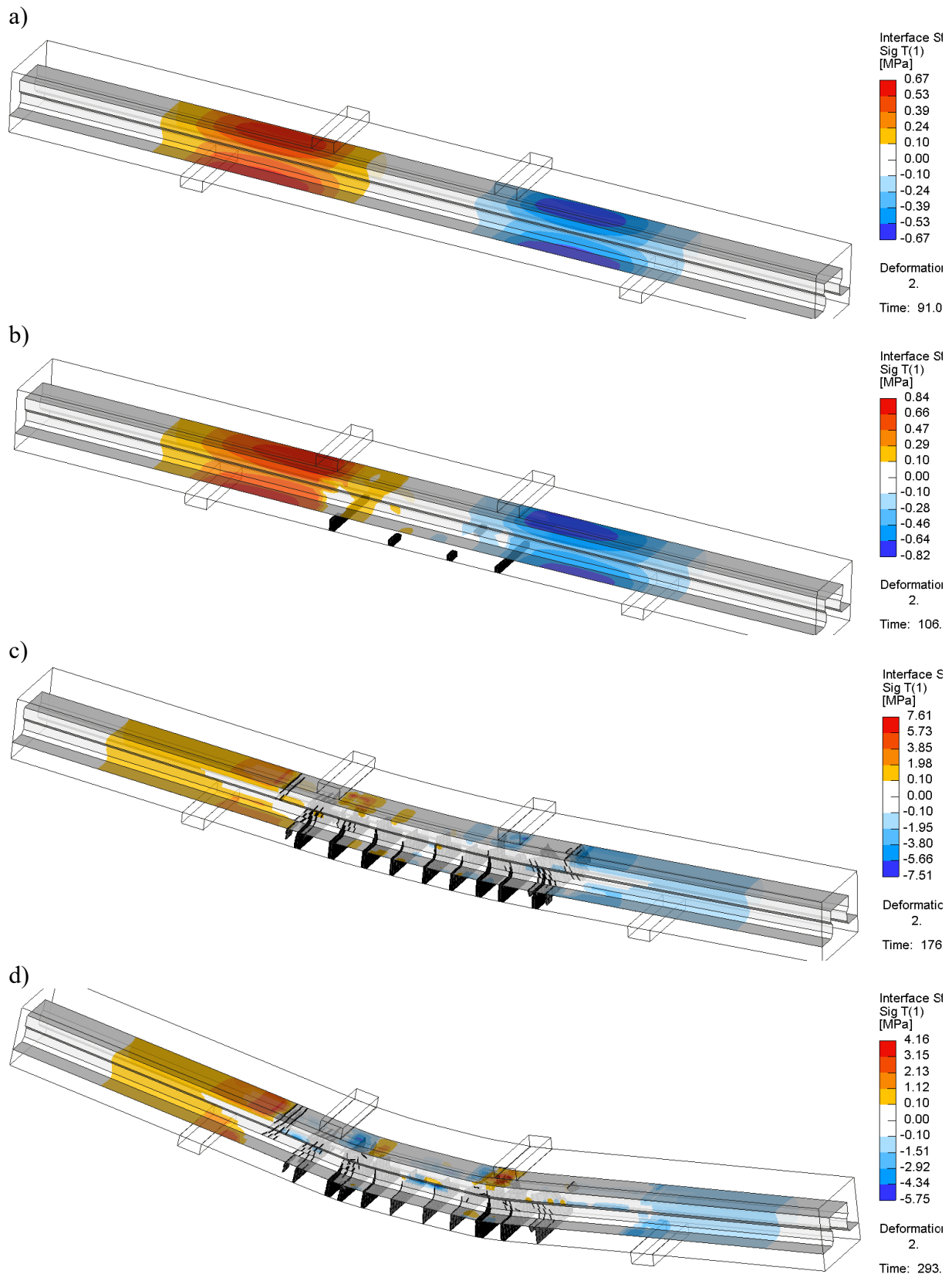


Fig. 7.30. Stress in the interface of the model Z1_C with the image of cracks for a load: a) 65.1 kN, b) 71.7 kN, c) 156.9 kN, d) 96.3 kN (post-peak)

Rys. 7.30. Naprężenia w styku modelu Z1_C z obrazem zarysowań dla siły o wartości: a) 65.1 kN, b) 71.7 kN, c) 156.9 kN, d) 96.3 kN (po osiągnięciu siły maksymalnej)

The described effect of the "anchoring zone of the interface" can be seen particularly for the Z2_AB model. Fig. 7.31a shows a map of shear stresses prior to the development of slip at the interface between the precast bottom flange and the concrete topping. Effective in transferring stresses are the horizontal zones at the pressure point from the reaction and the applied load. To a lesser extent, the horizontal zones from the edge of the support to the face of the element also transmit stresses. With the propagation of slip (plastic deformation of the interface), the pressure zones under the force and above the support and the section of the edge of the beam on the face side remain effective in transmitting stresses (Fig. 7.31b). Interestingly, the vertical surfaces of the rib also remain effective, while the horizontal surface becomes detached along most of its length. Once the peak load is exceeded (Fig. 7.31c), the only points for which it is possible to determine the stresses holding the interface are those immediately above the support and below the force, as a result of the effect of the force normal to the interface (pressure).

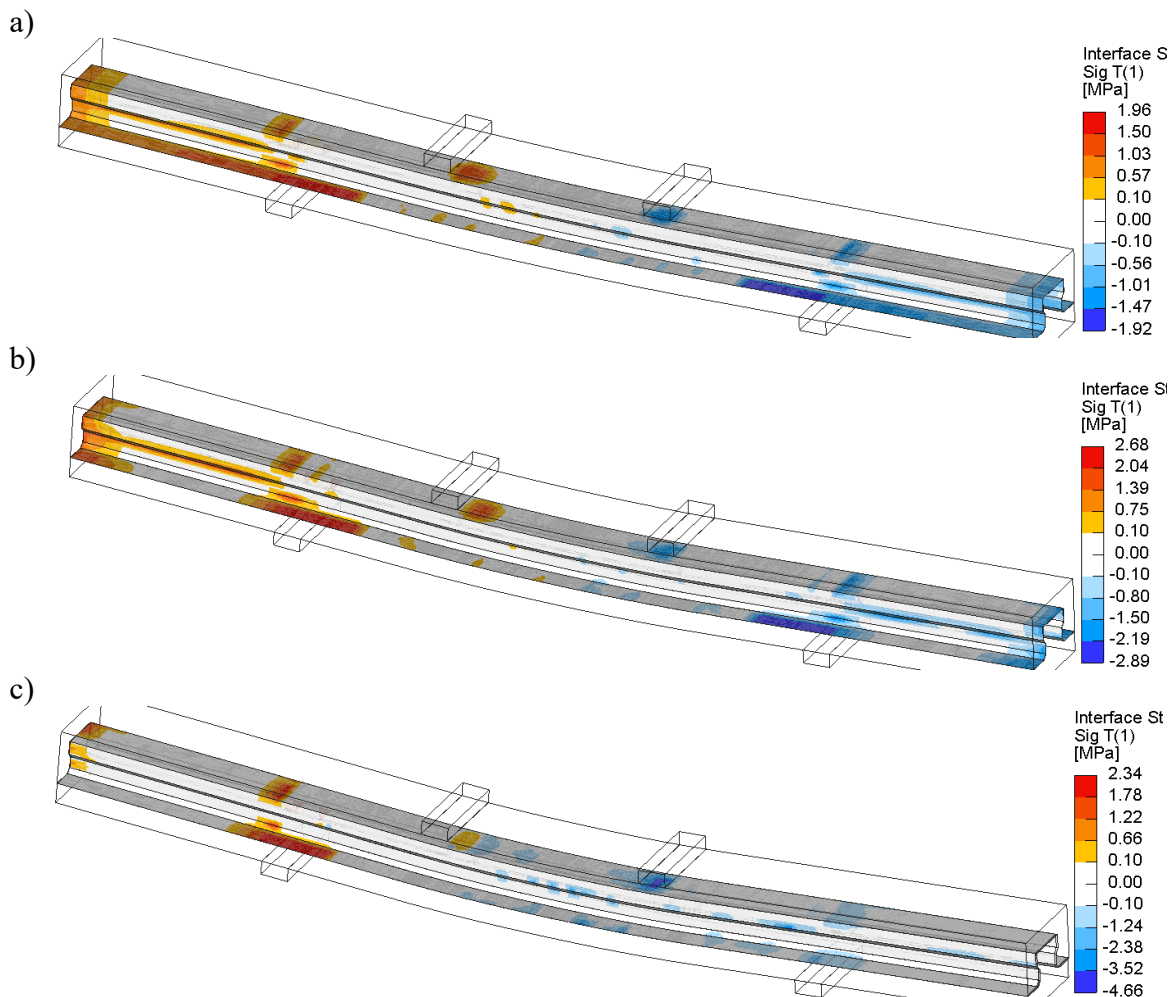


Fig. 7.31. Stress in the interface of the model Z2_AB: a) 139.4 kN, b) 150.8 kN, c) 135.4 kN (post-peak load)

Rys. 7.31. Naprężenia w styku modelu Z2_AB: a) 139.4 kN, b) 150.8 kN, c) 135.4 kN (po osiągnięciu siły maksymalnej)

7.5.3. Failure mechanism

Results for group I

The failure mechanism of the FEM models and the tested beam was similar. As the peak load was reached and displacements increased, the compression zone was crushed (Fig. 7.32). The strain of the concrete in the compressed zone on the inside of the load transfer plate was more than 3.5%. The increase in displacement was related to the slippage of the strands in the anchorage, which reached a constant value over the entire distance from the point of load to the edge of the element. In the Z1_C model, this was 5 mm for the last calculation step. The stresses in the bottom strands were 1445 MPa (Fig. 7.33). A similar failure pattern occurred for models Z2_AB and Z3_CB but was preceded by slippage at the interface up to the leading edge of the element.

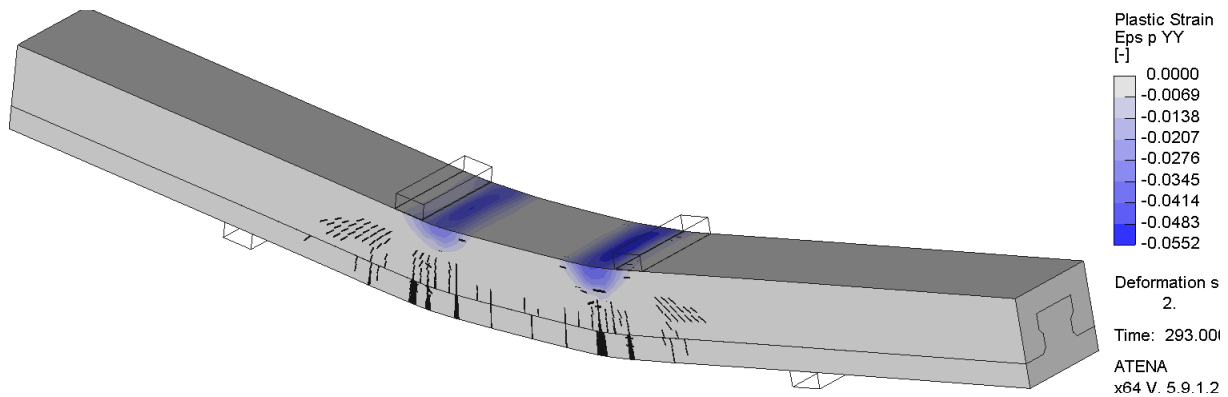


Fig. 7.32. Principal plastic strain of model Z1_C

Rys. 7.32. Główne naprężenia plastyczne dla modelu Z1_C

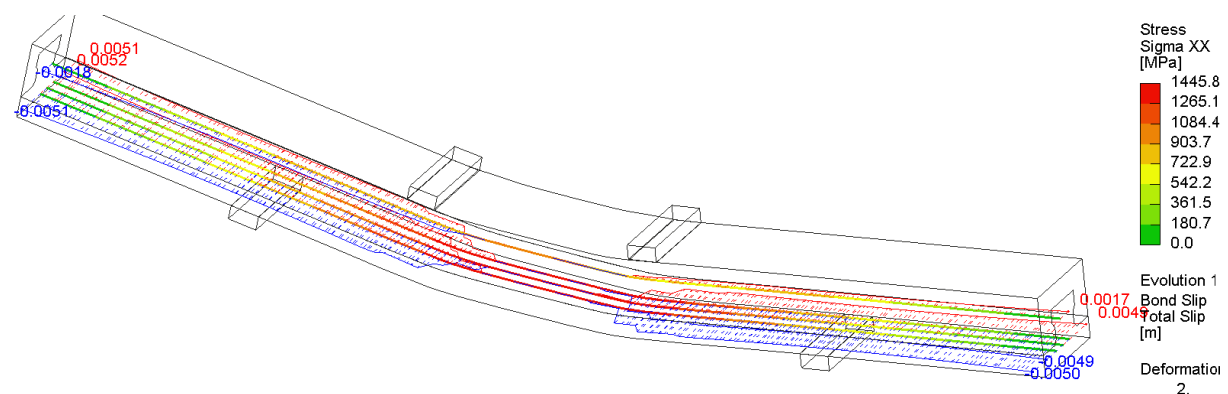


Fig. 7.33. Tensile stresses in strands and bond slip for model Z1_C

Rys. 7.33. Naprężenia rozciągające w splotach oraz poślizg zakotwienia dla modelu Z1_C

The crack pattern of the FEM models and the test elements was significantly convergence. The numerical model Z1_C fully represented the formation of a single flexural crack combined with a diagonal crack (Fig. 7.34). Single flexural cracks in the

zone between the force application points merged with cracks in the concrete topping, creating local areas of interface delamination. The location of the crack with the largest width converged for the model and the tested beam and occurred on the inner side relative to the force application point.

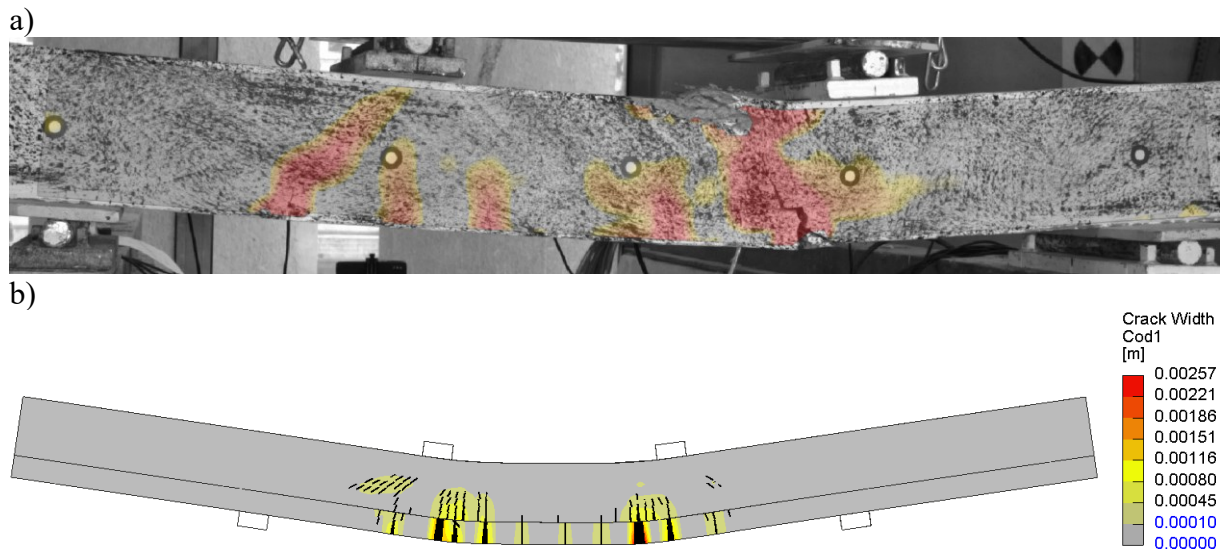


Fig. 7.34. Comparison of the failure image cracks for beam Z1.1_C (a) and model Z1_C (b)
 Rys. 7.34. Porównanie obrazu zarysowań po zniszczeniu dla belki Z1.1_C (a) i modelu Z1_C (b)

FEM model Z2_AB represented the formation of diagonal cracks directly at the outer edge of the load transfer plates (Fig. 7.35b). The concentration of flexural cracks in the concrete topping was higher than a of model Z1_C, which is consistent with the post-test view (Fig. 7.35a). The difference was the slip on both sides of the model up to its outer edges, compared to the slip on only one side of the beam in the test.

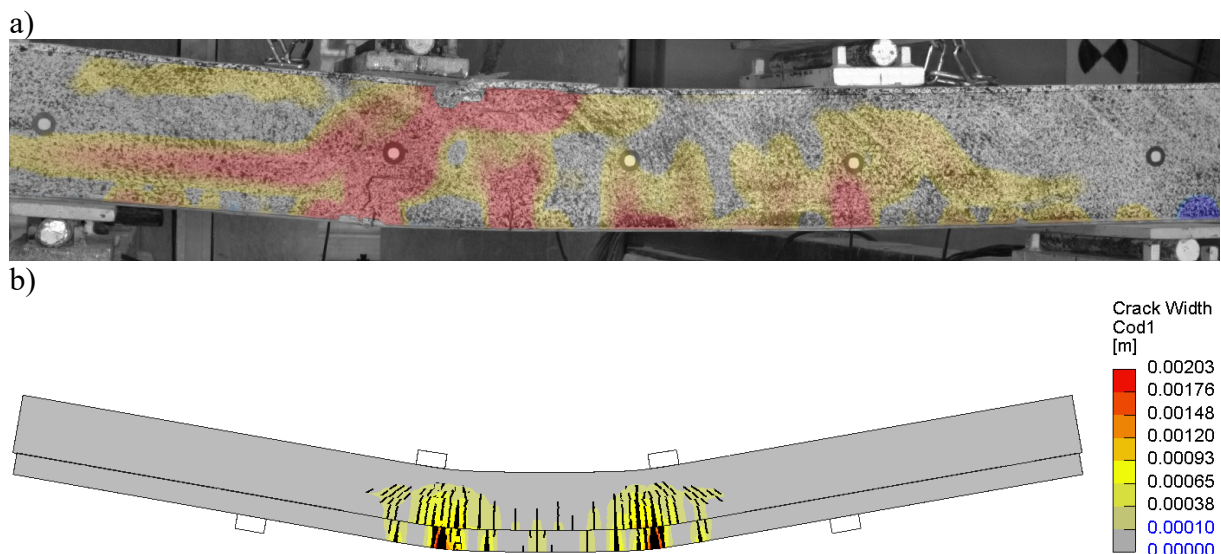


Fig. 7.35. Comparison of the failure image cracks for beam Z2.1_AB (a) and model Z2_AB (b)
 Rys. 7.35. Porównanie obrazu zarysowań po zniszczeniu dla belki Z2.1_AB (a) i modelu Z2_AB (b)

Significantly higher numbers of cracks in the precast element than in the tested beam Z3.1_CB were reached for the calculations of the FEM model Z3_CB. The number and course of concrete topping cracks was consistent with the FEM model. Once the cracking reached the compression zone, it was crushed, visible through horizontal cracks (Fig. 7.36b). In the numerical model, the concrete crushing occurred under both supports, whereas in the study, it only occurred under one (Fig. 7.36a). Slippage at the interface occurred as in the test on both sides of model Z1_C.

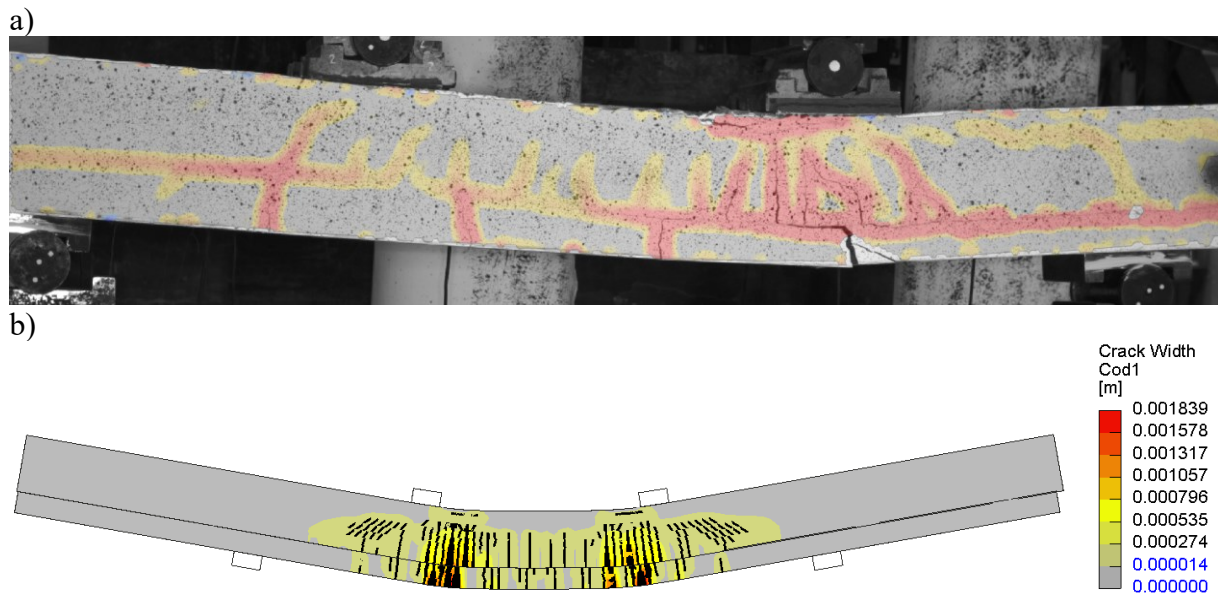


Fig. 7.36. Comparison of the failure image cracks for beam Z3.1_CB (a) and model Z3_CB (b)
Rys. 7.36. Porównanie obrazu zarysowań po zniszczeniu dla belki Z3.1_CB (a) i modelu Z3_CB (b)

Results for group II

As previously stated in Table 7.15, the failure mechanism of the Group II models was assigned to Type III failure. This is valid for both models Z5_S and Z6_TB despite the significantly different results of force and slip values, including the lack of slip of model Z6_TB up to the leading edge of the model. The Z5_S model represents to a satisfactory degree the numerous diagonal cracks (Fig. 7.37b) present on the tested Z5.1_S beam (Fig. 7.37a). The image of compression zone failure occurring on the inside of the applied load is also similar. The models were assigned a Type III failure due to slippage at the interface, which was combined with reaching the peak load and developing diagonal cracks.

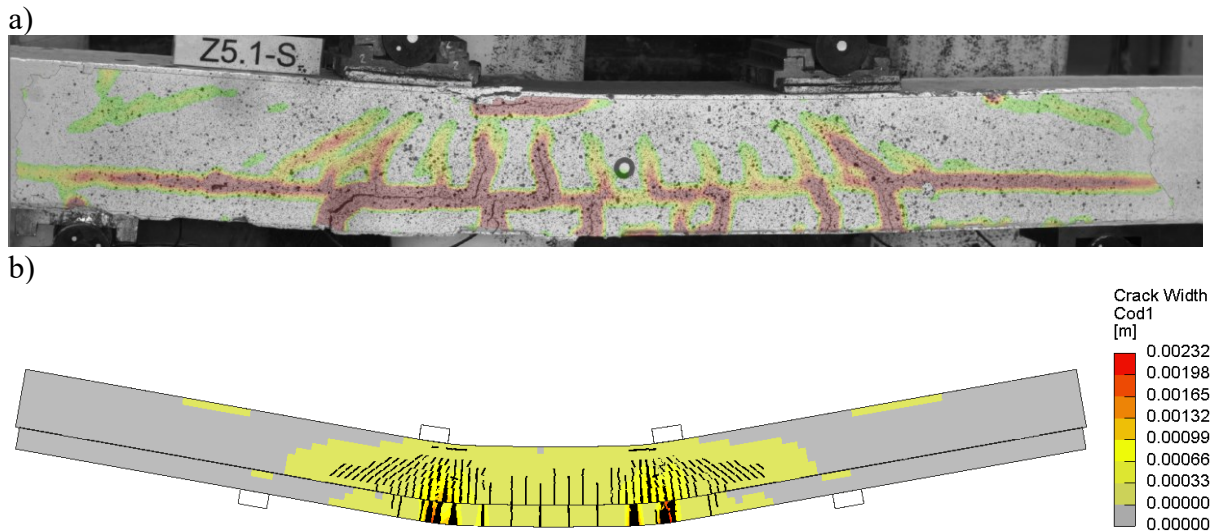


Fig. 7.37. Comparison of the failure image cracks for beam Z5.1_S (a) and model Z5_S (b)
 Rys. 7.37. Porównanie obrazu zarysowań po zniszczeniu dla belki Z5.1_S (a) i modelu Z5_S (b)

Despite the defect described in beam Z6.1_TB, its failure model is relatively similar to that of Z6_TB. In both, a dominant crack appears to be under the point of force application. Diagonal cracks propagate in the concrete topping, connecting to the interface. For the FEM model, the slip occurred on two sides and not on one side as in the tested beam. The failure picture for beam Z6.1_TB is justified by the early anchorage loss on one side (Fig. 7.38a). Despite the described very high convergence of the results for Z1_C and Z6_TB, the difference was a significant area covered by diagonal cracks (Fig. 7.38b), which was not the case in the fully composite beam (Fig. 7.32b). Type III failure was attributed to the numerous diagonal cracks connecting along the entire section length between the point of load application and the axis of support with an interface at the level of the bottom flange of the precast unit.

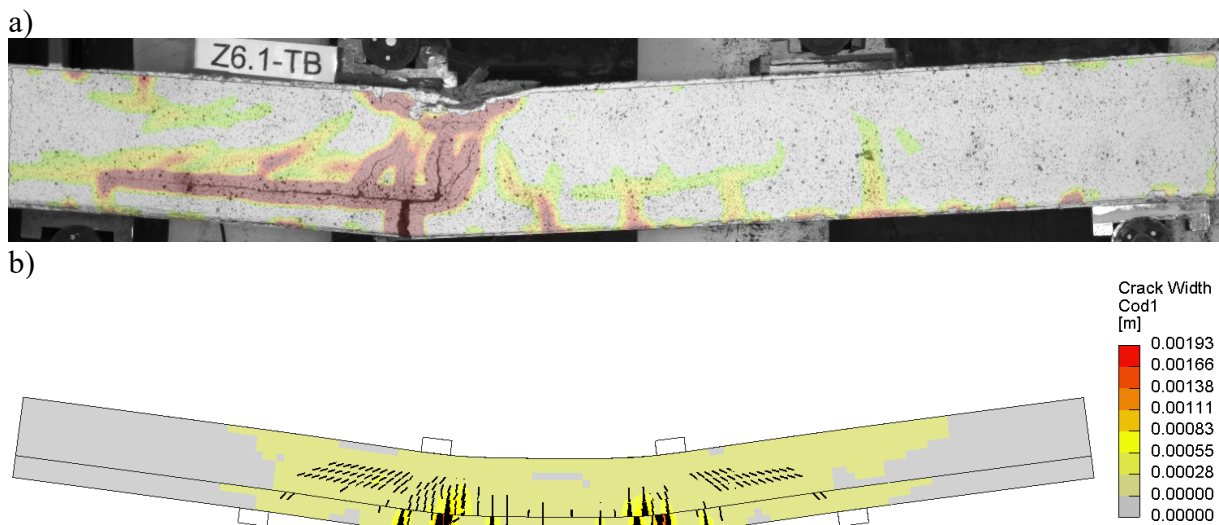


Fig. 7.38. Comparison of the failure image cracks for beam Z6.1_TB (a) and model Z6_TB (b)
 Rys. 7.38. Porównanie obrazu zarysowań po zniszczeniu dla belki Z6.1_TB (a) i modelu Z6_TB (b)

7.5.4. Analysis of supplementary models of type Z1_C

Following the FEM analyses presented, it was decided to make four additional models, divided into two groups. The first group will verify the influence of the applied load (local pressure) on the behaviour of the interface, and the second will verify the effective transmission of shear stresses through the element interface off the support axis. The first model was created with the same geometry as the basic model Z1_C, with only the friction coefficient parameter modified from 0.7 to 0.001, designated Z1_CFEM_u0.001. In order to verify the influence of the concrete topping interface beyond the support axis, an additional model was created, designated Z1_CFEM_Short. This model was created like the basic model Z1_C in terms of materials, the difference being the removal of the concrete topping from the off-axis zone of the support (Fig. 7.39). However, the extension of the precast was left in place, representing the length of the anchorage and the dispersion of the prestressing force.

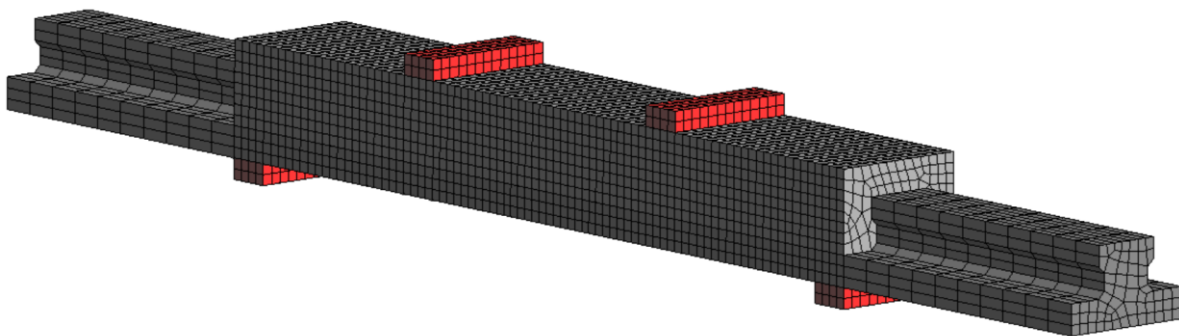


Fig. 7.39. View of the finite element mesh and boundary conditions of the “short” model
Rys. 7.39. Widok siatki elementów skończonych oraz warunków brzegowych modelu „skróconego”

The other two models were made to verify the effect of concrete topping deflecting outwards. These models can be seen as a preliminary to the development of a programme of further tests. At this stage, they were carried out on elements simulating integration in the slab. The models included lateral supports over the entire height and length of the topping to simulate, in a simplified way, the embedding of a beam in a slab in which the adjacent elements were the introduced lateral support. The third model was based on Z1_CFEM and designated Z1_CFEM_SC. The fourth model was based on an element with only the interface on the side surfaces Z5_SFEM and designated Z5_SFEM_SC. A view of the surface with additional side supports is shown in Fig. 7.40.

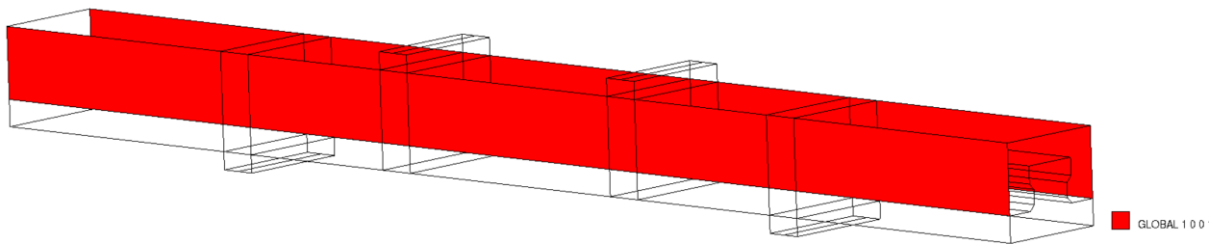


Fig. 7.40. Additional side supports (constraint) on models Z1_CFEM_SC and Z5_SFEM_SC
 Rys. 7.40. Dodatkowe podpory boczne na modelach Z1_CFEM_SC oraz Z5_SFEM_SC

The characteristics of the first two additional models remained consistent with the basic model in terms of crack force, diagonal crack, and maximum force. The main difference lay in slippage at the interface at high displacements. In the model with reduced friction, slippage was observed along the entire component length at a displacement of 18.5 mm. Once the adhesion between the precast and the concrete topping was broken, the model exhibited a brittle decrease in force and an increase in displacement, reaching a lower level than the Z2_ABFEM model (Fig. 7.41). Based on this failure model, it can be concluded that the roughness coefficient and the applied point load influence the interface's cracking, particularly in the high displacement range.

The failure scheme of the second model was more complex. At a displacement of 17 mm in model Z1_CFEM_Short (Fig. 7.41), interface slippage occurred up to the axis of the support on one side of the model. This was followed by a sudden drop in force. The model's stiffness from this stage was similar to the Z2_ABFEM model, for which there was only a slip on one side of the element. As the displacements increased, the interface slip also occurred on the other side of the element in model Z1_CFEM_Short. The above analysis clearly shows the influence of the interface of the element and the off-axis of the support on its behaviour, particularly after the maximum force is reached. The lack of “anchorage of the interface beyond the support axis” resulted in separating the precast element from the concrete topping, which was not the behaviour of the basic model. By comparing the failure type of the first model (Z1_CFEM_u0.001) and the second model (Z1_CFEM_Short), it is possible to conclude that the point application of the load (at a high friction coefficient) ensures a partial composite of the element even after the interface has been cracked.

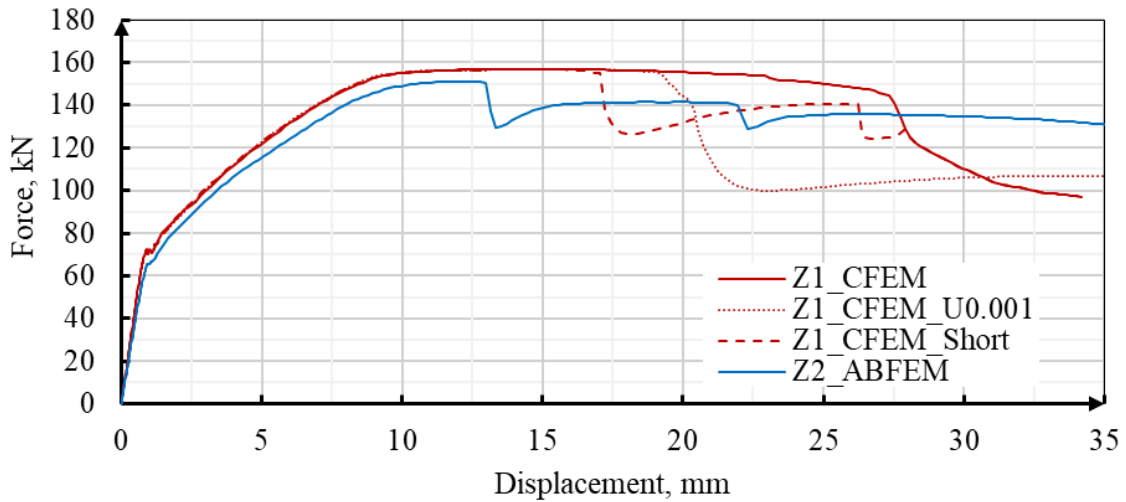


Fig. 7.41. Comparison of force-displacement characteristics for models Z1_CFEM, Z1_CFEM_u0.001, Z1_CFEM_Short and Z2_ABFEM

Rys. 7.41. Porównanie charakterystyk siła-przemieszczenia dla modeli Z1_CFEM, Z1_CFEM_u0.001, Z1_CFEM_Short oraz Z2_ABFEM

The models with added side support for the concrete topping had higher stiffness and maximum strength than the reference FEM models and beams from the experimental tests (Fig. 7.42). The main difference is the lack of interface slip in the Z5_SFEM_SC model relative to the Z5_SFEM model. Both models also had a high level of compliance with cracking in the concrete topping and precast. The highest stresses in the side supports were recorded in the middle of the height of the concrete topping section between the position of the force and the support. The results of the models with lateral supports are considered as a prelude to further research both experimentally and with FEM modelling. The models represent the potential and questions that can arise for vertical interfaces in elements that are part of a larger entity, such as a slab.

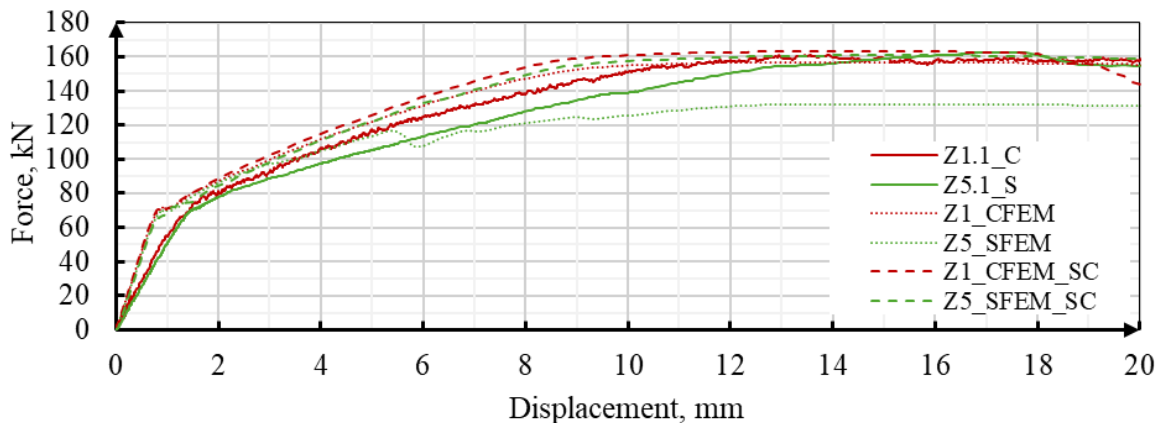


Fig. 7.42. Comparison of force-displacement characteristics for models without and with side support of concrete topping and experimental results

Rys. 7.42. Porównanie charakterystyk siła-przemieszczenia dla modeli bez oraz z podporą boczną nadbetonu i badaniami doświadczalnymi

7.5.5. Partial conclusions from the modelling of elements in the ZX.1 series

Based on the models in the ZX.1 series, the following conclusions can be drawn:

- The numerical model provides a very good representation of the behaviour of the fully composite element Z1.1_C, including force values and the cracking pattern.
- The modelled elements with correlated interface parameters enable the progressive failure character of the interface to be reproduced, including local cracking, slippage in the support axis and slippage to the face of the elements.
- Slippage of the interface to the support axis decreases stiffness, but the component remains partially composite due to the off-support length. Cracking the interface up to the face of the element is the point of failure of the composite element and a brittle decrease in the stiffness of the models.
- The lack of anchorage of the composite beyond the support axis decreases the force that slippage the interface along its entire length.
- Flexural and diagonal cracking affect the distribution of shear stresses in the models.
- Diagonal cracks limit the effective interface area, therefore the interface slip resistance decreases with increasing cracking.
- The beam model Z1.1_C showed a lack of effective cooperation of the vertical surfaces in transferring shear stresses at values close to the maximum force.
- Some of the vertical surfaces were subjected to normal tensile forces, which reduced the strength of the interface.
- The point application of force, combined with the roughness of the interface, provides a small partial bond after cracking the interface and affects the strength of the interface in the high displacement range.
- Despite correctly representing the cracking force and the interface slip in the support axis, the numerical model does not correctly represent the failure force for model Z5.1_S.
- For model Z5_SFEM_SC with constrained lateral strains in the concrete topping (outward displacement), a significantly higher maximum force was obtained with no slip at the interface relative to model Z5_SFEM and the experimental study (Z5.1_S). This model represents the potential for vertical interfaces in elements that are part of a larger whole, e.g. a slab.

7.6. Simplified 4PBT beam models

The basic numerical models reproduce the behaviour of the beams from the experimental tests to a very good convergence. The correlated interface characteristics for most of the models analysed provide a good representation of the development of local slip and the element's behaviour after the maximum force is reached. In these models, however, it was not always possible to separate the influences of the individual effects on the performance of the beam, understood as its stiffness and full slippage force of the interface. The additional models made in the Z1_C series partly allowed to identify the influence of some of the effects impacting the interface. However, simplified models were made to understand the influence of individual effects on the work of composite elements in detail.

The simplified models were made as beams with geometries like the basic models and with an interface of the type as in the basic models. Most models were based on the interface parameters, as in the Z1_CFEM model. The most crucial difference was replacing the concrete material model with a linear elastic model representing only stiffness and Poisson's ratio. This model is not subject to cracking or failure due to stress overrun. In this material model, the stiffness is the same in compression and tension. Fifteen simplified models were made, of which the first three belonged to one model group and the others were divided into a further three groups. The models in the first group were based on three geometries (Fig. 7.43a-c) designed to allow verification of the analysed features and behaviour of the interface. The others were based on the basic geometry (Fig. 7.43a). A brief description of the models and the groups assigned to them is given below:

Group I - models with the interface as for the basic model Z1_C:

1. Model 1 (ZS_1_C) - model with concrete topping and precast concrete modelled as a linearly elastic material. This model is intended to verify the maximum force cracking the interface.
2. Model 2 (ZS_2_C_Mesh) - a model with the same parameters as model 1 with a modified finite element mesh for the off-axis zone of the support (Fig. 7.43b). The model verifies the influence of the mesh dimensions in the anchorage zone on the obtained cracking force values. The model is intended to verify the correctness of the optimisation of the basic models in the ZX.1_FEM series.

3. Model 3 (ZS_3_C_Short) - a model in which sections of concrete topping and precast outside the support axis have been removed (Fig. 7.43c). The model is similar to the additional model Z1_CFEM_Short.

Group II - models with interface, such as the basic model Z1_C, with modification of selected individual contact parameters. Group II is an analysis of the effect of changing the interface parameters on the response of the model, the results for this group are mostly presented in tabular form only.

4. Model 4 (ZS_4_C_u0.001) - model in which the friction coefficient is reduced to a value of 0.001.
5. Model 5 (ZS_5_C_u1.0) - a model in which the friction coefficient is increased to a value of 1.0.
6. Model 6 (ZS_6_C_K_{NN}10⁴) - a model in which the normal stiffness is reduced to a value of 10⁴
7. Model 7 (ZS_7_C_K_{NN}10⁵) - model in which the normal stiffness is increased to 10⁵
8. Model 8 (ZS_8_C_K_{NN}2·10⁵) - model in which normal stiffness is increased to 2·10⁵
9. Model 9 (ZS_9_C_K_{TT}22.5) - a model in which the tangential stiffness is reduced twofold to 22.5 N/mm³
10. Model 10 (ZS_10_C_K_{TT}90), in which the tangential stiffness is doubled to 90 N/mm³

Group III - linear elastic models with modified interface parameters:

11. Model 11 (ZS_11_S) - model with interface as for beam type Z5_S
12. Model 12 (ZS_12_TB) - model with interface as for beam type Z6_TB. Models 11 and 12 verify the effect of the position of the interface on the interface cracking force.
13. Model 13 (ZS_13_AB) - a model in which the interface is defined as type Z2_AB. The model verifies the effect of roughness and stiffness of the interface after comparison with models 1 and 14.
14. Model 14 (ZS_14_CB) - a model in which the interface is defined as type Z3_CB, reproducing the applied mat to verify the influence of the roughness and stiffness of the composite.

Group IV - a group consisting of only one model with modified topping parameters:

15. Model 15 (ZS_15_CT) - model in which the concrete topping is modelled as in the basic models (allow cracking), including reinforcement and the precast element as a linear elastic model. The model aims to determine the effect of concrete topping cracking at, for example, a highly prestressed precast on the value of the interface cracking force. Due to the different material parameters, the model was assigned separately to the group.

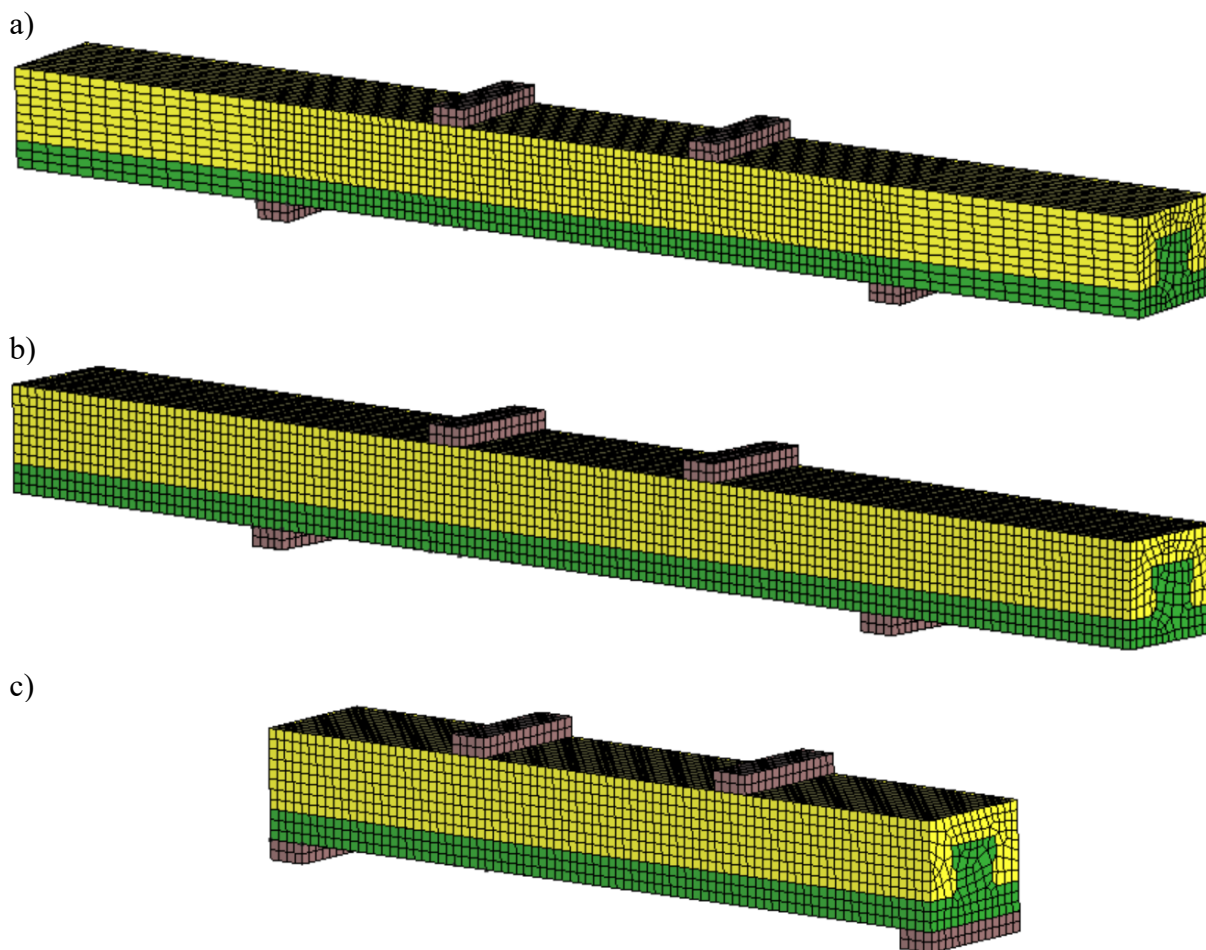


Fig. 7.43. View of the simplified numerical model: a) Model 1, 4-15, b) Model 2, c) Model 3
 Rys. 7.43. Widok uproszczonych modeli numerycznych: a) Model 1, 4-15, b) Model 2, c) Model 3

7.6.1. Results of Group I models

Comparison of the model with the mesh optimised in the edge zones (ZS_1) with the fully meshed model (ZS_2_Mesh) showed that the numerical model was not sensitive to mesh modification in the edge zone. The value of the cracking force and the displacement of the model was perfectly convergent between the models (Fig. 7.44). The adopted optimisation of the numerical model does not affect the obtained results.

The cracking force at the interface up to the support axis, i.e. along the entire length, obtained for model ZS_3_C_Short was 391.0 kN and was 9% lower than that of model ZS_1_C (425.1 kN). Model ZS_1_C remained composite with the concrete topping in the end zones after cracking in the axis of the support. A further increase in load and displacement resulted in a total interface cracking along the entire length at 436.4 kN, which is 12% higher than the model without concrete topping beyond the support axis.

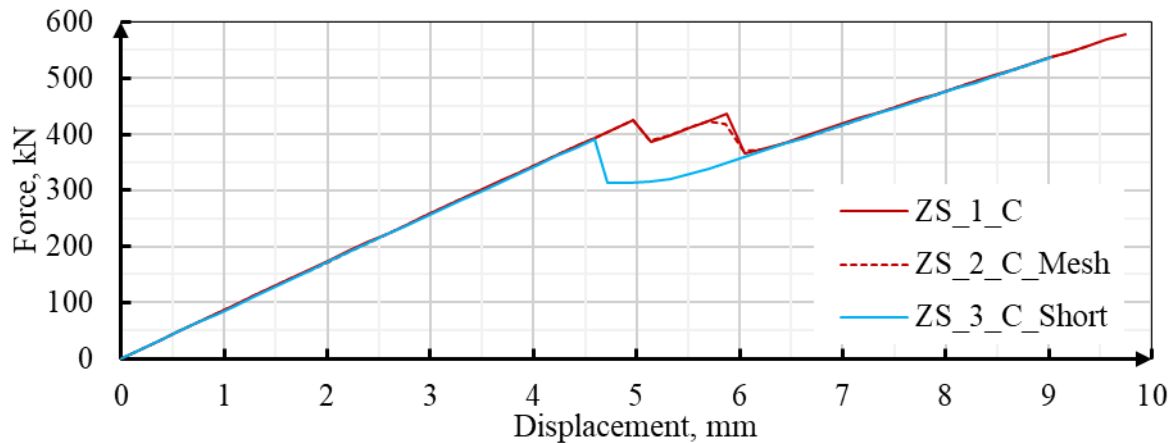


Fig. 7.44. Force-displacement characteristics for ZS_1_C, ZS_2_C_Mesh and ZS_3_C_Short models
 Rys. 7.44. Charakterystyka siła-przemieszczenie dla modeli ZS_1_C, ZS_2_C_Mesh i ZS_3_C_Short

Based on the ZS_1_C model, the stress distribution at the interface is briefly discussed. Fig. 7.45 shows the distribution of stresses before slip in the interface for a load of 159.5 kN. The highest tangential stresses were at the mid-length between the load and support axes (Fig. 7.45a). This zone also had minor normal force occurrence (Fig. 7.45b). For the lower lateral surface of the rib and the upper surface above the support, there were normal tensile forces of 0.68 MPa. For the top surface of the rib under load and the bottom surface of the rib flange above the support, there was a local pressure of 4.75 MPa. The tangential stresses transmitted through the interface were extinguished behind the support axis.

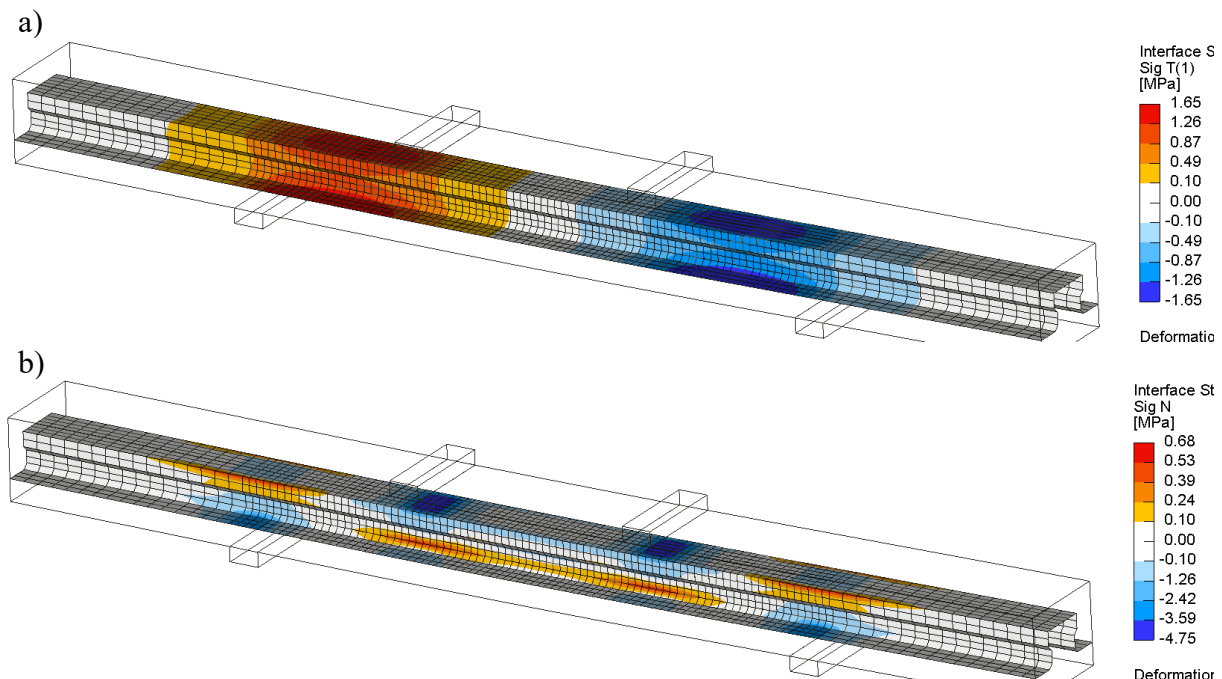


Fig. 7.45. Stress in the interface of the model ZS_1_C for a load of 159.5 kN: a) shear, b) normal
 Rys. 7.45. Naprężenia w styku modelu ZS_1_C dla siły 159.5kN: a) styczne, b) normalne

With increasing load, a local slippage had developed on the side surfaces of the rib (Fig. 7.46a) at the locations of the tensile forces as in Fig. 7.45b. The distribution of shear stresses over the height changed (Fig. 7.46a), with the highest stresses not being present halfway between the force and the support. When the interface was cracked over the support axis (Fig. 7.46b), the tangential stresses with the highest value occurred under the pressure points. The stresses took values between 0.0 and 0.5 MPa in the end zone. Once the interface was fully cracked, the only places where tangential stresses were effectively transferred remained the pressure points (Fig. 7.46c).

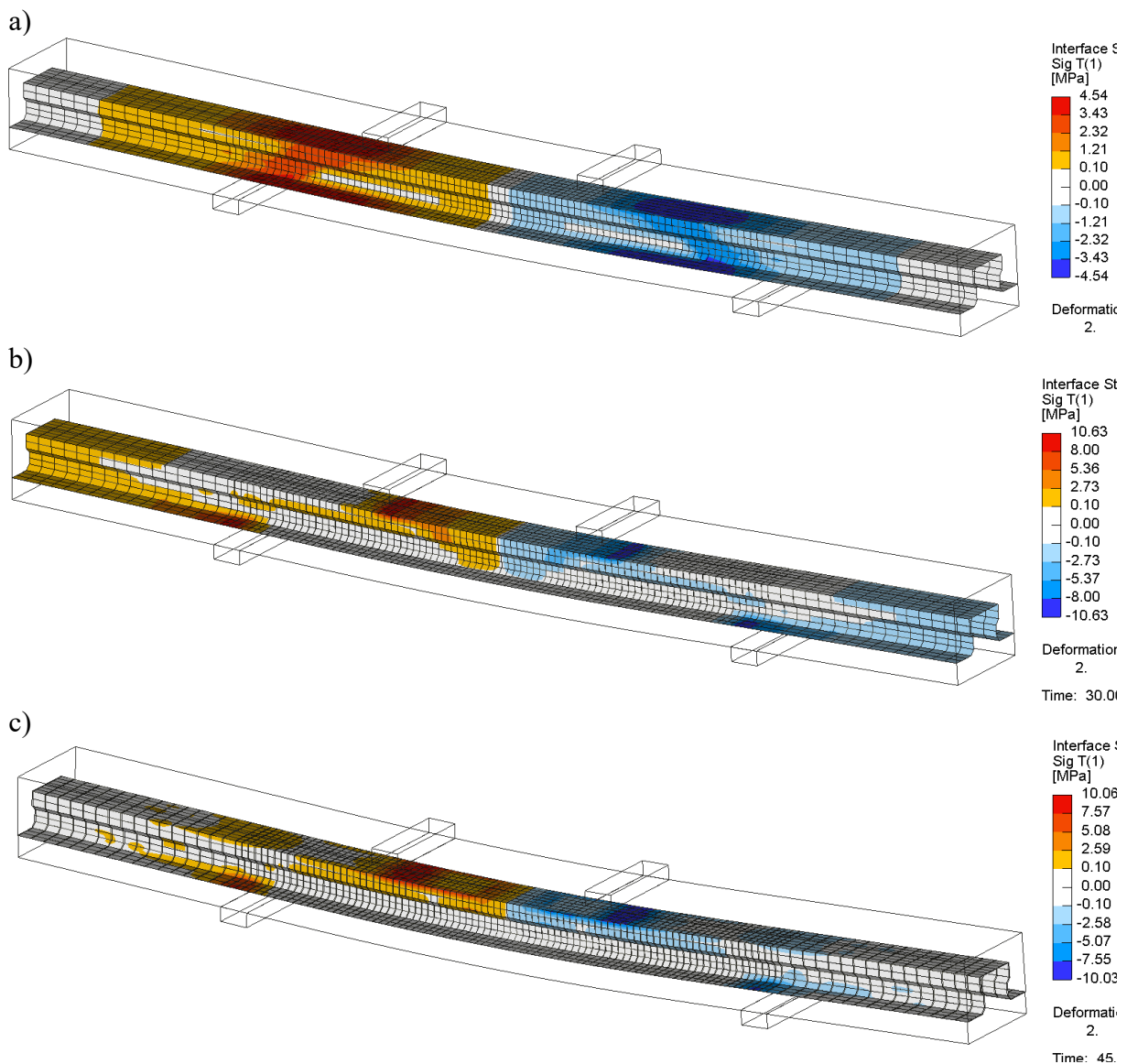


Fig. 7.46. Stress in the interface of the model ZS_1_C with the image of cracks for a load: a) 394.2 kN, b) 410.3 kN (post-peak), c) 493.2 kN

Rys. 7.46. Naprężenia w styku modelu ZS_1_C z obrazem zarysowań dla siły: a) 394.2 kN, b) 410.3 kN (po osiągnięciu siły maksymalnej), c) 493.2 kN

7.6.2. Results of Group II models

The second group is an analysis of the effect of varying the interface parameters on the response of the model, the results for this group, except for models ZS_4 and ZS_5, are presented in tabular form only. Changes made to models ZS_6 to ZS_10 only affected the values of the interface drawing force or flexural stiffness of the model without changing the failure mechanism.

Based on models ZS_4 and ZS_5 (Fig. 7.47), the effect of the friction coefficient on the interface's behaviour was verified. The models were compared with the basic model ZS_1_C. The first observation is significant from the point of view of correct calculation of the load capacity and cracking force of the interface. An interface with an almost zero friction coefficient allowed a higher interface cracking force (440.7 kN) than the basic model (425.1 kN - a difference of 3.7%), and a model with an increased friction coefficient (410.1 kN - a difference of 7.5%). The interface was cracked along its entire length in the reduced roughness model. There was no effect of the concrete topping being held by the pressure points and the end zone cooperation. Increasing the friction coefficient to a value of 1.0 made it possible to increase the described strengthening effect of the interface after local cracking to the support axis. The value of the cracking force along the entire length of the model was 525.1 kN, an increase of 20% compared to model ZS_1_C (436.4 kN) with a friction coefficient of 0.7.

Reducing the slight influence of the pressure point interaction allowed a higher interface drawing force for the given test configuration. This is the opposite effect of what was expected. The effect of the friction coefficient would require further study, particularly for components with relatively small normal loads uniformly distributed. However, this represents a different research issue. The resulting friction due to local pressure forces allows for an additional working phase, which should be counted as a “safety margin”.

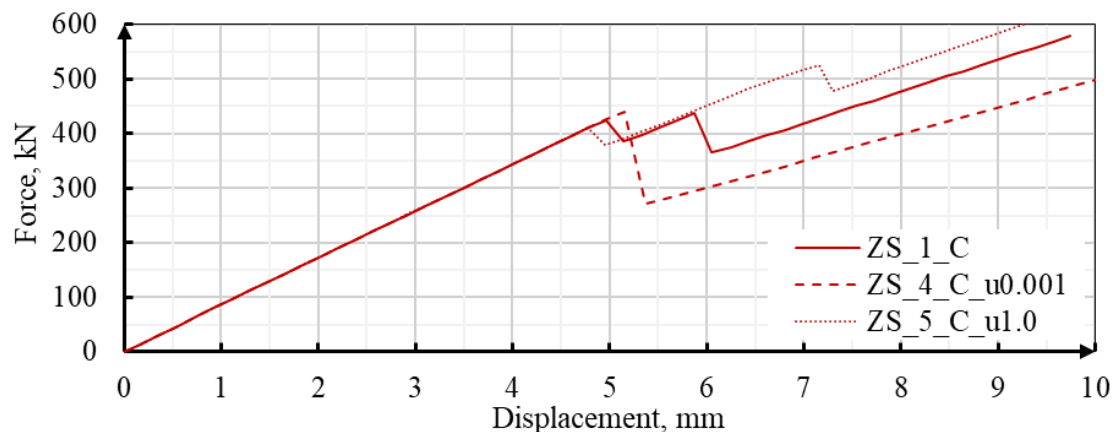


Fig. 7.47. Force-displacement characteristics for ZS_1_C, ZS_4_Cu0.001 and ZS_5_Cu1.0 models
Rys. 7.47. Charakterystyka siła-przemieszczenie dla modeli ZS_1_C, ZS_4_Cu0.001 i ZS_5_Cu1.0

Table 7.16 summarises the results for models with different interface normal stiffnesses. Modelling the interface 10x stiffer relative to the values adopted in the correlation process results in a 4.5% decrease in interface failure force. Adopting a lower normal stiffness allows for a slight increase in interface failure force of 3.1%. The effect of the interface's normal stiffness on the behaviour of the interface is relatively small. In the analysed range (full-length failure of the interface), the value of the friction coefficient has a more significant influence.

Table 7.16

Impact of the normal interface stiffness K_{NN}
Wpływ zmiany sztywności normalnej styku K_{NN}

Model	Normal stiffness K_{NN} , N/mm ³	Interface slip at face $V_{R,2}$, kN	Difference related to ZS_1_C %
ZS_1_C	21170	436.4	-
ZS_6_C_ $K_{NN}10^4$	10000	450.1	3.1%
ZS_7_C_ $K_{NN}10^5$	100000	422.02	-3.3%
ZS_8_C_ $K_{NN}2 \cdot 10^5$	200000	416.8	-4.5%

Table 7.17 summarises the results of the interface tangential stiffness analysis. A twofold increase in the interface tangential stiffness resulted in a 1.9% increase in the flexural stiffness of the beam. In the second case, the stiffness of the beam was reduced by 3.0%. Based on the results obtained, it can be concluded that the adopted interface stiffness provides the flexural stiffness of the tested beams as monolithic.

Table 7.17

Impact of the tangential interface stiffness K_{TT}
Wpływ zmiany sztywności stycznej styku K_{TT}

Model	Tangential stiffness K_{TT} , N/mm ³	Bending stiffness (at ~100 kN) kN·mm ²	Difference related to ZS_1_C %
ZS_1_C	45	3243	-
ZS_9_C_ $K_{TT}22.5$	22.5	3145	-3.0%
ZS_10_C_ $K_{TT}90$	90	3306	1.9%

7.6.3. Results of Group III models

The models with interface only on side surfaces and only on horizontal surfaces showed different behaviour concerning the failure model and the value of the force cracking the interface. The model with the interface on the side surfaces ZS_11_S was cracked over the entire interface length at a force of 185.8 kN. The model with the interface on the horizontal surfaces was cracked to the edge of the support at a force of 363.2 kN and over the entire length at 398.3 kN. This was 17% lower than that of model ZS_1_C. The forces cracking the model with an interface on all surfaces are not a simple sum of the forces cracking the interface of models ZS_11_S and ZS_12_TB. Despite the same coefficient of friction, model ZS_12_TB had slightly lower stiffness after interface slip than ZS_1_C (Fig. 7.48).

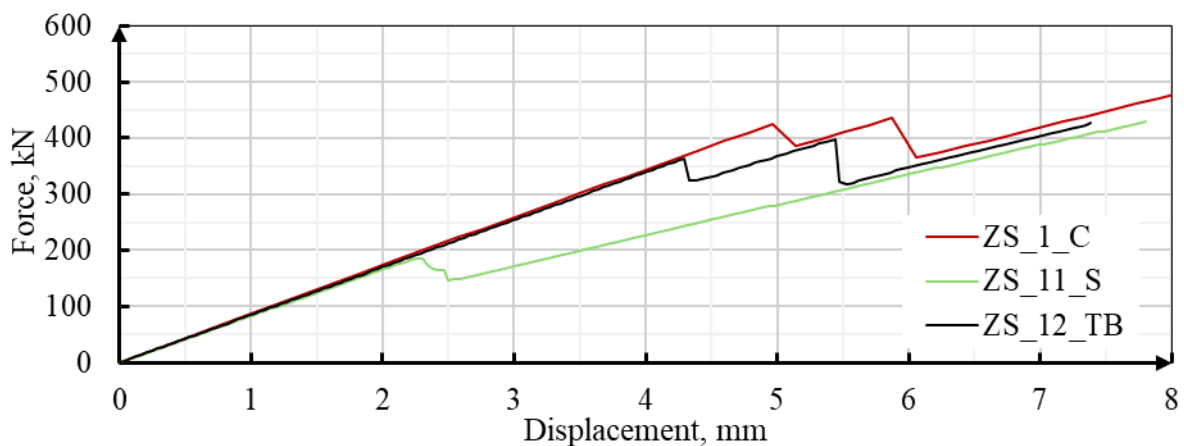


Fig. 7.48. Force-displacement characteristics for ZS_1_C, ZS_11_S and ZS_12_TB models
Rys. 7.48. Charakterystyka siła-przemieszczenie dla modeli ZS_1_C, ZS_11_S oraz ZS_12_TB

Analysing the results of model ZS_13_AB using only the force-displacement diagram (Fig. 7.48a), it can be concluded that, despite lower stiffness for this model, failure at the full-length interface occurred at a higher force (453.5 kN) than for model ZS_1_C (436.4 kN). The stiffness of model ZS_13_AB was significantly lower (18%) than that of model ZS_1_C prior to cracking (Fig. 7.48b). Despite the same friction coefficient, the stiffness after the complete cracking of the interface of model ZS_13_AB was lower than that of the basic model ZS_1_C. The failure of the interface over the entire length in model ZS_14_CB (full-length slip) occurred at a force of 297.4 kN. When comparing models with an interface with parameters such as those of the Z_AB and Z_CB series, it is noticeable that the difference in model stiffness is due to the elasticity of the interface even before it is cracked. These models were characterised

by a progressive degradation of flexural stiffness up to full-length failure of the interface. The progressive stiffness degradation was associated with an increasing slip area at the interface. For models ZS_13_AB and ZS_14_CB, the force resulting in the first local slipping was only 85.8 kN and 33.9 kN, respectively.

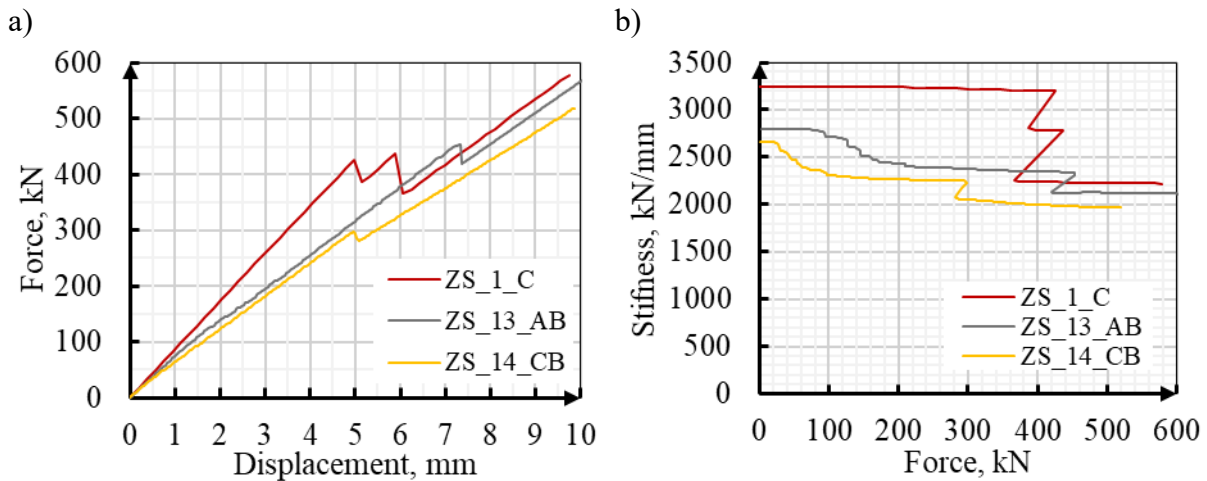


Fig. 7.49. Comparison of FEM results for ZS_1_C, ZS_13_AB and ZS_14_CB models: a) force-displacement characteristic, b) beam bending stiffness

Rys. 7.49. Porównanie wyników badań z obliczeniami MES dla modeli ZS_1_C, ZS_13_AB oraz ZS_14_CB: a) charakterystyka siła-przemieszczenie, b) sztywność giętna

Analysis of the slip values at the interface for successive calculation steps for ZS_13_AB showed increasing slip at the interface from low load values. Its extent increased with increasing load. The progressive degradation of the interface was responsible for the proceeding decrease in stiffness of the models (Fig. 7.49b). The first decrease in stiffness was associated with slippage of the interface beyond the edge of the support for the top and side surfaces of the rib, with the bottom surface remaining uncracked (Fig. 7.50a). Before failure, slippage was present along the entire length of the model except for the bottom surface from the axis of the support and the marginal rib section (Fig. 7.50b). With slippage along the entire interface length (Fig. 7.50c), the model noted a brittle decrease in stiffness.

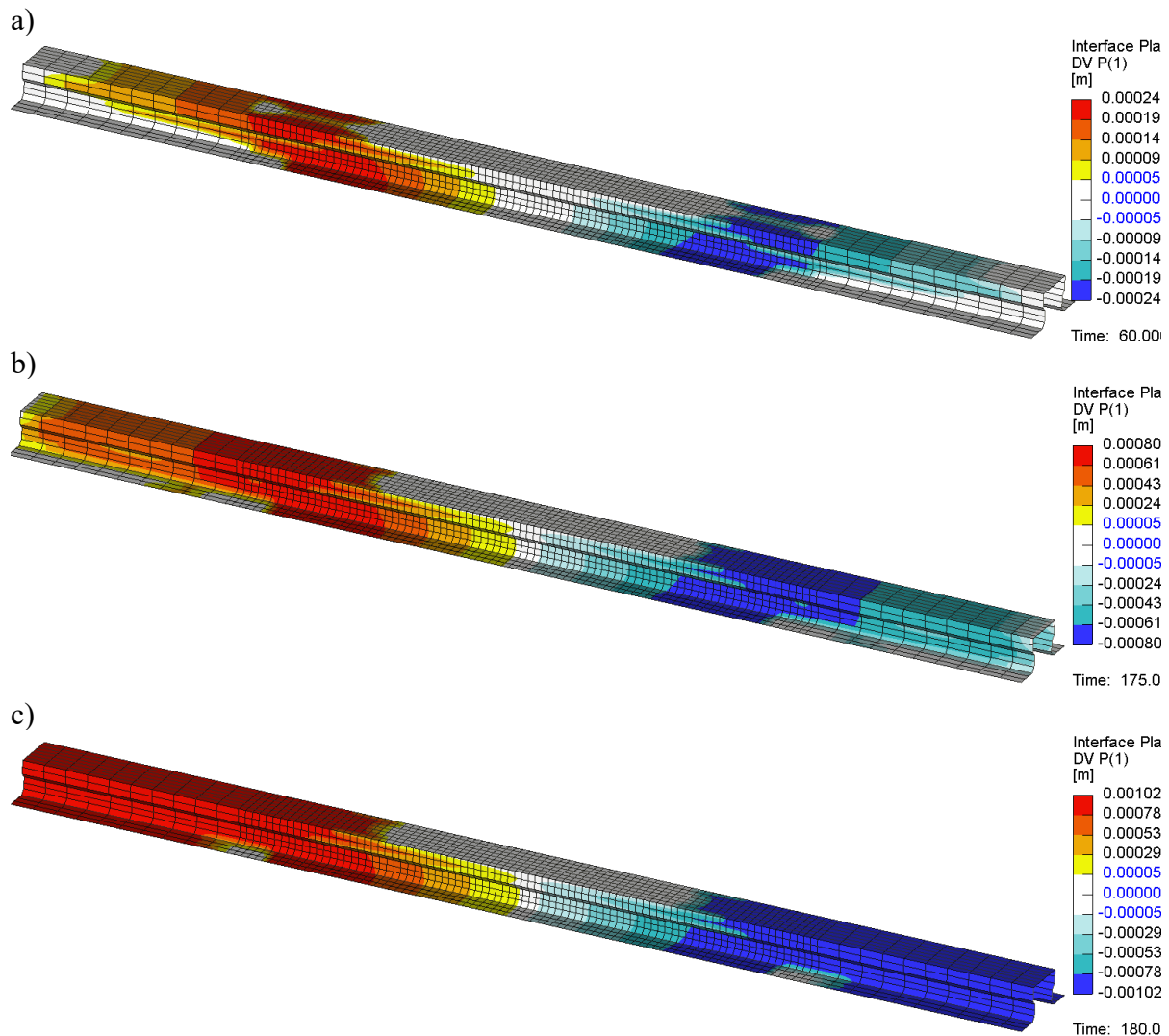


Fig. 7.50. Interface slip of model ZS_13_AB for the following load values: a) 164.4 kN, b) 450.6 kN, c) 419.5 kN

Rys. 7.50. Poślizg w styku modelu ZS_13_AB dla kolejnych wartości obciążenia: a) 164.4 kN, b) 450.6 kN, c) 419.5 kN

7.6.4. Results of the Group IV models

The last model differs from the previously described models due to the modified material model of the concrete topping. The concrete topping was modelled as a material subject to cracking and other effects according to the material model described for the main models. The model included concrete topping reinforcement. The model ZS_15_CT was intended to determine the effect of concrete topping on the cracking force of the interface. In a simplified manner, it can be assumed that the model represents the composite of a strongly prestressed or reinforced element for which flexural cracks will not occur before the interface is locally cracked, or their width will be small.

The resulting cracking value at the support axis was 240.1 kN, 77% lower than model ZS_1_C. The full-length cracking force at the interface was 335.7 kN and was 30% lower than that of model ZS_1_C. These values are higher than those obtained on the tested beam Z1.1_C and model Z1_CFEM (Fig. 7.51), for which no slip was obtained even in the support axis. At that point, the topping is completely crushed. It can be concluded that the flexural cracking of the concrete topping influences the value of the interface cracking force. The difference in the stress state between the main element (e.g. a highly prestressed precast unit) and the typical precast element (rebar reinforcement) may affect the actual value of the interface cracking force.

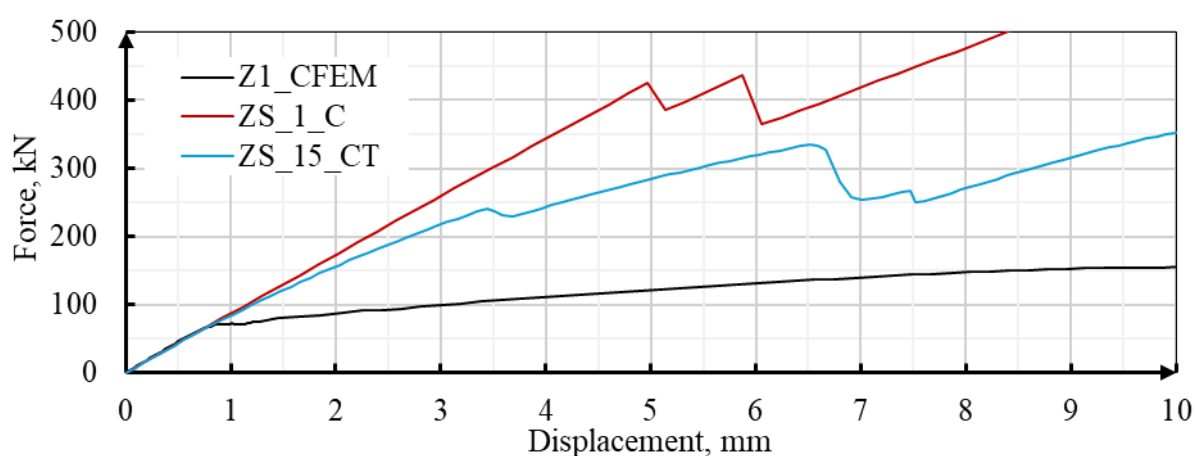


Fig. 7.51. Force-displacement characteristics for Z1_CFEM, ZS_1_C and ZS_15_CT models
Rys. 7.51. Charakterystyka siła-przemieszczenie dla modeli Z1_CFEM, ZS_1_C oraz ZS_15_CT

The first cracking of the concrete topping occurred when the tensile stresses of the main element were exceeded by as much as 54.9 MPa (Fig. 7.52a). The tensile strains of the concrete topping were 0.73‰, compared to those of 0.33‰ for which the cracking occurred in the Z1_CFEM model. The first flexural cracking (Fig. 7.52b) occurred with a local slip up to the support axis at the interface. At the same load (240.1 kN), plastic strains occurred in the compression zone of the concrete topping. Further interface degradation progressed as the amount and width of the concrete topping cracks and compression zone strains increased. After slippage of the interface along the entire length of the model, diagonal cracks appeared in the concrete topping (Fig. 7.52c). In the same step, there were also internal horizontal cracks indicative of crushing of the concrete topping zone.

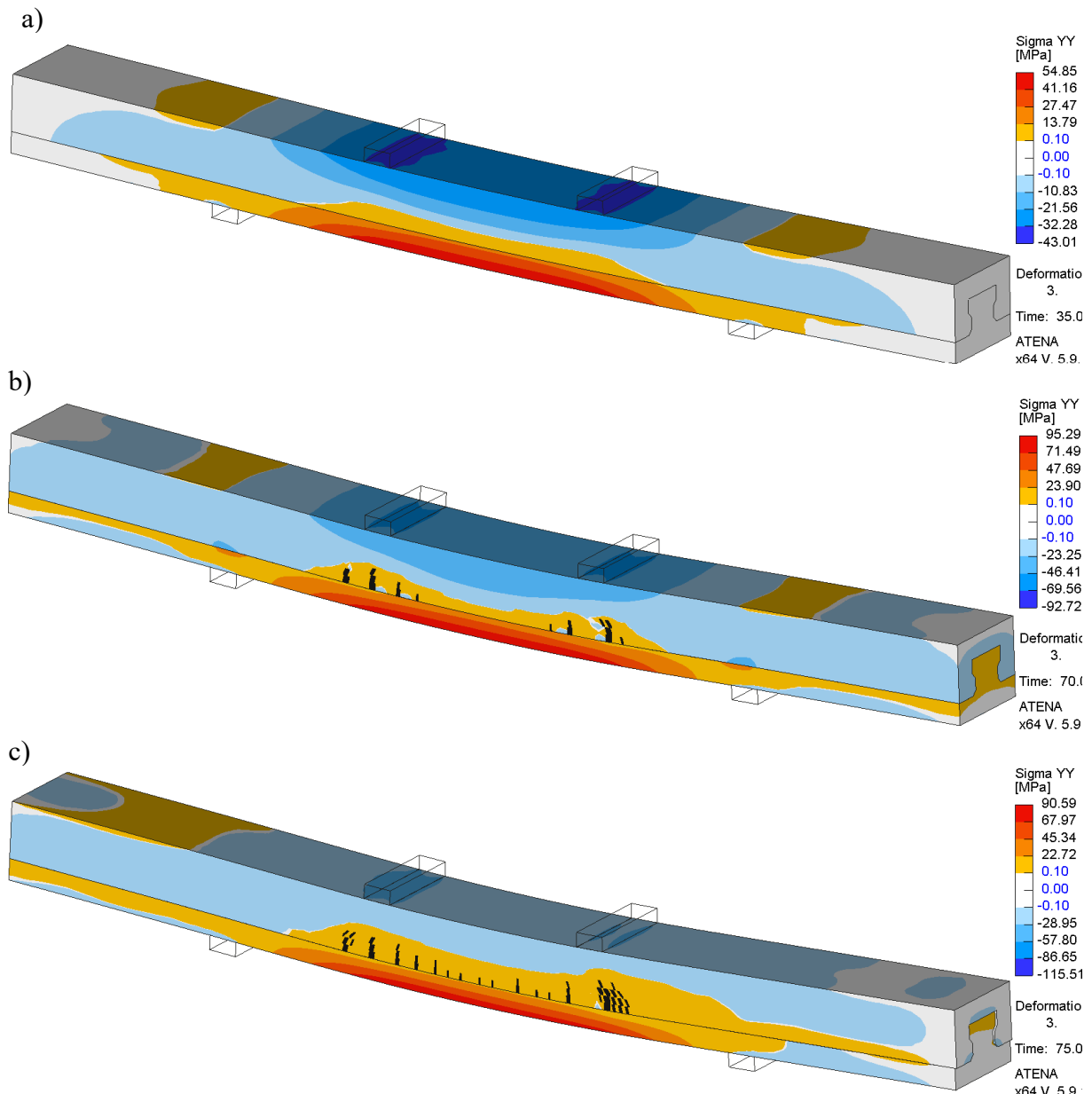


Fig. 7.52. Stress maps of the model ZS_15_CT with image of cracks for a load of: a) 231.4 kN – before bending cracks, b) 335.7 kN, c) 254.1 kN (post peak load)

Rys. 7.52. Mapy naprężeń modelu ZS_15_CT z obrazem zarysowań dla siły o wartości: a) 231.4 kN – przed zarysowaniami giętnymi, b) 335.7 kN, c) 254.1 kN (po sile maksymalnej)

7.7. FEM modelling conclusions

Based on the numerical analyses of the models representing the direct shear test, the 4PBT and the additional model in the 4PBT configuration, it is possible to state the following conclusions:

- **Correlation was possible with very high convergence of interface parameters in terms of stiffness and maximum force.** After cracking the models in the direct shear configuration, no post-cracking residual phase was obtained as in the tests.
- Models of all types were characterised by some non-linearity of the interface stiffness in terms of Phase I before cracking, but to a lower extent than in the direct shear experimental tests.
- The direct shear FEM models were characterised by only one type of failure, corresponding to slip along the entire length of the interface. The eccentric models affected the value of the maximum force and the slip on the sides of the model but did not change the type of failure.
- **For all the analysed FEM models, there was no concrete topping outward displacement relative to the precast element of a value similar to the tests.** The cracking that occurred in the cross-section of the models (at the corners) was of much smaller width than in the tests.
- The modelled beam elements with correlated interface parameters allow the degradation behaviour of the interface to be reproduced, including local cracking, slip in the axis of the support and slip to the face of the elements.
- Flexural and diagonal cracking affect the distribution of shear stresses in the models. Diagonal cracks limit the effective interface area of the composite, thus, as the cracks increase up to the edge of the support, the required force cracking the interface decreases.
- The FEM models showed the presence of a normal tensile force reducing the interface strength on the vertical surface parts. Further research is required to analyse the influence of the precast element geometry on the development of tensile forces at the interface.
- The interface efficiency of the vertical surfaces in the FEM models is significantly lower than that of the horizontal surfaces. This difference is particularly noticeable for the simplified model with the symbols ZS_11_S and ZS_12_TB. **The cracking force of a model with an interface on all surfaces is not a simple sum of the cracking force of the model with only vertical and horizontal interfaces.**
- **Cracking the interface in the support axis decreases stiffness, but the element remains partially composite due to the zone outside the support axis.** The additional models show that if the interface is not lengthened off the support axis as it were, there is a drop in the force that cracks the interface along its length,

in which case slippage in the support axis is the failure point of the element. From the point of view of the design of composite elements, it should be assumed that **the effect of partial composite through the end zones (composite outside the support zone) and the slight increase in interface cracking force at the support axis provides an additional safety margin.**

- The local point pressure of load to the interface does not increase the value of the cracking force. Local pressure points only allow partial interface bond after cracking of the interface. The resulting friction due to local pressure allows for an additional behaviour phase, which should be counted as a safety margin.
- For the Z5_SFEM_SC model with a constraint of lateral strains in the concrete topping (outward displacement), a significantly higher maximum force was obtained with no slip at the interface relative to the Z5_SFEM model and experimental studies (Z5.1_S). **This model represents the potential for vertical interfaces in elements that are part of a larger structure, e.g. a slab.**

8. ANALYSIS AND CONCLUSIONS

8.1. Analysis of the effectiveness of the interface surfaces

The analysis of experimental results and finite element method (FEM) modelling was conducted to assess the stresses present at the interface. The stress calculations were performed using formulas derived from the laminar structure mechanics [66]. A simplistic assumption of only two layers was made, even though each layer exists at multiple height levels. This approach should be regarded as considerably simplified.

$$V_{R,cr,exp} = \tau_{R,cr,exp} b_j \frac{\Delta_{11}(E_p J_p + E_{olc} J_{olc})}{w_0} \quad (8.1)$$

in which the distance between the centres of mass of the layers:

$$\Delta_{11} = \frac{1}{E_p A_p} + \frac{1}{E_{olc} A_{olc}} + \frac{w_0^2}{E_p J_p + E_{olc} J_{olc}} \quad (8.2)$$

in which,

E_p, A_p, J_p – modulus of elasticity, cross-sectional area, moment of inertia of the precast
 $E_{olc}, A_{olc}, J_{olc}$ - modulus of elasticity, cross-sectional area, moment of inertia of the overlay concrete (topping)

The initial assumption regarding the width of the interface was that it would account for the entire width of the interface for the specified element type, as outlined in Table 5.2. Subsequently, a factor was derived to account for the impact of the element's anchorage length beyond the support edge on the stresses at the interface. The factor assumed that some of the stresses are taken up by the interface beyond the support edge, reducing stresses within the shear zone. The presented equation 8.1 does not take this effect into account. As a result, the stress results obtained are overestimated due to the lack of stress reduction associated with the partial redistribution to the off-support zone. The calculations conducted with the FEM models ZS_1 and ZS_3 involved removing the section of the element located outside the support edge. The factor denoting the stress

reduction, referred to as the "beam support length reduction" factor, was determined using equation 8.3 and assigned a value of 0.92. As a result, extending the beam by 500 mm beyond the support axis corresponded to an 8% decrease in stress at the interface, indicating an 8% redistribution of stress.

$$r_{bsl} = \frac{\tau_{R,cr,exp.ZS_3}}{\tau_{R,cr,exp.ZS_1}} = \frac{3.75 \text{ MPa}}{4.08 \text{ MPa}} = 0.92 \quad (8.3)$$

in which,

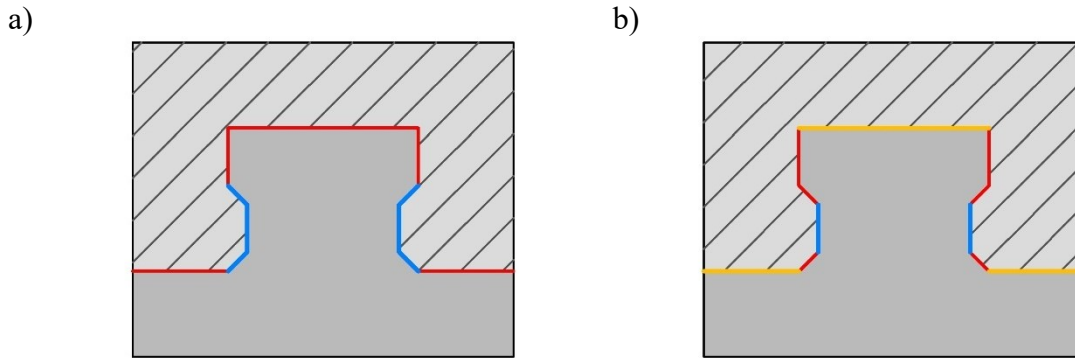
$\tau_{Rd,cr,exp.ZS_1}$ – tangential slip stress in ZS_1_C FEM model

$\tau_{Rd,cr,exp.ZS_3}$ – tangential slip stress in ZS_3_CShort FEM model

The stresses accounting for the redistribution effect were calculated for the four simplified models in Table 8.1. The calculated stresses for the entire interface ranged from 3.60 MPa to 5.88 MPa, with the lowest value observed for the model with a vertical interface (ZS_11_S) and the highest value observed for the model with a horizontal interface only (ZS_12_TB). Subsequently, the stresses at the interface were recalculated for the reduced width of the interface, referred to as the effective width. This width was determined based on the stress maps and the values of the normal forces at the interface, as shown for model ZS_1_C in Figures 7.45 and 7.46. The horizontal and upper vertical surfaces of the rib head were considered effective stress transfer surfaces. The resulting width of this area was determined to be 260 mm (Fig. 8.1a), compared to 367 mm for the entire member and 200 mm for the top and bottom surfaces only. The stress calculations performed, considering the described reduction in interface area, are summarised in Table 8.1. The resulting stresses were 5.30 MPa for models ZS_1 and ZS_3_Short, 3.60 MPa for model ZS_11_S, and 5.88 MPa for model ZS_12_TB.

It should be noted that the stresses calculated according to equation 8.1 and the presented procedure for determining the reduction factors do not account for local effects, such as cracks. Furthermore, they represent an average value of the stresses at the interface. The stresses for models ZS_1 and ZS_3_Short are consistent with expectations and correspond to the force at which slip occurs at the interface, precisely matching the cohesion value of the model. The recalculated stresses for model ZS_12_TB exceed the cohesion value and are 11% higher than the models with initially full interface width. This may indicate a more pronounced cooperative effect in the off-axis zone or an increased influence of localised pressure effects on the model. The stresses at the interface of model ZS_11_S are 32% lower than those of model ZS_1 due to the narrower interface width employed in the calculations, which is reduced before

reaching the maximum values. In order to achieve stresses of 5.30 MPa, it would be necessary to reduce the width of the anastomosis to approximately 115 mm. This reduction would entail an interface lacking a vertical surface at the rib web while still maintaining the interface on surfaces inclined at an angle to the element's base (Fig. 8.1b).



— "Effective" interface surface — "Ineffective" interface surface — Covered surface

Fig. 8.1. Effective tangential stress surfaces at the interface of beam types: a) Z1_C, b) Z5_S

Rys. 8.1. Efektywne powierzchnie naprężeń stycznych w styku belek typu: a) Z1_C, b) Z5_S

Table 8.1

Tangential stresses at the interface with reduction factors for FEM models

Naprężenia styczne w styku ze współczynnikami redukcyjnymi dla modeli MES

Model	$V_{R,cr,exp}$, kN	b_i , mm	$\tau_{R,cr,FEM}$, MPa	r_{bsl}	$\tau_{R,cr,FEM.red1}$, MPa	$b_{i,red}$, mm	$\tau_{R,cr,FEM.red2}$, MPa
ZS_1	212.6	367	4.08	0.92	3.75	260	<u>5.30</u>
ZS_3_Short	195.5	367	3.75		-	260	<u>5.30</u>
ZS_11_S	92.9	167	3.92		3.60	-	-
ZS_12_TB	181.6	200	6.39		<u>5.88</u>	-	-

According to the above procedure, stress calculations were conducted using the experimental results for Group I and Group II elements. The average stress at the interface for all elements was 1.72 MPa, with a standard deviation (SD) of 0.56 MPa and a coefficient of variation (COV) of 32.8%. After accounting for the reduction in stress due to the width of the interface and the anchorage length, the average stress was recalculated to be 2.53 MPa, with an SD of 0.21 MPa and a COV of 8.1%. These calculations demonstrate a significant convergence of the tangential stress values obtained at the element interfaces, notably when excluding beams Z2_AB, Z3_CB and Z5_S. The stress value obtained is lower than the tensile strength of the precast concrete

(3.34 MPa), but very close to the interface strength assumed on the pull-off test and correlated in the numerical models (2.71 MPa). For beams with only a vertical interface (Z5_S), the stresses at the interface were found to be 1.78 MPa and 2.04 MPa, 25% lower than the average for models with horizontal interfaces. The tests showed no difference between the average results for beams with the interface on the side and the top (Z10_TS) or bottom (Z9_SB) of the element. In the case of Z2_AB beams, the average stresses at the interface were measured at 1.17 MPa, compared to the tensile strength of 1.20 MPa obtained from the finite element method (FEM) model correlation. For Z3_CB beams, the stresses at the interface were recorded as 0.68 MPa, as opposed to the 0.45 MPa obtained through parameter correlation in the FE model.

The results indicate a correlation between interface stresses and the tensile strength of concrete. This finding contradicts the simplified finite element (FE) models, where interface stresses are aligned with the cohesion value. The disparity between experimental studies and simplified models can be attributed to the effects of flexural and diagonal cracking and the strain state of concrete in both tension and compression zones. By employing reduced interface widths, a significant level of convergence was achieved between models with only horizontal interfaces (Z6_TB) and those with vertical and horizontal interfaces. The tests showed no significant influence of the position of the interface planes on the element height. The same efficiencies were obtained for the bottom and top surfaces as indicated on beam types Z9_SB and Z10_TS. In the tested composite element geometry, the effective stress transfer at the interface did not involve the vertical surfaces at the rib web and inclined surfaces. When reduction factors were not considered, the Z5_S beams exhibited the highest stresses compared to beams for which calculations were performed for the entire interface prior to reduction. Despite cracking along the support axis, Z5.1_S beams demonstrated failure forces similar to those of Z1.1_C beams. They were comparable to other models in the 3PBT test, including those without slip from the face of the element. Relying solely on interface stresses for the composite surfaces, as indicated in Table 8.2 (column 4), would lead to incorrect conclusions.

Table 8.2

Tangential stresses at the interface with reduction factors for experimental test
 Naprężenia styczne w styku ze współczynnikami redukcijnymi dla badań doświadczalnych

Element	$V_{R,cr,exp}$, kN	b_i , mm	$\tau_{R,cr,exp}$, MPa	r_{bsl}	$\tau_{R,cr,exp,red1}$, MPa	$b_{i,red}$, mm	$\tau_{R,cr,exp,red2}$, MPa
Z1.1_C	-	367	-	0.92 - beam support length reduction coefficient	<i>No slip in the interface</i>		
Z1.3_C	101.1	367	1.94		1.78	260	<u>2.52</u>
Z2.1_AB	67.1	367	1.29		1.18	<i>No side surface reduction effect, different interface stiffness and failure behaviour</i>	
Z2.3_AB	65.4	367	1.26		1.15		
Z3.1_CB	30.4	367	0.58		0.54		
Z3.3_CB	46.1	367	0.89		0.81		
Z4.1_P	64.9	200	2.28		2.10	170	<u>2.47</u>
Z4.3_P	69.1	200	2.43		2.24	170	<u>2.63</u>
Z5.1_S	45.8	167	1.93		1.78	<i>Side surface only</i>	
Z5.3_S	52.6	167	2.22		2.04		
Z6.1_TB	45.8	200	1.61		1.48	<i>No side surface</i>	
Z6.3_TB	77.9	200	2.74		<u>2.52</u>		
Z9.1_SB	68.8	267	1.81		1.67	160	<u>2.78</u>
Z9.3_SB	59.0	267	1.56		1.43	160	<u>2.39</u>
Z10.1_TS	68.5	267	1.81		1.66	160	<u>2.77</u>
Z10.3_TS	53.2	267	1.40		1.29	160	<u>2.16</u>
	Mean, MPa		1.72	For $\tau_{Rd,cr,exp,red2}$, only comparable beam (underline values)	Mean, MPa		2.53
	SD, MPa		0.56		SD, MPa		0.21
	COV, %		32.8%		COV, %		8.1%
<p>$V_{Rd,cr,exp}$ – the lower of the slip in the support axis or the diagonal cracking force related to the local slip, reduced by 50% of the dead weight of the beam (100% - 1.74 kN) and 50% of the weight of the steel beam, force gauge and roller (100% - 1.17 kN); in the 3PBT the dead weight was subtracted, the forcehead weight was included in the measurements.</p> <p>b_i – width of the interface</p> <p>$\tau_{Rd,cr,exp}$ – experimental tangential slip stress (based on 7.1)</p> <p>r_{bsl} – beam support length reduction coefficient</p> <p>$\tau_{Rd,cr,exp,red1}$ – reduced by r_{bsl} factor tangential slip stress</p> <p>$b_{i,red}$ – reduced width of the interface based on FEM analysis</p> <p>$\tau_{Rd,cr,exp,red2}$ – tangential slip stress calculated on $b_{i,red}$</p>							

Based on the stress calculations conducted at the interface, it is possible to determine a reduction factor for the tested component geometry. This factor is determined based on the reduction in interface width associated with the lack of effective cooperation of the lateral surfaces. The factor is calculated by comparing the average stresses $\tau_{Rd,cr,exp.red2}$ to $\tau_{Rd,cr,exp.red1}$ of elements with side surfaces Z5.1_S and Z5.3_S. Comparisons between test elements and simplified models are made, with the results summarized in equation (8.4). Comparisons are made before and after the correction of the side surfaces for elements with vertical and horizontal surfaces. The resulting efficiency coefficient of vertical surfaces relative to horizontal surfaces is 0.68 for the FEM model and ranges from 0.70 to 0.81 for the experimental tests.

$$s_{red} = \frac{\tau_{R.cr.exp.red1.z5.1_S}}{\tau_{R.cr.exp.red2.mean}}; \frac{\tau_{R.cr.exp.red1.z5.3_S}}{\tau_{R.cr.exp.red2.mean}}; \frac{\tau_{R.cr.FEM.red1.ZS_11_S}}{\tau_{R.cr.FEM.red2}} \quad (8.4)$$

$$s_{red} = \left\langle \frac{1.78}{2.53} = 0.70 \mid \frac{2.04}{2.53} = 0.81 \mid \frac{3.60}{5.30} = 0.68 \right\rangle$$

The calculated values of the surface effectiveness factor confirm the lack of full cooperation of the lateral surfaces, even in a Z5_S-type element. The FEM analyses presented indicate that, before failure occurs, a specific area of the interface surface experiences slippage and fails to establish an effective stress transfer field. To capture this phenomenon accurately, a thorough analysis of a correlated FEM model is necessary. Due to the complexity of the interface degradation mechanism for Z1_C and Z5_S beams and the limited scope of geometry for the tested element, it is not feasible to propose a universally applicable reduction factor. It is worth mentioning, however, that the horizontal surfaces in the tested elements were positioned at the centre of the section height, which corresponds to the zone with the highest theoretical shear stresses, as illustrated in the FEM models. Simultaneously, the geometry of the tested beams resulted in tensile stresses on the vertical surfaces, thereby reducing their capacity of shear stresses.

The effective vertical interface area of beams in the Z5_S series surpasses that of beams with horizontal and vertical surfaces, previously specified as 60 mm. To ensure that the stresses on elements of type Z5_S align with the average for other elements, it is necessary to decrease the effective interface area to 135 mm for beam Z5.1_S and model ZS_11_S (a reduction of 20% concerning the total area), or to 115 mm for beam Z5.3_S. It should be noted that this reduction is due to the unique shape of the element.

However, the abovementioned calculations and reductions cannot be universally applied to a broader range of side surface geometries. Therefore, more research is required to confirm this reduction factor. Additionally, investigating the influence of interface geometry, including surface inclination, could be a topic for further research to supplement the analyses mentioned above. Based on additional FEM analyses and individual test models, it may be possible to establish guidelines for the preliminary assessment of element geometry, taking into account the surface inclination relative to the element base and the relative position of the layers' centres of mass.

8.2. Comparative analysis of EN series standards

The test results for beams of types Z1_C, Z5_S, and Z6_TB were compared with standard calculations. The calculations were performed using coefficients and formulas from PN-EN 1992-1-1:2008 (Eq. 8.5) and PN-EN 1992-1-1:2024 (Eq. 8.6), along with coefficients from PN-EN 15037-1:2011. The calculation procedure from PN-EN 1992-1-1:2008 was utilized, and the formulas were presented without the factor for reinforcement. The standard calculations, based on the average tensile strength of the reinforced concrete, were compared with the values obtained from the experimental tests. These test results were calculated for the shear force according to equation 8.1, and for the width of the interface as specified in Table 5.2. The calculations considered the entire area of the interface without the reduction mentioned in Section 8.1. To compare 4PBT and 3PBT, the load values were calculated as bending moments for the cracking force due to flexural cracks and the bending moment corresponding to the maximum load. The shear force values were calculated while considering the static scheme of the tested element (4PBT and 3PBT).

$$\tau_{Rdi} = c f_{ctd} + \mu \sigma_n \quad (8.5)$$

$$\tau_{Rdi} = c_{v1} \frac{\sqrt{f_{ck}}}{\gamma_c} + \mu_v \sigma_n \quad (8.6)$$

The test elements were specified and designed to observe horizontal cracking resulting from interface slip before diagonal cracking and flexural cracking (Table 8.3). Despite a prestressing force lower than initially assumed, the cracking moment still exceeds the corresponding diagonal cracking force and interface slip. The initial calculations were based on the standard interface parameters (EN 1992-1-1:2008) and

the average strength parameters of the materials. Using virtual strain gauges (described in Section 6.4.1), the height of the compression zone was determined to be 45 mm (Fig. 6.29). This measurement corresponds to the boundary between the concrete topping and the upper surface of the precast element. Finite element method (FEM) analysis shows compressive stresses within the top 5 mm of the precast. The standard calculation of the compression zone estimates a height of 39 mm, entirely within the concrete topping. Consequently, a β -factor of 1.0 was adopted for the calculations in accordance with EN standards.

The shear force values that induce cracking at the interface exhibit a high degree of consistency between the Z5_S and Z6_TB element types in both FEM analysis and experimental tests. Calculated shear force values leading to interface cracking are significantly lower in standard calculations than in experimental tests. Specifically, for PN-EN 1992-1-1:2008, the force was five times lower; for PN-EN 1992-1-1:2004, it was nearly seven times lower; and for PN-EN 15037-1:2011, the difference ranged from two to three times lower. The differences in results obtained between the different standards can reach up to 100%. The lowest interface cracking force was observed in the latest edition of PN-EN 1992-1-1:2024, where the formula calculations consider compressive stresses instead of tensile stresses as in the previous edition. The c factor can be utilized to compare the 2008 and 2011 standards in the context of beam-and-block slabs. In PN-EN 15037-1:2011, the c factor for the lowest category of slabs, after conversion from stresses, is up to 0.38, which is nearly equivalent to the rough surface in PN-EN 1992-1-1:2008. For a similarly defined surface, namely smooth, the standard assigns a coefficient of 0.2. Due to formulas 8.5 and 8.6 changes, a direct comparison of the coefficients between the 2008 and 2024 editions of the 1992-1-1 standard is not feasible. Nonetheless, none of the standards allow for determining close values for the slippage force. The closest value from the research is obtained through calculations based on the coefficient provided by the standard for beam-and-block slabs, which can also be applied to the tested elements. Moreover, this standard is the only one incorporating correlated coefficients for elements with a multiplanar interface.

The calculations of diagonal cracking force showed a significant difference of over 50% between the test results and the finite element method (FEM) models compared to the standard calculations. However, the difference between the 2008 and 2024 standards is only 4%. Considering the test configuration and resulting a/d parameter of 2.5, higher shear strengths were expected than those determined by the standard analysis. This observation aligns with the findings of other researchers who have studied composite prestressed elements with concrete topping [72]. It is important to note that the main

focus of this study is not the analysis of ultimate shear resistance; therefore, no further analysis and calculation in that direction was conducted. Nevertheless, the experimental results and FEM modelling presented in this study can serve as a valuable starting point for future analyses.

After incorporating prestressing stresses correlated into the FEM models, the calculated cracking moment closely matched the results of the experimental studies. The maximum bending moment closely approximated the test values, but there was a difference in the failure model. Specifically, the tests and FEM models showed crushing of the compression zone accompanied by strand slippage, while the calculations yielding the reinforcement (considering the compression bars in the concrete topping). Notably, the calculated values for reinforcement yielding and zone crushing due to strain are similar.

Table 8.3

Summary of calculated values of elements of types Z1_C, Z5_S and Z6_TB
 Zestawienie wartości obliczonych dla elementów typu Z1_C, Z5_S i Z6_TB

Description / Standard	Symbol	Element		
		Z1_C	Z5_S	Z6_TB
Interface cracking force				
Experimental value	$V_{R,cr,exp}$, kN	- 101.1 kN 4PBT 3PBT	45.8 52.6 4PBT 3PBT	45.8 77.9 4PBT 3PBT
FEM (4PBT)	$V_{R,cr,FEM}$, kN	-	49.2	65.2
PN-EN 1992-1-1:2008 ($c = 0.2$)	$V_{Rd,i(cr)}$, kN	26.23	11.94	14.30
PN-EN 1992-1-1:2024 ($c_{v1} = 0.08$)	$V_{Rd,i(cr)}$, kN	17.69	8.05	9.64
PN-EN 15037-1:2011 ($c_1 = 0.38$)	$V_{Rd,i(cr)}$, kN	49.84	22.68	27.16
Shear cracking force				
Experimental value	$V_{R,c,exp}$, kN	66.6 77.4 4PBT 3PBT	67.0 52.6 4PBT 3PBT	45.8 77.9 4PBT 3PBT
FEM (4PBT)	$V_{R,c,FEM}$, kN	65.1	49.2	65.2
PN-EN 1992-1-1:2008	$V_{Rd,c}$, kN	23.23 kN + 15.65 kN = 38.87 kN $V_{Rd,c} = V_{Rd,c,pc} + V_{Rd,c,top}$		
PN-EN 1992-1-1:2024	$V_{Rd,c}$, kN	23.92 kN + 16.49 kN = 40.4 kN $V_{Rd,c} = V_{Rd,c,pc} + V_{Rd,c,top}$		
Cracking moment				
Experimental value	$M_{R,cr,exp}$, kNm	11.48 14.22 4PBT 3PBT	12.37 11.36 4PBT 3PBT	3.38 12.72 4PBT 3PBT
FEM (4PBT)	$M_{R,cr,FEM}$, kNm	12.55	12.29	12.11
Calculation	$M_{R,cr}$ kNm	11.36		
Bending moment				
Experimental value	$M_{R,exp}$, kNm	28.63 39.06 4PBT 3PBT	28.47 33.19 4PBT 3PBT	17.66 34.70 4PBT 3PBT
FEM (4PBT)	$M_{R,FEM}$, kNm	27.46	23.15	27.49
Yielding of strands and rebars	M_R , kNm	33.44		

The interface force calculations for each stage, as per the three mentioned standards, are presented in Table 8.4. Notably, the coefficients obtained from the tests exceed those specified for any surface type in the 2008 or 2024 PN-EN 1992-1-1 standards. Specifically, the coefficients are 0.77 and 0.46, respectively. Nonetheless, it is important to acknowledge that these values should not be directly compared. When applying the procedure outlined in formula 8.1 to compute the shear force, the resulting coefficient, associated with PN-EN 15037-1, is 0.58.

Table 8.4

Summary of interface slip force calculation steps for selected standards
Zestawienie kroków obliczeniowych siły rozwarstwiającej dla wybranych norm

Formula component	PN-EN 1992-1-1: 2008	PN-EN 1992-1-1: 2024	According to formula 7.1
$V_{R,cr,exp,Z1.3_C}$, kN	101.1	101.1	101.1
$b_{Z1.3_C}$, mm	367	367	367
z , mm	0.107	0.107	-
β , -	1.0	1.0	-
$\frac{\Delta_{11}(E_p J_p + E_{olc} J_{olc})}{w_0}$, mm	-	-	0.142
$\tau_{Rd,cr,exp}$, MPa	2.55	2.55	1.94
$f_{ctm,ts,olc}$, MPa	3.34	-	3.34
$f_{cm,olc}$, MPa	-	31.70	-
c , -	0.77¹⁾	0.46²⁾	0.58³⁾
Cohesion factor calculation formula:			
1) $c_1 = \frac{V_{R,cr,exp,Z1.3_C}}{f_{ctm,ts,olc} z b_{Z1.3_C}}$;			
2) $c_2 = \frac{V_{R,cr,exp,Z1.3_C}}{\sqrt{f_{cm,olc}} z b_{Z1.3_C}}$;			
3) $c_3 = \frac{V_{R,cr,exp,Z1.3_C} w_0}{f_{ctm,ts,olc} b_{Z1.3_C} \Delta_{11}(E_p J_p + E_{olc} J_{olc})}$			

Based on the conducted calculations, there are significant differences in the calculation of identical components between successive editions of the PN-EN standard and the standard specifically designed for precast elements. More accurate results can be achieved by using the formula derived from the laminar mechanics instead of the standard formula for calculating shear forces. However, the cohesion coefficient values obtained for the examined elements are several times higher than the standard values.

Notably, the difference observed between the 2008 and 2024 standards can be attributed to the relatively high tensile strength compared to the compressive strength of the test specimens. When applying full-standard calculations based on the design concrete class values, the new edition of the standard allows for higher resistance values to be obtained for rough surfaces. However, it is important to emphasize that this study does not aim to conduct a comparative analysis of the standards regarding design parameters, and the above discussion serves solely as a point to prevent incorrect general conclusions.

8.3. Analysis of interface stiffness

When analyzing the behaviour of an interface, it is necessary to refer to its stiffness. A measure of stiffness is the stiffness coefficient, which is defined in three ways as [66]:

- the tangential force acting at the interface (in direct-shear tests the force F) and the displacement (slip) at the interface S . This measure has been used in previous stiffness diagrams of direct-shear tests and FEM models.

$$k_T = \frac{F}{S} \quad (8.7)$$

- shear stress at the interface and displacement at the interface (slip)

$$k_\tau = \frac{\tau}{S} \quad (8.8)$$

- shear stress at the interface and the difference in strain at the slip length:

$$k_{\tau,\varepsilon} = k_\tau \Delta x \quad (8.9)$$

The authors of this publication employ various measures, and following equation 8.7, the reported values are chosen to be aligned with the unit MPa. The analysis of interface stiffness is limited to two specific elements: Z1.2_C3, which demonstrates type I failure (slip); Z2.2_AB2, which exhibits an intermediate failure force value among the elements in group Z2_AB; and Z3.2_CB3, which has the highest stiffness within its group. The results present the calculated stiffness for the entire interface width and the width of the test element (200 mm) after modifying the interface width. The second

value is provided to compare the stiffness of the test element to other studies conducted by different authors on flat interfaces, where the composite width matches the beam width. This recalculation facilitates a comparison of the obtained interface stiffness with analyses performed by other authors while considering the impact of interface stiffness on beam behaviour. It should be noted that having an interface with higher stiffness in an element with a flat interface width than that of the analyzed beam does not necessarily result in a higher composite unit stiffness. The ratio of interface width to element width determines the stiffness of the interface relative to analyses conducted on flat interfaces.

The stiffness values obtained for the fully composite element, Z1.2_C3, were 4580 MPa for 80% of the load and 3790 MPa for 100% of the force. After accounting for the beam width, the corrected stiffness values were 8404 MPa and 6955 MPa, respectively (Fig 8.2a). In the case of the element with broken chemical adhesion, Z2.2_AB2, but with maintained mechanical adhesion, the stiffness values were 830 MPa for 80% of the load and 161 MPa for 100% of the force. After correction for the beam width, the corrected stiffness values were determined to be 1524 MPa and 294 MPa, respectively (Fig. 8.2b).

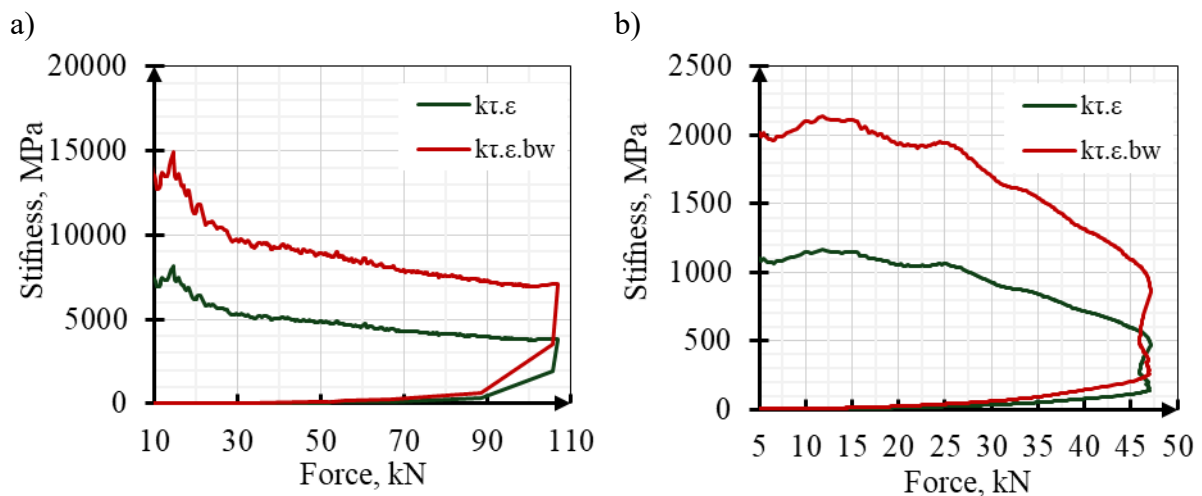


Fig. 8.2. Interface stiffness for the mean slip value: a) Z1.2_C3, b) Z2.2_AB2

Rys. 8.2. Sztywność styku dla średniej wartości poślizgu elementu: a) Z1.2_C3, b) Z2.2_AB2

The obtained stiffness values for the fully composite element fall within the range reported by other authors, approximately 4000 - 12000 MPa, as discussed in the literature review. Only Gremza's study [59] achieved higher stiffness values, ranging from 36000 - 54000 MPa, which can be attributed to the unique loading conditions of their specimen. The FEM analysis indicates that there are disturbances in the stress distribution at the boundaries of the analysed element. In Gremza's study, the uniform

distribution of tangential stresses resulted in higher stiffness values than those presented in this study and the works of other authors.

An analysis of the FEM model was conducted based on experimental tests to determine the stiffness. The definition of stiffness value aligns with equation (8.7). The ZS_1_C model had a stiffness value of 45 MPa/mm, equivalent to 9000 MPa. These values are nearly twice the calculated value for the entire interface at 80% load (4580 MPa) and almost three times that at 100% load (3790 MPa). This suggests that the disparity is due to the stress distribution explained in the preceding paragraph and the degradation of the interface during the test, as described by the FEM model analysis. The actual stiffness value of the tested interface exceeds the calculated value due to the reduced effective interface area. However, using this calculation method (for the entire interface) considering the element width allows for comparing the interface stiffness to the monolithicity of composite beams, as studied by other authors.

As discussed in Section 7.6.2, two finite element method (FEM) models were created with different interface stiffnesses. One model assumed an interface stiffness of 90 MPa/mm, while the other assumed 22.5 MPa/mm. The reference model defined an interface stiffness of 45 MPa/mm (Table 8.5). The impact on the distribution of shear stresses was not thoroughly examined, but rather, the tested beam's flexural stiffness. Doubling the interface stiffness resulted in a 1.9% increase in the beam's flexural stiffness. Conversely, the beam's stiffness was reduced by 3.0% in the second case. According to work [59], an interface stiffness of approximately 40 MPa/mm is necessary for the composite element to behave as a monolithic. In the tests, the interface stiffness was determined to be 22.9 MPa/mm and 42.0 MPa/mm after converting the stiffness from the entire composite's width to the beam's width. Both the experimental and FEM model values met the requirements for interface stiffness as a monolithic element. The interface stiffness at 80% of the maximum force (F_{max}) after conversion to the width of the element was 13.9 MPa/mm (2780 MPa) for Z2.2_AB2 and 7.8 MPa/mm (1560 MPa) for Z3.2_CB3. These values must be considered when analyzing bending composite elements due to their lower tangential stiffness. The reduced interface stiffness resulted in significantly lower flexural stiffness and flexural cracking force, as demonstrated in the FEM models Z2_ABFEM and Z3_CBFEM in Section 7.5.1.

Table 8.5

Impact of the tangential interface stiffness K_{TT} Wpływ zmiany sztywności stycznej styku K_{TT}

Model	Tangential stiffness K_{TT} , MPa/mm	Tangential stiffness $k_{\tau,\varepsilon}$, MPa	Bending stiffness (at ~100 kN) $\text{kN}\cdot\text{mm}^2$	Difference related to ZS_1_C %
ZS_1_C	45	9000	3243	-
ZS_9_C $K_{TT}22.5$	22.5	4500	3145	-3.0%
ZS_10_C $K_{TT}90$	90	18000	3306	1.9%

The influence of interface stiffness on shear stress distribution in beams has been analysed in Gremza [89] and Halicka's analyses [66]. The author argues that there is a significant difference between an interface with a stiffness of 1000 MPa and one with a stiffness of 10000 MPa, suggesting that a minimum threshold of 10000 MPa should be considered for a monolithic-like interface. This allows for the omission of interface stiffness in calculations, treating the interface as a monolithic element. The tested interface of the Z1.2_C3 element exhibited lower stiffness, even after correcting for the flat elements. Figure 8.2a demonstrates that as the load increased, the interface stiffness degraded, initially exceeding 10000 MPa and eventually dropping to approximately 14500 MPa and then halving. This highlights the need to analyze not only the interfaces before and after cracking along the component's length but also the stiffness of the multiplanar interfaces resulting from local cracking at the section's height. The occurrence of delaminated zones, which refer to slippage along the length of the element, is described in Section 7.3 through finite element method (FEM) analyses. However, it is important to consider the influence of the length of the test element and the configuration of the test stand on the obtained stiffness results. Conducting tests on longer elements would reduce the impact of local disturbances and result in higher interface stiffness. This, however, would require further research or testing of the cross-sections using a test stand consistent with Gremze's design.

The impact of tangential stiffness based on FEM analysis is presented and discussed in the context of simplified beam models ZS_8_AB and ZS_9_CB. The mechanism of interface degradation, as described, is justified by the distribution of tangential forces presented in Gremza's analyses. It is observed that for interfaces with low stiffness, the highest delamination forces occur at the midpoint between the force and the support. Conversely, the distribution of shear forces is more uniform for interfaces with higher stiffness. Notably, this conclusion contradicts the findings of the FEM direct shear test

results, where a more uniform distribution of stresses was obtained for less stiff interfaces (Section 7.3.3). However, it is important to consider the differences in test configurations (direct shear testing versus beam element analysis) and the influence of element geometry. Comparisons of stress distribution and stress redistribution between tests on beam elements and direct shear tests are not directly applicable.

Summarising, based on the findings from the literature and FEM analyses, the stiffness of the Z_C series was close to that of the interfaces. Therefore, the impact of tangential stiffness can be disregarded when calculating the flexural elements. The FEM analyses showed less than 2% difference in the flexural stiffness of the element for interfaces with doubled stiffness. According to the analyses in the papers discussed above, the effect of interface stiffness (as determined by the tests) can result in a difference in shear stress distribution in the end zones of ~3-4% [66].

8.4. Conclusions and discussion on the research program

The analysis of both experimental and numerical studies has revealed the complex behaviour of interfaces within the examined elements. It is important to note that local interface cracking does not indicate the composite beams' failure. The failure mechanism of composite elements consists of several stages. The initial stage is characterized by local cracking of the interface between flexural cracks, which does not impact the flexural stiffness of the beam. Subsequently, the second stage leads to the development of cracking at the interface, including between diagonal cracks. Local slippage at the interface in stage two still does not result in a loss of beam stiffness. However, local cracking reduces the effective stress transfer length at the interface. As diagonal cracks develop, the area narrows to a short distance at the support. In the third stage, the interface is cracked up to the support axis, resulting in a decrease in stiffness, but the beam still does not behave as if it were composed of two separate elements. Only cracking of the interface up to the face leads to slippage along the entire length, which must be considered as interface failure.

The failure force of the interface is influenced by both the applied load and the extent of cracking in the element caused by flexural and diagonal cracks. Numerical analysis has shown that different failure force values can be obtained in bent beams with the same interface parameters. Three numerical models were created: 1) a basic model accurately representing the test with high convergence, 2- a simplified model using a linear-elastic model for the precast and concrete topping, and 3- a model with the

concrete topping subject to cracking. These models provided a direct conclusion about the dependency of the interface failure force on the element's cracking. This conclusion aligns with the postulates presented by Halicka regarding the calculation of composite elements. Despite the demonstrated degradation model of interface failure, including the formation of successive diagonal cracks, one has to agree on the principle of designing only those elements in which the force cracking the interface exceeds the force of the diagonal cracks.

In this study, a 500 mm section of anchorage and prestressing force dispersion was left outside the support axis due to the use of a precast prestressed element. This section had an impact on the element's behaviour, allowing the interface's degradation beyond the support axis. As a result, the element exhibited partially composite behaviour, with a stiffness greater than the sum of its constituent elements' flexural stiffness. The numerical model used in the study demonstrated the significance of the beyond support axis section concerning interface failure, particularly in cases of significant deformation and cracking of the beam between the force and the support. Simplified models were used to estimate that the off-axis section of the support contributed to an 8% increase in the interface failure force. The section of beam anchorage beyond the support axis represents an area of tangential stress redistribution, the more significant, the shorter the interface section between force and support remains due to the development of diagonal cracks. This finding aligns with previous research, such as Gromysz's study, which highlighted the potential for composite behaviour in elements when their strains are agreed at their ends. In Gromysz's research, reinforcement provided this compatibility, while in the presented study, the beam section beyond the support axis fulfils this condition. However, this effect should be seen as an additional "undisclosed" safety margin resulting from the actual occurrence of the elements as a larger whole, such as slabs, rather than as separate beams, as in this research. For this reason, it is not suggested to add a factor to increase the resistance of the interface depending on, for example, the width of the tie beam or other structural elements that may constrain strains in the concrete topping.

An additional level of complexity in the analysed elements results from the existence of interfaces on the vertical and horizontal surfaces. As indicated by the numerical models and supported by the literature review on analytical models, the distribution of shear stresses in the beams is non-uniform in height. This distribution alters as flexural and diagonal cracking occurs. The interface is also subject to additional axial forces due to the cross-sectional geometry. Consequently, interface surfaces located at different heights of the components transmit tangential stresses with varying values. This leads

to a degraded failure model of the interface, where surfaces weakened by axial tensile forces crack before reaching the maximum failure force of the interface. These surfaces do not effectively contribute to stress transfer in the subsequent stages of the beam. From a design perspective, these surfaces can be considered ineffective and should not be considered in the interface resistance. The cracking force at the interface is not a simple sum of the vertical and horizontal surfaces, as demonstrated by the numerical models Z2_11_S and ZS_12_TB when compared with model ZS_1_C. The stress analysis performed on the interface (Table 8.2) proved that the effective interface area needs to be adjusted. Calculations adjusted for the effect of the beam length beyond the support axis and ineffective vertical surfaces exhibited a convergence of the obtained test results for the different beams in terms of the interface stresses obtained. Analyzing interface stresses solely based on the cracking force of the interface (considering the entire width) without numerical analysis could lead to the conclusion that vertical interfaces are the most effective. Such conclusions would be incorrect when evaluating transferred contact stresses per unit area. The analyses that were conducted need to be expanded with additional investigations of the interface shape, including the inclination of the surface on the development of axial tensile forces. The literature studies in the areas mentioned above remain limited in number, and their level of complexity is often inadequate.

The complex geometry of the analyzed beams can result in inefficient interface utilisation. However, in a different configuration, it can lead to a significant increase in the cracking force. If the analyzed beam is part of a larger structure, such as a slab, the vertical surfaces will be confined (restrained). However, the experimental investigations did not include slab element tests. Nevertheless, the tests and numerical analyses performed can provide some insight in this regard. The direct shear tests explicitly proved the interface opening at the elastic stage, resulting in an outward displacement of the precast concrete and cracking at the corners of the concrete cross-section. The same effect was observed on beam elements. Such behaviour is consistent with the theory that the development of a crack at an interface is associated with both displacement at the interface and its opening, and their relationship depends on the degree of roughness of the interface. Similar behaviour is supported by the studies presented in the literature review. The described effect also occurs for an interface through vertical surfaces (e.g., plates) for steel-concrete or composite-concrete interfaces. The effect of the concrete restraining the vertical interface and the opening due to the roughness of the surface-confined by the adjacent elements could significantly contribute to the load-bearing capacity of the interface in composite elements.

The numerical analysis conducted on the beam, which had lateral supports to simulate confinement (such as a slab), revealed the development of significant pressure stresses on the vertical surfaces. The absence of an interface opening at the elastic stage in the material model implies that the resulting contact force is solely a result of the cross-sectional geometry of the test element. The Z5_SFEM_SC model demonstrated a load increase of over 30% compared to the model without lateral support while maintaining an unslipped interface. This highlights the potential that can be achieved with an appropriate element geometry combined with a rigid slab. It can be assumed that a properly shaped slab surrounding the element or adequately shaped reinforcement could take up and transmit strains caused by interface opening, particularly in the case of horizontal interfaces that affect adjacent elements. The analysis of this effect and the ability to accommodate strains resulting from the opening of vertical interfaces is another comprehensive research program that requires experimental studies. Accurately understanding and describing the impact of interface opening during the elastic stage of slab-embedded elements may lead to further recommendations regarding the geometry of adjacent elements or the slab's reinforcement. Therefore, it appears possible to formulate a factor to increase the resistance of vertical interfaces in slab-embedded elements. Section 9 provides an initial approach to addressing this effect by establishing geometric relationships for determining effective interface areas.

The comparative analysis of the test results revealed significantly higher values for the force that cracks the interface compared to the standard calculations. This difference can be attributed to two main factors. Firstly, the coefficient of surface preparation varies significantly within a single Eurocode standard package (PN-EN 15037-1:2011 vs PN-EN 1992-1-1:2008), even for similar types of surfaces. Secondly, there are discrepancies in the model used to calculate the shear force and, consequently, the stresses at the interface. The standard models differ from the calculations based on the laminar construction mechanics. Depending on the calculation scheme used, surface factors of 0.77 (PN-EN 1992-1-1:2008) or 0.58 (Eq. 8.1) were obtained. These values are nearly three to four times higher than those for smooth surfaces and twice as high as predicted by the standard for beam-and-block slabs, which is the only one to include elements with vertical interfaces. Considering the above standard comparisons and the described effects for vertical surfaces, further research is required to determine appropriate design rules and geometric requirements for calculating and designing multiplanar interface elements.

The examination of shear resistance due to diagonal cracks was not the primary focus of the study, but it is closely connected with the tests conducted. The analyses were

limited to comparing the values of diagonal crack force with those obtained from the tests. At this stage, there was already a 50% difference between the calculations based on the standard model and the test results. The precast elements tested did not have any shear reinforcement, and the reinforcement used in the concrete topping did not extend to the prestressing strands. Therefore, the diagonal cracking force is assumed to correspond to the shear failure force, which is inconsistent with the observed data. The extensive research presented in this study and the results of the FEM models, which converge on the values of diagonal cracking and failure force, provide a strong starting point for the analysis of analytical models. The development of an analytical model reflecting the actual failure force representing the combined load capacity of the precast concrete topping and the effect of the applied reinforcement could serve as a point for further analysis in another study.

9. DESIGN RECOMMENDATIONS

9.1. Standard modification proposal – PN-EN 1992-1-1:2024

Based on the literature review, research performed, FEM calculations and analysis, it is proposed to expand the latest edition of PN-EN 1992-1-1:2024 and PN-EN 15037-1:2008 to include information relevant to the design of elements with multiple interfaces.

The first of the proposals for an addition arise from the consequences of adopting the standard for calculating interface stresses and resistance according to Mohr-Coulomb's theory. On this basis, it seems necessary to add the procedure for elements with vertical and horizontal interfaces, in which additional pressure from normal forces due to uniformly distributed loading is considered. It is reasonable to provide guidelines combining two design conditions with the logical disjunction ‘or’ for the calculation of interfaces without and with the consideration of the friction and uniform normal force component. According to the principles of the Mohr-Coulomb theory presented in the review and the description of the material model, the development of stresses that crack the interface with normal force and cohesion will occur when the displacement (slip) is greater than for interfaces with cohesion only (Fig. 7.4b). From the above relationship, it follows that it is not possible for the two planes to cooperate with a significant contribution from the normal force due to the previous failure of the interface with only the cohesion component. On this basis, it is proposed to give an additional guideline related to checking only unreinforced interfaces with vertical and horizontal planes (formula 9.1).

$$\tau_{Edi} \leq \tau_{Rdi} = \begin{cases} \tau_{Edi} = \frac{\beta_{new} V_{Ed}}{z b_{i,a}} \leq \tau_{Rdi} = c_{v1} \frac{\sqrt{f_{ck}}}{\gamma_c} \\ or \\ \tau_{Edi} = \frac{\beta_{new} V_{Ed}}{z b_{i,b}} \leq \tau_{Rdi} = c_{v1} \frac{\sqrt{f_{ck}}}{\gamma_c} + \mu_v \sigma_n \end{cases} \quad (9.1)$$

where:

$b_{i,a}$ – the width of the interface according to Fig. 9.1a (without normal force)

$b_{i,b}$ – the width of the interface according to Fig. 9.1b (with normal force)

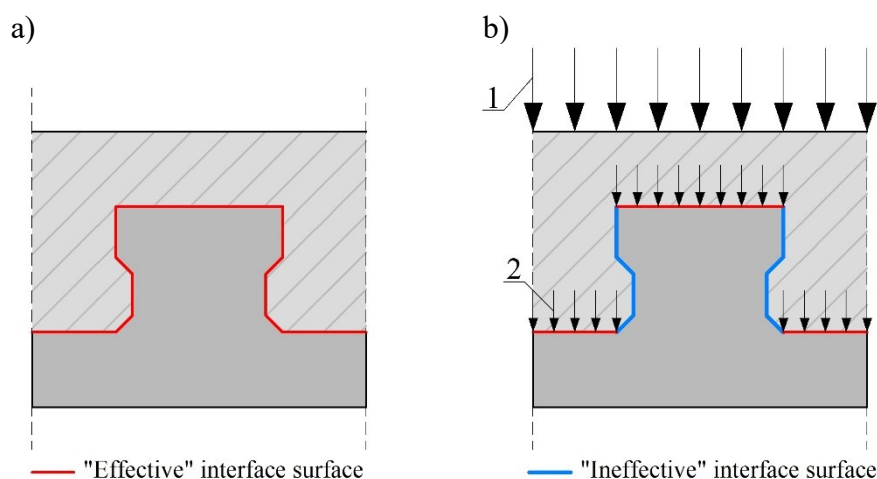


Fig. 9.1. Proposed concept for determining the unreinforced interface area A_i : a) without compressive stress, b) with permanent compressive stress; 1- external axial force, 2- distribution of axial force on the interface planes

Rys. 9.1. Proponowana koncepcja określania niezbrojonej powierzchni zespolenia A_i : a) bez naprężeń ściskających, b) ze stałym naprężeniem ściskającym; 1- zewnętrzna siła osiowa, 2- rozkład siły osiowej na płaszczyznach zespolenia

It is suggested that an additional note be added after the current point (7) – PN-EN 1992-1-1:2024 section 8.2.6 - indicating that there are additional standards on surface coefficients and the design and calculation of elements with a multiplanar interface in the scope of PN-EN 13747+A2:2011 and PN-EN 15037-1:2011 that can also be applied to individually designed and constructed elements.

The second proposed supplement concerns PN-EN 15037-1:2011 for Annex C and PN-EN 13747+A2:2011 for Annex D. The guidelines and figures below should be seen as an introduction to the discussion on changes in the scope of the standards and not as complete proposals. Discussed aspects require further research as described in sec. 9. For EN 15037-1:2011, it is proposed to include Fig. 8.1 in Figure C.1 (numbering of the standard) and the description as C.2 “Interface with axial force” before the current section C.2 on reinforcement. For PN-EN 13747+A2:2011, it is proposed to include Fig. 8.3, the description as section D.2 “Interface with axial force” before the current section D.2 on reinforcement.

The proposal only identifies the scope of points C.2 and D.2, which requires to be completed and expressed in the "language" and principles of the standard. The stated guidance can be divided into two main categories. The first relates to determining the effective interface area in beam-and-block slabs and composite slabs with infill not covering the rib area. The current distance-related guidelines (>20 mm, $>1.2 d_g$) are proposed to be replaced by a criterion based on the angle between the edge of the precast

element and its base. A straight line defined by the angle that does not intersect "flexible" elements such as hollow blocks or lightweight infill allows the height of vertical surfaces to be determined, which can be included in the interface calculations. Determination of the value of the alpha angle will be possible after additional research. A suggested range for determining the value should be between 26.6° and 45° . The calculation should not include the area defined below the straight line at the alpha angle. The basis for this is the outward pushing effect of the concrete topping observed in the tests. Determination of the permissible vertical area according to Fig. 9.2 and Fig. 9.3(1) will provide sufficient horizontal stiffening of the vertical surfaces to prevent the effect described in the tests. In the case under consideration, the slab must provide sufficient stiffening with the walls and the ring beam. As a result of further research, proposing an alternative approach with reinforcing concrete topping may be possible.

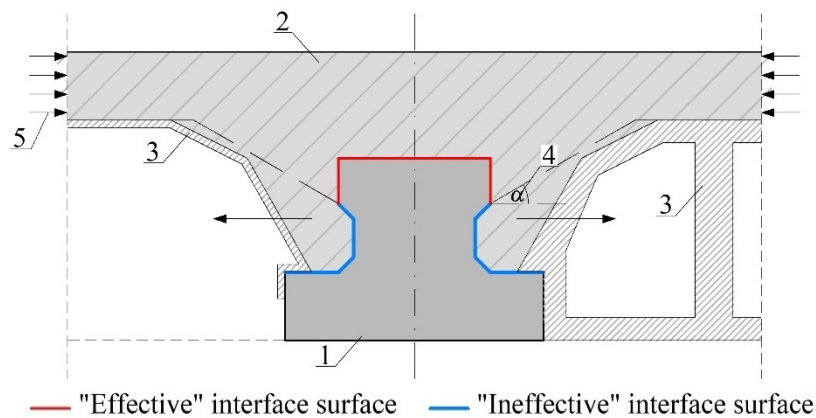


Fig. 9.2. Proposed concept for determining the interface area: 1- precast, 2- concrete topping, 3- block or light infill, 4- the angle of the line, 5- lateral restraint

Rys. 9.2. Proponowana koncepcja określania powierzchni zespolenia: 1- prefabrykat, 2- nadbeton, 3- pustak lub lekkie wypełnienie, 4- kąt nachylenia prostej, 5- sztywna tarcza stropowa

Four additional situations are proposed for consideration for composite slabs, which should be simplified to a single guideline based on further research. Possible situations requiring additional rules for determining the interface area include slab configurations with lightweight infill occurring between the ribs in every second pair of ribs. This solution is often applied in current precast elements. Based on experimental analysis and FEM, it will be necessary to establish rules related to the design of the rib to allow it to be assumed as a rigid element within the composite floor slab (in a horizontal plane). Assuming the rib to be flexible and therefore subject to deflection and cracking due to concrete topping pushing out will result in the vertical surfaces of the rib not being

considered if there are flexible infills on the other side of the rib (Fig. 9.3(3-4)). If the rib meets the geometrical requirements and is a “rigid element”, it will be possible to consider its vertical surfaces in the interface calculations. If the vertical surface is also allowed in situation 3, the rib could become flexible once the horizontal surfaces are cracked. Consequently, there would be a loss of effective constraint off the vertical surfaces, resulting in cracking of all surfaces. This approach could be on the unsafe side. Analysis of such situations requires further research. In the case of situation 4, if the diagonal cracking force is lower than the interface resistance or the interface resistance with shear reinforcement, the space between the ribs (Fig. 9.3(4)) in the composite slab (for ribs close to each other) requires additional consideration. In the case described above, such space should not be included due to local cracking and separation from the slab or reinforced with vertical reinforcement. This issue may provide another starting point for research investigation.

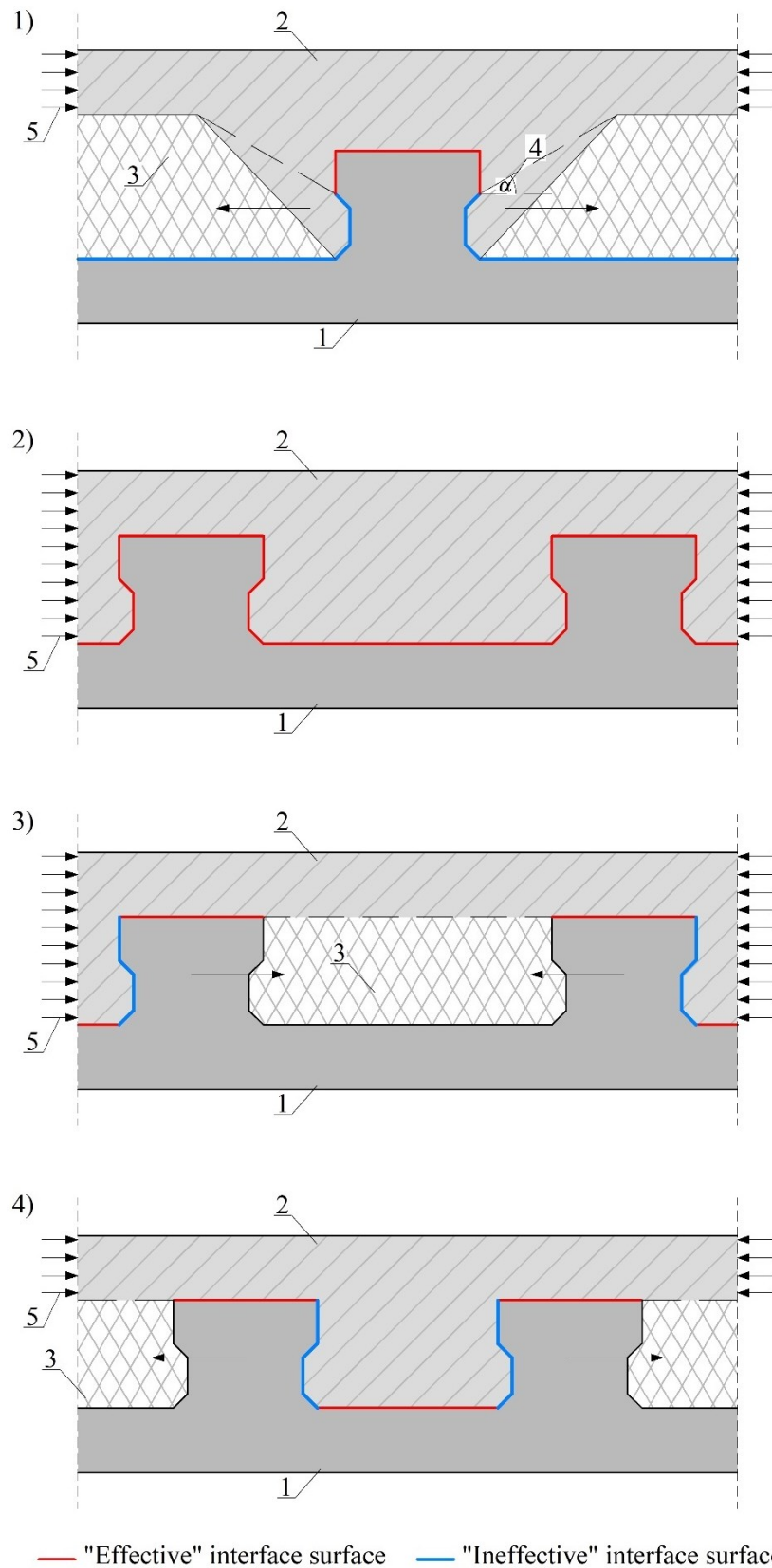


Fig. 9.3. Proposed concept for determining the interface area: 1- precast, 2- concrete topping, 3- light infill, 4- the angle of the line, 5- lateral restraint

Rys. 9.3. Proponowana koncepcja określania powierzchni zespolenia: 1- prefabrykat, 2- nadbeton, 3- lekkie wypełnienie, 4- kąt nachylenia prostej, 5- sztywna tarcza stropowa

An additional general comment concerns the scope of the standards relating to precast elements. The interface parameters given in PN-EN 15037-1:2011 by execution technology should also be included in PN-EN 13747, which, in the introduction in Fig. 2 (numbering of the standard), clearly shows the possible shapes of ribs within the scope of the standard in accordance with the shapes shown in the standard for beam-and-block slabs. Looking beyond the scope of this paper, it is the opinion of the author that the precast standards, including the formation and calculation of elements such as PN-EN 1168 (hollow core slabs), PN-EN 13747 (composite slabs), PN-EN 15037 (multi-storey slabs) need to be harmonised and agreed regarding interface parameters, deflection calculations, fire resistance and other guidelines. The above is a general comment on the EN series of standards for precast, which require unification and realignment with the basic standards of the PN-EN 199X series but leave evident scope for the detailing and changes allowed in standards dedicated to specific types of precast.

The possibility of including an additional factor in the current PN-EN 1992-1-1:2024 standard to increase the surface parameters of unreinforced interfaces for naturally rough surfaces without treatment could be discussed. A convention similar to the provisions as in clause 8.2.6(7) for increasing the c_{v2} parameter by 1.2 for slab structures could be proposed. Based on the literature review and own research, it is suggested that a factor for the c_{v2} parameter could be applied while ensuring the required level of surface preparation and roughness without using methods leading to micro-cracking. Determining the coefficient value requires safety analyses and a thorough review of existing research, as in the publications presented in the literature review [56].

9.2. General design recommendations

After verification and additional research, the above recommendations could cover cases that do not require additional calculations and analyses by standard users. For elements that do not meet the angle or lateral stiffening condition, it is possible to perform analyses based on experimental investigations and FEM modelling. In particular, such analyses should be carried out for new shapes of precast elements that are not explicitly addressed in the standard and for new materials. Particular attention should be paid to the potential occurrence of normal tensile forces at the interface due to the shape of the precast element. Another point of analysis should be the possible consideration of the effect of mutual stiffening of vertical surfaces through adjacent elements or appropriate concrete topping geometry.

The significant differences in the tensile strength of the interface shown in the example of the precast component tested and the consequent possible values for the surface coefficient concerning the current standard provisions suggest that a set of tests should be carried out to determine the exact parameters of the interface. Such tests should include precast units to determine the roughness of the interface resulting from the manufacturing process. It is important to note that different interface strengths can be obtained for the same roughness values determined using the sand path method solely due to variations in production processes. Before proceeding with computational analyses, attention must be given to the roughness development process. When mechanical treatments are necessary, a lower strength can be expected due to microcracking. It is recommended to strive for "natural" roughness due to technological processes.

10. FINAL CONCLUSION AND FUTHER RESEARCH AREA

This doctoral thesis focuses on the study of composite concrete elements with a multiplanar unreinforced interface. Elements with such an interface have been produced since the beginning of precast concrete and now constitute a significant part of the products sold. Despite this, the analysis of the interface behaviour in such elements has not received adequate recognition. Existing studies identified in the literature review primarily focus on isolated, small-scale specimens or flat single-plane interfaces. Only a few studies have addressed the interface behaviour of elements with multiple planes. The lack of a comprehensive analysis of the flexural behaviour of these elements, as well as computational methods that consider their unique characteristics, necessitated an experimental research program and numerical analysis to expand state of the art.

Based on the literature review, five main areas and objectives were identified at the beginning of the research program, along with several sub-areas that need to be developed to expand the state of the art related to the behaviour and analysis of the multiplanar unreinforced interface:

1. Behaviour of element with multiplanar unreinforced interface subjected to direct shear test.
2. Flexural behaviour of elements with multiplanar unreinforced interface.
3. Development of numerical models to represent the tested elements.
4. Recommendations for the design and calculation of the multiplanar interface.
5. Development of a foundation for further analyses on full-scale elements including composite slabs consisting of multiple elements with a multiplanar unreinforced interface.

To achieve the stated objectives, a programme of experimental testing was carried out in direct shear, 4PBT and 3PBT. FEM analyses and analytical calculations complemented the research. The main conclusions of the study can be summarised in the following brief points:

1. Behaviour of element with multiplanar unreinforced interface subjected to direct shear test.
 - 1.1. The interaction of the interface surfaces within a single element is limited due to the different resistances of the selected surfaces subjected to axial compressive and tensile actions.
 - 1.2. The element's geometry may cause the development of undesirable axial forces that reduce the resistance of the interface.
 - 1.3. Some non-linearity characterised the tested elements before cracking of the interface, affecting the redistribution of stresses at the interface between the planes of the composite.
2. Flexural behaviour of elements with multiplanar unreinforced interface.
 - 2.1. As in the direct shear test, the effective interaction of all interface planes was not achieved in the flexural element test. The element's geometry subjected the vertical surfaces to axial tensile forces.
 - 2.2. Diagonal cracking has a decisive impact on the effective interface length, which confirms the literature review's conclusions.
 - 2.3. Local cracking of the interface is not sufficient to indicate interface failure. The effect of local cracking on the behaviour of the tested beams was limited, only cracking of the interface along the length of the element resulted in a brittle decrease in stiffness.
 - 2.4. The presence of a beyond (off-axis) support beam length affects the interface resistance and behaviour of the beam, including its flexural stiffness. This effect should be considered as an additional safety margin.
 - 2.5. The concentrated load application does not affect the resistance of the interface due to the friction stresses induced. The effect of friction from the concentrated load only slightly impacts the stiffness of the flexural beam when the interface is cracked.
3. Numerical models that closely represent experimental studies can be developed.
 - 3.1. Based on direct shear tests, the interface parameters that also ensure the convergence of bending models can be correlated with experimental tests.
 - 3.2. The Mohr-Coulomb model of the interface does not fully reproduce the openings, which results from its roughness.
 - 3.3. Numerical models with a Mohr-Coulomb interface capture the interface cracking forces, diagonal cracks, flexural cracking, and failure pattern of a fully composite element and elements with limited interface.

- 3.4. The completed models allow the analysis to be extended to models with different geometries and selected modified material parameters, as shown in the ZS series numerical models.
4. FEM modelling makes it possible to isolate phenomena and their influence on the behaviour of the interface.
 5. Based on the studies carried out, a preliminary proposal for modifying the standard provisions and recommendations for design is presented. However, it should be noted that the rules for the interface between the PN-EN 199X series and the precast standards need to be aligned. There is a need for a broad discussion on changes to the interface parameters and guidelines for the design and calculation of elements with vertical interfaces.

The research and analysis conducted in this study provide an answer to the stated thesis (Table 10.1). Due to the complexity of the behaviour of multiplanar interfaces, an answer cannot always be given unambiguously. Thesis 1 has been positively verified through numerical analyses and experimental results. Thesis 2 has also been verified positively. The non-linear characteristic results mainly from material properties in tension and the degradation failure mechanism of the interface, which is related to Thesis 1. Further research is needed for Thesis 3 concerning vertical surfaces. Regarding the tested elements, the thesis has been negatively verified. However, if further tests on slab elements are conducted based on preliminary analyses of FEM models, the thesis can be confirmed. Nevertheless, the thesis and research need to be detailed with the range of element types analysed. Thesis 4 is partially confirmed. The element's interface over a significant length beyond the support axis allows the beam to behave as a composite. The flexural stiffness, however, is reduced and differs from that of a monolithic beam. The partial interface cooperation along the off-axis length of the support provides an additional safety margin, as described.

Table 10.1

Verification of the thesis statement of the dissertation
Weryfikacja postawionych tez w pracy

Number	Statement	Verification
1	The cooperation between the interface planes in the composite element dependent on the position at the height of the cross-section.	True
2	Multiplanar unreinforced interfaces responded non-linearly prior to slip failure.	True
3	The increased shear resistance of the vertical interface planes results from the restraint effect.	Partially confirmed
4	The lengthening of the composite beam beyond the support axis allows the quasi-monolithic behaviour despite slip in the interface up to support axis.	Partially confirmed

Based on the research conducted, the FEM analyses and the literature review presented, further research is planned in the area of elements with multiplanar interfaces. The proposed further research areas:

1. Direct shear tests with applied horizontal force control of concrete topping in the range of different strain levels. The research will be possible on a modified stand with force control based on displacement analysis and live strain from the image acquired from the ARAMIS system.
2. Research on beam elements with lateral concrete topping constraint.
3. Research on slab elements consisting of several ribs.
4. FEM analyses extended to the correlation of the residual force after failure and failure image and cracking of the elements. FEM analyses extended to include extensive material models of the interface considering deformations of the interface in the elastic range in both slip and opening representation due to roughness.
5. Analyses of the effects of shrinkage and creep on the behaviour of the interface, including the effect of multiplanar interface constraint.
6. Research regarding possible methods of determining interface delamination for multiplanar interface elements where not all planes are seen from the side of the element.

Regarding point 6, during the PhD, an attempt was made to determine interface local cracking on beam elements cut into 20 cm sections. Experiments were conducted with UV contrast, taking photographs without (Fig. 10.1a) and with a blue light filter (specific wavelength range). The pictures taken this way were subjected to graphic processing based on the developed filter algorithm (Fig. 10.1b). However, the tests were not fully completed due to the labour-intensive preparation of the elements, which involved pressure washing, applying UV contrast to the surface, and setting up the elements on the photographic stand. After the tests, the beam elements were cut into 12 sections, giving a total of 240 elements measuring 20 x 20 x 16.5 cm and weighing 16.5 kg per element. There were also some trials to identify local cracking during tests, using ultrasonic methods, but the results were unsatisfactory. Alternative approaches, such as thermographic identification, can be considered [37].

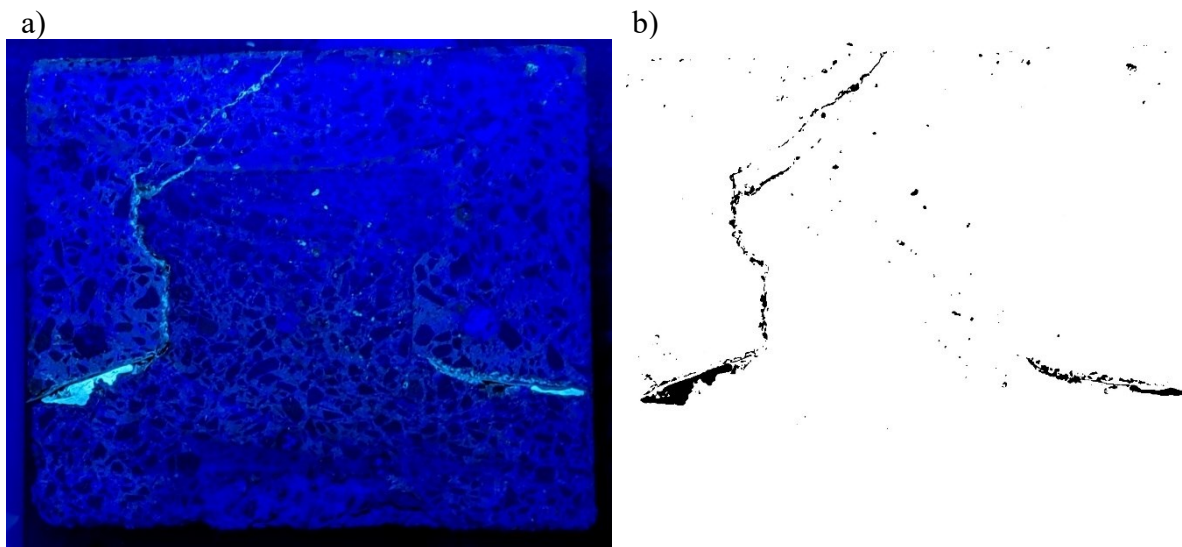


Fig. 10.1. Attempts to determine cracked areas based on UV contrast on the example of element type Z10_TS

Rys. 10.1. Próby określania obszarów zarysowany na bazie kontrastu UV na przykładzie elementu typu Z10_TS

The research presented in this thesis represents part of a broader programme covering several issues related to prestressed ribbed slab elements. The work carried out by the research group has resulted in several papers related to the interface [154–156,158], as well as two monographs on the market and design of precast slab systems [40,86]. Ongoing and planned research includes issues related to the behaviour of beams with multiplanar interface, not only focusing on the interface:

1. The behaviour of unreinforced in transverse direction slabs in four-edge support condition [38,152,153,157,159,160].
2. Analysis of the behaviour of shear-key at the longitudinal edges of slabs formed from the ribs.
3. Analysis of the shear resistance, including composite elements' cracking and failure forces with precast prestressed concrete.
4. Investigations into the effect of partial fixed and methods of determining the bending moment corresponding to partial fixed of one-way slabs supported on four edges.

BIBLIOGRAPHY

Publications

1. Adawi A., Youssef M.A., Meshaly M.E.: Experimental investigation of the composite action between hollowcore slabs with machine-cast finish and concrete topping. „Engineering Structures”, Vol. 91, 2015, doi:10.1016/j.engstruct.2015.02.018.
2. Afefy H.M., Kassem N.M., Taher S.E.-D.F.: Capacity magnification by imposing composite action of precast concrete flanged girders. „KSCE Journal of Civil Engineering”, Vol. 22, 2018, doi:10.1007/s12205-017-1563-0.
3. Ahmed I.M., Tsavdaridis K.D.: The evolution of composite flooring systems: applications, testing, modelling and eurocode design approaches. „Journal of Constructional Steel Research”, Vol. 155, 2019, doi:10.1016/j.jcsr.2019.01.007.
4. Ajdukiewicz A., Węglorz M., Kliszczewicz A.: Experimental study on effectiveness of interaction between pre-tensioned hollow-core slabs and concrete topping. „Architecture Civil Engineering Environment”, Vol. 1, 2008.
5. Al-Sherrawi M.H., Mahmoud K.S.: Shear and moment strength of a composite concrete beam. „International Research Journal of Advanced Engineering and Science”, Vol. 3, 2018.
6. Araújo D.L., El Debs M.K.: Strength of shear connection in composite bridges with precast decks using high performance concrete and shear-keys. „Materials and Structures”, Vol. 38, 2005, doi:10.1007/bf02479342.
7. Austin S., Robins P., Pan Y.: Shear bond testing of concrete repairs. „Cement and Concrete Research”, Vol. 29, 1999, doi:10.1016/S0008-8846(99)00088-5.
8. Bentz D.P., De La Varga I., Muñoz J.F., et al.: Influence of substrate moisture state and roughness on interface microstructure and bond strength: slant shear vs. pull-off testing. „Cement and Concrete Composites”, Vol. 87, 2018, doi:10.1016/j.cemconcomp.2017.12.005.
9. Beushausen H., Alexander M.G.: Bond strength development between concretes of different ages. „Magazine of Concrete Research”, Vol. 60, 2008, doi:10.1680/macr.2007.00108.
10. Beushausen H., Höhlig B., Talotti M.: The influence of substrate moisture preparation on bond strength of concrete overlays and the microstructure of the OTZ. „Cement and Concrete Research”, Vol. 92, 2017, doi:10.1016/j.cemconres.2016.11.017.
11. Birkeland P.W. and Birkeland, H.W.: Connections in precast concrete construction. „Journal of the American Concrete Institute”, Vol. 11, 1966.

12. Bissonnette B.: Bonded Cement-Based Material Overlays for the Repair, the Lining or the Strengthening of Slabs or Pavements: State-of-the-Art Report of the RILEM Technical Committee 193-RLS. 2011.
13. Bonaldo E., Barros J.A.O., Lourenço P.B.: Bond characterization between concrete substrate and repairing SFRC using pull-off testing. „International Journal of Adhesion and Adhesives”, Vol. 25, 2005, doi:10.1016/j.ijadhadh.2005.01.002.
14. Cavaco E., Camara J.: Experimental research on the behaviour of concrete-to-concrete interfaces subjected to a combination of shear and bending moment. „Engineering Structures”, Vol. 132, 2017, doi:10.1016/j.engstruct.2016.11.041.
15. Chilwesa M., Minelli F., Reggia A., et al.: Evaluating the shear bond strength between old and new concrete through a new test method. „Magazine of Concrete Research”, Vol. 69, 2017, doi:10.1680/jmacr.16.00327.
16. Cho K., Shin Y.S., Kim T.: Effects of half-precast concrete slab system on construction productivity. „Sustainability (Switzerland)”, Vol. 9, 2017, doi:10.3390/su9071268.
17. Colajanni P., Mendola L.L., Monaco A.: Review of push-out and shear response of hybrid steel-trussed concrete beams. „Buildings”, Vol. 8, No.10, 2018, doi:10.3390/buildings8100134.
18. Costa H., Carmo R.N.F., Júlio E.: Influence of normal stress and reinforcement ratio on the behavior of LWAC interfaces. „Construction and Building Materials”, Vol. 192, 2018, doi:10.1016/j.conbuildmat.2018.10.116.
19. Daneshvar D., Behnood A., Robisson A.: Interfacial bond in concrete-to-concrete composites: a review. „Construction and Building Materials”, Vol. 359, 2022, doi:10.1016/j.conbuildmat.2022.129195.
20. Dauner H. -G.: Techniken zum bau der fahrbahnplatte bei verbundbrücken. „Stahlbau”, Vol. 71, 2002, doi:10.1002/stab.200201990.
21. De La Varga I., Muñoz J.F., Bentz D.P., et al.: Grout-concrete interface bond performance: effect of interface moisture on the tensile bond strength and grout microstructure. „Construction and Building Materials”, Vol. 170, 2018, doi:10.1016/j.conbuildmat.2018.03.076.
22. Derkowski W.: Innowacje w stropach betonowych. „Wppk”, 2019.
23. Derkowski W.: Badania zespolenia między prefabrykowaną płytą kanałową a nadbetonem. „Materiały Budowlane”, Vol. 1, 2016, doi:10.15199/33.2016.09.42.
24. Derkowski W.: New solutions for prefabricated floor slabs. „Cement Wapno Beton”, Vol. 2019, 2019, doi:10.32047/CWB.2019.24.5.4.
25. Derkowski W., Kańka S.: Kompleksowe badania stropów gęstożebrowych na belkach strunobetonowych. „Materiały Budowlane”, 2013.
26. Derkowski W., Kańka S.: Comprehensive research on pretensioned beam-and-block floor systems. „Materiały Budowlane”, Vol. 3, 2013.
27. Derkowski W., Skalski P.: New concept of slimfloor with prestressed composite beams. „Procedia Engineering”, Vol. 193, 2017, doi:10.1016/j.proeng.2017.06.201.
28. Derkowski W., Surma M.: Composite Action of Precast Hollow Core Slabs With Structural Topping. „Technical Transactions”, Vol. 3-B, 2015, doi:10.4467/2353737XCT.15.159.4334.

29. Derkowski W., Surma M.: Prestressed hollow core slabs for topped slim floors – theory and research of the shear capacity. „Engineering Structures”, Vol. 241, 2021, doi:10.1016/J.ENGSTRUCT.2021.112464.
30. Derkowski W., Surma M.: Badania sprężonych stropów gęstożebrowych. In Proceedings of the Konferencja Naukowo-Techniczna KONSTRUKCJE SPREŻONE KS2012; 2012; 2012.
31. Derkowski W., Surma M.: Pretensioned beam-and-block floor systems - real scale tests. „Technical Transactions. Civil Engineering”, Vol. R. 109, z., 2012.
32. Derkowski W., Walczak R.: Effect of shear span-to-depth ratio on posttensioned concrete crane beams shear capacity. „MATEC Web of Conferences”, Vol. 323, 2020, doi:10.1051/matecconf/202032301019.
33. Dias-Da-Costa D., Alfaiate J., Júlio E.N.B.S.N.B.S.: FE modeling of the interfacial behaviour of composite concrete members. „Construction and Building Materials”, Vol. 26, 2012, doi:10.1016/j.conbuildmat.2011.06.015.
34. Dias-Da-Costa D., Alfaiate J., Sluys L.J., et al.: A comparative study on the modelling of discontinuous fracture by means of enriched nodal and element techniques and interface elements. „International Journal of Fracture”, Vol. 161, 2010, doi:10.1007/s10704-009-9432-6.
35. Diógenes H.J.F., El Debs A.L.H.C., Valente I.B.: Experimental analysis of new interfaces for connections by adhesion, interlocking and friction. „Journal of Constructional Steel Research”, Vol. 110, 2015, doi:10.1016/j.jcsr.2015.03.012.
36. D.L. Araujo M.K.E.D.: Beam-slab connection in precast bridge decks with pockets filled out with high-performance concrete and shear key. „IBRACON Structural Journal”, Vol. 1, 2005.
37. Domin J., Górski M., Bialecki R., et al.: Wheeled robot dedicated to the evaluation of the technical condition of large-dimension engineering structures. „Robotics”, Vol. 9, 2020, doi:10.3390/robotics9020028.
38. Drobiec Ł., Jasiński R., Mazur W., et al.: Half precast prestressed slab research under short-term and long-term load. In Proceedings of the 10th International Conference of Advanced Models and New Concepts in Concrete and Masonry Structures (AMCM 2020), Lublin, Poland, October 21-23, 2020. Proceedings; 2020; 2020.
39. Drobiec Ł., Jasiński R., Zając J., et al.: Wstępny raport badawczy. Badania doświadczalne pasm stropowych TerivaPanel oraz S-panel.
40. Drobiec Ł., Kisiołek A., Zając J.: Teriva Panel and Konbet S-Panel Ceilings Concept, Designing, Calculation, Execution. Monografia / Politechnika Śląska Wydawnictwo Politechniki Śląskiej, Gliwice, Poland . ISBN 978-83-7880-879-4.
41. Dudziak S., Jackiewicz-Rek W., Kozyra Z.: On the calibration of a numerical model for concrete-to-concrete interface. „Materials”, Vol. 14, No.23, 2021, doi:10.3390/ma14237204.
42. Dwyer-Joyce R.S., Gonzalez-Valadez M.: Ultrasonic Determination of Normal and Shear Interface Stiffness and the Effect of Poisson’s Ratio.; Elsevier, 2003; Vol. 43, 2003.
43. Dybeł P., Wałach D.: Evaluation of the Development of Bond Strength between Two Concrete Layers. In Proceedings of the IOP Conference Series: Materials Science and Engineering; Institute of Physics Publishing, 2017; Vol. 245, 2017.

44. Espeche A.D., León J.: Estimation of bond strength envelopes for old-to-new concrete interfaces based on a cylinder splitting test. „Construction and Building Materials”, Vol. 25, 2011, doi:10.1016/j.conbuildmat.2010.09.032.
45. Fernandes H., Lúcio V., Ramos A.: Strengthening of RC slabs with reinforced concrete overlay on the tensile face. „Engineering Structures”, Vol. 132, 2017, doi:10.1016/j.engstruct.2016.10.011.
46. Franczak D., Halicka A.: Wpływ wieku betonu na nośność styku w elementach zespolonych. „Przegląd Budowlany”, Vol. R. 83, nr, 2012.
47. Franczak D., Halicka A.: Wpływ Wieków Betonu Na Nośność Styku w Żelbetowych Elementach Zespolonych. Konstrukcje Zespolone, (in:); Konstrukcje Zespolone; Uniwersytet Zielonogórski,; Vol. IX, Zielona Góra 2011 ISBN 978-83-7481-410-2.
48. Franczak-Balmas D., Halicka A.: O efekcie skali w jednorodnych i zespolonych elementach betonowych. Cz.2: badanie efektu skali w pomiarze przyczepności betonu „starego” i „nowego” metodą rozłupywania. „Cement Wapno Beton”, 2014.
49. Franczak-Balmas D.: Analiza wpływu wytrzymałości betonów składowych jako czynnika kształtującego nośność niezbrojonego styku zespolonych elementów betonowych. „Budownictwo i Architektura”, Vol. 15, 2016, doi:10.24358/bud-arch_16_154_06.
50. Frenzel M., Curbach M.: Shear strength of concrete interfaces with infra-lightweight and foam concrete. „Structural Concrete”, Vol. 19, 2018, doi:10.1002/suco.201700015.
51. Garbacz A., Piotrowski T., Courard L.: Inżynieria powierzchni betonu. Część 1. Struktura geometryczna powierzchni. „Materiały Budowlane”, Vol. 9, 2006.
52. Garbacz A., Piotrowski T., Courard L.: Inżynieria powierzchni betonu. Część 2. Wpływ obróbki na powstawanie rys. „Materiały Budowlane”, Vol. 12, 2006.
53. Gebreyouhannes E., Kishi T., Maekawa K.: Shear fatigue response of cracked concrete interface. „Journal of Advanced Concrete Technology”, Vol. 6, 2008, doi:10.3151/jact.6.365.
54. Gohnert M.: Horizontal shear transfer across a roughened surface. „Cement and Concrete Composites”, Vol. 25, 2003, doi:10.1016/S0958-9465(02)00050-1.
55. Gohnert M.: Proposed theory to determine the horizontal shear between composite precast and in situ concrete. „Cement and Concrete Composites”, Vol. 22, 2000, doi:10.1016/S0958-9465(00)00050-0.
56. Gołdyn M.: Shear capacity of the interface between concretes cast at different time in the light of experimental investigations and codes of practice. „Archives of Civil Engineering”, Vol. 68, 2023, doi:10.24425/ACE.2022.140168.
57. Gołdyn M., Krawczyk Ł., Urban T.: Przyczynek do rozważań na temat nośności elementów z uwagi na przecinanie betonu. „Journal of Civil Engineering, Environment and Architecture”, 2017, doi:10.7862/rb.2017.123.
58. Gołdyn M., Urban T.: Experimental Investigations on Interface between Ordinary and Lightweight Aggregate Concretes Cast at Different Times. „Materials”, Vol. 14, 2021, doi:10.3390/ma14071664.
59. Gremza G.: Nośność i odkształcalność połączeń zespolonych typu beton - beton. rozprawa doktorska, 2006.

60. Gromysz K.: Dissipative forces in joint surface of composite reinforced concrete floors. „Czasopismo Techniczne”, Vol. 2013, 2013, doi:10.4467/2353737XCT.14.004.1922.
61. Gromysz K.: Nonlinear analytical model of composite concrete slab free and forced vibrations. „Procedia Engineering”, Vol. 193, 2017, doi:10.1016/j.proeng.2017.06.215.
62. Gromysz K.: Verification of the damping model vibrations of reinforced concrete composite slabs. „Procedia Engineering”, Vol. 57, 2013, doi:10.1016/j.proeng.2013.04.049.
63. Gromysz K.: Distribution of forces in composite concrete slabs between the joint and the reinforcement anchored on the support. „Procedia Engineering”, Vol. 65, 2013, doi:10.1016/j.proeng.2013.09.031.
64. Grzyb K.: The Behavior of Masonry Stiffening Walls Based on the Full-Scale Research. PhD Dissertation, Silesian University of Technology, Gliwice, Poland 2023.
65. Halicka A., Franczak D.: Rozwój przyczepności między dwoma betonami w czasie twardnienia betonu. „Budownictwo i Architektura”, Vol. 5, nr, 2009.
66. Halicka A.: Studium Stanu Naprężeń i Odkształceń w Płaszczyźnie Styku i Strefie Przypodporowej Elementów Zespolonych z Udziałem Betonów Skurczowych i Ekspansywnych. Wydawnictwo Politechniki Lubelskiej, Lublin 2007. ISBN 83-7497-022-7.
67. Halicka A.: Parameters of interface between shrinkable and expansive concrete resulting from their adhesion. „Electronic Journal of Polish Agricultural Universities”, Vol. 10, 2007.
68. Halicka A.: Shear Bond Tests for Analysis of Composite Concrete Structures,.; 2005; Ustroń, Poland 2005.
69. Halicka A.: Influence new-to-old concrete interface qualities on the behaviour of support zones of composite concrete beams. „Construction and Building Materials”, Vol. 25, 2011, doi:10.1016/j.conbuildmat.2011.04.045.
70. Halicka A., Franczak-Balmas D.: O efekcie skali w odniesieniu do jednorodnych i zespolonych elementów z betonu. Cześć I. „Cement Wapno Beton”, 2013.
71. Halicka A., Jabłoński Ł.: Shear failure mechanism of composite concrete T-shaped beams. „Proceedings of the Institution of Civil Engineers: Structures and Buildings”, Vol. 169, 2016, doi:10.1680/stbu.14.00127.
72. Han S.J., Jeong J.H., Joo H.E., et al.: Flexural and shear performance of prestressed composite slabs with inverted multi-ribs. „Applied Sciences (Switzerland)”, Vol. 9, 2019, doi:10.3390/APP9224946.
73. He Z.-Q., Ou C., Tian F., et al.: Experimental behavior of steel-concrete composite girders with UHPC-grout strip shear connection. „Buildings”, Vol. 11, No.5, 2021, doi:10.3390/buildings11050182.
74. Henin E., Morcou G., Tadros M.K.: Precast/prestressed concrete sandwich panels for thermally efficient floor/roof applications. „Practice Periodical on Structural Design and Construction”, Vol. 19, 2014, doi:10.1061/(ASCE)SC.1943-5576.0000213.
75. Huang H., Hu F., Most Zhu M., et al.: Influence of rib details on flexural behavior of concrete composite slab with precast prestressed ribbed panel. „J Build Struct”, Vol. 36–10, 2015.

76. Huang H., Li J., Zeng C., et al.: Simplified elastic design method using equivalent span ratio for two-way concrete composite slabs with precast ribbed panels. „Structural Concrete”, Vol. 20, 2019, doi:10.1002/suco.201800097.
77. Huang W., Ma X., Luo B., et al.: Experimental study on flexural behaviour of lightweight multi-ribbed composite slabs. „Advances in Civil Engineering”, Vol. 2019, 2019, doi:10.1155/2019/1093074.
78. Hui-cai X., Geng-ying L., Guang-jing X.: Microstructure model of the interfacial zone between fresh and old concrete. „Journal of Wuhan University of Technology-Mater. Sci. Ed.”, Vol. 17, 2002, doi:10.1007/BF02838421.
79. Ibrahim I.S., Padil K.H., Mansoor H., et al.: Ultimate Shear Capacity and Failure of Shear Key Connection in Precast Concrete Construction. „Malaysian Journal of Civil Engineering”, Vol. 26, 2014, doi:10.11113/mjce.v26n3.350.
80. Irawan D., Iranata D., Suprobo P.: Experimental study of two way half slab precast using triangular rigid connection of precast concrete component. „International Journal of Applied Engineering Research”, Vol. 12, 2017.
81. Jabłoński Ł.: Zagadnienie ścinania w żelbetowych belkach zespolonych o przekroju teowym. „Budownictwo i Architektura”, Vol. 9, nr, 2011.
82. Jabłoński Ł.: Wpływ położenia styku na wysokości żelbetowych elementów zespolonych o przekroju teowym na stan graniczny zarysowania styku. „Budownictwo i Architektura”, Vol. 13, 2014.
83. Jabłoński Ł.: Numerical Analyses of Concrete Composite T-Shaped Beams with Variously Arranged Interface. In Proceedings of the Proceedings of the 12th fib International PhD Symposium in Civil Engineering; Czech Technical University, 2018.
84. Jabłoński Ł., Halicka A.: Influence of surface based cohesive parameters on static performance of concrete composite T-shaped beams. „MATEC Web of Conferences”, Vol. 262, 2019, doi:10.1051/mateconf/201926208003.
85. Jasiński R., Grzyb K.: Proposal of Empirical Homogenization of Masonry Wall Made of AAC Masonry Units. 5th World Multidisciplinary Civil Engineering - Architecture - Urban Planning Symposium : WMCAUS 2020, 15-19 June 2020, Prague, Czech Republic [online], (in:); 2020.
86. Jasiński R., Kisiołek A., Zajac J.: Badania rynkowe systemów stropowych i potrzeb uczestników procesu budowlanego. Monografia / Politechnika Śląska Gliwice 2022.
87. Ju H., Han S.-J., Joo H.-E., et al.: Shear performance of optimized-section precast slab with tapered cross section. „Sustainability”, Vol. 11, 2018, doi:10.3390/su11010163.
88. Júlio E.N.B.S., Branco F.A.B., Silva V.D., et al.: Influence of added concrete compressive strength on adhesion to an existing concrete substrate. „Building and Environment”, Vol. 41, 2006, doi:10.1016/j.buildenv.2005.06.023.
89. Kamiński M., Kmiecik P.: Obliczanie połączenia prefabrykatów żelbetowych z nadbetonem konstrukcyjnym - przegląd wytycznych normowych. „Przegląd Budowlany”, Vol. 6, 2011.
90. Kim S.H., Lee K.K., Lee H.S., et al.: Bending and shear strength of I-slab with polystyrene forms. „Key Engineering Materials”, Vol. 385–387, 2008, doi:10.4028/www.scientific.net/KEM.385-387.353.

91. Kisiołek A.: The relation between the quality of building materials and customer preferences on the example of floor systems. „Zeszyty Naukowe Wyższej Szkoły Humanitas Zarządzanie”, Vol. 18, 2017, doi:10.5604/01.3001.0010.6502.
92. Kisiołek A.: The market of flooring systems in poland. „Innovative Marketing”, Vol. 14, 2018, doi:10.21511/im.14(1).2018.02.
93. Lebet J.-P.: New steel-concrete shear connection for composite bridges. „Composite Construction in Steel and Concrete VI”, 2011, doi:10.1061/41142(396)6.
94. Lemieux M., Gagné R., Bissonnette B., et al.: Behavior of overlaid reinforced concrete slab panels under cyclic loading - effect of interface location and overlay thickness. „ACI Structural Journal”, Vol. 102, 2005, doi:10.14359/14417.
95. Li M., Wang C., Tao W., et al.: Analysis of the shear force distribution of laminated slab with shear keys simply supported on four sides. „Proceedings of the 2015 International Conference on Mechatronics, Electronic, Industrial and Control Engineering”, Vol. 1, 2015, doi:10.2991/meic-15.2015.110.
96. Liang Y., Lei Z., Dong L., et al.: Shear Test of the Rectangular Beam on the New to Old Concrete Interface Based on Digital Image Correlation. In Proceedings of the IOP Conference Series: Earth and Environmental Science; Institute of Physics Publishing, 2019; Vol. 267, 2019.
97. Liu J., Hu H., Li J., et al.: Flexural behavior of prestressed concrete composite slab with precast inverted T-shaped ribbed panels. „Engineering Structures”, Vol. 215, 2020, doi:10.1016/j.engstruct.2020.110687.
98. Loov R.E.: Design of precast connections. „Compa International Pte, Ltd. Singapore”, 1978.
99. Loov R.E., Patnaik A.K.: Horizontal shear strength of composite concrete beams with a rough interface. „PCI Journal”, Vol. 39, 1994, doi:10.15554/pcij.01011994.48.69.
100. Lukovic M., Savija B., Dong H., et al.: Micromechanical study of the interface properties in concrete repair systems. „Journal of Advanced Concrete Technology”, Vol. 12, 2014, doi:10.3151/jact.12.320.
101. Luu X.-B., Kim S.-K.: Finite element modeling of interface behavior between normal concrete and ultra-high performance fiber-reinforced concrete. „Buildings”, Vol. 13, No.4, 2023, doi:10.3390/buildings13040950.
102. Mastali M., Valente I.B., Barros J.A.O.: Flexural performance of innovative hybrid sandwich panels with special focus on the shear connection behavior. „Composite Structures”, Vol. 160, 2017, doi:10.1016/J.COMPSTRUCT.2016.10.066.
103. Mastali M., Valente I.B.B., Barros J.A.O.: Development of innovative hybrid sandwich panel slabs: advanced numerical simulations and parametric studies. „Composite Structures”, Vol. 152, 2016, doi:10.1016/j.compstruct.2016.05.072.
104. Mattock A.H., Hawkins N.M.: Shear transfer in reinforced concrete - recent research. „PCI Journal”, Vol. 17, 1972, doi:10.15554/pcij.03011972.55.75.
105. Mohamad M., Ibrahim I., Abdullah R., et al.: Friction and cohesion coefficients of composite concrete-to-concrete bond. „Cement and Concrete Composites”, Vol. 56, 2015, doi:10.1016/j.cemconcomp.2014.10.003.
106. Mohamed M.S., Thamboo J.A., Jeyakaran T.: Experimental and numerical assessment of the flexural behaviour of semi-precast-reinforced concrete slabs.

- „Advances in Structural Engineering”, Vol. 23, 2020, doi:10.1177/1369433220904011.
107. Mohandoss P., Pillai R.G., Gettu R.: Determining bond strength of seven-wire strands in prestressed concrete. „Structures”, Vol. 33, 2021, doi:10.1016/j.istruc.2021.06.004.
 108. Momayez A., Ehsani M.R., Ramezani pour A.A., et al.: Comparison of methods for evaluating bond strength between concrete substrate and repair materials. „Cement and Concrete Research”, Vol. 35, 2005, doi:10.1016/j.cemconres.2004.05.027.
 109. Mones R.M., Breña S.F.: Hollow-core slabs with cast-in-place concrete toppings: a study of interfacial shear strength. „PCI Journal”, Vol. 58, 2013, doi:10.15554/pcij.06012013.124.141.
 110. Oh Y.-H., Moon J.-H.: Evaluation of design provisions for horizontal shear strength in composite precast concrete beams with different interface conditions. „Applied Sciences”, Vol. 11, No.9, 2021, doi:10.3390/app11094246.
 111. Ouyang H., Chen X.: 3D meso-scale modeling of concrete with a local background grid method. „Construction and Building Materials”, Vol. 257, 2020, doi:10.1016/j.conbuildmat.2020.119382.
 112. Park H.G., Kang S., Choi K.K.: Analytical model for shear strength of ordinary and prestressed concrete beams. „Engineering Structures”, Vol. 46, 2013, doi:10.1016/j.engstruct.2012.07.015.
 113. Park J., Choi J., Jang Y., et al.: An experimental and analytical study on the deflection behavior of precast concrete beams with joints. „Applied Sciences (Switzerland)”, Vol. 7, 2017, doi:10.3390/app7111198.
 114. Qian P., Xu Q.: Experimental investigation on properties of interface between concrete layers. „Construction and Building Materials”, Vol. 174, 2018, doi:10.1016/j.conbuildmat.2018.04.114.
 115. Rahman A., Ai C., Xin C., et al.: State-of-the-art review of interface bond testing devices for pavement layers: toward the standardization procedure. „Journal of Adhesion Science and Technology”, Vol. 31, 2017, doi:10.1080/01694243.2016.1205240.
 116. Randl N.: Investigations on Load Transfer between Old and New Concrete at Different Surface Roughnesses, University of Innsbruck, 1997.
 117. Randl N., Wicke M.: Schubübertragung zwischen Alt- und Neubeton. Experimentelle Untersuchungen, theoretischer Hintergrund und Bemessungsansatz. „Beton- und Stahlbetonbau”, Vol. 95, 2000, doi:10.1002/best.200000870.
 118. Randl N.: Design recommendations for interface shear transfer in fib model code 2010. „Structural Concrete”, Vol. 14, 2013, doi:10.1002/suco.201300003.
 119. Ribas C., Cladera A.: Experimental study on shear strength of beam-and-block floors. „Engineering Structures”, Vol. 57, 2013, doi:10.1016/j.engstruct.2013.10.001.
 120. Rueda-García L., Bonet Senach J.L., Miguel Sosa P.F., et al.: Experimental analysis of the shear strength of composite concrete beams without web reinforcement. „Engineering Structures”, Vol. 229, 2021, doi:10.1016/j.engstruct.2020.111664.

121. Sadowski G., Wiliński P., Halicka A.: Composite beams with indented construction joint – comparison of results of laboratory tests and numerical analysis. „Budownictwo i Architektura”, Vol. 19, No.4, 2020, doi:10.35784/bud-arch.2171.
122. Sadowski G., Wiliński P., Halicka A.: Analysis of the shear resistance in the indented interface between two concrete parts of concrete composite beam. „Civil and Environmental Engineering Reports”, Vol. 31, 2021, doi:10.2478/ceer-2021-0007.
123. Sadowski G., Wydra M.: Porównanie metod badawczych stosowanych w analizie procesu zarysowania belki zespolonej. „ACTA SCIENTIARUM POLONORUM - Architectura Budownictwo”, Vol. 18, 2019, doi:10.22630/aspa.2019.18.1.1.
124. Sadowski L.: Multi-scale evaluation of the interphase zone between the overlay and concrete substrate: methods and descriptors. „Applied Sciences (Switzerland)”, Vol. 7, 2017, doi:10.3390/app7090893.
125. Sadowski Ł.: Adhesion in Layered Cement Composites. Springer, 2018. ISBN 978-3-030-03783-3.
126. Sadowski Ł., Hoła J., Czarnecki S., et al.: Pull-off adhesion prediction of variable thick overlay to the substrate. „Automation in Construction”, Vol. 85, 2018, doi:10.1016/j.autcon.2017.10.001.
127. Sadowski Ł., Żak A., Hoła J.: Multi-sensor evaluation of the concrete within the interlayer bond with regard to pull-off adhesion. „Archives of Civil and Mechanical Engineering”, Vol. 18, 2018, doi:10.1016/j.acme.2017.09.008.
128. Saldanha R.F.S.M., Santos P.M.D., Júlio E.N.B.S.: fib model-code 2010 approach for concrete- to-concrete interfaces. 2010.
129. Saldanha R., Júlio E., Dias-Da-Costa D., et al.: A modified slant shear test designed to enforce adhesive failure. „Construction and Building Materials”, Vol. 41, 2013, doi:10.1016/j.conbuildmat.2012.12.053.
130. Santos P.D.D.: Assessment of the shear strenght between concrete layers. „Departemento De Engenharia Civil Faculdade De Ciencias E Tecnologia Unversidade De Coimbra”, 2009.
131. Santos P., Júlio E.: Shear-friction. Concept, codes and new trends. 2010.
132. Santos P., Júlio E.: Factors affecting bond between new and old concrete. „ACI Materials Journal”, Vol. 108, 2011, doi:10.14359/51683118.
133. Santos P.M.D.: Assessment of the bond strength in composite members. 2016.
134. Santos P.M.D., Júlio E.N.B.S.: A state-of-the-art review on roughness quantification methods for concrete surfaces. „Construction and Building Materials”, Vol. 38, 2013, doi:10.1016/j.conbuildmat.2012.09.045.
135. Santos P.M.D., Júlio E.N.B.S.: A state-of-the-art review on shear-friction. „Engineering Structures”, Vol. 45, 2012, doi:10.1016/j.engstruct.2012.06.036.
136. Shamass R., Zhou X., Wu Z.: Numerical analysis of shear-off failure of keyed epoxied joints in precast concrete segmental bridges. „Journal of Bridge Engineering”, Vol. 22, 2017, doi:10.1061/(asce)be.1943-5592.0000971.
137. Shan W., Liu J., Li J., et al.: Characterization of damage on precast pre-stressed concrete composite slabs under static loading based on acoustic emission parameters. „Structural Health Monitoring”, Vol. 19, 2020, doi:10.1177/1475921720919677.

138. Skupien P.: Composite slab made from precast, pre-tensioned concrete planks and lightweight concrete. „IOP Conference Series: Materials Science and Engineering”, Vol. 471, 2019, doi:10.1088/1757-899X/471/5/052055.
139. Supriyadi B., Siswosukarto S., Effi C.P.Y.P.: The Behavior Semi-Precast Slab under Dynamic Load. In Proceedings of the Procedia Engineering; Elsevier Ltd, 2017; Vol. 171, 2017.
140. Szydłowski R., Szreniawa M.: New Concept of Semi-Precast Concrete Slab on Pre-Tensioned Boards. In Proceedings of the IOP Conference Series: Materials Science and Engineering; 2017; Vol. 245, 2017.
141. Talbot C., Pigeon M., Beaupre D., et al.: Influence of surface preparation on long-term bonding of shotcrete. „ACI Materials Journal”, Vol. 91, 1994, doi:10.14359/1376.
142. Taylor R.: Interpretation of the Correlation Coefficient: A Basic Review. „Journal of Diagnostic Medical Sonography”, Vol. 6, 1990, doi:10.1177/875647939000600106.
143. Thomann M., Lebet J.-P.: Design method for connections by adherence for steel-concrete composite bridges. „Structural Engineering International”, Vol. 17, 2007, doi:10.2749/101686607779938778.
144. Van Damme H.: Concrete material science: past, present, and future innovations. „Cement and Concrete Research”, Vol. 112, 2018, doi:10.1016/j.cemconres.2018.05.002.
145. Wairaven J., Frenay J., Pruijssers A.: Influence of concrete strength and load history on the shear friction capacity of concrete members. „PCI Journal”, Vol. 32, 1987, doi:10.15554/pcij.01011987.66.84.
146. Walraven J.C., Reinhardt H.W.: Theory and Experiments on the Mechanical Behaviour of Cracks in Plain and Reinforced Concrete Subjected to Shear Loading. „HERON, 26 (1A), 1981”, 1981.
147. Wenzhong Z., Xueyuan L., Ying W.: Flexural behaviour of precast, prestressed ribbed RPC bottom panels. „The Open Civil Engineering Journal”, Vol. 9, 2015, doi:10.2174/1874149501509010535.
148. Wieneke K., Hegger J.: Fatigue of semi-precast slabs with lattice girders. „High Tech Concrete: Where Technology and Engineering Meet - Proceedings of the 2017 fib Symposium”, 2017, doi:10.1007/978-3-319-59471-2_107.
149. Wu F.B., Huang H.L., Chen W., et al.: Experimental analysis on the mechanical properties of concrete composite slabs with precast prestressed rectangular rib panels. „Tumu Jianzhu yu Huanjing Gongcheng/Journal of Civil, Architectural and Environmental Engineering”, Vol. 33, 2011.
150. Xia J., Shan K., Wu X., et al.: Shear-friction behavior of concrete-to-concrete interface under direct shear load. „Engineering Structures”, Vol. 238, 2021, doi:10.1016/j.engstruct.2021.112211.
151. Xu B., Luan L., Chen H., et al.: Experimental study on active interface debonding detection for rectangular concrete-filled steel tubes with surface wave measurement. „Sensors (Switzerland)”, Vol. 19, 2019, doi:10.3390/s19153248.
152. Zajac J.: Badania doświadczalne stropu panelowego vector III pod obciążeniem doraźnym oraz długotrwałym. „Materiały Budowlane”, Vol. 1, 2020, doi:10.15199/33.2020.04.01.

153. Zając J., Drobiec Ł.: Comparison of the performance of prestressed ribbed panels and hollow core panels supported on four-edges. „IOP Conference Series: Materials Science and Engineering”, Vol. 1203, 2021, doi:10.1088/1757-899X/1203/3/032049.
154. Zając J., Drobiec Ł., Blazy J., et al.: Flexural and Shear Performance of Precast Prestressed Composite Beams. International RILEM Conference on Synergising Expertise towards Sustainability and Robustness of Cement-based Materials and Concrete Structures, (in:); Jędrzejewska A., Kanavaris F., Azenha M., et al. (eds.); RILEM Bookseries; Springer Nature Switzerland,; Vol. 43, Cham 2023 ISBN 978-3-031-33210-4.
155. Zając J., Drobiec Ł., Grzyb K., et al.: Wpływ przekroju poprzecznego styku nadbetonu i prefabrykatu na pracę statyczną belek zespolonych. „Materiały Budowlane”, Vol. 1, 2022, doi:10.15199/33.2022.04.07.
156. Zając J., Drobiec Ł., Grzyb K.: Badania betonowych elementów sprężonych zespolonych z nadbetonem. „Przegląd Budowlany”, Vol. 94, 2023, doi:10.5604/01.3001.0053.8504.
157. Zając J., Drobiec Ł., Jasiński R., et al.: Research on semi-precast prestressed concrete slab under short-term and long-term load. „MATEC Web of Conferences”, Vol. 323, 2020, doi:10.1051/mateconf/202032302001.
158. Zając J., Drobiec Ł., Jasiński R., et al.: Experimental tests of the Vector II slab in field conditions, slab and strip model. „Civil and Environmental Engineering Reports”, Vol. 31, 2021, doi:10.2478/ceer-2021-0004.
159. Zając J., Drobiec Ł., Jasiński R., et al.: The behaviour of half-slabs and hollow-core slab in four-edge supported conditions. „Applied Sciences”, Vol. 11, 2021, doi:10.3390/app112110354.
160. Zając J., Drobiec Ł., Jasiński R., et al.: Badania doświadczalne stropu TERIVA PANEL pod obciążeniem krótko- i długotrwałym. „Materiały Budowlane”, Vol. 1, 2021, doi:10.15199/33.2021.11.03.
161. Zanotti C., Randl N.: Are concrete-concrete bond tests comparable?. „Cement and Concrete Composites”, Vol. 99, 2019, doi:10.1016/j.cemconcomp.2019.02.012.
162. Zareiyan B., Khoshnevis B.: Effects of interlocking on interlayer adhesion and strength of structures in 3D printing of concrete. „Automation in Construction”, Vol. 83, 2017, doi:10.1016/j.autcon.2017.08.019.
163. Zhang J.S., Nie H.H., Yang Y.L., et al.: Research and application of pre-stressed concrete composite slabs. „Applied Mechanics and Materials”, Vol. 166–169, 2012, doi:10.4028/www.scientific.net/AMM.166-169.131.
164. Zhang J., Liu B., Han B., et al.: Analysis of out-of-plane performance of composite slab with precast concrete ribbed panels under a hanging load. „PCI Journal”, Vol. 64, 2019, doi:10.15554/pcij64.5-02.
165. Zhang J., Yao Y., Zhou X., et al.: Failure mode and ultimate bearing capacity of precast ribbed panels used for concrete composite slabs. „Advances in Structural Engineering”, Vol. 16, 2013, doi:10.1260/1369-4332.16.12.2005.
166. Zilch K., Reinecke R.: Capacity of Shear Joints between High-Strength Precast Elements and Normal-Strength Cast-in-Place Decks.; 2000.

Standards

- N1. AASHTO-LRFD Bridge construction specifications, 2012
- N2. ACI 318-19 Building Code Requirements for Structural Concrete
- N3. EN 1992-1-1:2004 Eurocode 2: Design of concrete structures - Part 1-1: General rules and rules for buildings
- N4. EN 6892-1 Metallic Materials—Tensile Testing—Part 1: Method of Test at Room Temperature
- N5. EN 12390-3 Testing Hardened Concrete. Compressive Strength of Test Specimens.
- N6. EN 12390-2:2019, Testing Hardened Concrete—Part 2: Making and Curing Specimens for Strength Test; CEN: Brussels, Belgium, 2019.
- N7. EN 12390-13:2013 Testing Hardened Concrete Part 13: Determination of Secant Modulus of Elasticity in Compression
- N8. EN ISO 15630-1:2004, Steel for the Reinforcement and Prestressing of Concrete—Test Methods—Part 1: Reinforcing Bars, Wire Rod and Wire
- N9. *fib* Model Code for Concrete Structures 2010
- N10. PN-B-03264:2002 Plain, reinforced and prestressed concrete structures -- Analysis and structural design (in polish)
- N11. PN-EN 1168+A3:2011 Precast concrete products - Hollow core slabs (in polish)
- N12. PN-EN 13747+A2:2011 Precast concrete products - Floor plates for floor systems (in polish)
- N13. PN-EN 15037-1:2011 Precast concrete products - Beam-and-block floor systems - Part 1: Beams (in polish)
- N14. PN-EN 1992-1-1:2005 Eurocode 2: Design of concrete structures - Part 1-1: General rules and rules for buildings (in polish)
- N15. PN-EN 1992-1-1:2008 Eurocode 2: Design of concrete structures - Part 1-1: General rules and rules for buildings (in polish)
- N16. PN-EN 1992-1-1:2024-05 Eurocode 2: Design of concrete structures - Part 1-1: General rules and rules for buildings, bridges and civil engineering structures
- N17. prEN 1992-1-1:2020 Eurocode 2: Design of concrete structures – Part 1-1: General rules, rules for buildings, bridges and civil engineering structures

ZACHOWANIE SIĘ BETONOWYCH ELEMENTÓW ZESPOLONYCH Z WIELOPŁASZCZYZNOWYM NIEZBROJONYM STYKIEM

Streszczenie

Zespólone elementy betonowe wykonywane są najczęściej jako połączenie prefabrykatu i nadbetonu układanego na budowie. Elementy te projektowane są jak monolityczne, przy założeniu konieczności nieprzekroczenia dopuszczalnych naprężeń w styku. Pomimo stosunkowo prostych zapisów dotyczących wyznaczania nośności styku w normie PN-EN 1992-1-1:2008 uzupełnionej w zakresie prefabrykacji o zapisy z normy PN-EN 15037-1, procedury wymagają klaryfikacji w kilku aspektach projektowych. Wątpliwości te dotyczą wyznaczania naprężeń w stykach o wielu płaszczyznach zespolenia oraz przyjmowania parametrów powierzchni z uwagi na niespójne zalecenia pomiędzy normami z serii PN-EN. Zagadnienia te stanowiły punkt wyjścia do badań doświadczalnych mających na celu opisanie zachowania się elementów zespolonych z niezbrojonym stykiem wielopłaszczyznowym.

W ramach niniejszej pracy doktorskiej przeprowadzono obszerne studium literaturowe obejmujące analizę parametrów kształtujących zespolenie, mechanizmów odpowiadających za przenoszenie naprężeń w styku, ocenę zapisów krajowych oraz zagranicznych przepisów normowych wraz z przeglądem publikacji naukowych dotyczących badań elementów zespolonych. Opracowano autorski program badań doświadczalnych składający się z badań wstępnych przeprowadzonych na elementach z płaskim stykiem oraz badań na elementach z wielopłaszczyznowym stykiem w testach bezpośredniego ścinania, jak również trzy i czteropunktowego zginania. W ramach badań wykonano dziesięć różnych konfiguracji styku pozwalających na określenie efektywności stref zespolenia w zależności od ich położenia w przekroju poprzecznym. Analizy umożliwiły określenie faz pracy badanych elementów oraz identyfikację zakresu fazy sprężystej, opis fazy lokalnego zarysowania styku oraz fazy zarysowania do osi oparcia elementu, aż po jego zniszczenie. Wykazano niepełną efektywność stref zespolenia w przenoszeniu naprężeń stycznych.

Opracowano modele numeryczne o skalibrowanych parametrach zespolenia w oparciu o badania bezpośredniego ścinania. Modele pozwoliły na dokładny opis efektywności stref zespolenia oraz wydzielenie efektów wpływających na zachowanie się styku na skutek zarysowania oraz jego geometrii styku. Wykazano istotne różnice pomiędzy założeniami normowymi, a wynikami badań doświadczalnych i modelowaniem numerycznym. Zaproponowano modyfikację przepisów normowych w zakresie elementów o wielu płaszczyznach zespolenia. Wyznaczono dalsze kierunki prac badawczych dotyczących przedmiotu rozprawy.

THE BEHAVIOUR OF COMPOSITE CONCRETE ELEMENTS WITH UNREINFORCED MULTIPLANAR INTERFACE

Abstract

Composite concrete elements are typically constructed as a combination of precast concrete components and on-site concrete toppings. These elements are designed to function as monolithic structures, assuming that the stresses at the interface do not exceed resistance. Despite the relatively straightforward provisions for determining the load-bearing capacity of the interface in PN-EN 1992-1-1:2008, supplemented by provisions from PN-EN 15037-1 concerning precasting, several aspects of the design procedures require further clarification. These issues relate to the assessment of stresses in interfaces characterised by multiplanar interface and the adoption of surface parameters due to inconsistent recommendations between the PN-EN series of standards. This identification of gaps served as the starting point for experimental studies aimed at describing the behaviour of composite elements with unreinforced multiplanar interfaces.

This dissertation involved an extensive literature review that includes an analysis of the parameters influencing the interface, the mechanisms governing stress transfer at the interface, an evaluation of both national and international standard regulations, and a review of scientific publications on the testing of composite elements. An experimental research programme was developed consisting of preliminary tests conducted on elements featuring a flat interface, as well as tests on elements with a multiplanar interface subjected to direct shear, alongside three- and four-point bending tests. Ten distinct interface configurations were examined to assess the effectiveness of the interface zones in relation to their position within the cross-section. The analyses facilitated the identification of the phases of the tested elements and to identify the extent of the elastic phase, the description of the local cracking phase of the interface, the cracking phase up to the support axis of the element and subsequent element failure. The inefficiency of the interface zones in transferring shear stresses was indicated.

Numerical models with calibrated interface parameters were developed based on direct shear tests. The models allowed an in-depth description of the efficiency of the interface zones while enabling the distinction between the effects of cracking behaviour and interface geometry. Notable discrepancies between standard provisions, experimental results, and numerical modeling were identified. A modification to the standard provisions for elements featuring multiplanar interfaces was proposed. Further research directions for the subject of the dissertation were established.

ZACHOWANIE SIĘ BETONOWYCH ELEMENTÓW ZESPOLONYCH Z WIELOPŁASZCZYZNOWYM NIEZBROJONYM STYKIEM

Poszerzone streszczenie

Zespólone elementy betonowe wykonywane s najczściej jako poczenie prefabrykatu i nadbetonu ukadanego na budowie. Elementy te projektowane s jak monolityczne, przy zaozeniu koniecznoci nieprzekroczenia dopuszczalnych napreen w styku. Pomimo stosunkowo prostych zapisw dotyczcych wyznaczenia nonoci styku w normie PN-EN 1992-1-1:2008 uzupenionej w zakresie prefabrykacji o zapisy z normy PN-EN 15037-1, procedury wymagaj klaryfikacji w kilku aspektach projektowych. Wtpliwoci te dotycz wyznaczenia napreen w stykach o wielu paszczyznach zespolenia oraz przyjmowania parametrw powierzchni z uwagi na niespjne zalecenia pomidzy normami z serii PN-EN. Sformuowano zagadnienia, ktre stanowiy punkt wyjscia do badan dowiadczalnych majcych na celu opisanie zachowania sie elementw zespolonych z niezbrojonym stykiem wielopaszczyznowym:

- niespjne zapisy normowe dotyczce parametrw styku,
- niespjne ujcia zasad obliczania i okreslania efektywnych powierzchni zespolenia w elementach o wielopaszczyznowym styku,
- brak uwzgldnienia wpywu lokalnego polizgu oraz zarysowan ukonych na prac styku,
- niejasne zasady okreslania wpywu napreen spowodowanych zewnrznymi siami normalnymi w zalenoci od poozenia paszczyzny zespolenia (styki poziome i pionowe),
- niejednoznaczne wytyczne w zakresie uwzgldniania efektw skurczu oraz pezania.

Na podstawie powyszych zagadnien przeprowadzono studium literatury obejmujce przedstawienie parametrw ksztalujcych zespolenie, mechanizmw odpowiadajcych za przenoszenie napreen w styku, zapisw krajowych i zagranicznych przepisw normowych oraz przegld publikacji naukowych dotyczcych badan elementw zespolonych. Gwne wnioski i zagadnienia z przegldu literatury mona podsumowa w poniszych kilku punktach:

- szorstkoc powierzchni wpywa pozytywnie na wytrzymaoc styku,

- zwiększony okres pomiędzy wykonanie kolejnych warstw wpływa negatywnie na wytrzymałość zespolenia,
- wytrzymałość styku nie jest kształtowana tylko przez parametry słabszego z betonów, a stanowi sumę czynników betonów składowych,
- obecnie obowiązujące normy nie ujmują w pełni złożoności cech zespolenia, a obliczenia według procedur normowych prowadzą do istotnych rozbieżności względem wyników badań doświadczalnych,
- w ramach jednego pakietu norm PN-EN możliwe jest określenie parametrów zespolenia różniących się pomiędzy sobą ponad dwukrotnie dla zbliżonych charakterystyk powierzchni,
- styki ulegają lokalnemu zarysowaniu, które nie świadczy o zniszczeniu zespolenia pomiędzy elementami,
- zakotwienie zbrojenia w nadbetonie lub odpowiednio długa strefa zespolenia poza osią podpory pozwala nawet na uzyskanie pełnego zespolenia elementu pomimo zarysowania styku do osi oparcia,
- nieliczne badania na elementach o wielu płaszczyznach zespoleniu nie skupiają się na kwestii styku, a na ogólnym opisie pracy elementów poddanych zginaniu i ścinaniu.
- wykonywane modele numeryczne na stykach płaskich niezbrojonych oraz z zbrojeniem pozwalają na uzyskanie bardzo dobrej zgodności z badaniami doświadczalnymi,
- modele oparte na teorii Coulomba-Mohra nie odwzorowują wszystkich cech zespolenia, w tym rozwarcia przed i po jego zarysowaniu.

Głównym zagadnieniem badawczym pracy jest zachowanie się betonowych elementów zespolonych z wielopłaszczyznowym niezbrojonym stykiem. Na podstawie przeglądu literatury określono główne zagadnienia i cele pracy:

1. Opis zachowania się elementów zespolonych z wielopłaszczyznowym niezbrojonym stykiem w badaniu bezpośredniego ścinania.
2. Rozpoznanie charakterystyki pracy elementów zginanych o wielu płaszczyznach zespolenia.
3. Opracowanie modeli numerycznych odwzorowujących badane elementy.
4. Określenie zaleceń do projektowania i obliczeń.
5. Zakreślenie ram dla dalszych badań oraz analizy elementów płytowych z wielopłaszczyznowym niezbrojonym stykiem.

W ramach pracy sformułowano następujące tezy:

1. Współpraca pomiędzy płaszczyznami zespolenia jest zależna od położenia na wysokości przekroju poprzecznego.
2. Styku o wielu płaszczyznach zespolenia odznaczają się charakterystyką nieliniową przed zniszczeniem ze względu na poślizg w styku.
3. Zwiększona nośność zespolenia płaszczyzn pionowych wynika z efektu ich skrępowania.
4. Wydłużenie belki zespolonej poza oś podpory umożliwia zachowanie quasi-monolityczne pomimo zarysowaniu styku aż do osi oparcia.

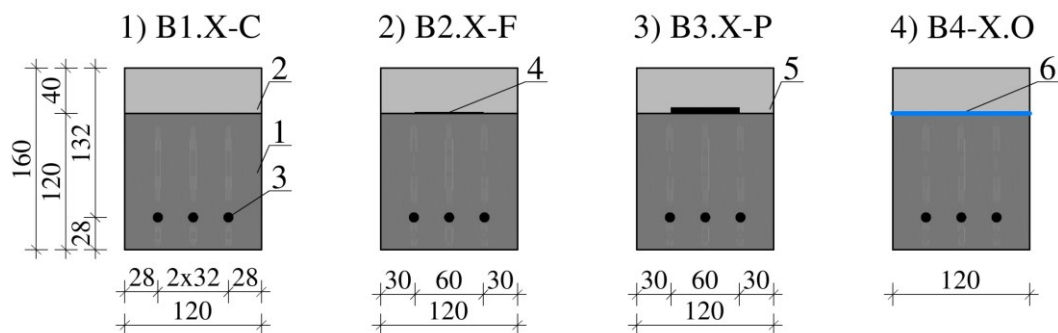
Rozprawa została podzielona na rozdziały poświęcone poszczególnym zagadnieniom. Rozdział 3 zawiera przegląd czynników determinujących parametry zespolenia, zapisy normowe dotyczące zespolenia beton-beton, badania próbek do określania parametrów zespolenia, wybrane badania elementów zespolonych oraz analizy numeryczne, rozdział zakończono wnioskami. Rozdział 4 zawiera sformułowanie tezy i określa szczegółowe cele pracy. W rozdziale 5 przedstawiono główne założenia programu badań. Opisano budowę stanowisk badawczych, geometrię badanych elementów oraz wybrane metody pomiarowe. W rozdziale 6 przedstawiono wyniki trzech rodzajów badań eksperymentalnych. Rozdział 7 zawiera analizy numeryczne wykonane metodą elementów skończonych. W rozdziale 8 przedstawiono analizę oraz obliczenia analityczne dla wyników badań eksperymentalnych oraz numerycznych w kontekście aktualnych norm i omówiono program badań. W rozdziale 9 zaproponowano modyfikacje i rozszerzenie obecnych norm z serii PN-EN. Rozdział 10 zawiera wnioski końcowe i określa kierunki przyszłych prac.

W celu wypełnienia stawionych celów oraz weryfikacji postawionych tez opracowano program badań doświadczalnych. Badania podzielone zostały na trzy główne etapy o następujących założeniach i celach:

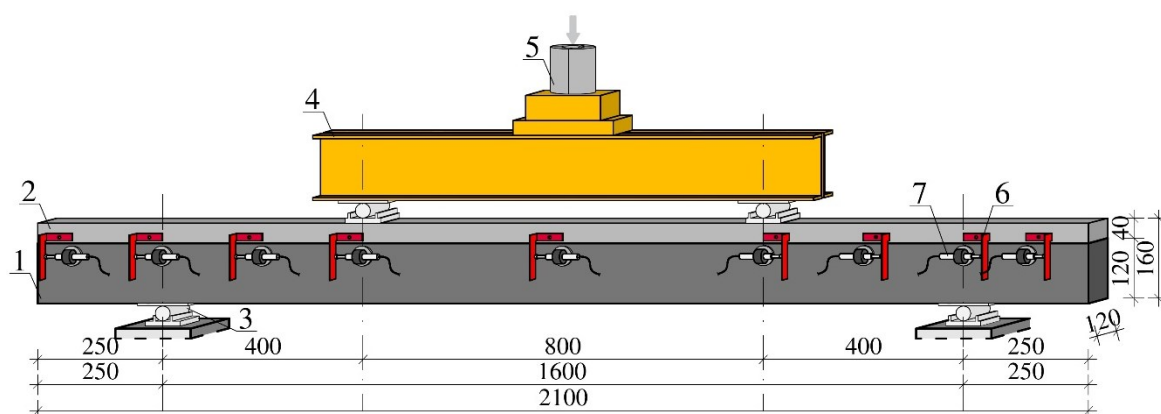
1. Badania wstępne:
 - 1.1. Elementy zostały wykonane z wykorzystaniem prefabrykowanych sprężonych belek o przekroju 120 x 120 mm o płaskiej powierzchni styku, grubość nadbetonu wynosiła 40 mm.
 - 1.2. Płaska powierzchnia zespolenia została wykonana w czterech wariantach, w celu dobór materiałów i metod do przygotowania głównych elementów badawczych.

- 1.3. Weryfikacji poddano zachowanie się elementów przed i po zerwaniu przyczepności w styku oraz schemat zniszczenia się elementów.
- 1.4. Celem badań było określenie materiałów do wykonania elementów głównych oraz zweryfikowanie przydatności planowanych metod pomiarowych tj. wykorzystania systemu cyfrowej korelacji obrazu Aramis oraz czujników indukcyjnych (LVDT) do pomiaru poślizgu w styku.
2. Badania bezpośredniego ścinania:
 - 2.1. Test wykonano na elementach stanowiących fragmenty belek przygotowanych do głównych badań.
 - 2.2. Badania wykorzystano do określenia charakterystyki styku oraz wartości poślizgu odpowiadającemu utracie zespolenia.
 - 2.3. Wyniki badań skorelowane z modelowaniem MES posłużą do określenia parametrów styku.
3. Badania trzy- i czteropunktowego zginania:
 - 3.1. Badania przeprowadzono na prefabrykowanych sprężonych elementach belkowych zespolonych z nadbetonem. Badany element odzwierciedla rzeczywiste element prefabrykowane, stanowiąc wycinek panelu stropowego.
 - 3.2. Długości oparcia i zakotwienia elementu dobrano tak aby zapewnić przekazanie siły sprężającej na element przed punktem przyłożenia obciążenia. Celem zabiegu była próba zweryfikowania i zminimalizowanie wpływu występowania zarysowań na poślizg w styku.
 - 3.3. Określenie charakterystyki pracy elementów zespolonych z wielopłaszczyznowym niezbrojonym stykiem poddanych zginaniu i ścinaniu.
 - 3.4. Określenie wpływu położenia powierzchni zespolenia.
 - 3.5. Weryfikacja wpływu odległości przyłożenia obciążenia oraz lokalnego docisku od przyłożonej siły skupionej.

W badaniach wstępnych wykonano elementy o czterech typach powierzchni przedstawionych na rysunku 1 zbadanych w teście czteropunktowego zginania (Rys. 2). Badania potwierdził skuteczność zastosowanego środka antyadhezyjnego oraz przekładki z maty PCW. Ze względu na brak zbrojenia i miejscowy docisk, nadbeton po zarysowaniu styku uległ podziałowi na wydzielone fragmenty. Pomiarzy czujnikami LVDT oraz z wykorzystaniem systemu cyfrowej korelacji obrazu umożliwiły określenie wartości poślizgu w styku oraz obrazu zarysowań belki.



Rys. 1. Przekrój poprzeczny belek do badań wstępnych: 1- prefabrykat, 2- nadbeton, 3- sploty, 4- folia PE, 5- mata PCW, 6- środek antyadhezyjny

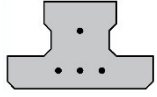


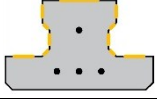
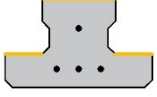
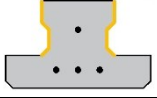
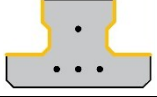
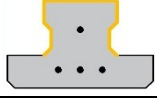
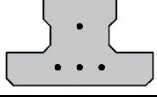
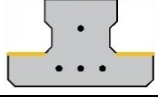


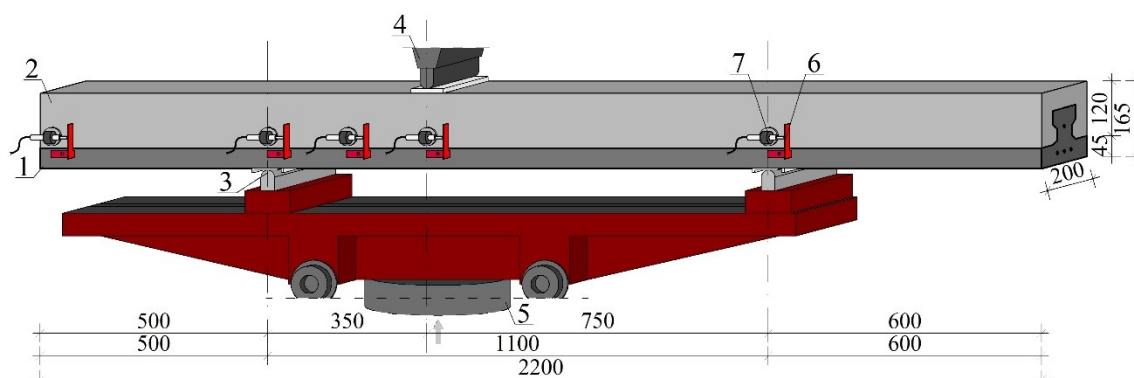
Rys. 2. Stanowisko badawcze belek wstępnych: 1- prefabrykat, 2- nadbeton, 3- podpora, 4- trawers stalowy, 5- siłomierz, 6- baza pomiarowa poślizgu, 7- czujnik LVDT

Badania główne przeprowadzono na sprężonych belkach żebrowych o szerokości 200 mm oraz wysokości 120 mm, z warstwą nadbetonu o grubości 45 mm. Powierzchnię styku przygotowano w dziesięciu wariantach (tabela 1). Typ podstawowy to element o powierzchni nieobrobionej, typ drugi to styk pokryty środkiem antyadhezyjnym, a typ trzeci to styk w całości przykryty matą Kevlarowo-gumową o grubości 0,3 mm. Dla pozostałych typów styk został częściowo zakryty matą. W tabeli określono rodzaj zakrytej powierzchni dzieląc je na powierzchnie górne, dolne oraz boczne. Badania główne przeprowadzono w próbie trzy- oraz czteropunktowego zginania (Rys. 3, 4) z pozostawieniem 500 mm długości elementu poza osią oparcia w celu uzyskania zakotwienia splotów oraz niezbędnej długości dyspersji sprężenia. Badania na elementach belkowych zostały poprzedzone testami bezpośredniego ścinania (Rys. 5) na elementach o długości 200 mm. W badaniu bezpośredniego ścinania wykorzystano czujniki laserowe o zwiększonej precyzji pomiaru oraz system cyfrowej korelacji obrazu o konfiguracji zwiększającej rozdzielczość obrazu w przeliczeniu na px/cm². Wariantom badanych elementów nadano oznaczenia zgodne z tabelą 1.

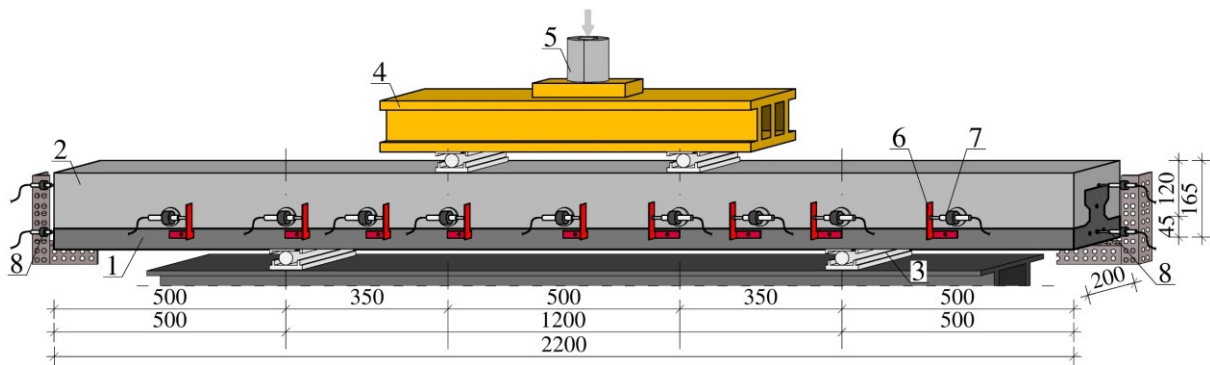
Tabela 1

Podział elementów ze względu na rodzaj powierzchni zespolenia

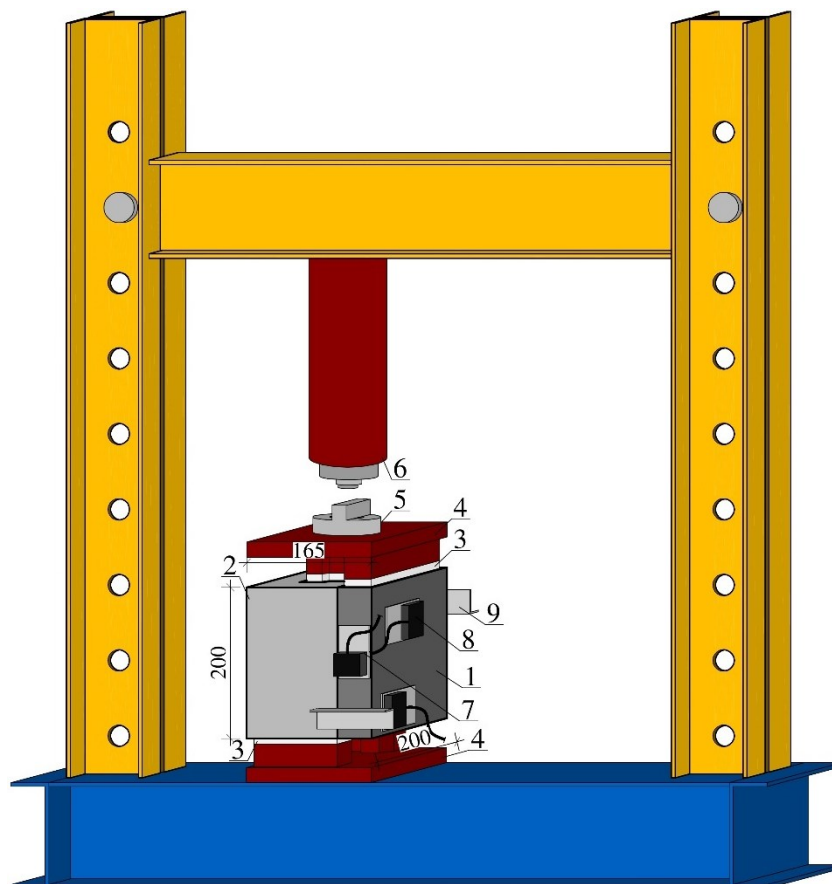
Symbol	Przekrój poprzeczny	Szerokość zespolenia, mm	Efektywna szerokość zespolenia	Pow. górna	Pow. dolna	Pow. dolna
Z1.X-C		367	1.0	x	x	x
Z2.X-AB		367* środek antyadhezyjny	1.0*	*	*	*
Z3.X-CB		-	-	-	-	-
Z4.X-P		183	0.50	x/2	x/2	x/2
Z5.X-S		167	0.46	x	-	x
Z6.X-TB		200	0.55	-	x	-
Z7.X-T		100	0.27	x	-	-
Z8.X-B		100	0.27	-	-	x
Z9.X-SB		267	0.73	-	x	x
Z10.X-TS		267	0.73	x	x	-



Rys. 3. Stanowisko badawcze trójpunktowego zginania (3PBT): 1- prefabrykat, 2- nadbeton, 3- podpora, 4- trawers stalowy, 5- siłownik i siłomierz, 6- baza pomiarowa poślizgu, 7- czujnik LVDT



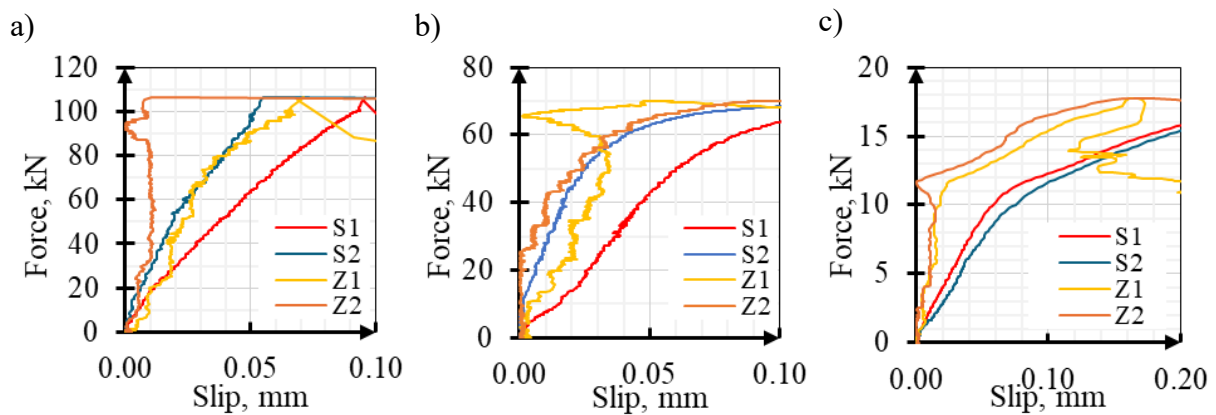
Rys. 4. Stanowisko badawcze czteropunktowego zginania: 1- prefabrykat, 2- nadbeton, 3- podpora, 4- trawers stalowy, 5- siłomierz, 6- baza pomiarowa poślizgu, 7- czujnik LVDT, 8- czujnik poślizgu splotu (LVDT)



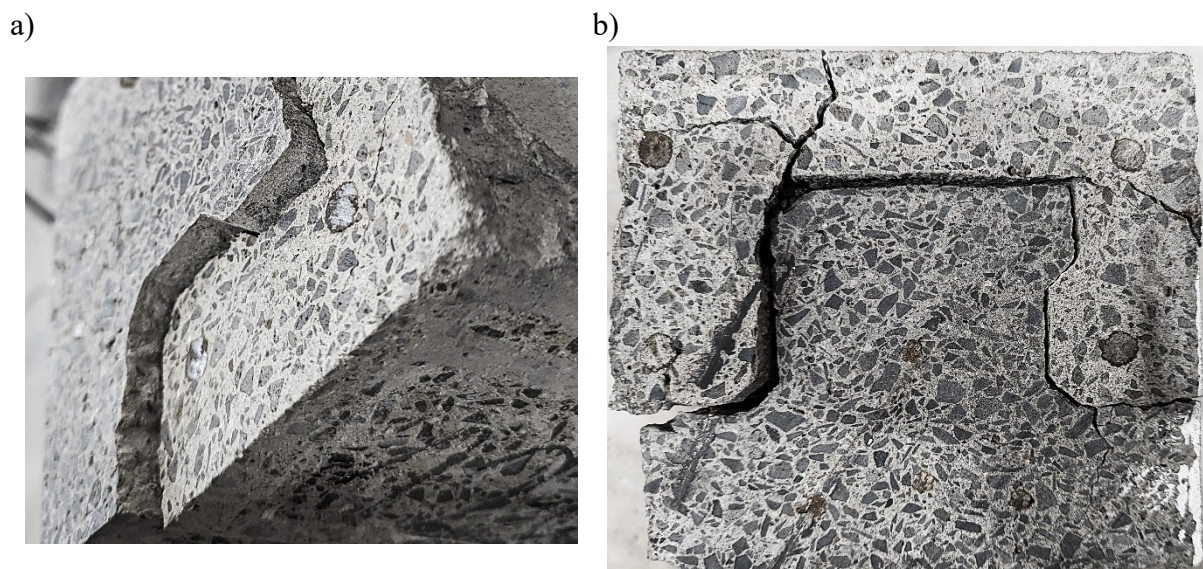
Rys. 5. Stanowisko badawcze bezpośredniego ścinania: 1- prefabrykat, 2- nadbeton, 3- podpora, 4- trawers stalowy, 5- siłomierz, 6- siłownik hydrauliczny, 7- pionowy czujnik laserowy, 8- poziomy czujnik laserowy, 9- baza pomiarowa

Na rysunku 6 zestawiono wyniki deformacji odczytany dla czujników laserowych mierzących poślizg oraz wychylenie nadbetonu względem prefabrykatu. Największą sztywność oraz siłę uzyskano dla elementu w pełni zespolonego. Na rysunku 7

przedstawiono obraz zniszczenia typu I (poślizg) oraz typu II (poślizg i zarysowanie/przecięcie nadbetonu) dla elementów z serii Z1.X_C.



Rys. 6. Zestawienie odczytów dla czujników w rozmieszczeniu typu S (poślizg) oraz Z (odchylenie nadbetonu): a) Z1.2_C3, b) Z2.2_AB1, c) Z3.2_CB2



Rys. 7. Widok elementów po badaniu: a) zniszczenie typu I, b) zniszczenie typu II

Na podstawie badań bezpośredniego ścinania sformułowane następujące główne wnioski:

- Charakterystyka siła/przemieszczenie badanych styków pozwalana na wyodrębnienie trzech faz pracy. Elementy pomimo braku zbrojenia w styku charakteryzowały się możliwą do wyodrębnienia fazą II związaną z siłą rezydualną przy narastającej wartości poślizgu.
- Elementy wszystkich typów charakteryzowały się pewną nieliniowością sztywności styku w zakresie Fazy I przed zarysowaniem.

- Pomiary LDS oraz analiza DIC wskazują na występowanie różnych wartości przemieszczenia styku na jego długości w ramach fazy I. Sugeruje to różny stopień obciążenia płaszczyzny zespolenia na jej długości.
- Zarysowanie styku występowało po osiągnięciu przemieszczenia o wartości >0.05 mm co jest zgodne z wnioskami przedstawionymi w przeglądzie literaturowym.

Analizując wyniki badań trzy- i czteropunktowego zginania (tabela 2 i 3) w tym wartość siły rysujące, siły skutkującej poślizgiem w styku, siły maksymalnej oraz mechanizm zniszczenia dla belek wyszczególniono cztery fazy pracy:

- Faza I – osiągnięcie siły rysującej przekrój, wyszczególnionej na podstawie analizy sztywności.
- Faza II – wystąpienie zarysowania styku aż do krawędzi jednej z podpór.
- Faza III – osiągnięcie siły maksymalnej
- Faza IV – spadek wartości siły do 50% wartości maksymalnej. W przypadku gwałtownego zniszczenia elementu, fazę IV przypisano do wartości siły bezpośrednio po osiągnięciu siły maksymalnej. Faza IV służy do opisu zniszczenia elementu, przy największym rozwarciu zarysowań.

Tabela 2

Zestawienie sił oraz typów zniszczenia belek z serii ZX.1 w teście czteropunktowego zginania

Element	Sztywność początkowa K_{init} , kNm ²	Siłą rysująca F_{cr} , kN	Poślizg w osi oparcia $V_{R,1,cr}$, kN	Poślizg do czola $V_{R,2,cr}$, kN	Rysa ukośna $V_{R,c}$, kN	Siła max. F_{max} , kN	Typ zniszcz.
Z1.1_C	2130	65.6	-	-	130.2	163.6	I
Z2.1_AB	1590	63.5	144.3	-	131.2	157.3	I
Z3.1_CB	1560	51.1	57.9	67.1	97.8	127.7	I
Z4.1_P	1730	67.6	126.8	108.8*	126.8	142.5	II
Z5.1_S	1910	70.7	88.7	149.6*	131.0	162.7	III
Z6.1_TB	1270	19.3	100.1	-	88.7	100.9	III
Z7.1_T	2260	52.0	119.1	119.1	103.3	119.1	II
Z8.1_B	1640	67.8	111.1	-	84.1	146.8	III
Z9.1_SB	1840	63.8	-	-	134.6*	144.8	I
Z10.1_TS	2010	68.3	-	-	134.0	161.4	I

*poślizg w styku lub rysa ukośna po osiągnięciu siły maksymalnej

Tabela 3

Zestawienie sił oraz typów zniszczenia belek z serii ZX.3 w teście trójpunktowego zginania

Element	Siła rysująca F_{cr} , kN	Poślizg w osi oparcia $V_{R,1,cr}$, kN	Poślizg do czoła $V_{R,2,cr}$, kN	Rysa ukośna $V_{R,c}$, kN	Siła max. F_{max} , kN	Typ zniszcz.
Z1.3_C	59.6	147.0	-	112.3	163.7	I
Z2.3_AB	46.5	94.7	-	94.7	124.0	II
Z3.3_CB	47.1	66.4	74.8(BF)	66.4	103.0	III
Z4.3_P	54.4	112.5	-	100.0	138.1	II
Z5.3_S	47.6	80.1	-	75.8	139.1	II
Z6.3_TB	53.3	113.0	-	113.0	145.4	II
Z7.3_T	48.1	80.4	88.9(BF)*	80.4	112.5	II
Z8.3_B	53.3	116.1	124.5(FF)	75.3	124.5	II
Z9.3_SB	48.6	110.9	-	85.3	143.3	II
Z10.3_TS	54.9	99.9	-	76.8	148.5	II

*poślizg w styku lub rysa ukośna po osiągnięciu siły maksymalnej

Na podstawie badań określono główne wnioski dotyczące elementów zginanych:

- W badaniu czteropunktowego zginania, dla belek których nie zaobserwowano poślizgu na styku aż do powierzchni czołowej oraz belki Z1.3_CB można przyporządkować zniszczenie typu I ze względu zmiążdżenia strefy ściskanej i rozwój dominującej rysy giętnej. Belki, w których wystąpił poślizg do czoła elementu, przyporządkowano zniszczeniu ze względu na rozwój rysy ukośnej przecinającej prefabrykat i nadbeton.
- W badaniu trójpunktowego zginania tylko belce Z1.3_C przyporządkowano zniszczenie typu I.
- Zarówno w badaniu trzy- jak i czteropunktowego zginania w na belce w pełni zespolonej (Z1_C) uzyskano zgodność zarysowań pomiędzy prefabrykatem, a nadbetonem.
- Rozwój rysy ukośnej skutkował był związany lub poprzedzał poślizg w styku aż do osi oparcia.
- Pomędzy kolejnymi rysami ukośnymi zaobserwowano powstanie lokalnych poślizgów w styku.
- **Lokalny poślizg w styku, nawet do osi oparcia, nie skutkował gwałtownym spadkiem sztywności giętnej belek.**

- W miejscu występowania poślizgu (w tym lokalnego), zaobserwowano oraz zmierzono wypychanie (poziome) nadbetonu względem prefabrykatu.
- Poślizg w zespoleniu aż do czoła elementu należy rozpatrywać jako zniszczenie elementu zespolonego.

Badania eksperymentalne belek nie pozwalają na jednoznaczną ocenę zjawisk wpływających na zachowanie się elementów ze względu na jednoczesne występowanie kilku efektów. Aby ocenić wpływ poszczególnych efektów, takich jak sztywność zespolenia, długość belki za krawędzią podpory, położenie płaszczyzn zespolenia oraz wpływ zarysowań giętnych i ukośnych, wykonano modele numeryczne. Modelowanie posłużyło jako kolejny oddzielny element do analizy zagadnień, których nie można wyodrębnić z programu badań eksperymentalnych ze względu na ograniczenia w metodach pomiarowych lub ilości badań w ramach programu badań eksperymentalnych. Analizy numeryczne podzielono szczegółowo na trzy etapy główne, dla których wydzielono konieczne do uzyskania cele, takie jak:

- Korelacja parametrów styku oraz siatki MES na modelach odwzorowujących badania bezpośredniego ścinania.
- Weryfikacja wartości zmierzonych deformacji w styku oraz typów zniszczenia w badaniu bezpośredniego ścinania.
- Określenie rozkładu naprężeń stycznych w styku.
- Odseparowania efektów wpływających na siłę rysującą oraz zachowanie się styku na podstawie zmodyfikowanego i uproszczonego modelu materiałowego nadbetonu oraz prefabrykatu w schemacie czteropunktowego zginania.

Szeroki program analiz numerycznych pozwolił na sformułowanie szeregu wniosków pozwalających na lepsze rozpoznanie charakterystyki pracy i zachowania się elementów zespolonych z programu badań eksperymentalnych:

- Korelacja styku na modelach z badania bezpośredniego ścinania, pozwoliła na uzyskanie bardzo wysokiej zgodności zachowania się zespolenia w modelach zginanych w tym lokalnego zarysowania w styku oraz wpływu rys ukośnych.
- Rysy giętne oraz ukośne wpływają na rozkład naprężeń stycznych w zespoleniu. Rysy ukośne ograniczają efektywną długość styku skutkując zmniejszeniem maksymalnej siły przenoszonej przez zespolenie.

- Efektywność powierzchni pionowych jest mniejsza niż powierzchni poziomych. Siła rysująca zespolenie nie jest prostą sumą wytrzymałości styków pionowych oraz poziomych.
- Zarysowanie zespolenia aż do osi podpory skutkuje spadkiem sztywności, lecz element pracuje nadal jako częściowo-zespolony z uwagi na zespolenie belki na długości 500 mm poza osią oparcia. Dodatkowy model bez przedłużenia poza oś oparcia uległ zarysowaniu przy mniejszej wartości siły, a siła rysująca styk aż do osi oparcia stanowi wartość niszczącą element zespolony.
- Żaden z modeli MES nie odwzorował wypychanie nadbetonu do zewnątrz względem prefabrykatu o wartości zbliżonej do badań eksperymentalnych.
- Na dodatkowym modelu MES z skrępowanymi powierzchniami bocznymi belki nie uzyskano poślizgu w styku. Model ten reprezentuje potencjał pionowych powierzchni zespolenia, dla których możliwe jest zablokowanie lub organicznie odkształceń poziomych.
- Z punktu widzenia projektowania elementów zespolonych należy przyjąć, że efekt częściowego zespolenia przez strefy krańcowe (poza strefą podparcia np. wieniec) i niewielki wzrost siły rysującej styk zapewnia dodatkowy margines bezpieczeństwa.

Uzyskane wyniki badań eksperymentalnych poddano analizie oraz przeliczeniu na wartości naprężeń zgodnie z wzorami dla mechaniki elementów warstwowych. Uwzględniając opisane i obliczone wartości efektów występowania zespolenia poza osią oparcia oraz redukując powierzchnie zespolenia z uwagi na niepełną efektywność powierzchni pionowych obliczono wartości naprężeń stycznych w styku. Uzyskano średnią wartość dla wszystkich badanych elementów poza belkami z serii Z5_S na poziomie 2.53 MPa przy współczynniku zmienności wynoszącym zaledwie 8.1%. Wartość naprężeń znajduje się w zakresie zbadanych wytrzymałości styku w metodzie pull-off. Naprężenia dla elementów z serii Z5_S wynosiły 1.78 MPa oraz 2.04 MPa co potwierdza niższą efektywność powierzchni pionowych, jeżeli ich szerokość zespolenia nie zostanie zredukowana do odpowiedniej wartości efektywnej. W przypadku przeprowadzenia obliczeń dla całej powierzchni zespolenia bez opisanych redukcji średnia wartość naprężeń w styku dla wszystkich badanych belek wynosiła 1.72 MPa przy współczynniku zmienności wynoszącym aż 32.8%.

Wykonano również sprawdzające obliczenia zgodne z procedurami normowymi. Uzyskane wartości naprężeń rysujących styk są znacząco mniejsze od uzyskanych z badań. Obliczona siła rysująca styk zgodnie z norma PN-EN 1992-1-1:2008 jest

pięciokrotnie niższa, a zgodnie z PN-EN 1992-1-1:2004 prawie siedmiokrotnie niższa, oraz od dwóch do trzech razy niższa przy obliczeniach zgodnych z normą PN-EN 15037-1:2011. Różnice obliczonej siły rysującej styk pomiędzy poszczególnymi normami z serii PN-EN sięgają do 100%.

Przeprowadzone badania eksperymentalne połączone z analizami na modelach MES oraz obliczeniami analitycznymi pozwoliły na sformułowanie propozycji modyfikacji normy PN-EN 1992-1-1:2024 oraz PN-EN 15037-1 w zakresie określania efektywnych powierzchni zespolenia dla elementów z wielopłaszczyznowym stykiem oraz obliczania naprężeń dopuszczalnych. Podane zalecenia stanowią wyłącznie punkt do dyskusji, która powinna obejmować również konieczność ujednoczenia zaleceń oraz wymogów względem zbliżonych z punktu widzenia cech zespoleni elementów prefabrykowanych objętych normami PN-EN 13747 oraz PN-EN 15037-1.

W ostatnim rozdziale pracy przedstawione wnioski końcowe ujęte w kolejności zgodnej z przedstawionym w pracy podziałem na pięć obszarów powiązanych z prowadzonymi badaniami eksperymentalnymi, analizami MES oraz obliczeniami analitycznymi. Niniejsze opracowanie stanowi część szerszego programu badań obejmującego szereg zagadnień dotyczących prefabrykowanych sprężonych stropów panelowych (żebrowych). Na podstawie zrealizowanych badań, których charakter można określić jako rozpoznawczy, możliwe jest określenie dalszych kierunków prac obejmujących:

- Badania eksperymentalne na elementach poddanych bezpośredniemu ścinaniu z dodatkową siłą krępującą styki pionowe.
- Badania elementów belkowych z zablokowaną swobodą odkształceń nadbetonu, w celu odwzorowania pracy w ramach stropu z sztywną tarczą.
- Badania na elementach płytowych składających się z kilku żeber.
- Analizy MES na podstawie podanych i skorelowanych w pracy parametrów materiałowych obejmują studium różnych kształtów żebra na rozkład naprężeń oraz efektywność stref zespolenia.
- Analizy wpływu skurczu oraz pełzania na wielopłaszczyznowe elementy zespolone.